AWARD NUMBER: W81XWH-15-1-0607

TITLE: The Effect of the Elimination of Micromotion and Tissue Strain on Intracortical Device Performance

PRINCIPAL INVESTIGATOR: Joseph J. Pancrazio

CONTRACTING ORGANIZATION: The University of Texas at Dallas

REPORT DATE: Dec 2019

TYPE OF REPORT: Final

PREPARED FOR: U.S. Army Medical Research and Materiel Command
Fort Detrick, Maryland 21702-5012

REPORT DOCUMENTATION PAGE

Form Approved
OMB No. 0704-0188

1. REPORT DATE	2. REPORT TYPE	3. DATES COVERED
Dec 2019	Final	30 Sep 2015 – 29 Sep 2019

4. TITLE AND SUBTITLE

The Effect of the Elimination of Micromotion and Tissue Strain on Intracortical Device Performance

5a. CONTRACT NUMBER

5b. GRANT NUMBER
W81XWH-15-1-0607

5c. PROGRAM ELEMENT NUMBER

6. AUTHOR(S)
Joseph J. Pancrazio

E-Mail: joseph.pancrazio@utdallas.edu

5d. PROJECT NUMBER

5e. TASK NUMBER

5f. WORK UNIT NUMBER

7. PERFORMING ORGANIZATION NAME(S) AND ADDRESS(ES)

The University of Texas at Dallas
800 W. Campbell Road
Richardson, Texas 75080

8. PERFORMING ORGANIZATION REPORT NUMBER

9. SPONSORING / MONITORING AGENCY NAME(S) AND ADDRESS(ES)

U.S. Army Medical Research and Materiel Command
Fort Detrick, Maryland 21702-5012

10. SPONSOR/MONITOR'S ACRONYM(S)

11. SPONSOR/MONITOR'S REPORT NUMBER(S)

12. DISTRIBUTION / AVAILABILITY STATEMENT

Approved for Public Release; Distribution Unlimited

13. SUPPLEMENTARY NOTES

14. ABSTRACT

Intracortical probes can be used to record brain signals to control paralyzed or robotic prosthetic limbs. Unfortunately, this technology is not reliable, likely for the reason that these devices are made of extremely stiff materials – 1 million times stiffer than the surrounding brain tissue. This difference in stiffness is believed to create inflammation which degrades the brain tissue and leads to device failure. While it has been previously proposed that flexible intracortical probes would exhibit an improved tissue response and enhanced device performance, there have been no definitive studies that definitively test this hypothesis. We are developing intracortical probes using shape memory polymers (SMPs): materials which have the capacity to transition from stiff to soft upon implantation. We will tune the degree of stiffness such that we can definitively address a fundamental question which limits progress in the field: Does probe softening improve the surrounding tissue response and recording performance of the device? The short term impact will be on the scientific community through publications and presentations. Over the long term, the core technology has exceptional promise for translation into the clinic. SMP-based probes are compatible with reliable manufacturing practices.

15. SUBJECT TERMS
Intracortical probe, neuroprosthesis, polymers, neural recording

16. SECURITY CLASSIFICATION OF:			17. LIMITATION OF ABSTRACT	18. NUMBER OF PAGES	19a. NAME OF RESPONSIBLE PERSON
a. REPORT	b. ABSTRACT	c. THIS PAGE			USAMRMC
Unclassified	Unclassified	Unclassified	Unclassified	30	19b. TELEPHONE NUMBER *(include area code)*

Table of Contents

INTRODUCTION

The goal of this research has focused on understanding how a key material property, stiffness, influences the robustness of implantable neuroprosthetic technologies. By bypassing damaged regions of the nervous system, brain machine interfaces (BMIs) offer the promise of reducing the burden of injury, a burden disproportionately borne by veterans, and enabling these injured individuals to live more full and interactive lives. Unfortunately, these devices, which take the form of implantable microelectrode arrays or intracortical probes, do not demonstrate long-term robustness. A major aspect of this issue has been hypothesized to be due to the differential stiffness between the implantable device and surrounding brain tissue. We are leveraging state-of-the-art shape memory polymer (SMP) material science where the degree of material softening can be precisely controlled in order to systematically address the importance of implantable device softening in the brain for robust intracortical probe performance. In addition, the fabrication approaches used to create these test structures takes advantage of industrial level manufacturing processes such that promising technology arising from this proposal has the capacity for translation by leveraging standard semiconductor processing techniques.

KEYWORDS

cyclic voltammetry, cytotoxicity, dynamic mechanical analysis, electrochemical impedance spectroscopy, immunohistochemistry, micromotion, modulus, shape memory polymer, sterilization, insulation

ACOMPLISHMENTS

The table below lists the specific aims as proposed and the status of the subtasks as identified in the SOW. This report covers the performance relative to Lead Investigators Dr. Pancrazio and Dr. Voit of the University of Texas at Dallas (Site 1) (for review of progress from Site 2, please refer to the companion report from Dr. Capadona from Cleveland VA which is Site 2 below).

Specific Aim (as specified in proposal)	Timeline	Site 1	Site 2	Status
Specific Aim 1: Quantitatively compare the tissue response evoked by short term and chronic implantation of non-softening, moderately softening, and softening shape memory polymer (SMP)-based intracortical probes.	**Months**	**Lead Investigator(s)**	**Lead Investigator**	**% complete**
Subtask 1: Fabricate non-functional SMP probes and verify physical and thermo-mechanical properties	1-6	Dr. Voit		100%
Subtask 2: Implant all variants of non-functional SMP probes into motor cortex of rats	6-18		Dr. Capadona	100%
Subtask 3: Harvest tissue from non-functional SMP probes implanted rat motor cortex	12-24		Dr. Capadona	100%
Subtask 4: Comprehensive immunohistochemical analysis of tissue response for acute and chronic SMP-based intracortical probes	18-30		Dr. Capadona	100%
Subtask 5: Dissemination of data through publication and presentation	24-36	Drs. Pancrazio & Voit	Dr. Capadona	100%

Milestone Achieved: Identification of distinctive tissue profiles due to differential modulus of non-functional SMP probes		Drs. Pancrazio & Voit	Dr. Capadona	100%
Milestone Achieved: Local IRB/IACUC approval	3		Dr. Capadona	100%
Milestone Achieved: HRPO/ACURO approval	6		Dr. Capadona	100%
Specific Aim 2: Quantitatively compare the long term recording capability of softening and non-softening SMP-based intracortical probes				
Subtask 1: Fabricate functional SMP probes and verify physical and thermo-mechanical properties	1-9	Drs. Voit & Pancrazio		100%
Subtask 2: Implant all variants of functional SMP probes into motor cortex of rats	6-30	Dr. Pancrazio		100%
Subtask 3: Perform bi-weekly recordings of single unit activity and electrochemical impedance spectroscopy using functional SMP probes	6-33	Dr. Pancrazio		100%
Subtask 4: Equivalent circuit modeling from EIS	27-36	Dr. Pancrazio		100%
Subtask 5: Comprehensive immunohistochemical analysis of tissue response for chronic SMP-based intracortical probes at identical time to non-functional, and at failure.	24-36	Dr. Pancrazio	Dr. Capadona	100%
Subtask 6: Dissemination of data through publication and presentation	24-36	Drs. Pancrazio & Voit	Dr. Capadona	100%
Milestone Achieved: Determination of differential device performance as a function of the modulus of SMP probes	30	Drs. Pancrazio & Voit	Dr. Capadona	100%
Milestone Achieved: Local IRB/IACUC approval	3	Dr. Pancrazio		100%
Milestone Achieved: HRPO/ACURO approval	6	Dr. Pancrazio		100%

Milestones: With the no-cost extension, we have completed all tasks and milestones associated with this project. We have performed comprehensive immunohistochemical analyses of non-functional probes as well as functional probes, demonstrated the ability to reliably fabricate multi-laminar devices comprised of shape memory polymer, insulating layers of Parylene-C, and gold electrical contacts. We moved beyond proof-of-concept to demonstrate the successful implantation and recording from a softening microelectrode array that does not require an insertion aid.

Specific Aim 1, Sub task 1: **Figure 1** illustrates the overall concept associated with the creation of fully encapsulated SMP intracortical devices consisting of materials of differential stiffness as demonstrated by dynamic mechanical analysis (DMA). We performed accelerated aging tests on all SMP formulations including the fully-softening formulation (SMP 7.1). Polymer samples were immersed for up to 8 weeks in 77 °C phosphate buffered saline (PBS) and for up to 4 weeks in 37°C in 1 molar sodium hydroxide solution. It was found that the SMP 7.1 starts to degrade after 4 weeks in 77 °C PBS, which can be projected to 13 months of aging at 37 °C. Similar results were observed with other SMP formulations. For our benchmark of 1 year in vivo for rat experiments, our results are satisfactory, although a clinical device will require a new SMP formulation that does not utilize ester chemistry which our data suggest will be far less susceptible to degradation. While beyond the scope of the present project, we have recently identified an entirely new SMP formulation that exhibits extreme softening but does not rely on ester chemistry. This SMP formulation (denoted as SMP-A in the figures below) performs very well in accelerated aging tests and appears to be highly promising.

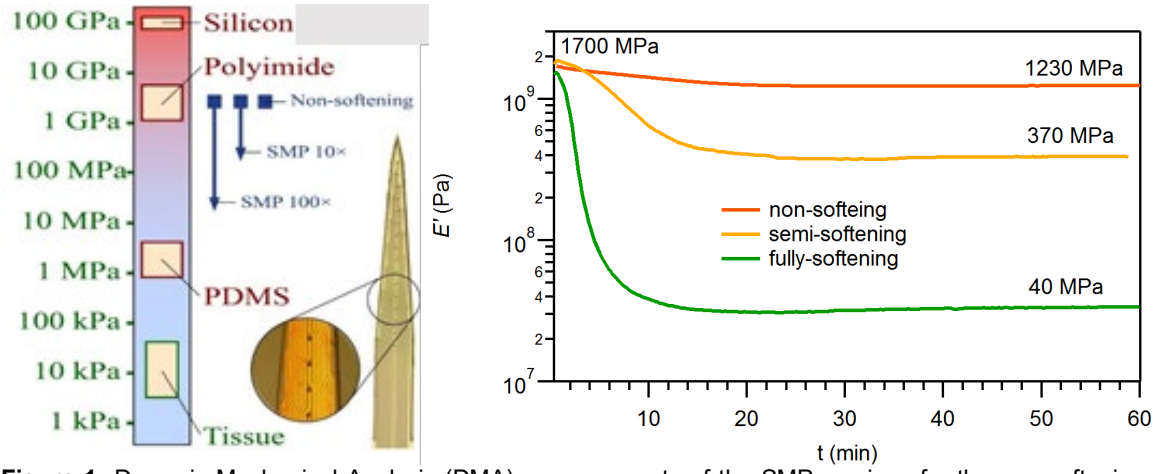

Figure 1: Dynamic Mechanical Analysis (DMA) measurements of the SMP versions for the non-softening, semi-softening and fully-softening SMP formulations for fabrication of neural probes. Measurements show the softening kinetics of SMP specimen of 30 µm thickness while immersed in 37 °C PBS.

Our hypothesis relative to the new formulation is based on the idea that the degradation can be attributed to hydrolysis of ester groups, which are part of the polymeric backbone of SMP 7.1. Thus, we have designed a new, ester-free formulation of SMP (SMP-A in **Figures 2 and 3**) which can soften to an even greater extent than SMP 7.1 to nearly ~10-20 MPa. It was verified with accelerated aging studies that the new SMP is comparatively more resistant to degradation and assuming a typical Q10 for degradation processes for polymeric materials, we anticipate that the new material will be stable for at least 8 years under in vivo conditions.

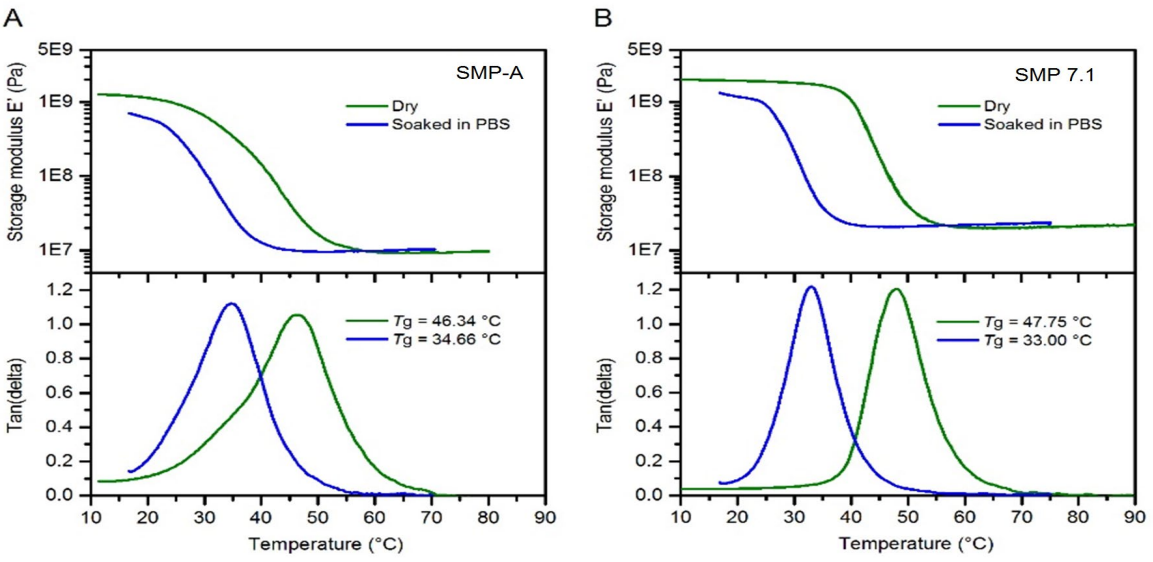

Figure 2: DMA measurements two fully softening SMP formulations. SMP-A which is ester-free (A) and SMP 7.1, which is ester containing (B).

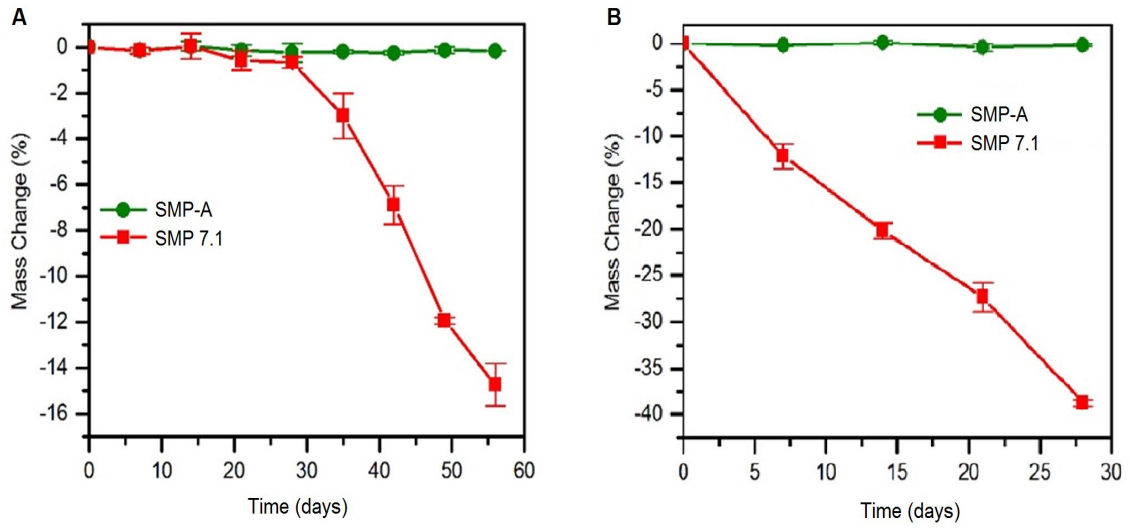

Figure 3: A measure of material stability, mass loss of SMP-A (ester free) and SMP-7.1 (ester containing) polymers, both of which are fully-softening polymer under aqueous conditions. Mass change under accelerated aging conditions at 77 °C in PBS (A), mass change with a 1 M sodium hydroxide solution also at 77 °C (B).

Specific Aim 1, Sub tasks 2-4: After successful fabrication shanks comprised of all formulations of SMP non-functional shanks, the Capadona Laboratory implanted all variants of non-functional SMP probes into motor cortex of rats. Tissue was harvested at the scheduled endpoints and comprehensive immunohistochemistry was performed. Two findings related to the problem of implantation of novel flexible cortical probes emerged: 1) To address difficulties in buckling associated with some of the SMP shanks that were too thin and long to tolerate insertion, the Capadona team developed a novel bio-inspired implantation method based on the mosquito proboscis (**Figure 4**). With the biomimetic guide in place, the rate of successful microprobe insertion increased from 37.5% to 100% due to the rise in the critical buckling force of the microprobes by 3.8-fold. The results were important for the field, and have been published in *Scientific Reports*. 2) We discovered the potential for thermal damage during the craniotomy to implant the microelectrodes. In our efforts to standardize implantation protocols, to ensure the most rigorous evaluation of our developed implants, we characterized the effects of craniotomy on the damage to the blood-brain barrier. These results were published in *Journal of Neural Engineering*.

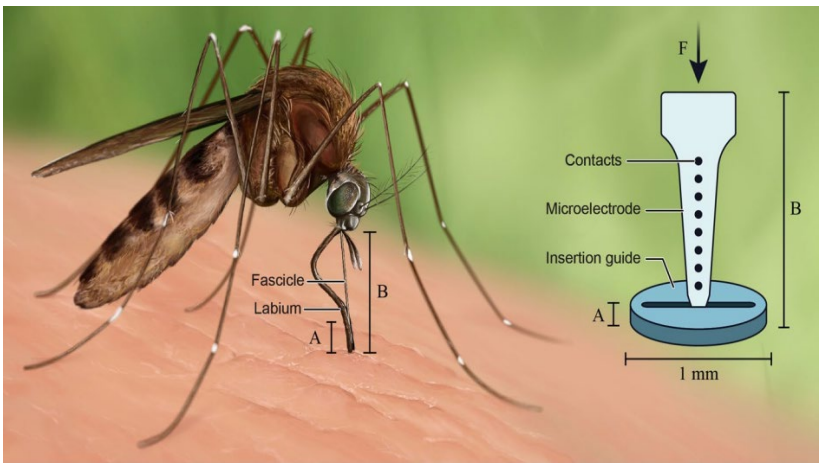

Figure 4: Mosquito-inspired guide to reduce buckling of flexible microelectrodes during insertion into brain tissue. Mosquitos use their labium (labeled above) to brace the fascicle during insertion through the tough skin. Mechanically, this changes the end-condition of the fascicle from a free- to a fixed-end condition and reduces the effective length. Similarly, our manufactured guide may be placed on the skull above the site of device implantation. A narrow slit, slightly wider than the microelectrode provides lateral support. The additional bracing prevents buckling.

With respect to the implantation results, two papers document our findings. The first, "Characterization of the Neuroinflammatory Response to Thiol-ene/Acrylate Shape Memory Polymer Coated Intracortical Microelectrodes" assessed the functionality of the materials we are testing within the added factor of mechanical changes. Surface properties contribute significantly to biocompatibility. Thus, we examined the SMP materials for intracortical neural electrodes by comparing standard state of the art devices with and without the SMP materials coated on the device. **Figure 5** shows the experimental comparisons between silicon and SMP-coated silicon shanks. Astrocytes, a glial cell, play a number of important roles in the brain, including contributing to the blood-brain barrier by reacting to injury and foreign implanted materials in the brain by changing morphology, migrating toward the implant, and expressing or upregulating the expression of a host of proteins, including glial fibrillary acidic protein (GFAP). While there were no significant differences between silicon and SMP dip-coated devices at 2 weeks (**Figure 6**), there was a small, yet significant reduction in astrocytic response for dip-coated implants at 16 weeks compared to the bare silicon control. Specifically, the statistically significant differences were in the concentric ranges 50–100 μm and 100–150 μm from the hole remaining after device extraction (**Figure 7**). With respect to other markers for neurons (NeuN), blood-brain barrier permeability (IgG), and activated microglia (CD68), no other statistical differences between the tissue responses from silicon and SMP-coated probes were determined.

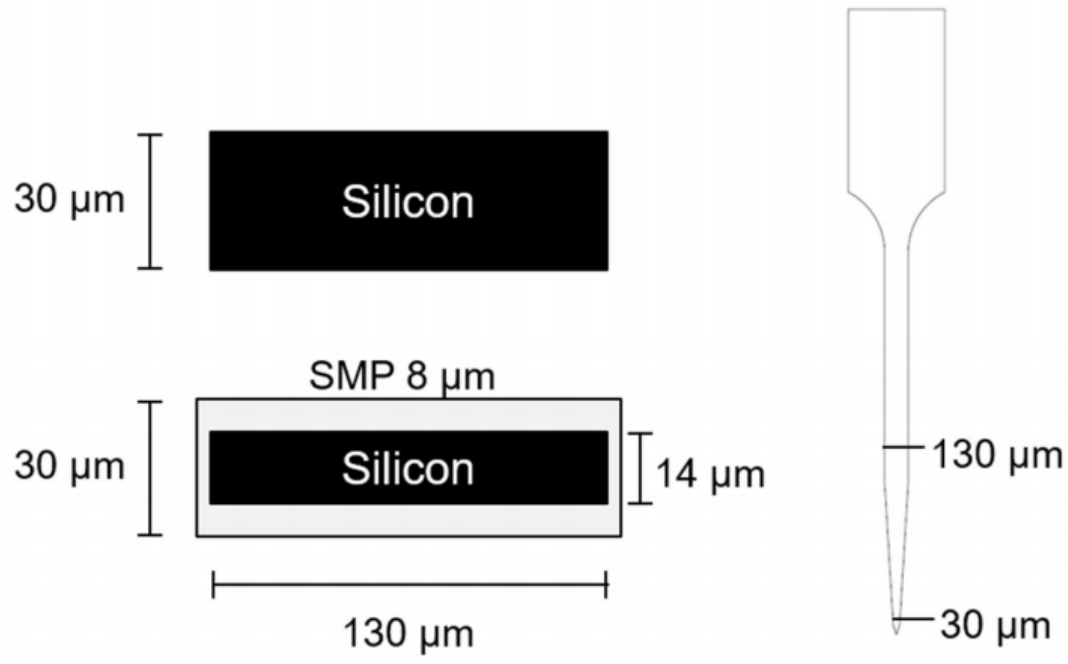

Figure 5: Probe design schematic. Cross-sectional dimensions of the silicon (top) and dip-coated (bottom) devices and view of the profile from the side (right). Here, 30 μm thick silicon wafers were used to fabricate the bare silicon probes whereas a 14 μm thick silicon wafer (after etching) was used to produce the dip-coating substrate so that the overall device thickness resulted as ~30 μm for both device types.

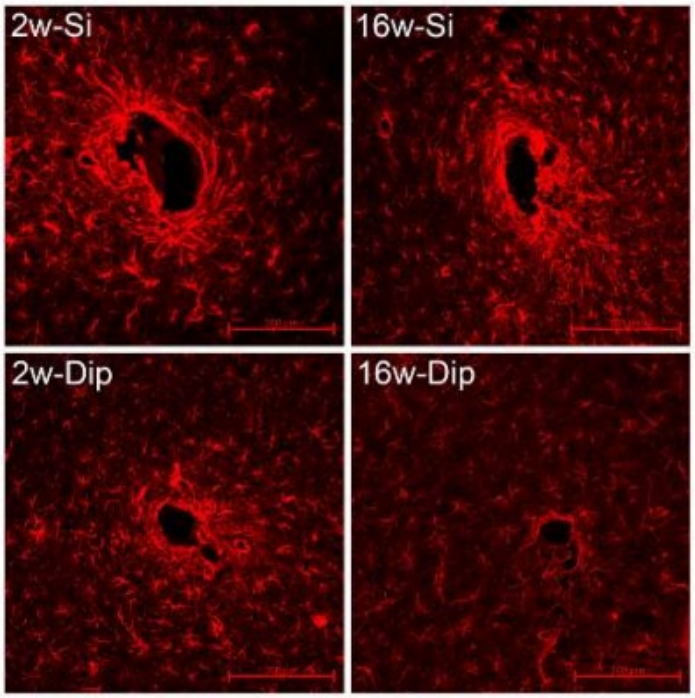

Figure 6: Representative images of horizontal (transverse) slices showing implantation site of silicon (Si) and SMP-coated silicon shanks. Activated astrocytes shown in red intensity by immunohistochemical labeling for GFAP. Scale bar is 200 μm. To account for the known variation of the histological response along the depth of the implant, slices were collected and compared at an array of locations spanning randomized depths of 500–1500 microns. Stained slides were imaged using a 10× objective on an AxioObserver Z1 and AxioCam MRm (Zeiss Inc.). The void in the tissue left by the explanted microelectrode was manually defined by tracing each image on-screen. The area defined by this tracing was collected and used to tabulate the explanted hole size. Fluorescent intensity was then tabulated in expanding concentric contours around the microelectrode-tissue interface edge.

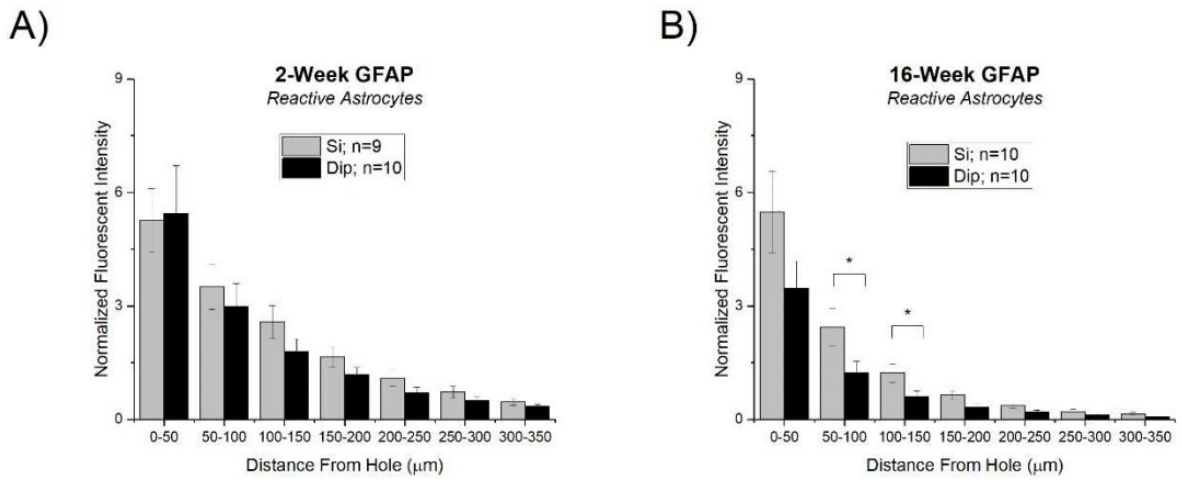

Figure 7: Astrocytic response to silicon vs. SMP dip-coated implants. (A) Astrocytic scarring at 2 weeks and (B) 16 weeks. There were significant differences between the silicon and dip-coated glial fibrillary acidic protein (GFAP) response at 16 weeks, specifically at bucketed distances 50–100 μm and 100–150 μm from the hole. There were no differences between the groups at 2 weeks or any other regions from the hole at 16 weeks post-implantation.

We also examined whether the dual targeting of the innate immune response by inhibiting innate immunity pathways associated with CD14, and the mechanical mismatch could improve the neuroinflammatory response to intracortical microelectrodes. A thiol-ene probe that softens on contact with the physiological environment was used to reduce mechanical mismatch. The thiol-ene probe was both softer and larger in size than the silicon control probe. *Cd14*$^{-/-}$ mice were used to completely inhibit contribution of CD14 to the neuroinflammatory response. Contrary to the initial hypothesis, dual targeting worsened the neuroinflammatory response to intracortical probes. Therefore, probe material and CD14 deficiency were independently assessed for their effect on inflammation and neuronal

density by implanting each microelectrode type in both wildtype control and Cd14-/- mice. IHC results show that 2 weeks after implantation, targeting CD14 results in higher neuronal density and decreased glial scar around the probe, whereas the thiol-ene probe results in more microglia/macrophage activation and greater blood-brain barrier disruption around the probe. Chronic IHC demonstrate no differences in the inflammatory response at 16 weeks. Over acute time points, results also suggest immunomodulatory approaches such as targeting CD14 can be utilized to decrease inflammation to intracortical microelectrodes. The results obtained in the current study highlight the importance of not only probe material, but probe size, in regards to neuroinflammation.

The final study conducted by the Capadona Lab, which concluded during the No Cost extension period, was to perform a highly controlled study on multiple microelectrodes fabricated of matched material properties, but with different stiffness. Within the bounds tested here ranging across three orders of magnitude of Young's modulus ("stiff", moderately softening or "medium", and "soft"), taken together, there were no significant differences in the neuroinflammatory response. Thiol-ene shape memory polymers are being used as a microelectrode substrate. Their mechanical stiffness can be modulated by changing the ratio of monomer concentrations and their cross-linking density. When heated above their glass transition temperature, T_g, they dramatically soften. Taking advantage of this property allows us to implant the devices while stiff, allowing them to soften only later in response to warming up to body temperature. We measured several neuroinflammatory markers. For example, we investigated the neuron density adjacent the implants (**Figure 8**), the accumulation of activated (CD68+) microglia and macrophages (**Figure 9**), the permeability of the local blood-brain barrier (**Figure 10**), and the progression of a GFAP+ glial scar (**Figure 11**) after devices were implanted in the rat cortex for 2- or 16-weeks.

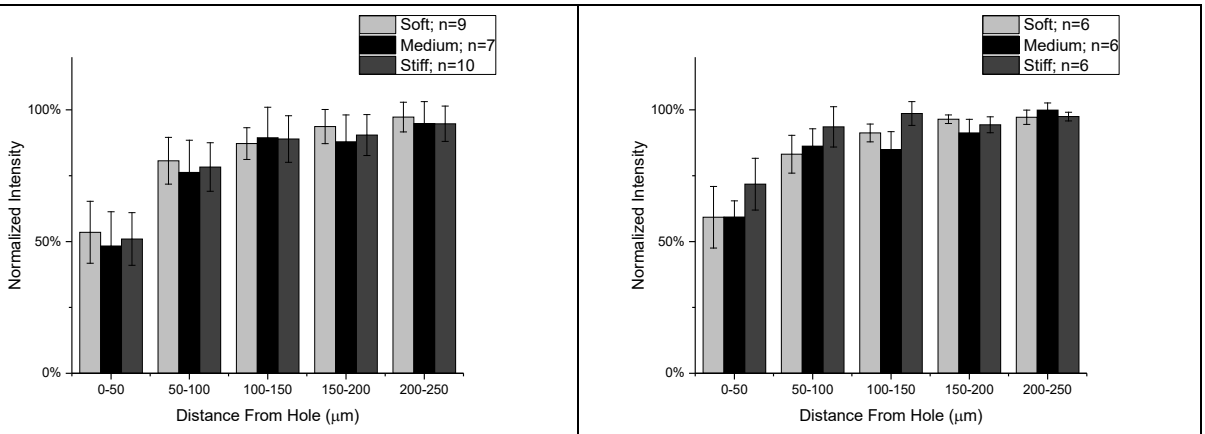

Figure 8: Neuronal density (NeuN staining) at (left) 2 weeks and (right) 16 weeks after microelectrode implantation. There were no significant differences between the three material stiffness implants, at the two time points tested.

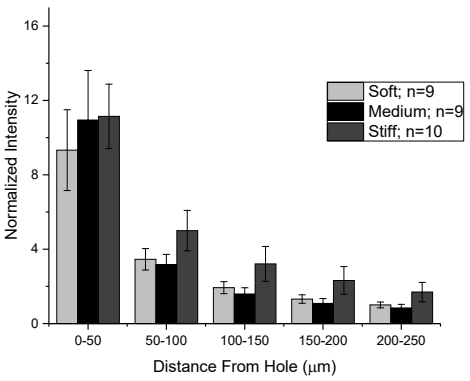

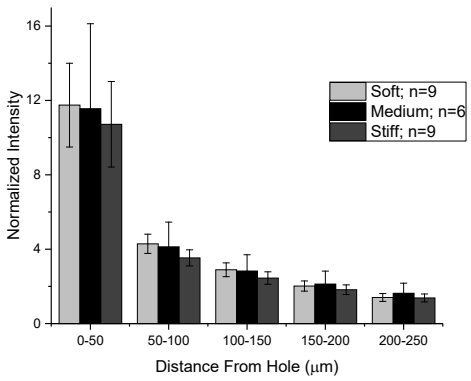

Figure 9: Microglia response to variable stiffness SMP implants. Activated macrophages and microglia (CD68) at (left) 2 weeks, and (right) 16 weeks. There were no differences between each probe type for either time point tested.

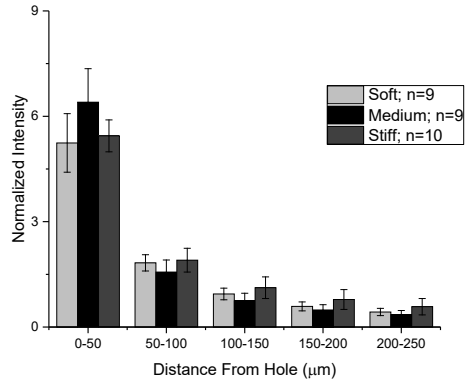

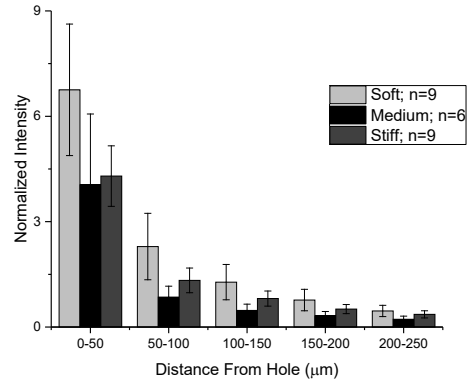

Figure 10: BBB response variable stiffness SMP implants. Blood-brain barrier (BBB) permeability marked by IgG staining at (left) 2 weeks and (right) 16 weeks after microelectrode implantation. There were no differences between each probe type for either time point tested.

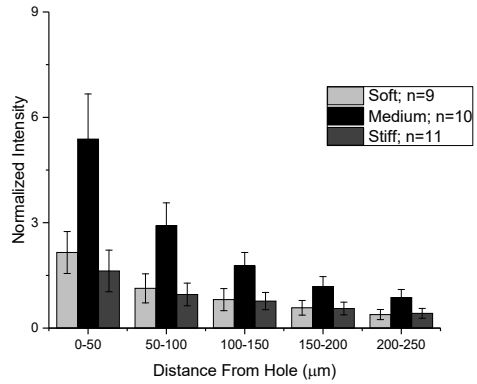

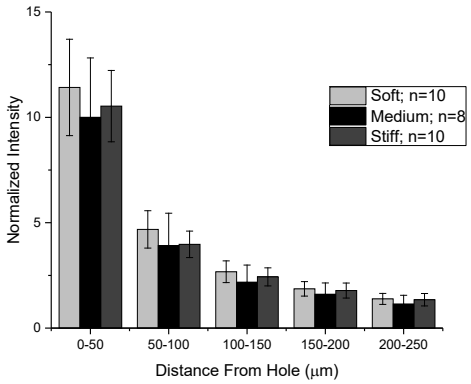

Figure 11: Astrocytic response to variable stiffness SMP implants. (left) Astrocytic scarring at 2 weeks, and (right) 16 weeks. There were no significant differences between the different stiffness probes with regards to GFAP response to the implants at either time point. The response to the medium stiffness probe at 2 weeks appeared to be higher compared to the other probe groups, although not significantly so. We do not have a specific explanation as to why the medium stiffness group performed differently than the soft and stiff probes. It is likely to be an aberration, given the generalized trends observed across the other stains.

In our study, we observed no differences in the markers tested at either of the time points. The thiol-ene devices appeared to be well-tolerated, but within the stiffness range tested,

there were no significant differences. The findings have implications for the field engaged in designing and evaluating flexible substrates for use as intracortical microelectrodes. In addition to softness/flexibility, we need to pay attention to size, geometry, surface chemistry, swelling behavior, and sterilization efficacy. These factors together likely determine the level of neuroinflammation elicited after implantation in the cortex.

Specific Aim 1, Subtask 5 Progress: As evidenced by the extensive list of peer-reviewed publications and presentations that comprise our product list, the Capadona laboratory, often in collaboration with the Pancrazio and Voit groups, has been extremely productive. This productivity positions the team well for pursuit of transitional research support and the continued development and demonstration of novel flexible intracortical probes.

Specific Aim 2, Subtask 1 Progress: Over the course of this project, we tackled a series of problems that ultimately were key for creating a functional device and we have disseminated our findings. Specifically, we have characterized the material dielectric properties, surface roughness, electrical continuity (through our innovative ZIF connector solution), internal layer adhesion optimization, optimization of UV curing, and particulate contamination. As a result, we have been able to create functional devices using industry standard photolithography that are robust and reliable. Our initial designs used an imbalanced layering strategy where one side of the probe consisted of a thicker layer of SMP than the other which supported the gold traces. The reason for this was that we wanted to only etch through a minimum layer of SMP to expose microelectrode sites since we were concerned that the etching process would not be uniform through depth of the material. The result with the imbalanced architecture was that devices would develop asymmetric intrinsic stress profiles and there was a greater propensity for device tips to bend after sterilization. Our last set of devices make use of a balanced layer architecture where the etching process has been refined and the tip bending is no longer a major issue.

Specific Aim 2, Subtasks 2 and 3 Progress:

Device Fabrication: For our functional recordings, we focused on two formulations of SMP as well as measurements from standard Neuronexus intracortical probes with similar dimensions and features. Utilizing both softening (SMP 7.1) and moderately softening (SMP 6) materials, we successfully fabricated devices and performed implantations into rat motor cortex for at least 13 weeks. All of our devices were fully encapsulated with SMP with a thin layer of Parylene-C around the gold traces for proper electrical insulation. Shanks were 5 mm long, 290 μm wide at the base, and 35 ± 5 μm thick with an asymmetric geometry that tapered toward the tip as seen in **Figure 12**. Electrode sites were 180 μm^2 and coated with sputtered iridium oxide film (SIROF).

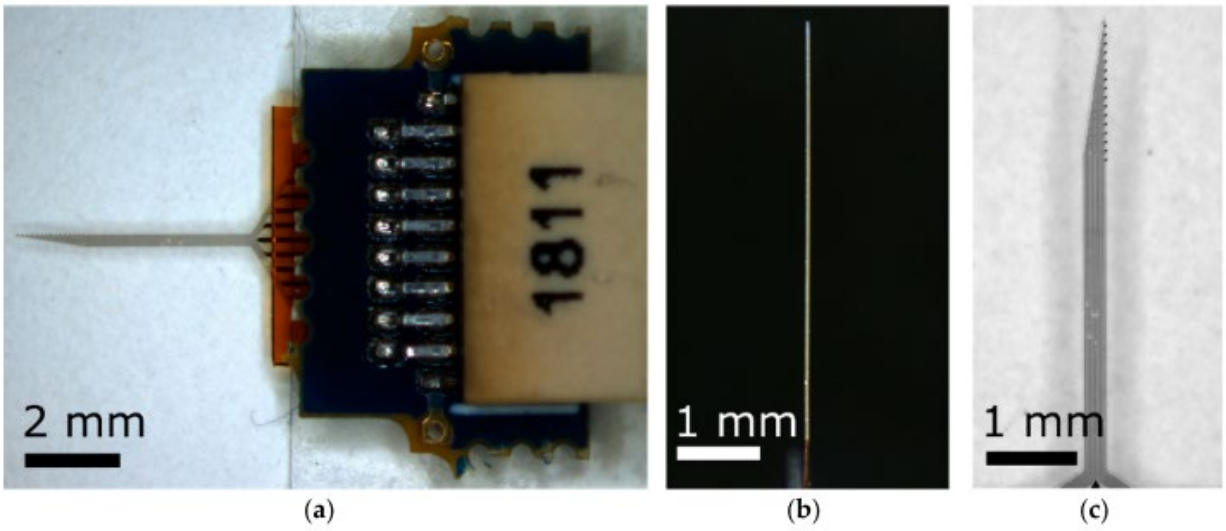

Figure 12: (a) full device with Omnetics connector, (b) side view to show straight shank, (c) intracortical probe shank with 15 electrode sites coated with SIROF.

Weekly recordings of single-unit activity: Electrophysiological recordings were carried out on lightly anesthetized animals (0.5–1.5% isoflurane) immediately following surgical implantation and once per week for 13 weeks afterward. Spontaneous wideband recordings (0.1–7000 Hz) were collected using 15-channel Michigan style SMP arrays (IC-5-16E, Qualia, Inc.) and an Omniplex acquisition system (Plexon, Inc., Dallas, TX, USA) from all 15 recording sites simultaneously at 40,000 Hz for 10 min. Wideband data were processed using a four-pole Butterworth high pass filter with a cutoff frequency of 250 Hz. Individual waveforms (spikes) were identified by filtered continuous data crossing a threshold of −4σ, based on the root mean square (RMS) of the filtered continuous signal. Single units were manually identified from collections of spikes using 2D principal component space, but were excluded from further analysis if they did not contain at least 100 individual spikes, or if >3% of spikes violated a 1.5-ms minimum refractory period. The signal to noise ratio (SNR) was calculated by dividing the mean peak-to-peak voltage of each unit (Vpp) by the RMS noise of its associated channel. The RMS noise was calculated as the RMS of the filtered continuous signal after removing all samples exceeding the 4σ threshold.

Recordings from SMP6 (moderately softening devices): Examples of recordings and analyses that were performed are shown in **Figure 13**. Well-resolved single units could be observed from each of the microelectrode sites along the length of the implanted intracortical probe. Findings are summarized in plots in **Figure 14** which suggests stability of the moderately softening devices during the 13-week study in terms of recording capability. Linear regression revealed no statistical changes in peak-to-peak voltage (Vpp), % active electrodes, or signal to noise ratio (SNR) over time, indicating relative stability of the implantable devices. Our findings for this class of device were documented in a special issue of the journal Micromachines in a publication entitled “Chronic intracortical recording and electrochemical stability of thio-lene / acrylate shape memory polymer electrode arrays”.

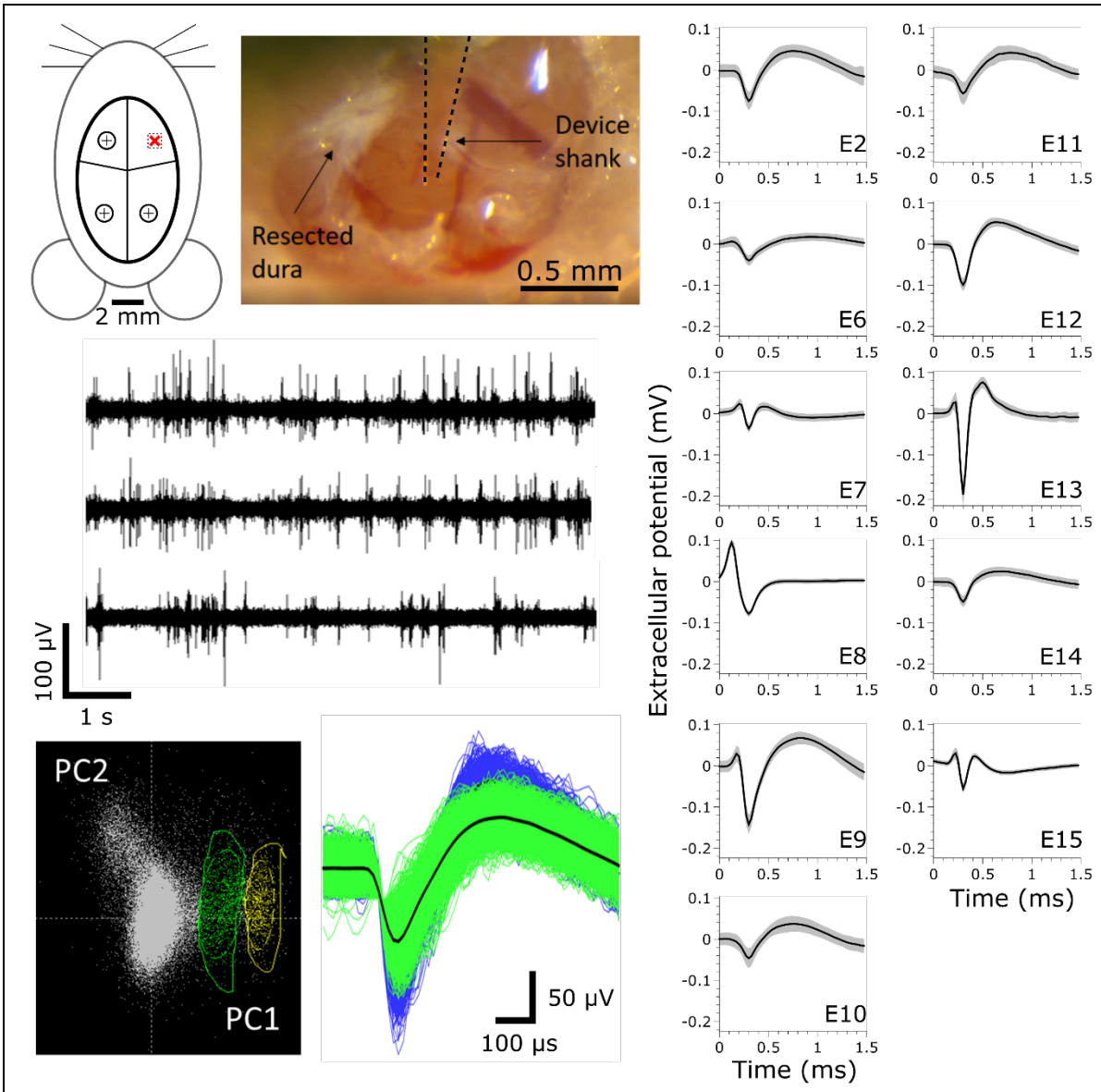

Figure 13: Neural data acquisition and waveform analysis. (a) Implantation schematic denoting the implantation site (red 'x') and stabilizing screws, (b) filtered continuous data from three representative electrodes on a single array, (c) representation of single-unit sorting principals (left) and representative multi-unit activity from a single recording electrode (right), (d) single units recorded on a single array during a single recording session, ordered from array tip (electrode E2) to base (electrode E15).

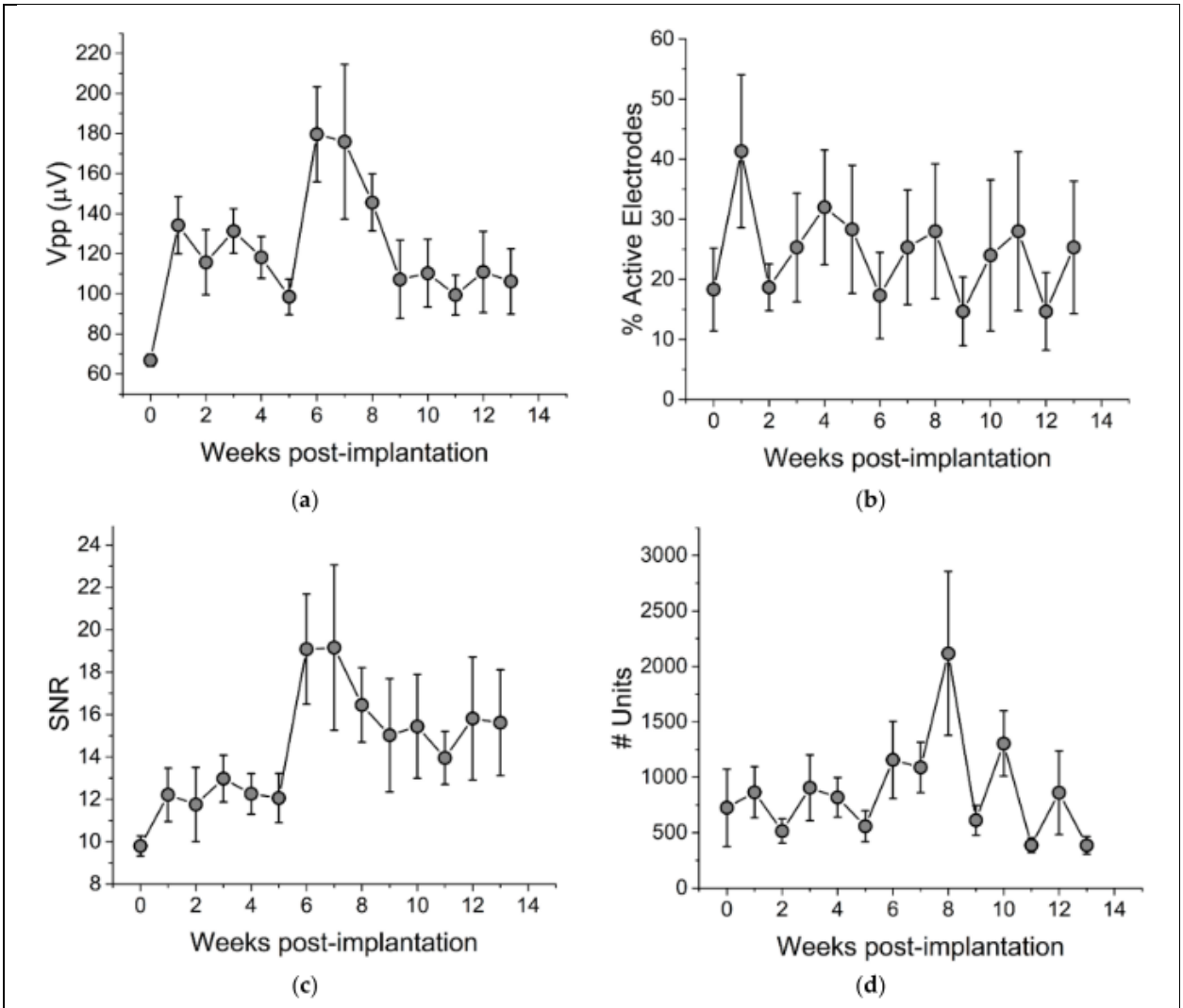

Figure 14: (a) Peak to peak voltage, (b) percent active electrodes, (c) signal to noise ratio, and (d) # units over 13 weeks. Linear regression revealed no statistical changes in peak-to-peak voltage (Vpp), % active electrodes, or signal to noise ratio (SNR) over time.

Recordings from SMP 7.1 (softening devices): SMP 7.1 exhibits an elastic modulus of ~2 GPa in dry, room temperature conditions but softens to ~20 MPa after implantation in the brain. SMP 7.1 devices were fabricating by spinning a 29 μm layer of SMP on a silicon wafer and curing for 3 min under 254 nm UV light followed by 1 hour under 365 nm UV light and 24 hrs in a vacuum oven. Next, 1 μm of Parylene C was deposited over the SMP, followed by 500 nm of gold. The gold was etched to create the appropriate metallization pattern. Another 1 μm layer of Parylene C was deposited, and then etched to form coaxial encapsulation of the gold. The wafer then received a top SMP layer of 6 μm. Electrode and bond pad sites were then etched to expose the gold. The electrode sites received a layer of SIROF to decrease the impedance of the sites. After etching, the devices were mounted to custom PCBs and attached to Omnetics connectors. We also fabricated size and shape-matched silicon shanks for histological comparisons. The devices were size matched with 3 mm long shanks, 290 μm base width and 36 μm thickness. **Figure 15** shows optical images of a fully packaged SMP 7.1 device and the non-functional silicon structure.

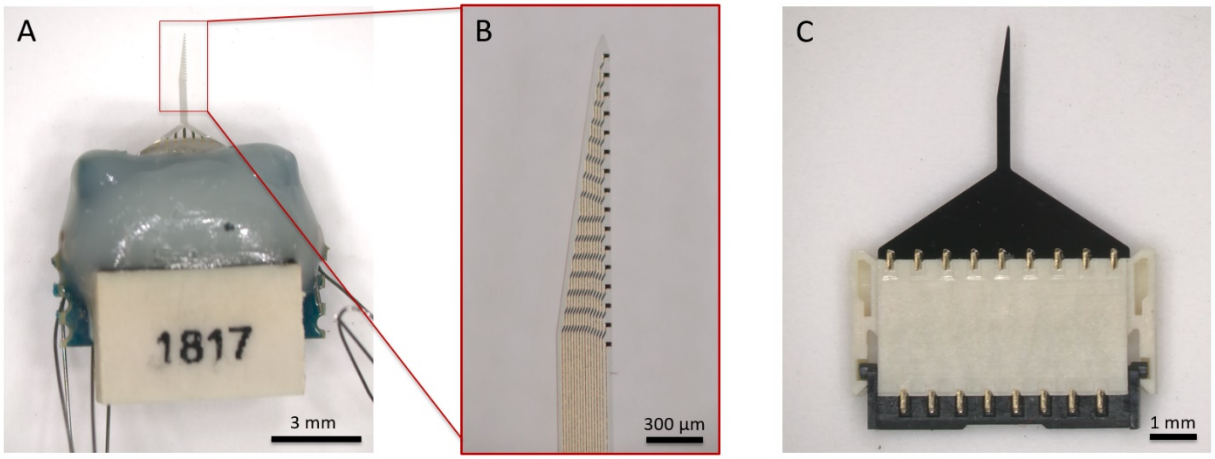

Figure 15: Optical images of probes. (A) A fully packaged SMP 7.1 device. The inset (B) is a close-up of the metallization leading to the microelectrode sites which appear black due to the SIROF coating). (C) A non-functional silicon shank mounted in a ZIF connector.

We implanted n=8 Long Evans rats with functional SMP 7.1 devices and non-function silicon shanks in either motor cortex. SMP devices featured 16 electrode contacts. Animals were anesthetized and mounted in a stereotaxic frame for surgery. An incision was made down the midline of the scalp to reveal the skull. Three stainless steel screws were drilled into the skull to serve as ground and reference points and provide mechanical stability for the skull cap. A craniotomy (approximately 1.5-2 mm^2) were performed over each motor cortex and the dura was resected. Devices were implanted using a hydraulic micropositioner (Kopf Instruments, Tujunga, CA, USA) at a speed of 2 mm/s to a depth of 2 mm. Following implantation of the SMP devices, ground and reference wires were wrapped around the screws. Dehydrated collagen was used to cover the brain tissue surrounding the devices to reseal the dura and then covered in a biocompatible cyanoacrylate. Finally, dental cement was used to create a skull cap that firmly mounted the devices to the skull and covered all exposed wires. Starting immediately after implantation, we took weekly 10 min electrophysiological recordings using an Omniplex system (Plexon, Inc., Dallas, TX) at 40 kHz for 16 weeks. Wideband data were process with a 4 pole Butterworth filter (250 Hz cutoff frequency) and then a -4σ threshold was used to identify potential spikes which were manually identified with 2D principal component analysis. The signal-to-noise ratio was calculated by dividing amplitude of each unit by the RMS of the channel noise.

We tracked single-unit amplitude, signal-to-noise ratio (SNR), RMS noise, and active electrode yield of 16 channel SMP 7.1 devices in rat motor cortex over 16 weeks. Representative single unit activity is shown in **Figure 16**.

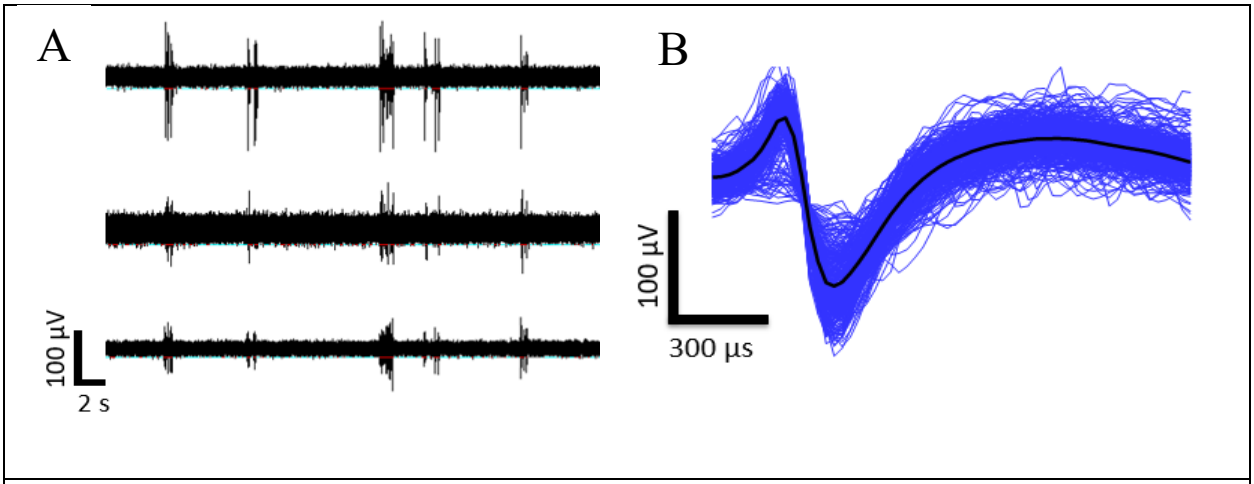

Figure 16: (A) Representative units from three channels on a single device. (B) A single representative unit from one electrode.

Figure 17 summarizes the results from the chronic study from fully softening probes. While amplitude, SNR, and RMS noise remained stable over that time, we saw a decrease in active electrode yield over time from 20% yield at week 0 vs 10% yield at Week 16.

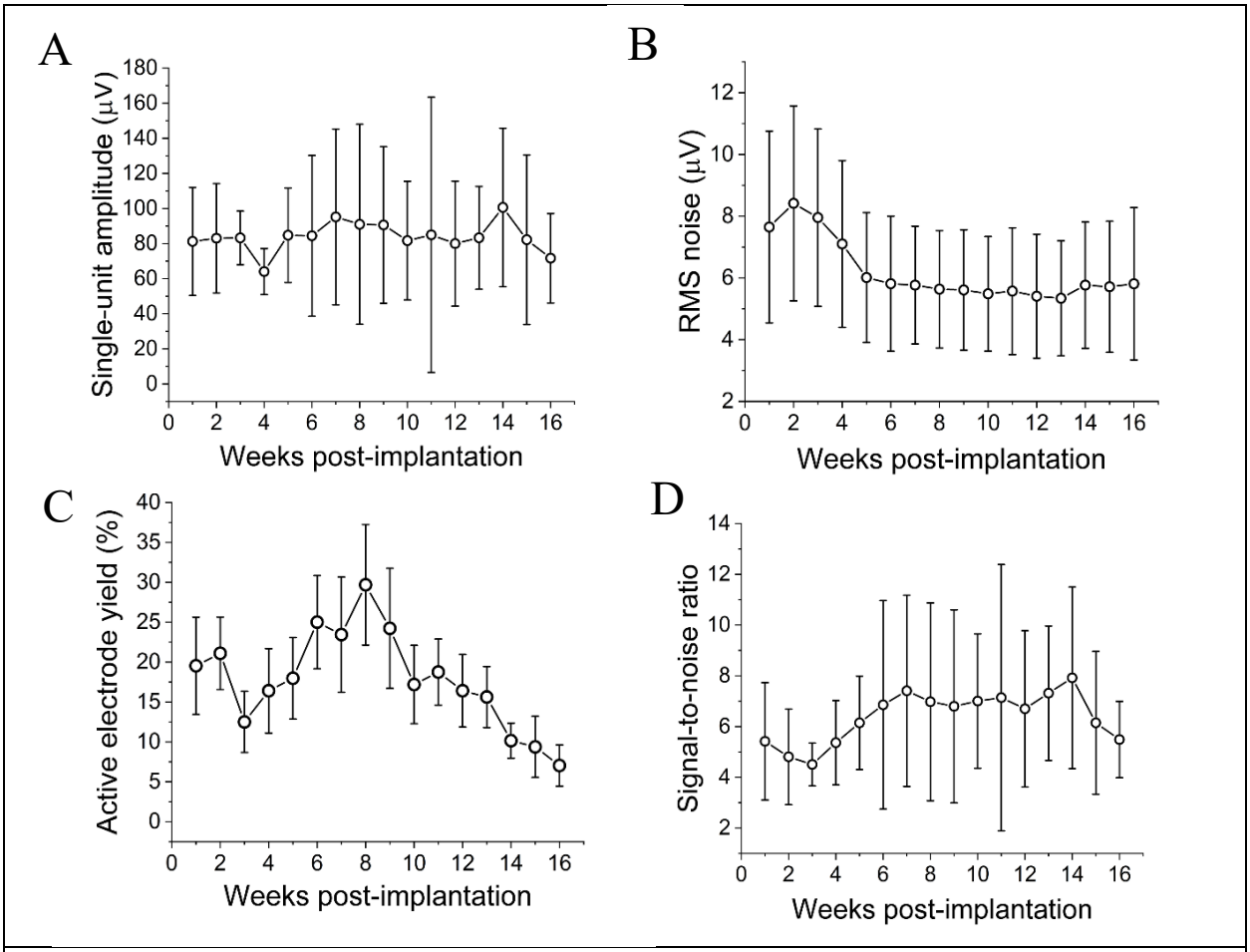

Figure 17: Neural data results. We tracked (A) single-unit amplitude, (B) RMS noise, (C) active electrode yield, and (D) signal-to-noise ratio over 16 weeks. All data are represented as mean ± standard error of the mean.

Recordings from Neuronexus Control Devices: For comparison purposes, we performed comparative intracellular recordings with Neuronexus commercially available devices. Similar to the SMP devices, NeuroNexus probes (A1x16-3mm-100-177, NeuroNexus Technologies Inc.) were implanted into the left motor cortex of female Sprague Dawley rats (n=3). The single shank 16-channel probes were 3 mm in length, with a 123 x 15 µm cross-section at the shank base with a tapered edge, and electrode surface area of 177 μm^2. Neuronal recordings were performed weekly over the course of 8 weeks. As summarized in **Figure 18**, approximately 50% of electrodes were able to record single unit activity (SUA) immediately after implantation. During the subsequent 6 weeks, this percent active electrode yield decreased to between 18-35%, before increasing back to near Week 0 levels. Single unit amplitude and signal-to-noise ratio (SNR) both decreased during the 8-week indwelling period.

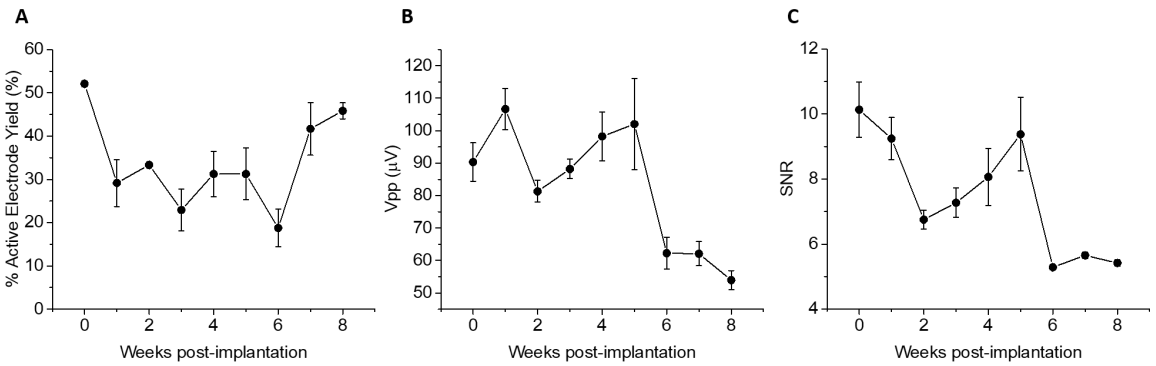

Figure 18: Chronic recording stability of silicon probes. (A) Percent active electrode yield over 8 weeks, defined as the percentage of electrodes that were able to record single unit activity. (B) Peak-to-peak voltage of sorted waveforms. (C) Signal-to-noise ratio of sorted waveforms. Data were averaged across all electrodes (n=48) and rats (n=3). Error bars are standard error of the mean.

Specific Aim 2, Subtask 4: Utilizing in vivo electrochemical impedance spectroscopy, we characterized the impedance across the microelectrode sites for each implanted array. Based on the impedance profile, we utilized a well-established equivalent circuit model for the sputtered iridium oxide microelectrode contacts and followed the derived values across time.

Weekly electrochemical impedance spectroscopy (EIS) and cyclic voltammetry (CV) measurements: EIS and CV measurements were carried out on all electrodes each week immediately following in vivo electrophysiological recordings. The Plexon headstage was removed and replaced with a pre-wired 18 pin dual strip Nano-D female connector (NSD-18-WD-18.0-C-GS, Omnetics Connector Corporation, Minneapolis, MN, USA) attached to multiplexor inputs of a model 604E Series Electrochemical Analyzer/Workstation (CH Instruments Inc., Austin, TX, USA). EIS was performed using a 10 mV RMS sinusoidal signal (Vrms), starting at a frequency of 100 kHz and decreasing to 1 Hz, recording current 12 times per decade of frequency**.** The impedance magnitude at each frequency was calculated by the CH instruments software.

Electrochemical impedance results from SMP6 probes: **Figure 19a** shows representative traces for mean EIS for a single device prior to implantation (in vitro), immediately following implantation, and at 5, 9, and 13 weeks following implantation. To evaluate the stability over a frequency relevant to extracellular spikes, the mean 1 kHz impedance across all devices

is plotted in **Figure 19b** over the 13-week time period. All electrodes exhibited a significant increase in impedance magnitude one week post-implantation (1.23 ± 0.07 MΩ) versus in vitro measurements (0.62 ± 0.09 MΩ), similar to observations made in previously. Impedance magnitudes remained largely consistent at this value across the first 7 weeks of the study, and then decreased slightly during the remaining 6 weeks. This decrease did not show any correlation with the mean active electrode yield however, suggesting that although there may have been degradation of the insulating material, this degradation did not hinder the devices' ability to resolve and record single unit activity.

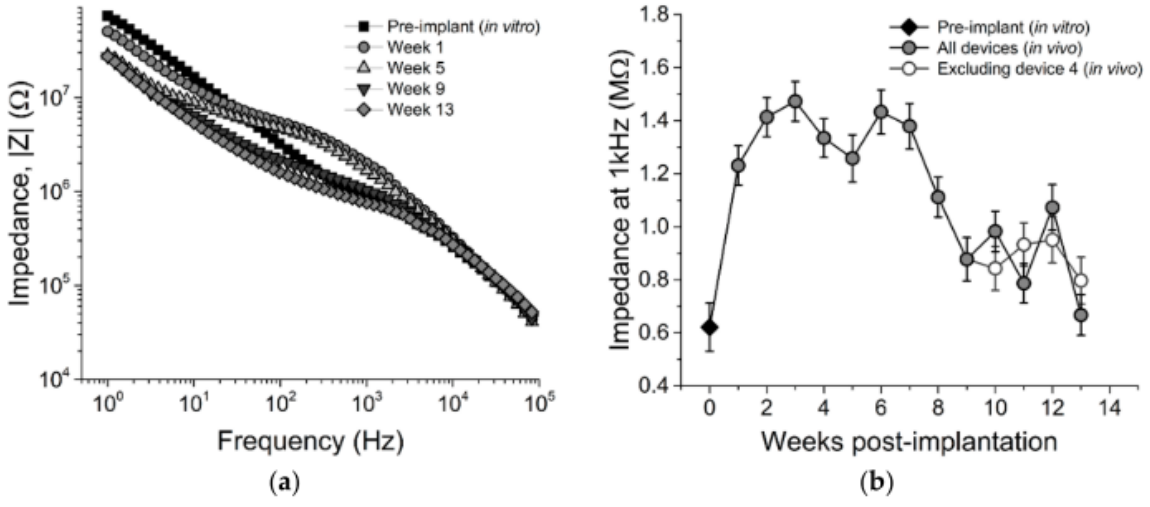

Figure 19: Electrochemical impedance spectroscopy for SMP6 (moderately softening) devices. (a) Impedance values for a single representative electrode over time. (b) Impedance (mean ± SEM) at 1 kHz for all electrodes over 13 weeks. After an initial increase in impedance after implantation at Week 0, likely due to the acute immune response, impedance gradually returned to its original, pre-implantation value.

The in vivo EIS experimental data were additionally analyzed in terms of equivalent electrical circuit modeling using ZSimpWin V3.60 software (Princeton Applied Research, Oak Ridge, TN). Equivalent circuit modeling can be useful in understanding the physiochemical properties of the device, as well as in monitoring the condition of the device in vivo. Several equivalent circuit models based on previously proposed circuits of iridium oxide films[1,2,3] were tested on individual electrode sites on SMP6 based intracortical probes over the course of the study in order to establish a representative model that fit the majority of the data. The quality of the fitted models was estimated using both the chi-square test (χ^2 values between 10^{-3} and 10^{-4}) and by minimizing the relative standard error between the experimental and calculated values for each individual circuit element.

Figure 20 shows the circuit model, along with a representative impedance and phase spectra for one SMP6 probe averaged across weeks 1, 5, 9, and 13 time points.

[1]Doyle RL, Lyons MEG (2013) An electrochemical impedance study of the oxygen evolution reaction at hydrous iron oxide in base. Phys. Chem. Chem. Phys. 15(14) 5224.
[2]Doyle et al. (2013) Redox and electrochemical water splitting catalytic properties of hydrated metal oxide modified electrodes. Phys. Chem. Chem. Phys. 15 (33) 13737.
[3]Weiland JD, Anderson DJ (2000) Chronic neural stimulation with thin-film, iridium oxide electrodes. IEEE Trans. Biomed. Eng. 47(7) 911–918.

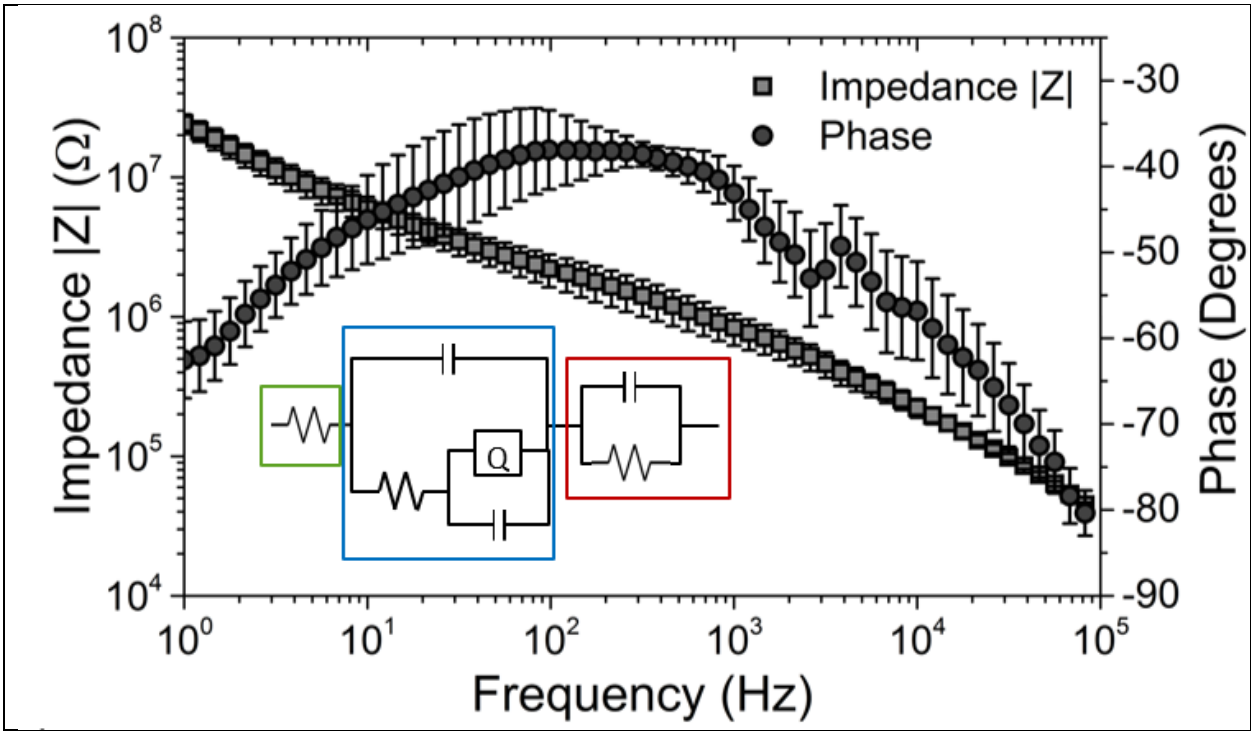

Figure 20: Equivalent circuit model for SIROF microelectrodes on SMP6 probes. The impedance and phase spectra are from a representative electrode and have been averaged across the Week 1, 5, 9, and 13 time points. The circuit model is divided into three sections. Circuit elements in green represent electrolyte resistance. Circuit elements in blue represent the double layer capacitance and charge transfer at the interface. Circuit elements in red represent the inner oxide layer.

Model elements in green represent active electrolyte resistance, while those in blue represent the double layer capacitance and charge transfer at the interface. Q is a generalized Warburg diffusion element referred to as a constant phase element (CPE) that represents the impedance of a capacitive process displaying frequency dispersion, i.e. an imperfect capacitor. Depending on its phase, the impedance of the CPE can reflect that of an ideal capacitor, a pure resistor, or somewhere in between. Circuit elements in red represent the interaction at the inner oxide layer. Overall, the model remained relatively stable over the duration of the in vivo study, which was expected given the stability of the impedance data**.** The stability of this model indicates that there were little to no unexpected interactions at the electrode-electrolyte interface indicating stability of the electrochemical interface.

Electrochemical impedance results from SMP 7.1 probes: Similar results emerged from data collected from the softening (SMP 7.1) probes as observed with the moderately softening devices, which is consistent with the stability of the SIROF microelectrode sites. The overall microelectrode electrode impedance measured at 1 kHz remained stable at ~600 kΩ through the duration of the in vivo recordings.

Electrochemical impedance results from Control Neuronexus probes: Electrochemical impedance spectroscopy (EIS) was performed to for comparison purposes using control single shank 16 microelectrode site laminar probes commercially provided by Neuronexus. As summarized in **Figure 21**, all microelectrode sites exhibited an increase in mean impedance at 1 kHz from *in vitro* (1.24 ± 0.0453 MΩ) to 1 week post-implantation (1.90 ± 0.674 MΩ) which is consistent with prior observations comparing *in vitro* and *in vivo*

impedances[1,2]. We anticipated higher impedances since these microelectrode sites consist of gold rather than SIROF. Impedance values decreased substantially over the 8-week period, falling below *in vitro* magnitudes, indicating possible encapsulation delamination or an increase in the conductive surface area of the probes. Overall, our results are consistent with previous literature investigating the chronic longevity of NeuroNexus probes[3,4], and are similar to the changes we observed with the SMP functional devices *in vivo*.

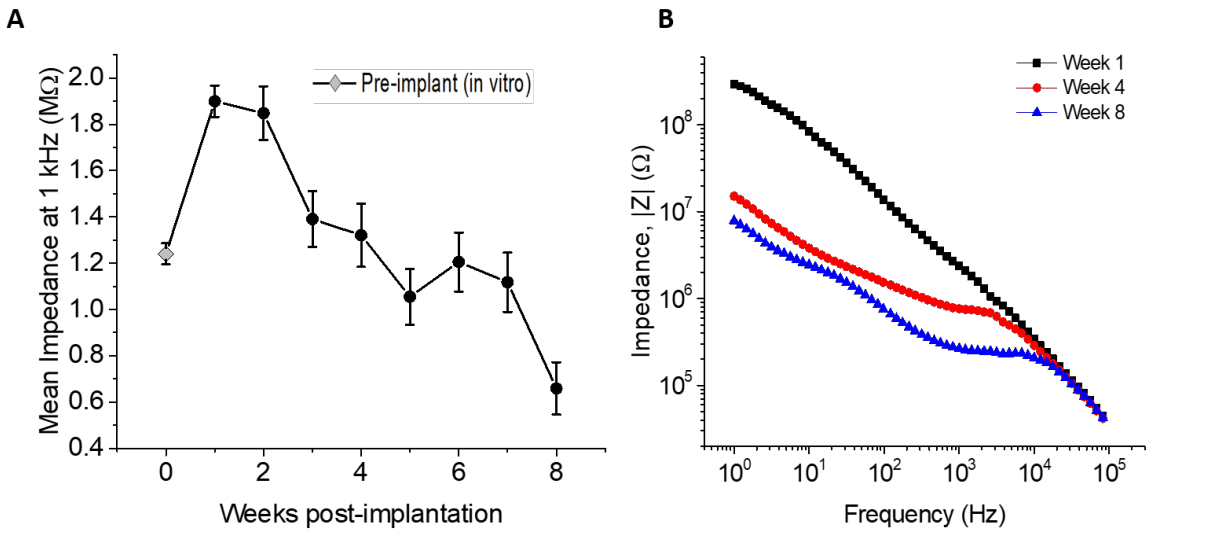

Figure 21: Electrochemical impedance spectroscopy (EIS) of silicon probes. (A) Mean impedance magnitude at 1 kHz measured over 8 weeks. The initial time point represents the impedance measured before implantation in vitro. (B) Representative traces of EIS spectrum at different time points. Traces were chose from the same electrode from the same animal. Mean impedance magnitude was averaged across all electrodes (n=48) and rats (n=3). Error bars are standard error of the mean.

Specific Aim 2, Subtask 5: To evaluate the induced foreign body response related to chronic implantation of functional SMP devices, we performed histology targeting neuronal cell bodies (NeuN), astrocytes (GFAP), and activated microglia/macrophages (CD68). Astrogliosis (GFAP intensity) and neuronal density were quantified as described previously[4]. Briefly, images were imported into Fiji, and open source imaging software package based on ImageJ. Using a custom macro, GFAP intensities and NeuN+ nuclei per area were calculated within at least 8 concentric bands of 50 µm thickness generated from a user-defined implant site. All reported values were normalized to measurements from the band located 350-400 µm from the device edge.

Immunohistochemical characterization of tissue after chronic implantation of moderately softening (SMP6) probes. **Figure 22a** shows representative fluorescence images for each marker with respect to increasing depth along the shank of the device. The most severe and apparent immune response was observed at the base of the shank, represented by "superficial" slices, within the first 50 µm of the device perimeter. However, this effect tapered off along the length of the probe, represented by "middle" and "deep" slices. Additionally, consistent with previous studies reporting histological outcomes, we observed slight astrogliosis in areas with neuronal dieback, again with the most severe response near the

4 Stiller, A.; Black, B.; Kung, C.; Ashok, A.; Cogan, S.; Varner, V.; Pancrazio, J. A Meta-Analysis of Intracortical Device Stiffness and Its Correlation with Histological Outcomes. Micromachines 2018, 9, 443, doi:10.3390/mi9090443.

base of the shank but tapered off toward the tip. This is in contrast to previous reports of significant neuroinflammatory response within 100 μm of the device when using silicon-based arrays. Additionally, there were few or no apparent activated microglia around the device at “middle” and “deep” slices (**Figure 22b**). It is important to note that the microelectrode sites on this device are located near the end of the device shank, and therefore best represented by the “middle” and “deep” slices. These results suggest that the neuroinflammatory response was modest proximal to the microelectrode site locations.

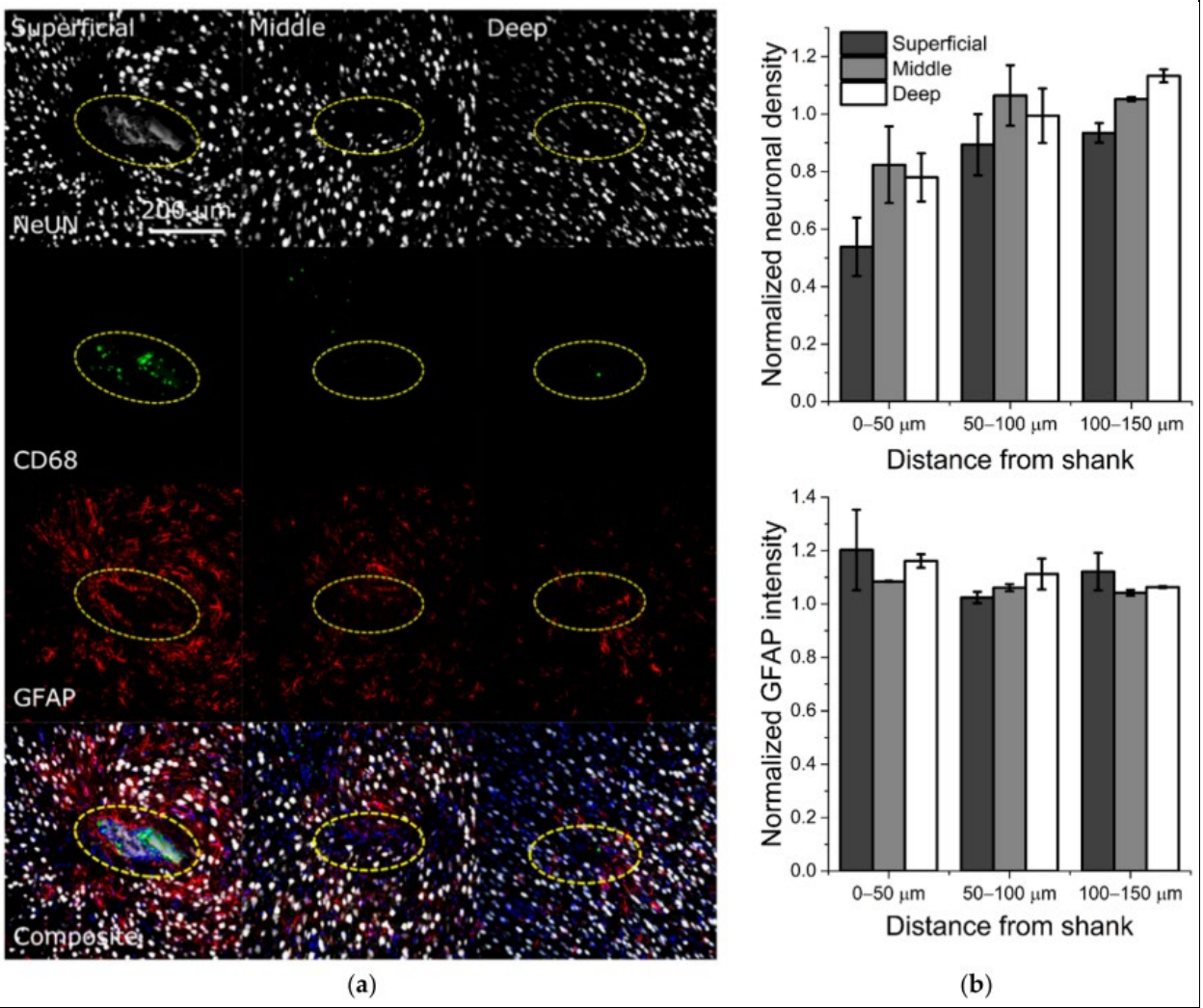

Figure 22: Immunohistochemistry for SMP6 moderately softening implant after 13 weeks in vivo. (a) Columns represent tissue collected at superficial, middle, and deep slices in relation to the surface of the motor cortex. Rows represent neuronal nuclei (NeuN) (gray, top), activated microglia/macrophages (CD68) (green), astrocytes (GFAP) (red), and Composite (bottom) images. Scale bar represents 200 μm in the transverse plane across all images. Yellow ellipses indicate probe location. (b) Quantification of NeuN and GFAP for n = 2 animals at varying slice depths (one slice per region) with respect to the shank location in the brain.

Immunohistochemical characterization of tissue after chronic implantation of fully softening (SMP7.1) probes: After 16 weeks, the animals were sacrificed with sodium pentobarbital and perfused with 4% paraformaldehyde. The probes were removed from the brains which were then sliced in a direction cross-sectional to the trajectory of the probe using a Leica CM 3050 Microtome Cryostat (Leica Biosystems, Buffalo Grove, IL, USA). After obtaining

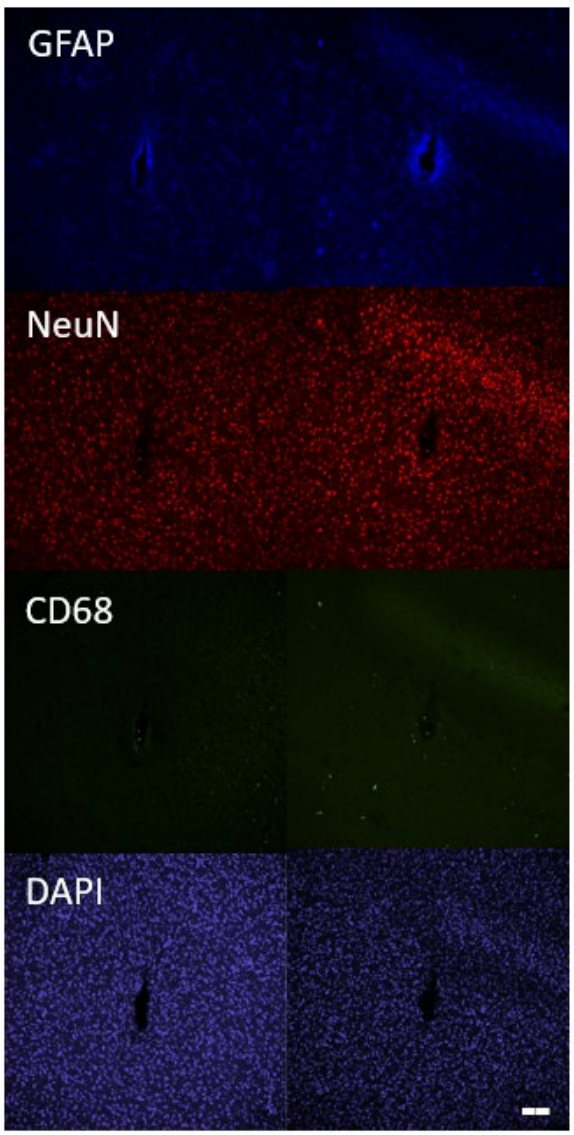

Figure 23: Representative immunohistochemistry at 1 mm slice depth for a SMP 7.1 device (left column) and silicon shank (right column). Scale bar = 100 µm.

50 µm slices, the tissue was placed on slides for staining. Brain slices were incubated with primary antibodies targeting NeuN, a marker for neuronal nuclei, glial fibrillary acidic protein (GFAP), a marker for astrocytes, CD68, a marker for activated macrophage and microglia, and DAPI. After staining, Z-stack images were taken using an inverted confocal microscope (Nikon Ti eclipse + A1R, Tokyo, Japan). Images were analyzed using a custom ImageJ macro that allowed the user to select the perimeter of the hole created by the probe. The macro then generated concentric 50 µm bands around the hole up to 400 µm away. For analysis of GRAP and CD68 stains, the macro calculated average intensity in each band. For analysis of NeuN, the area of each band was measured and the macro automatically counted the number of neurons in each band. From these measurements, cell density in each band was calculated. For all stains, values in the first three bands, 0-50 µm, 50-100 µm and 100-150 µm, were normalized to value in the last band, 350-400 µm. The figure below compares outcomes for GFAP, NeuN, and CD68 at a slice depth approximately 1 mm below the surface of the brain. **Figure 23** shows representative immunohistochemical images from horizontal brain slices. The summarized quantitative results for the softening SMP 7.1 probe versus silicon are shown in **Figure 24**. This analysis did not show a difference in histological results between SMP and silicon devices. However, these data were only from a single slice depth and restricted to three markers. We are considering a more comprehensive survey of various depths and markers (e.g., oxidative stress, blood-brain-barrier injury, etc.) to create a more comprehensive picture of tissue response to the devices. This subsequent analysis will compare SMP and silicon outcomes at multiple, distinct slice depths (e.g., near the surface of the brain, near the middle of the probe shank, and near the tip of the probe shank).

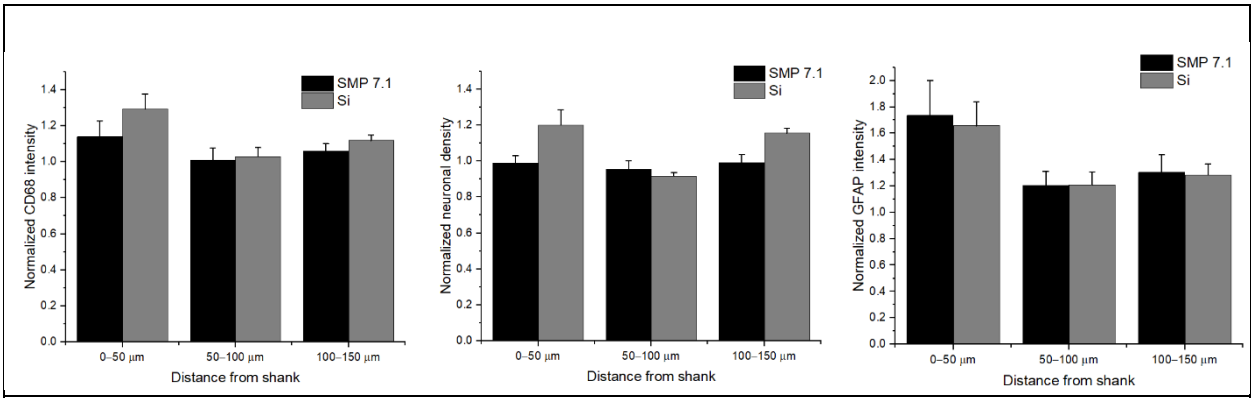

Figure 24: Immunohistochemistry results from 3 rats at a slice depth approximately 1 mm deep. In all panels, the black bars represent results for SMP 7.1 probes and the grey bars represent results for silicon shanks. All data are presented as mean ± standard error of the mean.

Summary of comparative immunohistochemical analyses of tissue after implantation with functional softening probes: One of our main hypotheses focused on the ability for softening probes fabricated from SMP to mitigate tissue response, where more flexible probes would exhibit both reduced tissue response and improved recording performance. The data, at this stage of inquiry, do not support that notion as SMP 6 based devices appeared to perform somewhat better or at least no worse than the SMP 7.1 based probes. It may be that there are additional factors (e.g., changes in constituent chemistry, surface hydrophobicity, etc) that have a more dominant influence on the performance of these devices in vivo.

Specific Aim 2, Subtask 6: Over the period of the project, our collective team spanning UT Dallas and Case Western Reserve University/Cleveland VA generated 17 peer-reviewed publications and 12 conference poster presentations tied to the CDMRP-supported work. Many of which were developed with co-authorship between group members spanning institutions.

IMPACT

Brain electrodes are typically fabricated from conductive and insulating materials such as metals and plastics that are inherently stiff, much stiffer than the surrounding brain tissue. The neuroscience community has known that the ability of these devices to record electrical activity is lost after 6 months to 1 year after implantation. The mismatch between the stiff devices and soft brain tissue is believed to be responsible for inflammatory tissue response that plays a major role as a mechanism of failure. Our work aimed to test the idea that if we can not only make a probe that softens in the brain, but more importantly, the performance of the softening device would improve over devices fabricated from non-softening materials. We are capitalizing on a novel material strategy: shape memory polymers (SMP). Our group, in collaboration with Dr. Capadona's team, are the world leaders in fabricating SMP based neuroelectronics and performing detailed physiological characterizations. To date, we have made significant progress in identifying the problems related to SMP-based devices and have developed and demonstrated solutions for each. Our data with the SMP based devices demonstrate that it is possible to create functional devices with performance and immunohistological profile that is at least no worse than silicon devices. **Our collaboration with Dr. Capadona and his group has been highly successful as evidenced by the large number of inter-group publications**.

There remains a need in the neuroscience community interested in basic science questions for devices capable of long-term chronic recording. It may be that future SMP based devices that soften to a much greater extent could address this need. It is evident from our work that in addition to the elastic modulus of the material comprising an intracortical probe, there must be consideration towards the size (cross-sectional area), geometry, surface chemistry, swelling behavior, and sterilization efficacy. These factors together likely determine the level of neuroinflammation elicited after implantation in the cortex. Beyond the use of SMPs as the penetrating probes themselves, material components of future implantable devices could leverage the SMPs to advance bioelectronics especially in the area of cabling or surface adherent non-penetrating electrode grids, not unlike paddle arrays used in spinal cord stimulation. SMP remains a viable candidate as a potentially useful material for implantable devices, as it is a material that can accommodate thin film processing for manufacturing reproducible devices.

CHANGES/ PROBLEMS

N/A

PRODUCTS

Journal publications:

- Frewin CL, Ecker M, Joshi-Imre A, Kamgue J, Waddell J, Danda VR Stiller AM, Voit WE, Pancrazio JJ (2019) Electrical properties of thiol-ene-based shape memory polymers intended for flexible electronics. Polymers 11 (5) 902.
- Bedell HW, Song S, Li X, Molinich E, Lin S, Stiller AM, Danda V, Ecker M, Voit WE, Pancrazio JJ, Capadona JR (2018) Understanding the effects of both CD14-meditated innate immunity and device/tissue mechanical mismatch in the neuroinflammatory response to intracortical microelectrodes. Frontiers in Neuroscience. DOI: 10.3389/fnins.2018.00772
- Stiller AM, Usoro J, Frewin CL, Danda VR, Ecker M, Joshi-Imre A, Musselman KC, Voit WE, Modi R, Pancrazio JJ, Black BJ (2018A) Chronic intracortical recording and electrochemical stability of thio-lene / acrylate shape memory polymer electrode arrays. Micromachines 9: 500. DOI: 10.3390/mi9100500
- Stiller AM, Black BJ, Kung C, Ashok A, Cogan SF, Varner VD, Pancrazio JJ (2018B) A meta-analysis of intracortical device stiffness and its correlation with histological outcomes. Micromachines 9: 443. DOI: 10.3390/mi9090443
- Shoffstall AJ, Ecker M, Danda V, Joshi-Imre A, Stiller A, Yu M, Paiz JE, Mancuso E, Bedell HE, Voit WE, Pancrazio JJ, Capadona JR (2018) Characterization of the neuroinflammatory response to thiol-ene shape memory polymer coated intracortical microelectrodes. Micromachines 9: 486. DOI: 10.3390/mi9100486
- Shoffstall AJ, Srinivasan S, Willis M, Stiller AM, Ecker M, Voit WE, Pancrazio JJ, Capadona JR (2018) A mosquito inspired strategy to implant microprobes into the brain. Scientific Reports 8: 122. DOI: 10.1038/s41598-017-18522-4
- Ecker M, Danda A, Shoffstall AJ, Mahmood SF, Joshi-Imre A, Frewin CL, Ware TH, Capadona JR, Pancrazio JJ, Voit WE (2017) Sterilization of thiol-ene/acrylate based

shape memory polymers for biomedical applications. Macromolecular Materials and Engineering 302: 1600331. DOI: 10.1002/mame.201600331

- Hosseini SM, Rihani R, Batchelor B, Stiller AM, Pancrazio JJ, Voit WE, Ecker M (2018) Softening shape memory polymer substrates for bioelectronic devices with improved hydrolytic stability. Frontiers in Materials. doi: 10.3389/fmats.2018.00066
- Ecker M, Joshi-Imre A, Modi R, Frewin CL, Garcia-Sandoval A, Maeng J, Gutierrez-Heredia G, Pancrazio JJ, Voit WE (2018) From softening polymers to multimaterial based bioelectronic devices. Multifunctional Materials 2(1) 012001.
- S.C. Lindner, M. Yu, J.R. Capadona, A.J. Shoffstall. (2019) A graphical user interface to assess the neuroinflammatory response to intracortical microelectrodes. J. Neurosci. Methods. doi: 10.1016/j.jneumeth.2019.01.003.
- K.R. Dona, M. Goss-Varley, A.J. Shoffstall, J.R. Capadona. (2018) A Novel Single Animal Motor Function Tracking System Using Simple, Readily Available Software. Journal of Visualized Experiments (JoVE) doi:10.3791/57917.
- M. Goss-Varley, A.J. Shoffstall1, K.R. Dona, J.A. McMahon, S.C. Lindner, E.S. Ereifej, J.R. Capadona. (2018) Rodent Behavioral Testing to Assess Functional Deficits Caused by Microelectrode Implantation in the Rat Motor Cortex. Journal of Visualized Experiments (JoVE) doi:10.3791/57829.
- A.J. Shoffstall, J. Paiz, D. Miller, G. Rial, M. Willis, D. Mendez, S. Hostler, J.R. Capadona. (2018) Potential for Thermal Damage to the Blood-Brain Barrier during Craniotomy Procedure: Implications for Intracortical Recording Microelectrodes. Journal of Neural Engineering. doi.org/10.1088/1741-2552/aa9f32.
- A.J. Shoffstall and J.R. Capadona. (2018) Chapter 28, Prospects for a Robust Cortical Recording Interface, Neuromodulation, 2nd Edition; Elsevier Ltd.
- A.J. Shoffstall, J.R. Capadona. (2018) Bio-Inspired Materials and Systems for Neural Interfacing. Current Opinions in Biomedical Engineering, doi.org/10.1016/j.cobme.2018.05.002.
- J.K. Hermann J.R. Capadona. (2018) Understanding the Role of Innate Immunity in the Response to Intracortical Microelectrodes. Critical Reviews in Biomedical Engineering. 2018, 46(4): 341-367.
- H.W. Bedell, J.R. Capadona. (2018) Anti-inflammatory approaches to mitigate the neuroinflammatory response to brain-dwelling intracortical microelectrodes. J. Immunol. Sci. 2(4): 15-21.

Conference presentations:

- 2018/10/19: A. M. Stiller, J. Usoro, C. L. Frewin, V. R. Danda, M. Ecker, A. Joshi-Imre, K. C. Musselman, R. Modi, W. E. Voit, J. J. Pancrazio, B. J. Black, Softening Shape Memory Polymer Intracortical Devices for Chronic Neural Recordings, *Biomedical Engineering Society Annual Meeting*, Atlanta, GA. (poster)
- 2018/10/16: M. Ecker**,** Softening Polymers for Biomedical Devices, *BMES - Biomedical Engineering Society - 2018 Annual Meeting*, Atlanta, GA, (poster at "*Meet the faculty candidate forum*")
- 2018/06/26: M. Ecker, S. M. Hosseini, Aldo Garcia Sandoval, W. E. Voit, Softening Polymeric Substrates for Bioelectronic Devices with Improved Hydrolytic Stability, *Neural Interfaces Conference (NIC) 2018*, Minneapolis, MN, (poster)

- 2018/06/25: A. M. Stiller, C. L. Frewin, J. Usoro, V. R. Danda, M. Ecker, R. Modi, W. Voit and J. J. Pancrazio, Softening Shape Memory Polymer Intracortical Probes for Chronic Neural Recordings, *Neural Interfaces Conference (NIC) 2018*, Minneapolis, MN, (poster)
- 2018/06/01: M. Ecker, S. M. Hosseini, R. Rihani, J. J. Pancrazio, W. E. Voit, Softening Substrates for Bioelectronics Devices with Improved Hydrolytic Stability, *Biomaterials Day at Texas A&M*, College Station, TX, (poster)
- 2018/03/28: M. Ecker, S. M. Hosseini, R. Rihani, J. J. Pancrazio, W. E. Voit, Softening Substrates for Bioelectronics Devices with Improved Hydrolytic Stability, *Neuroelectronic Interfaces Gordon Research Conference*, Galveston, TX, (poster)
- 2017/11/29: S. M. Hosseini, M. Ecker, K. Kupke, W. Voit, Ester-free thiol-ene shape memory polymers for neural interfaces, *2017 MRS Fall Meeting*, Boston, MA, (talk)
- 2017/10/12: A. Sridharan, V. Danda, M. Ecker, A. Stiller, W. Voit, J. J. Pancrazio, and J. Muthuswamy, Interfacial Mechanics of Shape Memory Polymers (SMPs) in Cortical Brain Tissue, *BMES - Biomedical Engineering Society - 2017 Annual Meeting*, Phoenix, AZ, (poster)
- 2017/10/11: M. Ecker, Self-softening shape memory polymers as a substrate for bioelectronic devices, *BMES - Biomedical Engineering Society - 2017 Annual Meeting*, Phoenix, AZ, (poster at "*Meet the faculty candidate forum*")
- 2017/08/21: M. Ecker, Self-softening shape memory polymers as a substrate for bioelectronic devices , *254th American Chemical Society National Meeting & Exposition*, Washington DC, (poster at AEI)
- 2017/04/05: M. Ecker, V. Danda, J. Pancrazio, W. Voit, Effects of sterilization on self-softening thiol-ene/acrylate polymers for bioelectronics, *ACS Meeting,* San Francisco, CA.
- 2017/04/20: M. Ecker, V. Danda, J. Pancrazio, W. Voit, Self-softening shape memory polymers as a scaffold for neural electrodes, *MRS Spring Meeting,* Phoenix, AZ.
- 2018/10/16: H.W. Bedell, S. Song, X. Li, E. Molinich, S. Lin, J. Pancrazio, W. Voit, J.R. Capadona, Contributions of the innate immune response and probe material properties to inflammation at the neural interface, *BMES - Biomedical Engineering Society - 2018 Annual Meeting*, Atlanta, GA, (podium)
- 2018/10/16: A. Shoffstall, V. Danda, M. Ecker, J. Pancrazio, W. Voit, J.R. Capadona. Evaluation of Thiol-ene/Acrylate Shape Memory Polymer as a Substrate for Intracortical Microelectrodes. *BMES - Biomedical Engineering Society - 2018 Annual Meeting*, Atlanta, GA, (podium)
- 2018/03/28: A. Shoffstall, V. Danda, M. Ecker, J. Pancrazio, W. Voit, J.R. Capadona. Neuroelectronic Interfaces Gordon Research Conference, Galveston, TX. (poster)
- 2017/04/20: M. Goss, K. Dona, J. McMahon, A. Shoffstall, E. Ereifej, J.R. Capadona. "The Effects of Chronic Intracortical Microelectrode Implantation In The Motor Cortex on Motor Behavior in Healthy Rats" Biomedical Engineering Society Meeting, Phoenix, AZ, October, 2017. (podium)
- 2017/04/20: A. Shoffstall, J. Paiz, D. Miller, M. Willis, G. Rial, D. Menendez, J.R. Capadona. Thermal Damage to the Blood-Brain Barrier during Craniotomy

Procedure—Implications for Intracortical Recording Microelectrodes. *MRS Spring Meeting,* Phoenix, AZ.

- 2017/04/20: J.R. Capadona, A. Shoffstall, J. Hermann, E. Ereifej. Materials-Based, Biologically-Inspired, Anti-Oxidative, Anti-Inflammatory Approaches to Enable Next Generation Intracortical Microelectrodes. *MRS Spring Meeting,* Phoenix, AZ. (podium)
- 2016/10/15: M.S. Goss, K.R. Dona, J.A. McMahon, A.J. Shoffstall, E.S. Ereifej, J.R. Capadona, "Effect On Rat Motor Behavior Of Chronic Intracortical Microelectrodes Implanted In The Motor Cortex." Society for Biomaterials, Regional Biomaterials Day, Cleveland, OH, (podium – Award Winner)
- 2016/10/15: A. Shoffstall, M. Ecker, J. Pancrazio, W. Voit, J.R. Capadona. Validation of Ethylene Oxide Sterilization for Shape Memory Polymer Microelectrodes. Society for Biomaterials, Regional Biomaterials Day, Cleveland, OH, (podium)

PARTICIPANTS & OTHER COLLABORATING ORGANIZATIONS

Name: Joseph J. Pancrazio, PhD
Project Role: Principal investigator
Researcher Identifier: 0000-0001-8276-3690
Nearest Person Month Worked: 48
Contribution to Project: project administration, technical supervision of electrochemical testing of intracortical probes and in vivo recordings, supervision of post-doctoral research associate and graduate student, and coordination with the Cleveland VA Site 2.
Funding Support: University faculty and administration.

Name: Jeffery R. Capadona, PhD
Project Role: Co-Principal investigator
Researcher Identifier: 0000-0001-8030-6947
Nearest Person Month Worked: 48
Contribution to Project: project administration, technical supervision of immunohistochemical characterization of non-functional intracortical probes, supervision of post-doctoral research associate and graduate student, and coordination with the University of Texas at Dallas team.
Funding Support: University faculty and VA staff.

Name: Walter Voit, PhD
Project Role: Co-investigator
Researcher Identifier: 0000-0003-0135-0531
Nearest Person Month Worked: 48
Contribution to Project: Overseeing shape memory polymer device fabrication, supervision of technical staff in the Cleanroom, and coordination with the PI and the Cleveland VA site.
Funding Support: University faculty.

Name: Andrew Shoffstall, PhD
Project Role: Post-Doctoral Research Associate
Researcher Identifier: 0000-0002-0881-2180

Nearest Person Month Worked: 36
Contribution to Project: Immunohistochemical characterization of non-functional intracortical probes and development of novel insertion technology to ameliorate problems associated with buckling.
Funding Support: N/A

Name: Melanie Ecker, PhD
Project Role: Post-Doctoral Research Associate
Researcher Identifier: 0000-0002-0603-6683
Nearest Person Month Worked: 22
Contribution to Project: Development and synthesis of new SMP formulations having various degrees of softening *in vivo*. Thermomechanical characterization of SMP formulations in dry and in soaked states order to verify the softening capabilities. Investigation of the impact of various sterilization methods on the thermomechanical properties and softening on SMP formulations.
Funding Support: N/A

Name: Christopher L. Frewin, PhD
Project Role: Post-Doctoral Research Associate
Researcher Identifier: 0000-0002-7591-0629
Nearest Person Month Worked: 24
Contribution to Project: Responsible for survival surgeries, in vivo recordings, electrochemical analysis, Histological analysis, and device design.
Funding Support: N/A

Name: Bryan J. Black, PhD
Project Role: Post-Doctoral Research Associate
Researcher Identifier: 0000-0002-7591-0629
Nearest Person Month Worked: 18
Contribution to Project: Biocompatibility analyses, led surgical planning and histological protocol implementation.
Funding Support: N/A

Name: Alexandra Joshi-Imre, PhD
Project Role: Research Assistant Professor
Researcher Identifier: 0000-0002-4271-1623
Nearest Person Month Worked: 6
Contribution to Project: Research management; Microfabrication process development; Microscopy; Materials characterization; Yield analysis and Failure analysis.
Funding Support: State funded position at the UT Dallas Center for Engineering Innovation.

Name: Romil Modi
Project Role: Research Engineer
Researcher Identifier: 0000-0002-0436-7403
Nearest Person Month Worked: 6
Contribution to Project: Aided in the design and fabrication the SMP implantation devices for the project. Development of the processes required to manufacture a complete device.
Funding Support: DARPA Phase II SBIR support to Qualia LLC

Name: Vindhya Reddy Danda
Project Role: Research Engineer
Researcher Identifier: 0000-0001-8670-8816
Nearest Person Month Worked: 30
Contribution to Project: Ms. Danda is in charge of fabricating the SMP implantation devices. She also has characterized the devices with DMA and light microscopy.
Funding Support: N/A

Name: Ms. Lisa Spurgin
Project Role: Technician
Researcher Identifier: 0000-0001-5240-2085
Nearest Person Month Worked: 8
Contribution to Project: Fabrication of shape memory polymer substrates
Funding Support: N/A

Name: Allison Stiller
Project Role: Graduate student
Researcher Identifier: 0000-0001-6326-890X
Nearest Person Month Worked: 48
Contribution to Project: Ms. Stiller performs device fabrication, device design, animal surgeries and recording of neural signals.
Funding Support: N/A

SPECIAL REPORTING REQUIREMENTS

As required for Collaborative awards, both PIs have submitted a report with tasks for each clearly delineated.

Journal of Neuroscience Methods 317 (2019) 141–148

Contents lists available at ScienceDirect

Journal of Neuroscience Methods

journal homepage: www.elsevier.com/locate/jneumeth

A graphical user interface to assess the neuroinflammatory response to intracortical microelectrodes

Sydney C. Lindner[a], Marina Yu[a,b], Jeffrey R. Capadona[a,b], Andrew J. Shoffstall[a,b,*]

[a] Department of Biomedical Engineering, Case Western Reserve University, Cleveland, OH 44106, United States
[b] Advanced Platform Technology Center, Louis Stokes Cleveland Department of Veterans Affairs Medical Center, Cleveland, OH, United States

ARTICLE INFO

Keywords:
Neuroinflammation
Intracortical microelectrode
Neurodegeneration
Brain implant
Craniotomy
Matlab

ABSTRACT

Background: Brain-implanted devices, including intracortical microelectrodes, are used in neuroscience applications ranging from research to rehabilitation and beyond. Significant efforts are focused on developing new device designs and insertion strategies that mitigate initial trauma and subsequent neuroinflammation that occurs as a result of implantation. A frequently published metric is the neuroinflammatory response quantified as a function of distance from the interface edge, using fluorescent immunohistochemical markers.

New method: Here, we sought to develop a graphical user interface software in Matlab to provide an objective, repeatable, and easy-to-use method for analyzing fluorescence immunohistochemistry images of neuroinflammation. The user interface allows for efficient batch-processing and review of images, and incorporates zoom and contrast features to improve the accuracy of identifying the 'region of interest' (ROI).

Results: The software was validated against previously published results and demonstrated equivalent scientific conclusions. Furthermore, a comparison between novice and expert users demonstrated consistency across levels of training and a rapid learning-curve.

Comparison with existing method(s): Existing methods published in the intracortical microelectrode literature include a wide variety of procedures within ImageJ and Matlab. However, specific procedural details are often lacking.

Conclusions: The distribution of the methodology may promote efficiency and reproducibility across the field seeking to characterize the tissue response to implanted neural interfaces. It may also serve as a template for researchers seeking to perform other types of histological quantification as a function of distance from an ROI.

1. Introduction

Brain-implanted devices have been utilized for a number of research and clinical purposes (Ajiboye et al., 2017; Hochberg et al., 2012; Pancrazio and Peckham, 2009). While we believe the following method has utility in multiple research areas, the current study focuses on intracortical microelectrodes. Intracortical recording microelectrodes are used for electrophysiology, cortical mapping, and studying neural circuitry. Within non-clinical research, microelectrodes are used ubiquitously and in large numbers, while within clinical research they are used selectively in smaller numbers of patients for exploratory rehabilitation applications. For example, they are often utilized in brain computer interface (BCI) systems that restore natural motion to patients with paralysis and limb loss. Certain entrepreneurs are simultaneously exploring their use in other, more futuristic, endeavors (Pancrazio and Peckham, 2009; Wu and Rao, 2017). While tremendous achievements have been made in the BCI field, there is a need for better neural interfaces that maintain viable levels of performance for longer duration (Jorfi et al., 2015). Typical implants begin degrading within the first weeks of implantation and many fail within just a few years (Jorfi et al., 2015).

For intracortical recording microelectrodes, it has become apparent that the neuroinflammatory response likely plays a role in their deterioration in recording performance over time (Barrese et al., 2016, 2013; Rennaker et al., 2005; Biran et al., 2005). Accordingly, the reduction of the neuroinflammatory response to implanted materials in the brain is an active area of research (Hermann et al., 2018; Bedell et al., 2018; Nguyen et al., 2016; Michelson et al., 2018; Cody et al., 2018). Efforts are focused both on understanding and mitigating initial iatrogenic trauma as well as the chronic neuroinflammatory foreign body response resulting from implantation of the devices (Goss-Varley et al., 2017).

* Corresponding author at: 2071 Martin Luther King Jr. Dr, Case Western Reserve University, United States.
E-mail address: Ajs215@case.edu (A.J. Shoffstall).

https://doi.org/10.1016/j.jneumeth.2019.01.003
Received 28 August 2018; Received in revised form 10 January 2019; Accepted 11 January 2019
Available online 18 January 2019
0165-0270/ Published by Elsevier B.V.

Several aspects of the neuroinflammatory response due to implantation are potentially detrimental to the efficacy of the intracortical microelectrode (Shoffstall and Capadona, 2018). The release of cytotoxic soluble factors by localized activated microglia and recruited macrophages contributes to oxidative corrosion and degradation of the microelectrode interface (Jorfi et al., 2015). Hypertrophic astrocytes in the region of the injury aid in scar formation around the implant, which may ultimately reduce recording quality over time (McCreery et al., 2016). Neurodegeneration around the implant can also reduce the functionality of the microelectrode (Biran et al., 2005). While many potential biological factors have been identified, there is still the need for continued research to improve our understanding of the biological system and the prognostic role of the various biomarkers (Michelson et al., 2018; McCreery et al., 2016). In addition to electrophysiological and motor behavioral studies, the majority of groups researching in this area rely on histological and immunohistochemistry methods to measure the biological response at the neural device-tissue interface (Jorfi et al., 2015; Hermann and Capadona, 2019).

Analysis of the neuroinflammatory response in post-implantation tissues can be accomplished using various histological techniques. There are dozens of groups actively working in this area and each has developed slightly different methods for their analyses (McCreery et al., 2016; Potter et al., 2012a, b; Sohal et al., 2016; Oakes et al., 2018; Lo et al., 2018). Histology can be used to categorize inflammatory markers based on their relative distance from the resulting hole after explanting the microelectrode implant in order to gain a greater understanding of the spatial reach of the neuroinflammatory response to implantation. For example, McCreery et al. refer to the measurement of neuron and glial fibrillary acidic protein (GFAP) density within 'overlapping concentric annuli' from the center of the microelectrode tip (McCreery et al., 2016). Some groups use Matlab to quantify fluorescence intensity via calculation of concentric ellipses or generation of rotational intensity sweeps around an implant region of interest; others use LabView to perform a pixel extraction algorithm (Sohal et al., 2016; Potter et al., 2012b; Sohal et al., 2016; Oakes et al., 2018; Lo et al., 2018). Similar measurements are reported with slight variations throughout the literature. The Capadona lab previously published a software called MINUTE ('Microelectrode INterface Universal Tool for Evaluation'), which semi-automates the process of generating intensity-based quantification as a function of distance from a selected region of interest. However, it has been cited relatively infrequently throughout the literature, potentially due to user-interface challenges (Potter et al., 2012a; Lee et al., 2017). Some of these challenges include long processing times for single-file sequential processing, inability to zoom or contrast images, an assumption that the implant hole geometry is purely elliptical, and difficulty in reviewing or updating analyses. Within the broader literature that provides openly available methods, various groups have demonstrated different strategies for quantifying histological outcomes. The efforts include pure intensity-based measurements and cellular counts using fully automated versus fully manual methods, but these methods often lack in simple user-interfaces and require a high level of training for proficiency [Shoffstall et al., 2018-26]. Additionally, variety among these histological quantification analysis methods contributes to a range in data error and reproducibility among specific users and groups.

There does not appear to be any obvious field-specific consensus regarding the best practices to study the neuroinflammatory response due to implanted intracortical microelectrodes. Therefore, we sought to develop an easy-to-use and open-source graphical user interface (GUI) in Matlab, coined 'SECOND' (alluding to both its improved speed compared to MINUTE, and its being the 2nd version of the program), to process and analyze immunohistochemistry fluorescence-based images. The methods of construction and use, as well as the code's validation, are presented here. The goal of this work was to achieve a software that is openly available to the field to improve the efficiency, accuracy, and standardization of results across groups.

2. Materials and methods

2.1. Overview

SECOND is a Matlab (Mathworks, Inc., Natick, MA) program with a basic Graphical User Interface (GUI) for histological image configuration and fluorescence intensity analysis. The histological images can be efficiently viewed and analyzed in large sets. The user-driven configuration and automated processing method in SECOND allows for variations in image quality and implantation procedures. SECOND can be used across various fields in need of analyzing fluorescence intensity as a function of distance from a defined region of interest (ROI).

The GUI for the program contains multiple tools necessary in order to work from image setup to data analysis and collection. The flow of the program follows the GUI toolbar from left to right, the details of which are outlined in Supplementary Figs. 1 and 2. The user first opens the desired set of images for analysis under the File menu in the toolbar. In the next step under the Setup menu, the program requires the user to manually configure the image parameters, including contrast adjustments and area definitions applied to all channels within the image, and to save the results in a Matlab file. After a set of images is configured, the user selects "Batch Run" from the Analysis menu for a collection of images and the corresponding configuration files are automatically processed for fluorescence intensity quantification. Once results are compiled under the Review menu, the script produces a collection of analysis files containing the averaged fluorescence intensities in each of the predefined buckets of distances emanating from the ROI.

The results are compiled and output three ways: a Matlab file with raw analysis data, a raw intensity plot, and a final contrast-adjusted image with overlaid exclusion and distance masks. The final "Compile Results" step is valuable for integrating the data into another program for more efficient review and revision of the total set of images. According to specific study requirements, the user may combine results further and perform statistical analysis with the resulting data after using SECOND for measuring intensities.

A step-by-step video tutorial has been uploaded to YouTube to help orient first-time users of the program: https://www.shofflab.com/research/videos

2.2. Sample images

For the purpose of demonstration, the sample images throughout the manuscript were taken from a previous study of cortical rat brain (Shoffstall et al., 2018). Tissue was sliced, 20 μm in the transverse direction after removal of a planar silicon microelectrode array implanted in the primary motor cortex. The removal of the device after perfusion-fixation with formaldehyde leaves a characteristic hole which is clearly visible in the center of the image (Fig. 1). The slides were stained for GFAP (glial fibrillary acidic protein) following published protocols (Shoffstall et al., 2018).

In order to be compatible with SECOND, image files must be saved in the TIFF grayscale format with 16-bit depth. Bit depths of 8 do not provide sufficient resolution of intensity levels for most analysis applications. If multiple channel analysis is being performed, each channel must be represented by a unique grayscale image file. All the files pertaining to a single multi-channel capture must be located in a single folder by themselves. It is recommended that each file be designated with a channel in its name with an underscore at the end. For example, a typical naming scheme we have adopted is "SpecimenID_#

(SliceID)_Channel.tif". There are no other defined limits as to the pixel resolution or other dimensions of the files. However, it is recommended that the images be of sufficient resolution to allow for all features to be resolved (i.e., not pixelated or blurry). Since the tissue response is normalized to a background level at a set distance from the region of interest, it is also important the images contain a sufficient distance away from the electrode such that the response plateaus to a baseline value. In our case, we perform image stitching on a 3-by-3 or 4-by-4 tiled region at 20x magnification to ensure a large enough region, roughly 1500 µm -by- 1500 µm microns has been captured. In our experience the inflammatory response for most of our markers (e.g. GFAP, CD68, IgG), return to baseline by 300–500 µm away from the implant edge. Pixel resolution is determined by the combination of the objective magnification and the resolution of the camera used to capture the images. The calibration factor must be determined for each experimental setup and input during the configuration process in SECOND.

2.3. Pre-analysis image configuration

16-bit monochrome TIF image files are loaded into the program, one for each channel (e.g., each fluorophore: DAPI, GFP, Cy5, etc.). The user performs contrast adjustments on each channel separately to view the details within the images (Fig. 1). Contrast adjustments allow the user to more easily define the implantation hole as the ROI and to define any necessary image exclusions, such as bubbles on the slide and tears in the tissue. The contrast bounds, ROI mask, and exclusion masks as a result of the user's adjustments are saved in a Matlab configuration file ('_sconfig.mat') for the image.

2.4. Data analysis

2.4.1. Load configuration and parameters

Further analysis requires the user to 'batch run' a set of microscope images and the configuration files. The code loads the configuration data, which includes image files for each channel, bounds for contrast adjustment, definitions for the ROI and any exclusions, and general settings. The settings include the grouping width for defining concentric distance buckets around the hole, micron-per-pixel conversion factor (determined by the microscope camera configuration), and configuration date. The code is optimized for use with 16-bit TIF monochrome images collected with 12–16 bit CCD cameras .

2.4.2. Generate exclusion mask

After loading all configuration data, the program creates an exclusion mask as a combination of the ROI (center) and exclusions (periphery) as defined by user input (Fig. 2). The exclusion mask initializes as an array of 'ones' that has the same dimensions as the image. The program inserts values of 'NaN' ('not a number') in the array for each pixel within the exclusion boundaries. The exclusion mask is applied to each channel within the image.

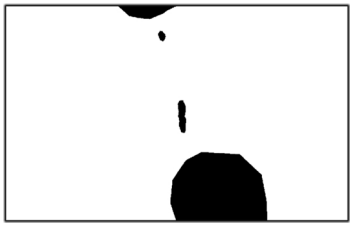

Fig. 2. Binary exclusion mask, showing the tissue void at the center from the explanted device as well as 3 other regions to remove bubbles as image artifact. The regions are all user-defined and saved in the image configuration file.

fx2

Code Snippet 2: An exclusion mask is generated from user-defined input of the 'hole' ROI and any other artifacts such as bubbles and tears. Again the functions are serialized using the built-in Matlab function 'cellfun' for efficiency and modularity.

2.4.3. Generate distance map

Next, the program creates a map of pixel distances emanating linearly outward from the ROI using the Matlab function 'bwdist' (Supplementary Fig. 3). These pixel distances are converted to micron distances based on the predefined conversion factor for the image. The distance map is further bucketed based on the predefined micron grouping width so that fluorescence intensity can be measured and averaged within each bucket. For a sample micron grouping width of 50 µm, the intensities would be calculated in a bucket of 0–50 µm, 50–100 µm, etc. around the hole (Supplementary Fig. 4, Fig. 3).

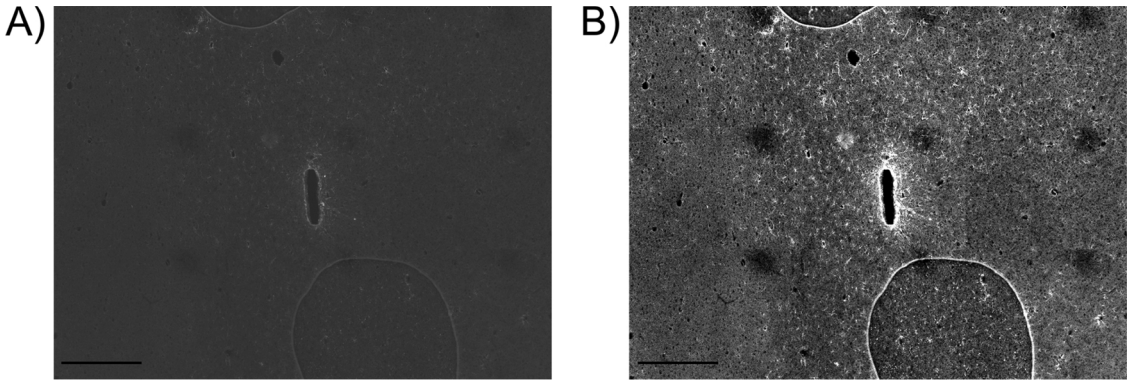

Fig. 1. Contrast adjustment within SECOND. A) Unadjusted monochrome GFAP-stained image showing a void in the center of the image created from explanting a single-shank silicon microelectrode device. B) Contrast-adjusted image according to user-selected bounds. Bubbles are obviously visible at the top and bottom edge of the images – the bubbles are excluded from the analysis in later steps. Scale bars = 400 µm.

fx1

Code Snippet 1: The built-in Matlab function 'cellfun' is used to call a custom function 'applyContrast' to adjust each of the channels loaded into the cell array image storage variable 'm1'.

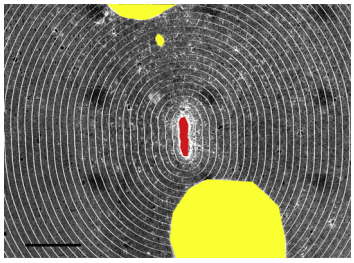

Fig. 3. Contrast-adjusted image with overlaid 'Bucket' grouping lines. Red denotes the hole. Yellow denotes exclusions applied to the image. Both are removed from the analysis. Scale bar = 400 µm.

fx3

Code Snippet 3: Sub-indices are generated from the distance map to aid in bucket grouping.

2.4.4. Fluorescence intensity analysis

Analysis of the fluorescence intensity in the non-excluded areas of the image is automatically performed by the program (Fig. 4). The mean intensity for the fluorescent objects of interest in each channel is measured and categorized based on the predefined distance buckets. Accordingly, the total number of pixels within each distance grouping increases at larger distances away from the ROI. The fluorescence intensity data is formatted into a plot and output by the program. The final image files with contrast adjustments, area definitions, and distance bucket mapping are also output by the program during this step, generating individual '_analysisresults.mat' MAT-files for each set of images.

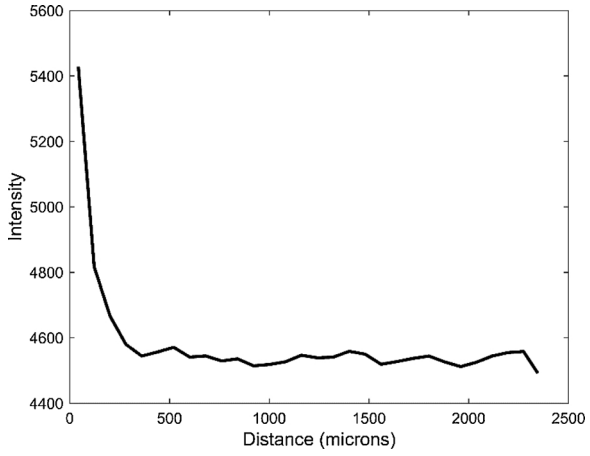

Fig. 4. Intensity profile as a function of distance from the neural interface region of interest. The intensity decays to a constant background level, typically within the first 500 µm from the hole edge. This example reflects a single trace of raw intensity data.

fx4

Code Snippet 4: Intensity profiles as a function of distance from the hole edge are calculated by leveraging the function 'accumarray' which allows for transformation of data along sub-indices.

2.5. Data compilation

After SECOND analyzes the fluorescence intensity data for each channel of a set of images, the user may compile the data for further analysis and review (Fig. 5). Compiling the results collates the data into the user's program(s) of choice for data processing and statistics (e.g. Excel, R, etc.), including intensity profiles and final images. This allows the user to perform further graphical and statistical analyses for entire batches of images, resulting in a wider view of the measurements of interest. As referenced in previously published papers, the raw intensity curves are further normalized to a baseline level established far from the injury site and aggregated using discrete area-under-the-curve tabulations (Bedell et al., 2018).

Image processing and fluorescence quantification via the script keeps the user blind to the experimental group, but further analyses can be accomplished after accumulating the data for a set. Blinding the user from knowing the specific experimental group aims to minimize bias in image configuration and masking selections. To categorize data after using SECOND, the compiled results should be given unique identifiers based on analysis user, date, or lab-specific attributes. These can be added as an additional column which can be used as a grouping variable in most data analytics software (e.g. Excel, Minitab, SPSS, SAS, R, etc.).

3. Results & discussion

3.1. Scientific validation testing

In order to validate that the software would perform similarly to previously published results, and result in equivalent scientific conclusions, we analyzed the same set of data using both SECOND and MINUTE. Additional details about the methods and data of the study represented in Fig. 6 can be found in the referenced publication (Potter et al. (2012a)). For the purposes of clarity in this manuscript, we have chosen to simply refer to the experimental groups as "1, 2, 3, etc.".

The Capadona lab previously studied the accuracy of fluorescence intensity quantification at the tissue-electrode interface using various immunohistochemical methods, and we used the same experimental images to compare the quantification methods in SECOND versus MINUTE (Fig. 6). We determined that the two analysis methods provided very similar data output, and as a result the scientific conclusions from the study would have been the same. Statistics were run using a ANOVA with Tukey tests for pairwise inter-group comparisons (Minitab).

3.2. Novice vs expert analysis (training efficiency testing)

Two groups, "expert" and "novice", were tested using SECOND to analyze three histological tissue images from two different animals for a total of six images. The six tissue samples were imaged with three fluorescent channels each, DAPI, ED1 (CD68), and GFAP. The findings from the GFAP analysis are shown in Fig. 7, while results from the other channels are shared in Supplementary Fig. 5. The "novice" testing group was comprised of nine students chosen from an undergraduate lab course. The novices were given no formal training to use SECOND, only told to follow the prompts from the program to analyze the

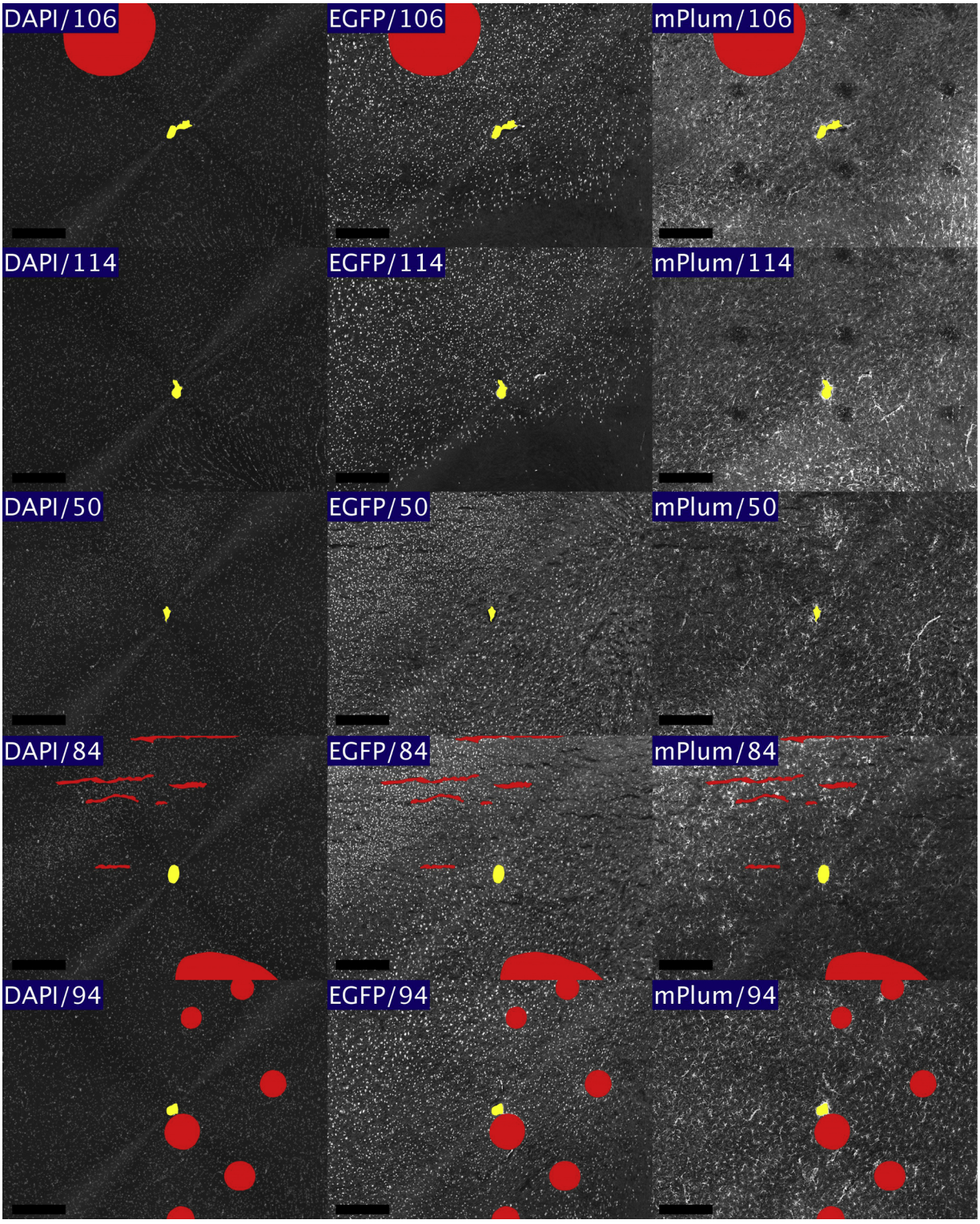

Fig. 5. Image Review. The panel shows the entire array of slices and stains performed for a given subject. The review makes it apparent that there are two panels that require re-masking. Panels "EGFP/106" and "EGFP/114", where there are two apparent areas void of cellular staining toward the bottom-right edge. Results from a minimum of 3-4 image replicates for a given tissue sample are suggested to be averaged together in order to achieve statistical power. Red denotes exclusion of imaging artifacts (bubbles, tears, etc.). Yellow denotes the hole definition. Scale bars = 400 μm.

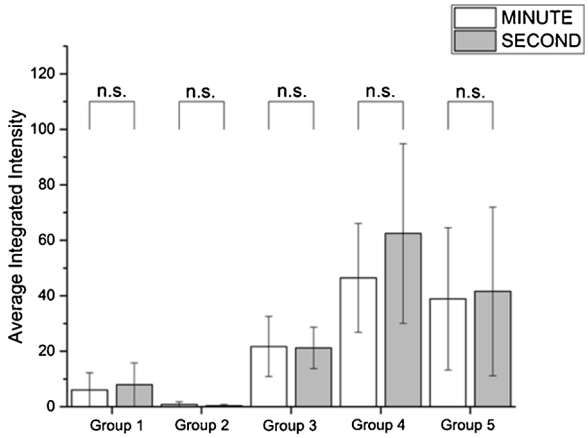

Fig. 6. SECOND versus MINUTE. A comparison between the data results found using the two different algorithms. There were not statistically significant differences between MINUTE and SECOND for any of the datasets tested.

intensities among the set of six images. The four experts were chosen from the Capadona lab, since they had regularly used SECOND to perform similar analyses. The two groups completed the program flow from manual contrast adjustments and area definitions to automated micron bucketing and analysis of fluorescence intensity.

The resulting intensity values from their analyses were normalized and bucketed into groups of 50 μm outwards from the implant hole (Fig. 7A). There were no statistically significant differences between the experts and the novices at any of the distance intervals (Table 1). The majority of the error was contributed by image-to-image variability rather than user-to-user variability (Extended ANOVA results are shown in Supplementary Table 1). However, it can be noted in Fig. 7B that there was at least one novice user that yielded outlier results. Given additional training, it is anticipated that the inconsistency could be resolved. On average, even with no training, the novices were able to obtain very similar intensity profiles for the images, showing that SECOND continues to be efficient among users of various training levels.

Table 1
Analysis of Variance (P-Value) Table. The image contributes most significantly to the source of variability. There were no significant differences between the expert and novice users in either of the image sets tested (stained with GFAP and ED-1).

P-Values from ANOVA-Tukey Tests	Distance Bucket (μm)			
Marker 1 (GFAP) Source	**0-50**	**50-100**	**100-150**	**150-200**
Expert/Novice	0.158	0.548	0.595	0.202
Image	< 0.001	< 0.001	< 0.001	< 0.001
Marker 2 (ED-1) Source				
Expert/Novice	0.753	0.838	0.869	0.947
Image	< 0.001	< 0.001	< 0.001	< 0.001

3.3. Processing algorithm & efficiency

Substantial efficiency was gained using SECOND compared to MINUTE, providing the ability to generate image masks and a compiled dataset within several hours compared to several days of analysis. The efficiency was primarily gained as a result of the following:

1) Batch-processing compared to sequential-processing allowing for user flexibility, and
2) Fast processing algorithm taking only 30–60 seconds compared to 15–20 minutes to analyze each image. Most of the efficiency was gained by using the 'bwdist' function rather than an iterative calculated expansion of concentric ellipses mapped to pixel-space.
3) Built-in image contrast and zoom to make hole and exclusion definition easier and more precise
4) Ability to define non-ellipsoidal holes

Data analysis was also made more efficient through a number of other means. The manual contrast adjustment by the user takes only a few seconds and allows for more accurate detection of image details. The adjustment is applied only to the visualization while the underlying data remains unaltered. Defining the implant hole and exclusions is additionally made simpler by a program prompt to zoom in on a smaller area of the image containing the definition of interest. These user-driven annotations take a few minutes to complete per image, but the

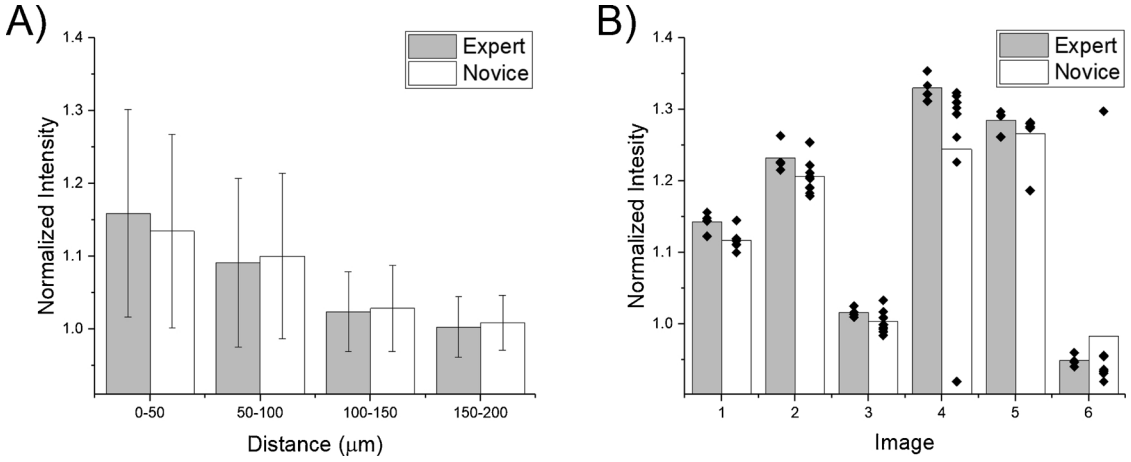

Fig. 7. Experts versus novices analysis. A) Expert users are compared to novice users in their analysis of the same set of 6 images stained with GFAP. Normalized intensities resulting from the two user groups and based on distance buckets are shown. The error bars represent the standard deviation of the average normalized intensities for each user group. B) The same data is shown with individual normalized intensity (0–50 μm bucket) measurements for each user (black-diamonds) overlaid on each group's average for each of the 6 images analyzed.

result is an image that can be automatically processed and analyzed in seconds with increased accuracy and ability for post-hoc review.

A distance map ('bwdist') is created in order to later measure the fluorescence intensity as a function of distance from the implant hole (Supplementary Fig. 3). The distance map for the image is generated more efficiently than other algorithms that rely on iterative methods, such as direct calculation of elliptical coordinates or image dilation (Potter et al., 2012a). Elliptical coordinates oversimplify the neural interface right at the edge where it matters most, and image dilation is a very processing-heavy task. Previous methods in MINUTE iteratively calculated ellipses expanding from the ROI before mapping discrete pixels to the area to determine distances. The built-in Matlab function 'bwdist' provides a very rapid and efficient method for tabulating the intensity as a function of distance, and does not force the geometry to be perfectly ellipsoidal.

The image (TIF format) is loaded into Matlab as an unsigned 16-bit integer array (Fig. 1A). Without any contrast and level adjustment, the image is dark with indistinguishable details. This would make any user interaction to define the hole edges very challenging. Therefore, a contrast procedure is performed (Fig. 1B). The contrast adjusted image is easier to see. While the display shown to the user is adjusted, the underlying pixel values are kept constant. This is accomplished by adjusting the image display bounds ('CLim') within Matlab image properties.

While the goal during sectioning and cover-slipping tissue slides is to minimize tears and bubbles, these issues are sometimes unavoidable. Artifact removal is a necessary part of research, so the methods provided give a simple means to annotate and review exclusions. An exclusion mask is created as a combination of the defined ROI and selected exclusions (Fig. 2). The exclusion mask serves to eliminate regions from the image that should not contribute to fluorescence intensity measurements. The inside area of the implant hole is excluded, because its perimeter is set as the origin for categorizing distances emanating outwards from the hole. Bubbles on the slide, major tissue tears, and any abnormalities to the image are excluded by the user to reduce error in the fluorescent intensity measurements. The user interface provides a simple method for removing artifacts from the analysis.

Due to the changes above, we estimate the average user-input time decreased by 2.5-fold, from 5 to 2 min, and computation time decreased by 20-fold, from 20 to 60 s, per image.

3.4. Special considerations

While SECOND attempts to generalize the analysis of neuroinflammation in histological images, there are a few factors to consider for each experiment-specific goal.

3.4.1. Pixel-to-Micron conversion factor

The conversion factor is a vital component to accurately reporting the image analysis and will vary based on lab-specific instrumentation. Pixel distances are converted to micron distances based on a predefined conversion factor (Supplementary Fig. 3). In order to perform analysis of the fluorescence intensity surrounding the hole, we further group micron distances into buckets based on a predefined group width. Therefore, it is highly recommended that users verify that the image processing techniques are accurately reporting distances. One possible method for checking accuracy would include collecting an image with a calibrated slide containing a ruler (Supplementary Fig. 6).

3.4.2. Intensity normalization

Specific selection of the normalization band should be done with care and justification. Near the implant hole, fluorescent intensity is typically highest due to the inflammatory response, and exponentially decreases to a dimmer background level. The separately included 'CompileResults' code normalizes the intensity data for each channel according to a selected band deemed far enough away from the hole that the inflammatory response has subsided to baseline. In our experience, depending on the stain, this can vary between 200–500 μm away (Bedell et al., 2018).

3.4.3. Image review for quality control

Especially for analysis being performed by multiple users, it is important to have a system for reviewing images for quality control. For this reason, the final image output displays the contrast adjustments, ROI definition, and perimeter lines for each micron bucket emanating from the ROI (Fig. 3). The review image is valuable for the user to manually check the details of the area definitions and boundaries of the measurements. Shown in Fig. 5 is a montage of the review JPG images for a single subject. While code for generating the panel montage is provided, it will require customization according to the user-specific naming scheme.

3.4.4. Appropriateness of intensity metric

Typical immunofluorescent labeling procedures used by the Capadona lab and analyzed with SECOND include GFAP, IgG, and CD68 stains, among others (Hermann et al., 2018; Bedell et al., 2018; Nguyen et al., 2016; Goss-Varley et al., 2017; Potter et al., 2012a, b). These stains correspond to protein biomarkers expressed at different amounts near the tissue-electrode interface, with quantities depending on the level of inflammation or injury to the tissue. While it is appropriate to analyze some IHC markers using an intensity-based approach, we have found that for some stains, including those that are sparsely populated and/or discretely stained (e.g., neuronal nuclei), the more scientifically relevant metric may rather be a cell count or density. In that case, an alternative analysis method would be required.

3.4.5. Considerations for multi-tined electrodes

The analysis of a matrix-style array type electrode would also be possible using the SECOND code. In this case, each tine would have to be analyzed one-at-a-time. While this is feasible, it would be highly cumbersome. In that case, it would be best to make a slight alteration to the code that would enable multiple ROIs to be defined (1 for each tine of the electrode). The remainder of the code would not require alteration.

4. Conclusion

Intracortical microelectrodes represent one of the principle types of brain-implanted devices currently under investigation. Beyond intracortical microelectrodes, there is interest in developing other novel neural interfaces for the central and peripheral nervous systems. A common goal is to develop interfaces that reduce the inflammatory response, so as to reduce tissue impedance and the distance between the device and neural tissue. Since many disparate research groups are each using slightly varied methods to achieve similar measurements of the neuroinflammatory response to implanted materials, reporting in the literature is equally varied and is potentially leading to inefficient duplication of efforts.

Using SECOND, the intensity of various fluorescent molecules on histological images can be quantified as a function of distance from a user-specified ROI. The code is openly available to the field, and if adopted, may improve the efficiency, accuracy, and standardization of results across groups. The ultimate goal of providing the analysis method here is to improve implanted neural device efficacy and longevity. While the code is currently optimized for use with microelectrodes implanted in cortical tissue, it may be adapted for broader study applications involving intensity based-measurements radiating from a specifically defined region of interest.

Funding

This work was supported in part by the Office of the Assistant Secretary of Defense for Health Affairs through the Peer Reviewed Medical Research Program under Award No. W81XWH-15-1-0608 (Capadona) in part by Merit Review Awards #B1495-R and #B2611 (Capadona), Presidential Early Career Award for Scientist and Engineers (PECASE, Capadona), and a Career Development Award-1 #1IK1RX002492-01 A2 (Shoffstall) from the United States (US) Department of Veterans Affairs Rehabilitation Research and Development Service, and by the National Institute of Health, National Institute of Neurological Disorders and Stroke, (Grant # 1R01NS082404). None of the funding sources aided in collection, analysis and interpretation of the data, in writing of the manuscript, or in the decision to submit the manuscript for publication. The contents do not represent the views of the U.S. Department of Defense, the U.S. Department of Veterans Affairs or the United States Government.

Conflicts of interest

The authors declare no conflict of interest.

Acknowledgements

The authors would like to acknowledge all the members of the Capadona lab for helping to rigorously test and validate the SECOND code.

Appendix A. Supplementary data

Supplementary material related to this article can be found, in the online version, at doi:https://doi.org/10.1016/j.jneumeth.2019.01.003.

References

Ajiboye, A.B., Willett, F.R., Young, D.R., Memberg, W.D., Murphy, B.A., Miller, J.P., Walter, B.L., Sweet, J.A., Hoyen, H.A., Keith, M.W., et al., 2017. Restoration of reaching and grasping movements through brain-controlled muscle stimulation in a person with tetraplegia: a proof-of-concept demonstration. Lancet 389, 1821–1830.

Barrese, J.C., Rao, N., Paroo, K., Triebwasser, C., Vargas-Irwin, C., Franquemont, L., Donoghue, J.P., 2013. Failure mode analysis of silicon-based intracortical microelectrode arrays in non-human primates. J. Neural Eng. 10, 066014.

Barrese, J.C., Aceros, J., Donoghue, J.P., 2016. Scanning electron microscopy of chronically implanted intracortical microelectrode arrays in non-human primates. J. Neural Eng. 13, 026003.

Bedell, H.W., Hermann, J.K., Ravikumar, M., Lin, S., Rein, A., Li, X., Molinich, E., Smith, P.D., Selkirk, S.M., Miller, R.H., et al., 2018. Targeting cd14 on blood derived cells improves intracortical microelectrode performance. Biomaterials 163, 163–173.

Biran, R., Martin, D.C., Tresco, P.A., 2005. Neuronal cell loss accompanies the brain tissue response to chronically implanted silicon microelectrode arrays. Exp. Neurol. 195, 115–126.

Cody, P.A., Eles, J.R., Lagenaur, C.F., Kozai, T.D.Y., Cui, X.T., 2018. Unique electrophysiological and impedance signatures between encapsulation types: an analysis of biological utah array failure and benefit of a biomimetic coating in a rat model. Biomaterials 161, 117–128.

Goss-Varley, M., Dona, K.R., McMahon, J.A., Shoffstall, A.J., Ereifej, E.S., Lindner, S.C., Capadona, J.R., 2017. Microelectrode implantation in motor cortex causes fine motor deficit: implications on potential considerations to brain computer interfacing and human augmentation. Sci. Rep. 7, 15254.

Hermann, J.K., Ravikumar, M., Shoffstall, A.J., Ereifej, E.S., Kovach, K.M., Chang, J., Soffer, A., Wong, C., Srivastava, V., Smith, P., et al., 2018. Inhibition of the cluster of differentiation 14 innate immunity pathway with iaxo-101 improves chronic microelectrode performance. J. Neural Eng. 15, 025002.

Hermann, J.K.; Capadona, J.R. Understanding the role of innate immunity in the response to intracortical microelectrodes. Critical Reviews in Biomedical Engineering (Under Review).

Hochberg, L.R., Bacher, D., Jarosiewicz, B., Masse, N.Y., Simeral, J.D., Vogel, J., Haddadin, S., Liu, J., Cash, S.S., van der Smagt, P., et al., 2012. Reach and grasp by people with tetraplegia using a neurally controlled robotic arm. Nature 485, 372–375.

Jorfi, M., Skousen, J.L., Weder, C., Capadona, J.R., 2015. Progress towards biocompatible intracortical microelectrodes for neural interfacing applications. J. Neural Eng. 12, 011001.

Lee, H.C., Gaire, J., Currlin, S.W., McDermott, M.D., Park, K., Otto, K.J., 2017. Foreign body response to intracortical microelectrodes is not altered with dip-coating of polyethylene glycol (peg). Front. Neurosci. 11, 513.

Lo, M.C., Wang, S., Singh, S., Damodaran, V.B., Ahmed, I., Coffey, K., Barker, D., Saste, K., Kals, K., Kaplan, H.M., et al., 2018. Evaluating the in vivo glial response to miniaturized parylene cortical probes coated with an ultra-fast degrading polymer to aid insertion. J. Neural Eng. 15, 036002.

McCreery, D., Cogan, S., Kane, S., Pikov, V., 2016. Correlations between histology and neuronal activity recorded by microelectrodes implanted chronically in the cerebral cortex. J. Neural Eng. 13, 036012.

Michelson, N.J., Vazquez, A.L., Eles, J.R., Salatino, J.W., Purcell, E.K., Williams, J.J., Cui, X.T., Kozai, T.D.Y., 2018. Multi-scale, multi-modal analysis uncovers complex relationship at the brain tissue-implant neural interface: new emphasis on the biological interface. J. Neural Eng. 15, 033001.

Nguyen, J.K., Jorfi, M., Buchanan, K.L., Park, D.J., Foster, E.J., Tyler, D.J., Rowan, S.J., Weder, C., Capadona, J.R., 2016. Influence of resveratrol release on the tissue response to mechanically adaptive cortical implants. Acta Biomater. 29, 81–93.

Oakes, R.S., Polei, M.D., Skousen, J.L., Tresco, P.A., 2018. An astrocyte derived extracellular matrix coating reduces astrogliosis surrounding chronically implanted microelectrode arrays in rat cortex. Biomaterials 154, 1–11.

Pancrazio, J.J., Peckham, P.H., 2009. Neuroprosthetic devices: How far are we from recovering movement in paralyzed patients? Expert Rev. Neurother. 9, 427–430.

Potter, K.A., Simon, J.S., Velagapudi, B., Capadona, J.R., 2012a. Reduction of autofluorescence at the microelectrode-cortical tissue interface improves antibody detection. J. Neurosci. Methods 203, 96–105.

Potter, K.A., Buck, A.C., Self, W.K., Capadona, J.R., 2012b. Stab injury and device implantation within the brain results in inversely multiphasic neuroinflammatory and neurodegenerative responses. J. Neural Eng. 9, 046020.

Rennaker, R.L., Street, S., Ruyle, A.M., Sloan, A.M., 2005. A comparison of chronic multichannel cortical implantation techniques: manual versus mechanical insertion. J. Neurosci. Methods 142, 169–176.

Shoffstall, A., Capadona, J.R., 2018. Prospects for a robust cortical recording interface. In: Krames, E.S., Peckham, P.H., Rezai, A.R. (Eds.), Neuromodulation, second edition. Academic Press, pp. 393–413.

Shoffstall, A.J., Ecker, M., Danda, V., Joshi-Imre, A., Stiller, A., Yu, M., Paiz, J.E., Mancuso, E., Bedell, H.W., Voit, W.E., et al., 2018. Characterization of the neuroinflammatory response to thiol-ene shape memory polymer coated intracortical microelectrodes. Micromachines (Basel) 9.

Sohal, H.S., Clowry, G.J., Jackson, A., O'Neill, A., Baker, S.N., 2016. Mechanical flexibility reduces the foreign body response to long-term implanted microelectrodes in rabbit cortex. PLoS One 11, e0165606.

Wu, J., Rao, R.P.N., 2017. How Close Are We to Elon Musk's Brain-computer Interface? In the Conversation. CNN.

micromachines

MDPI

Article

A Meta-Analysis of Intracortical Device Stiffness and Its Correlation with Histological Outcomes

Allison M. Stiller *, Bryan J. Black, Christopher Kung, Aashika Ashok, Stuart F. Cogan, Victor D. Varner and Joseph J. Pancrazio

Department of Bioengineering, The University of Texas at Dallas, 800W. Campbell Rd., Richardson, TX 75080, USA; bjb140530@utdallas.edu (B.J.B.); christopher.kung@utdallas.edu (C.K.); aashika.ashok@utdallas.edu (A.A.); sxc149830@utdallas.edu (S.F.C.); vdv@utdallas.edu (V.D.V.); joseph.pancrazio@utdallas.edu (J.J.P.)

* Correspondence: allison.stiller@utdallas.edu; Tel.: +1-972-883-2138

Received: 31 July 2018; Accepted: 30 August 2018; Published: 6 September 2018

Abstract: Neural implants offer solutions for a variety of clinical issues. While commercially available devices can record neural signals for short time periods, they fail to do so chronically, partially due to the sustained tissue response around the device. Our objective was to assess the correlation between device stiffness, a function of both material modulus and cross-sectional area, and the severity of immune response. Meta-analysis data were derived from nine previously published studies which reported device material and geometric properties, as well as histological outcomes. Device bending stiffness was calculated by treating the device shank as a cantilevered beam. Immune response was quantified through analysis of immunohistological images from each study, specifically looking at fluorescent markers for neuronal nuclei and astrocytes, to assess neuronal dieback and gliosis. Results demonstrate that the severity of the immune response, within the first 50 μm of the device, is highly correlated with device stiffness, as opposed to device modulus or cross-sectional area independently. In general, commercially available devices are around two to three orders of magnitude higher in stiffness than devices which induced a minimal tissue response. These results have implications for future device designs aiming to decrease chronic tissue response and achieve increased long-term functionality.

Keywords: intracortical implant; microelectrodes; stiffness; immunohistochemistry; immune response; neural interface response; neural interface

1. Introduction

Paralysis and limb loss pose significant personal, financial, and health burdens. Each year in the U.S. alone, there are over 17,500 cases of spinal cord injury where less than 1% achieve complete recovery [1]. The nationwide prevalence of amputees is even higher at 185,000 new cases each year [2]. To address this issue, engineers and scientists are developing a range of technologies with the intent of bypassing the damaged component of the peripheral or central nervous system, to replace or restore lost motor function [3]. State-of-the-art devices are implanted intracortically, or directly into the brain, where they can record biopotentials associated with voluntary movement [4]. Neural data can then be decoded and used to drive the movement of assistive devices and prosthetic limbs, or control stimulation for functional restoration of paralyzed limbs [5,6].

While many groups have demonstrated success resolving neural signals with intracortical probes for periods of about one year [7,8], these devices tend to lose their ability to record neural signals for longer time periods [4,8,9], limiting more widespread clinical use. While there are multiple factors influencing device performance, one prominent hypothesis for device failure pertains to a

chronic immune response characterized by glial encapsulation of the device, as well as local neuronal death [10,11]. Both of these compromise stable neural recordings over time. It has been suggested that a drastic mismatch in mechanical properties between the soft brain tissue and stiff neural implant may regulate the immune response [12–14]. Commercially available devices are fabricated using materials with a high elastic modulus, resulting in stiff devices that create concentrations of mechanical stress at the tissue interface [15], and provoke a significant, persistent immune response.

A common goal in the neuroengineering community is the development of more biocompatible implants, which elicit a decreased tissue response, with the intent of increasing their functional lifetime. These efforts are largely divided into two groups: (1) creating devices that are significantly smaller than the state-of-the-art [16,17], or (2) fabricating devices from softer materials to bridge the mechanical mismatch at the brain-device interface [18,19]. Both approaches have yielded promising results, such as decreased neuronal death and glial encapsulation, raising the possibility that a common link exists between both approaches. Our hypothesis is that these outcomes may be attributed to a single underlying parameter hereafter referred to as stiffness (k_b), a function of both the material properties and geometric dimensions of the device.

Based on the mechanics of static bodies, an implantable neural probe may be treated as a simple cantilevered beam, where the beam is fixed on one end, while a downward force is placed on the other end, causing a deflection [20]. The magnitude of the deflection is inversely proportional to the stiffness of the probe, with greater deflections associated with lower stiffness. Changes in the physical dimensions and/or the mechanical properties of the probe modulate its overall stiffness. The same is true for implantable devices. Devices with lower stiffness values, or greater flexibility, can be created by modifying the cross-sectional area (CSA) and/or by using softer constituent materials.

However, 'stiffness' (or 'flexibility') is often used synonymously to describe the softness or modulus of the implantable device or device substrate, even though stiffness must consider the contributions of device dimensions. For example, while polymer-based devices may be comprised of inherently soft materials, whether or not the device is highly flexible depends on more than just their material makeup. Instead, stiffness (k_b) assessments can be made based on calculations incorporating device dimensions to determine relative flexibility as compared to commercially available and other novel devices. The novelty of this study is the recognition that histological outcomes across material and geometric properties may be correlated to a single consolidated variable, k_b, as opposed to relating changes in histological outcomes to a single aspect of device design.

Here, we re-evaluated a number of studies reporting details on device design and the histological outcomes following implantation in rodent brain. The analysis draws upon studies utilizing a variety of devices fabricated from a wide range of materials and dimensions, yielding a range of stiffness values. Through quantitative analysis of previously published immunohistological images, we demonstrate that the severity of the immune response is highly correlated with device stiffness. This is a function of both elastic modulus and size, in contrast to correlations considering only modulus or cross-sectional dimensions independently.

2. Materials and Methods

2.1. Stiffness Calculations

Table 1 lists the studies and devices used in the meta-analysis. All devices were treated as simplified cantilevered beams (Figure 1) in order to solve for bending stiffness, k_b, as a function of area moment of inertia, I, device length, L, and Young's modulus, E, (Equation (1) [20]).

Device tip geometries and shank asymmetries were neglected for the sake of simplicity. It is important to note that many single shank devices do exhibit tapered geometries meaning that cross-sectional area, and area moment of inertia, are not necessarily uniform along the length of the device. However, preliminary computational modeling suggests that using average width values does not have a significant effect on stiffness calculations. Specifically, use of a simplified symmetric

model resulted in a 12% difference in maximum tip deflection in the cantilevered device bending simulation, when compared to the original tapered geometries (Figure 2). It is important to mention, however, that the tapering angle used in this simulation was relatively high when compared to those reported. Therefore, this represents a 'worst-case scenario' for difference in tip deflection.

Table 1. Devices from studies used in meta-analysis.

Author, Year	Material	Modulus	CSA (μm²)	Calculated Stiffness k_b (N/m)	Time Implanted	Stain Analyzed
Mercanzini et al., 2008 [21]	Polyimide	2.5 GPa	4200	0.00024	1 week	GFAP
Harris et al., 2011 [13]	Nanocomposite (poly(vinylacetate) and cellulose)	12 MPa	51,200	0.49	4 weeks	NeuN and GFAP
Biran et al., 2005 [11]	Silicon	179 GPa	3000	1.12	4 weeks	NeuN and GFAP
Knaack et al., 2016 [22]	Silicon	179 GPa	1875	0.15	4 weeks	NeuN and GFAP
Lee et al., 2017 [23]	OSTE soft (thiol-ene-epoxy)	6 MPa	5600	0.00016	4 weeks	NeuN and GFAP
Lewitus et al., 2014 [24]	Agarose with carbon nanotubes	Agarose-85 MPa	8220	0.02	4 weeks	GFAP
Kozai et al., 2012 [25]	Carbon fiber	234 GPa	38	0.01	2 weeks	NeuN and GFAP
Thelin et al., 2011 [26]	Stainless steel microwire (50 μm and 200 μm diameter)	200 GPa	50 μm: 1963 200 μm: 31416	50 μm: 32 200 μm: 8080	12 weeks	NeuN and GFAP
Lind et al., 2010 [27]	Bundled tungsten microwires in gelatin	Tungsten-411 GPa	70,686	7940	6 weeks	GFAP

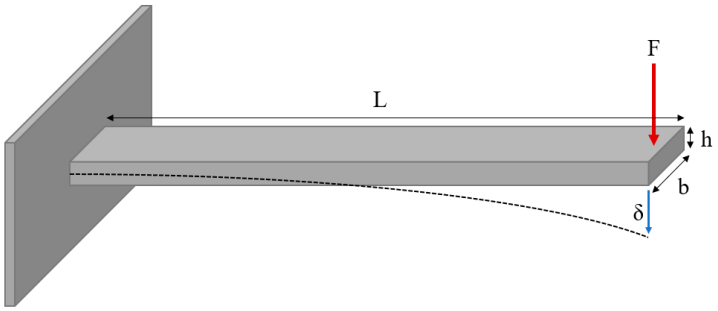

Figure 1. Diagram of a cantilevered beam. The beam is fixed on one end while a force on the opposite end produces a displacement, δ. Dimensions depicted are beam length, L, beam width, b, and beam thickness, h.

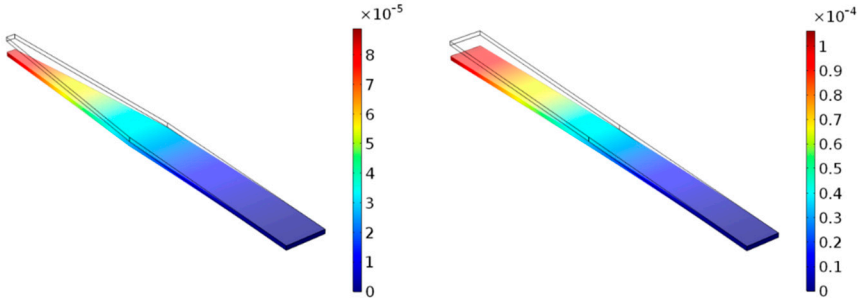

Figure 2. Computer simulated bend tests. Cantilever bend tests were used to determine the percent difference between device geometries with tapered and symmetrical shanks. In this case, shank (**A**) featured a width of 290 μm and tapered to 65 μm starting halfway down the shank. Shank (**B**) featured a width of 234 μm, calculated based on the weighted average of width down the length of shank (**A**). Both shanks were 30 μm thick and 3 mm long. Colored scale bars indicate deflection in meters.

Bending simulations were performed in COMSOL Multiphysics® v. 5.2. (COMSOL AB, Stockholm, Sweden) and the setup mirrored the cantilever-style bend test depicted in Figure 1. Further evaluation using Linear Buckling Analysis in COMSOL revealed only an 8% difference in critical buckling force between either geometries, indicating they are mechanically similar. Therefore, representative stiffness values (Equation (1) [20]) were calculated using average values of device width along the length of the shank. For devices with polymer coatings, stiffness was assumed to be dominated by the stiffest constituent material, and calculated accordingly. Most devices did not exhibit tapering as severe as the simulation presented above; rather, this was to illustrate the worst-case scenario. As such, most of the devices exhibit less than an 8 or 12% difference in critical buckling force and maximum tip deflection, respectively. All devices were treated as having either rectangular cross sections with height, h, and width, b, or circular cross sections with diameter, d, affecting the way in which moment of inertia of the cross-sectional area was calculated (Equations (2) and (3) [20]). Length was taken to be the overall length of the device shank, unless the implantation depth was otherwise stated in the study.

$$k_b = \frac{3EI}{L^3} \tag{1}$$

$$I_{rectangle} = \frac{bh^3}{12} \tag{2}$$

$$I_{circle} = \frac{\pi d^4}{64} \tag{3}$$

2.2. Image Analysis

The immune response for each study was quantified by analysis of fluorescent immunohistochemical images, from staining with several cell markers commonly associated with the immune response. For the purposes of this analysis, we focused on stains for neurons and astrocytes, specifically neuronal nuclei (NeuN) and glial fibrillary acidic protein (GFAP), a protein expressed in astrocytes.

Images were analyzed using Fiji [28], an open source image processing software based on ImageJ [29] (NIH). A custom macro was created to select the perimeter of the device within the image, and subsequently create concentric bands in 50 µm increments, while calculating the area in each band. For GFAP analysis, we computed the average intensity of GFAP immunofluorescence within each concentric band surrounding the probe (Figure 3a). For NeuN analysis, neurons were manually counted within each band using Fiji's Cell Counter plugin to quantify neuronal density (Figure 3b). Both GFAP intensity and neuronal density were normalized by dividing each band by the value in a band at least 200–250 µm from the device perimeter. This was done to ensure normalization with respect to tissue expected to be relatively unaffected by the implant. If healthy tissue samples were provided by the study, values were normalized with respect to areas from those samples.

While several of these studies reported their own analyses of fluorescent images, we chose not to include these quantifications in this meta-analysis. This was done in order to ensure that all NeuN density and GFAP intensity values were measured and normalized consistently across all studies, for accurate comparison. However, it is important to note that studies often feature figures that best illustrate the point of the study, i.e., fluorescent images that exemplify a reduced immune response. Therefore, our results likely reflect a conservative estimate of correlations between immune markers and device parameters.

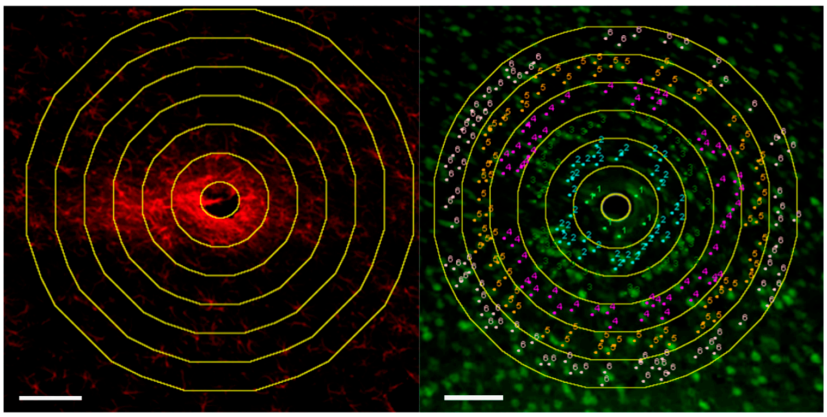

(**a**) (**b**)

Figure 3. Example image analysis on a stainless steel microwire. Scale bar 100 µm. (**a**) glial fibrillary acidic protein (GFAP) intensity and (**b**) neuronal density quantification in 50 µm concentric bands. Adapted from Thelin et al., 2011 [26]. Scale bar = 100 µm.

2.3. Statistical Analysis

To examine the possible relationships between material properties, dimensions, and device flexibility with both neuronal density and GFAP intensity, a Spearman rank correlation coefficient was calculated for each data set using functions available in MATLAB R2017a (MathWorks, Natick, MA, USA). Spearman correlation is a nonparametric test which assesses the monotonic relationship between ranked datasets. Good correlation is indicated by ρ values closest to 1 or 1 for positive and negative correlations respectively, with a high correlation being between 0.70 to 1.00 (or −0.70 to −1.0) [30]. A p-value less than 0.05 was taken as indicative of a significant correlation.

3. Results

Calculated stiffness levels varied over six orders of magnitude ranging from 8×10^3 to 1.6×10^{-4} N/m. Statistical analysis across multiple studies showed a high positive correlation ($\rho = 0.89$, $p < 0.05$) between device stiffness and normalized GFAP intensity, within a 50-µm band of the device perimeter, indicating that gliosis is more severe when using a stiffer implant (Figure 4).

Additionally, there was a high negative correlation ($\rho = -0.92$, $p < 0.05$) between device stiffness and normalized NeuN density in the same area, indicating that neuronal loss is increased when using a stiffer implant.

Device modulus and cross-sectional area did not exhibit significant correlation values within the same band, for either GFAP intensity or NeuN density, suggesting that the dependence on stiffness is a contributing factor in the severity of the immune response (Table 2). However, results also suggest that this trend is only relevant within the first 50 µm around the device. Outside of the first 50 µm band, neither GFAP intensity nor neuronal density show good, significant correlation with device stiffness, with the exception of GFAP intensity in the 100–150 µm band, therefore these data was not shown.

Table 2. Spearman's rho correlation results for 0–50 µm band.

			Stiffness	**Modulus**	**CSA**
Spearman's rho	GFAP Intensity	Correlation Coefficient	0.89 *	0.62	0.42
		Significance (two-tailed)	0.001	0.06	0.23
		N	10	10	10
	Neuronal Density	Correlation Coefficient	−0.92 *	−0.09	−0.5
		Significance (two-tailed)	0.01	0.85	0.27
		N	7	7	7

*: $p < 0.05$.

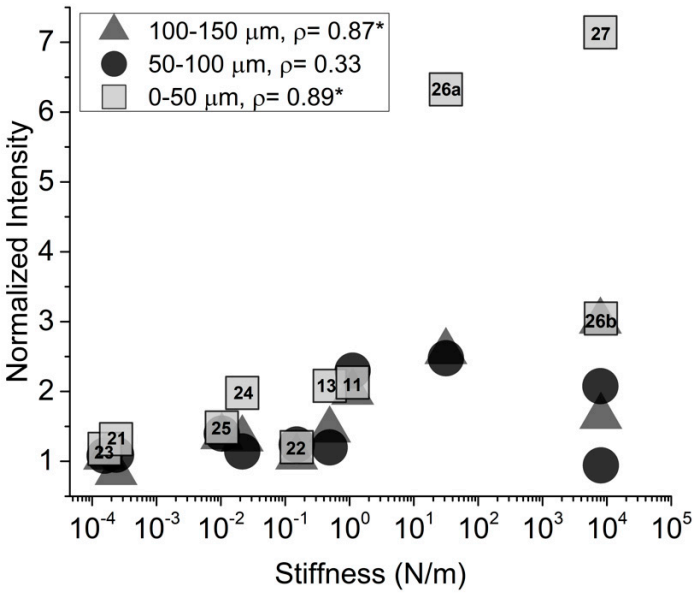

Figure 4. GFAP intensity analysis from GFAP-stained fluorescent images. Normalized intensity as a function of device stiffness three concentric 50 μm bands from device perimeter. * $p < 0.05$. Numbers indicate reference from Table 1. References are only included for 0–50 μm data, but all points aligned vertically are from the same reference. 26a and 26b reference the 50 μm and 200 μm stainless steel devices, respectively.

4. Discussion

Our meta-analysis across multiple studies indicated that the tissue response triggered during implantation may be most closely correlated with stiffness of an implanted device, as opposed to material moduli or geometric properties independently. Devices featured in this study exhibit stiffness values ranging from 10^{-4} to 10^{3} N/m. For reference, a commercially available Michigan-style silicon probe might exhibit a stiffness around 10^{2} N/m. Devices with a lower calculated bending stiffness exhibited decreased amounts of gliosis and neuronal death around the perimeter of the implant when compared with stiffer devices. These results were found to be significant within the first 50 μm of the device boundary, which is of critical importance in the context of functional neural recordings. Typically, neurons must be within 50 μm of the device electrodes in order to resolve single unit recordings at appropriate signal to noise ratios [31], and a severe immune response within this range would limit the device capabilities. Previously published studies have also reported on immune response with respect to 50 μm bands as important landmarks for histological outcomes [13,23]. Improved histological outcomes with respect to both GFAP intensity and NeuN density appeared to level off when a device reached the 10^{-1} to 10^{-2} N/m stiffness range (Figures 4 and 5) indicating that this could serve as a threshold for optimal device stiffness. This stiffness could be achieved with a commercially available Michigan-style probe by reducing the thickness from 50 μm to 10 μm while maintaining an average width of 125 μm and an implantation length of 2 mm. Stiffness of tapered devices may be more accurately calculated using cantilevered setups or computational models.

Overall, high correlation between device stiffness and the severity of the immune response may be a representation of how well these devices are able to move with the brain. Cross-sectional area or elastic modulus alone do not provide a full picture: a soft object may be so large that it is stiff and cannot flex with the brain. Conversely, a small device made from a material with a high elastic modulus may face the same issue. It has been well documented that the brain experiences significant micromotion due to breathing and vascular pulsation [32]. It is likely that decreased stiffness allows these devices to move with the brain, and therefore put less strain on the surrounding tissue, perhaps leading to a less significant tissue response.

In general, these findings support approaches to changing either the material properties, or physical dimensions of devices, to reduce the severity of the tissue response. Ideally, devices featuring both soft materials and small dimensions would offer improved tissue response, but in the absence of an insertion aid, mechanical considerations must also inform the minimal stiffness required to successfully penetrate the brain. This specific limitation explains a lack of histological studies in the literature performed, using highly soft and flexible devices which would provide additional insight into the relationship between flexibility and tissue response. Additionally, very stiff devices made from high modulus materials are prone to brittle fracture, which places limits on the minimum achievable dimensions during fabrication. Furthermore, ultra-small devices have limited available surface area for electrode sites on device structures, limiting the creation of high-density probes.

The results of this meta-analysis should however encourage further exploration of materials for devices which can be fabricated in a way that limits overall stiffness (k_b). This can be done through a reduction of material modulus (E) or a cross-sectional moment of inertia (I), with the goal of better matching stiffness to that of brain tissue, and subsequently improving chronic integration with surrounding tissue. Additionally, the possibility remains that the immune response may be a result of cells responding to stress concentrations due to material mismatch, as opposed to stiffness of the device itself. This hypothesis could be tested directly using an approach in which probe geometries are kept constant while varying material stiffness, or similarly, maintaining stiffness but using varied cross-sectional geometries.

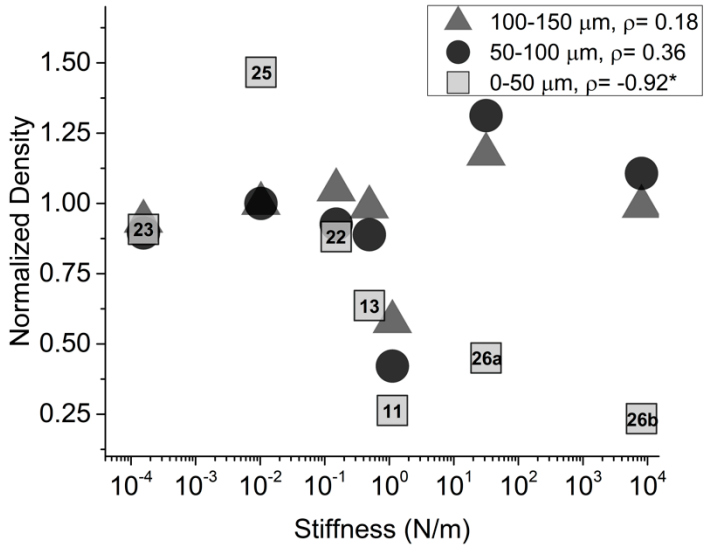

Figure 5. Neuronal density analysis from neuronal nuclei (NeuN)-stained fluorescent images. Normalized neuronal density as a function of device stiffness three concentric 50 μm bands from device perimeter. * $p < 0.05$. Numbers indicate reference from Table 1. References are only included for 0–50 μm data, but all points aligned vertically are from the same reference. 26a and 26b reference the 50 and 200 μm stainless steel devices, respectively.

5. Conclusions

Intracortical device stiffness may influence the severity of the chronic immune response, more than size or material properties of the device independently. Our novel results, which draw upon findings from multiple studies, indicate that device stiffness is especially important in close proximity to the device perimeter, which may profoundly affect the ability of devices to record from nearby neurons.

Author Contributions: Conceptualization, J.J.P. and A.M.S.; Methodology, A.M.S., B.J.B., and J.J.P.; Software, B.J.B. and A.M.S.; Validation, A.M.S.; Formal Analysis, A.M.S.; Investigation, A.M.S., C.K., and A.A.; Resources, J.J.P.; Data Curation, A.M.S.; C.K., and A.A.; Writing—Original Draft Preparation, A.M.S.; Writing—Review & Editing, A.M.S., B.J.B., S.F.C., V.D.V., and J.J.P.; Visualization, A.M.S. and B.J.B.; Supervision, J.J.P.; Project Administration, J.J.P.; Funding Acquisition, J.J.P.

Funding: This work was supported by the Office of the Assistant Secretary of Defense for Health Affairs through the Peer Reviewed Medical Research Program [grant No. W81XWH-15-1-0607]. Opinions, interpretations, conclusions and recommendations are those of the authors and are not necessarily endorsed by the Department of Defense. Additional support was provided by Defense Advanced Research Projects Agency (DARPA) BTO [grant No. HR0011-15-2-0017]; and the Eugene McDermott Graduate Fellowship Program, Richardson, TX [grant No. 201606] at University of Texas at Dallas.

Conflicts of Interest: The authors declare no conflicts of interest. The funders had no role in the design of the study; in the collection, analyses, or interpretation of data; in the writing of the manuscript, and in the decision to publish the results.

References

1. White, N.H.; Black, N.H. Spinal cord injury facts and figures at a glance. *Natl. Spinal Cord Inj. Stat. Cent.* **2017**, *35*, 197–198. [CrossRef]
2. Ziegler-Graham, K.; MacKenzie, E.J.; Ephraim, P.L.; Travison, T.G.; Brookmeyer, R. Estimating the prevalence of limb loss in the United States: 2005 to 2050. *Arch. Phys. Med. Rehabilit.* **2008**, *89*, 422–429. [CrossRef] [PubMed]
3. Tsu, A.P.; Burish, M.J.; GodLove, J.; Ganguly, K. Cortical neuroprosthetics from a clinical perspective. *Neurobiol. Dis.* **2015**, *83*, 154–160. [CrossRef] [PubMed]
4. Jorfi, M.; Skousen, J.L.; Weder, C.; Capadona, J.R. Progress towards biocompatible intracortical microelectrodes for neural interfacing applications. *J. Neural Eng.* **2015**, *12*, 011001. [CrossRef] [PubMed]
5. Hochberg, L.R.; Bacher, D.; Jarosiewicz, B.; Masse, N.Y.; Simeral, J.D.; Vogel, J.; Haddadin, S.; Liu, J.; Cash, S.S.; van der Smagt, P.; et al. Reach and grasp by people with tetraplegia using a neurally controlled robotic arm. *Nature* **2012**, *485*, 372–375. [CrossRef] [PubMed]
6. Pancrazio, J.J.; Peckham, P.H. Neuroprosthetic devices: How far are we from recovering movement in paralyzed patients? *Expert Rev. Neurother.* **2009**, *9*, 427–430. [CrossRef] [PubMed]
7. Chestek, C.A.; Gilja, V.; Nuyujukian, P.; Foster, J.D.; Fan, J.M.; Kaufman, M.T.; Churchland, M.M.; Rivera-alvidrez, Z.; Cunningham, J.P.; Ryu, S.I.; et al. Long-term stability of neural prosthetic control signals from silicon cortical arrays in rhesus macaque motor cortex. *J. Neural Eng.* **2011**, *8*, 045005. [CrossRef] [PubMed]
8. Barrese, J.C.; Rao, N.; Paroo, K.; Triebwasser, C.; Vargas-Irwin, C.; Franquemont, L.; Donoghue, J.P. Failure mode analysis of silicon-based intracortical microelectrode arrays in non-human primates. *J. Neural Eng.* **2013**, *10*, 066014. [CrossRef] [PubMed]
9. Ward, M.P.; Rajdev, P.; Ellison, C.; Irazoqui, P.P. Toward a comparison of microelectrodes for acute and chronic recordings. *Brain Res.* **2009**, *1282*, 183–200. [CrossRef] [PubMed]
10. Polikov, V.S.; Tresco, P.A.; Reichert, W.M. Response of brain tissue to chronically implanted neural electrodes. *J. Neurosci. Methods* **2005**, *148*, 1–18. [CrossRef] [PubMed]
11. Biran, R.; Martin, D.C.; Tresco, P.A. Neuronal cell loss accompanies the brain tissue response to chronically implanted silicon microelectrode arrays. *Exp. Neurol.* **2005**, *195*, 115–126. [CrossRef] [PubMed]
12. Andrei, A.; Welkenhuysen, M.; Nuttin, B.; Eberle, W. A response surface model predicting the in vivo insertion behavior of micromachined neural implants. *J. Neural Eng.* **2011**, *9*, 016005. [CrossRef] [PubMed]
13. Harris, J.P.; Capadona, J.R.; Miller, R.H.; Healy, B.C.; Shanmuganathan, K.; Rowan, S.J.; Weder, C.; Tyler, D.J. Mechanically adaptive intracortical implants improve the proximity of neuronal cell bodies. *J. Neural Eng.* **2011**, *8*, 066011. [CrossRef] [PubMed]
14. Moshayedi, P.; Ng, G.; Kwok, J.C.F.; Yeo, G.S.H.; Bryant, C.E.; Fawcett, J.W.; Franze, K.; Guck, J. The relationship between glial cell mechanosensitivity and foreign body reactions in the central nervous system. *Biomaterials* **2014**, *35*, 3919–3925. [CrossRef] [PubMed]
15. Sridharan, A.; Nguyen, J.K.; Capadona, J.R.; Muthuswamy, J. Compliant intracortical implants reduce strains and strain rates in brain tissue in vivo. *J. Neural Eng.* **2015**, *12*, 036002. [CrossRef] [PubMed]

16. Pancrazio, J.J.; Deku, F.; Ghazavi, A.; Stiller, A.M.; Rihani, R.; Frewin, C.L.; Varner, V.D.; Gardner, T.J.; Cogan, S.F. Thinking small: Progress on microscale neurostimulation technology. *Neuromodulation* **2017**, *20*, 745–752. [CrossRef] [PubMed]
17. Deku, F.; Cohen, Y.; Joshi-Imre, A.; Kanneganti, A.; Gardner, T.J.; Cogan, S.F. Amorphous silicon carbide ultramicroelectrode arrays for neural stimulation and recording. *J. Neural Eng.* **2018**, *15*. [CrossRef] [PubMed]
18. Simon, D.M.; Charkhkar, H.; John, C., St.; Rajendran, S.; Kang, T.; Reit, R.; Arreaga-Salas, D.; McHail, D.G.; Knaack, G.L.; Sloan, A.; et al. Design and demonstration of an intracortical probe technology with tunable modulus. *J. Biomed. Mater. Res. Part A* **2017**, *105*, 159–168. [CrossRef] [PubMed]
19. Weltman, A.; Yoo, J.; Meng, E. Flexible, penetrating brain probes enabled by advances in polymer microfabrication. *Micromachines* **2016**, *7*, 180. [CrossRef]
20. Hibbeler, R.C. *Mechanics of Materials*, 10th ed.; Pearson: London, UK, 2016; ISBN 0134319656.
21. Mercanzini, A.; Cheung, K.; Buhl, D.L.; Boers, M.; Maillard, A.; Colin, P.; Bensadoun, J.C.; Bertsch, A.; Renaud, P. Demonstration of cortical recording using novel flexible polymer neural probes. *Sens. Actuators A Phys.* **2008**, *143*, 90–96. [CrossRef]
22. Knaack, G.L.; McHail, D.G.; Borda, G.; Koo, B.; Peixoto, N.; Cogan, S.F.; Dumas, T.C.; Pancrazio, J.J. In vivo characterization of amorphous silicon carbide as a biomaterial for chronic neural interfaces. *Front. Neurosci.* **2016**, *10*, 301. [CrossRef] [PubMed]
23. Lee, H.C.; Ejserholm, F.; Gaire, J.; Currlin, S.; Schouenborg, J.; Wallman, L.; Bengtsson, M.; Park, K.; Otto, K.J. Histological evaluation of flexible neural implants; Flexibility limit for reducing the tissue response? *J. Neural Eng.* **2017**, *14*, 036026. [CrossRef] [PubMed]
24. Lewitus, D.Y.; Smith, K.L.; Landers, J.; Neimark, A.V.; Koh, J. Bioactive agarose carbon-nanotube composites are capable of manipulating brain-implant interface. *J. Appl. Polym. Sci.* **2014**, *131*, 317–323. [CrossRef] [PubMed]
25. Yoshida Kozai, T.D.; Langhals, N.B.; Patel, P.R.; Deng, X.; Zhang, H.; Smith, K.L.; Lahann, J.; Kotov, N.A.; Kipke, D.R. Ultrasmall implantable composite microelectrodes with bioactive surfaces for chronic neural interfaces. *Nat. Mater.* **2012**, *11*, 1065–1073. [CrossRef] [PubMed]
26. Thelin, J.; Jörntell, H.; Psouni, E.; Garwicz, M.; Schouenborg, J.; Danielsen, N.; Linsmeier, C.E. Implant size and fixation mode strongly influence tissue reactions in the CNS. *PLoS ONE* **2011**, *6*, e16267. [CrossRef] [PubMed]
27. Lind, G.; Linsmeier, C.E.; Thelin, J.; Schouenborg, J. Gelatine-embedded electrodes—A novel biocompatible vehicle allowing implantation of highly flexible microelectrodes. *J. Neural Eng.* **2010**, *7*. [CrossRef] [PubMed]
28. Schindelin, J.; Arganda-Carreras, I.; Frise, E.; Kaynig, V.; Longair, M.; Pietzsch, T.; Preibisch, S.; Rueden, C.; Saalfeld, S.; Schmid, B.; et al. Fiji: An open-source platform for biological-image analysis. *Nat. Methods* **2012**, *9*, 676–682. [CrossRef] [PubMed]
29. Schneider, C.A.; Rasband, W.S.; Eliceiri, K.W. NIH Image to ImageJ: 25 years of image analysis. *Nat. Methods* **2012**, *9*, 671–675. [CrossRef] [PubMed]
30. Mukaka, M.M. Statistics corner: A guide to appropriate use of correlation coefficient in medical research. *Malawi Med. J.* **2012**, *24*, 69–71. [CrossRef] [PubMed]
31. Buzsáki, G. Large-scale recording of neuronal ensembles. *Nat. Neurosci.* **2004**, *7*, 446–451. [CrossRef] [PubMed]
32. Gilletti, A.; Muthuswamy, J. Brain micromotion around implants in the rodent somatosensory cortex. *J. Neural Eng.* **2006**, *3*, 189–195. [CrossRef] [PubMed]

SCIENTIFIC REPORTS

OPEN

A Mosquito Inspired Strategy to Implant Microprobes into the Brain

Andrew J. Shoffstall[1,2], Suraj Srinivasan[1,2], Mitchell Willis[1,2], Allison M. Stiller[3], Melanie Ecker[4,6], Walter E. Voit[3,4,5,6], Joseph J. Pancrazio[3,4,6] & Jeffrey R. Capadona[1,2]

Received: 18 October 2017
Accepted: 13 December 2017
Published online: 09 January 2018

Mosquitos are among the deadliest insects on the planet due to their ability to transmit diseases like malaria through their bite. In order to bite, a mosquito must insert a set of micro-sized needles through the skin to reach vascular structures. The mosquito uses a combination of mechanisms including an insertion guide to enable it to bite and feed off of larger animals. Here, we report on a biomimetic strategy inspired by the mosquito insertion guide to enable the implantation of intracortical microelectrodes into the brain. Next generation microelectrode designs leveraging ultra-small dimensions and/or flexible materials offer the promise of increased performance, but present difficulties in reliable implantation. With the biomimetic guide in place, the rate of successful microprobe insertion increased from 37.5% to 100% due to the rise in the critical buckling force of the microprobes by 3.8-fold. The prototype guides presented here provide a reproducible method to augment the insertion of small, flexible devices into the brain. In the future, similar approaches may be considered and applied to the insertion of other difficult to implant medical devices.

The parasitic bite of a female mosquito allows it to both inject an anticoagulant to thin the host's blood, and then, like a miniature hypodermic needle, suck out blood to aid in egg production[1]. To enable the mosquito to penetrate the host's skin with a set of blood-sucking needles (fascicles), multiple mechanisms are employed[2]. Specifically, the mosquito must increase the critical buckling force of each fascicle, while also reducing the force required to penetrate the skin.

A series of recent studies have discussed strategies taken by nature to prevent buckling and, in effect, improve the performance of percutaneous instruments (e.g., microneedles)[3]. Sakes *et al.* categorized strategies to either increase the critical buckling load, or conversely decrease the required penetration load. Interestingly, the mosquito does both, inspiring the design of "painless" microneedles[2,4]. We are particularly intrigued by the mosquito's ability to increase the critical buckling force for adaptation to our application to implant intracortical microelectrodes into the brain. These devices offer a means of probing the functional neuronal network activity for both basic science and rehabilitation applications[5–7].

To increase the critical buckling load, the mosquito reduces the effective length of its fascicles by using a second structure, the labium, as an insertion guide (Fig. 1, left)[2,4]. To prevent fascicle buckling during insertion, the critical load must be higher than the penetration load. The mosquito fascicle and host tissue interface does not perfectly follow Euler's formula for critical buckling load of an ideal beam due to complementary mechanisms of insertion (violating both the static condition and rigid-beam condition). However, one of the takeaways remains true—the effective length of the implant dictates the critical load that it can withstand without buckling[4]. Length and end-conditions (combined to make up the denominator "effective length" or "KL") play an important role, defining an inverse-squared relationship to critical buckling force such that a 2-fold reduction of effective length results in a 4-fold increase of Euler critical load, $F_{\text{Euler Critical}}$ (Equation 1):

$$F_{Euler\ critical} = \frac{\pi^2 EI}{(KL)^2} \quad (1)$$

[1]Department of Biomedical Engineering, Case Western Reserve University, Cleveland, OH, USA. [2]Advanced Platform Technology Center, Rehabilitation Research and Development, Louis Stokes Cleveland Department of Veterans Affairs Medical Center, Cleveland, OH, USA. [3]Department of Bioengineering, The University of Texas at Dallas, Richardson, TX, USA. [4]Department of Materials Science and Engineering, The University of Texas at Dallas, Richardson, TX, USA. [5]Department of Mechanical Engineering, The University of Texas at Dallas, Richardson, TX, USA. [6]Center for Engineering Innovation, The University of Texas at Dallas, Richardson, TX, USA. Correspondence and requests for materials should be addressed to J.R.C. (email: jeffrey.capadona@case.edu)

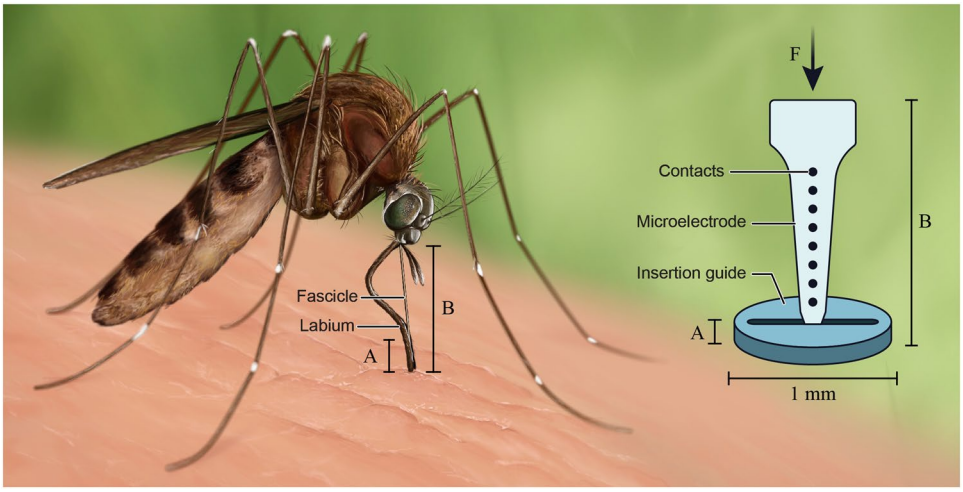

Figure 1. Mosquito-inspired guide to reduce buckling of flexible microelectrodes during insertion into brain tissue. Mosquitos use their labium (labeled above) to brace the fascicle during insertion through the tough skin. Mechanically, this changes the end-condition of the fascicle from a free- to a fixed-end condition and reduces the effective length. Similarly, our manufactured guide may be placed on the skull above the site of device implantation. A narrow slit, slightly wider than the microelectrode provides lateral support. The additional bracing prevents buckling. Figure was prepared by Erika Woodrum of the Cleveland FES Center, a contributor, with permission granted for use.

where *E* is the materials modulus of elasticity, I is the area moment of inertia, K is the effective length factor, and *L* is the unsupported length of the column. Through the use of the labium, the mosquito effectively reduces the length of the load bearing portion of the fascicle, enabling insertion of the higher aspect ratio needles, where the needles would not otherwise have been able to penetrate the skin. Intrigued by this capability, and with the goal of creating a new system for the implantation of ultra-small, flexible microelectrode devices into the brain, we set out to investigate whether a biomimetic strategy would enable an effective insertion guide approach (Fig. 1, right). Our work demonstrates for the first time that an insertion guide inspired by the fascicle/labium approach of the mosquito enables reliable insertion of microprobes within the brain.

Microelectrodes implanted in the cortex of the brain have the potential to be used in a number of exciting new neuroprosthetic applications specifically to enable brain-computer interface (BCI) and brain-machine interface (BMI) approaches. Neuroprostheses have the potential to improve the lives of individuals with paralysis and limb loss by reducing the burden of injury and enabling more full and interactive lives[5,8–10]. Unfortunately, penetrating intracortical microelectrodes such as those used for BMI applications demonstrate poor chronic neural recording performance and reliability[11,12]. The loss in performance is characterized by increased electrode contact and tissue impedance, decreased signal-to-noise ratio, and ultimately the inability to record from sufficient numbers of neurons to allow for robust decoding algorithms[13]. Performance typically degrades over several weeks-to-months, and is thought to result from both electromechanical and host tissue response mechanisms[13].

While the small size of microelectrodes minimizes, in part, the iatrogenic trauma to the brain during insertion, penetration of the brain tissue is still sufficient enough to damage the blood-brain barrier and initiate an immediate inflammatory response[14–16]. The resulting foreign body response yields encapsulation of the recording device and both physically and electrically isolates the device from the adjacent neurons[13,17]. The hypothesis that inflammation is a key mediator of device longevity has been supported by several key studies[13,17–22]. Therefore, many different designs for microelectrodes exist, with an ever increasing array of approaches to minimize both the injury from implantation, and the resulting neurodegenerative inflammatory response. Recent approaches have used smaller and smaller electrode designs as well as flexible materials to both minimize the microelectrode footprint and the resulting strain on the cortical tissue[23–36]. A challenge that arises, however, is that during insertion, the device must be stiff enough to pierce the brain tissue without buckling[13,37–40]. A number of innovative approaches to address the issue of buckling during insertion have been developed and has been recently reviewed[41]. Some of the reported approaches include coating microelectrodes with sacrificial polymers or coatings that dissolve away during or after insertion[42–47], fast insertion speeds[48], a variety of introducer designs[49–51], and materials that dynamically soften after insertion[38,40,52–54]. We recognized that the mosquito has solved the problem of reliable insertion of microscale needles into host tissue. Therefore, we sought to leverage the strategy used by the mosquito to enable robust insertion of novel microprobes into the brain. Mimicking the function should prove to be more broadly applicable to the various microelectrode designs currently under investigation.

To begin, guides were cut from plastic sheets made in varying dimensions ranging from 3 mm to 15 mm in diameter and 1/16″ to 1/8″ thickness using a laser cutter with motorized programmable x-y controls (150-Watt CO2 laser cutter, Universal ILS12.150D, Scottsdale, AZ). CAD drawings were created in CorelDRAW x6 (Ottawa, ON). During the optimization of the laser cutting process, we found that the following power settings to produce the highest quality cuts (achieving a balance between achieving the smallest kerf and least burnt edges possible): power (40%), speed (60%) and PPI (5000 dpi). A number of insertion guide materials were tested including

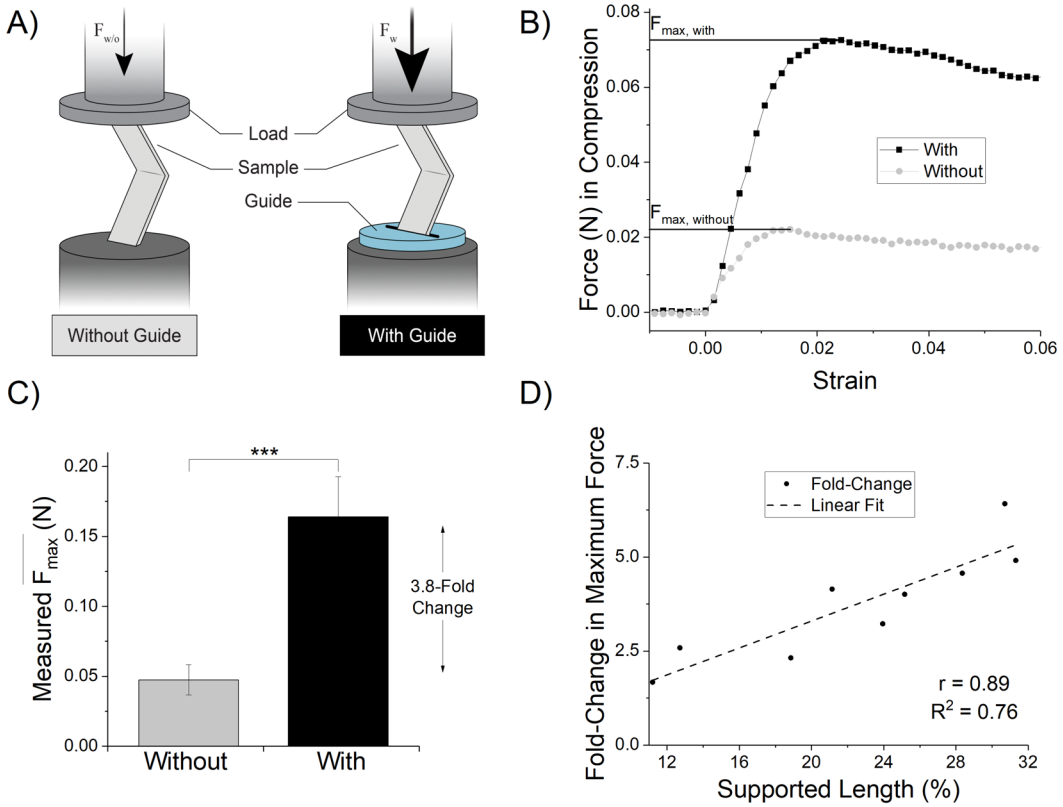

Figure 2. Mechanical testing of guide. (**A**) Illustration showing testing rig setup. Rectangular tests strips (n = 9) were placed in grips one side with a flat plate and force transducer opposing it. Maximal force in compression was measured with and without the guide in-place. (**B**) Representative mechanical testing traces for two back-to-back trials of the same dummy electrode. (**C**) Maximum force achieved in compression with and without the guide in-place, $p < 0.001$ (***), calculated by paired t-test of maximal achieved force with vs without guide in-place. (**D**) Scatterplot of fold-change in maximal force (i.e. fold-change = $(F_{max,with}/F_{max,without})$) for each sample plotted against supported length (%) of the sample. Samples were of varying lengths, while the guide remained a constant 1/16″ thickness. There is a very strong positive correlation as would be expected (i.e., the longer the probe, the more unsupported length there is to buckle). Part A of the figure was prepared by Erika Woodrum of the Cleveland FES Center, a contributor, with permission granted for use.

low-density polyethylene (LDPE), high-density polyethylene (HDPE), polyethylene terephthalate glycol (PETG), polytetrafluoroethylene (PTFE) and poly (methyl methacrylate) (PMMA). We found PTFE and PMMA provided the best machinability with our laser, allowing thin and uniform slits to be cut. Further, PMMA had the best post-processing transparency, allowing the ready visualization of underlying blood vessels and other brain structures. Additional design features were also possible, including angled slits for inserting at non-90° angles, guides with breakaway perforations, and guides with circular holes cut into them instead of slits (as would be used for fiber optic cables or microwires). The guides were produced such that a microelectrode could be inserted through the slit with the use of handheld forceps or custom-fit stereotaxic frames (Supplementary Figure 2).

With prototype labium mimetic guides fabricated, we next tested the buckling mechanics using a linear actuator and a force transducer (Fig. 2A). Thin rectangular films (n = 9 samples) were compressed axially with or without the guide in place in a paired fashion (n = 18 individual trials) and maximal force was recorded. Since the 2 mm displacement was not sufficient to cause plastic deformation of the PE dummy samples, we judged that randomized-paired testing (with and without the guide) on each sample would be appropriate.

Peak force was achieved rapidly followed by a sudden decline and plateau in force, characteristic of buckling (Fig. 2B). We found that the guide increased the average maximally achieved force ($\overline{F_{max}}$, Equation 2) by 3.8-fold (±1.5 S.D.; Fig. 2C), and that the effect on force augmentation was correlated with the length of the microprobe (Fig. 2D).

$$\overline{F_{max}} = \frac{\sum_{i=1}^{n}(F_{max})}{n} \quad (2)$$

The longer the microprobe, the less impact the 1/16″ guide (~1.6 mm) was able to effect. If we limited the microprobe lengths to 5-times that of the guide thickness (or the guide being 20% of the microprobe length), the ratio of $\overline{F_{max}}$ increase then became 4.5-fold (±1.1). The $\overline{F_{max}}$ for all microprobes was 160 mN with the guide, compared to 50 mN without the guide ($p < 0.001$).

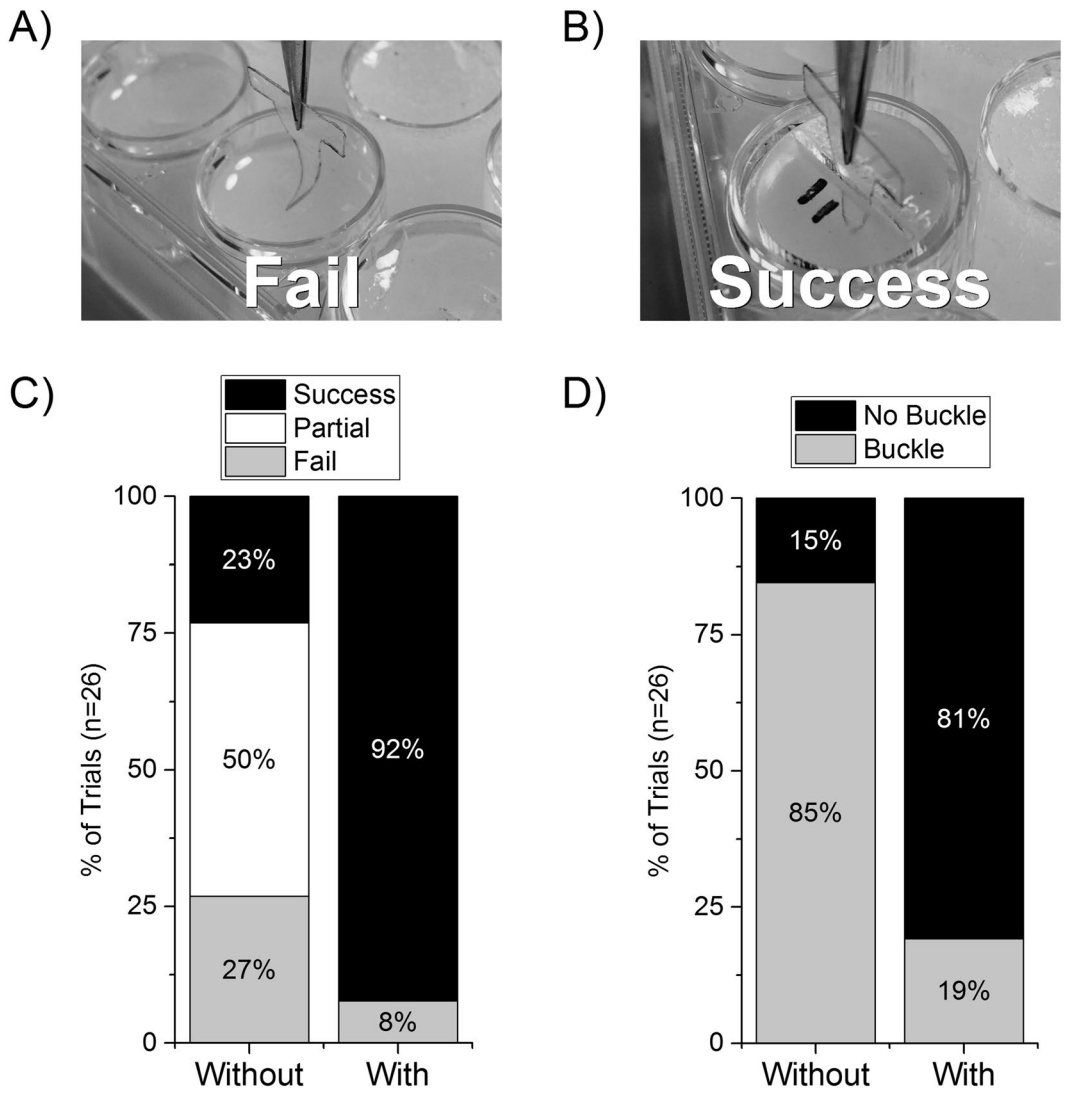

Figure 3. Agar gel model insertion with and without the guide. The microprobes were inserted using a stereotactic arm with a micropositioner. The microprobes were lowered to just above the surface of the gel, and inserted at a speed of ~1 mm/s. (**A**) Example of a failed insertion attempt without the guide in-place. Note the dummy microprobe buckling as it makes contact with the surface of the 0.6% agar model. (**B**) Example of a successful insertion with guide in place. (**C**) Successful rate of insertion with and without guides. (**D**) Rate of trials resulting in any buckling regardless of insertion status.

The critical design feature elucidated by this study was supported length, or the ratio of device length to guide thickness. This proportion was found to be largely determinant of maximal force before buckling. The design tradeoff of total device length versus desired depth of penetration is an important consideration. In this study, the depth of interest was set by the thickness of the rat cortex (~2 mm)[55]. Additional work is required to fully optimize and balance device length and cross-sectional geometry versus guide thickness. Furthermore, slit opening-thickness was minimized such that it was the smallest dimension possible, but still allowed the materials to slip between unimpeded. Operationally, this was approximately twice the film thickness (~150 µm). When testing, we found that a gap twice the thickness of the probe led to a good balance between easy slip between the two surfaces, without detrimentally impacting the bracing force of the guide. Tolerances 10–15 µm wider than the films themselves were too narrow and impeded insertion. Finer resolution laser cutting processes may enable a better optimization process to determine whether this gap thickness can be reduced further.

With an understanding of the design parameters between device and guide, we next developed a model of microprobe insertion with and without the guide, using 0.6% agar gel as a model for brain tissue[56]. Success was defined as complete insertion of the microprobe ~2 mm into the gel without any visible deformation of the microprobe; failure was everything else, including partial insertion or total deflection off the surface (Fig. 3A,B). Furthermore, insertion was still sometimes possible even in the event of buckling. However, buckling is potentially an undesirable outcome as it may mean the microprobe is then inserted at an angle and may not reach the desired brain structure target or perhaps be damaged. Interestingly, there was a marked difference in the number

Material		Approximate Young's Moduli (MPa)	Refs.
Silicon		~165,000	[61]
Pt/Ir (90%/10%)		~170,000	[62]
Cellulose nanocomposite	*(Pre/Stiff)(Post/Soft)*	4,2001.6	[40,63]
Thiol-ene/acrylateShape Memory Polymer	*(Pre/Stiff)(Post/Soft)*	~2,000~30	[28]
Rat brain tissue		0.015–0.45	[61,64,65]

Table 1. Young's moduli of example microelectrode substrates versus rat brain. While the methods and values vary in the reported literature, the relative magnitudes are conserved such that Young's moduli of typical electrode substrates are much greater than polymer-based microelectrode substrates, even dynamically changing materials in their 'stiff' state.

of successful attempts between those with and without the guide in place. The guide yielded successful insertion 92.3% of attempts versus 23.1% without the guide (Fig. 3C). Partial insertions, included as "failures" in the analysis, occurred 50% of the time without the guide and 0% with the guide (Fig. 3C). Moreover, with the guide, the dummy microprobes buckled only 19.2% of attempts versus 84.6% without the guide (Fig. 3D).

Encouraged by the substantial difference in implantation success rates achieved between conditions with and without the insertion guide, we next tested the impact of guided insertion on the implantation of intracortical microprobes into rat motor cortex. As mentioned above, many approaches have been developed to create intracortical microprobes that minimize implant mediated neuroinflammation[13], including those that involve materials that dynamically soften upon insertion into the brain[39,40,57–60]. Dynamically softening materials, rely on a responsive stimulus such as moisture or body heat to effect the change in material properties after insertion[40]. Dynamically softening microelectrodes are typically polymer nanocomposites or shape memory polymers (SMPs), and are thus orders of magnitude softer than traditional materials used in microelectrode design. For example, polymer microelectrodes remain softer at room temperature (2–5 GPa) than typical silicon, tungsten, or Pt/Ir microprobes (150–500 GPa) (Table 1)[28,39]. Furthermore, the extremely small size of the devices makes the implantation procedure challenging such that an insertion guide strategy could minimize the likelihood of SMP microprobe buckling.

In this study, fully softening thiol-ene SMP structures were fabricated similarly as previously reported[66] so that the onset of their glass-transition temperature was just above that of body temperature and moisture-induced plasticization of the polymer network would cause softening after rigid insertion (Supplementary Figure 1). Therefore, as the microprobes were implanted and heated above their glass transition temperature (T_g), the materials softened from ~2 GPa to ~30 MPa (indicated by vertical dashed gray line in Supplementary Figure 1).

While the system is designed to allow for successful insertion at room temperature, it was found that especially with an automated insertion system that controls the speed of insertion, the microprobes of chosen thickness were more prone to buckling, deflection and ultimately failed insertion without the use of an insertion guide (Fig. 4). With the insertion guide, we may be able to minimize device thickness in the future to achieve the same depth of penetration, leading to a less invasive implant.

We also examined the utility of the insertion guide in conjunction with the use of an automated motorized insertion system during *in vivo* implantations in the rat motor cortex (Kopf Instruments, Tujunga, CA, Model 2650 with a hydraulically driven micro-positioner). Due to the size of the guide, a large craniotomy was prepared (~1 cm^2), allowing the entire guide to be placed directly in contact with the dura. The guides significantly increased the rate of successful insertion of SMP microprobes ($p < 0.05$). Specifically, the insertion guide enabled 100% (8 of 8 trials) successful insertion using the automated system compared to 37.5% (3 of 8 trials) without the guide (Fig. 4). It was noted in an early experiment that the guides were not as effective if placed on the skull, leaving an air-gap in which the microprobes were not supported at the site of entry into the brain (Supplementary Figures 3 and 4). Future design iterations may include either (1) a smaller diameter guide that doesn't require such a large craniotomy, or (2) a beveled lip that allows the guide to be placed on the skull but with a recessed center which dips toward the brain surface.

Normally during intracranial microelectrode placement, the dura is reflected. As a demonstration of the added mechanical benefit to the insertion process, a dynamically softening SMP microprobe was inserted transdurally into rat brain (Supplementary Figure 5). Without the guide in place, buckling and failure to insert occurred every time. The microelectrodes (which are ~2 GPa at room temperature), buckled and deflected off the surface of the dura. With the guide in place, it became possible to insert the microelectrode through the tough dura. While it may still be preferred to reflect the dura to prevent shearing damage to the electronics on the face of the microelectrode, and to prevent an accelerated inflammatory response by dragging peripheral cells from the meninges into the parenchyma, insertion through the dura demonstrates the guide's value as added lateral support to prevent buckling.

In summary, inspired by the labium guide of the female mosquito, we developed a novel method for introducing flexible microprobes into the brain. The bioinspired insertion strategy significantly reduces the propensity for buckling during insertion by increasing the insertion force without buckling by a factor of ~4. While this is a great improvement, it should be noted that the mosquito achieves much higher insertion efficiency by using a multimodal delivery system including: 1) barbed maxillae integrated in their labrum that oppositely reciprocate and saw open the skin and break the surface tension[2,4], 2) an oscillatory insertion motion that results in a time-dependent shear thinning of the skin[3], and 3) a follower-force applied by the labrum that further optimizes

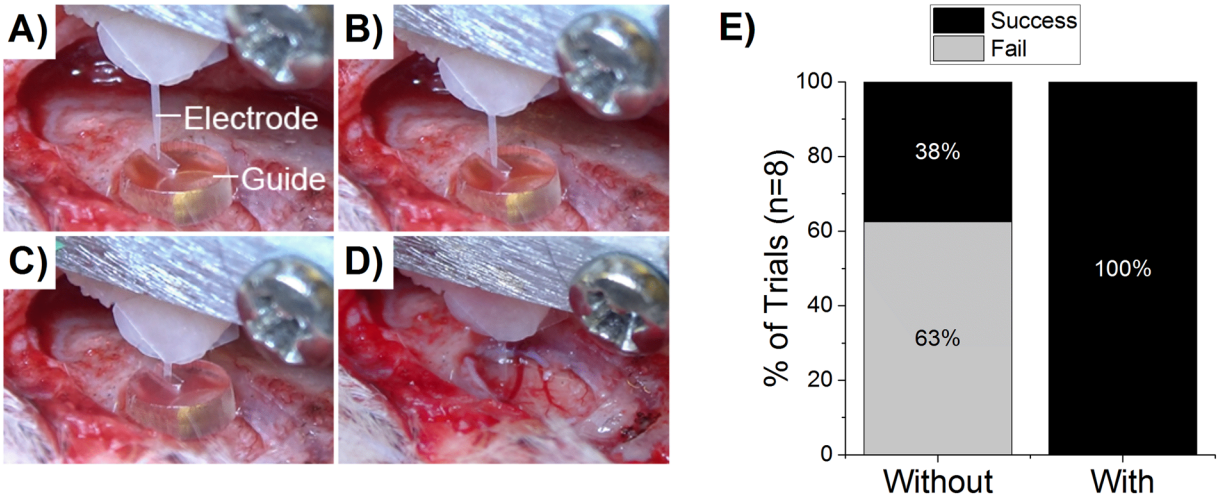

Figure 4. Implantation with shape memory polymer microelectrode with guide on brain surface. (**A**–**D**) feature progressive screen shots from a video taken during implantation of thiol-ene/acrylate microelectrodes. Guide thickness = 1 mm for reference. (**E**) 100% (8 of 8) insertion trials were successful with the automated insertion system and guide in place versus only 37.5% of trials without the guide.

	Critical Design Factors	Recommendations
Manufacturing	Heat Resistant Polymers; Laser Cutting Parameters (Speed, Power); Small Geometry, Precise Cuts; Scalability	PTFE, PMMA; Fast speed, low power <100 µm features; 100 devices in ~5 min
Mechanics	Supported Length; Slit Thickness; Guide Placement on Surface	>20% → >4x increase in F_{max}; 2x microelectrode thickness; Direct contact with dura
Usability	Visual characteristics; Placement and Removal Handling; Adherence to Surface During Insertion	Transparent materials; Design amenable to gripping tools; Thru holes for bonding to skull

Table 2. Critical Design Factors. A number of design factors were found to be critical to the manufacturability, mechanics, and usability of the guide.

the mechanics to reduce buckling[4]. The reader is referred to the above-referenced sources for additional information regarding the mosquito bite mechanism.

While acknowledging that the mosquito has a much more sophisticated delivery system for microneedles, our analog guides are more easily fabricated from off-the-shelf polymer sheeting and are readily implemented during surgery. Furthermore, it was possible to use our bioinspired guide as a complementary strategy to dynamically softening polymers which are themselves a promising strategy utilized to overcome buckling of microelectrodes during insertion. Together, using the combined strategy, it was possible to: 1) insert flexible devices transdurally (e.g. without prior reflection of the dura) and 2) insert flexible microelectrodes into rat brain using an automated motorized insertion device. The purpose of these experiments was to establish the proof-of-concept data and identify critical design factors in terms of manufacturing feasibility, buckle-prevention efficacy, and intraoperative usability (Table 2). The approach can be further optimized by tuning the guide's slit thickness and angle. While there are a number of other strategies to insert flexible electronics in the brain, the guide developed here is an additional tool and may be complementary to these other strategies. Finally, we envision the ease of implementation of our guide design to not just other microelectrode designs, but any other microscale medical device that suffers from difficulties in implantation.

Methods

Guide Design and Fabrication. Insertion guides were fabricated from various 1/16″ polymer sheets using a 150-Watt CO_2 laser cutter (Universal ILS12.150D). The width of the channel at the top was ~150–200 µm, and narrowed to ~75–150 µm at the bottom. The laser cutting method was the fastest method at our disposal to develop a workable prototype. However, we envision several other potential advanced manufacturing methods to meet more repeatable and precise design criteria (e.g., lithography, chemical/photo-etching, and others). For the purpose of these experiments, 1/16″ polytetrafluorethylene (PTFE) and poly (methyl methacrylate) (PMMA) were used. However, other thicknesses and materials could also be accommodated (e.g. polycarbonate, PETG, HDPE). Other incarnations of the device could include set non-90° angles to achieve specific targets or depths. The slit width and height may also be altered in order to accommodate electrodes of differing dimensions. Plastic

sheets were ordered from McMaster Carr. Part numbers include: LDPE (8657K111), HDPE (8619K421), PTFE (8545K22), PETG (85815K11), PMMA (8589K11).

Dummy Microelectrode Design, Characterization and Fabrication. For the purposes of testing the basic guide mechanics and insertion into agar gels, 'dummy' microelectrodes were fabricated from 3 mil (~75 µm) polyethylene (PE) films (Young's modulus ≈300 MPa). PE closely resembles the flexible and compliant nature of conventionally used flexible microelectrodes. Different electrode dimension configurations were examined to produce an electrode for 'dummy' insertion testing. To exaggerate the buckling effects of the material during insertion, the length was made extremely long (in comparison to typical microelectrodes), with a length of 13.5 mm, base thickness of 6 mm, with a straight taper (internal angle 25°). They were fabricated using a 40 Watt CO_2 laser cutter by placing the polyethylene films upon a sacrificial sheet of PTFE which absorbed the residual laser beam and heat. This ensured that the polyethylene was not burnt or singed during fabrication as the film tends to shrivel and form a blunt tip when heated to high temperatures.

Dynamically softening (dummy, non-functional) microelectrodes were provided by the Voit Lab (UT Dallas). The SMP-FS consists of a thiol-ene shape memory substrate composed of 0.5 mol% 1,3,5-Triallyl-1,3,5-triazine-2,4,6(1H,3H,5H)-trione (TATATO), 0.45 mol% trimethylolpropane tris(3-mercaptopropionate) (TMTMP), and 0.05 mol% tris [2-(3-mercaptopropionyloxy)ethyl] isocyanurate (TMICN). The SMP probes were prepared as previously described by radical initiated photo-polymerization[66,67].

Compression buckle testing. Compression buckle testing was performed using a universal testing apparatus (EnduraTec, Minnetonka, MN) equipped with a pneumatic linear actuator and load cell. Rectangular test strips (3-mil polyethylene film) were placed in clamps orthogonal to a custom-machined flat plate. The test strips, were advanced toward the flat plate either with or without the guide fixed in place to provide lateral support. Displacement was fixed to a maximum of 2 mm at a speed of 0.5–1.0 mm/s. Data was oversampled at 1000 Hz frequency to ensure capture of maximal forces attained during compression loading. Maximal force was determined with post-hoc analysis of the curves in Matlab (Natick, MA). Sample dimensions are shown in Supplementary Table 1.

Gel Model Fabrication (Agarose Hydrogels) and Testing. Agarose hydrogels (0.6% w/v, UltraPure™ Agarose from ThermoFisher Scientific) were prepared as a model of brain tissue[56]. Agarose solutions were heated and poured into a Pyrex petri dish to cool and solidify at room temperature. The temperature will greatly impact the nature of the agar gel model and to a much lesser degree our test strip made of polyethylene which we selected for its mechanical properties at room temperature and which has a glass-transition temperature of Tg ~ −125 °C (significantly lower than both room and body temperature). All testing was performed at room temperature, for which the probe stiffness and agar gel model were optimized[56]. A stereotaxic micromanipulator was used to lower flexible dummy polyethylene electrodes into the agar gels with and without the guides in-place. The microelectrodes were lowered to just above the surface of the gel and the insertion guide was positioned accurately such that the microelectrode would enter and be guided into the agarose. Subsequently, the microelectrode was lowered into the hydrogel through the insertion guide at ~1 mm/s. The judgement of success was based upon a human-objective standard and included two facets: insertion and buckling. Insertion was successfully achieved if the microelectrode vertically entered the agar to a depth of 2–3 mm below the surface. Partial insertions occurred when the microelectrode penetrated the surface of the agar and subsequently buckled within the testing medium. In some cases, successful or partial insertions were achieved but after the electrode had already undergone some buckling, and were noted separately.

Guide-Assisted Insertion of a Dynamically Softening Microelectrode. Rats were anesthetized with 5% isoflurane and given an intraperitoneal shot of a KXA (ketamine, xylazine, and atropine) cocktail as previously described[60]. The animal was then secured in a stereotaxic frame and then dexamethasone was administered subcutaneously. Lidocaine was then administered at the incision site. The scalp was shaved and the skin was removed from the skull area. Several craniotomies were created for the insertion tests. Insertion guides were fabricated from a clear plastic, PMMA with a diameter of 3 mm, a height of 1 mm, and a slit width of approximately 0.25 mm. The slit was accessible from the side of the device so that it could be removed after implantation. Implantation tests were completed using non-functional thiol-ene/acrylate SMP microprobes from the Voit lab (UT Dallas) with a 3 mm shank, approximately 200 µm width, and 30 µm thickness. Devices were manually positioned directly above the mosquito device slit. The micro-positioner motor drive was then activated to lower the device through the slit and into the brain at 2000 µm/s. All procedures and animal care practices were approved by, and performed in accordance with the Louis Stokes Cleveland Department of Veterans Affairs Medical Center Institutional Animal Care and Use Committees.

Statistics. Peak force from compression testing was analyzed by paired t-test in Minitab (State College, PA). Statistics were run on comparison of the average maximal forces achieved by each sample with and without the guide in place (n = 9, displayed as fold-change in the graph, Fig. 2B). Percentage of successful trials (Fig. 3C), was analyzed with a 2 × 2 probability table (Outcome A: 1 = success, 2 = partial/failure; Group B: 1 = With Guide, 2 = Without Guide) with Fisher's Exact test (n = 26 trials). Fishers Exact test and odds ratio 99% confidence interval were calculated in Matlab. Graphs were produced in Origin software (Northampton, MA).

References

1. Fradin, M. S. Mosquitoes and mosquito repellents: A clinician's guide. *Annals of Internal Medicine* **128**, 931–940, https://doi.org/10.7326/0003-4819-128-11-199806010-00013 (1998).
2. Kong, X. Q. & Wu, C. W. Mosquito proboscis: an elegant biomicroelectromechanical system. *Phys Rev E Stat Nonlin Soft Matter Phys* **82**, 011910, https://doi.org/10.1103/PhysRevE.82.011910 (2010).
3. Sakes, A., Dodou, D. & Breedveld, P. Buckling prevention strategies in nature as inspiration for improving percutaneous instruments: a review. *Bioinspir Biomim* **11**, 021001, https://doi.org/10.1088/1748-3190/11/2/021001 (2016).
4. Ramasubramanian, M. K., Barham, O. M. & Swaminathan, V. Mechanics of a mosquito bite with applications to microneedle design. *Bioinspir Biomim* **3**, 046001, https://doi.org/10.1088/1748-3182/3/4/046001 (2008).
5. Ajiboye, A. B. *et al*. Restoration of reaching and grasping movements through brain-controlled muscle stimulation in a person with tetraplegia: a proof-of-concept demonstration. *The Lancet* **389**, 1821–1830 (2017).
6. Hochberg, L. R. *et al*. Neuronal ensemble control of prosthetic devices by a human with tetraplegia. *Nature* **442**, 164–171 (2006).
7. Nicolelis, M. A. L. Brain–machine interfaces to restore motor function and probe neural circuits. *Nature Reviews Neuroscience* **4**, 417–422 (2003).
8. Hochberg, L. R. *et al*. Reach and grasp by people with tetraplegia using a neurally controlled robotic arm. *Nature* **485**, 372–375, https://doi.org/10.1038/nature11076 (2012).
9. Donoghue, J. Bridging the Brain to the World: A Perspective on Neural Interface Systems. *Neuron* **60**, 511–521, https://doi.org/10.1016/j.neuron.2008.10.037 (2008).
10. Sharma, G. *et al*. Using an Artificial Neural Bypass to Restore Cortical Control of Rhythmic Movements in a Human with Quadriplegia. *Sci Rep* **6**, 33807, https://doi.org/10.1038/srep33807 (2016).
11. Ludwig, K. A. *et al*. Using a Common Average Reference to Improve Cortical Neuron Recordings From Microelectrode Arrays. *J Neurophysiol* **101**, 1679–1689, https://doi.org/10.1152/jn.90989.2008 (2009).
12. Pancrazio, J. J. & Peckham, P. H. Neuroprosthetic devices: how far are we from recovering movement in paralyzed patients? *Expert Review of Neurotherapeutics* **9**, 427–430, https://doi.org/10.1586/ern.09.12 (2009).
13. Jorfi, M., Skousen, J. L., Weder, C. & Capadona, J. R. Progress towards biocompatible intracortical microelectrodes for neural interfacing applications. *Journal of Neural Engineering* **12**, 011001 (2015).
14. Biran, R., Martin, D. & Tresco, P. Neuronal cell loss accompanies the brain tissue response to chronically implanted silicon microelectrode arrays. *Exp Neurol* **195**, 115–126, https://doi.org/10.1016/j.expneurol.2005.04.020 (2005).
15. Polikov, V. S., Tresco, P. A. & Reichert, W. M. Response of brain tissue to chronically implanted neural electrodes. *J Neurosci Methods* **148**, 1–18 (2005).
16. Potter, K. A., Buck, A. C., Self, W. K. & Capadona, J. R. Stab injury and device implantation within the brain results in inversely multiphasic neuroinflammatory and neurodegenerative responses. *J Neural Eng* **9**, 046020 (2012).
17. Kozai, T. D. Y., Jaquins-Gerstl, A. S., Vazquez, A. L., Michael, A. C. & Cui, X. T. Brain Tissue Responses to Neural Implants Impact Signal Sensitivity and Intervention Strategies. *ACS Chemical Neuroscience* **6**, 48–67, https://doi.org/10.1021/cn500256e (2015).
18. Sommakia, S., Lee, H. C., Gaire, J. & Otto, K. J. Materials approaches for modulating neural tissue responses to implanted microelectrodes through mechanical and biochemical means. *Current Opinion in Solid State and Materials Science* **18**, 319–328, https://doi.org/10.1016/j.cossms.2014.07.005 (2014).
19. Tresco, P. A. & Winslow, B. D. The challenge of integrating devices into the central nervous system. *Critical Reviews in Biomedical Engineering* **39**, 29–44 (2011).
20. Gunasekera, B., Saxena, T., Bellamkonda, R. & Karumbaiah, L. Intracortical Recording Interfaces: Current Challenges to Chronic Recording Function. *ACS Chemical Neuroscience* **6**, 68–83, https://doi.org/10.1021/cn5002864 (2015).
21. Rennaker, R. L., Miller, J., Tang, H. & Wilson, D. A. Minocycline increases quality and longevity of chronic neural recordings. *J Neural Eng* **4**, L1–5 (2007).
22. Saxena, T. *et al*. The impact of chronic blood–brain barrier breach on intracortical electrode function. *Biomaterials* **34**, 4703–4713, https://doi.org/10.1016/j.biomaterials.2013.03.007 (2013).
23. Lacour, S. *et al*. Flexible and stretchable micro-electrodes for *in vitro* and *in vivo* neural interfaces. *Med Biol Eng Comput* **48**, 945–954, https://doi.org/10.1007/s11517-010-0644-8 (2010).
24. Köhler, P. *et al*. Influence of Probe Flexibility and Gelatin Embedding on Neuronal Density and Glial Responses to Brain Implants. *PLoS One* **10**, e0119340, https://doi.org/10.1371/journal.pone.0119340 (2015).
25. Jarchum, I. A flexible mesh to record the brain. *Nat Biotech* **33**, 830–830, https://doi.org/10.1038/nbt.3316 (2015).
26. Sohal, H. S. *et al*. The sinusoidal probe: a new approach to improve electrode longevity. *Front Neuroeng* **7**, 10, https://doi.org/10.3389/fneng.2014.00010 (2014).
27. Kim, E. G. R. *et al*. A hybrid silicon–parylene neural probe with locally flexible regions. *Sensors and Actuators B: Chemical* **195**, 416–422, https://doi.org/10.1016/j.snb.2014.01.048 (2014).
28. Simon, D. M. *et al*. Design and demonstration of an intracortical probe technology with tunable modulus. *J Biomed Mater Res A* **105**, 159–168, https://doi.org/10.1002/jbm.a.35896 (2017).
29. Huang, S.-H., Lin, S.-P. & Chen, J.-J. J. *In vitro* and *in vivo* characterization of SU-8 flexible neuroprobe: From mechanical properties to electrophysiological recording. *Sensors and Actuators A: Physical* **216**, 257–265, https://doi.org/10.1016/j.sna.2014.06.005 (2014).
30. Kim, T., Branner, A., Gulati, T. & Giszter, S. F. Braided multi-electrode probes: mechanical compliance characteristics and recordings from spinal cords. *Journal of Neural Engineering* **10**, 045001–045001, https://doi.org/10.1088/1741-2560/10/4/045001 (2013).
31. Lin, C.-M., Lee, Y.-T., Yeh, S.-R. & Fang, W. Flexible carbon nanotubes electrode for neural recording. *Biosensors and Bioelectronics* **24**, 2791–2797, https://doi.org/10.1016/j.bios.2009.02.005 (2009).
32. Tang-Schomer, M. D. *et al*. Film-based Implants for Supporting Neuron-Electrode Integrated Interfaces for The Brain. *Adv Funct Mater* **24**, 1938–1948, https://doi.org/10.1002/adfm.201303196 (2014).
33. Kolarcik, C. L. *et al*. Elastomeric and soft conducting microwires for implantable neural interfaces. *Soft Matter* **11**, 4847–4861, https://doi.org/10.1039/c5sm00174a (2015).
34. Luan, L. *et al*. Ultraflexible nanoelectronic probes form reliable, glial scar-free neural integration. *Sci Adv* **3**, e1601966, https://doi.org/10.1126/sciadv.1601966 (2017).
35. Subbaroyan, J. & Kipke, D. R. In *Conf Proc IEEE Eng Med Biol Soc*. 3588–3591.
36. Park, S. *et al*. One-step optogenetics with multifunctional flexible polymer fibers. *Nat Neurosci* **20**, 612–619, https://doi.org/10.1038/nn.4510 (2017).
37. Jorfi, M., Roberts, M. N., Foster, E. J. & Weder, C. Physiologically Responsive, Mechanically Adaptive Bio-Nanocomposites for Biomedical Applications. *ACS Appl. Mater. Interfaces* **5**, 1517–1526 (2013).
38. Capadona, J. R., Tyler, D. J., Zorman, C. A., Rowan, S. J. & Weder, C. Mechanically adaptive nanocomposites for neural interfacing. *Materials Research Society Bulletin* **37**, 581–589, https://doi.org/10.1557/mrs.2012.97 (2012).
39. Harris, J. P. *et al*. *In vivo* deployment of mechanically adaptive nanocomposites for intracortical microelectrodes. *Journal of Neural Engineering* **8**, 046010 (2011).
40. Capadona, J. R., Shanmuganathan, K., Tyler, D. J., Rowan, S. J. & Weder, C. Stimuli-responsive polymer nanocomposites inspired by the sea cucumber dermis. *Science* **319**, 1370 (2008).
41. Lecomte, A., Descamps, E. & Bergaud, C. A review on mechanical considerations for chronically-implanted neural probes. *J Neural Eng*. https://doi.org/10.1088/1741-2552/aa8b4f (2017).

42. Lewitus, D., Smith, K. L., Shain, W. & Kohn, J. Ultrafast resorbing polymers for use as carriers for cortical neural probes. *Acta biomaterialia* **7**, 2483–2491, https://doi.org/10.1016/j.actbio.2011.02.027 (2011).
43. Lind, G., Linsmeier, C. E., Thelin, J. & Schouenborg, J. Gelatine-embedded electrodes—a novel biocompatible vehicle allowing implantation of highly flexible microelectrodes. *Journal of Neural Engineering* **7**, 046005, https://doi.org/10.1088/1741-2560/7/4/046005 (2010).
44. Gilgunn, P. J. *et al.* In *IEEE 25th International Conference on Micro Electro Mechanical Systems (MEMS)*. 56–59.
45. Lo, M. C. *et al.* Coating flexible probes with an ultra fast degrading polymer to aid in tissue insertion. *Biomedical microdevices* **17**, 34, https://doi.org/10.1007/s10544-015-9927-z (2015).
46. Patel, P. R. *et al.* Insertion of linear 8.4 mum diameter 16 channel carbon fiber electrode arrays for single unit recordings. *J Neural Eng* **12**, 046009, https://doi.org/10.1088/1741-2560/12/4/046009 (2015).
47. Huijing, X. *et al.* A flexible parylene probe for *in vivo* recordings from multiple subregions of the rat hippocampus. *Conf Proc IEEE Eng Med Biol Soc* **2016**, 2806–2809, https://doi.org/10.1109/EMBC.2016.7591313 (2016).
48. Dryg, I. *et al.* Magnetically Inserted Neural Electrodes: Tissue Response and Functional Lifetime. *IEEE Transactions on Neural Systems and Rehabilitation Engineering* 1–1, doi:10.1109/tnsre.2015.2399856 (2015).
49. Kim, B. J. *et al.* 3D Parylene sheath neural probe for chronic recordings. *J Neural Eng* **10**, 045002, https://doi.org/10.1088/1741-2560/10/4/045002 (2013).
50. Kozai, T. D. & Kipke, D. R. Insertion shuttle with carboxyl terminated self-assembled monolayer coatings for implanting flexible polymer neural probes in the brain. *Journal of Neuroscience Methods* **184**, 199–205 (2009).
51. Gopalakrishnaiah, S. K., Joseph, K. & Hofmann, U. G. Microfluidic drive for flexible brain implants. *Current Directions in Biomedical Engineering* **3**, 675–678 (2017).
52. Capadona, J. R. *et al.* Polymer nanocomposites with nanowhiskers isolated from microcrystalline cellulose. *Biomacromolecules* **10**, 712–716 (2009).
53. Ware, T. *et al.* Thiol-ene/acrylate substrates for softening intracortical electrodes. *Journal of Biomedical Materials Research Part B: Applied Biomaterials*, doi:10.1002/jbmb.32946, https://doi.org/10.1002/jbmb.32946 (2013).
54. Ware, T., Simon, D., Rennaker, R. L. & Voit, W. Smart Polymers for Neural Interfaces. *Polymer Reviews* **53**, 108–129, https://doi.org/10.1080/15583724.2012.751924 (2013).
55. Defelipe, J. The evolution of the brain, the human nature of cortical circuits, and intellectual creativity. *Front Neuroanat* **5**, 29, https://doi.org/10.3389/fnana.2011.00029 (2011).
56. Pomfret, R., Miranpuri, G. & Sillay, K. The substitute brain and the potential of the gel model. *Ann Neurosci* **20**, 118–122, https://doi.org/10.5214/ans.0972.7531.200309 (2013).
57. Harris, J. P. *et al.* Mechanically adaptive intracortical implants improve the proximity of neuronal cell bodies. *Journal of neural engineering* **8**, 066011 (2011).
58. Nguyen, J. K. *et al.* Mechanically-compliant intracortical implants reduce the neuroinflammatory response. *Journal of neural engineering* **11**, 056014 (2014).
59. Potter, K. A. *et al.* Curcumin-releasing mechanically adaptive intracortical implants improve the proximal neuronal density and blood-brain barrier stability. *Acta Biomater* **10**, 2209–2222, https://doi.org/10.1016/j.actbio.2014.01.018 (2014).
60. Nguyen, J. K. *et al.* Influence of resveratrol release on the tissue response to mechanically adaptive cortical implants. *Acta biomaterialia* **29**, 81–93, https://doi.org/10.1016/j.actbio.2015.11.001 (2016).
61. Lee, H., Bellamkonda, R. V., Sun, W. & Levenston, M. E. Biomechanical analysis of silicon microelectrode-induced strain in the brain. *Journal of Neural Engineering* **2**, 81–89 (2005).
62. Johnson, M. D., Kao, O. E. & Kipke, D. R. Spatiotemporal pH dynamics following insertion of neural microelectrode arrays. *J Neurosci Methods* **160**, 276–287, https://doi.org/10.1016/j.jneumeth.2006.09.023 (2007).
63. Shanmuganathan, K., Capadona, J. R., Rowan, S. J. & Weder, C. Stimuli-responsive mechanically adaptive polymer nanocomposites. *ACS Appl Mater Interfaces* **2**, 165–174, https://doi.org/10.1021/am9006337 (2010).
64. Chatelin, S., Constantinesco, A. & Willinger, R. Fifty years of brain tissue mechanical testing: from *in vitro* to *in vivo* investigations. *Biorheology* **47**, 255–276, https://doi.org/10.3233/BIR-2010-0576 (2010).
65. Maikos, J. T., Elias, R. A. & Shreiber, D. I. Mechanical properties of dura mater from the rat brain and spinal cord. *J Neurotrauma* **25**, 38–51, https://doi.org/10.1089/neu.2007.0348 (2008).
66. Do, D.-H., Ecker, M. & Voit, W. E. Characterization of a Thiol-Ene/Acrylate-Based Polymer for Neuroprosthetic Implants. *ACS Omega* **2**, 4604–4611, https://doi.org/10.1021/acsomega.7b00834 (2017).
67. Ecker, M. *et al.* Sterilization of Thiol-ene/Acrylate Based Shape Memory Polymers for Biomedical Applications. *Macromolecular Materials and Engineering* **302**, 160331 (2017).

Acknowledgements

The authors would like to acknowledge Erika Woodrum from the Cleveland FES Center for her illustrations and other assistance with our figures. This work was supported in part by the Office of the Assistant Secretary of Defense for Health Affairs through the Peer Reviewed Medical Research Program under Award No. W81XWH-15-1-0608, and in part by Merit Review Award # B1495-R (Capadona) and Presidential Early Career Award for Scientist and Engineers (PECASE, Capadona) from the United States (US) Department of Veterans Affairs Rehabilitation Research and Development Service. None of the funding sources aided in collection, analysis and interpretation of the data, in writing of the manuscript, or in the decision to submit the manuscript for publication. The contents do not represent the views of the U.S. Department of Defense, the U.S. Department of Veterans Affairs or the United States Government.

Author Contributions

A.J.S. served as the study experimental lead and was responsible for experimental design, conducting experiments, data analysis, figure preparation, and writing the manuscript. S.S., M.W., A.M.S., and M.E. participated in conducting experiments and data analysis. W.E.V. and J.J.P. assisted in design of experiments and review of manuscript. J.R.C. served as scientific lead, oversaw the overall study design and rationale for the experiments, data analysis, and interpretation of results. A.J.S. and J.R.C. lead the team in preparation of the manuscript, while all authors reviewed the manuscript.

Additional Information

Supplementary information accompanies this paper at https://doi.org/10.1038/s41598-017-18522-4.

Competing Interests: The authors declare that they have no competing interests.

Video Article

A Novel Single Animal Motor Function Tracking System Using Simple, Readily Available Software

Keith R. Dona[1,2], Monika Goss-Varley[1,2], Andrew J. Shoffstall[1,2], Jeffrey R. Capadona[1,2]

[1]Advanced Platform Technology Center, Rehabilitation Research and Development, Louis Stokes Cleveland Department of Veterans Affairs Medical Center

[2]Department of Biomedical Engineering, Case Western Reserve University

Correspondence to: Jeffrey R. Capadona at jrc35@case.edu

URL: https://www.jove.com/video/57917
DOI: doi:10.3791/57917

Keywords: Behavior, Issue 138, Behavior, rat, ladder, open field grid, tracking algorithm, behavioral analysis, movement analysis

Date Published: 8/31/2018

Citation: Dona, K.R., Goss-Varley, M., Shoffstall, A.J., Capadona, J.R. A Novel Single Animal Motor Function Tracking System Using Simple, Readily Available Software. *J. Vis. Exp.* (138), e57917, doi:10.3791/57917 (2018).

Abstract

We have recently demonstrated that implanting intracortical microelectrodes in the motor corteces of rats results in immediate and lasting motor deficits. Motor impairments were manually quantified through an open field grid test to measure the gross motor function and through a ladder test to measure the fine motor function. Here, we discuss a technique for the automated quantification of the video-recorded tests using our custom Capadona Behavioral Video Analysis System: Grid and Ladder Test, or BVAS. Leveraging simple and readily available coding software (see the **Table of Materials**), this program allows for the tracking of a single animal on both the open field grid and the ladder tests. In open field grid tracking, the code thresholds the video for intensity, tracks the position of the rat over the 3 min duration of the grid test, and analyzes the path. It then computes and returns measurements for the total distance traveled, the maximum velocity achieved, the number of left- and right-handed turns, and the total number of grid lines crossed by the rat. In ladder tracking, the code again thresholds the video for intensity, tracks the movement of the rat across the ladder, and returns calculated measurements including the time it took the rat to cross the ladder, the number of paw slips occurring below the plane of the ladder rungs, and the incidence of failures due to stagnation or reversals. We envision that the BVAS developed here can be employed for the analysis of motor function in a variety of applications, including many injury or disease models.

Video Link

The video component of this article can be found at https://www.jove.com/video/57917/

Introduction

There are many established methods to assess both functional and behavioral motor and cognitive impairments[1,2,3]. Some of the more commonly employed methods include testing fine motor function *via* paw placement, stepping, and limb coordination on a ladder test[4], testing gross motor function and stress behavior *via* the open field grid test[5,6], and testing for fear, depression, and despair *via* the forced swim test[7,8] or rotor rod[9]. However, many of these methods rely on human researchers to "score" the animal or to judge its performance subjectively. The need for a subjective human assessment can slow the generation and analysis of the data, as well as present the opportunity for an intentional or unintentional influence of research bias in the study[10]. Further, subjective assessment of the data also presents the risk of inaccurate data representation, be it through forgetfulness, poor motivation, improper training, or negligence[11].

We have recently reported the use of both an open field grid test and a ladder test in rats implanted with intracortical microelectrodes[12,13]. Due to the novelty of the findings in those studies, we immediately began employing those and additional functional testing in many ongoing studies in the laboratory. In anticipation of unintentional human-generated variability resulting from an increase in the number of subjective evaluators, and to improve the analysis throughput, we set out to create an automated, computer-assisted program to score behavioral testing, and greatly limit the potential for error.

Here, we report on the development of the BVAS. The BVAS uses computer analysis to score an open field grid test and a ladder test as metrics of gross and fine motor function, respectively. The results can be used to elucidate possible motor function deficits caused by injury or disease, regardless of the injury or disease model. The analysis codes can be adapted to account for changes in behavioral testing equipment or to score various metrics of motor function. Therefore, the BVAS can be implemented in many applications, beyond our intended use or the intended use of those currently employed by other laboratories.

Note that the open field grid and ladder tests require video recording. Therefore, each test will require a video camera [1080 p, minimum 15 frames per second (fps)], a laptop, and a room to store the video data. For both tests, place the camera in a centered position, allowing for the whole apparatus to be seen on the frame. Anchor the camera on a tripod or scaffolding so that it does not move during the testing. Keep the edges of the video frame as close to parallel with the edges of the testing apparatus as possible. Be sure the same personnel complete all testing and the room is well-lit with a temperature-controlled system. Use the same room for all animals throughout the course of the testing, with minimal changes to the room. Cereals or banana chips make good rewards to encourage the animals to complete the behavior tests.

Protocol

All procedures and animal care practices were approved by and performed in accordance with the Louis Stokes Cleveland Department of Veterans Affairs Medical Center Institutional Animal Care and Use Committee. The behavioral testing protocol closely follows previously published work[12,13].

1. Behavioral Testing: Filming the Tasks

NOTE: Here, the animals were tested for 8 weeks to detect any chronic behavioral changes. The study duration is dependent on the application/injury/disease model used for the study.

1. **Open field grid testing**
   NOTE: The grid test has a 1 m^2 area with 40 cm walls and was built in-house. The bottom is partitioned into nine squares *via* brightly colored tape (**Figure 1A**). For the use of the automated BVAS, it is important that the color of the line and the grid contrast with the rat. Here, white Sprague Dawley rats were used; thus, the grid background was painted black, and the lines were created with bright pink tape.
   1. Test the animals 2x per week for all tests including the week before beginning the study in order to create a baseline score for use in later calculations.
   2. Clean all the testing equipment with a chlorine dioxide-based sterilant at the beginning of each testing session and between each animal.
   3. Bring the animals to the room for testing and allow them to adjust to the room for 20 min prior to starting the trials.
   4. Begin filming and place the animal in the center of the grid, facing away from the researcher, to begin the grid test.
   5. Allow the animal to run freely for 3 min while being video recorded from above.
   6. Stop filming when the 3 min time period has ended and return the animal to its home cage. Clean the grid with a chlorine dioxide-based sterilant, taking care to fully dry the surfaces before testing. Test each animal 1x per session.

2. **Ladder testing**
   NOTE: The ladder test was built in-house and consists of two acrylic side walls, each 1 m in length, connected by 3 mm diameter rungs spaced at 2 cm intervals (**Figure 2**). The animals require a week of ladder training before beginning the official testing. There is no difference between the training and the testing protocol. Note that the training does not need to be filmed.
   1. For the use with the BVAS, cover the wall behind the ladder with a black poster board and delineate the level of the rungs, start, and finish lines with bright tape to create a contrast with the white rats.
   2. Test the animals 2x per week for all tests including the week before beginning the study to create a baseline score for use in later calculations.
   3. Clean all the testing equipment with a chlorine dioxide-based sterilant at the beginning of each testing session and between each animal.
   4. Bring the animals to the room for testing and allow them to adjust to the room for 20 min prior to starting the trials.
   5. Place the animal in a clean temporary cage before the ladder testing.
      NOTE: A temporary cage is a short-term cage to hold the animal while the animal's home cage is used at the end of the ladder. There is no age bias as all animals used in the study are the same age and complete testing over the same time period. The control used here is a naïve animal having never received surgery.
   6. Set the ladder apparatus up to span two cages; the start cage is a clean cage, and the end cage is the animal's living cage, an incentive to complete the run.
   7. Place the camera on a tripod, centered on the length of the ladder. Extend the tripod so the lens of the camera is at the height of the ladder rungs. Position the camera so that the rungs are exactly aligned with the lens as this is important for the slip detection algorithm in the BVAS code.
   8. Start the video recording and allow the rat to begin the run by holding their front paws over the first rung of the ladder. Allow the animal to move onto the ladder unassisted.
   9. Allow the animal to move from the start line to the finish line at their own pace while filming. End the video recording and remove the animal from the ladder once the animal has completed the run.
   10. Consider the run a failed run if the animal turns around or remains stagnant for 20 s. End the video recording and remove the animal from the ladder if the animal fails the run. Assign a penalty score for failed runs which is equivalent to the slowest time recorded during the pre-surgery baseline testing.
   11. Ensure that each animal completes 5 runs per testing day and give them a 1 min rest period between each trial.
       NOTE: In this study, the animals were tested 2x per week for 8 weeks. However, the timeframe is up to the discretion of the researcher.

2. File Storage and Naming

NOTE: The BVAS code uses specifically designated video file and folder naming conventions so that videos may be reliably parsed and analyzed properly. Different naming conventions are currently not supported. After the completion of a testing session, the video file is saved in the default location under a default name.

1. **Individual video naming**
   1. Name each video with the animal's designation for all grid testing videos.
   2. Collect 5 ladder videos per testing session for each animal. Select all five videos and rename the first video, using the animal's designation. For example, if the animal's name is "C1NS", the files are named "C1NS (1)", "C1NS (2)", "C1NS (3)", *etc.*

2. **Storage folder naming**
    1. Take the videos now named after each animal and place the files in their own storage folder. Name this folder using the following convention: "TestingWeek_TestMode_MM_DD_YY".
    NOTE: For example, if this folder holds the first week of grid videos and was filmed on January 1st, 2018, the folder holding these videos is named "Week1_GridTest_01_01_18".
    2. Place this specifically named folder in another folder that will denote the larger study that this set of experiments belongs to.
    NOTE: There are no naming requirements for the folder tree system to keep studies and testing modes organized. The only folder the system selects is the folder holding videos named in step 2.2.1.

3. **Spreadsheet file creation**
    1. Using an outside spreadsheet program (see the **Table of Materials**), create a new empty spreadsheet file to store the data for each study and testing mode.
    NOTE: There are no naming or storage location requirements for this file. Each study requires two spreadsheet files for use with the system, one for grid testing and one for ladder testing. Leave these files empty for now.
    2. Check to ensure these spreadsheet files are not open on any computers while the BVAS is running.
    NOTE: If the BVAS attempts to open a spreadsheet file that is already open, this will result in an error.

3. System Installation

NOTE: The BVAS was built and tested on PC operating systems and leverages Runtime components from simple and readily available coding software. Other system configurations are currently not supported.

1. **Installing latest BVAS version**
    1. Run the installer by double-clicking on the installer icon labeled '*BVASX.XXinstaller*'. "X.XX" is the current version number, currently '*BVAS3.30installer*'.
    NOTE: This is open source software. Contact the corresponding author for the most recent version.
    2. Follow the on-screen instructions to install the BVAS.
    NOTE: The installer will check the system for the correct version of the software (*e.g.*, MATLAB Runtime) and if it is not found, it will install the software from the internet.
    3. Once installed, launch the program by clicking the '*BVAS.exe*' file.

4. System Use

1. **Opening the program**
    1. Double-click on the BVAS program icon to bring up the BVAS main menu which allows the following options: '*Grid Analysis*', '*Ladder Analysis*', '*Ladder Review*', or '*Quit*'.
    NOTE: There is also a drop-down menu located in the top left corner labeled '*Email Settings*' (**Figure 3A**).

2. **Email settings**
    1. Click on the '*Email Settings*' drop-down menu and first select '*Change email destination*'.
    2. Enter a preferred email address to receive updates on the analysis and select '*OK*'. Select 'Cancel' to not change the email currently saved.
    3. Click the '*Send Test Email*' button to send a test email to the email currently saved in the system. Close the '*Email Sent!*' window pop-up signifying the test's completion.

3. **Open Field Grid Test Analysis**
    1. Select '*Grid Analysis*' from the top menu screen.
    2. Ensure the toggle button labeled '*Single Video/Whole Session/Plot Data*' is displaying Whole Session to complete the analysis on a whole set of testing session videos.
    3. Utilize the '…' button next to the upper input box to browse the file system to find the file of videos to analyze. Select the folder labeled in the style discussed in step 2.2.1.
    4. Utilize the … button next to the lower input box to browse the file system to select the spreadsheet file in which to store the data.
    NOTE: Note that, as well as outputting the data to a spreadsheet file, the complete path data for each video is stored in a data file (.mat) in the same directory that holds the videos chosen in step 4.3.3.
    5. Ensure the toggle button mentioned in step 4.3.2 is set to '*Single Video*' to complete the analysis on a single video.
    6. Utilize the … button next to the upper input box to browse the file system to find the file of the video to analyze.
    7. Utilize the … button next to the lower input box to browse the file system to select a directory to save the data file (.mat) that results from the single video analysis.
    NOTE: The data file will be named after the video, which is named after the animal.
    8. Select '*Output Data*' from the toggle mentioned in step 4.3.2. to output the data from a previously analyzed grid video. Examples of this plotted data are shown in **Figures 1B** and **1C**.
    9. Utilize the … button next to the upper input box to browse the file system to select a previously created grid video data file. Select '*Go!*' to create the plot and data figure.
    NOTE: This function also creates a text file, named the same and located in the same directory as the data file, which has the animal's run data in it.

10. Once both necessary files have been located, select '*Go!*' to begin the video analysis. Note that the '*Return*' button will reopen the top menu and the '*Quit*' button will close the program completely. Choose the '*Debug Display*' toggle to show a visual representation of the tracking algorithm (**Figures 3C** and **3D**).
11. Select '*Go!*' to start the analysis process. Examine the images of each video on the reviewer screen. Use the '*Next*' and '*Previous*' page buttons if there are more than five videos.
12. To bring up a manual selection menu, select the '*Edit*' button if there are no green lines or the green line does not appear to be in the correct square around the testing area. To edit the corners, select the 'Edit Corners' button.
    NOTE: The '*Next Frame*' button changes the representative image to the next frame of the video in question. Select the '*Next Frame*' button if the frame given automatically is obstructed or out of focus.
13. Follow the instructions to the right of the representative image to select the testing area and hit '*Enter*' to complete the selection process.
    NOTE: The selected green lines will now be shown on the representative image.
14. Select '*Done*' to save the selection and return to the reviewer screen.
15. Select the center '*Done*' button to start the complete analysis process once the grid area for each video is selected correctly. Allow the program to run and, upon completion, a success prompt will appear.
    NOTE: The full analysis of a session of videos can take some time, approximately 10 min per animal.

4. **Ladder test analysis**
   NOTE: The protocol for the initial ladder test analysis is very similar to the protocol outlined in steps 4.3.10–4.3.15. The notable differences prior to those steps are as follows:
   1. Select '*Ladder Analysis*' from the top menu to open the ladder analysis menu.
   2. View the two options in the toggle, '*Single Video*' and '*Whole Session*' (**Figure 3B**).
   3. With '*Whole Session*', select the upper input … button to select the folder with ladder videos named in step 2.2.1.Select the lower … button to select a directory to save a folder with data from the ladder videos to review later.
   4. If '*Single Video*' is selected, select a single video file with the upper … button and a location the same as in step 4.4.3.
   5. Select '*Go!*' to start the analysis process and bring up the ladder test area reviewer screen.
   6. Follow steps 4.3.10–4.3.15 the same way for the ladder as for the grid. Allow the program to run and, upon completion, a success prompt will appear.
      NOTE: If something goes wrong during the analysis, an email is sent to the email address entered in step 4.2.2. Upon completion of an analysis of any kind, a completion email is sent to the same email address.

5. **Ladder image review**
   NOTE: The following protocol is to review previously analyzed ladder videos to confirm any failures and paw slips. Note, spreadsheet files for a ladder crossing are not generated to view until '*Ladder Image Review*' (steps 4.5.1–4.5.5) is completed.
   1. From the top menu, select '*Ladder Image Review*'. This brings up the Ladder Review file select screen.
   2. Select the top … button to select the folder of the data files.
      NOTE: The files are saved in the location chosen in step 4.4.2 and are named in the following format: "M1_D1_Y1 Ladder Video Session HH_MM M2_D2_YYYY". M1, D1, and Y1 are the date of the session being analyzed. "Ladder Video Session" will read "Single Video Analysis" if only a single video was analyzed. HH_MM and M2_D2_YYYY are the time and date that the review session was started.
   3. Select the bottom … to select the spreadsheet file created for the study.
   4. Select '*Go!*' to start the manual review process.
   5. View the automatically opened ladder data reviewer menu. If a slip is detected, use the '*Next Frame*' and '*Last Frame*' buttons to check any consecutively recorded frames if available.
   6. Utilize the slip toggle to denote what foot of the rat has slipped. Leave the toggle on '*No Slip*' if the detection is a false positive. Click '*Save/Continue*' to move on to the next detection (**Figure 2A**).
   7. In the case of failure, use the toggle to denote whether the failure is due to reversal (where the rat turned around during the run) or stagnation (where the rat failed to complete the run in a timely manner).
   8. Click '*Save/Continue*' to move on to the next detection. On the last detection, click '*Save/Continue*' to complete the analysis and save the data to the spreadsheet file chosen earlier. Dismiss the completion notice.
      NOTE: After the review is completed, the folder that was reviewed is renamed "REVIEWED M1_D1_Y1 Ladder Video Session HH_MM M2_D2_YYYY".

5. Output Data Analysis

1. **Grid spreadsheet file**
   1. Locate the created data in the spreadsheet file from each grid video.
      NOTE: The columns are left to right as follows: animal name, date of test, week of study number, total distance traveled, total time stopped, maximum velocity achieved, right turns, left turns, and grid line crosses (**Figure 1D**).
   2. Use these metrics to quantify the gross motor performance and create comparison plots between animals and time points.

2. **Ladder spreadsheet file**
   1. Locate the created data in the spreadsheet file from each ladder video following the failure and paw slip review.
      NOTE: The columns are left to right as follows: animal name, run number 1–5, week of study number, date of test, run type (either success or failure), time of run for successes, percent completion, paw slips on each paw, and failure mode. The time column is blank for a failure and the failure mode column will read either reversal or stagnation (**Figure 2B**).
   2. Use these metrics to quantify the fine motor performance and create comparison plots between animals and time points.

Representative Results

Following the methods presented here, rats completed the open field grid and ladder tests 2x per week. The data were analyzed both by using BVAS and manually with a stop-watch by trained and novice reviewers. The results presented are an average of the raw weekly scores from a single non-implanted control animal over an 8 week study, where week "0" corresponds to the baseline testing. Note there was no testing during week 1 as this was a rest week for the surgery animals. Because the open field grid is tested 1x per day, the ladder is tested 5x per day, and there are two testing days per week, there is a sample of 16 trials for open field grid whereas there are 80 trials for the ladder test in the same 8 week time period.

BVAS *vs.* manual analysis:
To confirm the consistency of the BVAS system and validate it against manual analysis, the results for grid lines crossed and ladder crossing time were compared to the manual results from three expert reviewers (*n* = 3) as a "gold standard." Novice users (*n* = 7) also reviewed the data both manually and using the BVAS. For the validation, each reviewer examined the same one day of experiments for one animal (grid testing = one video/trial; ladder testing = five independent trials). The results for the open field grid test showed that expert reviewers were more consistent than novice reviewers were (a variance of 0 *versus* a variance of 17.1, respectively), but when using the BVAS, there was zero variance for both expert and novice users (**Figure 4A**). Similarly, the results for the ladder test showed that expert reviewers were more consistent than novice reviewers were (~3.5x larger: a variance of 0.120 *versus* a variance of 0.414, respectively), but when using the BVAS, there was again zero variance for both expert and novice users (**Figure 4B**).

Therefore, where possible, behavior metrics for both the open field grid and ladder test were quantified manually by the same expert user and compared to the results generated using the BVAS. Here, the results from all included animals throughout the duration of the experiments were evaluated. All error is reported as a standard error of the mean (SEM) unless reported otherwise. The difference between the two methods ranged from an average of 0.64 ± 0.06 s for the ladder test and 3.56 ± 0.53 lines for the grid test. The average difference for the open field grid test over the course of 8 weeks between the two methods was 11.13 ± 3.03%. The average difference for the ladder test over the course of 8 weeks between the two methods was 9.05 ± 1.07%. The percent difference between the two methods was calculated following **Equation 1**.

Equation 1: $$\%\ difference\ between\ methods = \frac{(manual\ score - BVAS\ score)}{manual\ score} * (100)$$

Note also for the ladder test timing, the manual data collection is only precise to 1 s (which can change based on the device used to keep time), while the BVAS is precise to the inverse of the frame rate of the video being reviewed. For example, if the video is filmed at 15 frames per second, the BVAS data is precise to 1/15th of a second.

Open field grid test:
Following previously published protocols[12,13], animals were allowed to run freely in an open field grid test for 3 min to measure their gross motor function and stress behavior. The video recorded during the testing was analyzed using the BVAS to quantify the raw scores for the maximum velocity, the total distance, the number of gridlines crossed, and the percentage of right turns achieved by the animal (**Figure 5**). While this data is only representative of one animal, trends were seen over the course of the study of increased maximum velocity achieved, increased total distance traveled, and an increased number of gridlines crossed. Unsurprisingly, when compared to each other, the total distance traveled, and the total gridlines crossed had a strong positive correlation. Comparing the manual quantification to the BVAS gridline quantification revealed comparable results (**Figure 5C**). For this particular animal, the percentage of right turns largely hovered between 40% and 50% (**Figure 5D**). Of note, the metrics for the total distance traveled, maximum velocity, and turn direction were unable to be quantified manually, and represent another added feature of the automated BVAS program.

Ladder test:
As previously reported[4,14], the ladder testing was completed to measure the coordinated grasp and fine motor function. The video recorded during the testing was analyzed using the BVAS to quantify the raw scores for the time to cross and the number of paw slips (**Figure 6**).In this animal, there was a decreasing trend in the time to cross the ladder, followed by an increase in time starting around week 4. Comparing the manual quantification to the BVAS crossing time quantification revealed comparable results (**Figure 6A**). As the animal presented was a non-surgical control, paw slips were infrequent, and comparable in number between the left and right paw (**Figure 6B**).

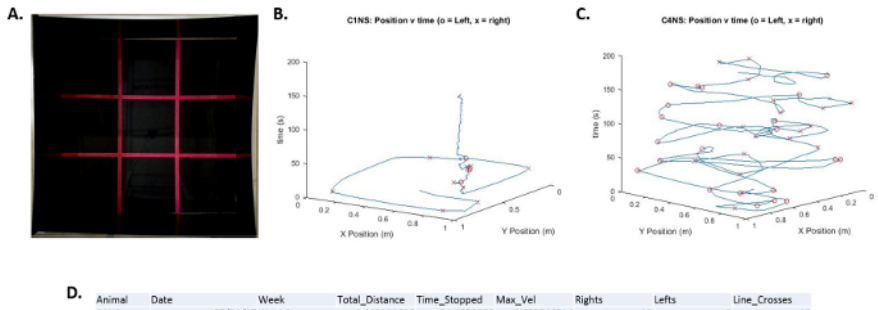

D.

Animal	Date	Week	Total_Distance	Time_Stopped	Max_Vel	Rights	Lefts	Line_Crosses
C1NS	07/24/17	Week6	4.449130018	24.1259968	0.329844714	10	3	10
C4NS	07/31/17	Week7	21.82123653	7.1303837	0.477236583	19	22	54

Figure 1: Example of open field grid test results. (**A**) This panel shows the behavioral testing 1 m^2 open testing area with a black background and pink grid lines. (**B**) This is an example of a plot of a single animal's 3-min grid run. This animal made one circuit of the grid and then remained mostly stationary for the remainder of the time. The red O's and X's denote where the turn detection algorithm detected a left (O) or a right (X) turn. (**C**) This is a second example of a plot of a single animal's 3-min grid run. This animal was extremely active for the entire 3-min testing period. The red O's and X's denote where the turn detection algorithm detected a left (O) or a right (X) turn. (**D**) This is an example of the output in the data file for the two runs seen in panels **B** and **C**. Please click here to view a larger version of this figure.

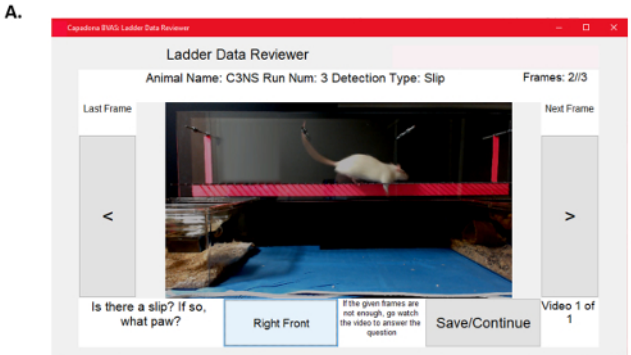

B.

Animal	Run_Number	Date	Week	Run_Type	Time_for_Successes	Percent_Completion	Right_Front_Slips	Left_Front_Slips	Right_Rear_Slips	Left_Rear_Slips	Failure_Mode
C3NS	3	07_26_17	Test	Success	2.9795704	100	1	0	0	0	

Figure 2: Example of a ladder data reviewer screen. (**A**) This panel shows the ladder data reviewer screen, complete with a screenshot demonstrating the ladder test set-up. This screen is where the user will confirm detected slips and failures. This example shows a positively detected right front paw slip. (**B**) This is an example of the output in the data file for the ladder run that was examined in panel **A**. Please click here to view a larger version of this figure.

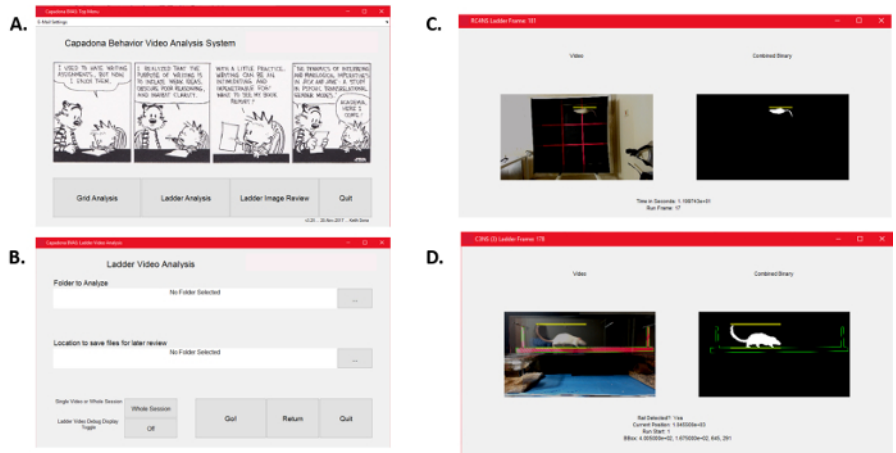

Figure 3: Example of BVAS analysis screens. (**A**) This panel shows the top menu of the BVAS. Note the four buttons along the bottom and the **Email Settings** drop-down menu in the top left corner. (**B**) This is an example of a file selection screen, in this case for the ladder video analysis. (**C**) This is an example of a debug analysis viewer for a grid test video. This demonstrates the detection algorithm during the analysis of a grid test. (**D**) This panel shows an example of a debug analysis viewer for a ladder test video. This demonstrates the detection algorithm during the analysis of a ladder test. Please click here to view a larger version of this figure.

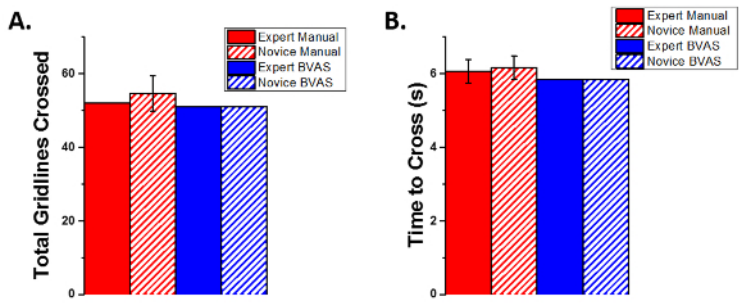

Figure 4: Example of expert and novice testing results. These panels show the results of a manual and a BVAS expert and novice testing for (**A**) the number of gridlines crossed on the open field grid test and (**B**) the time to cross on the ladder test. For both tests, the results showed that expert users had a lower variance than the novice users for the manual analysis, while using the BVAS resulted in zero variance, regardless of the user expertise. The standard deviation is reported. Please click here to view a larger version of this figure.

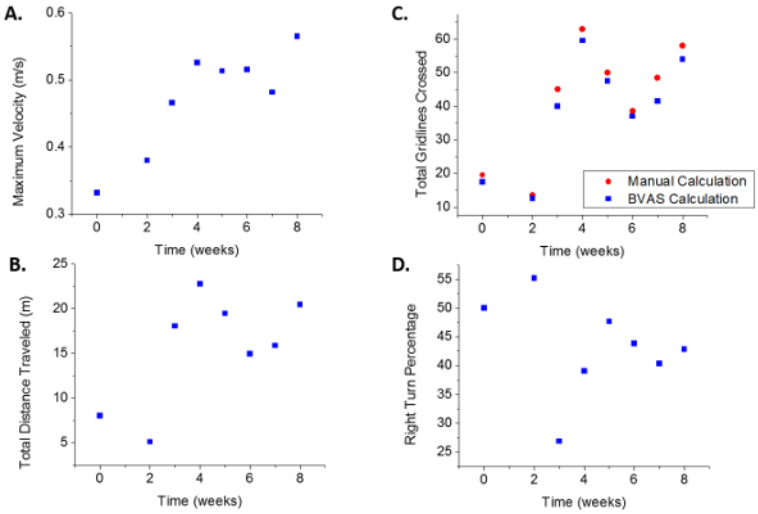

Figure 5: Representative open field grid test results. These panels show representative open field grid test results for a non-implanted control animal for (**A**) the maximum velocity achieved, (**B**) the total distance traveled, (**C**) the total number of gridlines crossed, and (**D**) the percentage of right turns made by the animal. Please click here to view a larger version of this figure.

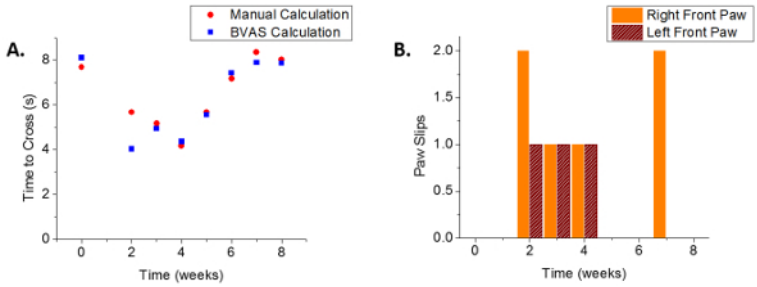

Figure 6: Representative ladder test results. These panels show representative ladder test results for a non-implanted control animal for (**A**) the time to cross the ladder, and (**B**) the number of right- and left-front-paw slips. Please click here to view a larger version of this figure.

Discussion

The most critical portion of the protocol to ensure a strong analysis is the consistent filming. If the videos are well lit and filmed at the correct position as discussed in the first section of the protocol, the system will be able to do a precise analysis. As with any image-processing problem, the work done in preprocessing will make the post-processing more accurate and simple. As such, making sure that the apparatus and animals are well-lit during the testing and any shadows or other motion in the frame is kept to a minimum will mean the BVAS can function at a higher level of accuracy.

The protocol presented here can be used to efficiently and reproducibly analyze results from both gross and fine motor function testing in rodents *via* an open field grid and a ladder test. Additionally, it reduces the possibility of human error or bias in the analysis process as the data analysis is largely completed by the self-functioning computer without any user input. Because of this feature, the BVAS system can be used with the same level of accuracy by both expert and novice users. The BVAS program is self-checking, easy to implement, and inexpensive to use.

Further, the code can be adapted to fit a researcher's individual needs. For example, the open field grid code can be used to analyze a variety of metrics including the total distance traveled, the maximum speed achieved, and the number of left and right turns, and could likely be easily modified for the tracking in a water maze or forced swim task. Additional modifications can be made to the code to account for varying room lighting, differences in grid and ladder line color, and differences in animal color. Although the testing apparatus and the BVAS code presented here were designed for their use in rat studies, we expect that either could be scaled up or down to be used with various sized animals, although this has not been verified to date.

As with all behavior testing and data analysis, it is important to maintain as much consistency as possible throughout the study and subsequent analyses. Although the presented BVAS greatly reduces any reliance on human input for the data analysis, human variance can come into play with the researcher working with the animals and handling the procedures[15]. Furthermore, changes in the testing location[16] or housing and husbandry conditions[17] can also influence the results. While the BVAS can be updated to account for lighting and camera angle, factors such as smells, personnel, or diet can only be accounted for at the time of the study. Therefore, researchers should take caution to remain as consistent as possible in the animal testing and housing conditions, testing personnel, and analytical methods, among others.

The BVAS is novel because of its compound detection system. Each frame of the video is passed through multiple image filters to create binary masks all calibrated to look for the rat in the frame. Each possible rat shape is then rated by the system on its likelihood of being the rat. This rating factors in size, the number of filters the shape is detected on, and the last known location and the predicted location of the animal based on the previous trajectory. This makes for a strong animal detection that can overcome most issues that arise based on shadows and changes in the lighting. Unlike current commercially available animal tracking systems, this method does not require any modifications to the animal to make it more visible and uses a single standard-speed webcam for the video recording. The BVAS system is also an improvement over conventional manually quantified behavior testing because all the metrics that are outputted are objectively measured from the videos. A human quantified behavioral study will have some subjectivity in nature as the researcher decides what constitutes a paw slip or grid line cross.

The system requires a somewhat specific setup to work to its fullest capabilities. While it is possible to adapt the system to changes in the apparatus, it would currently require some fluency in computer coding to edit the code. With some coding fluency, troubleshooting is made easy because the error notice emails include a full error information readout. If the videos fed into the system are not at the ideal resolution or frame rate (1080 p, 15 fps), the user is alerted *via* a warning message. This change will affect the accuracy of the system, but it still can run on lower resolution videos. Any lighting or shadow problems that cause an error during the analysis will lead to a dynamic error message sent to the user-entered email. The user can then use the debug viewer to watch the frame by frame analysis to understand what issue arose. The error message also includes an error report, so if it is a coding issue, it can be addressed simply.

In the future, the BVAS system may be able to be further adapted without any knowledge of the syntax from coding software. The addition of a tracking options menu could allow the user to select the color of the animal and grid lines simply and conveniently. The ladder test tracking will also increase in accuracy with the possible addition of a cascade object detector in the code and a better ladder lighting rig to accompany the ladder test and filming apparatus. Therefore, we expect that the BVAS system described here can be readily implemented into an array of behavioral and motor function tasks spanning a wide variety of disease and injury models.

Disclosures

The authors have nothing to disclose.

Acknowledgements

This study was supported by the Merit Review Award # B1495-R (to Jeffrey R. Capadona) and the Presidential Early Career Award for Scientist and Engineers (PECASE) (to Jeffrey R. Capadona) from the United States Department of Veterans Affairs Rehabilitation Research and Development Service. Additionally, this work was supported in part by the Office of the Assistant Secretary of Defense for Health Affairs through the Peer Reviewed Medical Research Program under Award No. W81XWH-15-1-0608. The authors acknowledge SOURCE for its summer research funding support. The contents do not represent the views of the United States Department of Veterans Affairs or the United States Government. The authors would like to thank Hiroyuki Arakawa in the CWRU Rodent Behavior Core for his guidance in designing and testing rodent behavioral protocols. The authors would also like to thank James Drake and Kevin Talbot from the CWRU Department of Mechanical and Aerospace Engineering for their help in designing and manufacturing the rodent ladder test.

References

1. Beery, A. K., Kaufer, D. Stress, social behavior, and resilience: insights from rodents. *Neurobiology of Stress.* **1**, 116-127 (2015).
2. Crawley, J. N. Behavioral phenotyping of rodents. *Comparative Medicine.* **53**, 140-146 (2003).
3. Wolf, A., Bauer, B., Abner, E. L., Ashkenazy-Frolinger, T., Hartz, A. M. A Comprehensive Behavioral Test Battery to Assess Learning and Memory in 129S6/Tg2576 Mice. *PLoS One.* **11**, e0147733 (2016).
4. Metz, G. A., Whishaw, I. Q. Cortical and subcortical lesions impair skilled walking in the ladder rung walking test: a new task to evaluate fore- and hindlimb stepping, placing, and co-ordination. *Journal of Neuroscience Methods.* **115**, 169-179 (2002).
5. Bailey, K. R., Crawley, J. N. Anxiety-Related Behaviors in Mice. in *Methods of Behavior Analysis in Neuroscience.* edited by Buccafusco, J. J., chapter 5, CRC Press/Taylor & Francis. Boca Raton, FL (2009).
6. Prut, L., Belzung, C. The open field as a paradigm to measure the effects of drugs on anxiety-like behaviors: a review. *European Journal of Pharmacology.* **463**, 3-33 (2003).
7. Porsolt, R. D., Bertin, A., Jalfre, M. Behavioral despair in mice: a primary screening test for antidepressants. *Archives Internationales de Pharmacodynamie et de Thérapie.* **229**, 327-336 (1977).
8. Porsolt, R. D., Brossard, G., Hautbois, C., Roux, S. Rodent models of depression: forced swimming and tail suspension behavioral despair tests in rats and mice. *Current Protocols in Neuroscience.* **Chapter 8**, Unit 8 10A (2001).

9. Dunham, N. W., Miya, T. S. A note on a simple apparatus for detecting neurological deficit in rats and mice. *Journal of the American Pharmaceutical Association.* **46**, 208-209 (1957).
10. Forstmeier, W., Wagenmakers, E. J., Parker, T. H. Detecting and avoiding likely false-positive findings - a practical guide. *Biological Reviews of the Cambridge Philosophical Society.* **92**, 1941-1968 (2017).
11. Reason, J. Human error: models and management. *The Western Journal of Medicine*. **172**, 393-396 (2000).
12. Goss-Varley, M. Rodent Behavioral Testing to Assess Functional Deficits Caused by Microelectrode Implantation in the Rat Motor Cortex. *Journal of Visualized Experiments.* **In Press** (2018).
13. Goss-Varley, M. *et al.* Microelectrode implantation in motor cortex causes fine motor deficit: Implications on potential considerations to Brain Computer Interfacing and Human Augmentation. *Scientific Reports.* **7**, 15254 (2017).
14. Metz, G. A., Whishaw, I. Q. The ladder rung walking task: a scoring system and its practical application. *Journal of Visual Experiments.* (28), e1204 (2009).
15. Chesler, E. J., Wilson, S. G., Lariviere, W. R., Rodriguez-Zas, S. L., Mogil, J. S. Influences of laboratory environment on behavior. *Nature Neuroscience.* **5**, 1101-1102 (2002).
16. Crabbe, J. C., Wahlsten, D., Dudek, B. C. Genetics of mouse behavior: interactions with laboratory environment. *Science.* **284**, 1670-1672 (1999).
17. Richter, S. H., Garner, J. P., Auer, C., Kunert, J., Wurbel, H. Systematic variation improves reproducibility of animal experiments. *Nature Methods.* **7**, 167-168 (2010).

Bedell HW, Capadona JR. Anti-inflammatory Approaches to Mitigate the Neuroinflammatory Response to Brain-Dwelling Intracortical Microelectrodes. J Immunol Sci. (2018); 2(4): 15-21

Journal of Immunological Sciences

Journal of Immunological Sciences

Mini Review Open Access

Anti-inflammatory Approaches to Mitigate the Neuroinflammatory Response to Brain-Dwelling Intracortical Microelectrodes

Hillary W. Bedell[1,2] and Jeffrey R. Capadona[1,2]*

[1]Department of Biomedical Engineering, Case Western Reserve University, School of Engineering, 2071 MLK Jr. Drive, Wickenden Bldg, Cleveland OH 44106, USA

[2]Advanced Platform Technology Center, L. Stokes Cleveland VA Medical Center, Rehab. R&D, 10701 East Blvd. Mail Stop 151 AW/APT, Cleveland OH 44106, USA

Article Info

Article Notes
Received: July 16, 2018
Accepted: August 03, 2018

***Correspondence:**
Dr. Jeffrey R. Capadona, Case Western Reserve University, 2071 Martin Luther King Jr. Drive, Cleveland, OH, 44107, USA; Email: jrc35@case.edu

Keywords
Intracortical Microelectrode
Brain
Anti-Inflammatory
Brain-Machine Interface
Neuroinflammation
Glial Response

ABSTRACT

Intracortical microelectrodes are used both in basic research to increase our understanding of the nervous system and for rehabilitation purposes through brain-computer interfaces. Yet, challenges exist preventing the widespread clinical use of this technology. A prime challenge is with the neuroinflammatory response to intracortical microelectrodes. This mini-review details immunomodulatory strategies employed to decrease the inflammatory response to these devices. Over time, broad-spectrum anti-inflammatory approaches, such as dexamethasone and minocycline, evolved into more targeted treatments since the underlying biology of the neuroinflammation was elucidated. This review also presents studies which examine novel prospective targets for future immunomodulatory targeting.

Introduction: Brain-dwelling Intracortical Microelectrodes—Uses and Limitations

Intracortical microelectrodes were created as a tool for basic neuroscience research to understand the normal and diseased physiology of the brain for the treatment of neurological disorders, and they have since expanded to become critical components for brain-machine interfacing (BMI)[1-3]. BMI technologies have shown great success in enabling locked-in patients to interact with computers, robotic limbs, and their own electrically driven limbs[3,4]. The recent advances have inspired worldwide enthusiasm resulting in billions of dollars of federal and industrial sponsorships to promote understanding the brain for rehabilitative and preventative medicine applications. Additionally, private philanthropists have also demonstrated excitement in the field by investing in the use of brain interfacing technologies as a means to human augmentation[5,6]. In the future, brain-dwelling microelectrodes could restore patterns of normal brain function in diseased or injured patients through therapeutic modulation of dysfunctional pathways. Thus, implantable microelectrodes in the future can be transformative in not only restoring sensorimotor abilities but also improving the treatment of brain disorders and augmenting human capabilities.

While the promise of these incredible technologies is real, caution must be taken as implications regarding optimal performance and unforeseen side effects following device implantation into the brain are not fully characterized. For example, we recently demonstrated that rats with intracortical microelectrodes implanted in the primary motor cortex exhibited a remarkable 527% increase in the

time required to complete a fine motor task[7]. Notably, the increased time to complete fine motor tasks was correlated with persistent damage to the blood-brain barrier, as a result of the neuroinflammatory response.

Despite the incredible enthusiasm for brain interfacing technologies, it is widely understood that microelectrodes for BMI technologies exhibit limited long-term viability where recordings typically fail 6 months to 1 year after implantation, due to multimodal failure mechanisms.[8] One of the primary causes for this failure is believed to originate from the perpetual inflammatory response following implantation[9,10]. Since the neurodegenerative progression of the disease and injured states are often associated with the progression of cognitive and motor-related disease symptoms, the relative contribution of implanting potentially restorative devices that could actually contribute to the perceived progression of disease-like symptoms remains unclear, and in most cases untested. Therefore, these critical questions need to be answered in respect to both understanding disease progression and the role of interfacing technologies in both treating and propagating disease-like symptoms of deteriorated cognitive and motor abilities.

Fortunately, much work is being done surrounding microelectrode design to reduce the inflammatory response (for review see[8,11]). Although significant progress has been made fabricating ultra-small implants, a universal approach to reduce inflammation regardless of the device decreases the need for design restrictions for successful tissue integration. For example, larger brain-dwelling electrodes are necessary to reach deep brain structures such as nucleus accumbens[12]. Additionally, in order to input/output more degrees of freedom from these neural prostheses, many electrode sites are needed resulting in designs with greater surface area[13]. Larger electrodes result in more foreign material in the brain disrupting tissue; the more invasive the implant, the more tissue is damaged during implantation. Ideally, lessons learned about the neuroinflammatory response to smaller intracortical microelectrodes can be applied to future applications of any brain-dwelling electrode, regardless of size or design. The factors that drive the inflammatory response must be targeted to reduce neuronal dysfunction and damage, to lead to improved signal for any application using implantable microelectrodes to ensure chronic, high-fidelity function.

An active immunomodulatory approach should afford the resolution of the damage caused during the implantation of the microelectrode, while also curtailing the chronic neurodegenerative aspects of the neuroinflammatory response to enhance the long-term function of the device. Furthermore, an immunomodulatory approach should also work in combination with innovative design strategies to combat the foreign body response, as no one solution can adapt as fast as the dynamic temporally facilitated biological response. In addition to modifications in the design of the probe to mitigate the inflammatory response, there are also biological and materials-based approaches undertaken to reduce neuroinflammation to chronically implanted intracortical microelectodes (reviewed in [8]). In this mini-review, however, we focus on only direct immunomodulatory approaches applied to reduce the inflammatory response and improve the function of implantable intracortical microelectrodes, and we provide our current vision of the leading prospects moving forward.

Discussion

The following sections will discuss leading active anti-inflammatory approaches to mitigate microelectrode-induced neuroinflammation.

Steroids: Dexamethasone (DEX)

The first method to directly modulate the immune system after implantation of microelectrodes was the use of systemic injection of dexamethasone (DEX), commonly used for the treatment of multiple sclerosis in the clinic. DEX is a synthetic glucocorticoid that induces pleiotropic anti-inflammatory functions through cellular glucocorticoid receptors. Most cells, including microglia, express receptors for glucocorticoids such as dexamethasone[14].

The first group to report the use of DEX to minimize neuroinflammation in response to intracortical microelectrodes peripherally injected DEX (200 mg/kg) in rats daily for six days beginning the day of surgery. The systemic administration of DEX led to decreased astrocytic response at 1 and 6 weeks post-implantation[15]. However, the same systemic repeated administration of DEX at a lower dose (200 μg/kg) in rats, led to a "transient increase" in both microglial/macrophage responses and laminin deposition which was interpreted by the authors as a response to injury, repair, and/or angiogenesis[16]. Since high systemic delivery of steroids can have serious side effects, DEX has also been incorporated into different probe coatings: poly(ethyl-vinyl) acetate, nitrocellulose, carbon nanotubes, and poly(lactic-co-glycolic acid) nanoparticles within alginate hydrogel matrices[17,18]. Each of the studies delivering DEX locally examined different markers of neuroinflammation. Benefits common to all the studies included decreased astrocytic response, reduced microglial/macrophage activity, mitigated neuronal loss, and minimized chondroitin sulfate proteoglycan expression[15,19-21].

DEX has also been shown to improve the functional recording performance of intracortical microelectrode. For example, DEX was loaded into electrospun biodegradable nano-fibers followed by an alginate hydrogel encapsulation

to allow for long-term release. Poly (3,4-ethylene dioxythiophene) (PEDOT) was then electrochemically polymerized on the electrode sites within the scaffold. The composite coating with PEDOT elicited decreased impedance compared to non-PEDOT coated electrodes and allowed for higher applied charge density than traditional electrodes[22]. DEX incorporated into nanoparticle embedded coatings reduced impedance compared to no-drug controls by 25%, likely due to the demonstrated decreased tissue response[23]. Zhong and colleagues were able to release DEX from nitrocellulose coatings for 16 days *in vitro*. However, once the drug is depleted from the probe material, it is currently not possible to reload the material with the drug, Furthermore, acute strategies to mitigate the inflammatory response have not been completely successful at more chronic time points[24,25]. Currently, continuous local delivery of a drug such as DEX can be delivered *in vitro* on a 1.5 mm metal neural probe using microfluidic technology[26]. As the development of this technology progresses to incorporate a microfluidic delivery system into smaller, functional, neural probes, local continuous delivery of DEX can be a promising strategy in a larger multifaceted anti-inflammatory approach.

Antibiotics

Another broad-spectrum drug that has been investigated to decrease neuroinflammation associated with microelectrode implantation is minocycline. Minocycline is a semi-synthetic tetracycline shown to be neuroprotective in brain and spinal cord injury[27]. Rennekar and colleagues were the first group to use minocycline to improve neural recordings from intracortical microelectrodes. The team dissolved minocycline-HCl in the drinking water of experimental rats for 2 days prior to probe implantation through 5 days post-implantation. It was estimated that the rats received about 4 mg minocycline per day (13–20 mg kg^{-1}), based on water consumption. After 6 days, the group receiving minocycline yielded significantly higher signal to noise ratios (SNR) and the percentage of active channels detecting neural activity was higher than the control group. Both metrics for improved recording quality were maintained through 4 weeks post-implantation (study completion). Additionally, glial scarring was reduced with minocycline administration at both of the time points in which histology was examined, 1 and 4 weeks post-implantation [28]. Unfortunately, no report of neuronal density, known to die back around the implants, was provided in Rennekar's study.

An earlier study had previously shown that to achieve neuroprotective effects, minocycline must be present by the neurons at much higher levels[29,30]. Thus, Zhang *et al*. incorporated minocycline into thin film coatings on oxidized silicon, a common material for neural electrodes[31]. The thin film coatings allow for increased loading and local, sustained release of higher concentrations of minocycline (over 46 days). In preliminary *in vitro* testing, minocycline incorporated in thin film coatings were able to elicit neuroprotective activity similar to controls dispersed directly into the culture media. Although these studies were conducted *in vitro*, the results demonstrated promise for the extended delivery of minocycline via neural probes. Additionally, recent work showed that minocycline delivered through microfluidic channels fabricated within an implanted neural probe led to reductions in microglial reactions between 200-400 μm from the probe interface[32]. Such distances are unlikely to impact neural recording quality. Interestingly, minocycline delivery had no effect on astrocyte density, inconsistent with the original findings from Rennekar *et al.* Similarly, in concordance to the previously mentioned studies, Hayn *et al*. (2017) administered minocycline in a single local dose (20 μg/μL) via cannula implantation in the motor cortex of rats and found decreased neuronal death and anti-inflammatory effects with improved motor function[33]. Overall, these studies demonstrate promise for minocycline to mitigate the neuroinflammatory response around implanted microelectrodes.

However, long-term dosing of minocycline begets an increased risk of adverse events—including hyperpigmentation of the skin and other organs [34,35]. Minocycline possesses an increased chance of serious adverse events relative to other tetracyclines[35]. Thus, minocycline could be part of a multi-faceted approach to reduce initial neuroinflammation, but less risky alternative therapies are needed for chronic applications.

Because of an increased understanding of the biological response to microelectrode implantation, more specific immunomodulatory approaches are being utilized to mitigate the inflammatory response and improve the chronic performance of these devices.

Mitigating the Glial Response

Both microglia and astrocytes contribute to the biological response affecting electrode function. Thus, an effective way to modulate the immune response would be to mitigate the glial response. The Bellamkonda group utilized alpha-melanocyte stimulating hormone (MSH) (an endogoneous tridecapetide) to target the microglial response[36]. Alpha-MSH has been shown to inhibit both nitric oxide and pro-inflammatory cytokines produced by activated microglia—both of which are detrimental to neuronal health[37]. In their study, the Bellamkonda group coupled the Alpha-MSH peptide to silicon single shank planar microprobes and implanted the probes into the motor cortex of rats. The astrocytic and activated microglial response was examined via histology at 1 and 4 weeks post-implantation. At both time points, the activated

microglial response was significantly decreased compared to a non-coated control probe. There was no notable difference in astroglial scarring at 1 week, but at 4 weeks post-implantation significantly less scarring was present[36].

Purcell *et al*. administered flavopiridol to rats implanted with Michigan-style single shank silicon multi-channel intracortical electrodes[38]. Flavopiridol arrests progression into the cell cycle, yet, re-entry into the cell cycle has been demonstrated in glial activation as shown by upregulation of cell-cycle components[39]. Thus, flavopiridol was hypothesized to lead to decreased glial activation and improved intracortical microelectrode recording performance. However, Purcell *et al*. were unable to demonstrate improved neural recording or decreased presence of glial cells (astrocytes and microglia combined)[38].

Another immunomodulatory approach that has been explored was to use a cytokine receptor antagonist to reduce neuroinflammation. Interleukin- 1 receptor antagonist (IL-1Ra) has been used in human clinical trials for rheumatoid arthritis treatment and is endogenously released by microglia to facilitate neuroprotection [40,41]. Neural probe coatings incorporated with IL-1Ra have been successfully used to improve neuronal survival and reduce glial scarring as long as four weeks post-implantation[42,43]. Unfortunately, no information has been reported to date about either chronic time points or the effects on recording performance.

Targeting the Inflammasome

Given the role of the inflammasome in brain injury models, targeting the players of this construct can be pivotal in reducing neuroinflammation following intracortical microelectrode implantation. The inflammasome is an innate immune protein complex. The inflammasome activates caspase-1, an enzyme which allows a pivotal pro-inflammatory cytokine, IL- 1β, to achieve its active form. IL-1β has been shown to be significantly upregulated around intracortical probes and plays a role in blood-brain barrier (BBB) dysfunction[11,44]. Kozai *et al*. used a knock-out mouse model to demonstrate caspase-1 as a promising immunomodulatory target for improving chronic single-unit recordings by intracortical microelectrodes implanted in the visual cortex of mice[45]. Data obtained by Kozai *et al*. suggested that pharmacologic interventions which target the components and downstream players of the inflammasome can yield more stable chronic neural recordings. Future studies could entail using a caspase inhibitor such as VX-765 or Ac-YVAD-cmk, both of which have demonstrated neuroprotection in various models[46-48].

Targeting Blood-derived Cells

Blood-derived cells have been shown to be major contributors to the inflammatory response of brain-dwelling intracortical microelectrode, despite the perception of the immune privileged brain[49,50]. Thus, a recently developed hypothesis is that immunomodulatory strategies that limit blood-derived immune cells from the area within the brain, surrounding the implanted neural electrodes, could mitigate the inflammatory response and concurrently improve recording performance. Targeting monocyte chemoattractant protein-1 (MCP-1) using a knock out mouse model was found to decrease the inflammatory response to intracortical microelectrode implantation[51]. MCP-1 is a chemoattractant which attracts monocytes to areas of inflammation, such as the response to a neural electrode in the brain. Although this study did not directly evaluate reductions to blood-derived cells, they found that MCP-1 knock-out mice reduced BBB leakage, microglia/macrophage response, and astrocytic response, all leading to an increased neuronal density at acute and chronic time points. Notably, the improved neuroinflammatory response was recapitulated with pharmacological inhibition of MCP-1 via daily intraperitoneal injections[51]. It will be critical for future studies to also investigate the impact on neural recordings.

Pattern Recognition Receptors

Given the presence of blood and cellular damage present at the tissue-device interface after implantation, targeting cellular receptors that recognize damage and initialize the production of pro-inflammatory cytokines promises to reduce the inflammatory response and improve intracortical microelectrode performance. Pattern recognition receptors detect cellular damage and blood proteins and are found on microglia, neurons, astrocytes, and blood-derived macrophages present at the probe interface. Through the use of knock-out mouse models and a small-molecule inhibitor, we have previously shown that targeting the toll-like receptor (TLR)/cluster of differentiation 14 (CD14) pathways can improve both acute and chronic microelectrode performance[49,52]. Thus, pattern recognition receptors are amenable targets to improve neural recording from brain-dwelling intracortical microelectrodes, yet appropriate dosing regimens for optimal wound healing and anti-inflammatory responses remains to be determined.

Conclusion and Perspectives

The goal of our mini-review was to highlight key studies in the many parallel approaches to mitigating the neuroinflammatory response to brain-dwelling neural electrodes **(Table 1)**. The mini-review was intended as a starting point for discussion towards the integration of a more targeted approach to device integration. As the list of interesting targets within the brain for interfacing continues to grow, a more comprehensive and specific

Table 1. Summary of strategies to mitigate the neuroinflammatory response to intracortical microelectrodes.

Strategy	Approaches	Suggested next steps/remarks
Broad anti-inflammatory strategies		
Steroids	Peripheral injections Probe coatings Electrode site coatings Local delivery via microfludics in probe	Development of continuous local delivery platform, determine effect on neural recording
Antibiotics	Add to drinking water Incorporate in thin film coatings Local delivery via microfludics in probe Single local dose via cannula	Determine effect local delivery has on neural recording. Other strategies might be less risky.
Targets of more specific immunomodulatory strategies		
Glial Response	Alpha-MSH probe coating	Determine effect on neural recording
	Single dose of flavopiridol	Did not result in improvement in neural recording performance
	IL-1Ra probe coating	Determine effect on neural recording
Inflammasome	Caspase knock-out model	Determine effect small molecule or other clinically relevant therapy has on neural recording
Blood-derived cells	MCP-1 knock out model Pharmacological inhibition of MCP-1	Determine effect on neural recording
Pattern recognition receptors	CD14 knock out model Pharmacological inhibition of CD14	Determine dosing regimens of small molecule or other clinically relevant therapy

strategy for device integration will be required. Electrode design alone will not be the answer. As a more detailed understanding of the biology at the probe-tissue interface is elucidated, more directed therapeutic interventions which modulate the immune system will be required to improve device performance to a long-term, reliable system. It should be clear that many promising approaches to mitigation of inflammation are under development and studies looking at the effects of neural recording to many of these approaches need to be conducted before the aforementioned approaches are widely adapted. Strategies that utilize immunomodulatory interventions already in the clinic will need to be coupled with responsive local delivery platforms to avoid peripheral anti-inflammatory treatment that should not be a long-term solution. Large animal and clinical demonstration of such approaches will soften the barrier to novel immunomodulatory strategies at earlier stages of development and ultimately bring forth significant benefit to the function of these devices and the rehabilitation of disabled individuals.

Funding Sources

Support for the authors was provided in part by the National Institute of Health, National Institute of Neurological Disorders and Stroke, (Grant # 1R01NS082404-01A1), the Office of the Assistant Secretary of Defense for Health Affairs through the Peer Reviewed Medical Research Program (Award No. W81XWH-15-1-0608), the Presidential Early Career Award for Scientists and Engineers (PECASE), and by Merit Review Award (B1495-R and B2611-R) from the United States (US) Department of Veterans Affairs Rehabilitation Research and Development Service. None of the funding sources aided in collection, analysis and interpretation of the data, in writing of the manuscript, or in the decision to submit the manuscript for publication. The authors have no conflict of interest related to this work to disclose. The contents do not represent the views of the U.S. Department of Veterans Affairs or the United States Government.

References

1. Golub MD, Chase SM, Batista AP, et al. Brain–computer interfaces for dissecting cognitive processes underlying sensorimotor control. *Current opinion in neurobiology.* 2016; 37: 53-58.
2. Collinger JL, Wodlinger B, Downey JE, et al. High-performance neuroprosthetic control by an individual with tetraplegia. *The Lancet.* 2013; 381(9866): 557-564.
3. Ajiboye AB, Willett FR, Young DR, et al. Restoration of reaching and grasping movements through brain-controlled muscle stimulation in a person with tetraplegia: a proof-of-concept demonstration. *The Lancet.* 2017; 389(10081): 1821-1830.
4. Donoghue J. Bridging the Brain to the World: A Perspective on Neural Interface Systems. *Neuron.* 2008; 60(3): 511-521.
5. Winkler R. Elon Musk Launches Neuralink to Connect Brains With Computers. *The Wallstreet Journal.* 2017.

6. Wu J, Rao RPN. How close are we to Elon Musk's brain-computer interface? 2017; http://www.cnn.com/2017/04/12/health/brain-computer-interface-partner/.

7. Goss-Varley M, Dona KR, McMahon JA, et al. Microelectrode implantation in motor cortex causes fine motor deficit: Implications on potential considerations to Brain Computer Interfacing and Human Augmentation. *Scientific Reports.* 2017; 7: 15254.

8. Jorfi M, Skousen JL, Weder C, et al. Progress towards biocompatible intracortical microelectrodes for neural interfacing applications. *J Neural Eng.* 2015; 12(1): 011001.

9. Nolta NF, Christensen MB, Crane PD, et al. BBB leakage, astrogliosis, and tissue loss correlate with silicon microelectrode array recording performance. *Biomaterials.* 2015; 53: 753-762.

10. Barrese JC, Rao N, Paroo K, et al. Failure mode analysis of silicon-based intracortical microelectrode arrays in non-human primates. *J Neural Eng.* 2013; 10(6): 066014.

11. Karumbaiah L, Saxena T, Carlson D, et al. Relationship between intracortical electrode design and chronic recording function. *Biomaterials.* 2013; 34(33): 8061-8074.

12. Wu H, Miller KJ, Blumenfeld Z, et al. Closing the loop on impulsivity via nucleus accumbens delta-band activity in mice and man. *Proceedings of the National Academy of Sciences.* 2018; 115(1): 192-197.

13. Lebedev MA, Nicolelis MA. Brain–machine interfaces: past, present and future. *TRENDS in Neurosciences.* 2006; 29(9): 536-546.

14. Reichardt HM, Tuckermann JP, Göttlicher M, et al. Repression of inflammatory responses in the absence of DNA binding by the glucocorticoid receptor. *The EMBO journal.* 2001; 20(24): 7168-7173.

15. Shain W, Spataro L, Dilgen J, et al. Controlling cellular reactive responses around neural prosthetic devices using peripheral and local intervention strategies. *IEEE transactions on neural systems and rehabilitation engineering.* 2003; 11(2): 186-188.

16. Spataro L, Dilgen J, Retterer S, et al. Dexamethasone treatment reduces astroglia responses to inserted neuroprosthetic devices in rat neocortex. *Experimental neurology.* 2005; 194(2): 289-300.

17. Hempen C, Weiss E, Hess CF. Dexamethasone treatment in patients with brain metastases and primary brain tumors: do the benefits outweigh the side-effects. *Supportive care in cancer.* 2002; 10(4): 322-328.

18. Heimdal K, Hirschberg H, Slettebø H, et al. High incidence of serious side effects of high-dose dexamethasone treatment in patients with epidural spinal cord compression. *Journal of neuro-oncology.* 1992; 12(2): 141-144.

19. Kim DH, Martin DC. Sustained release of dexamethasone from hydrophilic matrices using PLGA nanoparticles for neural drug delivery. *Biomaterials.* 2006; 27(15): 3031-3037.

20. Zhong Y, Bellamkonda RV. Dexamethasone-coated neural probes elicit attenuated inflammatory response and neuronal loss compared to uncoated neural probes. *Brain research.* 2007; 1148: 15-27.

21. Luo X, Matranga C, Tan S, et al. Carbon nanotube nanoreservior for controlled release of anti-inflammatory dexamethasone. *Biomaterials.* 2011; 32(26): 6316-6323.

22. Abidian MR, Martin DC. Multifunctional Nanobiomaterials for Neural Interfaces. *Advanced Functional Materials.* 2009; 19(4): 573-585.

23. Mercanzini A, Reddy ST, Velluto D, et al. Controlled release nanoparticle-embedded coatings reduce the tissue reaction to neuroprostheses. *Journal of Controlled Release.* 2010; 145(3): 196-202.

24. Potter KA, Jorfi M, Householder KT, et al. Curcumin-releasing mechanically adaptive intracortical implants improve the proximal neuronal density and blood–brain barrier stability. *Acta biomaterialia.* 2014; 10(5): 2209-2222.

25. Szarowski D, Andersen M, Retterer S, et al. Brain responses to micro-machined silicon devices. *Brain research.* 2003; 983(1-2): 23-35.

26. Frey L, Bandaru P, Zhang YS, et al. A Dual-Layered Microfluidic System for Long-Term Controlled In Situ Delivery of Multiple Anti-Inflammatory Factors for Chronic Neural Applications. *Advanced Functional Materials.* 2018; 28(12): 1702009.

27. Yong VW, Wells J, Giuliani F, et al. The promise of minocycline in neurology. *The Lancet Neurology.* 2004; 3(12): 744-751.

28. Rennaker R, Miller J, Tang H, et al. Minocycline increases quality and longevity of chronic neural recordings. *Journal of neural engineering.* 2007; 4(2): L1.

29. Pi R, Li W, Lee NT, et al. Minocycline prevents glutamate-induced apoptosis of cerebellar granule neurons by differential regulation of p38 and Akt pathways. *Journal of neurochemistry.* 2004; 91(5):1219-1230.

30. Garcia-Martinez EM, Sanz-Blasco S, Karachitos A, et al. Mitochondria and calcium flux as targets of neuroprotection caused by minocycline in cerebellar granule cells. *Biochemical pharmacology.* 2010; 79(2): 239-250.

31. Zhang Z, Nong J, Zhong Y. Antibacterial, anti-inflammatory and neuroprotective layer-by-layer coatings for neural implants. *Journal of neural engineering.* 2015; 12(4): 046015.

32. Liu B, Kim E, Meggo A, et al. Enhanced biocompatibility of neural probes by integrating microstructures and delivering anti-inflammatory agents via microfluidic channels. *Journal of neural engineering.* 2017; 14(2): 026008.

33. Hayn L, Deppermann L, Koch M. Reduction of the foreign body response and neuroprotection by apyrase and minocycline in chronic cannula implantation in the rat brain. *Clinical and Experimental Pharmacology and Physiology.* 2017; 44(2): 313-323.

34. Reed DN, Gregg FO, Corpe RS. Minocycline-induced black bone disease encountered during total knee arthroplasty. *Orthopedics.* 2012; 35(5): e737-e739.

35. Ochsendorf F. Minocycline in acne vulgaris. *American journal of clinical dermatology.* 2010; 11(5): 327-341.

36. He W, McConnell GC, Schneider TM, et al. A novel anti-inflammatory surface for neural electrodes. *Advanced Materials.* 2007; 19(21): 3529-3533.

37. Galimberti D, Baron P, Meda L, et al. α-MSH peptides inhibit production of nitric oxide and tumor necrosis factor-α by microglial cells activated with β-amyloid and interferon γ. *Biochemical and biophysical research communications.* 1999; 263(1): 251-256.

38. Purcell EK, Thompson DE, Ludwig KA, et al. Flavopiridol reduces the impedance of neural prostheses in vivo without affecting recording quality. *Journal of neuroscience methods.* 2009; 183(2): 149-157.

39. Di Giovanni S, Movsesyan V, Ahmed F, et al. Cell cycle inhibition provides neuroprotection and reduces glial proliferation and scar formation after traumatic brain injury. *Proceedings of the National Academy of Sciences of the United States of America.* 2005; 102(23): 8333-8338.

40. Pinteaux E, Rothwell NJ, Boutin H. Neuroprotective actions of endogenous interleukin-1 receptor antagonist (IL-1ra) are mediated by glia. *Glia.* 2006; 53(5): 551-556.

41. Arend WP. The balance between IL-1 and IL-1Ra in disease. *Cytokine & growth factor reviews.* 2002; 13(4-5): 323-340.

42. Gutowski SM, Shoemaker JT, Templeman KL, et al. Protease-degradable PEG-maleimide coating with on-demand release of IL-1Ra to improve tissue response to neural electrodes. *Biomaterials.* 2015; 44: 55-70.

43. Taub AH, Hogri R, Magal A, et al. Bioactive anti-inflammatory coating

for chronic neural electrodes. *Journal of biomedical materials research Part A.* 2012; 100(7): 1854-1858.

44. Tian W, Kyriakides TR. Matrix metalloproteinase-9 deficiency leads to prolonged foreign body response in the brain associated with increased IL-1β levels and leakage of the blood-brain barrier. *Matrix Biology.* 2009; 28(3): 148-159.

45. Kozai TD, Li X, Bodily LM, et al. Effects of caspase-1 knockout on chronic neural recording quality and longevity: Insight into cellular and molecular mechanisms of the reactive tissue response. *Biomaterials.* 2014; 35(36): 9620-9634.

46. Wannamaker W, Davies R, Namchuk M, et al. (S)-1-((S)-2-{[1-(4-Amino-3-chloro-phenyl)-methanoyl]-amino}-3, 3-dimethyl-butanoyl)-pyrrolidine-2-carboxylic acid ((2R, 3S)-2-ethoxy-5-oxo-tetrahydro-furan-3-yl)-amide (VX-765), an Orally Available Selective Interleukin (IL)-Converting Enzyme/Caspase-1 Inhibitor, Exhibits Potent Anti-Inflammatory Activities by Inhibiting the Release of IL-1β and IL-18. *Journal of Pharmacology and Experimental Therapeutics.* 2007; 321(2): 509-516.

47. Rabuffetti M, Sciorati C, Tarozzo G, et al. Inhibition of caspase-1-like activity by Ac-Tyr-Val-Ala-Asp-chloromethyl ketone induces long-lasting neuroprotection in cerebral ischemia through apoptosis reduction and decrease of proinflammatory cytokines. *Journal of Neuroscience.* 2000; 20(12): 4398-4404.

48. Bassil F, Fernagut PO, Bezard E, et al. Reducing C-terminal truncation mitigates synucleinopathy and neurodegeneration in a transgenic model of multiple system atrophy. *Proceedings of the National Academy of Sciences.* 2016; 113(34): 9593-9598.

49. Bedell HW, Hermann JK, Ravikumar M, et al. Targeting CD14 on blood derived cells improves intracortical microelectrode performance. *Biomaterials.* 2018; 163: 163-173.

50. Ravikumar M, Sunil S, Black J, et al. The Roles of Blood-derived Macrophages and Resident Microglia in the Neuroinflammatory Response to Implanted Intracortical Microelectrodes. *Biomaterials.* 2014; S0142-9612(35): 8049-8064.

51. Sawyer AJ, Tian W, Saucier-Sawyer JK, et al. The effect of inflammatory cell-derived MCP-1 loss on neuronal survival during chronic neuroinflammation. *Biomaterials.* 2014; 35(25): 6698-6706.

52. Hermann JK, Ravikumar M, Shoffstall AJ, et al. Inhibition of the cluster of differentiation 14 innate immunity pathway with IAXO-101 improves chronic microelectrode performance. *Journal of Neural Engineering.* 2018; 15(2): 025002.

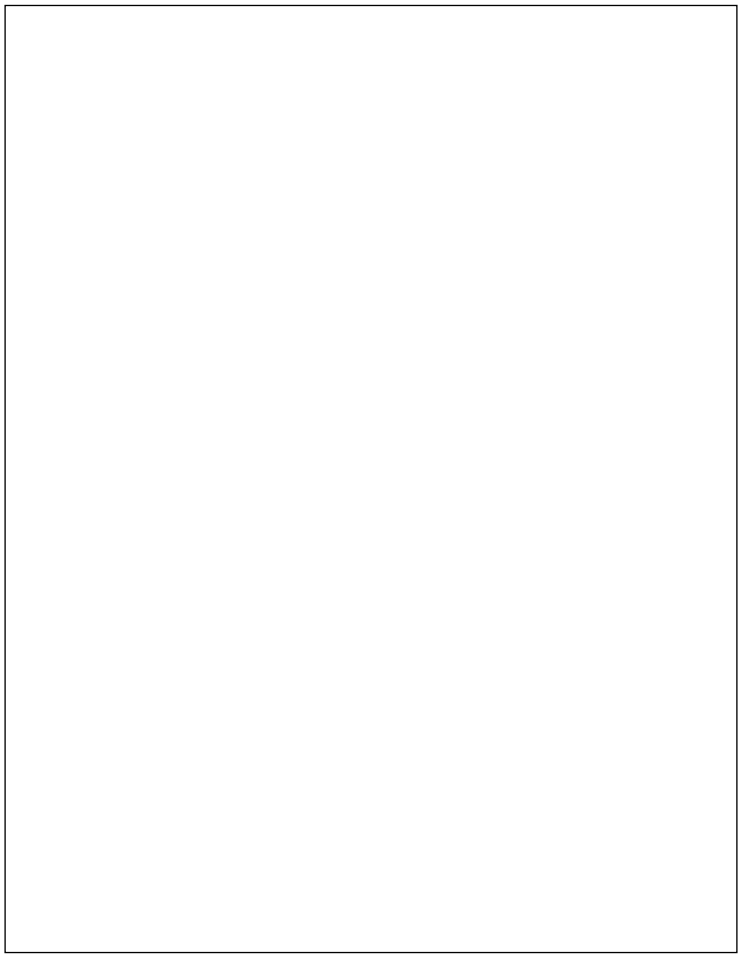

Available online at www.sciencedirect.com

ScienceDirect

Current Opinion in
Biomedical Engineering

Bioinspired materials and systems for neural interfacing

Andrew J. Shoffstall[1,2] and Jeffrey R. Capadona[1,2]

Abstract

Brain-implanted devices have a number of applications with significant potential. Widespread adoption hinges on the ability to produce an interface that can engage with neural tissue over long periods of time. Biomimetic approaches can help camouflage implants by altering their characteristics to better reflect the neural environment, which may promote an attenuated inflammatory response, improving integration into native tissue, and ultimately improve device performance. Additionally, as new neural interfacing technologies are developed, unexpected challenges can arise, requiring novel tools to enable their implementation. Unlikely inspiration from the mechanically-dynamic sea-cucumber-dermis, mechanism of a mosquito bite, squid beak mechanics, and the woodpecker's dynamic control of intracranial pressure represent some of the exciting bioinspired systems that may lead to unique solutions to recent challenges in neural interfacing.

Addresses

[1] Department of Biomedical Engineering at Case Western Reserve University, Cleveland, OH 44106, USA

[2] Advanced Platform Technology Center at Louis Stokes Cleveland VA Medical Center, Cleveland, OH 44106, USA

Corresponding author: Capadona, Jeffrey R (jeffrey.capadona@case.edu)

Current Opinion in Biomedical Engineering 2018, **6**:110–119

This review comes from a themed issue on **Biomaterials: Neural Interfaces & Neuro-prosthetics**

Edited by **Wutian Wu** and **Seeram Ramakrishna**

Received 30 January 2018, revised 12 April 2018, accepted 15 May 2018

https://doi.org/10.1016/j.cobme.2018.05.002

Keywords

Biomimetic, Bio-inspired, Materials, Neural interfacing.

Introduction

The first generations of chronic intracortical recording microelectrodes were introduced in their current forms starting in the 1970s and consisted of either metal microwires, silicon-based planar substrates ("Michigan-type"), or the multidimensional Pt/Ir-based "Utah Array" [1–3]. While significant strides in manufacturing, connectors and wireless telemetry have been made, surprisingly, the substrates for the neural interface itself, be it steel, gold, silicon or platinum/iridium, have remained relatively consistent across commercially available systems [4]. In the last two decades however, a new focus on designing a more biocompatible neural interface has expanded the neural engineer's toolbox beyond silicon and purely metallic substrates to a host of polymers, flexible carbon-based systems, and other systems that more closely resemble the endogenous biological environment.

Potential applications of neural interfaces vary, ranging from electrical stimulation vs. recording, pain management vs. restoration of sensation, clinical vs. research, and these applications may even possess potential for human augmentation and eventual integration with consumer electronics [5,6]. Each approach presents unique challenges for an optimal neural interface. Non-invasive technologies such as electroencephalography (EEG) controlled prostheses aim to reduce the risk of neural recording, but unfortunately do not currently produce signal quality as robust as their more invasive counterparts [7]. More invasive approaches like intracortical implants, produce high fidelity signals, but performance degrades over time due in part to degradation of the materials as well as the synergistic changing of the microenvironment near the device [4]. Placement and location also matter. The brain comprises a unique environment compared to other tissues in the body, owing to the blood–brain barrier, and is considered *immune privileged* [8]. Peripheral immune cells are typically prevented from escaping the vascular space since the environment being tightly regulated by lymph- and glymph-atic systems [9,10].

As recently highlighted by multiple labs, the role of neuroinflammation in the failure of recording microelectrode is still not entirely understood [11–13]. When a neural device is placed near the site of interest, that site is inherently changed and immediately begins remodeling. The remodeled tissue produces a scar, altering both actual and detectable neural activity and circuits. Depending on electrode placement in or next to neural tissue, the impact of scarring can have a more severe impact on device performance or on surrounding tissue. For example, new evidence further demonstrates that microelectrodes implanted in the motor cortex of the brain alters the motor behavior of rats, a finding that is highly correlated with chronic blood–brain barrier damage [14]. An ideal electrode would be one that can interface with the neural tissue without affecting any changes in the local environment.

Bioinspired and biomimetic approaches to neural Interfacing have the potential to help solve the issue of achieving more seamless device integration within the brain (Figure 1). Biomimicry is defined here as altering the physical, chemical, or electrical characteristics of an implanted material to more closely match the endogenous neural environment (Table 1). Bioinspiration, on the other hand, enhances neural systems by leveraging materials, methods, or other cues from nature and applying them toward analogous functions to improve the implantation and implementation of the device. This review discusses the recent advances (focusing on the last two-to-three years, 2015–2017) in both biomimetic and bioinspired approaches to improve the performance of neural interfaces.

It should be noted that while many groups have not specifically identified their research or developments as "biomimetic", the field of neural engineering is moving knowingly or unknowingly toward a more integrated biological approach. Therefore, the broad definition stated above has been adopted to the work discussed in the current review.

Mimicking physical aspects of the brain

Bulk stiffness & flexibility

Mechanical mismatch between the traditionally rigid materials used for neural interfaces and the pliant neural tissue is thought to play a role in recording longevity [15]. Strain generated by the device on the tissue is a function of micromotion, tethering, bulk stiffness and flexibility [16]. It has been postulated that there may be a threshold or limit for reducing the tissue response [17]. While a number of groups have published studies comparing the inflammatory response of stiff versus soft microelectrodes [4], few have been able to achieve devices in the same order-of-magnitude range as brain tissue.

Recently, Cui's research group has developed an ultrasoft (~1 MPa) material as well as a delivery vehicle system to produce an electrode that closely resembles the brain's stiffness (Figure 2A) [18,19]. Cui and colleagues demonstrated the ability to reduce the inflammatory response, improve neural integration, and reduce mechanical damage to nearby neurons [18]. Their microwires (125 μm diameter), made from an elastomeric and conductive PEG/PEDOT blend, were also capable of acute signal recordings [18,19]. Dissolvable adhesives on needles allowed the probes to be easily introduced into the brain.

Beyond just modifying bulk stiffness, multiaxial flexibility is likely to be in important factor. Luan et al. demonstrated an ultra-pliant probe made from nanothreads [20]. To achieve mechanical pliance on the same magnitude as the brain, the Durand lab developed what they call nanotube (CNT) "yarns" which are extremely

Figure 1

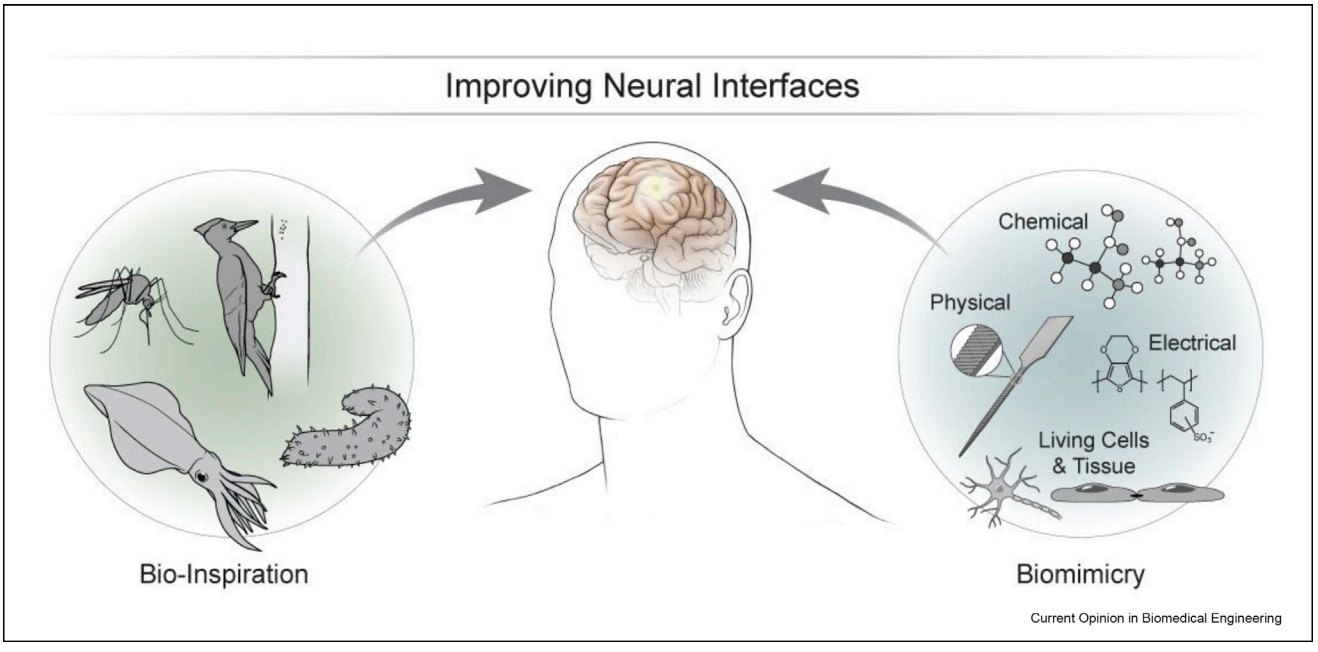

Overview schematic of biomimetic vs. bioinspired systems. Bioinspired and biomimetic systems for next generation neural interfaces have the potential to produce a robust neural interface that can engage with neural tissue over long periods of time. Biomimetic devices camouflage implanted materials by altering their characteristics to better reflect the local neural environment (e.g., physically, chemically, and electrically) which may promote a weaker inflammatory/immune response and improve device performance. Bioinspired neural systems leverage materials, methods, or other cues from nature and apply them toward analogous functions to improve the use or integration of the device. Figure courtesy of Cleveland FES Center.

Table 1

Table of some common biomimetic approaches. Implanted devices are mechanically, chemically, or electrically altered to exhibit similar properties to the natural neural environment. Features in the brain are small and mechanically pliant (Physical). Proteins are the first molecules to react to device implantation and their conformation determines downstream effects (Chemical). Neural tissues are excitable by ionic currents (Electrical). Ultimately, the brain is a dynamic, living environment. Permanent synthetic structures are more likely to cause inflammation and damage over time. Living systems have the advantage of being able to dynamically respond to a changing environment.

Mechanical	Chemical	Electrical	Living/Dynamic
➢ Bulk stiffness & flexibility ➢ Surface topography ➢ Size & form-factor	➢ Managing the protein corona ➢ Bioactive surfaces ➢ Antioxidants & free-radical scavengers	➢ Ionic conductors ➢ Flexible conductors ➢ Electrically responsive materials	➢ Cell-seeded scaffolding ➢ Tissue ingrowth/remodeling ➢ Biodegradable systems

small and ultra-pliant (Figure 2B) [21]. While the bulk materials themselves may be very stiff (on the order of several hundred GPa), they are easily flexed in any direction, thus mitigating any unnatural strains or stresses on the brain tissue.

Surface topography

At the microscale perspective, brain tissue is not a smooth surface. It is comprised of a vast network of extracellular matrix scaffolding, cytoskeleton structure, and is organized by distinct meningeal layers and distinct cortical layers, permeated throughout with vasculature. Each niche environment has a distinct set of mechanical properties and presentation to cells involved in the inflammatory response such as macrophages, microglia, and astrocytes. This complicated architecture is in contrast to the smooth fabricated electrodes typically implanted in the brain.

Therefore, it is not surprising that surface topography appears to be an important factor in the development of the inflammatory response surrounding the electrode [22]. Aiming to better match the brain's natural topography, Ereifej et al. demonstrated a method for manufacturing precise parallel grooves etched into the surface of a silicon device (Figure 2C) [23]. While their results indicated that their nanopatterned devices did not reduce histological markers of neuroinflammation compared to control implants, they did significantly alter gene expression. The authors have previously suggested a positive influence of nanopatterning on astrocytes that has the potential to better stabilize the device [24].

Size & form factor

Brain cells are soft, amorphous and on the microscale, while proteins are even smaller, with features at the pico- and nano-scale. Leading thoughts on the subject of microelectrode design have suggested that "smaller is better," and that scaling the devices to the subcellular level has the potential to largely reduce penetrating trauma during insertion and thus preventing the inflammatory or immune responses to the materials [25]. However, at that scale, traditional materials are challenging to manufacture. The choice of materials is balanced by the need for high conductivity and surface area and having enough strength to withstand implantation and indwelling tissue strains. Consequently as microelectrode sizes have gotten smaller, high charge capacity coatings (e.g., poly(3,4-ethylenedioxythiophene) (PEDOT)) combined with new substrates with better mechanical properties (e.g., silicon carbine (SiC) and carbon nanotubes (CNT)) have yielded ultra-small microelectrodes capable of implantation without shattering [25]. Silicon amorphous SiC has the benefit of being corrosion resistant, and has thus been studied as an alternative, more inert coating layer for Si-devices [26]. Along those lines, graphene and other next-generation materials also hold significant potential for developing ultrasmall, flexible, durable and conductive electrodes [27].

Neurons form intricate branched structures that sprawl many orders of magnitude greater than their individual size. Therefore, 3D macroporous nanoelectronic injectable mesh networks that form a sprawling neural interface mimicking the native network design, hold significant promise for developing a truly minimally invasive brain probe, (Figure 2D) [28,29]. "Neural dust" takes a similar approach as the injectable meshes but instead uses miniaturized devices integrated with piezocrystal transceivers which communicate to an externally placed transceiver via ultrasound energy, (Figure 2E) [30]. Such approaches have significant advantages of being able to interface with larger tissue volumes without the need for placing a large electrode into the tissue.

Managing and mimicking chemical aspects of the brain

In order for neurons and nerve cells to communicate with one another, complex chemical reactions send chemical signals from cell to cell. Unfortunately, some of the chemical and biological signaling molecules used by glial cells within neural tissue can lead to undesirable chemical reactions in neural cells, leading to neurodegenerative states. Many neurodegenerative glial cell

Figure 2

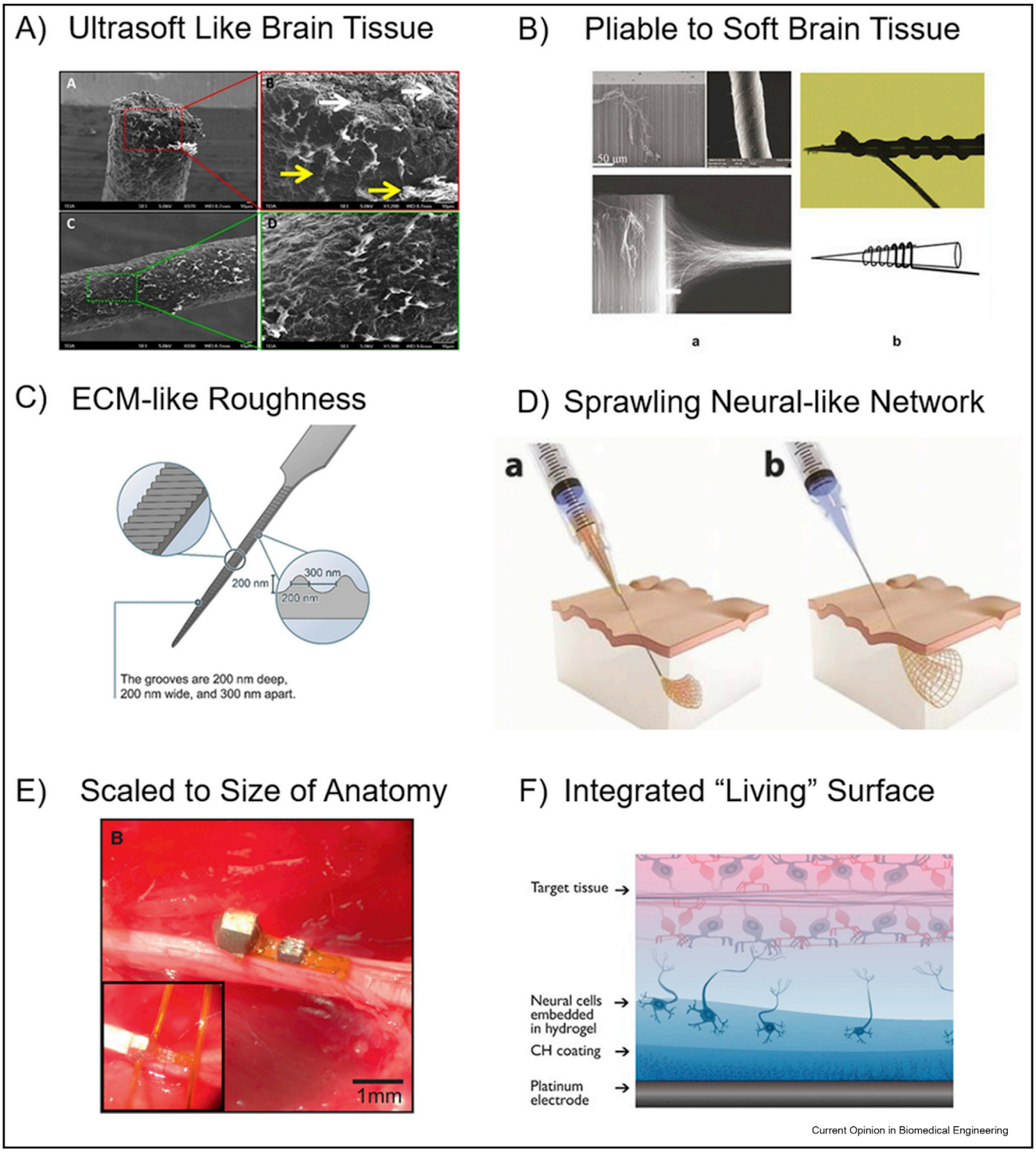

Examples from recent neural interface approaches in literature. A) Kolarcik et al. developed an electrically conductive soft polymer electrode by coating extruded PDMS wires with PEDOT [19]. These implants aim to match the mechanics and conductivity of native tissue. B) McCallum et al. developed an ultrasmall and flexible probe for electrophysiological recordings, made from a CNT yarn [21], reproduced under the creative commons license https://creativecommons.org/licenses/by/4.0/. C) Nanopatterned silicon substrate microelectrodes attempt to better mimic the innate microenvironment as extracellular matrix and cells form intertwining networked structures rather than smooth planar sheets that are currently present on the surface of microelectrode devices [23]. D) Injected polymer mesh electrodes unfold in situ to form sprawling network of microelectrode contacts, better mimicking the neural environment, and allowing for greater volume coverage without requiring a more invasive procedure [29]. E) "Neural dust" developed by researchers at Stanford University and funded by DARPA represents an attempt to even further miniaturize electrophysiological recording technology so that it can be deployed to and interact seamlessly with nerves [30,31]. F) Goding et al. generated "living electrodes" by layering multiple coatings, including a hydrogel scaffold which could support neural cell seeding and tissue in-growth [32]. Figures reproduced with copyright permission.

processes can be initiated by the inflammatory response to neural interfaces. Therefore, it is not surprising that chemistry has also been employed as a tool to inhibit unwanted inflammatory responses to neural interfaces. The biochemical methods for altering implanted microelectrode surfaces has been previously reviewed by Sommakia et al. [33] and Jorfi et al. [4], therefore this review will focus on only the most recent advances in managing and mimicking the chemistry of the brain.

Managing the protein corona

Protein adsorption to the surface of an implanted material is the first observable event upon the contact of a synthetic material with physiological fluids [34]. When soluble protein encounters implanted synthetic materials or devices, non-covalent interactions facilitate the denaturing of the protein. The denatured adsorbed protein then initiates an inflammatory response. The extent of denaturation of the protein and the amount of protein that adsorbs is largely controlled by the chemistry of the material [35,36]. Therefore, managing the protein corona to camouflage an implanted device remains the holy grail of surface modification for biomedical engineering applications.

Many approaches have been employed to create non-fouling surfaces [37]. Glycocalyx–like and carbohydrate decorated materials have an obvious biomimetic inspiration. However, polyethylene glycol (PEG) surface modification remains a common strategy for managing the protein corona for implanted devices. The extent of biomimicry in PEG approaches varies in the secondary modifications to the PEG itself, to incorporate additive features, such as drug delivery and crosslinking to control mechanics. Regardless, inert substrates in general are at least in part inspired by a natural analog in structure, chemistry, or function.

One of the most recent attempts to utilize PEG in neural interfacing was by the Otto laboratory. Otto's group showed that dip-coating intracortical microelectrode with PEG appears to be relatively ineffective at altering the foreign body response [38] despite the studies that have incorporated these coatings [39]. While the results may be discouraging, it has been widely recognized that not all PEG coatings are created equal. The PEG chain length and grafting density is a major factor for determining the coatings hydrodynamic mobility and therefore its efficacy of managing protein adsorption [40]. With the dip-coating (non-covalently bound) approach, limited efficacy may have been attributable to premature dissolution from the surface.

Bioactive surfaces, antioxidants, & free-radical scavengers

While the above section described the requirement to inhibit nonspecific protein-material interactions, there are equally as desirable interactions and reactions that are often the inspiration for biomaterials design of neural interfaces. Two of the most recent strategies to incorporate bioactive design into neural interfacing come from the Cui and Capadona laboratories. First, building from earlier work from the Tresco group [41], the Cui lab has spent years developing neural interfaces which incorporate the neuroadhesive L1 coating on neural interfaces to attenuate acute microglial attachment to neural electrodes [42], and which demonstrate improved neuronal density surrounding the implanted device [43]. Alternatively, the Capadona lab was the first to investigate the use of natural and biomimetic antioxidants such as resveratrol and curcumin, as well as free radical scavengers (MnTBaP) that may reduce local tissue response [44–46]. Anti-oxidative enzyme secretion is regulated during neuroinflammation to protect neurons from oxidative damage, which is often a consequence of frustrated phagocytosis [47]. The development of biomimetic and bioinspired systems to regulate oxidative damage promises to stabilize the neural interface and lead to improved tissue health and device performance.

Mimicking electrical aspects of the brain

Electrical signals are primarily transmitted in the brain by ions; devices transmit electrons. At the interface of these two systems is the Helmholtz double layer, where the ionic charges are converted to Faradaic or electron-based charge [48]. Therefore, many bioinspired systems have been explored to facilitate the transfer of charge between tissues and neural interfaces.

Ionic conductors (PEDOT)

Similar to nervous system tissue, poly(3,4-ethylenedioxythiophene):polystyrene sulfonate (PEDOT:PSS, or simply PEDOT) is a water-permeable volume-conductor. PEDOT along with a counter-ion, e.g., PSS, has been investigated extensively over the last several years [49–53]. PEDOT increases the surface area of the microelectrodes, decreasing impedance and increasing charge transfer capacity, and can facilitate ultra-small high-density arrays [54]. Significant work has been performed to characterize and improve PEDOT's performance and biocompatibility [55–57].

Flexible conductors

The brain conducts ionic currents through soft pliable nerves. Wang et al. developed stretchable, conductive polymers that may serve as interconnects [58]. The flexibility may improve the mechanical stability and integrity over repeated strain cycles. There are undoubtedly new polymers and materials yet to be discovered that may play a significant role in improving the device-tissue interface to transfer charge most efficiently from biological to *in silico*. Other applications may

even require ionically responsive materials as developed by Meng and Wnek et al. [59,60].

Dynamic (living) systems

At the cellular and molecular level, everything within the body is in a permanent state of flux and remodeling. Dynamically changing materials and systems may therefore have an advantage in their interacting with living neural tissue.

The ultimate biomimetic electrode may incorporate actual living elements. Cells attached to the electrode surface or incorporated into a scaffold have the advantage of being able to dynamically respond to changes in the local environment. Goding et al. developed a construct for seeding cells onto extracellular matrix components, (Figure 2F) [32]. Cui's group developed PEDOT/graphene-oxide (GO) materials that may improve the stability of neural stem cells during transplantation [61]. While the study was performed for a different purpose, the substrate may also be used for camouflaging implanted microelectrodes or providing sustained release of factors from an attached layer of mesenchymal stem cells. A third approach, developing macroporous nanowire nanoelectronic scaffolds, allows for the ingrowth of tissue [62,63], enabling the device to becomes tightly incorporated in the tissue environment after implantation. Having the biology interface well with the device opens up possibilities for introducing therapeutic cells (e.g. stem cells) or engineered cells as well as physiological recording with minimal disturbance to the tissues. Unfortunately, a significant concern with dynamic living systems is the possible complication if the device were to ever need removal.

Bioinspired systems for the neural interface

Developing new materials and systems to mimic the brain has also elicited the requirement of novel methods

Figure 3

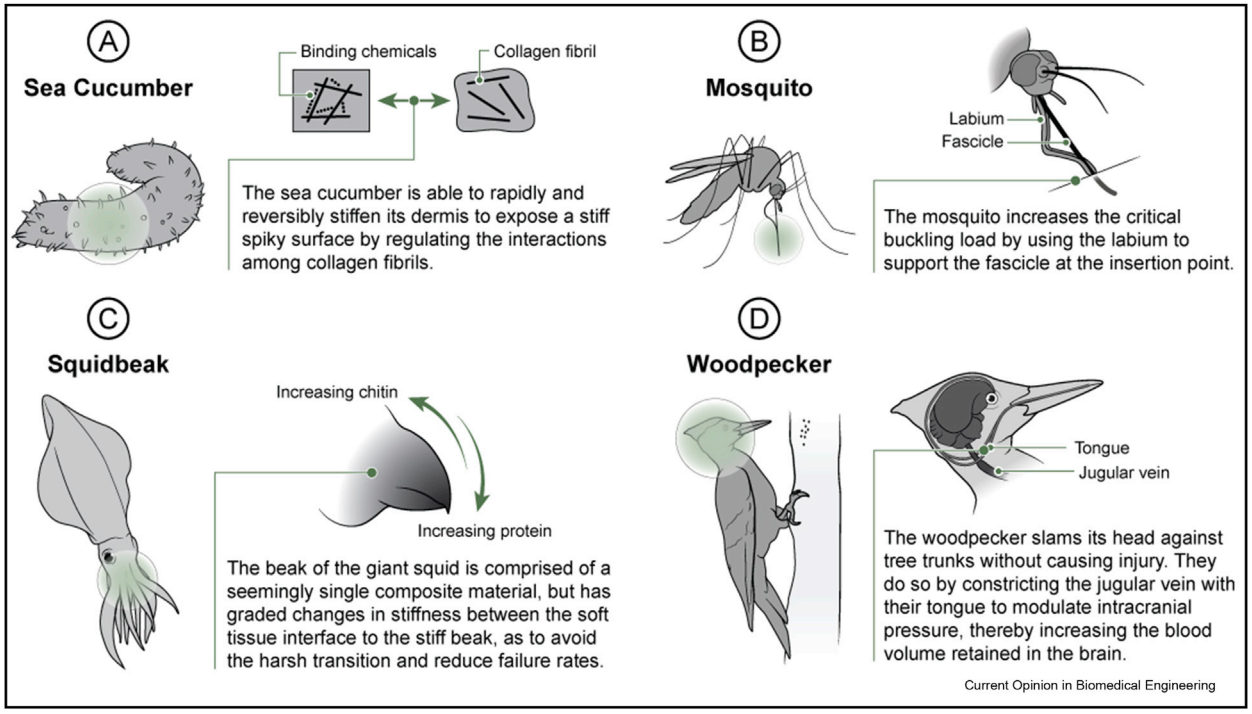

Bioinspired neural engineering solutions. A) The sea cucumber regulates interactions among collagen fibrils which organize in a chemo-responsive manner to transition from ~5 to ~50 MPa, upon exposure to a chemical regulator. Using a polymer analog, Capadona et al. produced an implant material that transitions from 4200 to 1.6 MPa upon exposure to emulate physiological conditions, enabling implantation into the brain in the "stiff" state, and mechanical matching of the pliant tissue in the "soft state" [64]. B) The squid beak comprises a single composite material that undergoes a continuous transition from soft-to-hard regions. Similar to the squid beak, Fox et al. developed nanocomposites with a controllable degree of cross-linking along the length of the device [65]. They utilized tunicate cellulose nanocrystals as the nanofiller which where functionalized with allyl moieties, allowing the team to use photo-induced thiol-ene chemistry to cross-link the nanofiller in a controlled fashion. Ultimately, the team was able to produce an increase in wet modulus from 60 to 300 MPa (~500% increase). C) The female mosquito uses its labium to help brace and guide its fascicle through the skin of its host prey. Taking inspiration from this, Shoffstall et al. developed a simple guide to brace planar microelectrodes at their tip during insertion to reduce effective length and increase the critical buckling load [66]. D) The woodpecker repeatedly slams its head against tree trunks with apparently little-to-no long-term consequences to its well-being due to its ability to temporarily regulate intracranial pressure to reduce dead-volume in the skull. A group of researchers and physicians invented a method of recreating the effect with the use of a simple compression brace placed around the neck [67,68]. Figure courtesy of Cleveland FES Center.

and tools to overcome new challenges which require thinking outside the box. Scientists and engineers have looked to nature for inspiration (Figure 3).

Sea cucumber inspired dynamic stiffness material

Over time, the quality of electrophysiological recordings from intracortical microelectrodes degrades. The result is likely due to a combination of changes within the material as well as neural degeneration along with other physiological changes occurring around the implant [4]. As discussed above in Bulk Stiffness & Flexibility, neuroinflammation is thought to play a role in the sequelae of the degeneration and micro-motion, and repeated tissue strain from mechanical mismatch between the electrode material (stiff) and the brain tissue (soft) is thought to play a major role [16,17]. While a number of soft substrates had been investigated for use in microelectrodes, purely soft, flexible materials suffer from the challenge of buckling during insertion. To overcome this hurdle, Capadona et al. took their inspiration from the sea cucumber which is able to rapidly and reversibly stiffen its dermis as a defense mechanism when threatened (Figure 3A) [64]. Capadona applied the same design used by the sea cucumber to develop a polymer matrix that changes its stiffness in response to a chemical trigger (i.e., water hydration). The result was a material that was capable of being implanted into the brain while stiff to avoid buckling during insertion, and only subsequently softens after hydration in the brain tissues.

Squid beak inspired stiffness-graded transition material

The use of soft polymer systems with hard engineered devices leads to a significant challenge and a frequent failure point: the interface between the two dissimilar materials. Fox et al. looked to the squid's beak for inspiration (Figure 3B) [65]. The team noticed that the beak of the giant squid is comprised of a seemingly single composite material, but had graded changes in stiffness between the soft tissue interface of the stiff beak portion. The authors sought to develop a system that mimicked this gradual change in stiffness, so to avoid the harsh transition and reduce failure rates. Such systems may provide significant advantages in interconnects (transition from head-stage to flexible wires) which are a major failure point in current neural implants.

Mosquito bite inspired insertion guide

While dynamically softening polymers aid in the insertion of the devices into the brain, the systems are still relatively flexible due to their form factor (often thin films or microwires), and thus can be more challenging to implant than their very stiff (>700 GPa) silicon or metallic counterparts. Inspiration was taken from the mosquito, which uses a combination of mechanisms that includes an insertion guide to enable the mosquito to insert a set of micro-sized needles through the skin to reach vascular structures (Figure 3C) [66]. By bracing the needle at its base during insertion, the critical buckling force of the microprobes increased by 3.8-fold. With the guide in place, the rate of successful microprobe insertion increased from 37.5% to 100%. The prototype guides provided a reproducible method to augment the insertion of small, flexible devices into the brain, and can potentially be scaled for use in inserting other micro-scaled medical devices that suffer from challenges in implantation due to buckling.

Woodpecker inspired method to prevent chronic traumatic encephalopathy

While not directly related to devices implanted in the brain, it was worth mentioning this very interesting bioinspired method for interfacing with the brain non-invasively. This example shows how thinking creatively and looking to nature which has evolved over millennia may provide significant inspiration to solve new scientific and technical challenges.

Chronic traumatic encephalopathy appears to be linked to repeated trauma to the skull/brain, especially relevant to sports and battlefield injuries. The woodpecker amazingly slams its head against tree trunks without causing unintentional damage. Trauma is avoided by modulating intracranial pressure via constriction of the jugular vein. Constriction increases the blood volume retained in the brain (Figure 3D) [67]. Researchers have mimicked this action with a neck collar that contracts the omohyoid neck muscles to gently apply pressure to the jugular veins [68,69]. The mechanism of protection is hypothesized to be due to the reduction of "slosh" in the brain upon skull impact, thereby reducing risk of brain injury. In preclinical models, axonal amyloid precursor proteins, degenerative neurons, reactive astrocytes, and microglial activation have been reduced [67]. Perhaps future generations of neural interfaces can dynamically sense the impact to the head, and responsively initiate jugular compression to prevent trauma in a dynamically-responsive biomimetic design.

Conclusion

Biological systems have evolved over millions of years. Bioinspired and biomimetic strategies can leverage those advances to improve engineered neural interface devices. Biomimetic approaches taken over the last few years have included physical, chemical, and electrical modifications, and have even begun to incorporate living elements (e.g., seeded with cells). All these approaches have the potential to aid in forming a more compatible neural interface that causes less disruption to the existing physiology which may enable innovative medical applications in the fields of neural-controlled prosthetics and brain-computer interfacing. Despite all the knowledge gained through decades of research, a better

appreciation of what biological factors impact neural recordings is still required so that new microelectrode neural interfacing technology may be rationally designed. As new systems are developed, neural engineers will be presented with unique challenges relating to miniaturization, surgical delivery, manufacturing, and other technical aspects. Looking to nature for bio-inspired ideas may yield interesting and unforeseen approaches that take advantage of evolutionarily-optimized systems.

Acknowledgements

The authors would like to acknowledge Erika Woodrum from the Cleveland FES Center for her illustrations and other assistance with our figures. This work was supported in part by the Office of the Assistant Secretary of Defense for Health Affairs through the Peer Reviewed Medical Research Program under Award No. W81XWH-15-1-0608 in part by Merit Review Award #B1495-R (Capadona) and Presidential Early Career Award for Scientist and Engineers (PECASE, Capadona) from the United States (US) Department of Veterans Affairs Rehabilitation Research and Development Service, and by the National Institute of Health, National Institute of Neurological Disorders and Stroke, (Grant # 1R01NS082404-01A1). None of the funding sources aided in collection, analysis and interpretation of the data, in writing of the manuscript, or in the decision to submit the manuscript for publication. The contents do not represent the views of the U.S. Department of Defense, the U.S. Department of Veterans Affairs or the United States Government.

Conflict of interest statement

Nothing declared.

References

Papers of particular interest, published within the period of review, have been highlighted as:

- • of special interest

1. Salcman M, Bak MJ: **A new chronic recording intracortical microelectrode**. *Med Biol Eng* 1976, **14**:42–50.

2. BeMent SL, Wise KD, Anderson DJ, Najafi K, Drake KL: **Solid-state electrodes for multichannel multiplexed intracortical neuronal recording**. *IEEE Trans Biomed Eng* 1986, **33**: 230–241.

3. Campbell PK, Jones KE, Huber RJ, Horch KW, Normann RA: **A silicon-based, three-dimensional neural interface: manufacturing processes for an intracortical electrode array**. *IEEE Trans Biomed Eng* 1991, **38**:758–768.

4. • Jorfi M, Skousen JL, Weder C, Capadona JR: **Progress towards biocompatible intracortical microelectrodes for neural interfacing applications**. *J Neural Eng* 2015, **12**:011001.

5. Winkler R: **Elon musk launches neuralink to connect brains with computers**. *Wallstr J* March 28, 2017. Print edition as 'Brain Is Musk's New Frontier.

6. Clifford C: **Ahead of Elon Musk, this self-made millionaire already launched a company to merge your brain with computers**. In *CNBC*; 2017. Accessed at: https://www.cnbc.com/2017/04/12/self-made-millionaire-leads-elon-musk-in-fusing-brains-and-computers.html.

7. Bright D, Nair A, Salvekar D, Bhisikar S: **EEG-based brain controlled prosthetic arm**. In *2016 Conference on Advances in Signal Processing (CASP)*; 2016:479–483.

8. Louveau A, Harris TH, Kipnis J: **Revisiting the mechanisms of CNS immune privilege**. *Trends Immunol* 2015, **36**:569–577.

9. Engelhardt B, Carare RO, Bechmann I, Flugel A, Laman JD, Weller RO: **Vascular, glial, and lymphatic immune gateways of the central nervous system**. *Acta Neuropathol* 2016, **132**: 317–338.

10. Louveau A, Plog BA, Antila S, Alitalo K, Nedergaard M, Kipnis J: **Understanding the functions and relationships of the glymphatic system and meningeal lymphatics**. *J Clin Invest* 2017, **127**:3210–3219.

11. Michelson NJ, Vazquez AL, Eles JR, Salatino JW, Purcell EK, Williams JJ, Cui T, Kozai TDY: **Multi-scale, multi-modal analysis uncovers complex relationship at the brain tissue-implant neural interface: new emphasis on the biological interface**. *J Neural Eng* 2018 Jun, **15**:033001. https://doi.org/10.1088/1741-2552/aa9dae [Epub 2017 Nov 28].

12. Wellman SM, Kozai TDY: **Understanding the inflammatory tissue reaction to brain implants to improve neurochemical sensing performance**. *ACS Chem Neurosci* 2017 Dec 20, **8**: 2578–2582. https://doi.org/10.1021/acschemneuro.7b00403 [Epub 2017 Nov 9].

13. Shoffstall A, Capadona JR: **Prospects for a robust cortical recording interface**. In *Neuromodulation*. Edited by Krames E, Peckham PH, Rezai A. 2nd ed., Elsevier; 2018.

14. Goss-Varley M, Dona KR, McMahon JA, Shoffstall AJ, Ereifej ES, Lindner SC, Capadona JR: **Microelectrode implantation in motor cortex causes fine motor deficit: implications on potential considerations to brain computer interfacing and human augmentation**. *Sci Rep* 2017, **7**:15254.

15. Kozai TD, Catt K, Li X, Gugel ZV, Olafsson VT, Vazquez AL, Cui XT: **Mechanical failure modes of chronically implanted planar silicon-based neural probes for laminar recording**. *Biomaterials* 2015, **37**:25–39.

16. Sridharan A, Nguyen JK, Capadona JR, Muthuswamy J: **Compliant intracortical implants reduce strains and strain rates in brain tissue in vivo**. *J Neural Eng* 2015, **12**:036002.

17. Lee HC, Ejserholm F, Gaire J, Currlin S, Schouenborg J, Wallman L, Bengtsson M, Park K, Otto KJ: **Histological evaluation of flexible neural implants; flexibility limit for reducing the tissue response?** *J Neural Eng* 2017, **14**:036026.

18. Du ZJ, Kolarcik CL, Kozai TDY, Luebben SD, Sapp SA, Zheng XS, Nabity JA, Cui XT: **Ultrasoft microwire neural electrodes improve chronic tissue integration**. *Acta Biomater* 2017, **53**:46–58.

19. Kolarcik CL, Luebben SD, Sapp SA, Hanner J, Snyder N, Kozai TD, Chang E, Nabity JA, Nabity ST, Lagenaur CF, *et al.*: **Elastomeric and soft conducting microwires for implantable neural interfaces**. *Soft Matter* 2015, **11**:4847–4861.

20. Luan L, Wei X, Zhao Z, Siegel JJ, Potnis O, Tuppen CA, Lin S, Kazmi S, Fowler RA, Holloway S, *et al.*: **Ultraflexible nanoelectronic probes form reliable, glial scar-free neural integration**. *Sci Adv* 2017, **3**:e1601966.

21. McCallum GA, Sui X, Qiu C, Marmerstein J, Zheng Y, Eggers TE, Hu C, Dai L, Durand DM: **Chronic interfacing with the autonomic nervous system using carbon nanotube (CNT) yarn electrodes**. *Sci Rep* 2017, **7**:11723.

22. Ereifej ES, Cheng MM, Mao G, VandeVord PJ: **Examining the inflammatory response to nanopatterned polydimethylsiloxane using organotypic brain slice methods**. *J Neurosci Methods* 2013, **217**:17–25.

23. • Ereifej ES, Smith CS, Meade SM, Chen K, Feng H, Capadona JR: **The neuroinflammatory response to nanopatterning parallel grooves into the surface structure of intracortical microelectrodes**. *Adv Funct Mater* 2018, **28**. 1704420-n/a.

24. Ereifej ES, Matthew HW, Newaz G, Mukhopadhyay A, Auner G, Salakhutdinov I, VandeVord PJ: **Nanopatterning effects on astrocyte reactivity**. *J Biomed Mater Res A* 2013, **101**: 1743–1757.

25. • Pancrazio JJ, Deku F, Ghazavi A, Stiller AM, Rihani R, Frewin CL, Varner VD, Gardner TJ, Cogan SF: **Thinking small: progress on microscale neurostimulation technology**. *Neuromodulation* 2017 Dec, **20**:745–752. https://doi.org/10.1111/ner.12716 [Epub 2017 Oct 27].

26. Knaack GL, McHail DG, Borda G, Koo B, Peixoto N, Cogan SF, Dumas TC, Pancrazio JJ: **In vivo characterization of amorphous silicon carbide as a biomaterial for chronic neural interfaces**. *Front Neurosci* 2016, **10**:301.

27. Liu N, Chortos A, Lei T, Jin L, Kim TR, Bae WG, Zhu C, Wang S, Pfattner R, Chen X, *et al.*: **Ultratransparent and stretchable graphene electrodes**. *Sci Adv* 2017, **3**:e1700159.

28. Xie C, Liu J, Fu TM, Dai X, Zhou W, Lieber CM: **Three-dimensional macroporous nanoelectronic networks as minimally invasive brain probes**. *Nat Mater* 2015, **14**:1286–1292.

29. Liu J, Fu TM, Cheng Z, Hong G, Zhou T, Jin L, Duvvuri M, Jiang Z, Kruskal P, Xie C, *et al.*: **Syringe-injectable electronics**. *Nat Nanotechnol* 2015, **10**:629–636.

30. Seo D, Neely RM, Shen K, Singhal U, Alon E, Rabaey JM, Carmena JM, Maharbiz MM: **Wireless recording in the peripheral nervous system with ultrasonic neural dust**. *Neuron* 2016, **91**:529–539.

31. Seo D, Carmena JM, Rabaey JM, Maharbiz MM, Alon E: **Model validation of untethered, ultrasonic neural dust motes for cortical recording**. *J Neurosci Methods* 2015, **244**:114–122.

32. • Goding J, Gilmour A, Robles UA, Poole-Warren L, Lovell N, Martens P, Green R: **A living electrode construct for incorporation of cells into bionic devices**. *MRS Commun* 2017, **7**: 487–495.

33. Sommakia S, Lee HC, Gaire J, Otto KJ: **Materials approaches for modulating neural tissue responses to implanted microelectrodes through mechanical and biochemical means**. *Curr Opin Solid State Mater Sci* 2014, **18**:319–328.

34. Anderson JM, Rodriguez A, Chang DT: **Foreign body reaction to biomaterials**. *Semin Immunol* 2008, **20**:86–100.

35. Capadona JR, Collard DM, Garcõa AJ: **Fibronectin adsorption and cell adhesion to mixed monolayers of tri(ethylene glycol)- and methyl-terminated alkanethiols**. *Langmuir* 2003, **19**:1847–1852.

36. Capadona JR, Petrie TA, Fears KP, Latour RA, Collard DM, García AJ: **Surface-nucleated assembly of fibrillar extracellular matrices**. *Adv Mater* 2005, **17**:2604–2608.

37. Raynor JE, Capadona JR, Collard DM, Petrie TA, Garcia AJ: **Polymer brushes and self-assembled monolayers: versatile platforms to control cell adhesion to biomaterials (Review)**. *Biointerphases* 2009, **4**. FA3–16.

38. Lee HC, Gaire J, Currlin SW, McDermott MD, Park K, Otto KJ: **Foreign body response to intracortical microelectrodes is not altered with dip-coating of polyethylene glycol (PEG)**. *Front Neurosci* 2017, **11**:513.

39. Sommakia S, Rickus JL, Otto KJ: **Glial cells, but not neurons, exhibit a controllable response to a localized inflammatory microenvironment in vitro**. *Front Neuroeng* 2014, **7**:41.

40. Faulon Marruecos D, Kastantin M, Schwartz DK, Kaar JL: **Dense poly(ethylene glycol) brushes reduce adsorption and stabilize the unfolded conformation of fibronectin**. *Biomacromolecules* 2016, **17**:1017–1025.

41. Webb K, Budko E, Neuberger TJ, Chen S, Schachner M, Tresco PA: **Substrate-bound human recombinant L1 selectively promotes neuronal attachment and outgrowth in the presence of astrocytes and fibroblasts**. *Biomaterials* 2001, **22**:1017–1028.

42. • Eles JR, Vazquez AL, Snyder NR, Lagenaur C, Murphy MC, Kozai TD, Cui XT: **Neuroadhesive L1 coating attenuates acute microglial attachment to neural electrodes as revealed by live two-photon microscopy**. *Biomaterials* 2017, **113**:279–292.

43. Kolarcik CL, Bourbeau D, Azemi E, Rost E, Zhang L, Lagenaur CF, Weber DJ, Cui XT: **In vivo effects of L1 coating on inflammation and neuronal health at the electrode–tissue interface in rat spinal cord and dorsal root ganglion**. *Acta Biomater* 2012, **8**:3561–3575.

44. Nguyen JK, Jorfi M, Buchanan KL, Park DJ, Foster EJ, Tyler DJ, Rowan SJ, Weder C, Capadona JR: **Influence of resveratrol release on the tissue response to mechanically adaptive cortical implants**. *Acta Biomater* 2016, **29**:81–93.

45. Potter-Baker KA, Stewart WG, Tomaszewski WH, Wong CT, Meador WD, Ziats NP, Capadona JR: **Implications of chronic daily anti-oxidant administration on the inflammatory response to intracortical microelectrodes**. *J Neural Eng* 2015, **12**:046002.

46. Potter KA, Jorfi M, Householder KT, Foster EJ, Weder C, Capadona JR: **Curcumin-releasing mechanically adaptive intracortical implants improve the proximal neuronal density and blood-brain barrier stability**. *Acta Biomater* 2014, **10**: 2209–2222.

47. Ereifej ES, Rial G, Hermann JK, Smith CS, Meade S, Rayyan J, Chen K, Feng H, Capadona JR: **Implantation of neural probes in the brain elicits oxidative stress**. *Front Bioeng Biotechnol* 2018 Feb 12, **6**:9. https://doi.org/10.3389/fbioe.2018.00009 [eCollection 2018].

48. Geddes LA: **Historical evolution of circuit models for the electrode-electrolyte interface**. *Ann Biomed Eng* 1997, **25**: 1–14.

49. • Kozai TD, Catt K, Du Z, Na K, Srivannavit O, Haque RU, Seymour J, Wise KD, Yoon E, Cui XT: **Chronic in vivo evaluation of PEDOT/CNT for stable neural recordings**. *IEEE Trans Biomed Eng* 2016, **63**:111–119.

50. Patel PR, Zhang H, Robbins MT, Nofar JB, Marshall SP, Kobylarek MJ, Kozai TD, Kotov NA, Chestek CA: **Chronic in vivo stability assessment of carbon fiber microelectrode arrays**. *J Neural Eng* 2016, **13**:066002.

51. Alba NA, Du ZJ, Catt KA, Kozai TD, Cui XT: **In vivo electrochemical analysis of a PEDOT/MWCNT neural electrode coating**. *Biosensors* 2015, **5**:618–646.

52. • Kolarcik CL, Catt K, Rost E, Albrecht IN, Bourbeau D, Du Z, Kozai TD, Luo X, Weber DJ, Cui XT: **Evaluation of poly(3,4-ethylenedioxythiophene)/carbon nanotube neural electrode coatings for stimulation in the dorsal root ganglion**. *J Neural Eng* 2015, **12**:016008.

53. Patel PR, Na K, Zhang H, Kozai TD, Kotov NA, Yoon E, Chestek CA: **Insertion of linear 8.4 mum diameter 16 channel carbon fiber electrode arrays for single unit recordings**. *J Neural Eng* 2015, **12**:046009.

54. • Charkhkar H, Knaack GL, McHail DG, Mandal HS, Peixoto N, Rubinson JF, Dumas TC, Pancrazio JJ: **Chronic intracortical neural recordings using microelectrode arrays coated with PEDOT-TFB**. *Acta Biomater* 2016, **32**:57–67.

55. Mandal HS, Kastee JS, McHail DG, Rubinson JF, Pancrazio JJ, Dumas TC: **Improved poly(3,4-ethylenedioxythiophene) (PEDOT) for neural stimulation**. *Neuromodulation* 2015, **18**: 657–663.

56. Mandal HS, Cliff RO, Pancrazio JJ: **Freeze drying improves the shelf-life of conductive polymer modified neural electrodes**. *Bioengineering* 2015, **2**:176–183.

57. Du ZJ, Luo X, Weaver C, Cui XT: **Poly (3, 4-ethylenedioxythiophene)-ionic liquid coating improves neural recording and stimulation functionality of MEAs**. *J Mater Chem C Mater Opt Electron Devices* 2015, **3**:6515–6524.

58. Wang Y, Zhu C, Pfattner R, Yan H, Jin L, Chen S, Molina-Lopez F, Lissel F, Liu J, Rabiah NI, *et al.*: **A highly stretchable, transparent, and conductive polymer**. *Sci Adv* 2017, **3**: e1602076.

59. • Wnek GE: **Perspective: do macromolecules play a role in the mechanisms of nerve stimulation and nervous transmission?** *J Polym Sci B Polym Phys* 2016, **54**:7–14.

60. Meng L, Klinkajon W, K-hasuwan P-R, Harkin S, Supaphol P, Wnek GE: **Electrospun crosslinked poly(acrylic acid) fiber constructs: towards a synthetic model of the cortical layer of nerve**. *Polym Int* 2015, **64**:42–48.

61. Weaver CL, Cui XT: **Directed neural stem cell differentiation with a functionalized graphene oxide nanocomposite**. *Adv Healthc Mater* 2015, **4**:1408–1416.

62. Tan Y, Richards D, Xu R, Stewart-Clark S, Mani SK, Borg TK, Menick DR, Tian B, Mei Y: **Silicon nanowire-induced maturation of cardiomyocytes derived from human induced pluripotent stem cells**. *Nano Lett* 2015, **15**:2765–2772.

63. Tian B, Liu J, Dvir T, Jin L, Tsui JH, Qing Q, Suo Z, Langer R, Kohane DS, Lieber CM: **Macroporous nanowire nanoelectronic scaffolds for synthetic tissues**. *Nat Mater* 2012, **11**: 986–994.

64. • Capadona JR, Shanmuganathan K, Tyler DJ, Rowan SJ, Weder C: **Stimuli-responsive polymer nanocomposites inspired by the sea cucumber dermis**. *Science* 2008, **319**: 1370–1374.

65. • Fox JD, Capadona JR, Marasco PD, Rowan SJ: **Bioinspired water-enhanced mechanical gradient nanocomposite films that mimic the architecture and properties of the squid beak**. *J Am Chem Soc* 2013, **135**:5167–5174.

66. • Shoffstall AJ, Srinivasan S, Willis M, Stiller AM, Ecker M, Voit WE, Pancrazio JJ, Capadona JR: **A mosquito inspired strategy to implant microprobes into the brain**. *Sci Rep* 2018 Jan 9, **8**:122. https://doi.org/10.1038/s41598-017-18522-4.

67. • Smith DW, Bailes JE, Fisher JA, Robles J, Turner RC, Mills JD: **Internal jugular vein compression mitigates traumatic axonal injury in a rat model by reducing the intracranial slosh effect**. *Neurosurgery* 2012, **70**:740–746.

68. Myer GD, Yuan W, Barber Foss KD, Thomas S, Smith D, Leach J, Kiefer AW, Dicesare C, Adams J, Gubanich PJ, *et al.*: **Analysis of head impact exposure and brain microstructure response in a season-long application of a jugular vein compression collar: a prospective, neuroimaging investigation in American football**. *Br J Sports Med* 2016, **50**:1276–1285.

69. Myer GD, Yuan W, Barber Foss KD, Smith D, Altaye M, Reches A, Leach J, Kiefer AW, Khoury JC, Weiss M, *et al.*: **The effects of external jugular compression applied during head impact exposure on longitudinal changes in brain neuroanatomical and neurophysiological biomarkers: a preliminary investigation**. *Front Neurol* 2016, **7**:74.

micromachines

MDPI

Article

Characterization of the Neuroinflammatory Response to Thiol-ene Shape Memory Polymer Coated Intracortical Microelectrodes

Andrew J. Shoffstall [1,2], Melanie Ecker [2,3], Vindhya Danda [3,4,5,6], Alexandra Joshi-Imre [4], Allison Stiller [5], Marina Yu [1,2], Jennifer E. Paiz [1,2], Elizabeth Mancuso [1,2], Hillary W. Bedell [1], Walter E. Voit [3,4,5,6], Joseph J. Pancrazio [5] and Jeffrey R. Capadona [1,2,*]

1 Department of Biomedical Engineering, Case Western Reserve University, Cleveland, OH, USA; andrew.shoffstall@case.edu (A.J.S.); mhy7@case.edu (M.Y.); jep141@case.edu (J.E.P.); mancuso.33@buckeyemail.osu.edu (E.M.); hillary.bedell1@gmail.com (H.W.B.)
2 Advanced Platform Technology Center, Rehabilitation Research and Development, Louis Stokes Cleveland Department of Veteran Affairs Medical Center, Cleveland, OH, USA
3 Department of Materials Science and Engineering, The University of Texas at Dallas, Richardson, TX, USA; melanie.ecker@utdallas.edu (M.E.); vxd160030@utdallas.edu (V.D.); walter.voit@utdallas.edu (W.E.V.)
4 Center for Engineering Innovation, The University of Texas at Dallas, Richardson, TX, USA; alexandra.joshi-imre@utdallas.edu
5 Department of Bioengineering, The University of Texas at Dallas, Richardson, TX, USA; axs169031@utdallas.edu (A.S.); joseph.pancrazio@utdallas.edu (J.J.P.)
6 Department of Mechanical Engineering, The University of Texas at Dallas, Richardson, TX, USA
* Correspondence: jrc35@case.edu; Tel.: +1-(216)-368-5486

Received: 31 July 2018; Accepted: 18 September 2018; Published: 24 September 2018

Abstract: Thiol-ene based shape memory polymers (SMPs) have been developed for use as intracortical microelectrode substrates. The unique chemistry provides precise control over the mechanical and thermal glass-transition properties. As a result, SMP substrates are stiff at room temperature, allowing for insertion into the brain without buckling and subsequently soften in response to body temperatures, reducing the mechanical mismatch between device and tissue. Since the surface chemistry of the materials can contribute significantly to the ultimate biocompatibility, as a first step in the characterization of our SMPs, we sought to isolate the biological response to the implanted material surface without regards to the softening mechanics. To accomplish this, we tightly controlled for bulk stiffness by comparing bare silicon 'dummy' devices to thickness-matched silicon devices dip-coated with SMP. The neuroinflammatory response was evaluated after devices were implanted in the rat cortex for 2 or 16 weeks. We observed no differences in the markers tested at either time point, except that astrocytic scarring was significantly reduced for the dip-coated implants at 16 weeks. The surface properties of non-softening thiol-ene SMP substrates appeared to be equally-tolerated and just as suitable as silicon for neural implant substrates for applications such as intracortical microelectrodes, laying the groundwork for future softer devices to improve upon the prototype device performance presented here.

Keywords: intracortical; microelectrodes; shape-memory-polymer; electrophysiology

1. Introduction

Intracortical microelectrodes are used for electrophysiology recordings from the brain in a number of applications across both basic neuroscience and rehabilitation [1–4]. The specific needs of the given application dictate how long the microelectrode must endure, what type of signal is required

(e.g., single units versus local field potential), and the design of the electrode required for reaching the targeted location [5–9]. Unfortunately, the currently available implantable microelectrode arrays do not demonstrate long-term robustness, as evidenced by a gradual decline in the signal-to-noise ratio and ultimately a diminishing percentage of contacts that are able to record spiking behavior [10–13]. Therefore, there are many types of intracortical microelectrodes under development [3,4].

The failure mechanisms of recording microelectrodes are multifaceted and include a number of interrelated processes involving mechanical, material, and biological pathways [14–18]. Among these interrelated processes, the neuroinflammatory response is thought to play a central role in microelectrode failure. Prolonged neuroinflammation can cause a build-up of oxidative species that can promote neurodegeneration while also initiating the degradation of implanted materials, resulting in a positive feedback cycle [19,20]. Numerous materials-based and therapeutic strategies have the potential to intervene in several of the failure modes by combining mechanical strategies, bioactive coatings, and/or drug-eluting substrates [21].

To reduce the tissue response and combat chronic neurodegeneration around implanted intracortical microelectrodes, the neural engineering field has been increasingly moving toward smaller, softer materials and electrode designs [21–23]. Using soft polymer substrates, like polyimides [24–26] or Parylene-C [27], compliant devices appear to reduce the appearance of chronic inflammation in end-point histology [28–30]. Ultra-small concepts have also proven to work well for reaching superficial cortical targets of the brain [28,31–33]. However, such devices may not be compatible with implantation strategies for more difficult to access structures of the brain.

Thiol-ene and thiol-ene/acrylate shape memory polymers (SMPs) comprise a new class of substrate under development for neural interfaces [34,35]. Thiol-ene/acrylate acts as a versatile material that is stiff at room temperature and softens after implantation in response to body temperatures and fluid exposure. The softening effect can be as large as a transition from 1 GPa to 18 MPa [35]. The combination of thiol, alkene and acrylate monomers modulates the rubbery modulus and allows for the adjustment of the glass transition temperature via a composition ratio (i.e., relative concentrations of multivalent monomers from all three groups) [36–38]. Sterilization methods have been optimized [39], allowing for the first demonstration of acute recordings signals from the primary auditory cortex of rats [40]. While thiol-ene-based SMPs appear to be promising, thus far, there have not been robust analyses of the neuroinflammatory response elicited by their long-term implantation in the cortex.

The objective of the current study was to quantify the neuroinflammatory response to implanted SMP materials. Here, we chose to first compare our SMP to a bare silicon substrate similar to those used in commercially available planar microelectrodes. The goal was to first understand the biological response to the thiol-ene material itself, without the confounding variable of stiffness (and resulting differential tissue strains). To that end, the SMP material was dip-coated onto a silicon surface and compared to a size-matched bare silicon substrate. As a result, the bulk flexibility of the microelectrode was held consistent, while only the tissue-exposed surface varied. Given the similar size and stiffness, we hypothesized that stiff silicon microelectrodes dip-coated with a shape memory polymer would elicit a similar or reduced neuroinflammatory response compared to size-matched bare silicon microelectrodes after implantation into the rat cortex.

2. Materials and Methods

2.1. Study Design

Male Sprague Dawley rats (200–250 g, n = 11 per group) were implanted with either stiff silicon microelectrode probes dip-coated with shape memory polymer or size-matched bare silicon microelectrode probes. As performed previously by our group and others, microelectrode probes were implanted bilaterally (one in each hemisphere) and treated as independent of one another [41,42]. After implantation, animals were housed for 2 or 16 weeks, spanning the periods of initial and late-onset

neurodegeneration [43,44]. Immunohistochemistry markers tested included neuronal density (NeuN), activated microglia (CD68), blood-brain barrier permeability (Immunoglobulin G (IgG)), and reactive astrocytes (glial fibrillary acidic protein (GFAP)) [20,43,45–49].

2.2. Device Fabrication and Sterilization

Silicon 'dummy' probe devices, substrates without a recording functionality, were fabricated by a photolithographic process using a deep-reactive ion etching procedure as described below. In detail, silicon shanks of the desired thickness were fabricated from the appropriate SOI (silicon on insulator) wafer. These SOI wafers contained a device silicon layer and a buried oxide layer of 2 µm on top of 400 µm silicon handle layer. A hard mask of 2 µm thermal oxide was grown on these SOI wafers using a Tystar Diffusion/Oxidation Furnace. The wafers were then patterned using standard lithography techniques to yield the desired probe pattern. The thermal oxide hard mask and the device silicon layer were etched using CHF_3/Ar plasma and a Bosch sequence (SF_6/Ar and C_4F_8 plasmas) using a Plasma-Therm deep silicon etcher respectively. The buried oxide layer was used as the etch stop layer for the device silicon etch. The wafers were then soaked in solvent to remove the photoresist residues and in diluted 10:1 hydrofluoric acid overnight to lift-off the silicon shanks before they were triple rinsed in distilled water. The silicon shanks were further singulated from each other by breaking the tab that connects them using very fine metal tweezers under a microscope. The use of two different thickness of silicon wafers allowed us to generate devices that were either 30 µm or 14 µm thick (25 µm prior to etching). The latter devices were then modified with a dip-coating process to add a thiol-ene shape memory polymer to generate a nearly equivalent ~30 µm thick SMP dip-coated device (Figure 1).

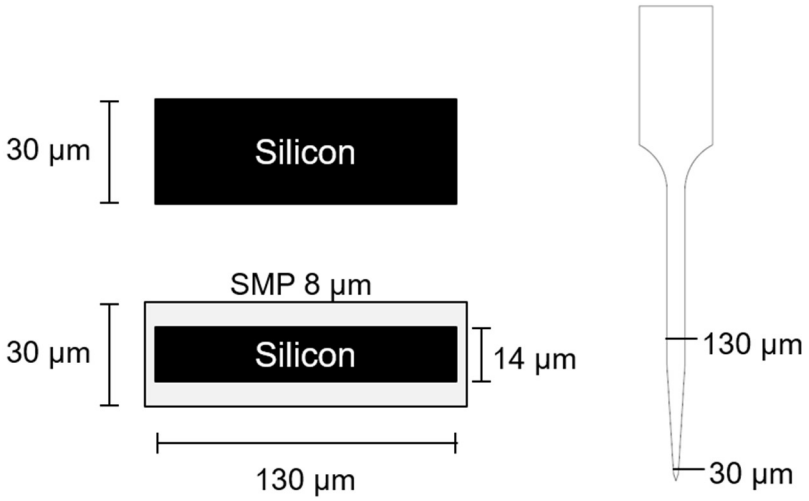

Figure 1. Probe design schematic. Cross-sectional dimensions of the silicon (**top**) and dip-coated (**bottom**) devices and view of the profile from the side (right). Here, 30 µm thick silicon wafers were used to fabricate the bare silicon probes whereas a 14 µm thick silicon wafer (after etching) was used to produce the dip-coating substrate so that the overall device thickness resulted as ~30 µm for both device types. Due to the photomasks used, the widths of the etched silicon devices were held constant so that the bare silicon probes were 130 µm in width and after coating, the dip-coated probes were slightly larger, ~135 µm, in width. The actual coating thickness varied slightly along the length of the probe as shown in Supplementary Figure S1.

SMP pre-polymer solution was prepared as described previously [39]. The material is characterized by a glass transition temperature (T_g) of 45 °C in the dry state, and a T_g of 30 °C after being soaked in phosphate buffered saline (PBS) at 37 °C for at least 30 min. The storage modulus E' of the materials decreases from 1.7 GPa (dry) to 20 MPa (wet) due to plasticization effects. The monomer ratios were 50 mol% 1,3,5-Triallyl-1,3,5-triazine-2,4,6(1H,3H,5H)-trione

(TATATO), 45 mol% trimethylolpropane tris(3-mercaptopropionate) (TMTMP), and 5 mol% Tris[2-mercaptopropionyloxy)ethyl] isocyanurate (TMICN). All monomers were mixed with 0.1 wt% of photoinitiator 2,2-dimethoxy-2-phenylacetophenone (DMPA) before they were used for dip coating.

The silicon shanks were individually mounted on ethylene oxide indicator tape for handling purposes. To enhance the SMP adhesion, bare silicon shanks were subjected to a surface treatment prior to the dip-coating which included a roughening step via O_2/Ar plasma in a March reactive ion etching (RIE) system for 16 min at 200 mT/50 W followed by SF_6 plasma treatments at 120 mT/100 W for 5 min in a Technics RIE system on both sides. The surface-treated silicon shanks were then held with tweezers and dipped manually at an average speed of 7–13 mm·s^{-1} (assessed by videotaping) into the pre-polymer solution. The viscosity (h) of the thiol-ene pre-polymer solution was 0.18 $\pm$ 0.1 Pa·s (TA discovery HR3 rheometer (TA Instruments, New Castle, DE, USA), sweep from 1 to 1000 s^{-1}). The SMP solution was prepared immediately before dip-coating. The coated pre-polymer was cured on all sides using a 365 nm handheld UV gun for about 30 s. The probes were inspected under an optical microscope to ensure the shank was coated successfully (i.e., showing full polymer coverage and no beads). Only sufficiently coated probes were selected and fully cured for 1 h in a cross-linking chamber (UVP CL-1000 (UVP, LLC, Upland, CA, USA) with five overhead bulbs) followed by an overnight post-cure at 120 °C under vacuum. To verify the thickness of the SMP layer and to ensure evenly coated surfaces, the fully cured samples were investigated using scanning electron microscope (SEM) (Zeiss Supra 40 and Zeiss EVO LS 15 Scanning Electron Microscopes, Zeiss, Inc., Oberkochen, Germany). SEM parameters included: EHT (accelerating voltage) between 0.5 kV and 5.0 kV and various magnifications. Individual parameters are displayed at the bottoms of the SEM images. The contact angle of water for the SMP material was ~70° while the silicon had a contact angle of ~40°.

Devices were sterilized using ethylene oxide (EtO) as previously described [39]. Briefly, the devices were loaded into a liner bag along with gas indicator tape and a glass ampoule containing 18 g of liquid EtO before it was sealed using Velcro wrap and placed into the ethylene oxide sterilizer (AN 74i, Anprolene, Andersen Sterilizers Inc., Haw River, NC, USA). The sterilization cycle at atmospheric pressure lasted for 24 h followed by a 2 h purge/aeration. To remove any residual EtO from the samples, they were subjected to an addition degassing for 72 h at 37 °C under vacuum. To validate the effectiveness of this sterilization method, we have previously performed residual endotoxin testing on pre- and post-sterilization materials as well as a host of mechanical testing (e.g., dynamic mechanical analysis (DMA)) to ensure that the mechanical properties were not adversely impacted in the described process [39].

2.3. Device Implantation

All procedures were reviewed and approved by the Louis Stokes Cleveland Department of Veterans Affairs Institutional Animal Care and Use Committee. Sprague Dawley rats were anesthetized (3–5%) and kept under anesthesia (1–3%) using an isoflurane vaporizer to maintain a surgical plane of anesthesia. Once anesthetized, eye lubricant was applied and the fur on the scalp was shaved and cleaned. Prior to surgery, the rats received 16 mg/kg cefazolin and 1 mg/kg meloxicam subcutaneously as a prophylactic antibiotic and analgesic, respectively. Additionally, a single dose of 0.2 mL of 0.25% bupivacaine (local anesthetic) was administered subcutaneously at the incision site. The surgical site was cleaned in triplicate with betadine followed by isopropyl alcohol scrubs. Surgery was performed under an operating microscope. Craniotomies were performed carefully with a combination of intermittent pausing and saline application, to prevent overheating from drilling [50]. A sterile ruler and forceps were used to mark the area to be drilled, 2 mm lateral to midline, 3 mm posterior to bregma (corresponding to a region of the sensory cortex). Removal of the final thinned bone flap was performed with ultrafine rongeurs to prevent incidental mechanical damage to the brain from the drill tip. After careful reflection of the dura, microelectrodes were implanted ~2 mm deep by hand using micro-forceps, avoiding superficially visible vasculature. Kwik-Cast was applied to cover the craniotomy and allowed to cure, followed by application of cold-cure dental acrylic to build up a stable

cement base around the implant. Given the low profile of the dummy probe implants (e.g., as compared to functional recording microelectrodes that require an exposed head-stage), the skin was sutured together and treated with a non-prescription triple-antibiotic cream. A post-operative analgesic was provided for 2 days following implantation (1 mg/kg meloxicam q.d.) and post-operative prophylactic antibiotics were provided for 1 day following implantation (16 mg/kg cefazolin, b.i.d.). There were no complications with post-operative infection or observations of overtly unmanaged pain from the procedure.

2.4. Tissue Extraction and Preparation

At the pre-determined end points (2 or 16 weeks), animals were perfused transcardially under deep anesthesia to prepare the tissue for histological processing. After achieving a deep plane of anesthesia, using a ketamine/xylazine cocktail (80 mg/kg and 10 mg/kg respectively), rat aortas were cannulated with a gavage needle via an incision in the left ventricle and connected to a perfusion pump. Phosphate buffered saline (1×) was perfused until the fluid exiting the excised vena cava/right atrium appeared clear. Tissue was then fixed by perfusion with ~200 mL of 4% *w*/*v* paraformaldehyde solution. The tissue was post-fixed in 4% *w*/*v* paraformaldehyde solution overnight. After careful extraction, brains were subsequently cryoprotected with a gradient of sucrose (with 0.1% sodium azide) from 10 % to 30% *w*/*v* and frozen in OCT (Opjmal Cu ng. Temperature) blocks and stored at −80 °C until sectioning. Tissue sections, 20 µm thick, were generated on a cryostat and were collected on Fisherbrand 'Superfrost Plus' glass slides.

2.5. Quantification of Immunohistochemistry

Immunohistochemistry was performed as previously described for neuronal density (NeuN), activated microglia (CD68), blood-brain barrier permeability (IgG), and astrocytes (GFAP) [45,51]. To account for the known variation of the histological response along the depth of the implant, horizontal (transverse) slices were collected and compared at an array of locations spanning randomized depths of 500–1500 microns. Stained slides were imaged using a 10× objective on an AxioObserver Z1 (Zeiss, Inc.) and AxioCam MRm (Zeiss Inc.). All images except those stained for NeuN were analyzed using SECOND (version 030918, MathWorks, Inc., Natick, MA, USA), a custom MATLAB program developed to analyze fluorescent intensity profiles around the electrode [52]. In summary, the void in the tissue left by the explanted microelectrode was manually defined by tracing each image on-screen. The area defined by this tracing was collected and used to tabulate the explanted hole size. Fluorescent intensity was then tabulated by the program in expanding concentric contours around the microelectrode-tissue interface edge. To quantify neuron populations around the implant site, the number of neurons in each ring was manually counted to obtain the number of neurons per area for each radial distance [19,43]. In each case a normalized metric was generated, where the average intensity for a given concentric bin was divided by a concentric bin far enough away from the microelectrode implant that the neuroinflammatory response was minimal: 600–650 µm for intensity-based measures (IgG, GFAP, CD68), and 250–300 µm for count-based measures (NeuN).

Statistics were calculated in Minitab 18 (State College, PA, USA). The continuous outcome measures, including neuronal density, captured at endpoint histology were evaluated to compare inter-group differences for individual distance buckets (i.e., 0–50 µm, 50–100 µm,) using two-sample *t*-tests, with a significance at level $p < 0.05$. Intensity-based histological measures (GFAP, CD68, IgG) were analyzed using previously established quantification methods [43,46], wherein the fluorescent intensity was plotted as a function of distance from the electrode surface and the statistical outcome was the area-under-the-curve, corresponding to the level of overall tissue response for a given stain. Similarly, inter-group differences for individual distance buckets were calculated by two-sample *t*-tests, with a significance at level $p < 0.05$.

2.6. Characterization

2.6.1. Dip-Coating Silicon 'Dummy' Microelectrodes with Thiol-ene Polymer

Dummy microelectrodes were successfully dip-coated with a thiol-ene polymer (Figure 2). Multiple parameters appeared to influence the coating thickness and ability to form a uniform layer, especially the surface of the silicon shanks and the rate of removal from the polymer solution. If the silicon shanks were unmodified, the SMP did not adhere well to the surface (Figure 2A). However, after applying a surface treatment to the bare silicon shanks (O_2/Ar and SF_6 plasma), the shanks could be uniformly coated with SMP (Figure 2B). The viscosity of the pre-polymer solution, $h = 0.18 \pm 0.1$ Pa·s, was set by the previously defined composition of monomers. A change in the composition would result in a change of thermomechanical properties and was therefore not desired. Another way to change the viscosity of the solution would be by the addition of solvent. However, the addition of solvent would alter the curing kinetics and cross-link density and thus the thermomechanical properties as well. Therefore, only the removal speed could be varied to alter the surface coating. An average speed of 7 to 13 mm·s^{-1} of manual dip-coating turned out to result in sufficient coatings (Figure 2B). In some cases, more dominant at lower speeds, beading of the coating was visible along the microelectrode shank (Figure 2C). Only probes which showed full coating and no visible beads were used for the in vivo study.

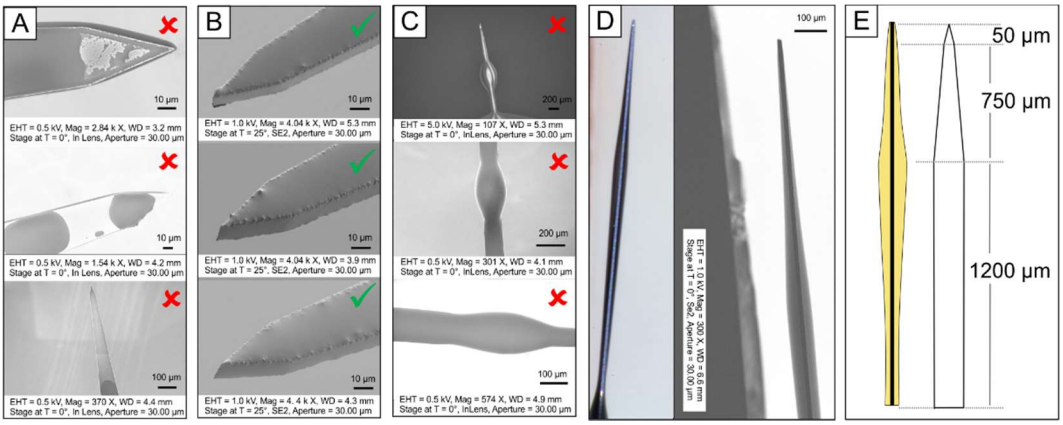

Figure 2. Characterization of silicon 'dummy' microelectrode with thiol-ene polymer. Dip coating of 25 µm thick microelectrodes with a uniform layer of shape memory polymer (SMP) to generate approximately 30 µm thick coated devices; (**A**) the polymer detached before surface modification of silicon probes, (**B**) nicely coated the silicon shanks after surface modification. (**C**) In some cases, the coating would form 'beads' due to slow removal. Checkmarks and crosses indicate whether probes were used for in vivo studies or not. (**D**) Optical and scanning electron microscope (SEM) images in the side view to assess the thickness of the coating, and (**E**) schematic drawing of coating thickness with respect to the shank geometry.

Dip coating quality and uniformity were approximated using optical microscopy and SEM on several representative devices. We found that the coating profile was consistent across various probes. The thickness of the coating, however, had no uniform thickness throughout the length of the shanks (Figure 2D). The tip of the probes had a very thin layer of polymer (less than 1 µm), whereas the rest of the probe had a layer thickness of about 10 to 30 µm on the top and bottom, respectively. The thickest coating was consistently found at the part of the probes where the shank started to narrow down about 850 µm distance from the tip (Figure 2E). This can be explained by the dipping process. The pre-polymer solution was flowing down the probes due to gravity before they were cured and accumulated at the abovementioned part of the probe due to an abrupt change of geometrical surface area. After the surface modification of the bare silicon shank, which included reactive ion etching, the thickness of the shanks was reduced from 25 µm to 14 µm. The averaged thickness of the SMP

coating across the surface was approximately 8 µm on either side, which adds up to an overall probe thickness of about 30 µm. Even if the coating had no consistent thickness throughout the probe, the overall probe volume, and with that the averaged footprint of the implanted part of the dip-coated probes, was still similar to that of bare silicon probes.

2.6.2. Durability of Dip Coated Probes

The thiol-ene formulation used here was stable under physiological conditions for up to 13 months without any signs of hydrolytic degradation (paper under review). In order to directly test the dip-coating stability after in vivo implantation, explanted polymer coated silicon probes were investigated after 2 weeks (Figure 3A,B) and 16 weeks of dwelling in the rat cortex (Figure 3C,D). The coating of the probes was investigated before and after aging by means of SEM imaging. It was found that the coating was stable and did not show any signs of degradation over the course of implantation. The coating looked intact after being implanted into rat cortex for 2 weeks and 16 weeks, as demonstrated by the representative SEM images in Figure 3. In order to further assess the durability of the SMP coating and its adhesion to the silicon shanks, the dip-coated probes were further tested in vitro under accelerated aging conditions. The dip-coated probes were mounted onto the cap of a glass jar and were immersed into phosphate buffered saline (PBS) at 57 °C for a minimum of 84 h. While the surfaces of the probes became rougher, they remained visibly intact under SEM imaging (Supplementary Figure S2).

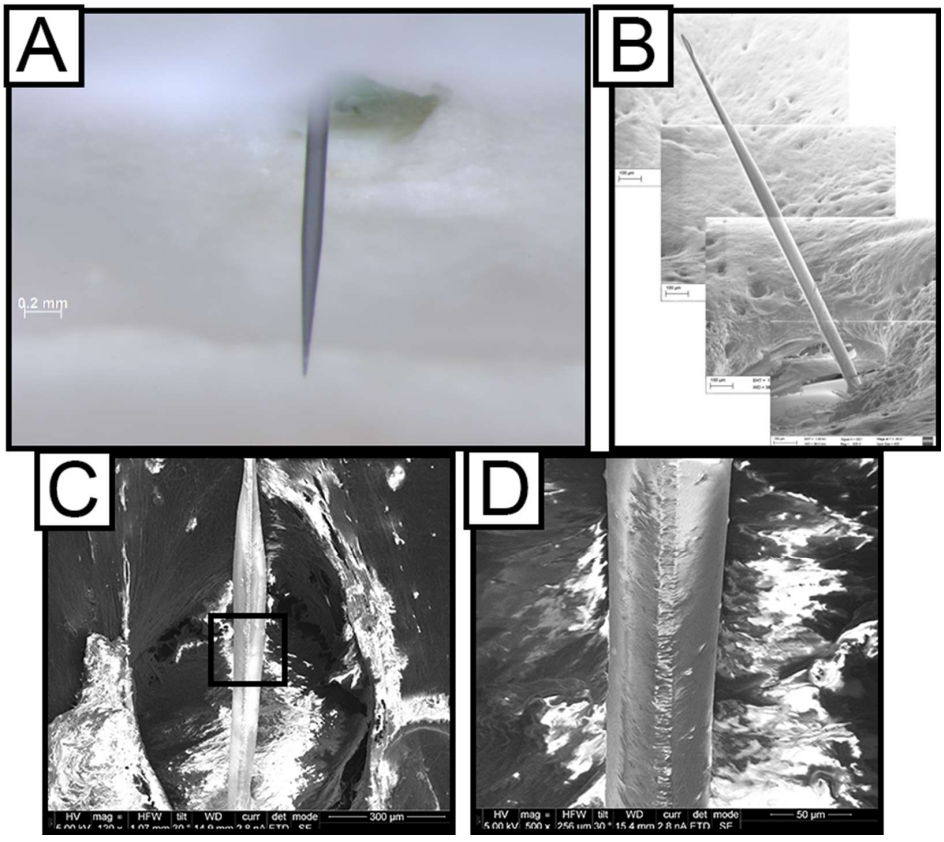

Figure 3. Ex vivo Characterization of coating stability. Dip-coated probes inside the skull with all tissue removed captured using optical microscopy (**A**) and SEM (**B**) showing that the SMP coating of the silicon shanks is still intact after two weeks. (**C**) Side-view SEM image of a dip-coated probe, explanted after 16 weeks in the rat cortex, showing the SMP coating intact. Black rectangle inset is blown up further in (**D**).

2.6.3. Tissue Void from Device Explantation

To verify that the cross-sectional area was held consistent between the two types of implants, we quantified the remnant hole in the tissue after device explantation. As expected, the hole sizes were similar to, but slightly larger than, the cross-sectional area of the actual probe devices (~3900 μm^2, Figure 4A,B). The difference in the hole to device size could be due to a thin layer of tissue remaining adhered to the microelectrode, or any slicing (edge) artifact. Interestingly, the remnant tissue hole size variability appeared to be higher at 2 weeks compared to 16 weeks and may have resulted from a looser, more immature scar or increased edema at that time.

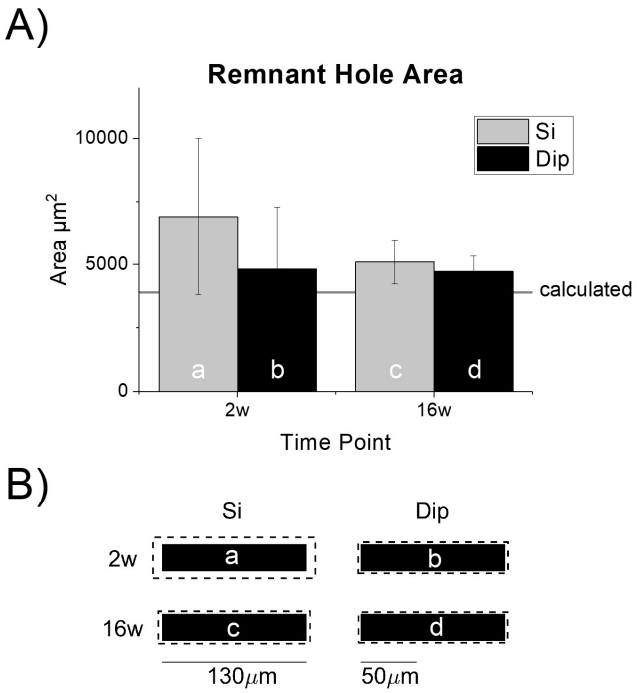

Figure 4. Characterization of the remnant tissue hole after explantation and 'dummy' probe device dimensions. (**A**) Remnant hole size after probe extraction was consistent (no statistically significant differences) across both implant types. The hole was slightly larger than the theoretical cross-sectional area denoted by the horizontal line; n = 9 (Si-2w), 10 (Si-16w), 10 (dip-2w), 10 (Dip-16w). (**B**) Mean explanted hole size (dashed line) drawn in relative scale to the actual device dimensions. The letters correspond with the matching bar in the chart shown in (**A**). The 130 μm scale bar is shown to provide context for the microelectrode dummy probe width. The 50 μm scale bar provides context for the analysis of bucket widths for the histological analysis. Tissue responses can extend several hundred microns away from the tissue-device interface.

As described above, the size of the dip-coated probe devices was controlled by applying a ~8 μm thick layer of SMP to a bare silicon device with 14 μm thickness to achieve an approximately 30 μm overall thickness (Figure 1). Compared to the actual device sizes, the increased hole diameters appeared to be marginal (Figure 4B). In the largest group, two-week silicon implants ('2w-Si'), the equivalent mean increase in radius was calculated to be ~16 microns (Figure 4B).

3. Results

3.1. Endpoint Histological Analysis

3.1.1. Astrocyte Response

Astrocytes, a glial cell, play a number of important roles in the brain, including contributing to the blood-brain barrier [16,53]. They react to injury and foreign implanted materials in the brain by changing morphology, migrating toward the implant, and expressing or upregulating the expression of a host of proteins, including glial fibrillary acidic protein (GFAP) [18,54].

While there were no significant differences between silicon and SMP dip-coated devices at 2 weeks (Figure 5A), there was a significantly lower response for dip-coated implants at 16 weeks compared to the bare silicon control. Specifically, the statistically significant differences were in the concentric ranges 50–100 μm and 100–150 μm from the hole remaining after device extraction (Figure 5B).

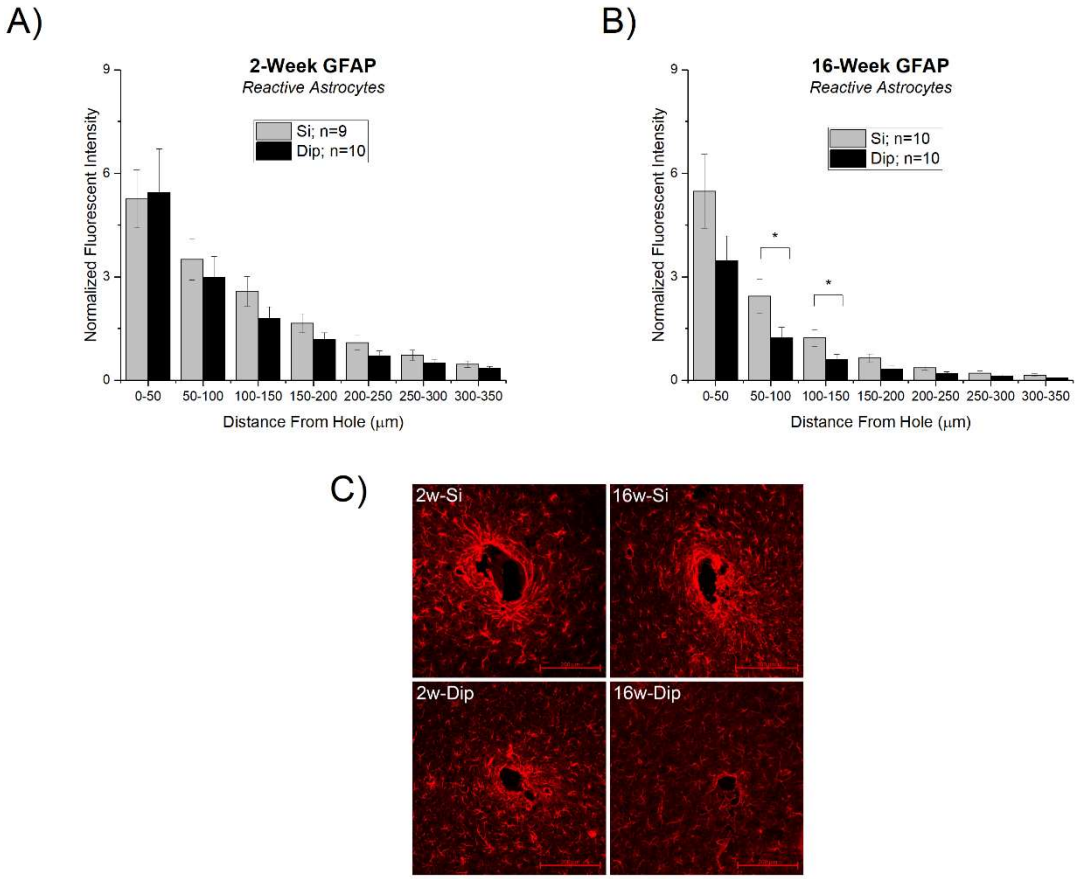

Figure 5. Astrocytic response to silicon vs. SMP dip-coated implants. (**A**) Astrocytic scarring at 2 weeks and (**B**) 16 weeks. There were significant differences between the silicon and dip-coated glial fibrillary acidic protein (GFAP) response at 16 weeks, specifically at bucketed distances 50–100 μm and 100–150 μm from the hole. There were no differences between the groups at 2 weeks or any other regions from the hole at 16 weeks post-implantation. (**C**) Representative images of the GFAP staining results with 200 μm scale bars in the bottom right-hand corner.

3.1.2. Activation of Microglia and Macrophages and Blood-Brain Barrier Permeability

CD68 is a marker of activated microglia and macrophages and has been associated with heightened neuroinflammatory responses to implanted foreign materials in the brain [55–58]. IgG is a blood immunoglobulin protein not normally found in the brain and is therefore commonly used as a marker for blood-brain barrier permeability [59]. All the stains followed a typical decay profile with

the largest expression at the explant hole edge, returning to a baseline response within a few hundred microns. While overall there was a trend of a reduced response in both CD68 (Figure 6A,B) and IgG (Figure 6C,D), there were no statistically significant differences between any of the silicon and SMP dip-coated implants for either stain at each time point.

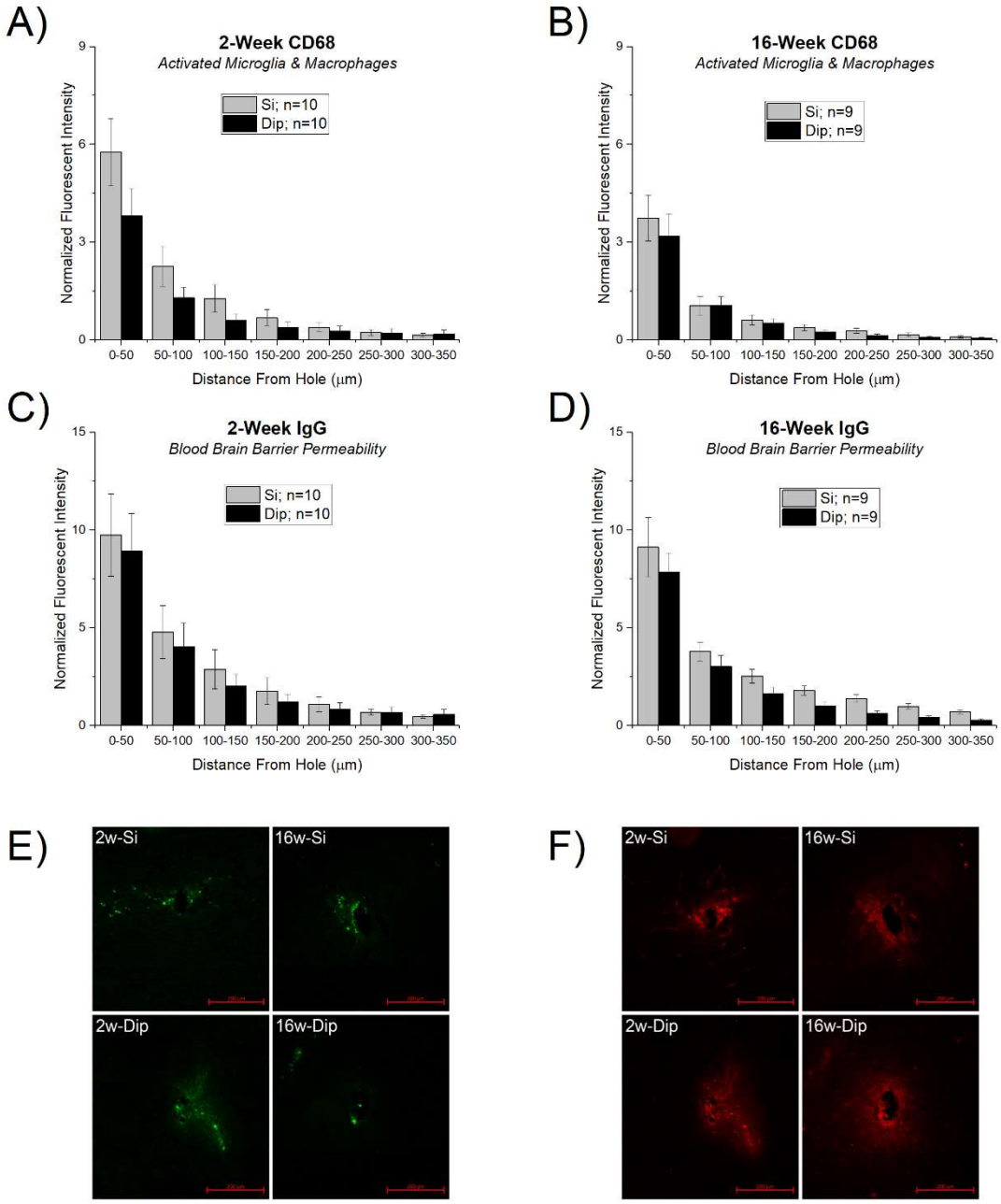

Figure 6. Microglia and BBB response to silicon vs. SMP dip-coated implants. Activated macrophages and microglia (CD68) at (**A**) 2 weeks and (**B**) 16 weeks. Blood-brain barrier (BBB) permeability marked by immunoglobulin G (IgG) staining at (**C**) 2 weeks and (**D**) 16 weeks after microelectrode implantation. There were no differences in either stain between each probe type for either time point tested. (**E**,**F**) Representative images of the CD68 (**E**) and IgG (**F**) staining results with 200 μm scale bars in the bottom right-hand corner.

3.1.3. Neuronal Density

Insertion surgery and the subsequent neuroinflammatory response is thought to contribute to neuronal loss near the microelectrode interface [60]. In our studies, a decrease in neuronal density near the explanted microelectrode site was observed both at 2 weeks and 16 weeks for both probe types (Figure 7). For both probe types, neuronal densities returned to background levels by 200–250 µm at 2 weeks post-implantation and by 50–100 µm at 16 weeks post-implantation. There were no statistically significant differences between the silicon and dip-coated implants.

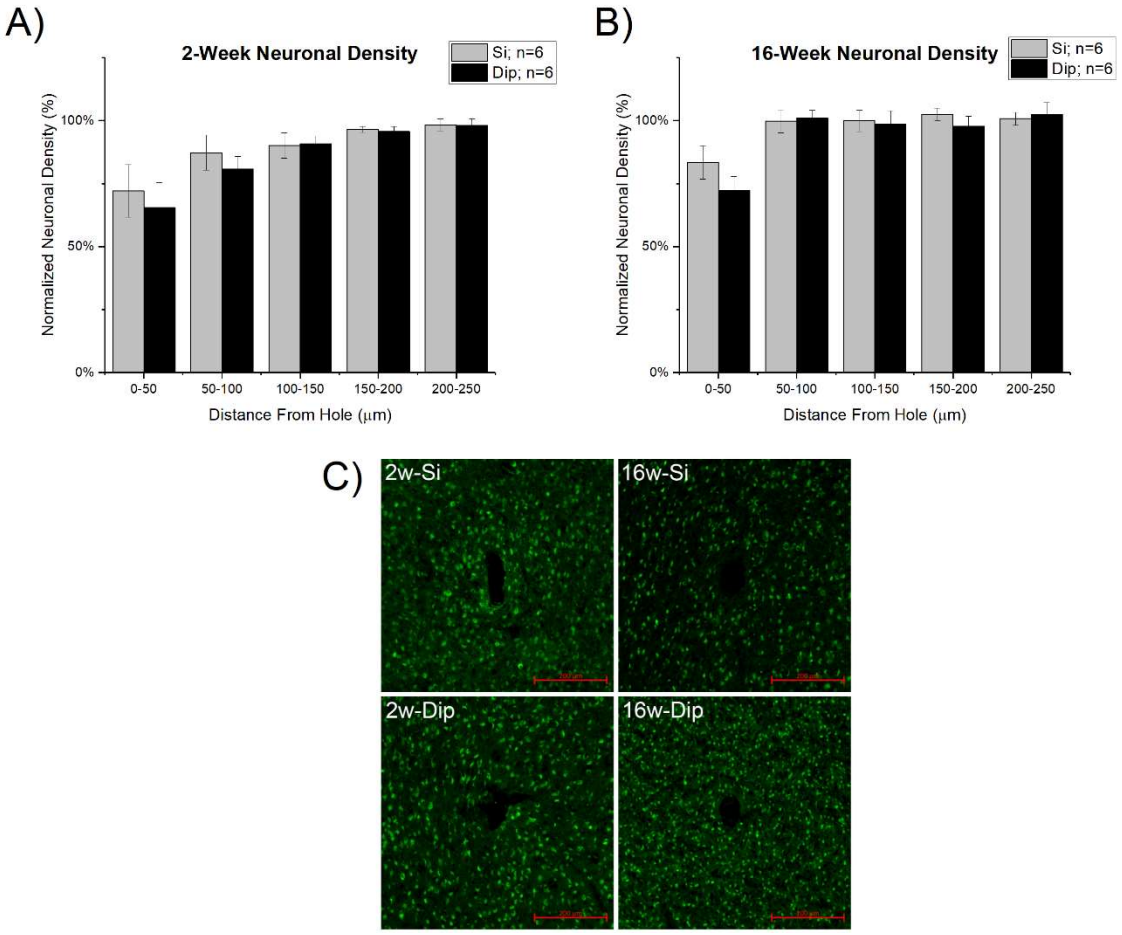

Figure 7. Neuronal density (NeuN staining) at (**A**) 2 weeks and (**B**) 16 weeks after microelectrode implantation. There were no significant differences between either material group, silicon vs dip-coated, at the two time points tested. (**C**) Representative images of the NeuN staining results with 200 µm scale bars in the bottom right-hand corner.

4. Discussion

Thiol-ene and thiol-ene/acrylate shape memory polymers (SMP) are under development for use as an implanted microelectrode substrate [35]. The materials are advantageous owing to their unique and highly tunable chemistry, the potential for reproducible manufacturing, and ability to soften after implantation in the brain [40]. We have previously demonstrated that intracortical probes that reduce their modulus after implantation into the brain significantly reduce the resulting neuroinflammatory response [45,61–63], likely due to the reduction in tissue strain and micro-motion [64]. We have also shown that the protein, cellular, and tissue responses to synthetic materials are highly correlated to the surface chemistry [65–69]. Therefore, in order to disentangle the potential differential effects on the biological response from both the new material chemistry and the unique mechanics, in this study, we first sought to hold the bulk mechanics as constant as possible while only varying the surface exposed

to the brain tissue after implantation. By dip-coating SMP onto the surface of silicon probe devices, we were able to compare the biological response to implanted thiol-ene polymer materials without regards to their bulk stiffness or flexibility.

The only marker with statistically significant results was in the astrocytic response after 16 weeks of implantation, where the dip-coated silicon devices exhibited a significantly lower response than the bare silicon control devices at distances of 50–150 µm from the implant surface (Figure 5B). We found no statistically significant differences between the two implanted probes with regards to microglia and macrophage activation, blood-brain barrier permeability, or neuronal density. While the surface mechanics of the dip-coating layer may have played a minor role, we have shown before that the overall flexibility of the devices is driven by the underlying silicon [62]. Several studies have investigated the effects of substrate stiffness (modulus) on the astrocytic response, both in vitro [70,71] and in vivo [70,72], showing an enhanced response around stiff materials (~10 kPa) compared to softer materials (~100 Pa). While consistent with our overall observations of a decrease in activated astrocytes proximal to the implant, it is important to note that the modulus of the SMP coating here was at least twice as stiff as the "stiffer" substrates in each of the mentioned studies, with "soft" substrates often an order(s) of magnitude softer than the SMP reported here.

As the neuroinflammatory events surrounding the implanted microelectrode are constantly changing with respect to glial cell density, biochemical environment, neuron viability, and blood-brain barrier leakage [13,73,74], it is important to consider several time points. Here, we chose 2 weeks and 16 weeks, as they correspond with both early-onset and late-stage neurodegeneration [43]. Upon implantation, microelectrodes immediately disrupt brain tissue and neurovasculature, initiating a multi-phasic inflammatory response [3,43]. The acute response plateaus within the first few weeks of implantation and inflammation thereafter is driven in a chronic state by various mechanisms, including the fibrotic glial scar formation, microglial and macrophage activation, free radical oxidation and chronic dysfunction of the blood-brain barrier [43,49,75,76].

In the current study, the astrocytic response was observed to be greater for the non-coated silicon at the 16 week time point but not the 2 week time point. Since GFAP expression was only greater at the later-stage time point, our results suggest that the main differences appear after the normal wound-healing response has subsided. The overall magnitude of the response to the silicon implants at 16 weeks was similar to that of the silicon and dip-coated material at 2 weeks. Therefore, the increased astrocyte response for silicon versus the dip-coated at 16 weeks appears as a prolonged state of activation phase (or inability to 'de-activate') rather than the increased initial magnitude of astrocyte activation. Furthermore, differences were not observed in any of the other markers, including microglial/macrophage activation, blood-brain barrier permeability, or neuronal density, suggesting that the different response may be uniquely centered around astrocytes (at least of the markers tested). Increased astrocytic scarring has been associated with negatively impacting signal quality, either through directly increasing tissue impedance, or through physical separation and increased distance between the microelectrode contacts and viable neurons [77]. Results demonstrating that the SMP material exhibits a reduction in GFAP expression at 16 weeks are promising and deserve further exploration in future recording studies.

The SMP polymer formulation used here demonstrated a slightly higher contact angle (more hydrophobic) compared to bare silicon. We have previously demonstrated that slight changes in contact angle measurements can have profound impacts on the nature of protein adsorption and the resulting cell adhesion [68]. Upon initial observation, the higher contact angle (more hydrophobic) SMP material would have been thought to lend itself to a greater adsorption of proteins that promote the development of the glial scar. On the contrary, we found less GFAP expression for the SMP group compared to bare silicon at 16 weeks. It is possible that the dip-coated surface may preferentially attract a different composition or conformation of adsorbed proteins that does not react with astrocytes as strongly. Similar results have been demonstrated with other coating approaches to microelectrode substrates.

By comparison, Lee found that coating planar silicon microelectrodes with polyethylene glycol (PEG) previously demonstrated no effect on the foreign body response [41]. Considering that PEG is highly hydrophilic, this is somewhat contradictory to the expected results. However, as noted by the authors of the paper, it is unlikely the PEG coatings remained intact over the course of the entire 4 week study. Considering the work reported by Lee, and our current study together, it is unclear if a high degree of hydrophobicity alone is enough to influence the long-term foreign body response.

Future studies will investigate the recording performance and neuroinflammatory response to probes made entirely from the SMP materials. Preliminary experiments with dummy (non-functional) SMP probes have suggested that stereotactic insertion of the SMP microelectrodes will be challenging. Due to their thin and flexible nature, many of the fabricated SMP devices have a curved surface that prevents their successful insertion using stereotactic methods. The probes bend, deflect, or buckle at a relatively high frequency. Since the current study was planned to be compared to a study of microelectrodes made completely of the SMP material, all implantations were performed by-hand to allow for cross-comparability between the experimental conditions. However, it is likely that the error injected into the study is minimal compared to other experimental confounds. We have previously compared the neuroinflammatory response of microelectrodes implanted by either stereotactic or by-hand method and found the variability of the histological responses to be negligible compared the larger subject-to-subject variability inherent with both methods (Supplementary Figure S3). While the magnitude of the impact may be debated, the discrepancy must be noted as a known limitation of the present study.

In conclusion, thiol-ene and thiol-ene/acrylate shape memory polymers are currently under development for a wide range of neural implant applications, including intracortical microelectrodes, spinal cord stimulators, sciatic-tibial-sural 'Y' electrodes, longitudinal intrafascicular electrodes, and self-coiling nerve cuff electrodes [22,35,40,78–80]. Here, our initial study sought to investigate the foreign body response to the material in absence of its mechanical softening properties so that as many extra and potentially confounding variables as possible could be eliminated. From the results of the current study, we can conclude that the thiol-ene polymer material performs similar to, or better than, bare silicon in terms of the biological markers tested over 16 weeks of implantation in the rat cortex. It is well documented that silicon-based microelectrodes, such as the controls used here, are not a long-term solution for intracortical microelectrodes. Therefore, the fact that our thiol-ene shape memory polymer merely performs as well is not overly inspiring. However, the anticipated advantage of the thiol-ene shape memory polymer system is in the mechanical softening, which was not exploited here. Therefore, at worst, our SMP is adequate as an intracortical microelectrode substrate. Additional studies are required to test how the mechanics (dynamically softening after implantation) will affect the neuroinflammatory response.

Supplementary Materials: The following are available online at http://www.mdpi.com/2072-666X/9/10/486/s1, Figure S1: SEM measurement of dip-coating thickness along the length of the probe, Figure S2: Accelerated aging representative SEM, Figure S3: Comparing neuronal density around stereotactically and hand inserted Michigan-style microelectrodes 16 weeks post implantation.

Author Contributions: Conceptualization W.E.V., J.J.P., J.R.C.; methodology A.J.S., M.E., V.D.; software A.J.S.; validation M.E., V.D., A.S.; formal analysis A.J.S., M.E., V.D., M.Y., J.E.P., E.M.; investigation A.J.S., M.E., V.D., H.W.B., A.S.; resources W.E.V., J.J.P., J.R.C.; data curation A.J.S., M.Y., J.E.P., E.M.; writing—original draft preparation A.J.S., M.E., A.J.-I., V.D., H.W.B.; writing—review and editing A.J.S., M.E., V.D., W.E.V., J.J.P., J.R.C.; visualization A.J.S.; supervision W.E.V., J.J.P., J.R.C.; project administration W.E.V., J.J.P., J.R.C.; funding acquisition W.E.V., J.J.P., A.J.S., J.R.C.

Funding: This work was supported in part by the Office of the Assistant Secretary of Defense for Health Affairs through the Peer Reviewed Medical Research Program under Award No. W81XWH-15-1-0607 (Pancrazio) and W81XWH-15-1-0608 (Capadona) in part by Merit Review Awards #B1495-R and #B2611 (Capadona), Presidential Early Career Award for Scientist and Engineers (PECASE, Capadona), and a Career Development Award-1 #1IK1RX002492-01A2 (Shoffstall) from the United States (US) Department of Veterans Affairs Rehabilitation Research and Development Service, and by the National Institute of Health, National Institute of Neurological Disorders and Stroke, (Grant # 1R01NS082404-Q3 01A1). None of the funding sources aided in collection, analysis and interpretation of the data, in writing of the manuscript, or in the decision to submit the manuscript for

publication. The contents do not represent the views of the U.S. Department of Defense, the U.S. Department of Veterans Affairs or the United States Government.

Acknowledgments: We would like to acknowledge the following individuals for their contribution to the image process and surgical assistance: Suraj Srinivasan, Mitchell Willis, Dhariyat Menendez, Carmen Toth, Rachel Welscott, Noel Jeansonne.

Conflicts of Interest: The authors declare no conflicts of interest.

References

1. Pancrazio, J.J.; Peckham, P.H. Neuroprosthetic devices: How far are we from recovering movement in paralyzed patients? *Expert Rev. Neurother.* **2009**, *9*, 427–430. [CrossRef] [PubMed]
2. Ajiboye, A.B.; Willett, F.R.; Young, D.R.; Memberg, W.D.; Murphy, B.A.; Miller, J.P.; Walter, B.L.; Sweet, J.A.; Hoyen, H.A.; Keith, M.W.; et al. Restoration of reaching and grasping movements through brain-controlled muscle stimulation in a person with tetraplegia: A proof-of-concept demonstration. *Lancet* **2017**, *389*, 1821–1830. [CrossRef]
3. Jorfi, M.; Skousen, J.L.; Weder, C.; Capadona, J.R. Progress towards biocompatible intracortical microelectrodes for neural interfacing applications. *J. Neural Eng.* **2015**, *12*, 011001. [CrossRef] [PubMed]
4. Seymour, J.P.; Wu, F.; Wise, K.D.; Yoon, E. State-of-the-art MEMS and microsystem tools for brain research. *Microsyst. Nanoeng.* **2017**, *3*, 16066. [CrossRef]
5. Teleńczuk, B.; Dehghani, N.; Le Van Quyen, M.; Cash, S.S.; Halgren, E.; Hatsopoulos, N.G.; Destexhe, A. Local field potentials primarily reflect inhibitory neuron activity in human and monkey cortex. *Sci. Rep.* **2017**, *7*, 40211. [CrossRef] [PubMed]
6. Turner, D.A.; Patil, P.G.; Nicolelis, M.A.L. Conceptual and technical approaches to human neural ensemble recordings. In *Methods for Neural Ensemble Recordings*, 2nd ed.; Nicolelis, M.A.L., Ed.; CRC Press/Taylor & Francis: Boca Raton, FL, USA, 2008.
7. Perel, S.; Sadtler, P.T.; Oby, E.R.; Ryu, S.I.; Tyler-Kabara, E.C.; Batista, A.P.; Chase, S.M. Single-unit activity, threshold crossings, and local field potentials in motor cortex differentially encode reach kinematics. *J. Neurophysiol.* **2015**, *114*, 1500–1512. [CrossRef] [PubMed]
8. Sendhilnathan, N.; Basu, D.; Murthy, A. Simultaneous analysis of the LFP and spiking activity reveals essential components of a visuomotor transformation in the frontal eye field. *Proc. Natl. Acad. Sci. USA* **2017**, *114*, 6370–6375. [CrossRef] [PubMed]
9. Sharma, G.; Annetta, N.; Friedenberg, D.; Blanco, T.; Vasconcelos, D.; Shaikhouni, A.; Rezai, A.R.; Bouton, C. Time stability and coherence analysis of multiunit, single-unit and local field potential neuronal signals in chronically implanted brain electrodes. *Bioelectron. Med.* **2015**, *2*, 63–71.
10. Rennaker, R.L.; Miller, J.; Tang, H.; Wilson, D.A. Minocycline increases quality and longevity of chronic neural recordings. *J. Neural Eng.* **2007**, *4*, L1–L5. [CrossRef] [PubMed]
11. Williams, J.C.; Rennaker, R.L.; Kipke, D.R. Long-term neural recording characteristics of wire microelectrode arrays implanted in cerebral cortex. *Brain Res.* **1999**, *4*, 303–313. [CrossRef]
12. Tresco, P.A.; Winslow, B.D. The challenge of integrating devices into the central nervous system. *Crit. Rev. Biomed. Eng.* **2011**, *39*, 29–44. [CrossRef] [PubMed]
13. McConnell, G.C.; Rees, H.D.; Levey, A.I.; Gutekunst, C.-A.; Gross, R.E.; Bellamkonda, R.V. Implanted neural electrodes cause chronic, local inflammation that is correlated with local neurodegeneration. *J. Neural Eng.* **2009**, *6*, 056003. [CrossRef] [PubMed]
14. Kozai, T.D.Y.; Catt, K.; Li, X.; Gugel, Z.V.; Olafsson, V.T.; Vazquez, A.L.; Cui, X.T. Mechanical failure modes of chronically implanted planar silicon-based neural probes for laminar recording. *Biomaterials* **2015**, *37*, 25–39. [CrossRef] [PubMed]
15. Shoffstall, A.; Capadona, J.R. Prospects for a robust cortical recording interface. In *Neuromodulation*, 2nd ed.; Krames, E.S., Peckham, P.H., Rezai, A.R., Eds.; Academic Press: Cambridge, MA, USA, 2018; pp. 393–413.
16. Michelson, N.J.; Vazquez, A.L.; Eles, J.R.; Salatino, J.W.; Purcell, E.K.; Williams, J.J.; Cui, X.T.; Kozai, T.D.Y. Multi-scale, multi-modal analysis uncovers complex relationship at the brain tissue-implant neural interface: New emphasis on the biological interface. *J. Neural Eng.* **2018**, *15*, 033001. [CrossRef] [PubMed]

17. Miranda, R.A.; Casebeer, W.D.; Hein, A.M.; Judy, J.W.; Krotkov, E.P.; Laabs, T.L.; Manzo, J.E.; Pankratz, K.G.; Pratt, G.A.; Sanchez, J.C.; et al. Darpa-funded efforts in the development of novel brain–computer interface technologies. *J. Neurosci. Methods* **2015**, *244*, 52–67. [CrossRef] [PubMed]
18. Cody, P.A.; Eles, J.R.; Lagenaur, C.F.; Kozai, T.D.Y.; Cui, X.T. Unique electrophysiological and impedance signatures between encapsulation types: An analysis of biological utah array failure and benefit of a biomimetic coating in a rat model. *Biomaterials* **2018**, *161*, 117–128. [CrossRef] [PubMed]
19. Potter-Baker, K.A.; Nguyen, J.K.; Kovach, K.M.; Gitomer, M.M.; Srail, T.W.; Stewart, W.G.; Skousen, J.L.; Capadona, J.R. Development of superoxide dismutase mimetic surfaces to reduce accumulation of reactive oxygen species surrounding intracortical microelectrodes. *J. Mater. Chem. B* **2014**, *2*, 2248–2258. [CrossRef] [PubMed]
20. Potter-Baker, K.A.; Stewart, W.G.; Tomaszewski, W.H.; Wong, C.T.; Meador, W.D.; Ziats, N.P.; Capadona, J.R. Implications of chronic daily anti-oxidant administration on the inflammatory response to intracortical microelectrodes. *J. Neural Eng.* **2015**, *12*, 046002. [CrossRef] [PubMed]
21. Wellman, S.M.; Eles, J.R.; Ludwig, K.A.; Seymour, J.P.; Michelson, N.J.; McFadden, W.E.; Vazquez, A.L.; Kozai, T.D.Y. A materials roadmap to functional neural interface design. *Adv. Funct. Mater.* **2018**, *28*. [CrossRef] [PubMed]
22. Ware, T.; Simon, D.; Arreaga-Salas David, E.; Reeder, J.; Rennaker, R.; Keefer Edward, W.; Voit, W. Fabrication of responsive, softening neural interfaces. *Adv. Funct. Mater.* **2012**, *22*, 3470–3479. [CrossRef]
23. Pancrazio, J.J.; Deku, F.; Ghazavi, A.; Stiller, A.M.; Rihani, R.; Frewin, C.L.; Varner, V.D.; Gardner, T.J.; Cogan, S.F. Thinking small: Progress on microscale neurostimulation technology. *Neuromodulation* **2017**, *20*, 745–752. [CrossRef] [PubMed]
24. Mercanzini, A.; Cheung, K.; Buhl, D.L.; Boers, M.; Maillard, A.; Colin, P.; Bensadoun, J.-C.; Bertsch, A.; Renaud, P. Demonstration of cortical recording using novel flexible polymer neural probes. *Sens. Actuators A Phys.* **2008**, *143*, 90–96. [CrossRef]
25. Cheung, K.C.; Renaud, P.; Tanila, H.; Djupsund, K. Flexible polyimide microelectrode array for in vivo recordings and current source density analysis. *Biosens. Bioelectron.* **2007**, *22*, 1783–1790. [CrossRef] [PubMed]
26. Metz, S.; Bertsch, A.; Bertrand, D.; Renaud, P. Flexible polyimide probes with microelectrodes and embedded microfluidic channels for simultaneous drug delivery and multi-channel monitoring of bioelectric activity. *Biosens. Bioelectron.* **2004**, *19*, 1309–1318. [CrossRef] [PubMed]
27. Takeuchi, S.; Ziegler, D.; Yoshida, Y.; Mabuchi, K.; Suzuki, T. Parylene flexible neural probes integrated with microfluidic channels. *Lab Chip* **2005**, *5*, 519–523. [CrossRef] [PubMed]
28. Luan, L.; Wei, X.; Zhao, Z.; Siegel, J.J.; Potnis, O.; Tuppen, C.A.; Lin, S.; Kazmi, S.; Fowler, R.A.; Holloway, S.; et al. Ultraflexible nanoelectronic probes form reliable, glial scar-free neural integration. *Sci. Adv.* **2017**, *3*, e1601966. [CrossRef] [PubMed]
29. Liu, J.; Fu, T.-M.; Cheng, Z.; Hong, G.; Zhou, T.; Jin, L.; Duvvuri, M.; Jiang, Z.; Kruskal, P.; Xie, C.; et al. Syringe-injectable electronics. *Nat. Nanotechnol.* **2015**, *10*, 629. [CrossRef] [PubMed]
30. Sohal, H.S.; Jackson, A.; Jackson, R.; Clowry, G.J.; Vassilevski, K.; O'Neill, A.; Baker, S.N. The sinusoidal probe: A new approach to improve electrode longevity. *Front. Neuroeng.* **2014**, *7*, 10. [CrossRef] [PubMed]
31. Kozai, T.D.; Gugel, Z.; Li, X.; Gilgunn, P.J.; Khilwani, R.; Ozdoganlar, O.B.; Fedder, G.K.; Weber, D.J.; Cui, X.T. Chronic tissue response to carboxymethyl cellulose based dissolvable insertion needle for ultra-small neural probes. *Biomaterials* **2014**, *35*, 9255–9268. [CrossRef] [PubMed]
32. McCallum, G.A.; Sui, X.; Qiu, C.; Marmerstein, J.; Zheng, Y.; Eggers, T.E.; Hu, C.; Dai, L.; Durand, D.M. Chronic interfacing with the autonomic nervous system using carbon nanotube (cnt) yarn electrodes. *Sci. Rep.* **2017**, *7*, 11723. [CrossRef] [PubMed]
33. Patel, P.R.; Zhang, H.; Robbins, M.T.; Nofar, J.B.; Marshall, S.P.; Kobylarek, M.J.; Kozai, T.D.; Kotov, N.A.; Chestek, C.A. Chronic in vivo stability assessment of carbon fiber microelectrode arrays. *J. Neural Eng.* **2016**, *13*, 066002. [CrossRef] [PubMed]
34. Reit, R.; Zamorano, D.; Parker, S.; Simon, D.; Lund, B.; Voit, W.; Ware, T.H. Hydrolytically stable thiol-ene networks for flexible bioelectronics. *ACS Appl. Mater. Interfaces* **2015**, *7*, 28673–28681. [CrossRef] [PubMed]
35. Ware, T.; Simon, D.; Liu, C.; Musa, T.; Vasudevan, S.; Sloan, A.; Keefer, E.W.; Rennaker, R.L., 2nd; Voit, W. Thiol-ene/acrylate substrates for softening intracortical electrodes. *J. Biomed. Mater. Res. B Appl. Biomater.* **2014**, *102*, 1–11. [CrossRef] [PubMed]

36. Senyurt, A.F.; Wei, H.; Hoyle, C.E.; Piland, S.G.; Gould, T.E. Ternary thiol−ene/acrylate photopolymers: Effect of acrylate structure on mechanical properties. *Macromolecules* **2007**, *40*, 4901–4909. [CrossRef]
37. Wei, H.; Senyurt Askim, F.; Jönsson, S.; Hoyle Charles, E. Photopolymerization of ternary thiol–ene/acrylate systems: Film and network properties. *J. Polym. Sci. Part A: Polym. Chem.* **2007**, *45*, 822–829. [CrossRef]
38. Do, D.-H.; Ecker, M.; Voit, W.E. Characterization of a thiol-ene/acrylate-based polymer for neuroprosthetic implants. *ACS Omega* **2017**, *2*, 4604–4611. [CrossRef] [PubMed]
39. Ecker, M.; Danda, V.; Shoffstall Andrew, J.; Mahmood Samsuddin, F.; Joshi-Imre, A.; Frewin Christopher, L.; Ware Taylor, H.; Capadona Jeffrey, R.; Pancrazio Joseph, J.; Voit Walter, E. Sterilization of thiol-ene/acrylate based shape memory polymers for biomedical applications. *Macromol. Mater. Eng.* **2016**, *302*, 1600331. [CrossRef]
40. Simon, D.M.; Charkhkar, H.; St. John, C.; Rajendran, S.; Kang, T.; Reit, R.; Arreaga-Salas, D.; McHail Daniel, G.; Knaack Gretchen, L.; Sloan, A.; et al. Design and demonstration of an intracortical probe technology with tunable modulus. *J. Biomed. Mater. Res. Part A* **2016**, *105*, 159–168. [CrossRef] [PubMed]
41. Lee, H.C.; Gaire, J.; Currlin, S.W.; McDermott, M.D.; Park, K.; Otto, K.J. Foreign body response to intracortical microelectrodes is not altered with dip-coating of polyethylene glycol (peg). *Front. Neurosci.* **2017**, *11*, 513. [CrossRef] [PubMed]
42. Lind, G.; Gallentoft, L.; Danielsen, N.; Schouenborg, J.; Pettersson, L.M. Multiple implants do not aggravate the tissue reaction in rat brain. *PLoS ONE* **2012**, *7*, e47509. [CrossRef] [PubMed]
43. Potter, K.A.; Buck, A.C.; Self, W.K.; Capadona, J.R. Stab injury and device implantation within the brain results in inversely multiphasic neuroinflammatory and neurodegenerative responses. *J. Neural Eng.* **2012**, *9*, 046020. [CrossRef] [PubMed]
44. McConnell, G.C. *Chronic Inflammation Surrounding Intra-Cortical Electrodes Is Correlated with a Local Neurodegenerative State*; Georgia Institute of Technology: Atlanta, GA, USA, 2008.
45. Harris, J.P.; Capadona, J.R.; Miller, R.H.; Healy, B.C.; Shanmuganathan, K.; Rowan, S.J.; Weder, C.; Tyler, D.J. Mechanically adaptive intracortical implants improve the proximity of neuronal cell bodies. *J. Neural Eng.* **2011**, *8*, 066011. [CrossRef] [PubMed]
46. Potter, K.A.; Simon, J.S.; Velagapudi, B.; Capadona, J.R. Reduction of autofluorescence at the microelectrode-cortical tissue interface improves antibody detection. *J. Neurosci. Methods* **2012**, *203*, 96–105. [CrossRef] [PubMed]
47. Potter, K.A.; Buck, A.C.; Self, W.K.; Callanan, M.E.; Sunil, S.; Capadona, J.R. The effect of resveratrol on neurodegeneration and blood brain barrier stability surrounding intracortical microelectrodes. *Biomaterials* **2013**, *34*, 7001–7015. [CrossRef] [PubMed]
48. Potter, K.A.; Jorfi, M.; Householder, K.T.; Foster, E.J.; Weder, C.; Capadona, J.R. Curcumin-releasing mechanically-adaptive intracortical implants improve the proximal neuronal density and blood-brain barrier stability. *Acta Biomater.* **2014**, *10*, 2209–2222. [CrossRef] [PubMed]
49. Potter-Baker, K.A.; Ravikumar, M.; Burke, A.A.; Meador, W.D.; Householder, K.T.; Buck, A.C.; Sunil, S.; Stewart, W.G.; Anna, J.P.; Tomaszewski, W.H.; et al. A comparison of neuroinflammation to implanted microelectrodes in rat and mouse models. *Biomaterials* **2014**, *34*, 5637–5646. [CrossRef] [PubMed]
50. Shoffstall, A.J.; Paiz, J.E.; Miller, D.M.; Rial, G.M.; Willis, M.T.; Menendez, D.M.; Hostler, S.R.; Capadona, J.R. Potential for thermal damage to the blood-brain barrier during craniotomy: Implications for intracortical recording microelectrodes. *J. Neural Eng.* **2018**, *15*, 034001. [CrossRef] [PubMed]
51. Potter, K.; Gui, B.; Capadona, J.R. Biomimicry at the cell-material interface. In *Biomimetics—Innovation Thru Mimicking natures Inventions*; Bar-Cohen, Y., Ed.; CRC Press: Boca Raton, FL, USA, 2011; Volume 2, pp. 95–129.
52. Hermann, J.K.; Ravikumar, M.; Shoffstall, A.J.; Ereifej, E.S.; Kovach, K.M.; Chang, J.; Soffer, A.; Wong, C.; Srivastava, V.; Smith, P.; et al. Inhibition of the cluster of differentiation 14 innate immunity pathway with iaxo-101 improves chronic microelectrode performance. *J. Neural Eng.* **2018**, *15*, 025002. [CrossRef] [PubMed]
53. Abbott, N.J. Astrocyte–endothelial interactions and blood–brain barrier permeability. *J. Anat.* **2002**, *200*, 629–638. [CrossRef] [PubMed]
54. Cavanagh, J.B. The proliferation of astrocytes around a needle wound in the rat brain. *J. Anat.* **1970**, *106*, 471–487. [PubMed]
55. Woolley, A.J.; Desai, H.A.; Otto, K.J. Chronic intracortical microelectrode arrays induce non-uniform, depth-related tissue responses. *J. Neural Eng.* **2013**, *10*, 026007. [CrossRef] [PubMed]

56. Hanisch, U.-K. Microglia as a source and target of cytokines. *Glia* **2002**, *40*, 140–155. [CrossRef] [PubMed]
57. Bedell, H.W.; Hermann, J.K.; Ravikumar, M.; Lin, S.; Rein, A.; Li, X.; Molinich, E.; Smith, P.D.; Selkirk, S.M.; Miller, R.H.; et al. Targeting cd14 on blood derived cells improves intracortical microelectrode performance. *Biomaterials* **2018**, *163*, 163–173. [CrossRef] [PubMed]
58. Graeber, M.B.; Streit, W.J.; Kiefer, R.; Schoen, S.W.; Kreutzberg, G.W. New expression of myelomonocytic antigens by microglia and perivascular cells following lethal motor neuron injury. *J. Neuroimmunol.* **1990**, *27*, 121–132. [CrossRef]
59. Aihara, N.; Tanno, H.; Hall, J.J.; Pitts Lawrence, H.; Noble, L.J. Immunocytochemical localization of immunoglobulins in the rat brain: Relationship to the blood-brain barrier. *J. Comp. Neurol.* **1994**, *342*, 481–496. [CrossRef] [PubMed]
60. Biran, R.; Martin, D.C.; Tresco, P.A. Neuronal cell loss accompanies the brain tissue response to chronically implanted silicon microelectrode arrays. *Exp. Neurol.* **2005**, *195*, 115–126. [CrossRef] [PubMed]
61. Nguyen, J.K.; Jorfi, M.; Buchanan, K.L.; Park, D.J.; Foster, E.J.; Tyler, D.J.; Rowan, S.J.; Weder, C.; Capadona, J.R. Influence of resveratrol release on the tissue response to mechanically adaptive cortical implants. *Acta Biomater.* **2016**, *29*, 81–93. [CrossRef] [PubMed]
62. Nguyen, J.K.; Park, D.J.; Skousen, J.L.; Hess-Dunning, A.E.; Tyler, D.J.; Rowan, S.J.; Weder, C.; Capadona, J.R. Mechanically-compliant intracortical implants reduce the neuroinflammatory response. *J. Neural Eng.* **2014**, *11*, 056014. [CrossRef] [PubMed]
63. Capadona, J.R.; Tyler, D.J.; Zorman, C.A.; Rowan, S.J.; Weder, C. Mechanically adaptive nanocomposites for neural interfacing. *MRS Bull.* **2012**, *37*, 581–589. [CrossRef]
64. Sridharan, A.; Nguyen, J.K.; Capadona, J.R.; Muthuswamy, J. Compliant intracortical implants reduce strains and strain rates in brain tissue in vivo. *J. Neural Eng.* **2015**, *12*, 036002. [CrossRef] [PubMed]
65. Raynor, J.E.; Capadona, J.R.; Collard, D.M.; Petrie, T.A.; Garcia, A.J. Polymer brushes and self-assembled monolayers: Versatile platforms to control cell adhesion to biomaterials (review). *Biointerphases* **2009**, *4*, FA3–FA16. [CrossRef] [PubMed]
66. Petrie, T.A.; Capadona, J.R.; Reyes, C.D.; Garcia, A.J. Integrin specificity and enhanced cellular activities associated with surfaces presenting a recombinant fibronectin fragment compared to rgd supports. *Biomaterials* **2006**, *27*, 5459–5470. [CrossRef] [PubMed]
67. Capadona, J.R.; Petrie, T.A.; Fears, K.P.; Latour, R.A.; Collard, D.M.; García, A.J. Surface-nucleated assembly of fibrillar extracellular matrices. *Adv. Mater.* **2005**, *17*, 2604–2608. [CrossRef]
68. Capadona, J.R.; Collard, D.M.; García, A.J. Fibronectin adsorption and cell adhesion to mixed monolayers of tri(ethylene glycol)- and methyl-terminated alkanethiols. *Langmuir* **2003**, *19*, 1847–1852. [CrossRef]
69. Kovach, K.M.; Capadona, J.R.; Gupta, A.S.; Potkay, J.A. The effects of peg-based surface modification of pdms microchannels on long-term hemocompatibility. *J. Biomed. Mater. Res. A* **2014**, *102*, 4195–4205. [PubMed]
70. Moshayedi, P.; Ng, G.; Kwok, J.C.F.; Yeo, G.S.H.; Bryant, C.E.; Fawcett, J.W.; Franze, K.; Guck, J. The relationship between glial cell mechanosensitivity and foreign body reactions in the central nervous system. *Biomaterials* **2014**, *35*, 3919–3925. [CrossRef] [PubMed]
71. Wilson, C.L.; Hayward, S.L.; Kidambi, S. Astrogliosis in a dish: Substrate stiffness induces astrogliosis in primary rat astrocytes. *RSC Adv.* **2016**, *6*, 34447. [CrossRef]
72. Spencer, K.C.; Sy, J.C.; Ramadi, K.B.; Graybiel, A.M.; Langer, R.; Cima, M.J. Characterization of mechanically matched hydrogel coatings to improve the biocompatibility of neural implants. *Sci. Rep.* **2017**, *7*, 1952. [CrossRef] [PubMed]
73. McConnell, G.C.; Butera, R.J.; Bellamkonda, R.V. Bioimpedance modeling to monitor astrocytic response to chronically implanted electrodes. *J. Neural Eng.* **2009**, *6*, 055005. [CrossRef] [PubMed]
74. He, W.; Bellamkonda, R.V. A molecular perspective on understanding and modulating the performance of chronic central nervous system (CNS) recording electrodes. In *Indwelling Neural Implants: Strategies for Contending with the In Vivo Environment*; Reichert, W.M., Ed.; CRC Press: Boca Raton, FL, USA, 2008.
75. Skousen, J.L.; Bridge, M.J.; Tresco, P.A. A strategy to passively reduce neuroinflammation surrounding devices implanted chronically in brain tissue by manipulating device surface permeability. *Biomaterials* **2015**, *36*, 33–43. [CrossRef] [PubMed]
76. Nguyen, D.; Cho, N.; Satkunendrarajah, K.; Austin, J.W.; Wang, J.; Fehlings, M.G. Immunoglobulin g (IgG) attenuates neuroinflammation and improves neurobehavioral recovery after cervical spinal cord injury. *J. Neuroinflamm.* **2012**, *9*, 224. [CrossRef] [PubMed]

77. Douglas, M.; Stuart, C.; Sheryl, K.; Victor, P. Correlations between histology and neuronal activity recorded by microelectrodes implanted chronically in the cerebral cortex. *J. Neural Eng.* **2016**, *13*, 036012.
78. Ware, T.; Simon, D.; Hearon, K.; Liu, C.; Shah, S.; Reeder, J.; Khodaparast, N.; Kilgard, M.P.; Maitland, D.J.; Rennaker, R.L., 2nd; et al. Three-dimensional flexible electronics enabled by shape memory polymer substrates for responsive neural interfaces. *Macromol. Mater. Eng.* **2012**, *297*, 1193–1202. [CrossRef] [PubMed]
79. Ware, T.; Simon, D.; Hearon, K.; Kang, T.H.; Maitland, D.J.; Voit, W. Thiol-click chemistries for responsive neural interfaces. *Macromol. Biosci.* **2013**, *13*, 1640–1647. [CrossRef] [PubMed]
80. Garcia-Sandoval, A.; Pal, A.; Mishra, A.M.; Sherman, S.; Parikh, A.R.; Joshi-Imre, A.; Arreaga-Salas, D.; Gutierrez-Heredia, G.; Duran-Martinez, A.C.; Nathan, J.; et al. Chronic softening spinal cord stimulation arrays. *J. Neural Eng.* **2018**, *15*, 045002. [CrossRef] [PubMed]

micromachines

MDPI

Article

Chronic Intracortical Recording and Electrochemical Stability of Thiol-ene/Acrylate Shape Memory Polymer Electrode Arrays

Allison M. Stiller [1,*], Joshua Usoro [1], Christopher L. Frewin [1], Vindhya R. Danda [1,2], Melanie Ecker [3], Alexandra Joshi-Imre [1], Kate C. Musselman [1], Walter Voit [2,3], Romil Modi [2], Joseph J. Pancrazio [1] and Bryan J. Black [1]

1 Department of Bioengineering, The University of Texas at Dallas, Richardson, TX 75080, USA; Joshua.usoro@utdallas.edu (J.U.); Christopher.frewin@utdallas.edu (C.L.F.); vxd160030@utdallas.edu (V.R.D.); Alexandra.Joshi-imre@utdallas.edu (A.J.-I.); kate.musselman@utdallas.edu (K.C.M.); joseph.pancrazio@utdallas.edu (J.J.P.); bjb140530@utdallas.edu (B.J.B.)
2 Qualia, Inc., Dallas, TX 75252, USA; walter.voit@utdallas.edu (W.V.); romil@qualiamedical.com (R.M.)
3 Department of Materials Science and Engineering, The University of Texas at Dallas, Richardson, TX 75080, USA; Melanie.ecker@utdallas.edu
* Correspondence: Allison.stiller@utdallas.edu; Tel.: +1-972-883-2138

Received: 18 August 2018; Accepted: 27 September 2018; Published: 29 September 2018

Abstract: Current intracortical probe technology is limited in clinical implementation due to the short functional lifetime of implanted devices. Devices often fail several months to years post-implantation, likely due to the chronic immune response characterized by glial scarring and neuronal dieback. It has been demonstrated that this neuroinflammatory response is influenced by the mechanical mismatch between stiff devices and the soft brain tissue, spurring interest in the use of softer polymer materials for probe encapsulation. Here, we demonstrate stable recordings and electrochemical properties obtained from fully encapsulated shape memory polymer (SMP) intracortical electrodes implanted in the rat motor cortex for 13 weeks. SMPs are a class of material that exhibit modulus changes when exposed to specific conditions. The formulation used in these devices softens by an order of magnitude after implantation compared to its dry, room-temperature modulus of ~2 GPa.

Keywords: intracortical implant; microelectrodes; softening; immunohistochemistry; immune response; neural interface; shape memory polymer

1. Introduction

Successful clinical application of brain-machine interfaces (BMIs) requires stable, chronic, selective recordings from task-associated neural networks. Noninvasive techniques for the acquisition of neural signals include electroencephalography and electrocorticography [1–3]; however, these methods cannot achieve high-density, single-unit resolution, and are therefore limited as high information content BMI systems [4–6]. Multichannel intracortical microelectrode arrays (MEAs) are able to record single units and local field potentials from adjacent neural tissue within the brain. While several styles of intracortical MEAs are commercially available, they are limited in clinical implementation due to a relatively short functional lifetime, only recording distinguishable units in non-human primates for an average of 1-6 years post-implantation [7–10].

While there are various factors that contribute to MEA failure, findings suggest that the tissue response may be one component that contributes to the premature loss of stable neural recordings [11–14]. The chronic foreign body response stems from the recruitment of activated support cells to the injury site,

initiating signaling cascades that result in upregulated local production of inflammatory and neurotoxic cytokines [14,15]. This leads to the accumulation of glial cells around the implant (i.e., encapsulation) concurrent with local neuronal death [11,15–18], both of which are obstacles for reliable signal acquisition.

State-of-the-art, commercially available devices are fabricated using very stiff (high elastic modulus) materials, such as silicon or tungsten (50–400 GPa). Current research suggests that this mechanical mismatch between the low modulus of the brain (~1–10 kPa) and the high modulus of the device may play a major role in aggravating the chronic immune response [17,19,20]. This effect is exacerbated by constant micromotion of the brain around the implant [21], which results in the development of strain fields in tissue adjacent to the probe [22,23]. Several groups have demonstrated that softer implants may mitigate the tissue response over time when compared to stiffer counterparts [24,25]. However, these materials are often too soft to provide appropriate mechanical support for successful penetration into the brain tissue without the aid of insertion guides [26,27]. Conversely, stiffer devices are brittle and prone to fracture, making them difficult to handle in a clinical setting.

Shape memory polymers (SMPs) are a class of materials that undergo dramatic programmed mechanical deformations or modulus changes when exposed to external stimuli such as light, electric currents, or heat [28–30]. Recently, softening thiol-ene/acrylate-based SMPs, which exhibit changes in modulus when transitioning from ambient to physiological conditions, have been investigated for their use as substrate and encapsulation materials for neural interfaces [31,32]. Specifically, this type of SMP can maintain a high modulus and mechanical stability necessary for the implantation of a thin device, but softens by an order of magnitude within only a few minutes [33]. However, to date, no published study has evaluated the chronic recording and electrochemical performance of fully encapsulated thiol-ene/acrylate-based SMP MEAs in vivo. To address this issue, we have implanted 15-channel Michigan-style SMP devices in the motor cortex of five rats and conducted electrophysiological recordings as well as electrochemical impedance spectroscopy (EIS) and cyclic voltammetry (CV) over a 13-week period. Additionally, we have performed immunohistochemistry (IHC) to evaluate tissue response. Our results demonstrate that these SMP devices consistently recorded units for 13 weeks and induced a minimal immune response in the surrounding tissue.

2. Materials and Methods

2.1. Shape Memory Polymer Devices

All experiments were carried out using IC-5-16E devices (Figure 1) provided by Qualia, Inc. (Dallas, TX, USA). Devices featured 15 electrode sites coated with sputtered iridium oxide film (SIROF) with an electrode area of 180 μm^2. Parylene C encapsulated the thin metal traces to ensure proper electrical insulation. Shanks were 5 mm long, 290 µm wide at the base, and 35 $\pm$ 5 µm thick, with an asymmetric geometry that tapered toward the device tip. The SMP formulation used in these devices softens by an order of magnitude from its dry room-temperature modulus of ~2 GPa to ~300 MPa after implantation. This transition occurs within a few minutes of implantation.

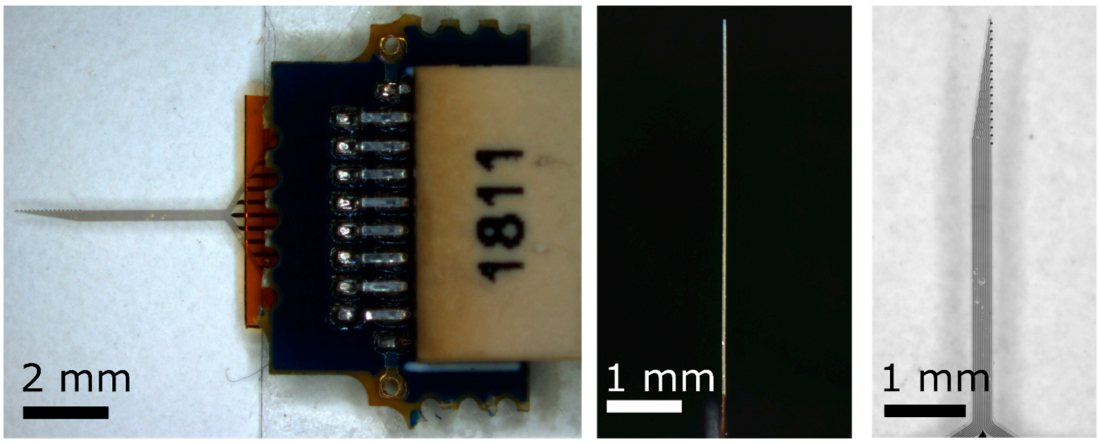

(**a**) (**b**) (**c**)

Figure 1. Optical images of shape memory polymer (SMP) probes. (**a**) Device with Omnetics connector, (**b**) side view demonstrating a straight shank prior to implantation, (**c**) tip with sputtered iridium oxide film (SIROF)-coated electrodes.

2.2. Surgical Implantation

All animal handling, housing, and surgical procedures were approved by the University of Texas Institutional Animal Care and Use Committee. Long Evans rats (n = 5, Charles River), weighing 300–450 g, were implanted with functional SMP devices. Devices underwent brief electrochemical impedance testing before implantation to ensure all electrode sites were below 1 MΩ at 1 kHz frequency. Animals were anesthetized by an intraperitoneal (IP) injection of KXA cocktail consisting of ketamine (65 mg/kg), xylazine (13.33 mg/kg) and acepromazine (1.5 mg/kg) followed by an intramuscular injection of atropine sulfate (0.05 mg/kg) to counteract the cardiovascular depression induced by KXA. After reaching a deep anesthesia plane, confirmed by tail and toe pinches, the scalp was shaved using small hair clippers. Ophthalmic ointment was applied to the animal's eyes to mitigate drying and post-operative irritation. The anesthetic plane was supplemented and maintained using 1–2% isoflurane mixed with 100% oxygen for the duration of the surgery.

Three alternating rounds of 10% iodine solution and 70% ethanol, ending with ethanol, were used to sterilize and clean the point of incision on the scalp. Dexamethasone was then administered subcutaneously between the shoulders (2 mg/kg), followed by subcutaneous injection of 0.4 mL 0.5% lidocaine at the incision cite. A surgical blade was used to make a midline incision down the scalp and the surrounding skin and muscle were retracted with hemostatic forceps. All loose tissue and debris was removed from the skull surface using sterile cotton swabs, and the skull was roughened using the surgical blade to promote binding of the head cap post-surgery.

A surgical drill was used to create a 1–2 mm^2 craniotomy centered in the right motor cortex, approximately 2.5 mm rostral and 2.5 mm lateral from bregma. Three anchoring screws were positioned approximately 1 cm from the perimeter of the insertion site. The dura was resected and the device was implanted at 1000 μm/s to a depth of 1.5–2 mm using a pneumatically controlled micropositioner (Kopf Instruments, Tujunga, CA, USA). No significant curvature or bending of the device was observed prior to or during implantation. Collagen-based dural grafts (Biodesign Dural Graft, Cook Medical, Bloomington, IN, USA) were placed around the implanted device to act as a dura replacement, and then set in place with Gluture topical adhesive (World Precision Instruments, Sarasota, FL, USA). We applied dental cement around the device and all three anchoring screws to construct a protective head cap, promoting chronic mechanical stability. Before being removed from the isoflurane, the animal was given 0.15 mg/kg of sustained release buprenorphine SR LAB (ZooPharm, Windsor, CO, USA) and 5 mg/kg of cefazolin antibiotic along with subcutaneous sterile saline to prevent dehydration. All animals received follow-up analgesic injections of buprenorphine SR 72 h following surgery. None

of the animals showed signs of post-operative complications including chronic bleeding, signs of infection, or skin ulcers.

2.3. Electrophysiological Recordings and Single-Unit Analysis

Electrophysiological recordings were carried out on lightly anesthetized animals (0.5–1.5% isoflurane) immediately following surgical implantation and once per week for 13 weeks afterward. Spontaneous wideband recordings (0.1–7000 Hz) were collected using 15-channel Michigan style SMP arrays (IC-5-16E, Qualia, Inc.) and an Omniplex acquisition system (Plexon, Inc., Dallas, TX, USA) from all 15 recording sites simultaneously at 40,000 Hz for 10 min. Wideband data were processed using a four-pole Butterworth high pass filter with a cutoff frequency of 250 Hz. Individual waveforms (spikes) were identified by filtered continuous data crossing a threshold of -4σ, based on the root mean square (RMS) of the filtered continuous signal. Single units were manually identified from collections of spikes using 2D principal component space, but were excluded from further analysis if they did not contain at least 100 individual spikes, or if >3% of spikes violated a 1.5-ms minimum refractory period. The signal to noise ratio (SNR) was calculated by dividing the mean peak-to-peak voltage of each unit (Vpp) by the RMS noise of its associated channel. The RMS noise was calculated as the RMS of the filtered continuous signal after removing all samples exceeding the 4σ threshold.

2.4. EIS and CV Measurements

EIS and CV measurements were carried out on all electrodes each week immediately following in vivo electrophysiological recordings. The Plexon headstage was removed and replaced with a pre-wired 18 pin dual strip Nano-D female connector (NSD-18-WD-18.0-C-GS, Omnetics Connector Corporation, Minneapolis, MN, USA) attached to multiplexor inputs of a model 604E Series Electrochemical Analyzer/Workstation (CH Instruments Inc., Austin, TX, USA). EIS was performed using a 10 mV RMS sinusoidal signal (Vrms), starting at a frequency of 100 kHz and decreasing to 1 Hz, recording current 12 times per decade of frequency. The impedance magnitude at each frequency was calculated by the CH instruments software. CV evaluations were performed by applying a negative potential ramp starting at the open circuit potential (vs. 316 stainless steel) with no external direct current bias applied. The potential was reduced to -0.6 V and then cycled at 50 mV/s for two complete cycles between -0.6 V and 0.8 V while recording current every 10 ms. A second CV measurement was performed under the same conditions, but at a sweep rate of 50,000 mV/s.

Electrochemistry results were process in MATLAB to extract the values of real impedance (Ω) directly from the EIS recordings at the physiological frequencies of 0.01, 1, and 10 kHz. MATLAB scripts also determined cathodal charge storage capacity (CSCc), a measure of the total cathodal charge available per unit of geometric area, from the CV cathodal current between the limits of -0.6 to 0.8 V.

2.5. Immunohistochemistry

2.5.1. Tissue Preparation

Rats were administered a 200 mg/kg IP injection of sodium pentobarbital. After confirming unconsciousness through tail and toe pinches, the rats were transcardially perfused with room-temperature phosphate buffered saline (PBS) followed by room-temperature 4% paraformaldehyde (PFA) solution. The brain was removed such that the device was kept intact with the connector and surrounding skull. The brain was stored in PFA at 4 °C overnight, then transferred to PBS with sodium azide and stored at 4 °C until sectioning.

Prior to sectioning, brains were submerged in a 4% (m/V) agarose solution for stability. Vibratome sections (Leica VT 1000 S, Leica Biosystems Inc., Buffalo Grove, IL, USA) were collected from the surface of the brain to a 2 mm depth (200 µm slices) and then stored in PBS with 0.1% (w/v) sodium azide (Alfa Aesar, Tewksbury, MA, USA) at 4 °C until staining.

2.5.2. Antibody Staining

Brain slices were blocked in 4% (*v*/*v*) normal goat serum (Abcam Inc., Cambridge, UK) with 0.3% (*v*/*v*) Triton X-100 (Sigma-Aldrich, Saint Louis, MO, USA) in 1× PBS with 0.1% sodium azide (Alfa Aesar) for one hour. Slices were then incubated overnight with primary antibodies targeting neuronal nuclei (NeuN), astrocytes (GFAP), and activated microglia/macrophages (CD68) (Table 1) at 4 °C in a buffer solution containing only 0.1% (*v*/*v*) Triton X-100.

Table 1. Primary antibodies.

Primary	Vendor	ID#	Dilution	Labeling
NeuN	Sigma-Aldrich	ABN91	1:500	Neuronal nuclei
GFAP	Millipore-Sigma	AB5541	1:500	Astrocytes
CD68	Fisher Scientific	MS397P0	1:1000	Activated microglia/macrophages

The following day, slices were washed and incubated for one hour in blocking solution with secondary antibodies, goat anti-rabbit IgG (TRITC), goat anti-mouse IgG (Alexa Fluor 488), goat anti-chicken IgY (Alexa Fluor 647), at 1:1000 dilution, and DAPI (0.6 µM) (Abcam Inc.). Slices were subsequently washed and mounted on glass slides with Fluoromount aqueous mounting medium (Sigma-Aldrich).

2.5.3. IHC Imaging

Stained tissue slices were imaged using an inverted confocal microscope (Nikon Ti eclipse + A1R, Tokyo, Japan) controlled by Nikon Instruments Software package (version AR 4.40.00). Briefly, z-stack images were collected at 1024 × 1024 transverse resolution and 5 µm per axial slice using a 20× Ph2 objective. Fluorescence signal-to-noise was increased by enabling 2× pixel averaging and bleed-over between emission lines was reduced by collecting each emission line in series. All microscope hardware and software settings were conserved between individual image collections and imaging sessions. Following acquisition, z-stack images were collapsed to single maximum intensity projection image.

2.5.4. IHC Quantification

Astrogliosis (GFAP intensity) and neuronal density were quantified as described in [34]. Briefly, images were imported into Fiji [35], and open source imaging software based on ImageJ [36]. Using a custom macro, GFAP intensities and NeuN+ nuclei per area were calculated within at least eight concentric bands of 50 µm thickness generated from a user-defined implant site. All reported values were normalized to measurements from the band located 350–400 µm from the device edge.

2.6. Statistical Analysis

Statistical analysis and graphing were carried out in OriginPro 2017 (Origin Lab, Northampton, MA, USA). In all cases, statistical significance of increasing/decreasing differences ($p < 0.05$) was determined by carrying out analysis of variance (ANOVA) tests on residuals. In the case of both EIS and CV measurements, a single-tiered Grubb's test was applied at a 0.05 significance level to exclude aberrant statistical outliers.

3. Results

3.1. Chronic Single Unit Recordings

To evaluate the chronic recording performance of thiol-ene/acrylate-based SMP devices, we implanted 15-channel Michigan-style single shank electrode arrays in the motor cortex of five Long Evans rats and collected spontaneous wide-band 10-min recordings for 13 weeks post-implantation (Figure 2). Immediately following implantation, we observed that 18.3 ± 6.9% (mean ± SEM, $n = 60$)

of electrode sites across all devices exhibited distinguishable single units (termed "Active electrode yield %") (Figure 3b). At this time, the mean peak-to-peak voltage of sorted waveforms (Figure 3a) was 66.8 ± 3.1 µV, n = 75, resulting in an excellent mean signal-to-noise ratio (SNR) of 9.80 ± 0.47 (Figure 3c). One week post-implantation, the active electrode yield increased to 41.3 ± 12.7%. While, there was no significant change in active electrode yield or SNR over the remaining 13-week period, the total number of recorded units (Figure 2d) increased slightly (R^2 = 0.02, p = 0.02). Overall, these data suggest that our SMP electrodes were stable with regard to their recording capabilities.

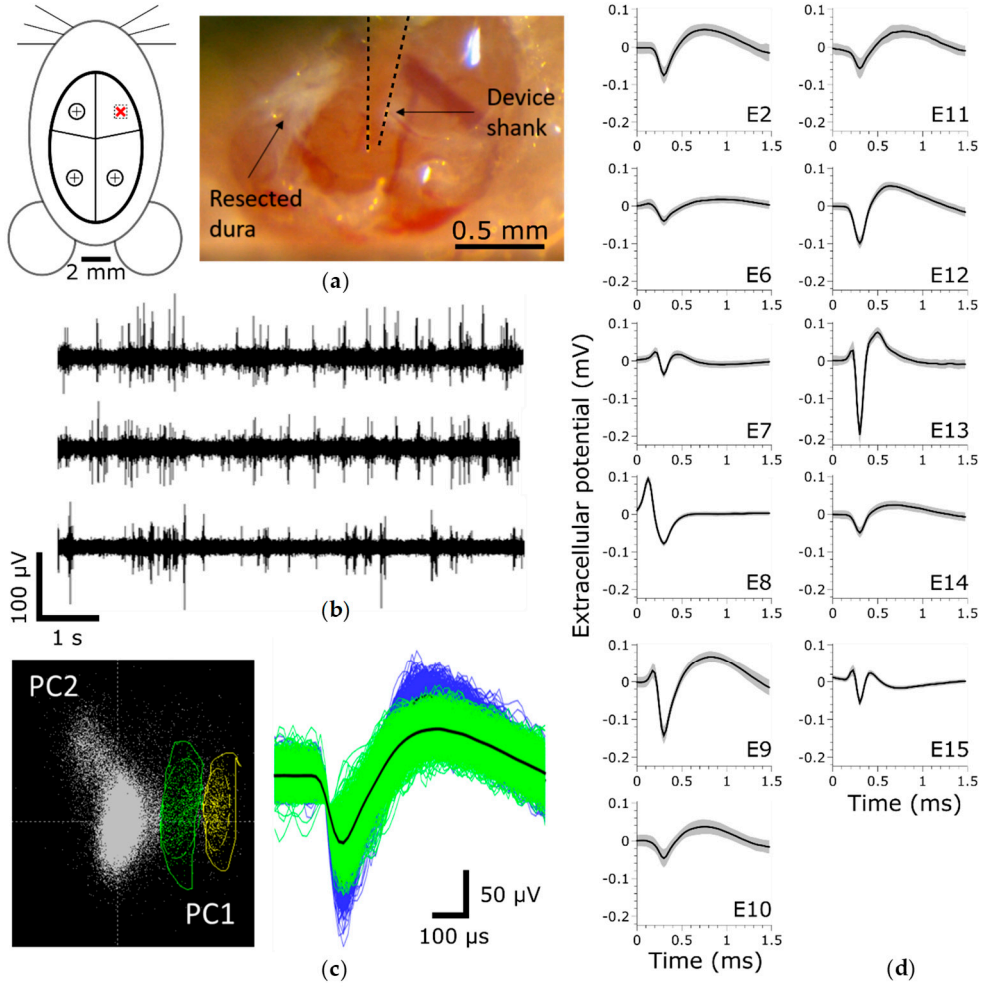

Figure 2. Neural data acquisition and waveform analysis. (**a**) Implantation schematic denoting the implantation site (red "x") and stabilizing screws, (**b**) filtered continuous data from three representative electrodes on a single array, (**c**) representation of single-unit sorting principals (left) and representative multi-unit activity from a single recording electrode (right), (**d**) single units recorded on a single array during a single recording session, ordered from array tip (E2) to base (E15).

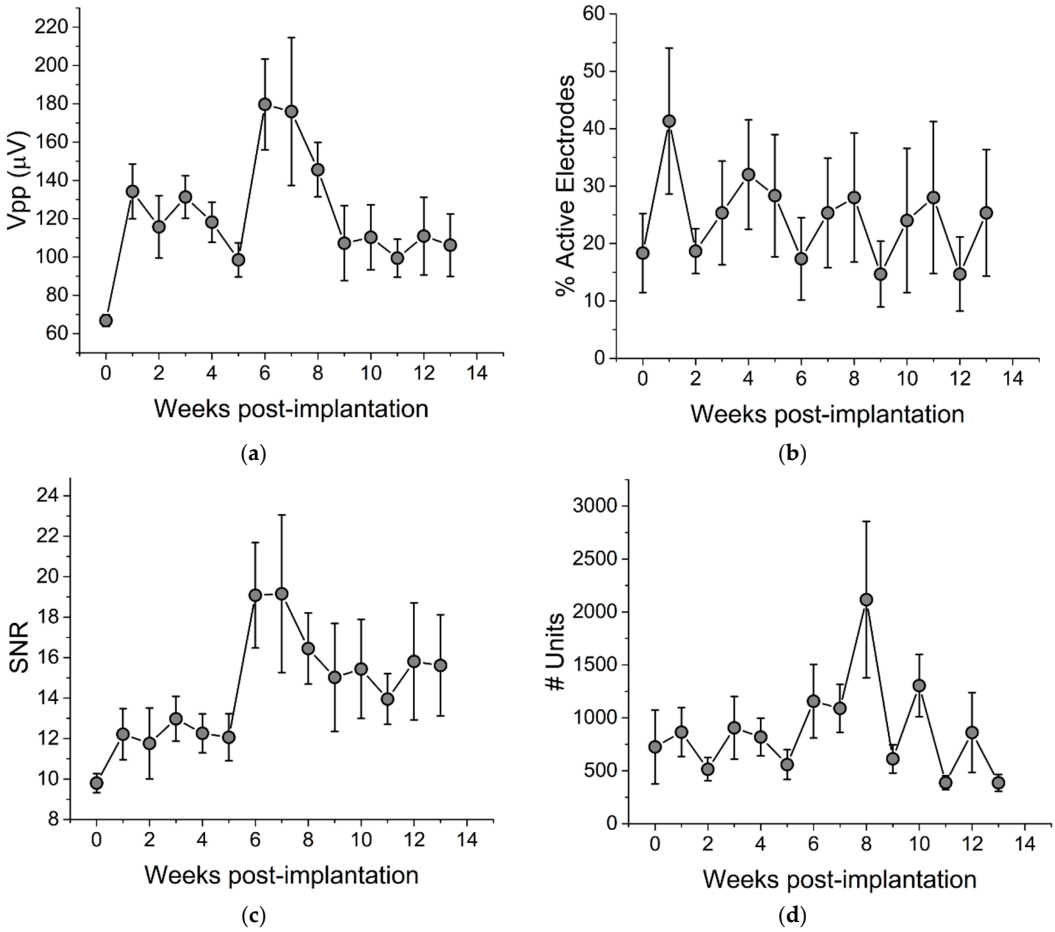

Figure 3. Chronic recording stability. (**a**) peak-to-peak voltage (Vpp), (**b**) active electrode yield %, (**c**) signal-to-noise ratio (SNR), and (**d**) number of units. Each time point reflects n = 75 electrodes, except weeks 0 and 5, which reflect n = 60 electrodes. Linear regression analysis indicates no change in Vpp, active electrode yield %, or SNR, while number of units increased slightly (R^2 = 0.016, p = 0.02). Week 0 represents data taken on the day of implantation. Data are shown as mean ± SEM.

3.2. Chronic In Vivo Electrochemistry

To evaluate the electrochemical stability of the SMP devices over time, we performed EIS and CV measurements on each array across all electrode sites for 13 weeks post-implantation. EIS and CV data are also presented for week 0 data points indicating pre-implantation measurements taken in room temperature PBS. Figure 4a shows representative traces for mean EIS for a single device prior to implantation (in vitro), immediately following implantation, and at five, nine, and 13 weeks following implantation. To evaluate the stability over a frequency relevant to extracellular spikes, the mean 1 kHz impedance across all devices is plotted in Figure 4b over the 13-week time period.

All electrodes exhibited a significant increase in impedance magnitude one week post-implantation (1.23 ± 0.07 MΩ) versus in vitro measurements (0.62 ± 0.09 MΩ), similar to observations made in [37]. Impedance magnitudes remained largely consistent at this value across the first seven weeks of the study, and then decreased slightly during the remaining six weeks. This decrease did not show any correlation with the mean active electrode yield, however, suggesting that although there may have been degradation of the insulating material, this degradation did not hinder the devices' ability to resolve and record single unit activity.

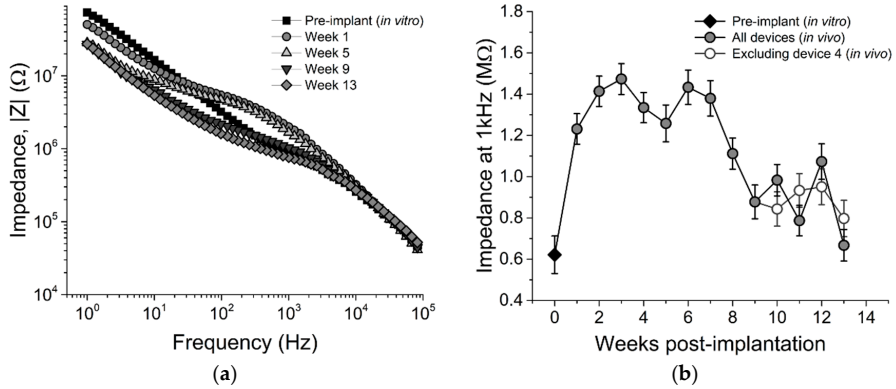

Figure 4. Electrochemical impedance spectroscopy. (**a**) Impedance across 1–10 kHz frequency range for a representative electrode at five time points and (**b**) impedance magnitude at 1 kHz across all electrodes on all devices. Impedance was initially low (~600 kΩ) upon testing before implantation, but increased following implantation. From week 1 until week 13, impedance magnitude decreased over time. Pre-implantation data are from n = 45 electrodes. All other time point reflect n = 75 electrodes, except weeks 0 and 5, which reflect n = 60 electrodes.

Figure 5a–d shows representative CV traces for a single electrode at two different sweep rates (50 and 50,000 mV/s) at selected time points, as well as mean CSC_C for both sweep rates across all devices and time points. Faster sweep rates are indicative of conductive pathways that are near the tip of the device, while slower sweep rates allow access to conductive pathways proximal to the tip.

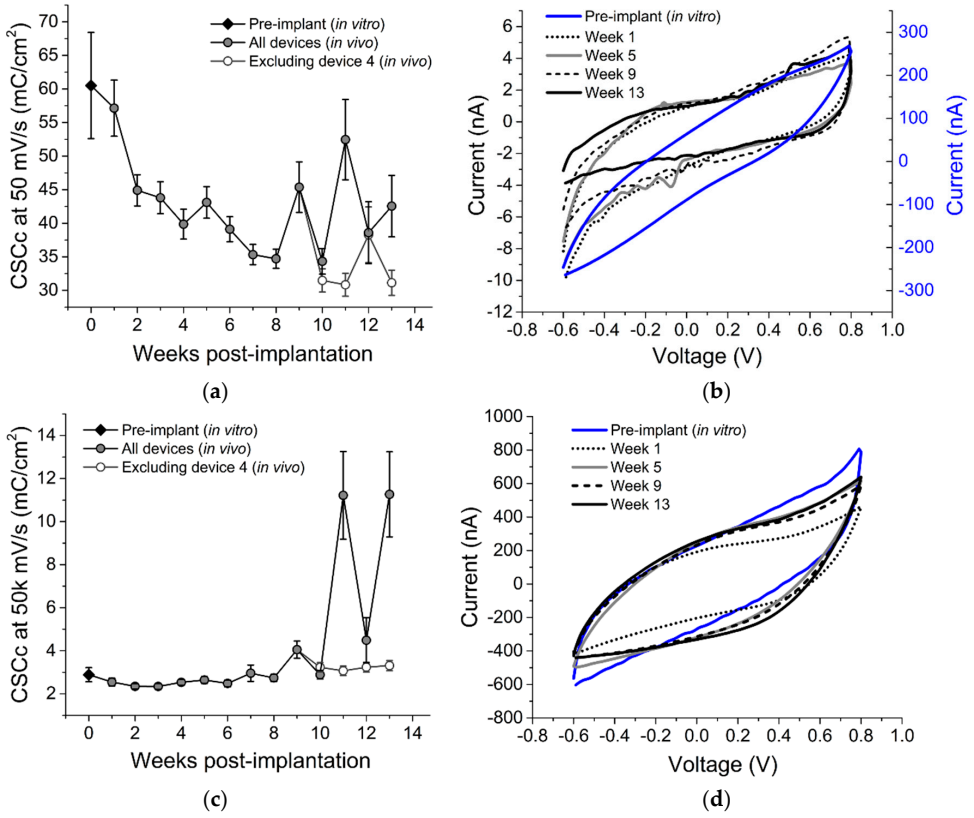

Figure 5. Cyclic voltammetry (CV) results. (**a**,**c**) slow (50 mV/s) and fast (50 k mV/s) CV over 13 weeks, (**b**,**d**) slow and fast CV curves across five time points on a representative electrode.

We observed an increase over time in CSC_C at 50,000 mV/s, (R^2 = 0.07, $p < 0.001$) likely indicating increased access to conductive paths that could be due to cracks or separation between the insulating and conductive layers near the tip. CSC_C at 50 mV/s decreased within the first two weeks post-implantation as compared to in vitro measurements, and continued to decrease until week 8, suggesting a possible loss of the SIROF coating. After week 10, however, the CSC_C increased. This change was attributable to values recorded from a single device (device 4), as demonstrated in Figure 5a,c, and also supported by EIS results (Figure 4b). Nevertheless, the majority of the devices exhibited stable electrochemistry over time, as also supported by the stable neural recordings.

3.3. Histology

To evaluate the induced FBR related to chronic implantation of softening SMP devices, we performed histology targeting neuronal cell bodies (NeuN), astrocytes (GFAP), and activated microglia/macrophages (CD68). Figure 6a shows representative fluorescence images for each marker with respect to increasing depth along the shank of the device.

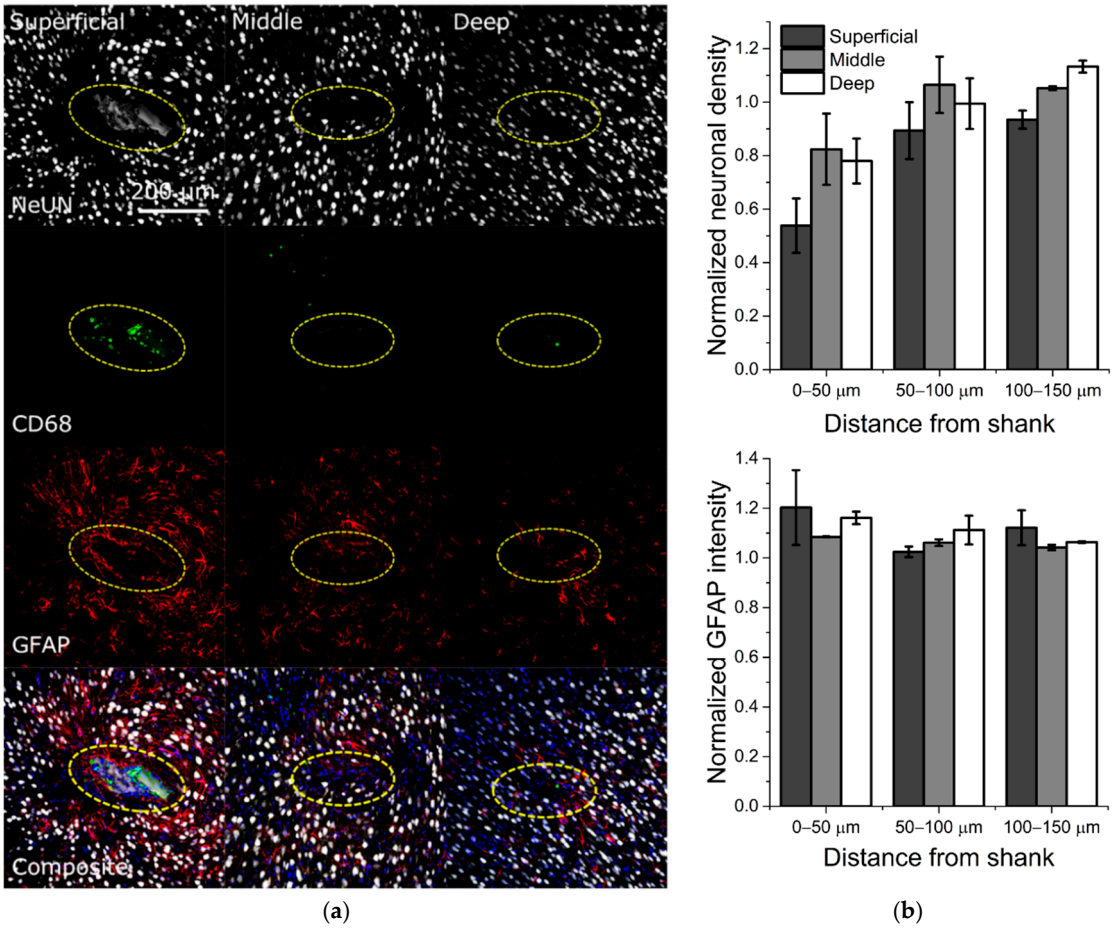

(**a**) (**b**)

Figure 6. Immunohistochemistry for SMP implant after 13 weeks in vivo. (**a**) Columns represent tissue collected at superficial, middle, and deep slices in relation to the surface of the motor cortex. Rows represent neuronal nuclei (NeUN) (gray, top), activated microglia/macrophages (CD68) (green), astrocytes (GFAP) (red), and Composite (bottom) images. Scale bar represents 200 µm in the transverse plane across all images. Yellow ellipses indicate probe location. (**b**) Quantification of NeuN and GFAP for n = 2 animals at varying slice depths (one slice per region) with respect to the shank location in the brain.

While Figure 6 demonstrates promising histological outcomes, these results are preliminary and require a more comprehensive analysis comparing SMP with standard silicon devices to make statistical claims. The most severe apparent immune response was observed at the base of the shank, represented by "superficial" slices, within the first 50 µm of the device perimeter (Figure 6b). However, this effect tapered off along the length of the probe, represented by "middle" and "deep" slices. Additionally, consistent with previous studies reporting histological outcomes, we observed slight astrogliosis in areas with neuronal dieback, again with the most severe response near the base of the shank but tapered off toward the tip. This is in contrast to previous reports of significant neuroinflammatory response within 100 µm of the device when using silicon-based arrays [15]. Additionally, there were few or no apparent activated microglia around the device at "middle" and "deep" slices. It is important to note that the microelectrode sites on this device are located near the end of the device shank, and therefore best represented by the "middle" and "deep" slices. Therefore, it appears that the neuroinflammatory response was modest proximal to the microelectrode site locations.

4. Discussion

Significant efforts have been directed toward developing penetrating intracortical MEAs that mitigate the FBR. Prior work has made use of three general strategies or combinations thereof: (1) decreasing MEAs dimensions [38,39], (2) utilizing soft or softening materials for MEAs [24,25], and (3) coating MEAs with biomimetic gels, proteins, or growth factors to depress the foreign body response or facilitate local regeneration [40,41]. While these approaches have all yielded varying levels of success in terms of histological response, the chronic recording reliability of penetrating intracortical MEAs remains a significant challenge. Here, for the first time, we have demonstrated stable chronic recordings from a fully encapsulated softening SMP-based electrode array implanted in the motor cortex of rats. Importantly, we observed no significant decrease in active electrode yield over a 13-week indwelling period. Additionally, we performed electrochemical measurements to evaluate the electrical stability of these arrays. While we initially observed an increase in 1 kHz impedance magnitude, most likely associated with acute inflammation, the impedance approached its pre-implantation values over time, suggesting a resolution of the acute immune response over the first eight weeks in vivo [42]. This is further supported by the limited FBR we observed following device explantation. Cathodal charge storage capacity was also found to be largely consistent over the indwelling period. However, in the case of one electrode array, the CSC increased dramatically over the final three weeks of implantation (approximately 2 orders of magnitude). Concurrently, this electrode array exhibited reduced impedances. This was most likely due to trace or wire bundle breakage.

Table 2 summarizes previous studies using state-of-the-art single-shank silicon- and SMP-based electrode arrays. While there are important differences in all these studies in terms of N number, study duration, implantation site, single-unit sorting criteria, and electrode material/deposition, our results (top row) compare well in terms of terminal AEY% with the current state of the art ($25 \pm 11\%$ versus 10–59%). Additionally, there have been significant prior efforts to leverage soft or softening polymers as either an insulator or a structural material for intracortical MEAs. Luan et al. demonstrated chronic recording capability with a comparable active electrode yield (20–25%), and also exhibited minimal tissue response [43]. However, due to their extreme flexibility, they required an insertion guide, which may not be practical for applications using multi-shank structures. This highlights one of the inherent advantages of softening over soft material approaches. Other groups have investigated Parylene C [44,45] and polyimide [46], but have not achieved chronic recordings up to or longer than one month. Others have investigated softening polymers [24,25], but face significant challenges in fabricating functional devices due to water absorption during softening.

Table 2. Planar single-shank electrode array comparison. Active electrode yield (AEY) percentage represents spontaneous single-unit activity unless otherwise indicated.

Ref	Model (R/M), Implant Site	*N*, Study Duration	AEY%	Substrate, Electrode Material
-	R, MC	*N* = 5, 13 weeks	25 ± 11%	SMP, SIROF
[32]	R, MC	*N* = 2, 11 weeks	* 37 ± 13%	SMP, PEDOT:PSS
[47]	R, MC	*N* = 8, 6 weeks	59% (Ir, SNR > 2)	Si, Ir or PEDOT
[37]	R, MC	*N* = 5, 12 weeks	33 and 39%	Si, Au or PEDOT:TFB
[7]	R, MC	*N* = 4, 4 weeks	* 27%	Si, Ir
[48]	M, VC	*N* = 4, 27 weeks	* 10% (spontaneous)	Si, Ir

* Represents approximate or recalculated values in the case that AEY was not reported. (R/M)—Rat or Mouse model. MC—motor cortex, VC—visual cortex.

The feasibility of SMP-based recording MEAs has been demonstrated in both rat auditory [31] and motor cortex [32]. The work presented here takes full advantage of SMP as an encapsulation material. Whereas previous studies have assessed devices that are SMP on one side and Parylene C on the other, the devices used here are completely sandwiched between layers of both Parylene C and SMP. In this way, we show that SMP is viable for use as a substrate material for neural device encapsulation, along with a thin layer of Parylene C necessary for electrical isolation. Additionally, SEM images collected post-explantation (Figure 7) reveal no evident signs of encapsulation failure or cracking.

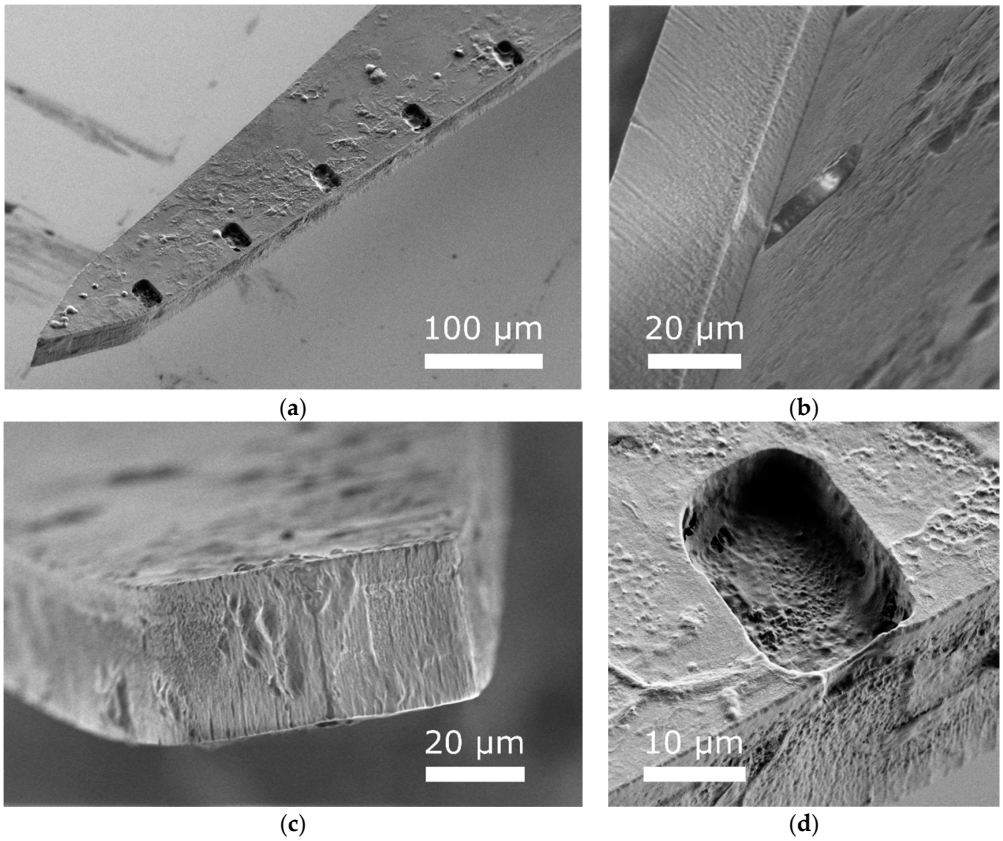

Figure 7. SEM post-explantation. (**a**) Explanted array showing some, but limited, biofouling, (**b**) interface between SMP layers at an electrode site, indicating no apparent layer separation, (**c**) interface between SMP layers at the tip of the array, (**d**) representative electrode site, showing no apparent signs of SIROF delamination.

Future studies focused on the design and development of SMP-based MEAs should take advantage of both geometrical and chemical considerations. For example, recently developed SMP formulations may extend the dynamic softening range of SMP devices [48]. Additionally, one inherent disadvantage

of thiol-ene/acrylate polymers based on ester linkages is that they may exhibit degradation due to hydrolysis. The development of hydrolytically stable SMP formulations may provide a more chronically useful substrate. Nevertheless, for experiments over the time course of 13 weeks in vivo, the present SMP formulation appears sufficient to realize functional devices.

5. Conclusions

Here we demonstrated stable neural recordings and electrochemistry using IC-5-16E devices fully encapsulated with SMP. Devices consistently recorded single units for 13 weeks in the rat motor cortex and preliminary histology demonstrated only a modest tissue response in the tissue adjacent to the insertion site. Our results establish a valuable baseline for the evaluation of other softening probe technologies including devices comprised of SMPs capable of increased softening after implantation.

Author Contributions: Conceptualization, A.M.S., B.J.B. and J.J.P.; Methodology, A.M.S., B.J.B., J.U. and C.L.F.; Software, A.M.S., B.J.B. and C.L.F.; Validation, A.M.S. and B.J.B.; Formal Analysis, A.M.S., J.U. and B.J.B.; Investigation, A.M.S., B.J.B., J.U. and C.L.F.; Resources, J.J.P.; Data Curation, A.M.S., J.U., C.L.F., K.C.M. and A.J.-M. and B.J.B.; Writing—Original Draft Preparation, A.M.S., J.U. and B.J.B.; Writing—Review & Editing, A.M.S., B.J.B., M.E., W.V., R.M., V.R.D., C.L.F. and J.J.P.; Visualization, A.M.S. and B.J.B.; Supervision, B.J.B. and J.J.P.; Project Administration, A.M.S., B.J.B. and J.J.P.; Funding Acquisition, J.J.P.

Funding: This work was supported by the Office of the Assistant Secretary of Defense for Health Affairs through the Peer-Reviewed Medical Research Program (grant number W81XWH-15-1-0607). Opinions, interpretations, conclusions, and recommendations are those of the authors and are not necessarily endorsed by the Department of Defense. Additional support was provided by the Eugene McDermott Graduate Fellowship Program, Richardson, TX (grant number 201606) at the University of Texas at Dallas.

Conflicts of Interest: Qualia Labs, Inc. provided the intracortical electrodes used in this study. W.V. is the president of Qualia Labs, Inc. R.M. and V.D. are paid employees of Qualia Labs, Inc. W.V., R.M., and V.D. had no role in the design of the study; in the collection, analysis, or interpretation of the data; or in the decision to publish the results. The senior author of this work (B.B.) serves as an unpaid advisor to Qualia Labs, Inc.

References

1. Kübler, A.; Kotchoubey, B.; Kaiser, J.; Wolpaw, J.R.; Birbaumer, N. Brain-computer communication: Unlocking the locked in. *Psychol. Bull.* **2001**, *127*, 358–375. [CrossRef] [PubMed]
2. Obermaier, B.; Müller, G.R.; Pfurtscheller, G. "Virtual keyboard" controlled by spontaneous EEG activity. *IEEE Trans. Neural Syst. Rehabil. Eng.* **2003**, *11*, 422–426. [CrossRef] [PubMed]
3. Pailla, T.; Jiang, W.; Dichter, B.; Chang, E.F.; Gilja, V. ECoG data analyses to inform closed-loop BCI experiments for speech-based prosthetic applications. In Proceedings of the 38th Annual International Conference of the IEEE Engineering in Medicine and Biology Society (EMBC), Orlando, FL, USA, 16–20 August 2016; pp. 5713–5716.
4. Birbaumer, N. Brain-computer-interface research: Coming of age. *Clin. Neurophysiol.* **2006**, *117*, 479–483. [CrossRef] [PubMed]
5. Lebedev, M.A.; Nicolelis, M.A. Brain-machine interfaces: Past, present and future. *Trends Neurosci.* **2006**, *29*, 536–546. [CrossRef] [PubMed]
6. Kipke, D.R.; Shain, W.; Buzsaki, G.; Fetz, E.; Henderson, J.M.; Hetke, J.F.; Schalk, G. Advanced neurotechnologies for chronic neural interfaces: New horizons and clinical opportunities. *J. Neurosci.* **2008**, *28*, 11830–11838. [CrossRef] [PubMed]
7. Ward, M.P.; Rajdev, P.; Ellison, C.; Irazoqui, P.P. Toward a comparison of microelectrodes for acute and chronic recordings. *Brain Res.* **2009**, *1282*, 183–200. [CrossRef] [PubMed]
8. Barrese, J.C.; Rao, N.; Paroo, K.; Triebwasser, C.; Vargas-Irwin, C.; Franquemont, L.; Donoghue, J.P. Failure mode analysis of silicon-based intracortical microelectrode arrays in non-human primates. *J. Neural Eng.* **2013**, *10*, 066014. [CrossRef] [PubMed]
9. Barrese, J.C.; Aceros, J.; Donoghue, J.P. Scanning electron microscopy of chronically implanted intracortical microelectrode arrays in non-human primates. *J. Neural Eng.* **2016**, *13*, 026003. [CrossRef] [PubMed]
10. Suner, S.; Fellows, M.R.; Vargas-Irwin, C.; Nakata, G.K.; Donoghue, J.P. Reliability of signals from a chronically implanted, silicon-based electrode array in non-human primate primary motor cortex. *IEEE Trans. Neural Syst. Rehabil. Eng.* **2005**, *13*, 524–541. [CrossRef] [PubMed]

11. Polikov, V.S.; Tresco, P.A.; Reichert, W.M. Response of brain tissue to chronically implanted neural electrodes. *J. Neurosci. Methods* **2005**, *148*, 1–18. [CrossRef] [PubMed]
12. Seymour, J.P.; Kipke, D.R. Neural probe design for reduced tissue encapsulation in CNS. *Biomaterials* **2007**, *28*, 3594–3607. [CrossRef] [PubMed]
13. Leach, J.; Achyuta, A.K.H.; Murthy, S.K. Bridging the divide between neuroprosthetic design, tissue engineering and neurobiology. *Front. Neuroeng.* **2010**, *2*, 1–19. [CrossRef] [PubMed]
14. Karumbaiah, L.; Saxena, T.; Carlson, D.; Patil, K.; Patkar, R.; Gaupp, E.A.; Betancur, M.; Stanley, G.B.; Carin, L.; Bellamkonda, R.V. Relationship between intracortical electrode design and chronic recording function. *Biomaterials* **2013**, *34*, 8061–8074. [CrossRef] [PubMed]
15. Biran, R.; Martin, D.C.; Tresco, P.A. Neuronal cell loss accompanies the brain tissue response to chronically implanted silicon microelectrode arrays. *Exp. Neurol.* **2005**, *195*, 115–126. [CrossRef] [PubMed]
16. McConnell, G.C.; Rees, H.D.; Levey, A.I.; Gutekunst, C.-A.; Gross, R.E.; Bellamkonda, R.V. Implanted neural electrodes cause chronic, local inflammation that is correlated with local neurodegeneration. *J. Neural Eng.* **2009**, *6*, 056003. [CrossRef] [PubMed]
17. Moshayedi, P.; Ng, G.; Kwok, J.C.; Yeo, G.S.; Bryant, C.E.; Fawcett, J.W.; Franze, K.; Guck, J. The relationship between glial cell mechanosensitivity and foreign body reactions in the central nervous system. *Biomaterials* **2014**, *35*, 3919–3925. [CrossRef] [PubMed]
18. Nolta, N.F.; Christensen, M.B.; Crane, P.D.; Skousen, J.L.; Tresco, P.A. BBB leakage, astrogliosis, and tissue loss correlate with silicon microelectrode array recording performance. *Biomaterials* **2015**, *53*, 753–762. [CrossRef] [PubMed]
19. Andrei, A.; Welkenhuysen, M.; Nuttin, B.; Eberle, W. A response surface model predicting the in vivo insertion behavior of micromachined neural implants. *J. Neural Eng.* **2011**, *9*, 016005. [CrossRef] [PubMed]
20. Karumbaiah, L.; Norman, S.E.; Rajan, N.B.; Anand, S.; Saxena, T.; Betancur, M.; Patkar, R.; Bellamkonda, R.V. The upregulation of specific interleukin (IL) receptor antagonists and paradoxical enhancement of neuronal apoptosis due to electrode induced strain and brain micromotion. *Biomaterials* **2012**, *33*, 5983–5996. [CrossRef] [PubMed]
21. Gilletti, A.; Muthuswamy, J. Brain micromotion around implants in the rodent somatosensory cortex. *J. Neural Eng.* **2006**, *3*, 189–195. [CrossRef] [PubMed]
22. Sridharan, A.; Nguyen, J.K.; Capadona, J.R.; Muthuswamy, J. Compliant intracortical implants reduce strains and strain rates in brain tissue in vivo. *J. Neural Eng.* **2015**, *12*, 036002. [CrossRef] [PubMed]
23. Subbaroyan, J.; Martin, D.C.; Kipke, D.R. A finite-element model of the mechanical effects of implantable microelectrodes in the cerebral cortex. *J. Neural Eng.* **2005**, *2*, 103–113. [CrossRef] [PubMed]
24. Harris, J.P.; Capadona, J.R.; Miller, R.H.; Healy, B.C.; Shanmuganathan, K.; Rowan, S.J.; Weder, C.; Tyler, D.J. Mechanically adaptive intracortical implants improve the proximity of neuronal cell bodies. *J. Neural Eng.* **2011**, *8*, 066011. [CrossRef] [PubMed]
25. Lee, H.C.; Ejserholm, F.; Gaire, J.; Currlin, S.; Schouenborg, J.; Wallman, L.; Bengtsson, M.; Park, K.; Otto, K.J. Histological evaluation of flexible neural implants; Flexibility limit for reducing the tissue response? *J. Neural Eng.* **2017**, *14*, 036026. [CrossRef] [PubMed]
26. Shoffstall, A.J.; Srinivasan, S.; Willis, M.; Stiller, A.M.; Ecker, M.; Voit, W.E.; Pancrazio, J.J.; Capadona, J.R. A mosquito inspired strategy to implant microprobes into the brain. *Sci. Rep.* **2018**, *8*, 1–10. [CrossRef] [PubMed]
27. Lo, M.C.; Wang, S.; Singh, S.; Damodaran, V.B.; Kaplan, H.M.; Kohn, J.; Shreiber, D.I.; Zahn, J.D. Coating flexible probes with an ultra fast degrading polymer to aid in tissue insertion. *Biomed. Microdevices* **2015**, *17*. [CrossRef] [PubMed]
28. Mather, P.T.; Luo, X.; Rousseau, I.A. Shape memory polymer research. *Annu. Rev. Mater. Res.* **2009**, *39*, 445–471. [CrossRef]
29. Wang, K.; Strandman, S.; Zhu, X.X. A mini review: Shape memory polymers for biomedical applications. *Front. Chem. Sci. Eng.* **2017**, *11*, 143–153. [CrossRef]
30. Leng, J.; Lan, X.; Liu, Y.; Du, S. Shape-memory polymers and their composites: Stimulus methods and applications. *Prog. Mater. Sci.* **2011**, *56*, 1077–1135. [CrossRef]
31. Ware, T.; Simon, D.; Liu, C.; Musa, T.; Vasudevan, S.; Sloan, A.; Keefer, E.W.; Ii, R.L.R.; Voit, W. Thiol-ene/acrylate substrates for softening intracortical electrodes. *Appl. Biomater.* **2013**, *102*, 1–11.

32. Simon, D.M.; Charkhkar, H.; St. John, C.; Rajendran, S.; Kang, T.; Reit, R.; Arreaga-Salas, D.; McHail, D.G.; Knaack, G.L.; Sloan, A.; et al. Design and demonstration of an intracortical probe technology with tunable modulus. *J. Biomed. Mater. Res. Part A* **2017**, *105*, 159–168. [CrossRef] [PubMed]
33. Do, D.-H.; Ecker, M.; Voit, W.E. Characterization of a thiol-ene/acrylate-based polymer for neuroprosthetic implants. *ACS Omega* **2017**, *2*, 4604–4611. [CrossRef] [PubMed]
34. Stiller, A.; Black, B.; Kung, C.; Ashok, A.; Cogan, S.; Varner, V.; Pancrazio, J. A meta-analysis of intracortical device stiffness and its correlation with histological outcomes. *Micromachines* **2018**, *9*, 443. [CrossRef]
35. Schindelin, J.; Arganda-Carreras, I.; Frise, E.; Kaynig, V.; Longair, M.; Pietzsch, T.; Preibisch, S.; Rueden, C.; Saalfeld, S.; Schmid, B.; et al. Fiji: An open-source platform for biological-image analysis. *Nat. Methods* **2012**, *9*, 676–682. [CrossRef] [PubMed]
36. Schneider, C.A.; Rasband, W.S.; Eliceiri, K.W. NIH Image to ImageJ: 25 years of image analysis. *Nat. Methods* **2012**, *9*, 671–675. [CrossRef] [PubMed]
37. Charkhkar, H.; Knaack, G.L.; Mchail, D.G.; Mandal, H.S.; Peixoto, N.; Rubinson, J.F.; Dumas, T.C.; Pancrazio, J.J. Chronic intracortical neural recordings using microelectrode arrays coated with PEDOT-TFB. *Acta Biomater.* **2016**, *32*, 57–67. [CrossRef] [PubMed]
38. Pancrazio, J.J.; Deku, F.; Ghazavi, A.; Stiller, A.M.; Rihani, R.; Frewin, C.L.; Varner, V.D.; Gardner, T.J.; Cogan, S.F. Thinking small: Progress on microscale neurostimulation technology. *Neuromodul. Technol. Neural Interfaces* **2017**, *20*, 745–752. [CrossRef] [PubMed]
39. Deku, F.; Cohen, Y.; Joshi-Imre, A.; Kanneganti, A.; Gardner, T.J.; Cogan, S.F. Amorphous silicon carbide ultramicroelectrode arrays for neural stimulation and recording. *J. Neural Eng.* **2018**, *15*, 016007. [CrossRef] [PubMed]
40. Lewitus, D.Y.; Smith, K.L.; Landers, J.; Neimark, A.V.; Koh, J. Bioactive agarose carbon-nanotube composites are capable of manipulating brain-implant interface. *J. Appl. Polym. Sci.* **2014**, *131*. [CrossRef] [PubMed]
41. Spencer, K.C.; Sy, J.C.; Ramadi, K.B.; Graybiel, A.M.; Langer, R.; Cima, M.J. Characterization of mechanically matched hydrogel coatings to improve the biocompatibility of neural implants. *Sci. Rep.* **2017**, *7*, 1–16.
42. Cody, P.A.; Eles, J.R.; Lagenaur, C.F.; Kozai, T.D.Y.; Cui, X.T. Unique electrophysiological and impedance signatures between encapsulation types: An analysis of biological Utah array failure and benefit of a biomimetic coating in a rat model. *Biomaterials* **2018**, *161*, 117–128. [CrossRef] [PubMed]
43. Luan, L.; Wei, X.; Zhao, Z.; Siegel, J.J.; Potnis, O.; Tuppen, C.A.; Lin, S.; Kazmi, S.; Fowler, R.A.; Holloway, S.; et al. Ultraflexible nanoelectronic probes form reliable, glial scar–free neural integration. *Sci. Adv.* **2017**, *3*, e1601966. [CrossRef] [PubMed]
44. Takeuchi, S.; Ziegler, D.; Yoshida, Y.; Mabuchi, K.; Suzuki, T. Parylene flexible neural probes integrated with microfluidic channels. *Lab Chip* **2005**, *5*, 519–523. [CrossRef] [PubMed]
45. Xu, H.; Weltman, A.; Scholten, K.; Meng, E.; Berger, T.W.; Song, D. Chronic multi-region recording from the rat hippocampus in vivo with a flexible Parylene-based multi-electrode array. In Proceedings of the 39th Annual International Conference of the IEEE Engineering in Medicine and Biology Society (EMBC), Seogwipo, Korea, 11–15 July 2017; pp. 1716–1719.
46. Mercanzini, A.; Cheung, K.; Buhl, D.L.; Boers, M.; Maillard, A.; Colin, P.; Bensadoun, J.C.; Bertsch, A.; Renaud, P. Demonstration of cortical recording using novel flexible polymer neural probes. *Sens. Actuators A Phys.* **2008**, *143*, 90–96. [CrossRef]
47. Ludwig, K.A.; Uram, J.D.; Yang, J.; Martin, D.C.; Kipke, D.R. Chronic neural recordings using silicon microelectrode arrays electrochemically deposited with a poly (3,4-ethylenedioxythiophene)(PEDOT) film. *J. Neural Eng.* **2006**, *3*, 59–70. [CrossRef] [PubMed]
48. Kozai, T.D.Y.; Du, Z.; Gugel, Z.V.; Smith, M.A.; Chase, S.M.; Bodily, L.M.; Caparosa, E.M.; Friedlander, R.M.; Cui, X.T. Comprehensive chronic laminar single-unit, multi-unit, and local field potential recording performance with planar single shank electrode arrays. *J. Neurosci. Methods* **2015**, *242*, 15–40. [CrossRef] [PubMed]

polymers

MDPI

Article

Electrical Properties of Thiol-ene-based Shape Memory Polymers Intended for Flexible Electronics

Christopher L. Frewin [1], Melanie Ecker [2,*], Alexandra Joshi-Imre [2], Jonathan Kamgue [1], Jeanneane Waddell [1], Vindhya Reddy Danda [1], Allison M. Stiller [1], Walter E. Voit [2] and Joseph J. Pancrazio [1]

1 Department of Bioengineering, The University of Texas at Dallas, Richardson, TX 75080, USA; cfrewin@neuronexus.com (C.L.F.); Jonathan.Kamgue@utdallas.edu (J.K.); jeanneane@me.com (J.W.); VindhyaReddy.Danda@utdallas.edu (V.R.D.); allison.stiller@utdallas.edu (A.M.S.); Joseph.Pancrazio@utdallas.edu (J.J.P.)

2 Center for Engineering Innovation, The University of Texas at Dallas, Richardson, TX 75080, USA; Alexandra.Joshi-Imre@utdallas.edu (A.J.-I.); walter.voit@utdallas.edu (W.E.V.)

* Correspondence: Melanie.Ecker@utdallas.edu

Received: 15 April 2019; Accepted: 15 May 2019; Published: 17 May 2019

Abstract: Thiol-ene/acrylate-based shape memory polymers (SMPs) with tunable mechanical and thermomechanical properties are promising substrate materials for flexible electronics applications. These UV-curable polymer compositions can easily be polymerized onto pre-fabricated electronic components and can be molded into desired geometries to provide a shape-changing behavior or a tunable softness. Alternatively, SMPs may be prepared as a flat substrate, and electronic circuitry may be built directly on top by thin film processing technologies. Whichever way the final structure is produced, the operation of electronic circuits will be influenced by the electrical and mechanical properties of the underlying (and sometimes also encapsulating) SMP substrate. Here, we present electronic properties, such as permittivity and resistivity of a typical SMP composition that has a low glass transition temperature (between 40 and 60 °C dependent on the curing process) in different thermomechanical states of polymer. We fabricated parallel plate capacitors from a previously reported SMP composition (fully softening (FS)-SMP) using two different curing processes, and then we determined the electrical properties of relative permittivity and resistivity below and above the glass transition temperature. Our data shows that the curing process influenced the electrical permittivity, but not the electrical resistivity. Corona-Kelvin metrology evaluated the quality of the surface of FS-SMP spun on the wafer. Overall, FS-SMP demonstrates resistivity appropriate for use as an insulating material.

Keywords: Polymer; Dielectric; Resistivity; Permittivity; Curing; Corona-Kelvin

1. Introduction

Thermoset thiol-ene and thiol-ene/acrylate shape memory polymers (SMPs) have been demonstrated lately as attractive substrate materials in flexible electronics. That includes organic and inorganic thin film transistors and diodes [1–6] as well as multi-electrode arrays for biomedical applications. [7–12] Shape memory polymers (SMPs) have the ability to change shape and/or softness in response to external stimuli [13–17] and therefore enable multifunctional and responsive devices. The use of highly tunable thiol click chemistry allows for the design of substrate and packaging materials having the desired mechanical and thermomechanical properties for a particular application. This can be achieved by controlling the cross-link density and the glass transition temperature (T_g) of the polymer [7,18].

The fabrication of electronic circuits, semiconductors, and diodes on flexible polymeric substrates has been enabled by low-temperature processing techniques [19,20]. Our group successfully demonstrated the fabrication, electrical stability, and lifetime of hafnium oxide (HfO_2) dielectric [2] and indium–gallium–zinc-oxide (IGZO) [1,3] thin film transistors on top thiol-ene/acrylate-based flexible substrates with softening capabilities. Additionally, SMP materials can be used for deployable devices, or parts thereof, and for the molding of specific device's components. With this, the polymer can not only serve as a substrate, but also as an encapsulant or packaging material for electronic circuitries.

One example where responsive SMP substrates may be used is bioelectronics devices. In this case, the polymers have been engineered to transition from a stiffness of 2 GPa to as low as ~20 MPa in vivo [10,18,21–25]. These particular polymers undergo plasticization upon immersion into aqueous environments, and with this, their glass transition temperature (T_g) shifts towards lower temperatures [23,24,26,27]. The associated transition in Young's modulus allows SMP-based devices to be rigid during handling and insertion in air but soften to a more compliant modulus soon after implantation if the right polymer composition was chosen. For implantable devices that form intimate contact with soft tissue, the resulting interface with these SMP materials effectively decreases mechanical mismatch at the device–tissue interface. In the case of neural recording probes, commonly used devices have mechanical mismatch due to composition with stiff materials, like metal and silicon. The mismatch poses a source of constant inflammation and has been proposed as a basis for probe failure under chronic conditions [28–30]. Therefore, interest in softening SMPs as an integral material component for implantable bioelectronics devices has grown [10,14,31–34]. If SMPs are to serve not only as substrate material but also as an electrical insulation between electronic components, it is imperative to characterize their electric behavior.

Flexible electronic devices mainly consist of conductive traces surrounded by an electrically insulating material. As we consider the move to device miniaturization, these component layers, especially the insulation, can become thinned to the point that electrical properties, like polarization, breakdown, and resistivity becomes an extremely important consideration in device performance. Additionally, these properties are directly linked to the electrical issues of leakage, cross-talk, and parasitic shunt capacitance [35–37]. The goal of the present work was to characterize the electrical permittivity and resistivity of a representative thiol-ene SMP candidate. We have selected an SMP we named fully softening (FS-SMP) in previous studies [23,38] because it has a low glass transition temperature (between 40 and 60 °C dependent on the curing process), which allowed us to easily examine material parameters in the glassy as well as in the rubbery state. Additionally, we have considered two different curing approaches for the FS-SMP materials, which can affect the mechanical properties of the material [18,23].

The relative permittivity was 5.26 ± 0.11 and 6.38 ± 0.11, below and above T_g respectively, determined for FS-SMP cured under 254 nm wavelength (λ) ultraviolet (UV) radiation for 2 h. Reducing the curing exposure time under 254 nm UV to 3 min, followed by 1 h at 365 nm UV, increased the relative permittivity to 5.87 ± 0.08 below, and 7.79 ± 0.09 above T_g. Unlike relative permittivity, resistivity for FS-SMP was only modestly altered between glassy and rubbery states. Surface resistivity, irrespective of cure, was just above 10^{14} Ω/sq in the glassy state, which was reduced by 10% in the rubbery state. The volume resistivity was reduced by an additional order of magnitude from 10^{14} Ω·cm in the glassy state to 10^{13} Ω·cm in the rubbery state. Finally, preliminary work with corona-Kelvin metrology, a non-contact method employed in the semiconductor industry to detect defects in dielectrics, suggested that while FS-SMP-spun films are heterogeneous, there were also large areas of homogeneity which might be suitable for device fabrication.

2. Materials and Methods

2.1. Materials and Fabrication

The fabrication of FS-SMP was previously described [38]. The formulation described in Ecker et al. [23] was a slight variation thereof. The polymer is composed of a mixture of three monomer components (Figure 1): 0.5 mol% 1,3,5-Triallyl-1,3,5-triazine-2,4,6(1H,3H,5H)-trione (TATATO) (Sigma Aldrich, St. Louis, MO, USA), 0.45 mol% trimethylolpropane tris(3-mercaptopropionate) (TMTMP) (Sigma Aldrich, St. Louis, MO, USA), and 0.05 mol% Tris[2-(3-mercaptopropionyloxy)ethyl] isocyanurate (TMICN) (Evans Chemetics, Teaneck, NJ, USA). 2,2-dimethoxy-2-phenylacetophenone (DMPA) (Sigma Aldrich, St. Louis, MO, USA) was used as a photo-initiator. All of the chemicals were used as received without further purification.

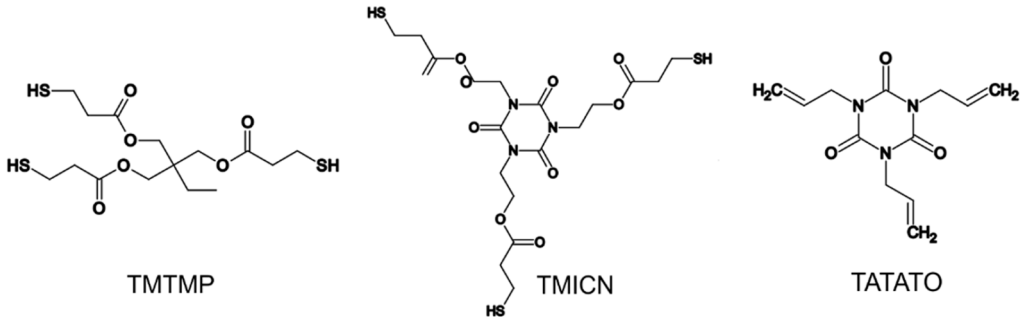

Figure 1. Chemical structures of monomers used for the synthesis of the fully softening shape memory polymer (FS-SMP).

FS-SMP was prepared by mixing exact mole fractions of the liquid monomers, TATATO, TMTMP, and TMICN, with 0.1 wt.% of DMPA into a vial at room temperature (~22 °C). The vial was covered in aluminum foil to prevent incident light from contacting the solution and mixed thoroughly using a DAC150.1 FV planetary speed mixer (FlackTec Inc., Landrum, SC, USA). The mixed solution was spin cast upon substrates consisting of a 100 mm diameter silicon wafer (University Wafers, Boston, MA, USA) using a Laurell WS-650-8B spin coater (Laurel Technologies, North Wales, PA, USA). Prior to spinning, each of the substrates had 20 nm of titanium followed by 400 nm of gold evaporated onto the surface using a Temescal 1800 single chamber evaporation system (FerroTec Inc, Santa Clara, CA, USA) to serve as the ground plate for the test capacitors.

We have evaluated two curing methods for the FS-SMP polymer fabrication. Figure 2 demonstrates that the two processes produce equivalent moduli in the glassy and rubbery state but shifted T_g. The first process, previously reported in [23], involved spinning the mixed monomers onto silicon substrates followed by exposure to 254 nm UV radiation at room temperature (~22 °C) and ambient atmosphere within an UVP CL-1000 cross-linking chamber (UVP LLC, Upland, CA, USA) containing five overhead UV bulbs for 120 min (2 h cure). The second polymerization condition was performed at ambient temperature under 254 nm with a reduced time of three minutes, which was immediately followed by 1 h of exposure to 365 nm UV light (3 min cure). At the completion of polymerization, the samples were placed in a vacuum oven, at 120 °C and 127.5 Torr, for 18 h to achieve complete curing. The resulting thickness of each wafer or slide was individually characterized to the nearest 0.1 μm using a Dektak 8 profilometer (Veeco, Plainview, NY, USA) to facilitate capacitance calculations.

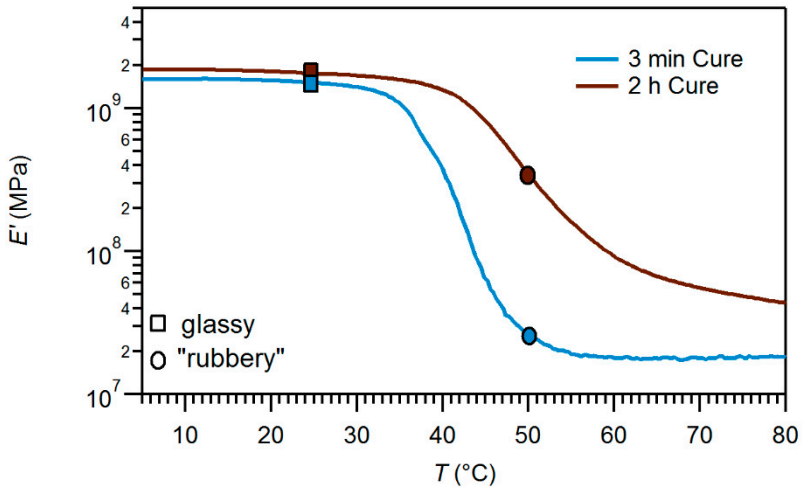

Figure 2. Graphs of storage modulus, E', for fully softening shape memory polymers obtained using dynamic material analysis in air using the two curing methods discussed in this study. At temperatures below 37 °C, both curing formulations were in the glassy state, with E' above 10^9 Pa. However, while the 3 min curing process nearly reached its fully softened, rubbery state at 50 °C, the 2 h cure became only semi-soft with an E' of ~500 MPa.

To determine the electrical properties of FS-SMP, we crafted physical capacitors (Figure 3) for testing. The top plate of the physical capacitors and outer ring were fabricated using the following methodology. First, 20 nm of titanium, followed by 400 nm of gold, were blanket evaporated onto a silicon wafer. Next, FS-SMP was spin-coated and cured on top before another layer of Ti/Au was evaporated. The capacitors having sizes of 2, 3, and 4 mm, surrounded by 1 mm wide rings with gaps between of 0.5, 1, 1.5, and 2 mm, were patterned using photolithography via positive photoresist. The gold was wet-etched using Iodine-based etchant, and 10:1 Hydrofluoric acid solution was used to remove the underlying titanium adhesion layer.

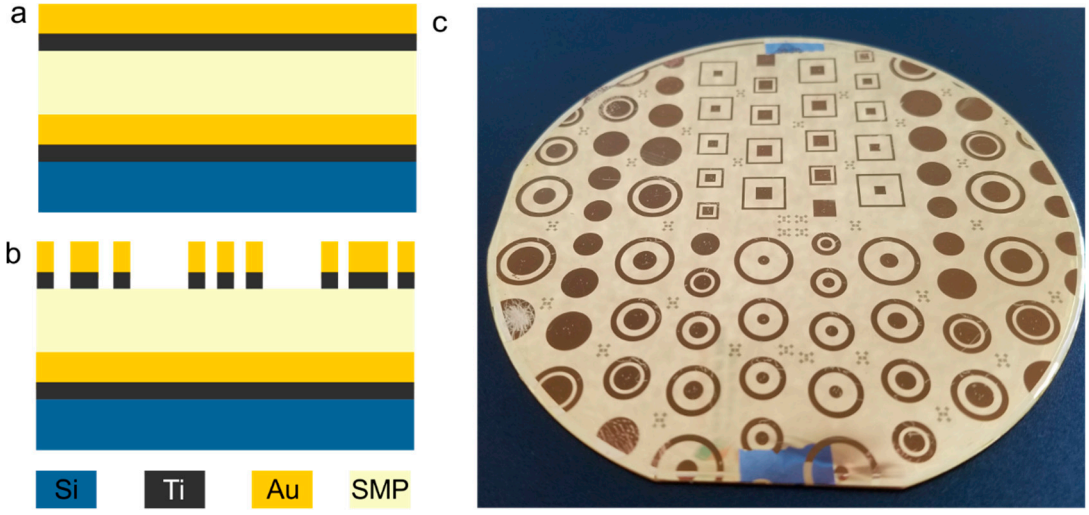

Figure 3. Fabrication of physical capacitors for testing. (**a**) shows a schematic of the sequence of the materials used for the fabrication of capacitors, (**b**) displays the stack after photolithography, and (**c**) shows a photograph of a typical device having differently sized capacitors.

2.2. Electrical Characterization

The electrical properties of resistivity and permittivity for SMP were measured and evaluated using guidelines published by the American Society for Testing and Materials (ASTM International)

and the Association Connecting Electronics Industries (IPC) [39–41]. Round, parallel plate SMP capacitors were used for all measurements (Figure 3). The outer rings facilitated measurement of the leakage current across the surface of the material, while volume resistivity through the bulk of the SMP was measured between top and bottom plates. Leakage currents were used to calculate average surface and volume resistivity, while capacitance was used to calculate the relative permittivity for the FS-SMP [39–41]. In detail, capacitance was determined using the characteristic time (RC time constant t) required to charge a resistor-capacitor (RC) circuit. A carbon fiber resistor, characterized at 6,997 Ω, was connected in series with the top plate of the FS-SMP capacitor using a Model S-926 micro-positioner with a P pivot head and ST-T 5 µm point tungsten tips (Signatone, Gilroy, CA, USA). An RG-174/U coaxial cable containing a low-density polyethylene dielectric was utilized to connect the voltage source, a Keithley 3390 50 MHz Arbitrary Waveform Generator (Tektronix, Inc., Beaverton, OR, USA). Square wave pulses with an amplitude of 10 V_{pp} and periods of 0.01, 0.001, 1.0×10^{-4}, and 1.0×10^{-5} s with equal high and low phases were continuously delivered. The output voltage waveforms were measured with a TBS 1052B Digital Oscilloscope Generator (Tektronix, Inc., Beaverton, OR, USA) using 10X attenuated voltage probes (TPP0051, Tektronix, Inc., Beaverton, OR, USA), which were characterized to have ~12 pF capacitance and 10 MΩ input resistance. The RC time constant was determined for the different square wave frequencies and the corresponding capacitance was calculated. These capacitances where then used to calculate the relative permittivity of the SMP-FS according to ASTM D150-11 [40], using the parallel plate equation.

Volumetric leakage current through the bulk of the material and surface current leakage through the top plate and outer ring electrode were measured using a 9103 USB Auto-Ranging Picoammeter (RBD Instruments, Bend, OR, USA) in response to DC voltage biasing. The 9103 provided a battery-powered voltage source of 90 V. The current was recorded every 50 ms for a total of 3 min using software provided by RBD Instruments. The initial current pulse was removed from the recordings, and the current was averaged across the total time period. The measured leakage currents were used to calculate the volume and surface resistivity according to ASTM 257-14 [39].

The electrical impedance of the wires and carbon resistors were considered in the calculations for all resistivity and permittivity calculations. Approximations for capacitance due to electrical fringing effects were removed using equations provided in the standards document [40].

Given that the FS-SMP was designed to operate over a specific temperature range, we examined the temperature dependence of the FS-SMP electrical properties. We placed the FS-SMP devices on a Fisherbrand™ Isotemp™ Stirring Hotplate, which included a Thermo Scientific FS PT100 external probe (Fisher Scientific, Waltham, MA, USA) for thermal feedback control. The polymer was heated to 50 °C, and the samples were held at this temperature for 10 min before measuring the capacitance and leakage currents again.

In total, two different wafers were fabricated, one for each polymer curing scenario, namely the 3 min and 2 h cure. Measurements were performed on individual, differently sized capacitors within these wafers. For the relative permittivity, N = 9 (2 h cure) and N = 14 (3 min cure) capacitors were measured at four different frequencies each. Thus, a total number of N = 36 (2 h cure) and N = 56 (3 min cure) measurements were performed at 22 and 50 °C, respectively. For the surface resistivity, N = 7 (2 h cure glassy), N = 8 (2 h cure rubbery), N = 18 (3 min cure glassy), and N = 16 (3 min cure glassy) measurements were performed. Volume resistivity was measured on N = 8 (2 h cure glassy), N = 8 (2 h cure rubbery), N = 19 (3 min cure glassy), and N = 16 (3 min cure rubbery) capacitors, respectively. All results are given as mean values ± standard deviation (SD).

2.3. Kelvin Force Probe Characterization

Non-contact voltage mapping has been used in the silicon circuit industry as a quick, non-destructive method to detect defects in insulators [42–45]. While the process has been described in detail previously, a brief explanation of the process is as follows. The Si wafer containing the FS-SMP thin film was placed on a grounded vacuum chuck. A 2 mm diameter vibrating Kelvin probe,

accompanied with a vibrating reference electrode, was placed approximately 1 mm above the surface of the FS-SMP. The reference electrode is DC-biased and vibrates normally to the measured surface. The time-variation in capacitance, caused by the changes in the angular frequency of the vibration, was monitored using a lock-in amplifier in response to reference electric potential sweeps to determine the contact potential difference (V_{cpd}). V_{cpd} was a series system composed of the potentials from the work function difference from the metal probe and references, the air insulation, the insulating film, and the semiconductor space charge region. The DC voltage applied to the reference electrode generated current due to the changes in the capacitance and was then adjusted to reduce the current to zero, at which point $V_{cpd} = -V_{DC}$. Equipment calibration removed the contact potential of the Kelvin probe and reference electrode. Contributions from the potential due to the semiconductors surface barrier, V_{SB}, were removed by subtracting the potential obtained under wafer illumination, producing excess carriers to reduce surface band bending, and the wafer recorded in the dark. The remaining potential was the contribution of the dielectric material, V_D. As this potential is proportional to the dielectric charge-to-permittivity ratio, variations indicated changes in material electronic properties. The entire wafer surface was scanned by moving the wafer under the probe.

3. Results

Figure 4 displays the relative permittivity obtained for the two curing processes of FS-SMP evaluated at two temperatures that provide for the thermomechanical state of the FS-SMP. At room temperature, FS-SMP was in a glassy state, and the relative permittivity of the 2 h cure FS-SMP was 5.26 ± 0.11. The 3 min cure FS-SMP at the same temperature produced a permittivity of 5.87 ± 0.08. Increasing the temperature to change the state of the FS-SMP to rubbery demonstrated that the 2 h cure FS-SMP relative permittivity elevated to 6.38 ± 0.11, whereas the 3 min cure FS-SMP relative permittivity levels were 7.79 ± 0.09, respectively.

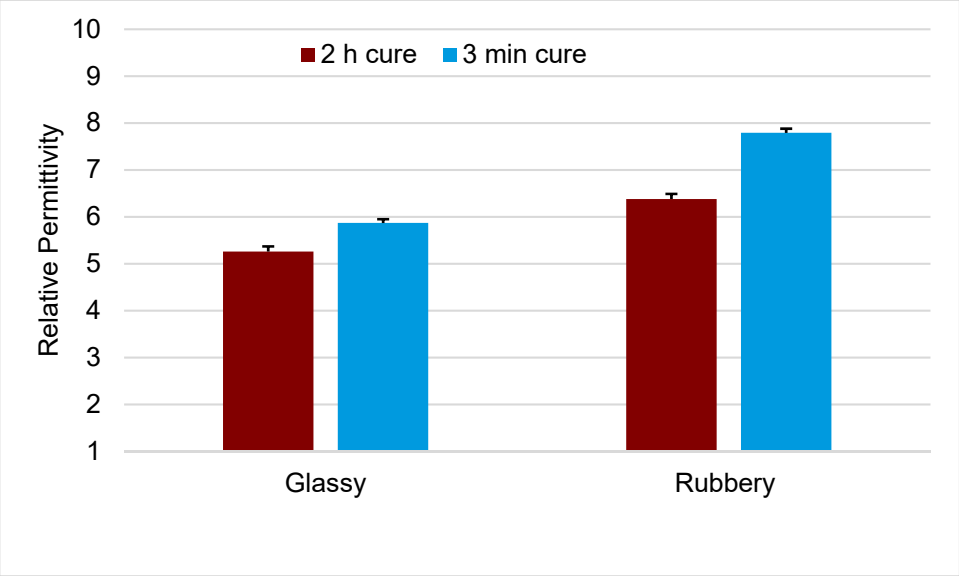

Figure 4. Mean relative permittivity of fully-softening shape memory polymer (FS-SMP) obtained at glassy and rubbery thermomechanical states. $N = 36$ ($N = 9$ capacitors with 4 replicate measurements each) for the 2 h cure FS-SMP and $N = 56$ ($N = 14$ capacitors with 4 replicate measurements each) for the 3 min cure FS-SMP. Standard deviation is represented through the positive error bars. The temperatures of measurement for the glassy state were 22 °C and for the rubbery, 50 °C.

A three-way ANOVA was performed with a threshold of 0.05 between the variables of square-wave voltage signal frequency, the thermomechanical state of the polymer, and the curing method. Statistics for the tested factors are reported listing the F value, including the associated degree of freedom and N

value separated in parenthesis, as well as the p value for the test. The permittivity was found to be statistically independent from changes in the frequency range from 100 to 10,000 Hz ($F(3,332) = 0.02465$, $p = 0.99476$). Thus, the measurements at the different frequencies were grouped together (Figure 4). Additionally, the interaction between frequency and thermomechanical state ($F(3,332) = 0.62841$, $p = 0.5971$), and the interaction for the factors for frequency, curing, and thermomechanical state ($F(9,332) = 0.26987$, $p = 0.98231$) demonstrated no statistically significant effect on the overall mean relative permittivity. Removing the frequency as an independent variable, we compared the factors of polymeric state ($F(1,214) = 81.76$, $p = 9.4 \times 10^{-17}$), and curing ($F(3,214) = 92.61$, $p = 1.89 \times 10^{-38}$), as well as the interactions between these factors ($F(3,214) = 6.59$, $p = 2.81 \times 10^{-4}$), and demonstrated evidence of significantly different mean values for relative permittivity.

In summary, the method of polymer curing, along with the thermomechanical state of the polymer, has an influence on the relative permittivity.

A post hoc Tukey test was used to investigate specific factors which influenced the relative permittivity at a threshold level of $p < 0.05$. The 3 min cure produced a significantly higher mean relative permittivity than the 2 h cure when both samples were evaluated within the same environment and the thermomechanical state remained constant. A change in thermomechanical state from glassy to rubbery produced a significant increase in relative permittivity. To summarize, the change in state from glassy to rubbery produced a significant increase in relative permittivity, the longer curing process significantly reduced molecular polarization within the FS-SMP.

While the electric property of relative permittivity is an important factor in the consideration of AC leakages, electrical resistivity is an extremely important factor when considering DC leakages in an insulating material. We measured not only the resistivity of bulk FS-SMP, but also the resistivity across the skin, or surface, of the polymer. The mean surface and volume resistivity ± standard deviation of FS-SMP samples fabricated with the two curing techniques is displayed in Figure 5. The surface resistivity for the 2 h cure FS-SMP was $1.47 \times 10^{14} \pm 5.60 \times 10^{13}$ Ω/sq in its glassy state, and $1.20 \times 10^{13} \pm 2.01 \times 10^{13}$ Ω/sq in the rubbery state. The 3 min cure FS-SMP possessed a mean surface resistivity of $1.25 \times 10^{14} \pm 1.35 \times 10^{14}$ Ω/sq below T_g, and $2.50 \times 10^{12} \pm 2.72 \times 10^{12}$ Ω/sq above T_g.

The volume resistivity in the glassy state was $4.55 \times 10^{14} \pm 3.83 \times 10^{14}$ Ω·cm for the 2 h cure FS-SMP, and $8.13 \times 10^{14} \pm 9.24 \times 10^{14}$ Ω·cm for the 3 min cure. The volume resistivity in the rubbery state was $4.75 \times 10^{13} \pm 7.99 \times 10^{13}$ Ω·cm for the 2 h cure, and $3.37 \times 10^{13} \pm 3.87 \times 10^{13}$ Ω·cm for the 3 min cure.

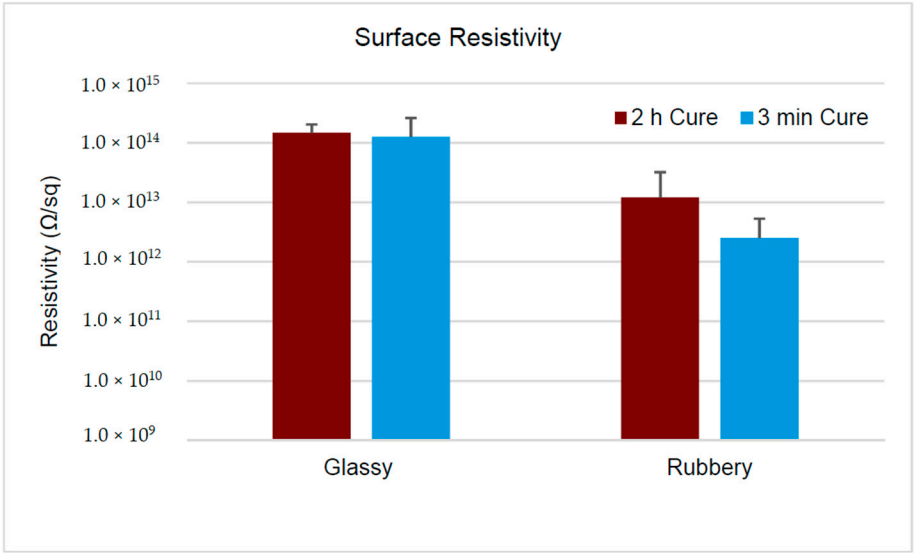

Figure 5. *Cont.*

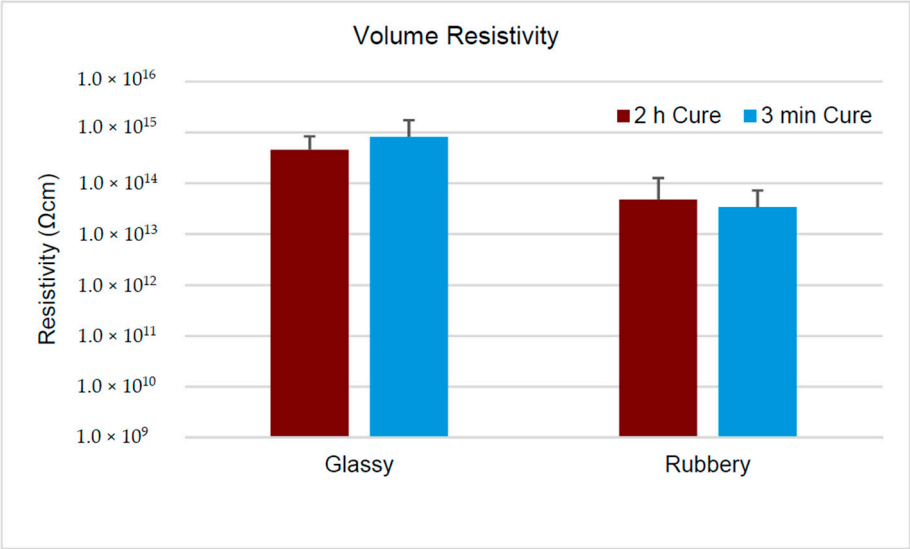

Figure 5. Two bar graphics displaying the mean surface and volume resistivity of FS-SMP, respectively. N = 7–8 (2 h cure) and N = 16–19 (3 min cure) measurements were performed for surface and volume resistivity at 22 and 50 °C, respectively. Standard deviation is represented through the positive error bars.

Figure 6 displays an example of the contact potential voltage, V_{CPD}, mapped across the surface of a 100 mm diameter, boron-doped P-type silicon wafer of 1 Ω·m resistivity, 7 µm thick film of FS-SMP, and cured with the 3 min FS-SMP methodology. V_{CPD} value ranges between 1.6 V and −2.8 V with an average of −0.885 V and a standard deviation of 0.691 V across the wafer. Positive V_{CPD} are mostly confined near the edges of the wafer. V_{CPD} below −2 V appear as islands, and the two dominant such islands are approximately 10–15 mm in size. There are large areas of V_{CPD} values possessing homogeneous potential.

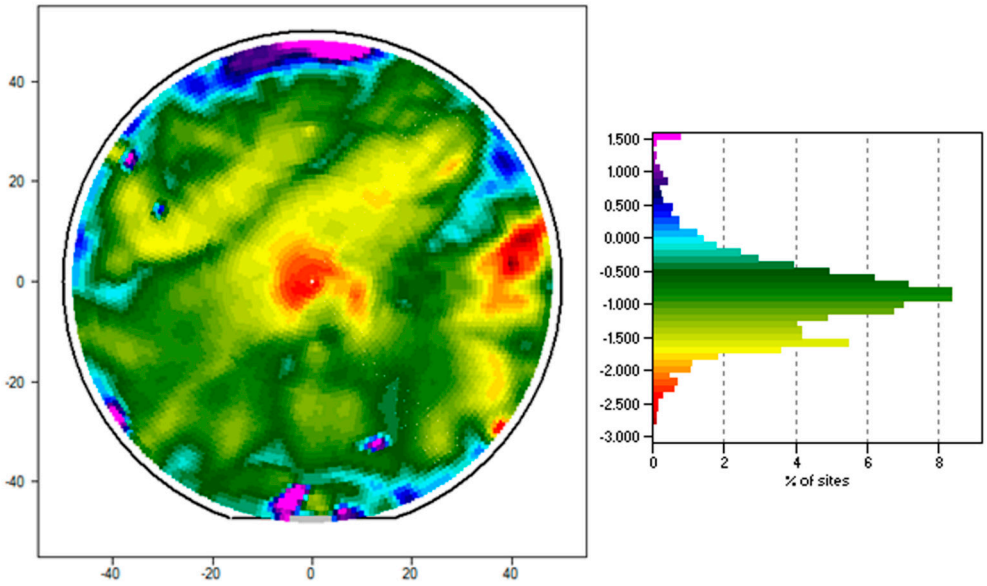

Figure 6. A contact potential voltage map (V_{CPD}) displaying charge variation in a dielectric film of FS-SMP spun onto a 100 mm diameter p-doped silicon wafer and cured using the 3 min FS-SMP process.

4. Discussion

Relative permittivity in amorphous polymers has been theorized to arise from two main molecular interactions. The first is from charge polarization due to dipoles within the polymer chain. Another is the relaxation process which has been associated with the mobility of molecules and motion within portions of the main chain, side chains, or side groups [46]. This relaxation has been generally linked to thermal processes which rise in effective strength with an increase in temperature. As FS-SMP does not possess side chains or groups, one must consider the overall chain rigidity and the chemical composition of the polymer. It has been shown that these latter factors are extremely important in the formation of permanent dipoles and increase in relative permittivity [46,47].

Our study focuses on a single polymer chemistry under two different polymerization methods. As discussed previously, the method of polymerization by exposure to 254 nm wavelength UV light for two hours has demonstrated a wider transition window in FS-SMP as well as an up-shift of T_g by about 10 °C as compared to the 3 min method, which is attributed to differences in the cross-linking mechanism [18,23]. In the case of the 3 min method, where exposure to 254 nm wavelength UV radiation is limited to 3 min and polymerization is completed by subsequent exposure to 365 nm wavelength UV light, our DMA findings suggest a reduction in cross-link density and a more homogenous network formation (Figure 2). Although dielectric relaxation has been demonstrated to greatly increase at the glass transition temperature [47], we have seen a much larger proportional increase in relative permittivity during the physical transformation from glassy to rubbery for the 3 min cure process than the 2 h cure. Most likely, this effect is attributable to the lower overall curing dose (short amount of exposure to the high energy/lower wavelength followed by one hour of exposure to the lower energy/higher wavelength), as opposed to two hours exposure with the high energy/lower wavelength, which would create a polymer inherent with additional relaxation during cross-linking (less curing stress) and increased chain mobility compared to the 2 h cure. However, it should be noted that the 2 h cure is still within its transition temperature and not fully rubbery at the high-temperature measurement (50 °C). This might also contribute to the mobility of the polymer and associated relaxation. The hydrophobicity of both polymer films was similar. The contact angle of water droplets was measured to be (70.7 ± 5.5°) for the 2 h cure and (80.3 ± 2.9°) for the 3 min cure. Thus, the samples of the 3 min cure resulted in slightly higher hydrophobicity.

We found that the surface and volume resistivity of FS-SMP exceeded the thresholds of 1.0×10^{12} Ω/sq, and 1.0×10^{9} Ω·cm respectively, while in glassy or rubbery states and regardless of the curing methodology, and therefore classifies as an insulating polymer [48,49]. Since the mean and standard deviation values of measured resistivities were close together, we also looked at the sample percentiles (Table 1). We found that the majority (at least 90%) of the measured samples were above that threshold that classifies them as insulating polymer. The only exception was the 3 min cure FS-SMP in the rubbery state that had only 71% of the measured samples above the threshold of 1.0×10^{12} Ω/sq for the surface resistivity, while the volume resistivity was still above 90%.

Table 1. Mean values ± standard deviation (SD) and values for surface and volume resistivity at the 10th percentile.

Material	Surface Resistivity (Ω/sq)		Volume Resistivity (Ω·cm)	
	Mean ± SD	10th Percentile	Mean ± SD	10th Percentile
2 h cure glassy	$1.47 \times 10^{14} \pm 5.60 \times 10^{13}$	7.58×10^{13}	$4.55 \times 10^{14} \pm 3.83 \times 10^{14}$	2.03×10^{12}
2 h cure rubbery	$1.20 \times 10^{13} \pm 2.01 \times 10^{13}$	2.41×10^{13}	$4.75 \times 10^{13} \pm 7.99 \times 10^{13}$	1.09×10^{11}
3 min cure glassy	$1.25 \times 10^{14} \pm 1.35 \times 10^{14}$	1.23×10^{13}	$8.13 \times 10^{14} \pm 9.24 \times 10^{14}$	1.33×10^{12}
3 min cure rubbery	$2.50 \times 10^{12} \pm 2.72 \times 10^{12}$	2.44×10^{11}	$3.37 \times 10^{13} \pm 3.87 \times 10^{13}$	3.22×10^{9}

When we compare the SMP-FS with other insulating materials at room temperature (Table 2), we can see that it falls well within their values for volume and surface resistivity.

Table 2. Comparison of dielectric properties of various insulating materials from [50] if not stated differently.

Material	Volume Resistivity (Ω·cm)	Surface Resistivity (Ω/sq)
SMP-FS	10^{14}	10^{14}
Ceramics	10^{11}–10^{14}	-
Soda-lime glass	10^{11}–10^{13}	10^{10}–10^{12}
Hard rubber	10^{15}–10^{17}	10^{10}–10^{18}
Epoxy cast resin	10^{14}–10^{15}	10^{7} –>10^{14}
Acrylic	>10^{15}	>10^{14}
Polypropylene	10^{15}–10^{17}	>10^{15}
Parylene C	10^{12}–10^{16} [51]	10^{15}
Polyimide (Kapton)	10^{17} [52]	

Uniformity is an important aspect of processing micro- and nano-sized devices, and insulating materials should perform as designed. Kelvin force probe characterization is widely used in the semiconductor industry to quickly scan entire production wafers with the aims to ensure quality of dielectric materials, detect possible device destroying defects, and increase the product yield. We utilized this technique to assess charge distribution in spin-coated FS-SMP. The film was found to be mostly homogeneous at around −900 mV contact potential with some isolated area showing potential differences. Unfortunately, the measurement from the Kelvin probe process only allows detection of differences in potential. It is not possible to accurately use the method to attribute the changes to variations in surface thickness or to chemical defects within the matrix. Future investigations will be needed to characterize the mechanisms behind the potential variations. We also conducted atomic force microscopy (AFM) measurements to investigate the surface roughness of the samples and found that the spin coating resulted in relatively smooth polymer surfaces. The surface roughness of SMP samples after both curing scenarios was similar. AFM measurements revealed root mean square averages of height deviations of the assessed profile R_q of 0.291 and 0.316 nm for the 2 h and 3 min cure samples, respectively.

5. Conclusions

Thiol-ene and thiol-ene/acrylate-based shape memory polymers have been developed by our group to demonstrate desirable mechanical properties for flexible electronics, such as organic and inorganic thin film transistors and diodes, and multi-electrode arrays for biomedical applications. Although the mechanical properties have been reported across multiple investigations, the electrical properties have not been reported for this promising material.

Our investigations demonstrated that reducing the exposure of the FS-SMP monomer mixture to 254 nm UV light from 2 h to 3 min during polymerization changes the polymer network slightly and increases the relative permittivity: 5.3 to 5.8 in the glassy state. Relative permittivity measured in the rubbery state was consistently higher than that in the glassy state for both curing methods.

FS-SMP, according to the standards established by the ESD Association, displays good electrical properties when compared to other thin film materials. The surface and volume resistivity of the material classifies as an insulating polymer, independent of curing or thermomechanical state. FS-SMP may also be considered as a dielectric for use in flexible capacitors.

Author Contributions: Conceptualization, C.L.F. and J.J.P.; methodology, C.L.F., M.E., J.K., J.W., V.R.D., A.M.S.; software, C.L.F. and J.K.; validation, C.L.F., A.J.-I. and M.E.; formal analysis, C.L.F.; data curation, C.L.F., M.E., J.K., J.W.; writing—original draft preparation, C.L.F.; writing—review and editing, C.L.F., A.J.-I., M.E.; visualization, C.L.F. and M.E.; funding acquisition, W.E.V. and J.J.P.

Funding: This work was supported by the Office of the Assistant Secretary of Defense for Health Affairs through the Peer Reviewed Medical Research Program under Award Nos. W81XWH-15-1-0607 and W81XWH-15-1-0608. Opinions, interpretations, conclusions, and recommendations were those of the authors and were not necessarily endorsed by the Department of Defense. Additionally, the contents did not represent the views of the U.S. Department of Veterans Affairs or the United States Government.

Acknowledgments: The authors would like to thank Lisa Spurgin for her help with the fabrication of capacitors, Manasvini A for conducting AFM measurements, and Andrew Hoff from the Department of Electrical Engineering at the University of South Florida, for his use of the Corona-Kelvin technique to characterize the surface of FS-SMP.

Conflicts of Interest: The authors declare no conflict of interest.

References

1. Gutierrez-Heredia, G.; Maeng, J.; Conde, J.; Rodriguez-Lopez, O.; Voit, W.E. Effect of annealing atmosphere on IGZO thin film transistors on a deformable softening polymer substrate. *Semicond. Sci. Technol.* **2018**, *33*, 095001. [CrossRef]
2. Gutierrez-Heredia, G.; Pineda-Leon, H.A.; Carrillo-Castillo, A.; Rodriguez-Lopez, O.; Tishechkin, M.; Ong, K.M.; Castillo, J.S.; Voit, W.E. Lifetime of hafnium oxide dielectric in thin-film devices fabricated on deformable softening polymer substrate. *Mater. Sci. Semicond. Process.* **2018**, *88*, 273–277. [CrossRef]
3. Gutierrez-Heredia, G.; Rodriguez-Lopez, O.; Garcia-Sandoval, A.; Voit, W.E. Highly Stable Indium-Gallium-Zinc-Oxide Thin-Film Transistors on Deformable Softening Polymer Substrates. *Adv. Electron. Mater.* **2017**, *3*, 1700221. [CrossRef]
4. Choi, S.; Fuentes-Hernandez, C.; Wang, C.-Y.; Wei, A.; Voit, W.; Zhang, Y.; Barlow, S.; Marder, S.R.; Kippelen, B. Top-gate organic field-effect transistors fabricated on shape-memory polymer substrates. *Proc. SPIE* **2015**, *9568*. [CrossRef]
5. Reeder, J.; Kaltenbrunner, M.; Ware, T.; Arreaga-Salas, D.; Avendano-Bolivar, A.; Yokota, T.; Inoue, Y.; Sekino, M.; Voit, W.; Sekitani, T.; et al. Mechanically Adaptive Organic Transistors for Implantable Electronics. *Adv. Mater.* **2014**, *26*, 4967–4973. [CrossRef] [PubMed]
6. Avendano-Bolivar, A.; Ware, T.; Arreaga-Salas, D.; Simon, D.; Voit, W. Mechanical Cycling Stability of Organic Thin Film Transistors on Shape Memory Polymers. *Adv. Mater.* **2013**, *25*, 3095–3099. [CrossRef] [PubMed]
7. Ecker, M.; Joshi-Imre, A.; Modi, R.; Frewin, C.; Garcia Sandoval, A.; Maeng, J.; Gutierrez, G.; Pancrazio, J.; Voit, W. From Softening Polymers to Multi-Material Based Bioelectronic Devices. *Multifunct. Mater.* **2019**, *2*, 012001. [CrossRef]
8. Stiller, A.M.; Usoro, J.; Frewin, C.L.; Danda, V.R.; Ecker, M.; Joshi-Imre, A.; Musselman, K.C.; Voit, W.; Modi, R.; Pancrazio, J.J.; et al. Chronic Intracortical Recording and Electrochemical Stability of Thiol-ene/Acrylate Shape Memory Polymer Electrode Arrays. *Micromachines* **2018**, *9*, 500. [CrossRef]
9. González-González, M.A.; Kanneganti, A.; Joshi-Imre, A.; Hernandez-Reynoso, A.G.; Bendale, G.; Modi, R.; Ecker, M.; Khurram, A.; Cogan, S.F.; Voit, W.E.; et al. Thin Film Multi-Electrode Softening Cuffs for Selective Neuromodulation. *Sci. Rep.* **2018**, *8*, 16390. [CrossRef]
10. Simon, D.M.; Charkhkar, H.; St. John, C.; Rajendran, S.; Kang, T.; Reit, R.; Arreaga-Salas, D.; McHail, D.G.; Knaack, G.L.; Sloan, A.; et al. Design and demonstration of an intracortical probe technology with tunable modulus. *J. Biomed. Mater. Res. Part A* **2017**, *105*, 159–168. [CrossRef]
11. Ware, T.; Simon, D.; Hearon, K.; Kang, T.H.; Maitland, D.J.; Voit, W. Thiol-Click Chemistries for Responsive Neural Interfaces. *Macromol. Biosci.* **2013**, *13*, 1640–1647. [CrossRef]
12. Ware, T.; Simon, D.; Hearon, K.; Liu, C.; Shah, S.; Reeder, J.; Khodaparast, N.; Kilgard, M.P.; Maitland, D.J.; Rennaker, R.L., II; et al. Three-Dimensional Flexible Electronics Enabled by Shape Memory Polymer Substrates for Responsive Neural Interfaces. *Macromol. Mater. Eng.* **2012**, *297*, 1193–1202. [CrossRef] [PubMed]
13. Sokolowski, W.; Metcalfe, A.; Hayashi, S.; Yahia, L.; Raymond, J. Medical applications of shape memory polymers. *Biomed. Mater.* **2007**, *2*, 23–27. [CrossRef]
14. Small, W.; Singhal, P.; Wilson, T.S.; Maitland, D.J. Biomedical applications of thermally activated shape memory polymers. *J. Mater. Chem.* **2010**, *20*, 3356–3366. [CrossRef] [PubMed]
15. Yakacki, C.M.; Gall, K. Shape-Memory Polymers for Biomedical Applications. *Adv. Polym. Sci.* **2010**, *226*, 147–175.

16. Serrano, M.C.; Ameer, G.A. Recent Insights Into the Biomedical Applications of Shape-memory Polymers. *Macromol. Biosci.* **2012**, *12*, 1156–1171. [CrossRef] [PubMed]
17. Wang, K.; Strandman, S.; Zhu, X.X. A mini review: Shape memory polymers for biomedical applications. *Front. Chem. Sci. Eng.* **2017**, *11*, 143–153. [CrossRef]
18. Do, D.-H.; Ecker, M.; Voit, W.E. Characterization of a Thiol-Ene/Acrylate-Based Polymer for Neuroprosthetic Implants. *ACS Omega* **2017**, *2*, 4604–4611. [CrossRef] [PubMed]
19. Nomura, K.; Takagi, A.; Kamiya, T.; Ohta, H.; Hirano, M.; Hosono, H. Amorphous Oxide Semiconductors for High-Performance Flexible Thin-Film Transistors. *Jpn. J. Appl. Phys.* **2006**, *45*, 4303–4308. [CrossRef]
20. Nomura, K.; Ohta, H.; Takagi, A.; Kamiya, T.; Hirano, M.; Hosono, H. Room-temperature fabrication of transparent flexible thin-film transistors using amorphous oxide semiconductors. *Nature* **2004**, *432*, 488. [CrossRef]
21. Ware, T.; Simon, D.; Liu, C.; Musa, T.; Vasudevan, S.; Sloan, A.; Keefer, E.W.; Rennaker, R.L.; Voit, W. Thiol-ene/acrylate substrates for softening intracortical electrodes. *J. Biomed. Mater. Res. Part B Appl. Biomater.* **2014**, *102*, 1–11. [CrossRef]
22. Arreaga-Salas, D.E.; Avendaño-Bolívar, A.; Simon, D.; Reit, R.; Garcia-Sandoval, A.; Rennaker, R.L.; Voit, W. Integration of High-Charge-Injection-Capacity Electrodes onto Polymer Softening Neural Interfaces. *ACS Appl. Mater. Interfaces* **2015**, *7*, 26614–26623. [CrossRef]
23. Ecker, M.; Danda, V.; Shoffstall, A.J.; Mahmood, S.F.; Joshi-Imre, A.; Frewin, C.L.; Ware, T.H.; Capadona, J.R.; Pancrazio, J.J.; Voit, W.E. Sterilization of Thiol-ene/Acrylate Based Shape Memory Polymers for Biomedical Applications. *Macromol. Mater. Eng.* **2017**, *302*, 1600331. [CrossRef]
24. Reit, R.; Zamorano, D.; Parker, S.; Simon, D.; Lund, B.; Voit, W.; Ware, T.H. Hydrolytically Stable Thiol–ene Networks for Flexible Bioelectronics. *ACS Appl. Mater. Interfaces* **2015**, *7*, 28673–28681. [CrossRef]
25. Ware, T.; Hearon, K.; Lonnecker, A.; Wooley, K.L.; Maitland, D.J.; Voit, W. Triple-Shape Memory Polymers Based on Self-Complementary Hydrogen Bonding. *Macromolecules* **2012**, *45*, 1062–1069. [CrossRef]
26. Crampon, M.A.; Sawan, M.; Brailovski, V.; Trochu, F. New nerve cuff electrode based on a shape memory alloy armature. In Proceedings of the 20th Annual International Conference of the IEEE Engineering in Medicine and Biology Society, Hong Kong, China, 1 November 1998; Volume 20.
27. Hardy, J.G.; Palma, M.; Wind, S.J.; Biggs, M.J. Responsive Biomaterials: Advances in Materials Based on Shape-Memory Polymers. *Adv. Mater.* **2016**, *28*, 5717–5724. [CrossRef]
28. Gilletti, A.; Muthuswamy, J. Brain micromotion around implants in the rodent somatosensory cortex. *J. Neural Eng.* **2006**, *3*, 189. [CrossRef]
29. Elias, C.N.; Lima, J.H.C.; Valiev, R.; Meyers, M.A. Biomedical applications of titanium and its alloys. *JOM* **2008**, *60*, 46–49. [CrossRef]
30. Helton, K.L.; Ratner, B.D.; Wisniewski, N.A. Biomechanics of the sensor-tissue interface-effects of motion, pressure, and design on sensor performance and foreign body response-part II: Examples and application. *J. Diabetes Sci. Technol.* **2011**, *5*, 647–656. [CrossRef]
31. Lendlein, A.; Langer, R. Biodegradable, Elastic Shape-Memory Polymers for Potential Biomedical Applications. *Science* **2002**, *296*, 1673–1676. [CrossRef]
32. El Feninat, F.; Laroche, G.; Fiset, M.; Mantovani, D. Shape Memory Materials for Biomedical Applications. *Adv. Eng. Mater.* **2002**, *4*, 91–104. [CrossRef]
33. Lendlein, A.; Behl, M.; Hiebl, B.; Wischke, C. Shape-memory polymers as a technology platform for biomedical applications. *Expert Rev. Med. Devices* **2010**, *7*, 357–379. [CrossRef]
34. Hearon, K.; Wierzbicki, M.A.; Nash, L.D.; Landsman, T.L.; Laramy, C.; Lonnecker, A.T.; Gibbons, M.C.; Ur, S.; Cardinal, K.O.; Wilson, T.S.; et al. A Processable Shape Memory Polymer System for Biomedical Applications. *Adv. Healthc. Mater.* **2015**, *4*, 1386–1398. [CrossRef] [PubMed]
35. Ahmad, Z. Polymer Dielectric Materials. In *Dielectric Material*; Silaghi, M.A., Ed.; InTechOpen: London, UK, 2012. [CrossRef]
36. Farrell, R.; Goshal, T.; Cvelbar, U.; Petkov, N.; Morris, M.A. Advances in Ultra Low Dielectric Constant Ordered Porous Materials. *Electrochem. Soc. Interface* **2011**, *20*, 39–46. [CrossRef]
37. Scholvin, J.; Kinney, J.P.; Bernstein, J.G.; Moore-Kochlacs, C.; Kopell, N.J.; Fonstad, C.G.; Boyden, E.S. Heterogeneous neural amplifier integration for scalable extracellular microelectrodes. In Proceedings of the 38th Annual International Conference of the IEEE Engineering in Medicine and Biology Society (EMBC), Orlando, FL, USA, 16–20 August 2016; pp. 2789–2793.

38. Black, B.J.; Ecker, M.; Stiller, A.; Rihani, R.; Danda, V.R.; Reed, I.; Voit, W.E.; Pancrazio, J.J. In vitro compatibility testing of thiol-ene/acrylate-based shape memory polymers for use in implantable neural interfaces. *J. Biomed. Mater. Res. Part A* **2018**, *106*, 2891–2898. [CrossRef]
39. ASTM. *Standard Test Methods for DC Resistance or Conductance of Insulating Materials*; D257-14; ASTM International: West Conshohocken, PA, USA, 2014; Volume D257-14.
40. ASTM. *Standard Test Methods for AC Loss Characteristics and Permittivity (Dielectric Constant) of Solid Electrical Insulation*; D150-11; ASTM International: West Conshohocken, PA, USA, 2011; Volume D150-11.
41. IPC. *Permittivity (Dielectric Constant) and Loss Tangent (Dissipation Factor) if Insulating Material a 1 MHz (Contacting Electrode Systems)*; IPC-TM-650; Institute for Inteerconnecting and Packaging ELectronic Circuits: Bannockburn, IL, USA, 1986; Volume 2.5.5.1, p. 5.
42. Findlay, A.; Marinskiy, D.; Edelman, P.; Wilson, M.; Savtchouk, A.; Lagowski, J. Non-Visual Defect Monitoring with Surface Voltage Mapping. *ECS J. Solid State Sci. Technol.* **2016**, *5*, P3087–P3095. [CrossRef]
43. Hoff, A.M.; Esry, T.C.; Nauka, K. Monitoring Plasma Damage: A Real-time, Non-contact Approach. *Solid State Technol.* **1996**, *39*, 139–152.
44. Lagowski, J.; Hofl, A.; Jastrzebski, L.; Edelman, P.; Esry, T. A Novel Method For Studying Degradation Related To Plasma Processing Of Silicon Wafers. *MRS Proc.* **2011**, *428*, 437. [CrossRef]
45. Marinskiy, D.; Lagowski, J.; Wilson, M.; Findlay, A.; Almeida, C.; Edelman, P. New Approach to Surface Voltage Based Non-Visual Defect Inspection. *ECS Trans.* **2014**, *60*, 917–922. [CrossRef]
46. Vassilikou-Dova, A.; Kalogeras, I.M. Dielectric analysis (DEA). In *Thermal Analysis of Polymers: Fundamentals and Applications*; Menczel, J.D., Prime, R.B., Eds.; John Wiley & Sons, Inc.: Hoboken, NJ, USA, 2008; pp. 497–613. [CrossRef]
47. Bocharova, V.; Wojnarowska, Z.; Cao, P.-F.; Fu, Y.; Kumar, R.; Li, B.; Novikov, V.N.; Zhao, S.; Kisliuk, A.; Saito, T.; et al. Influence of Chain Rigidity and Dielectric Constant on the Glass Transition Temperature in Polymerized Ionic Liquids. *J. Phys. Chem. B* **2017**, *121*, 11511–11519. [CrossRef]
48. Biron, M. 1—Thermoplastic Material Selection: Some Ways of Thinking for a Systematic Approach. In *Material Selection for Thermoplastic Parts*; Biron, M., Ed.; William Andrew Publishing: Oxford, UK, 2016; pp. 1–38. [CrossRef]
49. Biron, M. Chapter 3—Basic criteria for the selection of thermosets. In *Thermosets and Composites*; Biron, M., Ed.; Elsevier Science: Oxford, UK, 2004; pp. 145–181. [CrossRef]
50. Laby, K.A. Electrical Insulating Materials. Available online: http://www.kayelaby.npl.co.uk/general_physics/2_6/2_6_3.html (accessed on 4 December 2019).
51. Hassler, C.; von Metzen, R.; Stieglitz, T. Deposition Parameters Determining Insulation Resistance and Crystallinity of Parylene C in Neural Implant Encapsulation. In *4th European Conference of the International Federation for Medical and Biological Engineering*; Springer: Berlin/Heidelberg, Germany, 2009; pp. 2439–2442.
52. *DUPONT™ KAPTON®Summary Of Properties*; DuPond: Wilmington, DE, USA, 2017.

TOPICAL REVIEW

From softening polymers to multimaterial based bioelectronic devices

To cite this article: Melanie Ecker *et al* 2019 *Multifunct. Mater.* **2** 012001

Multifunctional Materials

TOPICAL REVIEW

From softening polymers to multimaterial based bioelectronic devices

Melanie Ecker[1,2,3,6], **Alexandra Joshi-Imre**[1,2,3], **Romil Modi**[4], **Christopher L. Frewin**[2], **Aldo Garcia-Sandoval**[2], **Jimin Maeng**[2], **Gerardo Gutierrez-Heredia**[5], **Joseph J Pancrazio**[2] and **Walter E. Voit**[1,2,3,4]

[1] Center for Engineering Innovation, The University of Texas at Dallas, Richardson, TX, USA
[2] Department of Bioengineering, The University of Texas at Dallas, Richardson, TX, USA
[3] Department of Materials Science and Engineering, The University of Texas at Dallas, Richardson, TX, USA
[4] Qualia Inc., Richardson, TX, USA
[5] Centro de Investigaciones en Optica A. C. Leon Gto, Mexico
[6] Author to whom any correspondence should be addressed.

E-mail: melanie.ecker@utdallas.edu **and** walter.voit@utdallas.edu

RECEIVED
7 May 2018

REVISED
26 October 2018

ACCEPTED FOR PUBLICATION
1 November 2018

PUBLISHED
11 December 2018

Keywords: shape memory polymer, softening polymer, neural interfaces, microfabrication, bioelectronic devices, material interfaces

Abstract

A recent development in bioelectronic devices involves the utilization of multifunctional polymers as substrate material. Dynamically softening, thin-film polymers reduce the mechanical mismatch between device and tissue after implantation and therefore improves the device–tissue interaction. However, when implementing a new material into the fabrication of fully functional and chronically viable devices, there are specific challenges that need to be addressed. The key for all multimaterial devices is to ensure a good adhesion and connectivity between the different layers. That is especially true if one of the materials is sensitive to stimuli such as temperature and moisture. This review will give an overview on the development of a variety of neural interfaces for recording and stimulation with softening shape memory polymers (SMPs) as substrate material. This review discusses specific requirements for device fabrication, testing, and durability.

1. Introduction

The field of bioelectronic devices [1] comprises non-invasive wearable devices such as temperature and pressure sensors [2–9], as well as implantable devices such as neural interfaces [10–17] and pacemakers [18, 19]. All of these devices have in common the fact that they are built of multiple materials, resulting in multimaterial based bioelectronics devices. The range of applied materials within these devices is wide and spans organic materials such as polymers to inorganic materials such as metals [20–23]. A relatively new development is the use of multifunctional polymers as substrate material for various bioelectronic devices [22, 24].

The challenge when fabricating devices comprised of multiple materials, independent of the materials used, is to ensure a good interlayer adhesion such that the resulting device is appropriate for chronic applications without early failure. For devices consisting of layers of materials that are capable of dynamic shape and stiffness changes, interlayer adhesion is particularly challenging. Therefore, it is essential to perform sufficient durability testing to ensure reliable and long-lasting devices through in vitro and in vivo experiments [25–28].

Another important aspect when using multifunctional materials such as shape memory polymers (SMPs) is the processing. Often, the fabrication of bioelectronic devices involves exposure to harsh conditions, which may impact the multifunctionality of these materials. These processing conditions include high temperatures, plasma treatments, and chemicals. Therefore, it is important to ensure that the fabrication is performed in a way that is compatible with the temperature and moisture sensitive materials [29].

Finally, when multifunctional materials are being used for biomedical devices, it needs to be ensured that these materials are biocompatible and can be sterilized without losing their functionality.

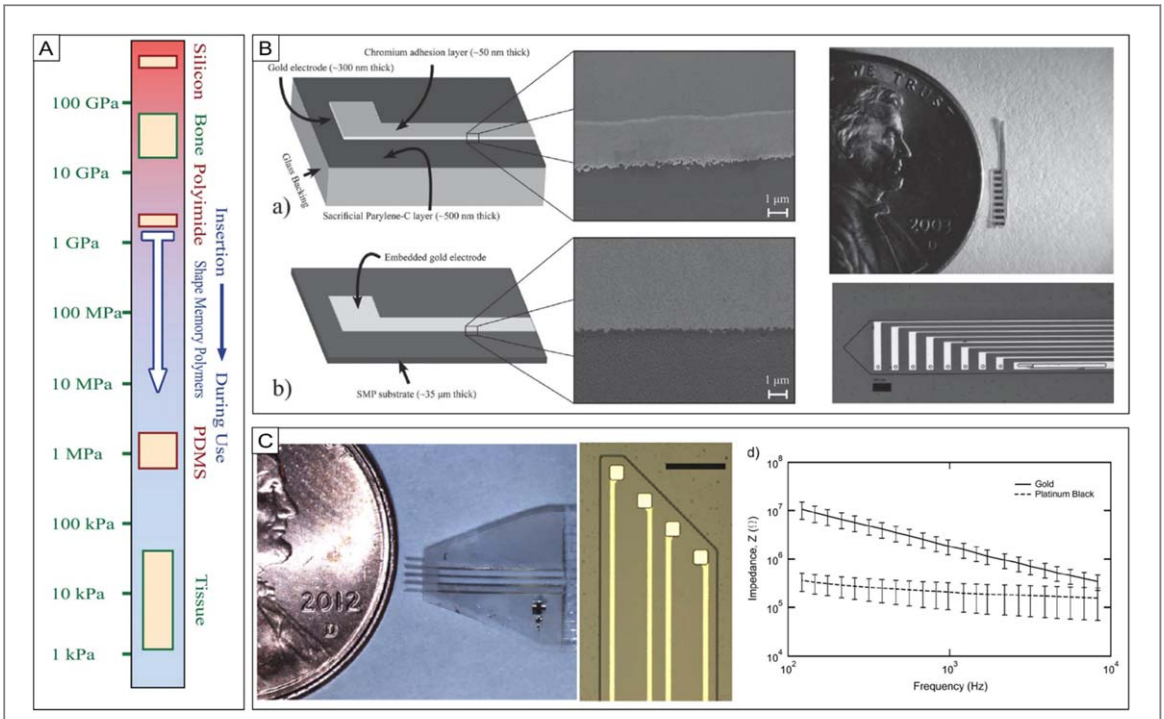

Figure 1. (A) Schematic illustration indicating the modulus of materials used in neural interfaces relative to biological tissues. (B) Process schematics (left) and images (right) demonstrating the utilized transfer by polymerization process. Substrate prepared for the transfer of patterned devices from the sacrificial to the final substrate (top left) schematic. Devices after synthesis of the final substrate and removal of the sacrificial substrate (bottom left). Optical microscopy images of example cortical probes fabricated using the transfer by polymerization process. Cortical probe with eight recording channels and a ground fabricated and insulated with patterned Parylene-C (right). (C) Photograph of a 16-channel intracortical electrode array next to an American penny with an optical micrograph of a single penetrating shank (scale bar 60 mm) and impedance spectroscopy of electrodes (n 5 16) before and after electroplating platinum (error bars represent 95% CI). (A) was reproduced from Ware *et al* [38], (B) was reproduced from Ware *et al* [31], and (C) was reproduced from Ware *et al* [38]

This review will focus on specific requirements when using multifunctional polymers for the fabrication of multimaterial electronic devices for biomedical applications. We will discuss in particular the use of softening polymeric substrates for neural interfaces that have been first reported in 2012 by Ware *et al* (figure 1) [30, 31]. Since its introduction, the technology has constantly evolved, and a variety of material and device iterations have been developed.

2. Types of devices

Bioelectronic devices are electronic devices to be used to interact with biological systems and function as information processing systems. They can be used to extract biological relevant information from the body through recording and monitoring of physiological signals, including temperature, blood pressure, and neural activity. They can also be used to manipulate the body by altering electrical signals to activate muscles and modulate neural activity.

Depending on the task, the device design can vary greatly. Devices for monitoring may be non-invasive, wearable devices; whereas devices for neural stimulation are often invasive and need to be implanted in close proximity to the neural tissue to achieve specificity. This paper will give a general overview about implantable neural interfaces that are fabricated from responsive polymeric substrate materials.

In general, neural interfaces are small electronic devices that interact with the neural system [15, 32]. They can either record electrical signals associated with neural activity, or they can stimulate to modulate the activity of the central nervous system (CNS) or the peripheral nervous system (PNS). Depending on the targeted area, neural interfaces can differ in their invasiveness. There are electrodes that are entirely non-invasive, e.g., scalp electrodes for electroencephalography (EEG). In order to monitor single neuronal units, it is necessary to place the electrodes closer to the neurons, which makes these devices much more invasive. The specifics of the device design depend on the targeted neurons. This includes the overall device shape and the substrate material, choice of electrode size and materials, as well as integration of active elements such as transistors or diodes. The use of softening polymeric substrates has been shown to be amenable to many of these design permutations. Three implantable device types were identified, which seem to benefit from softening polymeric substrates for various reasons: cortical probes, spinal cord stimulators, and nerve cuffs.

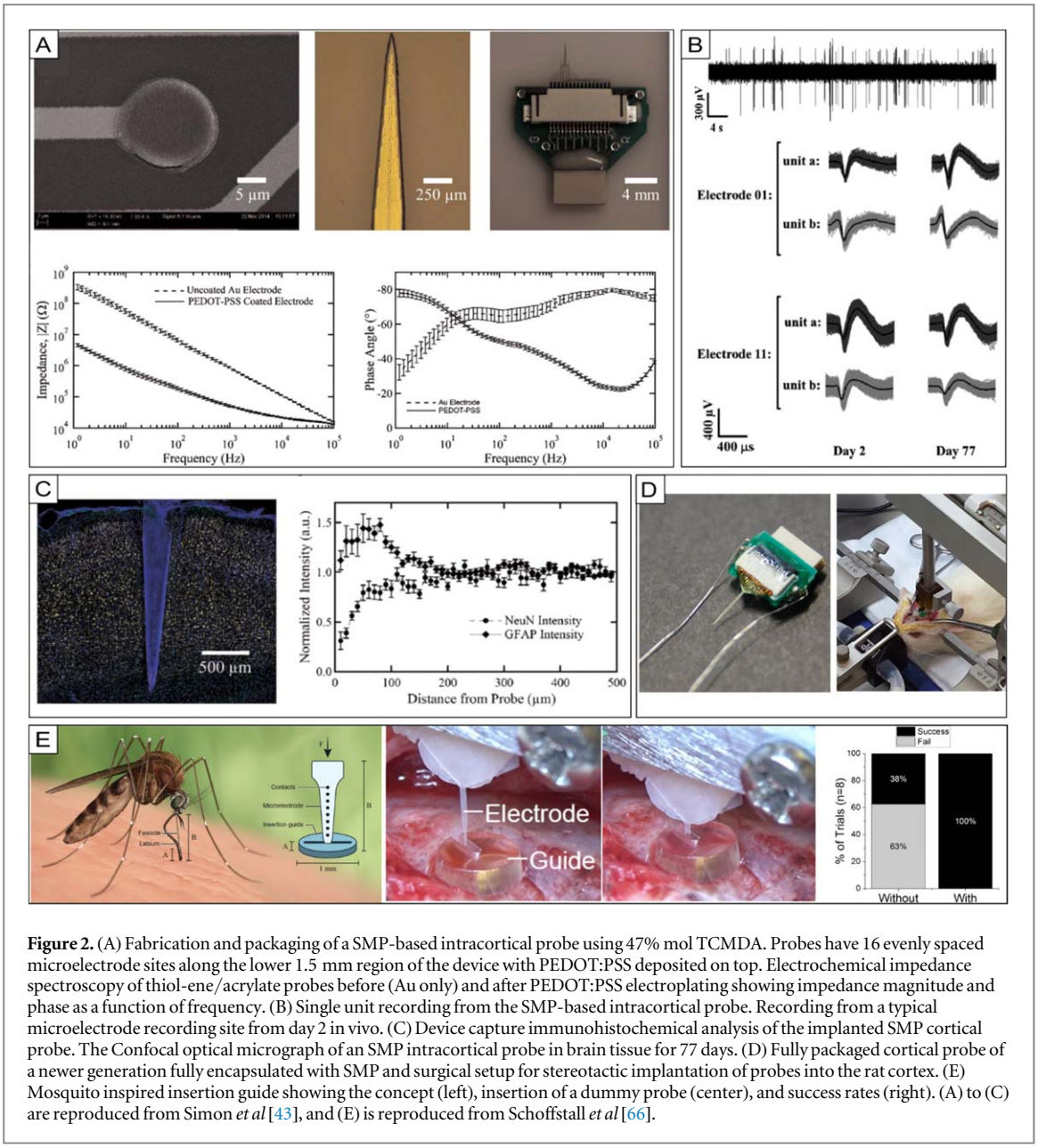

Figure 2. (A) Fabrication and packaging of a SMP-based intracortical probe using 47% mol TCMDA. Probes have 16 evenly spaced microelectrode sites along the lower 1.5 mm region of the device with PEDOT:PSS deposited on top. Electrochemical impedance spectroscopy of thiol-ene/acrylate probes before (Au only) and after PEDOT:PSS electroplating showing impedance magnitude and phase as a function of frequency. (B) Single unit recording from the SMP-based intracortical probe. Recording from a typical microelectrode recording site from day 2 in vivo. (C) Device capture immunohistochemical analysis of the implanted SMP cortical probe. The Confocal optical micrograph of an SMP intracortical probe in brain tissue for 77 days. (D) Fully packaged cortical probe of a newer generation fully encapsulated with SMP and surgical setup for stereotactic implantation of probes into the rat cortex. (E) Mosquito inspired insertion guide showing the concept (left), insertion of a dummy probe (center), and success rates (right). (A) to (C) are reproduced from Simon *et al* [43], and (E) is reproduced from Schoffstall *et al* [66].

2.1. Cortical probes

Traditional cortical probes consist primarily of silicon which has an elastic modulus that exceeds the surrounding tissue by 6 orders of magnitude (figure 1(A)). One major limitation observed with current cortical probes is the low level of long-term reliability, where neural activity can become variable and decrease months after implantation [33]. One of the causes attributed to this overall failure may originate from the inflammatory response initiated following intracortical probe implantation, in addition to biotic factors including tissue encapsulation and astroglial scarring [22, 34, 35]. This foreign body response has often been attributed in large part to the mechanical mismatch that exists between the materials that comprise intracortical probes and the surrounding brain tissue [35]. The magnitude of the strain field in highly compliant cortical tissue can be minimized through the reduction of implant elastic modulus [36]. Therefore, by creating cortical probes that are less stiff, tissue strain would be reduced, resulting in an improved tissue response and device performance.

The use of softening polymers is an approach to minimize the mechanical mismatch and associated tissue response to improve the device–tissue interaction. Softening polymers offer the advantage of being stiff enough during the implantation to ensure that they can penetrate the tissue. However, the polymers change their mechanical modulus and become much softer in an aqueous environment (figure 1(A)). The underlying effect is the so-called "solvent induced plasticization," which will be discussed in more detail in the section 3.1.1.

The Voit group has developed a series of thiol-ene/acrylate polymers that can undergo various degrees of softening under physiological conditions [31, 37–42] and fabricated Michigan style multi-electrode arrays to study neural activity in the rat cortex (figures 1 and 2) [38, 43]. Studying the physiological response to devices

possessing different overall stiffness may give important insights to the hypothesis that stiffer materials are linked to increased foreign body responses. Early devices (figure 1(B) and (C)), which were fabricated between 2012 and 2013, used the transfer by polymerization method. Their design was simple and the probes were still rather big, but successfully demonstrated the compatibility of the SMP substrate with standard photolithographical processes. These devices were used for acute [31] and subchronic (4 weeks) [38] in vivo studies. Devices that were fabricated later (figure 2) became more advanced. Their overall size was reduced, their channel count was increased, and they were fully packaged. These devices allowed single unit recordings from the rat cortex for durations up to 77 days [43] and 13 weeks [44], respectively.

An approach used by other groups to minimize the foreign body response is by minimizing the probe size to reduce the overall footprint [45–47]. Additionally, by reducing the thickness, the probe becomes more flexible since flexural/bending modulus is not only dependent on the Young's modulus, but also on the thickness of the material. Common materials used for polymeric cortical probes are polyimide [21, 48–52], SU-8 [12, 53–55], and Parylene-C [56–59]. However, these polymers remain stiff after implantation due to a high glass transition temperature and are therefore not responsive to the body environment. The insertion of cortical probes is usually performed using a stereotaxic surgery (figure 2(D)), following the procedure described by Fornari *et al* [60], which helps to standardize the procedure and to minimize variations during the procedure. That method allows the exact positioning of the probe, set angle, and insertion speeds. However, even if the polymeric substrate materials of the devices are still in the glassy state, the devices may buckle during the insertion depending on their geometry. While for 30 μm-thick and 3 to 5 mm-long probes the insertion works adequately, buckling becomes more relevant as the shank length of the probes increases and their thickness decreases. This general phenomenon independent of the materials arises when probes become thinner and more flexible. They lose their stiffness and mechanical support, which are needed in order to overcome insertion forces. In the past, some approaches have been identified to enable the implantation of devices that would otherwise buckle because of their flexibility or softness. These strategies include insertion shuttles [55, 61–63], and coatings that make probes temporarily stiffer and that dissolve after implantation [59, 64, 65]. However, these techniques increase the footprint of the probe, may have negative impact on the tissue response, and are therefore contradictory to the general trend of probe miniaturization. To eliminate the risk of buckling and bending for thin and flexible electrode materials without the need for probe manipulation or modification, Shoffstall *et al* have developed a mosquito inspired insertion guide (figure 2(E)) [66]. That allows the insertion of the microprobe through a small slit (~150 μm), which provides lateral support, reduces the effective length of the device, and increases the critical buckling load during insertion.

2.2. Nerve cuffs

Nerve cuff electrodes have been used for years on relatively large and accessible somatic nerves. However, new clinical applications targeting smaller autonomic nerves composed mostly of unmyelinated axons present new challenges. Current silicone cuff electrodes have a medium-soft shore hardness with thick (200–600 μm) walls, and they cannot be size-adjusted during surgery. These characteristics contribute to fibrotic tissue growth over and inside the device, which restricts nerve movement, alters nerve conduction, and often causes nerve damage [67, 68]. These adverse reactions can also be the result of cuff thickness (200–600 μm), sharp edges, inadequate cuff-nerve fitting, a mechanical mismatch between silicone/platinum-iridium electrodes and the nerve tissue, and tissue damage due to stimulation or electrode dissolution [69, 70]. To address several of the limitations of the silicone cuff electrodes, flexible thin-film electrode arrays using polyimide or silicone as substrates are under investigation [22, 70–72]. The Voit lab has also developed a new type of thin-film cuffs that are based on softening polymers that can soften from the GPa range to the MPa range under physiological conditions and can be wrapped around nerves of different sizes, providing optimal nerve–electrode contact [68, 73]. These unique characteristics are likely to contribute to the fabrication of clinical electrodes that will offer more sensitive recording and safer electrical stimulation of small and fragile peripheral nerves, thus enabling access to a number of autonomic nerve targets for clinical neuromodulation applications. The first generation of cuff electrodes were hook-like and self-coiling utilizing the shape memory effect (figures 3(A) and (B)) [30]. Stimulation of the vagus nerve was demonstrated in an acute setup through a marked decrease in heart rate and arterial oxygen saturation. These early devices were limited to acute applications only. However, they demonstrated the overall concept and feasibility. The newer generations are folding electrodes that can wrap tightly around the tissue and comprise of various electrode sizes to address differently sized nerves for acute and chronic studies [68, 73] (figures 3(C) to (F)). Although the thin-film cuffs show advantages over the silicone cuff/tunnel devices in terms of device–tissue interaction, one major limitation is that they do not offer a self-closing mechanism and therefore need to be anchored by adhesives or sutures as visible in figures 3(C) and (E), respectively.

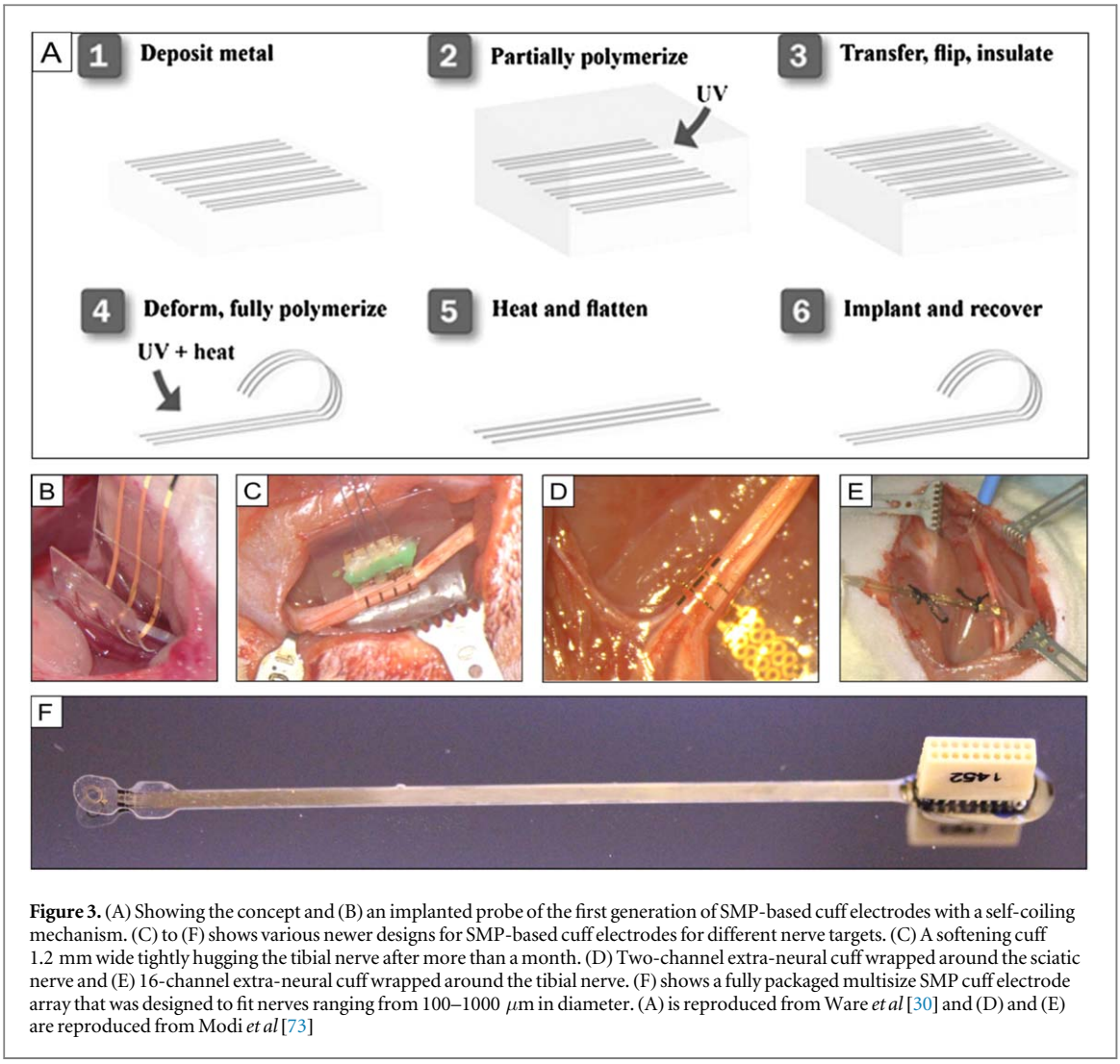

Figure 3. (A) Showing the concept and (B) an implanted probe of the first generation of SMP-based cuff electrodes with a self-coiling mechanism. (C) to (F) shows various newer designs for SMP-based cuff electrodes for different nerve targets. (C) A softening cuff 1.2 mm wide tightly hugging the tibial nerve after more than a month. (D) Two-channel extra-neural cuff wrapped around the sciatic nerve and (E) 16-channel extra-neural cuff wrapped around the tibial nerve. (F) shows a fully packaged multisize SMP cuff electrode array that was designed to fit nerves ranging from 100–1000 μm in diameter. (A) is reproduced from Ware *et al* [30] and (D) and (E) are reproduced from Modi *et al* [73]

2.3. Spinal cord stimulators

The spinal cord has a large range of motion which creates a difficult environment for neural prostheses within the spinal canal [74], therefore such devices need to be tough enough to withstand high mechanical stress and strain. However, such devices need to be soft to prevent damage to the spinal cord tissue, which is highly supple and flexible [75]. Current commercially available devices are usually made of soft materials, e.g., silicone, in paddle or cylindrical shapes integrating different electrode materials, for instance, platinum, iridium, and Pt/Ir alloys. Nonetheless, these devices often fail due to migration or glia scar encapsulation and they can also cause epidural hematomas, spinal tissue damage, and painful stimulation [76]. Also, an invasive surgery (laminectomy) is required to implant such a paddle-shaped device in which vertebrae is removed. Overall, polymeric substrates are preferred over stiffer materials as the mechanical mismatch between the spinal cord tissue and the electrode leads is reduced. The Voit lab has demonstrated the fabrication process of thin-film softening spinal cord stimulation arrays integrating gold interconnections and titanium nitride stimulating electrodes (figure 4) [77]. These devices are stiff at room temperature and become supple once exposed to physiological conditions, allowing the surgeon for an easy device handling and reducing their elastic modulus once implanted. Tensile tests and dynamic mechanical analysis (DMA) were performed to the neat softening polymer and to fabricated softening devices, respectively, to determine the modulus in dry (room temperature) and wet (body temperature) conditions, as shown in figure 4(F). Figure 4(B) displays a 3D rendering of the implanted device based on a computed tomography (CT) scan. The softening property of SMP-based devices allows for an easy implantation, which requires a single laminectomy and sliding the thin-film implant in the epidural space which becomes soft and conforms around the spinal cord. These devices were tested in vitro in an accelerated aging paradigm for a simulated time of 29 weeks. They have also been implanted for up to 29 weeks in the cervical spinal cord of a rat model and were able to deliver stimulation pulses and evoke muscle responses, which were recorded by electromyograms throughout the time implanted showing stable performance in terms of their stimulation threshold and electrode impedance.

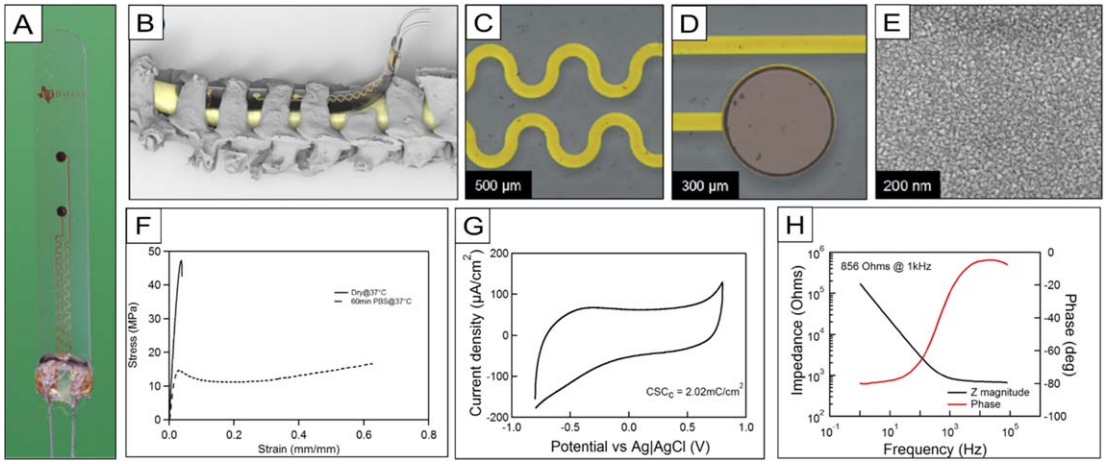

Figure 4. (A) Softening spinal cord stimulator (SCS) as fabricated. (B) CAD rendering obtained by magnetic resonance images of the spinal cord of a rat model with a softening SCS array implanted in the epidural space with electrodes at the C4 and C5 sections. The optical pictures express detail at 20 × magnification of the SMP-based SCS array showing (**C**) the serpentine 100 μm-wide gold interconnects and (D) one of the device's two high-charge injection capacity TiN electrodes. (E) A scanning electron micrograph (SEM) shows the inherently rough, nanostructured TiN surface that enables large electrochemical surface area per geometric surface area. (F) Tensile test shows the mechanical properties of the SCS array when tested at dry conditions and in phosphate buffered saline (PBS), both at 37°C. (G) Cyclic voltammetry of a TiN electrode. Charge storage capacity (CSC) was calculated to be 2.02 mC cm^{-2} and the impedance at 1 kHz is 856 ohms. (H) Electrochemical impedance spectroscopy of TiN electrodes. The graph shows both the impedance magnitude and the phase angle. Adapted from Garcia-Sandoval *et al* [77] with permission from IOP Publishing.

3. Fabrication of multimaterial devices

This section will focus on the fabrication of multifunctional and multimaterial devices for recording and/or stimulation of neural activity [29–31, 38–40, 73, 78–81]. In order to fabricate fully functional neural interfaces, multiple materials need to be integrated into one device. These materials include substrate materials, interlayers for encapsulation, and materials for electrodes and interconnects. As Szostak *et al* [11] have already pointed out for cortical probes, there are variety of key requirements for the successful fabrication of neural recording and stimulating devices. Won *et al* [82] have also just recently summarized the recent developments in material selections for durable neural interfaces. That includes the selection of materials used for the different parts of the devices, material interfaces, and the processing.

3.1. Materials

3.1.1. Substrate material: softening polymers

As already mentioned earlier, the use of softening polymers is beneficial for many bioelectronic device applications. With softening, devices become more compliant and reduce the mismatch in modulus that otherwise exists between the device and the tissue.

Ware *et al* have reported the first versions of dynamically softening polymers in 2012 [31]. These substrates comprised of the monomers methyl acrylate (MA), isobornyl acrylate (IBoA), and 1 wt% poly(ethylene glycol) diacrylate as crosslinker. Shortly thereafter, thiol-ene/acrylate click-chemistry have been explored as an ideal chemistry to create a softening substrate for neural interfaces [30, 39]. Common monomers used include di- and tri-functional alkenes, thiols, and acrylates such as 1,3,5-Triallyl-1,3,5-triazine-2,4,6(1H,3H,5H)-trione (TATATO), trimethylolpropanetris(3-mercaptopropio-nate) (TMTMP), and tricyclodecanedimethanoldiacrylate (TCMDA) (figure 5(A)). The softening effect of the polymers can be explained by the solvent induced plasticization effect [83]. When the polymer swells in water, the free volume of the polymer chains increase and with this, the glass transition temperature (T_g) drops (figure 5(C)). This effect is also used to trigger the shape recovery of shape memory polymers.

By tuning the polymers to have a T_g that is above body temperature when dry, but below after soaking and plasticizing in 37 °C warm water or phosphate buffered saline (PBS), the material will soften from its glassy state to the rubbery regime (figure 5(C)). By tuning both the T_g and the crosslink-density of the polymers, the degree of softening can be varied, resulting in polymers that do not soften at all under physiological conditions to polymers with a modulus that drops over orders of magnitudes during the plasticization process.

The degree of softening can easily be tuned by tailoring the polymer composition (figure 5(D)) [37, 41], which allows for a detailed study of the relationship between the properties of the materials and the tissue response. However, not only the choice and quantity of the monomers have influence over the resulting polymer

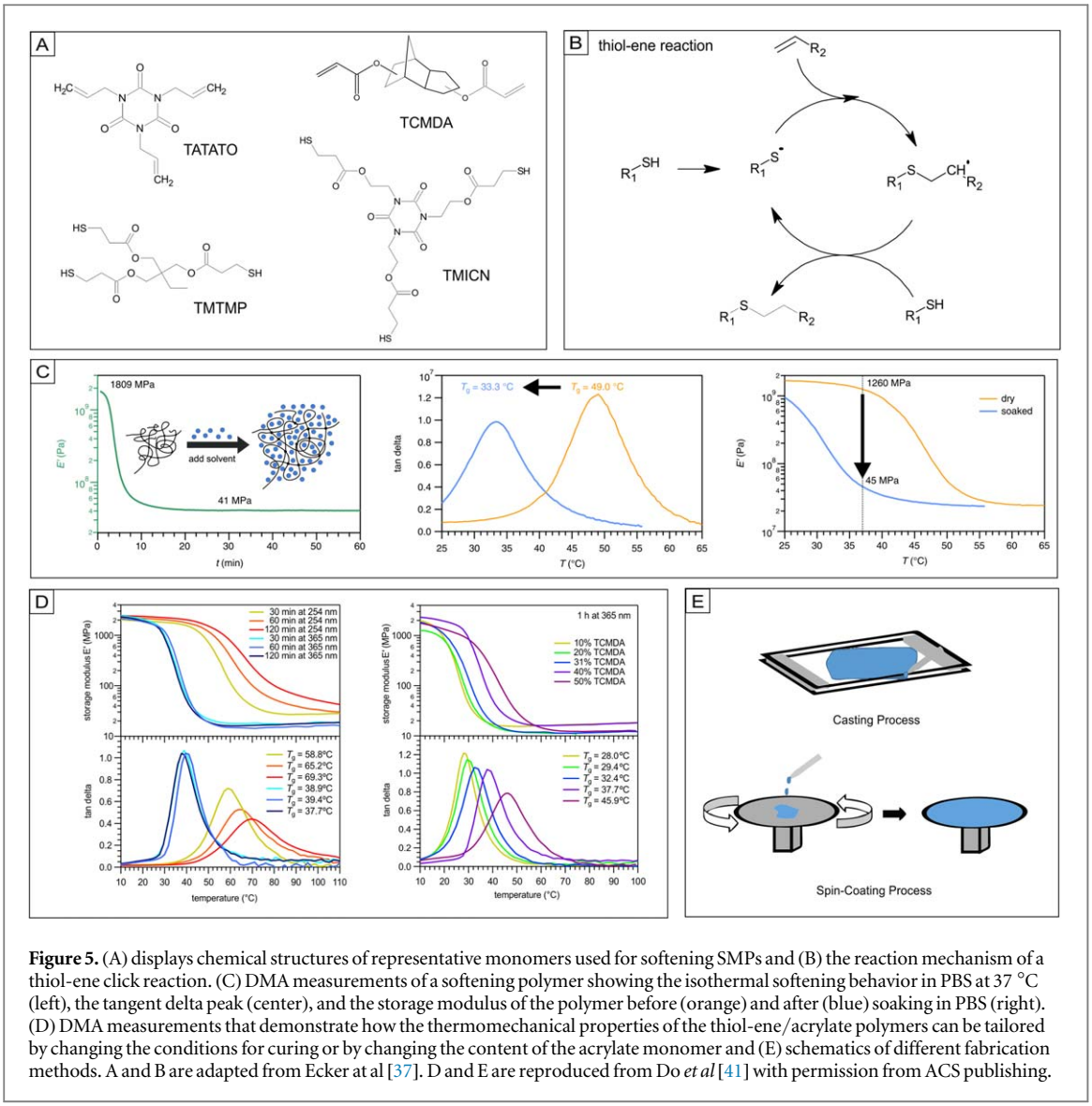

Figure 5. (A) displays chemical structures of representative monomers used for softening SMPs and (B) the reaction mechanism of a thiol-ene click reaction. (C) DMA measurements of a softening polymer showing the isothermal softening behavior in PBS at 37 °C (left), the tangent delta peak (center), and the storage modulus of the polymer before (orange) and after (blue) soaking in PBS (right). (D) DMA measurements that demonstrate how the thermomechanical properties of the thiol-ene/acrylate polymers can be tailored by changing the conditions for curing or by changing the content of the acrylate monomer and (E) schematics of different fabrication methods. A and B are adapted from Ecker at al [37]. D and E are reproduced from Do *et al* [41] with permission from ACS publishing.

properties, but also the fabrication parameters. For example, the wavelength and time for curing and the film casting technique (e.g., spin coating and injection casting) alter the thermomechanical properties of the polymer (figures 5(D) and (E)) [41]. The use of thiol-ene and thiol-ene/acrylate polymers offer a huge toolbox to design softening polymers. These polymers undergo a photo-initiated radical reaction (figure 5(B)), which is a step growth reaction. Therefore, the curing stresses are minimized, which is important to maintain dimensional stability of the cured polymer films during the electrode fabrication and later during their application as a final device. Another important factor is the swelling behavior of the polymer. Since the polymers need to absorb water in order to undergo the plasticization induced softening (figure 5(C)), they will also swell to some extent. However, the thiol-ene/acrylate polymers swell only up to 3%, which ensures dimensional stability after softening [29, 41].

The thermal stability of the thermoset thiol-ene/acrylate polymers was determined by a thermal gravimetric analysis (TGA). It was found that these polymers start to decompose at temperatures higher than 300 °C [41, 84]. The fabrication of functional devices is therefore limited by this temperature.

3.1.2. Interlayers for encapsulation

The solvent induced plasticization phenomenon described earlier has an effect not only on the thermomechanical properties but also on the electromagnetic properties of the polymer. Water uptake, in general, increases the dielectric constant and decreases the volume resistivity, hindering electrical insulation functionality [82]. Electrical leakage across the softened polymer substrate may be tolerable when the exposed electrodes of a neural interface device are large in size, which provide a low impedance pathway to electrical currents typically in the kΩ range, and when the embedded metal traces are separated by a sufficient amount of polymer. A thicker polymer encapsulation has the effect of increasing the resistance between traces, and

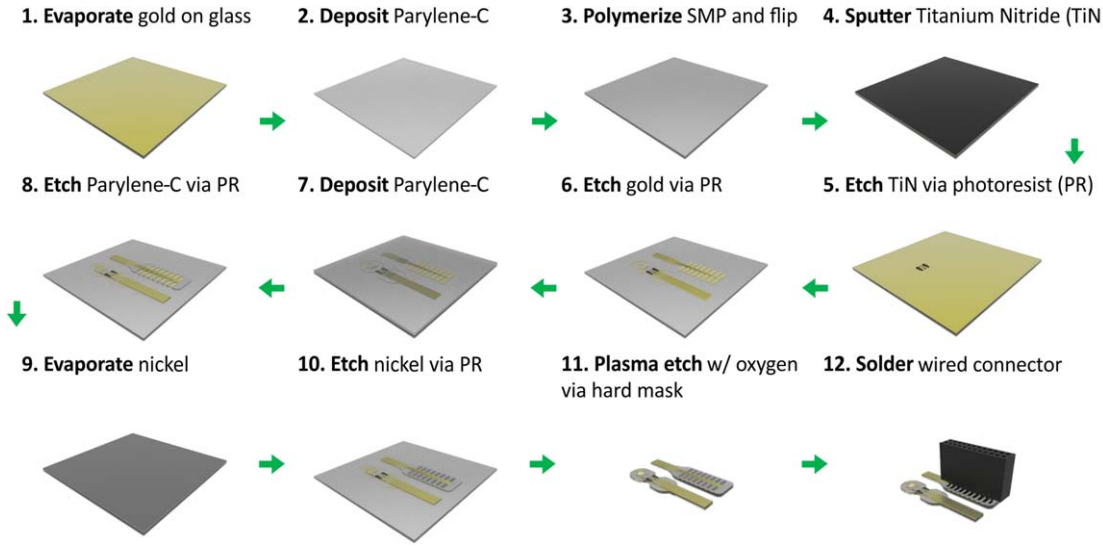

Figure 6. Depicts the photolithographic process for the fabrication of 16-channel TiN electrodes using the transfer by the polymerization process.

therefore decreasing the current leakage. However, when small electrode sites are used, electrode impedance will most likely increase well into the MΩ range. Additionally, down-scaled devices limit real estate and require closer spacing of the metal traces, and the reduced distance between traces increases the current leakage. The increasing impedance of the electrode sites and the decreasing impedance of the leakage pathways then can create a situation when shunting through the softened substrate becomes unreasonably high. In this situation, the use of an interlayer material of better barrier properties becomes desirable. Simon *et al* [43] have presently employed minimal amounts of Parylene-C, which has been widely used [56, 85–87] as a liner between the gold wiring and the softening polymer. Since this Parylene-C liner comprises a relatively small volume contribution to the overall device, effects of the liner on device mechanics are virtually negligible. Other polymeric materials that are used as material for encapsulation in (flexible) microelectronics are SU-8 [53, 54], polyimide [88, 89], and PDMS [90–93]. Besides that, inorganic materials, such as silicon carbide (SiC) [94, 95], silicon nitride (SiN_x) [8, 96, 97], silicon oxide (SiO_2) [98], aluminum oxide (Al_2O_3) [99], and hafnium oxide (HfO_2) [100] have shown some promise. Some of them, however, show also leakage over time when fully immersed in physiological environment [96].

3.1.3. Selection of electrode material

The electrode material provides an electrochemically reliable interface to neural tissue. In order to be able to fabricate devices with reasonable electrochemical properties, it is important that the substrate is compatible with microfabrication processes [101, 102]. Platinum (Pt), titanium nitride (TiN), and sputtered iridium oxide (SIROF) coatings have been used as a method to reduce interface impedance and to increase charge storage capacity (CSC) [11, 13, 17, 23, 25, 42, 78, 82, 102–104]. The Voit lab has developed a fabrication process to incorporate reliable high-performance electrode materials onto the thiol-ene-based softening substrate such as TiN [68, 105] and activated iridium electrodes [78]. Material selection is of high importance for the integration of electronic elements onto the flexible substrate. Especially for the softening neural interfaces, thin-film stress, interlayer adhesion, and strain tolerance are critical factors. In addition, SMP-based devices are compatible with electroplating of poly(3,4-ethylenedioxythiophene) polystyrene sulfonate (PEDOT-PSS) [43], iridium oxide (EIROF) [73], and carbon nanomaterials [106] which aim to reduce interface impedance.

3.1.4. Materials for Interconnects

Besides the material for the electrodes, the material used for traces and interconnects is equally important [107]. The traces are needed to transport the electrical signals from the electrode side to the connector and ultimately to an external device for data interpretation. Widely used materials in flexible devices are noble metals, such as gold (Au), platinum (Pt), and iridium (Ir). The traces are traditionally patterned through microfabrication including photolithography as displayed in figure 6.

Gold has the advantage that it has a high electrical conductivity and is more malleable compared to other metals. The thickness of such Au traces is usually between 100 to 500 nm. While neural interfaces are implanted, they may experience various degrees of deformation such as bending and torsion, depending on their

surroundings, which increase the risk of trace cracking and breaking. In order to minimize internal stresses, it is recommended to have the interconnects in the so-called "neutral plane" of the device [108, 109]. Another common method is tracing the pattern in the shape of the serpentines (figures 4(A) and (C)), which give additional stress relief [110–112].

3.2. Material interfaces

A typical stack of a simple SMP bioelectronic device may consist of SMP/Parylene-C/Au/Parylene-C/SMP. In this architecture, there are three different interfaces involved, SMP to Parylene-C, Parylene-C to Au, and SMP to SMP. To evaluate the strength of interfaces/adhesion between various layers, the tests are typically done directly after fabrication. These tests may include scratch and tape tests [113, 114] and T-peel tests [115]. Often, the results may show good adhesion of the materials when dry. However, when using these devices for functional tests in vitro as well as in vivo, one can see that the devices are not robust enough and that delamination between layers occurs. Therefore, it is necessary to test the interface adhesion under accelerated aging conditions that represent the actual environment. That will be addressed in more detail in section 5.2.

If the adhesion between layers is not sufficient, the performance may be improved by the use of adhesion promoters such as A-174 silane, thiol-based adhesion promoters, and surface treatment such as etching (RIE) [116–118].

3.3. General processing

The fabrication of early softening neural interface devices (produced between 2011 and 2014) was based on a molding process termed "transfer by polymerization" [30, 31, 40]. This method uses two glass slides, strips of spacer materials of a desired thickness and spring-loaded clips to create the mold in which the monomer solution is photopolymerized and cured as displayed in figure 5(E). By having one of the glass slides coated with a thin layer of gold and using the other glass slide as window for the photopolymerization process, the polymer film cures in contact with the gold surface and likely develops covalent bonding through the available thiol groups. After curing, at disassembly of the mold, the weakly adhering gold to glass interface separates, and the gold layer becomes essentially "transferred" to the polymer film (figure 1(B)) [31, 38]. The gold film then can be patterned by standard photolithography and wet chemical etching using potassium iodide and iodine (KI/I_2) chemistry at room temperature (figure 6). The surface of polymer with patterned gold is then coated with a few microns thick layer of Parylene-C (room temperature Gorham method), and windows on the Parylene-C are opened by photolithography and oxygen plasma-based reactive ion etching through the photoresist mask. The final device outline is etched out by laser micromachining. The main advantage of the 'transfer by polymerization' based fabrication is its simplicity, but it has limitations to how accurately the molded polymer film thickness could be controlled.

More recently, the Voit lab began making the polymer substrate by a spin-coating process (figure 5(E)). Spin coating provides precise control over polymer film thickness and allows for additional softening polymer layers to be incorporated into the devices [37, 41, 77]. Disadvantages of the spin-coating process as compared to transfer by polymerization includes larger amounts of wasted monomer solution, and challenges associated with open-surface polymerization in air. Nevertheless, spin-coated polymer thin films of thiol-ene/acrylate composition were found to be extremely smooth at 0.3 nm rms surface roughness (unpublished), providing an excellent substrate for thin-film microfabrication. On this surface, gold is deposited and patterned to serve as electrical wiring, with or without an interlayer of Parylene-C (as discussed earlier in section 3.1.2). Gold is still the choice for making the conductive traces because of its high electrical conductivity (4E7 Sm^{-1}) and its favorable mechanical properties (78 GPa Young's modulus and 27 GPa rigidity modulus) when compared to other metals. A novel solution to pattern high-resolution gold traces was developed in the Voit laboratory (unpublished). It was sought to replace the wet isotropic etching process that produces significant feature edge roughness and size irregularity with polycrystalline gold films deposited by thermal evaporation. "Lift-off" patterning methods use sacrificial photoresist materials to define patterns by blocking and shadowing regions during the deposition process and are known to produce smoother feature edges; however, conventional photoresist-based lift-off layers are incompatible with thiol-ene polymers due to swelling by solvents and etch non-specificity. The Voit group has identified low-stress silicon nitride (SiN) produced by plasma-enhanced chemical vapor deposition (PECVD) as a highly compatible sacrificial material, and developed a bi-layer based lift-off process (unpublished). With this new approach, a gold patterning resolution can be achieved that is only limited by the photolithography equipment, which is approximately 2-micron minimal feature sizes. PECVD SiN became key in another microfabrication process, as it can be employed as hard mask material for the dry etching of the softening polymer thin films. Using a hard mask material (that is of high etch selectivity and virtually acts as an etch stop layer) allows for extended plasma processing and results in high fidelity patterning of polymer thicknesses up to 100 μm or so. The last step of the device fabrication consists of the device release from the carrier substrate, which is either a glass slide or a silicon wafer, by soaking in de-ionized water.

3.4. Processing of active devices

Low-temperature electronics have enabled the capability to add active devices on top of flexible substrates. This represents the possibility to leverage advances from diverse areas such as materials science, the physics of semiconductors, mechanical engineering, chemistry, and biomedical engineering, among others. However, the combination of different disciplines also may increase the complexity required to achieve functional applications. For instance, the synthesis of the flexible substrate is a clear example of combining several disciplines to achieve bioelectronic applications. It requires an appropriate level of chemical knowledge, biocompatibility, and an affinity for semiconductor processing. The fabrication of electronic circuits on top of the flexible substrate will allow addressability in order to stimulate and read electrical signals from the nerves. In addition, mechanical stability plays an important role due to the bending stresses between the substrate and electronic devices, which can affect their performance and lifetime.

Once all the requirements have been met, future active devices should be able to interact with a larger number of stimulation/sensing electrodes. The entire system will be controlled by electronic circuitry and powered/communicated via wireless. Previously, the fabrication of active devices such as thin-film transistors (TFTs) [119–122] and Schottky diodes [123–127] on top of polymer substrates has been reported to achieve the control and communication/energy for flexible applications, respectively.

The fabrication of active or semiconductor devices on top of softening polymer substrates has been previously reported; where standard photolithographic processes are used with photomasks, wet and dry etch, as well as lift-off technique (figure 7) [128–131]. Once the softening polymer is deposited by transfer or spin coating, on top of a glass slide which is its mechanical carrier, the active structure fabrication is done by depositing and patterning multiple layers of films, such as conductors, semiconductors, and dielectrics.

Besides the previous reports about active devices fabricated on top of a softening polymer, there are still issues that need to be addressed to ensure their reliability, such as methods of encapsulation, electrical stability, and mechanical resilience.

3.4.1. Fabrication of transistors

The fabrication of transistors on softening polymeric substrates has been successfully demonstrated [128–130, 132]. The transistors or TFTs were fabricated using a bottom-gate/top-contact configuration (figure 7(D)). First, a gold (Au) layer of 200 nm is deposited by thermal evaporator to define the gate contact. After each film deposition, a patterning process is done using a photolithographic process and using wet etching. Next, 50 nm of hafnium oxide (HfO_2), by atomic layer deposition, is deposited using a chamber temperature of 100 °C as a gate dielectric. The active layer or semiconductor (IGZO) is deposited by sputtering at room temperature. Then, another Au layer of 100 nm is deposited to define the source and drain contacts. Figures 7(A), (B), and (D) show examples of the 3D structures of a transistor fabricated on top of the softening substrate. Finally, the sample with the TFTs is subjected to a temperature treatment of 200 °C for 2 hours.

Posterior to the fabrication, the sample is released from the glass slide for bending stress and electrical characterizations (figure 7). Each transistor is tested, with a semiconductor analyzer, by sweeping the applied voltage at the gate contact (V_{GS}), keeping a constant voltage between the drain source (V_{DS}) and evaluating the current flow through the drain (I_{DS}) and gate (I_{GS}) electrodes. The electrical performance is evaluated by the transfer curve (figure 7(C)) and the transistors channel dimensions (width: W and length: L). The well-accepted MOSFET model (equation (1)) is used to analyze the transistor performance, where C_i is the capacitance density of the HfO_2, μ is the saturation mobility, and V_{TH} the threshold voltage of the transistor:

$$I_{DS} = \frac{W}{2 \cdot L} \mu \cdot C_i \cdot (V_{GS} - V_{TH})^2 \quad (1)$$

Commonly, the IGZO TFTs SMP exhibit a mobility value and V_{TH} of approximately 10 $cm^2V^{-1}s^{-}1$ and 2 V, respectively [132]. Another parameter representing transistor performance is the on/off current ratio, which is 10^6 with a subthreshold swing of 200 mV/decade. Presently, the V_{TH} hysteresis is approximately 0.5 V after 100 electrical cycles (not shown), which could become a problem if the V_{TH} increased. However, this electrical stability can be affected by the lack of an appropriate encapsulation or with a very pronounced physical bend. For this reason, it is also important to perform a durability test with accelerated aging to predict the operational lifetime.

3.4.2. Fabrication of diodes

To minimize risk associated with percutaneous and to reduce the overall size of biosensors and other implantable devices, wireless power transmission is desirable. Wireless power transfer can be accomplished through the transmission of an external radio-frequency (RF) power, a signal receiving it with an antenna, and by performing rectification. One promising approach for implementing rectifiers in neural interfaces is utilizing Schottky diodes based on a semiconductor suitable for thin-film processing [127, 133–137]. Schottky diodes, being majority-carrier devices, possess advantageous properties such as fast switching and high cut-off frequency, making them an

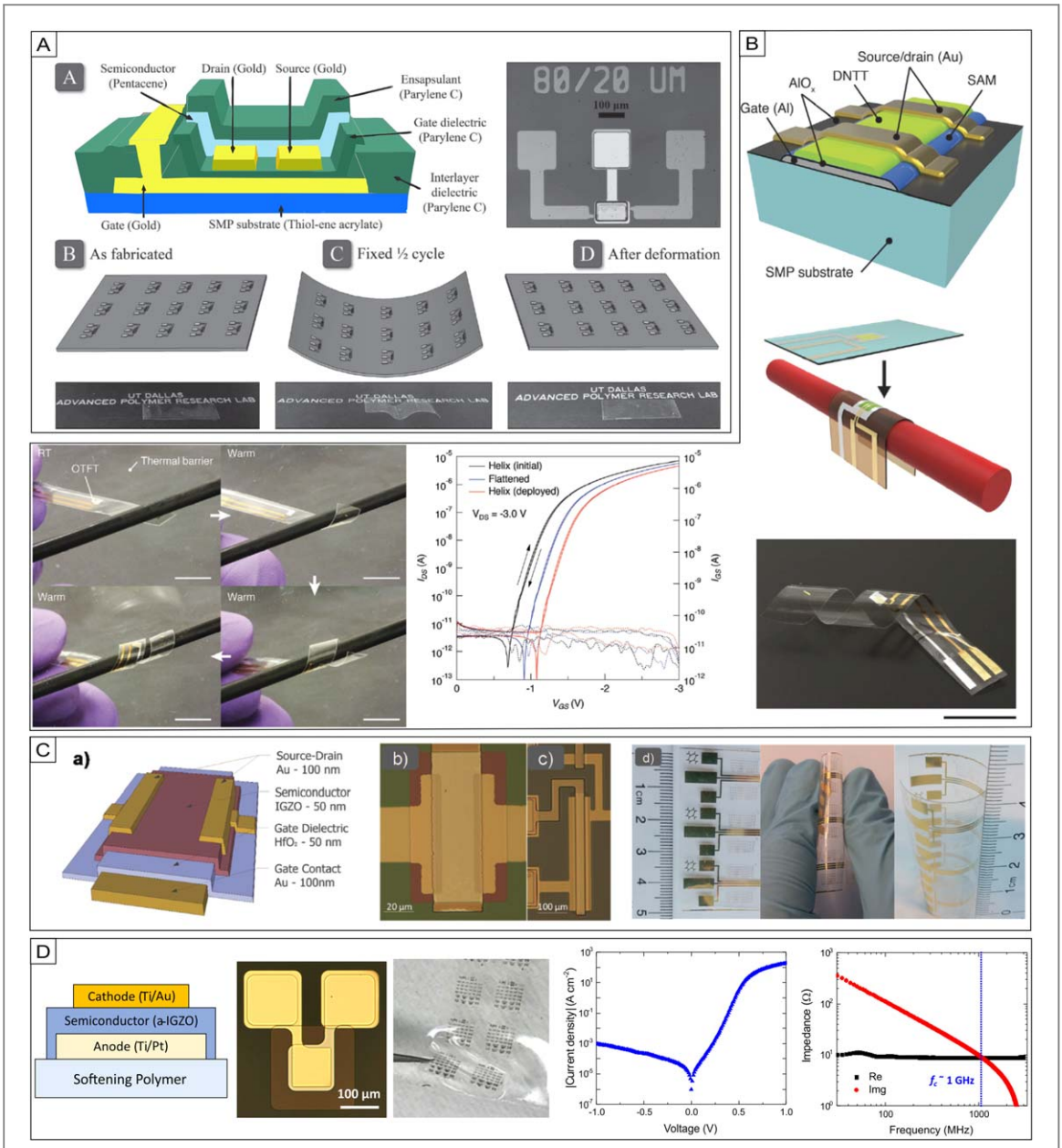

Figure 7. (A) A cross-section schematic (recolored) and optical micrograph of an organic thin-film transistor are shown on top. Devices are pictured on SMP substrates after fabrication, at the fixed (bent) meta-stable shape and after a full shape memory cycle on the bottom. (B) Cross section of an OTFT fabricated on an SMP substrate (top), illustration of an OTFT on an SMP substrate conforming to warm surface (center), and OTFTs are able to deploy from their planar fabrication state to helices with r = 2.25 mm where the scale bar is 10 mm (bottom right). A planar OTFT deploys into a helix and wraps around a rod (r = 2.25 mm) after it passes through a 150 μm-thick opening in a thermal barrier (bottom left). Comparing the transfer curves shows slight shifting of the V_{th} after both thermal deformation steps (bottom center). (C) Indium-gallium-zinc-oxide (IGZO) thin-film transistors (TFTs) shown as a 3D diagram (left) and in optical microscopy images of a single IGZO TFT and a logic inverter circuit using two IGZO TFTs (center). Optical images highlight the thiol-ene-based SMP substrate as it is fixed into a meta-stable shape by applying mechanical deformation and a temperature cycle (right). (D) Thin-film IGZO Schottky diodes on a softening polymer. (a) Cross-sectional device structure. (b) Fabricated single diode (100 μm × 100 μm). (c) Fabricated diodes on a softening polymer. (d) Rectification characteristics. (e) Radio-frequency characteristics. (A) is reproduced from Avendano-Bolivar *et al* [129], (B) is reproduced from Reeder *et al* [128], and (C) is reproduced from Gutierrez-Heredia *et al* [130]

ideal candidate for wireless applications. While there has been an increasing interest in thin-film Schottky diodes [127, 133–137], the current scientific literature gives no reports detailing implementation on multifunctional materials, such as SMPs. There are two challenges in fabricating thin-film Schottky diodes on such novel polymers as a substrate: (1) limited process temperature (<250 °C) and (2) incompatibility of these polymers with organic solvents regularly used in cleanroom photolithography (e.g., acetone). Therefore, both the selection of appropriate anode/semiconductor/cathode materials as well as the modification of conventional fabrication processes are essential for implementing these devices on such polymers.

Figure 7(D) illustrates a preliminary (not published) study on the fabrication of thin-film Schottky diodes on a thiol-ene/acrylate-based SMP. Here, amorphous indium-gallium zinc-oxide (a-IGZO) is used as the

semiconductor and Pt as an anode metal, forming a Pt-IGZO Schottky junction (figure 7). IGZO is chosen due to its high electron mobility >10 $cm^2 V^{-1}s^{-}1$ and low fabrication temperature (<250 °C). Processing techniques, including the use of a sacrificial layer and UV-ozone surface treatment, were employed to make the device fabrication process viable. Figure 7 shows images of a single device and multiple devices fabricated on SMP, respectively. These devices exhibit a maximum rectification ratio of ~105 and a cut-off frequency of approximately 1 GHz. Based on the demonstrated rectification capability and the high operational frequency, these devices may serve as a building block toward more complex circuits that enable wireless powering. Future work includes integration of these diodes with other thin-film components (i.e., antenna and capacitors) to form fully integrated wireless energy harvesting technology.

4. Biocompatibility and sterilization

All devices which are meant to be used for in vivo applications need to be tested toward biocompatibility and need to withstand sterilization to gain regulatory approval [138]. Different SMPs have been tested toward their compatibility to various sterilization methods, which include autoclave, radiation, and ethylene oxide (EtO) [37, 139–141]. Based on these measurements, EtO emerged as a sufficient method that did not change the thermomechanical properties of the temperature and moisture sensitive thiol-ene/acrylate polymers. The sufficiency of the sterilization was confirmed by the low endotoxin levels [37].

The biocompatibility of materials is often initially tested in vitro by cytotoxicity assays following ISO 10993–5 [142]. Various thiol-ene/acrylate SMPs have been tested using fibroblast and cortical neuron cell lines and have proven to be non-cytotoxic [143]. Tests have been performed on material extracts. In all cases the cell viability was significantly above 70%, which is considered to be the threshold for ISO guidance.

Another way to test the biocompatibility of new materials is to test them in vivo in a comparative study to already established materials [144, 145], such as silicone or tungsten. That allows for a study of the biological responses to the materials, which may differ from in vitro testing due to the complexity of the biological tissue in a live environment. Neural devices often lose their recording capabilities due to astrogliosis and neuronal loss near the implant as a result of foreign body responses.

In the case of the softening polymers, silicon devices dip-coated with thiol-ene polymers were compared to pristine silicon shanks having the same dimensions toward their biological response [146]. That study aimed to investigate the influence of the surface chemistry of new materials only, and therefore the factor of the materials stiffness was eliminated. The neuroinflammatory response was evaluated after devices were implanted in the rat cortex for 2 and 16 weeks. It was found that the dip-coated probes are equally tolerated and just as suitable as silicon for neural implant substrates.

5. Durability of devices

It is important to ensure that the bioelectronic devices are durable and stable before they can be translated as commercial products. In vitro methodologies are less expensive and less time consuming than extensive testing in animal models.

The durability of devices can be evaluated in different ways. It is common, to test the basic materials or full devices under aggravated and accelerated aging conditions, to speed up the normal aging process of the materials. The choice of the medium and the storage temperature are important parameters that should be chosen in accordance to the expected in vivo conditions. A typical experiment to speed up the aging process of implantable devices is storage in PBS at temperatures higher than body temperature. Molecular activity doubles in organic molecules for every 10 °C according to a derivation of the Arrhenius equation where the temperature coefficient Q_{10} is chosen to be two, which is a good approximation for most polymers [147–149]. Therefore, storing a product for one month at 47 °C will result in a two-month accelerated aging. Similarly, storing a product at 57 °C for one month will result in an accelerated aging period of four months, and so on.

Another commonly used method for aggravated aging is the use of different, harsher media for aging tests. To accelerate chemical processes such as hydrolysis, samples are aged in a sodium hydroxide (NaOH) solution [28] or with reactive oxygen species such as hydrogen peroxide [26]. However, it is not clear how well such tests mimic degradation processes in vivo.

5.1. Testing of the material

The first step is to test the durability of the substrate material [26, 28, 50, 150, 151]. Only when the basic material is sufficiently stable, can the material be used to fabricate fully functional devices. After the functional polymers are subjected to various aging scenarios and aging times, the durability of the materials is tested with various analytical methods [84, 150]. First, the mass loss of the samples is monitored to detect degradation and estimate the overall

robustness of the material. The aging media can be investigated with methods such as nuclear magnetic resonance (NMR) and gas chromatography–mass spectrometry (GS-MS) to detect degradation products and to validate degradation mechanisms. Especially when functional materials are tested, it also important to determine any changes in thermomechanical properties using a dynamic mechanical analysis (DMA), differential scanning calorimetry (DSC), a thermal gravimetric analysis (TGA), and tensile testing. These methods can provide information on structural changes of the polymer due to degradation and decomposition. It was found that the thiol-ene/acrylate polymers are stable up to four weeks under accelerated aging in PBS at 75 °C, roughly translating to 13 months at body temperature before initiating hydrolysis [84]. While this time period is enough for most of the chronic small animal experiments, which usually last three to six months, for pursuing clinical applications it is necessary to have polymers that are stable for years. A newly developed thiol-ene polymer consists of ester-free monomers and may therefore become a promising candidate for future, long-use devices. A recent study has shown that this polymer is stable for the equivalent of years under hydrolytic conditions [84].

Many neural interfaces utilize a very simple device component, the electrode, which is simply composed of a conductive material as the interface sending and receiving electrical signals, and an insulator to specify the target area of interaction and prevent unwanted signal transmission between traces and outside the device. With larger implant devices, like the stimulators used in deep brain implantation therapeutics, insulation can be nearly a millimeter thick, which is very adequate for the application, but as many neural implants are reduced in size to decrease implantation invasiveness and increase target specificity, the insulation is often reduced to only a few micrometers. Electrical properties like electrical permittivity and resistivity now become extremely important as they directly affect negative qualities like shunt capacitance and electrical leakage [152–154].

While there are many different methods to evaluate a materials electrical property, a few have been selected as guidelines by standards groups like by the American Society for Testing and Materials (ASTM International) and the Association Connecting Electronics Industries (IPC) [155–158]. Insulators, which are utilized for low power signal applications, would optimally have a low permittivity to reduce parasitic capacitance, and a high resistivity to reduce electrical leakage between adjacent traces and the external electrolytic environment. The standards use capacitors that would then be characterized across a large range of frequencies for complex impedance, while resistivity is usually determined using the actual leakage current measured between two electrodes after the application of DC voltage.

Neural interfaces function within an electrolytic environment, and many are required to function chronically. Many of these standard techniques evaluating electrical properties of dielectric materials become complicated or even impossible due to the presence of mobile ionic substances in the environment around the capacitor and its electrodes. Additionally, it has been shown that insulator properties for many materials change within the electrolyte when compared to the parameters obtained in a dry environment. The absorption of water, an easily polarizable substance, into the matrix of a material tends to increase relative permittivity and can lead to physical insulation failure due to swelling and degeneration [159–162]. Ionic substances have also been shown to diffuse into the material, creating both conductive pathways as well as the formation of random electrical fields that can influence overall relative permittivity [163, 164]. J Murry [165–167] describes the methodology to examine dielectric properties of insulation immersed within electrolytes. The material under test is placed on a conductive medium on one side, while the opposite side is placed in contact with an electrolyte, creating a parallel plate capacitor. A counter electrode is placed into the electrolyte completing the circuit and allowing an electrochemical impedance analysis and subsequent characterization to determine the overall electrical properties. When the characterization is complete, it can be determined if any novel material would be appropriate for applications for neural interface insulation, and this characterization is extremely important when considering the fabrication of chronic devices that require months, to even years, of reliable device functionality.

5.2. Testing of material interfaces

For the fabrication of multimaterial devices, it is important to ensure sufficient interlayer adhesion so that the devices will not fail due to delamination or leakage [107]. There are multiple material interfaces within one device, including polymer–polymer, polymer–metal, and metal–metal. The adhesion between two materials can be tested by peel tests, which include a T-peel test [115, 168, 169], by scratch tests [113], and by tape tests [114]. Usually these tests are done directly after fabrication and test how much force is needed to delaminate the two layers. However, in the case of the implantable devices, it is also necessary to test the interlayer adhesion after soaking under physiological conditions. The adhesion properties might change upon soaking in various media due to differences in swelling and hydrophobicity. It is also helpful to optically inspect the samples for defects. Typical procedures to enhance the adhesion between layers include plasma treatment or the use of adhesion promoting substances including A-174 silane [87, 116, 170, 171]. In the case of an unpublished study where the influence of various surface treatments, including mild oxygen plasma and A-174 adhesion promoter on the

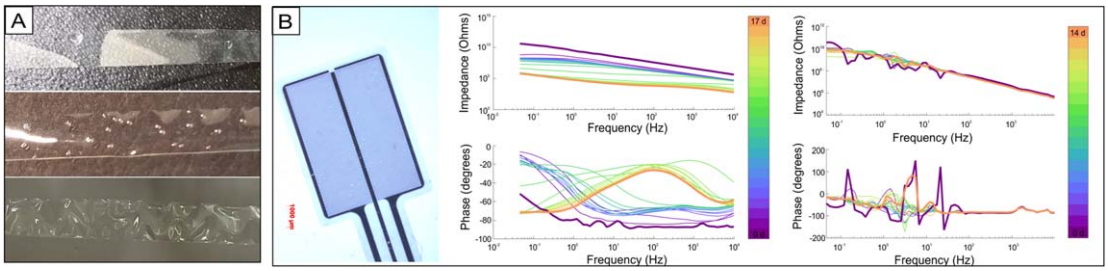

Figure 8. (A) SMP to SMP adhesion after accelerated aging in PBS at 75 °C. (B) Optical micrograph of a shape memory polymer interdigitated electrode (SMP-IDE) used for the testing (left), a Bode plot displaying real impedance and phase obtained from a SMP-IDE using electrochemical impedance spectroscopy (EIS; center), and a Bode plot obtained from EIS data showing an SMP-IDE supported by a 1 μm-thick Parylene-C inner insulator surrounding the electrode and traces (right).

adhesion, were tested in over the course of four weeks in 77 °C warm PBS, obvious defects like solvent pockets were visible to the naked eye (figure 8(A)). It tuned out that the oxygen plasma alters the polymeric surface in a way that reduces the adhesion to its adjacent layers. These findings are in line with a study of Vishnuvarthanan *et al* [170] who have investigated the effect of the oxygen plasma treatment of polypropylene films.

The variable reliability of chronically implanted neural interface devices has been one of the factors reducing their use in widespread clinical translation [172–177]. Many novel materials have been proposed as a solution to these issues; for instance, shape memory polymers may provide an ideal platform to increase device reliability by becoming more compliant after implantation [37, 38, 41]. However, many of these materials have only been characterized individually, and nothing is known about the complete interaction with other materials. As expounded upon in the last section, an physical failure mechanism has been identified as insulation failure attributed to moisture absorption and ionic uptake. This, in turn, leads to the modulation of dielectric properties and plays a contributing factor to material degradation, swelling, and delamination [20, 38, 178]. To ensure that novel materials can be utilized in a neural interface, evaluation should include an examination of the ability of the insulating material to reliably withstand a simulated physiological environment while also providing protection for the conductive electrode materials.

Investigating the integrity of the novel neural device insulation material has been demonstrated using specialized interdigitated electrode devices (IDE) [179]. These specialized IDE contain at least two electrodes totally encapsulated within the insulation materials, and should use the final material stack that has been exposed to the full array of fabrication processes. IDE characterization consists of at least three electrochemical measurements, performed using a two-contact measurement mode, and performed within an appropriate electrolytic environment. These methods include electrochemical impedance spectroscopy (EIS), cyclic voltammetry (CV), and chronoamperometry (CA) [179–182]. Conductive pathways in either the insulating material between the electrodes or formed from one electrode to the outside electrolytic environment will decrease the high impedance and increase the leakage current. In addition to testing under ambient conditions, the IDE characterization provides methods to examine device performance over time through accelerated aging based on the Arrhenius' relationship [179–181].

Interdigitated devices have been used to verify thiol-ene/acrylate-based shape memory polymers with gold electrodes within PBS (unpublished work). The initial device consisted simply of 15 μm of SMP surrounding gold electrodes and was evaluated at 37 °C. Figure 8(B) shows the impedance and phase obtained from EIS plotted for each day. Failure was quantitatively determined if the impedance at 1 Hz fell below 10^8 Ω, while a qualitative analysis was required if the phase angle increased above −80° at 1 Hz. Failure criteria was achieved six days after PBS immersion, although changes in phase hinted to the instability of the device just hours after immersion as the phase increased to −60° at 1 Hz. Figure 8(b) demonstrates a more complicated IDE device. 30 μm of SMP serves as a back substrate for mechanical stability, while 5 μm of SMP on the top side serves to maintain a small relative distance to the surface to reduce signal degradation. 1 μm of Parylene-C surrounds each of the electrodes to provide a boost to insulation. The device was measured under accelerated conditions at a temperature of 60 °C, increasing the time of exposure from 14 to 70 days. The addition of a small amount of Parylene-C around the electrodes allowed the integrity of the insulation to be maintained, with impedance well above 10^9 Ω and a phase pf ~80° at 1 Hz. The data in Figure 8 shows that while SMP is a material with the mechanical advantage to soften into a more compliant state when exposed to water, the absorption of water has a negative effect on its ability to provide adequate insulation for small devices, like cortical implants. The addition of a small layer of Parylene-C directly around the electrode and trace materials provides an adequate amount of protection and will be used in the fabrication of future devices.

5.3. Testing of device functionality

The development of novel multifunctional materials for biomedical devices requires many hours of characterization and design. We have discussed the importance of the characterization for both physical and electrical properties as well as the evaluation of material reliability. A full characterization of these factors will enable the intelligent design of a neural interface device that can be designed to optimally interact with the neural environment for long periods. After the fabrication of the final device, device characterization is normally conducted with a focus on the electrochemical interaction between a working electrode and the external electrochemical environment. These tests will evaluate not only the electrochemical impedance of the electrode and its ability to send and store charge, but it can also detect possible issues with the insulating materials. Many publications used these methods to establish functionality of neural interface devices, reporting on electrodes not only composed of commonly used conductors like gold, platinum, and iridium, but also many other novel materials like the ceramic-like conductor coatings titanium nitride (TiN) and iridium oxide, and conductive polymer coatings like PEDOT [102, 183–185].

6. Future directions and conclusions

The use of multifunctional materials as a substrate material for neural interfaces is a promising approach, which helps to improve the device–tissue interaction for multiple applications. These applications range from cortical probes to spinal cord stimulators and peripheral nerve cuffs. The benefit of the softening, thin-film devices is not only that they approach the tissue modulus after implantation and that they are compliant, but they are also far less brittle than traditional silicon devices and are therefore robust against fracture upon insertion. Another benefit of the use of softening polymeric substrates is that they are compatible with most of the microfabrication processes, which enables the fabrication of complex and versatile devices, similar to other polymeric substrates such as polyimide [48, 49], SU-8 [55], and Parylene-C [14, 186]. Although the basic concepts could be successfully demonstrated, and first chronic in vivo studies have been performed, there remain several technological challenges. The long-term stability and robustness of these SMP devices have yet to be proven. Interlayer adhesion seems to be one of the next critical hurdles, which needs to be surmounted to fabricate chronically reliable devices. Another important aspect for future devices is the integration of active components, such as transistors and diodes, to create complex and high throughput devices capable of wireless signaling and powering.

Acknowledgments

This work was supported by the Office of the Assistant Secretary of Defense for Health Affairs through the Peer Reviewed Medical Research Program under Award No. W81XWH-15-1-0607. Opinions, interpretations, conclusions, and recommendations are those of the authors and are not necessarily endorsed by the Department of Defense. In addition, this work was supported by a DARPA subcontract to D17PC00111 and the Center for Engineering Innovation at the University of Texas at Dallas. Lastly, this work was supported by NIH R21EB020318.

ORCID iDs

Melanie Ecker https://orcid.org/0000-0002-0603-6683
Alexandra Joshi-Imre https://orcid.org/0000-0002-4271-1623
Romil Modi https://orcid.org/0000-0002-0436-7403
Aldo Garcia-Sandoval https://orcid.org/0000-0002-6616-1179
Gerardo Gutierrez-Heredia https://orcid.org/0000-0002-9198-1822
Joseph J Pancrazio https://orcid.org/0000-0001-8276-3690
Walter E. Voit https://orcid.org/0000-0003-0135-0531

References

[1] Choi S, Lee H, Ghaffari R, Hyeon T and Kim D-H 2016 Recent advances in flexible and stretchable bio-electronic devices integrated with nanomaterials *Adv. Mater.* **28** 4203–18
[2] Yokota T *et al* 2015 Ultraflexible, large-area, physiological temperature sensors for multipoint measurements *Proc. Natl. Acad. Sci. USA* **112** 14533–8
[3] Lee S *et al* 2016 A transparent bending-insensitive pressure sensor *Nat Nano* **11** 472–8

[4] Nakamura T, Yokota T, Terakawa Y, Reeder J, Voit W, Someya T and Sekino M 2016 Development of flexible and wide-range polymer-based temperature sensor for human bodies *2016 IEEE-EMBS Int. Conf. on Biomedical and Health Informatics (BHI) 24-27 Feb. 2016* pp 485–8
[5] Lu H, Yao Y and Lin L 2015 Temperature sensing and actuating capabilities of polymeric shape memory composite containing thermochromic particles *Pigm. Resin. Technol.* **44** 224–31
[6] Schlierf R, Horst U, Ruhl M, Schmitz-Rode T, Mokwa W and Schnakenberg U 2007 A fast telemetric pressure and temperature sensor system for medical applications *J. Micromech. Microeng.* **17** S98
[7] Moser Y and Gijs M A M 2007 Miniaturized flexible temperature sensor *J. Microelectromech. Syst.* **16** 1349–54
[8] Urban G *et al* High-resolution thin-film temperature sensor arrays for medical applications *Sensors and Actuators A: Physical* 1990 **22** 650–4
[9] Gaj M P, Wei A, Fuentes-Hernandez C, Zhang Y, Reit R, Voit W, Marder S R and Kippelen B 2015 Organic light-emitting diodes on shape memory polymer substrates for wearable electronics *Org. Electron.* **25** 151–5
[10] Pancrazio J J, Deku F, Ghazavi A, Stiller A M, Rihani R, Frewin C L, Varner V D, Gardner T J and Cogan S F 2017 Thinking small: progress on microscale neurostimulation technology *Neuromodulation: Technology at the Neural Interface* n/a-n/a (https://doi.org/10.1111/ner.12716)
[11] Szostak K M, Grand L and Constandinou T G 2017 Neural interfaces for intracortical recording: requirements, fabrication methods, and characteristics *Frontiers in Neuroscience* **11** 665
[12] Luan L *et al* 2017 Ultraflexible nanoelectronic probes form reliable, glial scar–free neural integration *Science Advances* **3** E1601966
[13] Patil A C and Thakor N V 2016 Implantable neurotechnologies: a review of micro- and nanoelectrodes for neural recording *Med. Biol. Eng. Comput.* **54** 23–44
[14] Hara S A, Kim B J, Kuo J T W, Lee C D, Meng E and Pikov V 2016 Long-term stability of intracortical recordings using perforated and arrayed Parylene sheath electrodes *J. Neural Eng.* **13** 066020
[15] Lee J H, Kim H, Kim J H and Lee S-H 2016 Soft implantable microelectrodes for future medicine: prosthetics, neural signal recording and neuromodulation *Lab on a Chip* **16** 959–76
[16] Sridharan A, Nguyen J K, Capadona J R and Muthuswamy J 2015 Compliant intracortical implants reduce strains and strain rates in brain tissue *in vivo J. Neural Eng.* **12** 036002
[17] Jorfi M, Skousen J L, Weder C and Capadona J R 2015 Progress towards biocompatible intracortical microelectrodes for neural interfacing applications *J. Neural Eng.* **12** 011001
[18] Hudson F, Coulshed D, D'Souza E and Baker C 2010 Effect of radiation therapy on the latest generation of pacemakers and implantable cardioverter defibrillators: a systematic review *Journal of Medical Imaging and Radiation Oncology* **54** 53–61
[19] Beck H, Boden W E, Patibandla S, Kireyev D, Gupta V, Campagna F, Cain M E and Marine J E 50th anniversary of the first successful permanent pacemaker implantation in the united states: historical review and future directions *American Journal of Cardiology* **106** 810–8
[20] Teo A J T, Mishra A, Park I, Kim Y-J, Park W-T and Yoon Y-J 2016 Polymeric Biomaterials for Medical Implants and Devices *ACS Biomaterials Science & Engineering* **2** 454–72
[21] Hassler C, Boretius T and Stieglitz T 2011 Polymers for neural implants *J. Polym. Sci., Part B: Polym. Phys.* **49** 18–33
[22] Lacour S P, Courtine G and Guck J 2016 Materials and technologies for soft implantable neuroprostheses *Nature Reviews Materials* **1** 16063
[23] Fattahi P, Yang G, Kim G and Abidian M R 2014 A review of organic and inorganic biomaterials for neural interfaces *Adv. Mater.* **26** 1846–85
[24] Fekete Z and Pongrácz A 2017 Multifunctional soft implants to monitor and control neural activity in the central and peripheral nervous system: a review *Sensors Actuators B: Chem.* **243** 1214–23
[25] Green R A, Lovell N H, Wallace G G and Poole-Warren L A 2008 Conducting polymers for neural interfaces: challenges in developing an effective long-term implant *Biomaterials* **29** 3393–9
[26] Takmakov P, Ruda K, Phillips K S, Isayeva I S, Krauthamer V and Welle C G , 2015 Rapid evaluation of the durability of cortical neural implants using accelerated aging with reactive oxygen species *J. Neural Eng.* **12** 026003
[27] Ryu S I and Shenoy K V 2009 Human cortical prostheses: lost in translation ? *Neurosurgical Focus* **27** E5
[28] Reit R, Zamorano D, Parker S, Simon D, Lund B, Voit W and Ware T H 2015 Hydrolytically stable thiol–ene networks for flexible bioelectronics *ACS Appl. Mater. Interfaces* **7** 28673–81
[29] Simon D, Ware T, Marcotte R, Lund B, Smith D Jr, Prima M, Rennaker R and Voit W 2013 A comparison of polymer substrates for photolithographic processing of flexible bioelectronics *Biomed. Microdevices* **15** 925–39
[30] Ware T *et al* Three-dimensional flexible electronics enabled by shape memory polymer substrates for responsive neural interfaces *Macromol. Mater. Eng.* 2012 **297** 1193–202
[31] Ware T, Simon D, Arreaga-Salas D E, Reeder J, Rennaker R, Keefer E W and Voit W 2012 Fabrication of responsive, softening neural interfaces *Adv. Funct. Mater.* **22** 3470–9
[32] Grill W M, Norman S E and Bellamkonda R V 2009 Implanted neural interfaces: biochallenges and engineered solutions In *Annu. Rev. Biomed. Eng.* **11** 1–24
[33] Barrese J C, Rao N, Paroo K, Triebwasser C, Vargas-Irwin C, Franquemont L and Donoghue J P 2013 Failure mode analysis of silicon-based intracortical microelectrode arrays in non-human primates *J. Neural Eng.* **10** 066014
[34] Biran R, Martin D C and Tresco P A 2005 Neuronal cell loss accompanies the brain tissue response to chronically implanted silicon microelectrode arrays *Exp. Neurol.* **195** 115–26
[35] Polikov V S, Tresco P A and Reichert W M 2005 Response of brain tissue to chronically implanted neural electrodes *J. Neurosci. Methods* **148** 1–18
[36] Subbaroyan J, Martin D C and Kipke D R 2005 A finite-element model of the mechanical effects of implantable microelectrodes in the cerebral cortex *J. Neural Eng.* **2** 103
[37] Ecker M, Danda V, Shoffstall A J, Mahmood S F, Joshi-Imre A, Frewin C L, Ware T H, Capadona J R, Pancrazio J J and Voit W E 2017 Sterilization of thiol-ene/acrylate based shape memory polymers for biomedical applications *Macromol. Mater. Eng.* **302** 1600331
[38] Ware T, Simon D, Liu C, Musa T, Vasudevan S, Sloan A, Keefer E W, Rennaker R L II and Voit W 2014 Thiol-ene/acrylate substrates for softening intracortical electrodes *J. Biomed. Mater. Res. Part* B **102** 1–11
[39] Ware T, Simon D, Hearon K, Kang T H, Maitland D J and Voit W 2013 Thiol-click chemistries for responsive neural interfaces *Macromol. Biosci.* **13** 1640–7
[40] Ware T, Simon D, Rennaker R L II and Voit W 2013 Smart polymers for neural interfaces *Polymer Reviews* **53** 108–29

[41] Do D-H, Ecker M and Voit W E 2017 Characterization of a thiol-ene/acrylate-based polymer for neuroprosthetic implants *ACS Omega* **2** 4604–11
[42] Stiller A M *et al* 2018 Chronic intracortical recording and electrochemical stability of thiol-ene/acrylate shape memory polymer electrode Arrays. *Micromachines* **9** 500
[43] Simon D M *et al* Design and demonstration of an intracortical probe technology with tunable modulus *J. Biomed. Mater. Res. Part* A 2017 **105** 159–68
[44] Stiller A *et al* Chronic intracortical recording and electrochemical stability of thiol-ene/acrylate shape memory polymer electrode arrays *Micromachines* 2018 **9** 500
[45] Weltman A, Yoo J and Meng E 2016 Flexible, penetrating brain probes enabled by advances in polymer microfabrication *Micromachines* **7** 180
[46] Seymour J P and Kipke D R 2007 Neural probe design for reduced tissue encapsulation in CNS *Biomaterials* **28** 3594–607
[47] HajjHassan M, Chodavarapu V and Musallam S 2008 NeuroMEMS: neural probe microtechnologies *Sensors* **8** 6704
[48] Stieglitz T, Beutel H R, Schuettler M and Meyer J U 2000 Micromachined, polyimide-based devices for flexible neural interfaces *Biomed. Microdevices* **2** 283–94
[49] Rousche P J, Pellinen D S, Pivin D P, Williams J C, Vetter R J and Kipke D R 2001 Flexible polyimide-based intracortical electrode arrays with bioactive capability *IEEE Trans. Biomed. Eng.* **48** 361–71
[50] Rubehn B and Stieglitz T 2010 *In vitro* evaluation of the long-term stability of polyimide as a material for neural implants *Biomaterials* **31** 3449–58
[51] Tooker A, Tolosa V, Shah K G, Sheth H, Felix S, Delima T and Pannu S 2012 Polymer neural interface with dual-sided electrodes for neural stimulation and recording *2012 Annual Int. Conf. of the IEEE Engineering in Medicine and Biology Society Aug. 28 2012–Sept. 1 2012* pp 5999–6002
[52] Mercanzini A, Cheung K, Buhl D L, Boers M, Maillard A, Colin P, Bensadoun J-C, Bertsch A and Renaud P 2008 Demonstration of cortical recording using novel flexible polymer neural probes *Sensors and Actuators A: Physical* **143** 90–6
[53] Fernández L J, Altuna A, Tijero M, Gabriel G, Villa R, Rodríguez M J, Batlle M, Vilares R, Berganzo J and Blanco F J 2009 Study of functional viability of SU-8-based microneedles for neural applications *J. Micromech. Microeng.* **19** 025007
[54] multimodal A 2015 SU-8—platinum—polyimide microelectrode array for chronic *in vivo* neurophysiology *PLoS One* **10** e0145307
[55] Wei X, Luan L, Zhao Z, Li X, Zhu H, Potnis O and Xie C Nanofabricated ultraflexible electrode arrays for high-density intracortical recording *Adv. Sci.* **0** 1700625
[56] Takeuchi S, Ziegler D, Yoshida Y, Mabuchi K and Suzuki T 2005 Parylene flexible neural probes integrated with microfluidic channels *Lab on a Chip* **5** 519–23
[57] Rodger D C *et al* 2008 Flexible parylene-based multielectrode array technology for high-density neural stimulation and recording *Sensors and Actuators B-Chemical* **132** 449–60
[58] Kim B J, Gutierrez C A and Meng E 2015 Parylene-based electrochemical-MEMS force sensor for studies of intracortical probe insertion mechanics *J. Microelectromech. Syst.* **24** 1534–44
[59] Lo M-C *et al* 2018 Evaluating the *in vivo* glial response to miniaturized parylene cortical probes coated with an ultra-fast degrading polymer to aid insertion *J. Neural Eng.* **15** 036002
[60] Fornari R V, Wichmann R, Atsak P, Atucha E, Barsegyan A, Beldjoud H, Messanvi F, Thuring C M A and Roozendaal B 2012 Rodent stereotaxic surgery and animal welfare outcome improvements for behavioral neuroscience *J. Vis. Exp.* 3528
[61] Kozai T D Y and Kipke D R 2009 Insertion shuttle with carboxyl terminated self-assembled monolayer coatings for implanting flexible polymer neural probes in the brain *J. Neurosci. Methods* **184** 199–205
[62] Sohal H S, Jackson A, Jackson R, Clowry G J, Vassilevski K, O'Neill A and Baker S N 2014 The sinusoidal probe: a new approach to improve electrode longevity *Frontiers in Neuroengineering* **7** 10
[63] Felix S, Shah K, George D, Tolosa V, Tooker A, Sheth H, Delima T and Pannu S 2012 Removable silicon insertion stiffeners for neural probes using polyethylene glycol as a biodissolvable adhesive *Conf. Proc. IEEE Eng. Med. Biol. Soc.* pp 871–4
[64] Foley C P, Nishimura N, Neeves K B, Schaffer C B and Olbricht W L 2009 Flexible microfluidic devices supported by biodegradable insertion scaffolds for convection-enhanced neural drug delivery *Biomed. Microdevices* **11** 915
[65] Lewitus D, Smith K L, Shain W and Kohn J 2011 Ultrafast resorbing polymers for use as carriers for cortical neural probes *Acta Biomater.* **7** 2483–91
[66] Shoffstall A J, Srinivasan S, Willis M, Stiller A M, Ecker M, Voit W E, Pancrazio J J, Capadona J R and Mosquito A 2018 Inspired strategy to implant microprobes into the brain *Sci. Rep.* **8** 122
[67] Grill W M and Mortimer J T 1994 Electrical properties of implant encapsulation tissue *Ann. Biomed. Eng.* **22** 23–33
[68] González-González M A, Kanneganti A, Joshi-Imre A, Hernandez-Reynoso A G, Bendale G, Modi R, Ecker M, Khurram A, Cogan S F, Voit W E and Romero-Ortega M I 2018 Thin film multi-electrode softening cuffs for selective neuromodulation *Sci. Rep.* **8** 16390
[69] Loeb G E and Peck R A 1996 Cuff electrodes for chronic stimulation and recording of peripheral nerve activity *J. Neurosci. Methods* **64** 95–103
[70] Lacour S P, Benmerah S, Tarte E, FitzGerald J, Serra J, McMahon S, Fawcett J, Graudejus O, Yu Z and Morrison B 2010 Flexible and stretchable micro-electrodes for *in vitro* and *in vivo* neural interfaces *Med. Biol. Eng. Comput.* **48** 945–54
[71] Guo L, Ma M, Zhang N, Langer R and Anderson D G 2014 Stretchable polymeric multielectrode array for conformal neural interfacing *Advanced materials (Deerfield Beach, Fla.)* **26** 1427–33
[72] Lee S H, Jung J H, Chae Y M, Suh J-K F and Kang J Y 2010 Fabrication and characterization of implantable and flexible nerve cuff electrodes with Pt, Ir and IrOx films deposited by RF sputtering *J. Micromech. Microeng.* **20** 035015
[73] Modi R M and Voit W V 2017 High-density neural interface on softening substrate *Brain Stimul.* **10** 455
[74] Panjabi M M, Crisco J J, Vasavada A, Oda T, Cholewicki J, Nibu K and Shin E 2001 Mechanical properties of the human cervical spine as shown by three-dimensional load-displacement curves *Spine (Phila Pa 1976)* **26** 2692–700
[75] Minev I R *et al* 2015 Electronic dura mater for long-term multimodal neural interfaces *Science* **347** 159
[76] Epstein L J and Palmieri M 2012 Managing chronic pain with spinal cord stimulation *The Mount Sinai journal of medicine, New York* **79** 123–32
[77] Garcia-Sandoval A *et al* 2018 Chronic softening spinal cord stimulation arrays *J. Neural Eng.* **15** 045002
[78] Arreaga-Salas D E, Avendaño-Bolívar A, Simon D, Reit R, Garcia-Sandoval A, Rennaker R L and Voit W 2015 Integration of high-charge-injection-capacity electrodes onto polymer softening neural interfaces *ACS Appl. Mater. Interfaces* **7** 26614–23
[79] Ecker M, Danda V, Pancrazio J and Voit W 2016 Sterilization of softening shape memory polymers used as substrate for neural devices *NANS 2 NIC-Neural Interfaces Joint Meeting (Baltimore, MD Vol. June 25–29, 2016)*

[80] Modi R and Voit W 2016 Recent advances in photolithographically defined neural interfaces on softening substrates *NANS2-Neural Interfaces Joint Meeting (Baltimore, MD)*
[81] Modi R and Voit W 2016 Neural interfaces with photolithographically-defined softening substrates *BMES—Biomedical Engineering Society—2016 Annual Meeting* (Minneapolis, MN)
[82] Won S M, Song E, Zhao J, Li J, Rivnay J and Rogers J A 2018 Recent advances in materials, devices, and systems for neural interfaces *Adv. Mater.* **30** 1800534
[83] Immergut E H and Mark H F 1965 Principles of plasticization *Plasticization and Plasticizer Processes* vol 48 (Washington, DC: American Chemical Society) pp 1–26
[84] Hosseini S M, Rihani R, Batchelor B, Stiller A M, Pancrazio J J, Voit W E and Ecker M 2018 Softening shape memory polymer substrates for bioelectronic devices with improved hydrolytic stability *Front. in Mater.* **5:66**
[85] Zeniieh D, Ledernez L and Urban G 2014 Parylene-C as High Performance Encapsulation Material for Implantable Sensors *Procedia Engineering* **87** 1398–401
[86] Rizzi F, Qualtieri A, Chambers L D, Megill W M and De Vittorio M 2013 Parylene conformal coating encapsulation as a method for advanced tuning of mechanical properties of an artificial hair cell *Soft Matter* **9** 2584–8
[87] Hassler C, von Metzen R P, Ruther P and Stieglitz T 2010 Characterization of parylene C as an encapsulation material for implanted neural prostheses *Journal of Biomedical Materials Research Part B: Applied Biomaterials* **93B** 266–74
[88] Park S I *et al* , 2015 stretchable, fully implantable miniaturized optoelectronic systems for wireless optogenetics *Nat. Biotechnol.* **33** 1280
[89] Wurth S *et al* 2017 Long-term usability and bio-integration of polyimide-based intra-neural stimulating electrodes *Biomaterials* **122** 114–29
[90] Subbaroyan J and Kipke D R 2006 The role of flexible polymer interconnects in chronic tissue response induced by intracortical microelectrodes—a modeling and an *in vivo* study *Engineering in Medicine and Biology Society, 2006. EMBS '06. 28th Annual Int. Conf. of the IEEE* Aug. 30 2006–Sept. 3 2006 pp 3588–91
[91] Nedoma J, Fajkus M and Vasinek V 2016 *Proc. SPIE* **9994** 99940P
[92] Lachhman S, Zorman C A and Ko W H 2012 Multi-layered poly-dimethylsiloxane as a non-hermetic packaging material for medical MEMS *Conference proceedings : ... Annual International Conference of the IEEE Engineering in Medicine and Biology Society. IEEE Engineering in Medicine and Biology Society. Conference* **2012** 1655–8
[93] Kim S H, Moon J-H, Kim J H, Jeong S M and Lee S-H 2011 Flexible, stretchable and implantable PDMS encapsulated cable for implantable medical device *Biomedical Engineering Letters* **1** 199
[94] Rajaraman V, Pakula L S, Pham H T M, Sarro P M and French P J 2009 Robust Wafer-level thin-film encapsulation of microstructures using low stress PECVD silicon carbide *2009 IEEE 22nd Int. Conf. on Micro Electro Mechanical Systems* 25–29 Jan. 2009 pp 140–3
[95] Hsu J-M, Tathireddy P, Rieth L, Normann A R and Solzbacher F 2007 Characterization of a-SiC(x):H thin films as an encapsulation material for integrated silicon based neural interface devices *Thin Solid Films* **516** 34–41
[96] Song E *et al* 2017 Thin, transferred layers of silicon dioxide and silicon nitride as water and ion barriers for implantable flexible electronic systems *Advanced Electronic Materials* **3** 1700077
[97] Krimmel E F, Hezel R, Nohl U and Bohrer R 1991 Silicon nitride in encapsulation and recrystallization *Si Silicon: Silicon Nitride in Microelectronics and Solar Cells* ed E F Krimmel, R Hezel, U Nohl, R Bohrer, A Pebler and F Schröder (Berlin, Heidelberg: Springer Berlin Heidelberg) pp 99–118
[98] Lee Y K, Yu K J, Kim Y, Yoon Y, Xie Z, Song E, Luan H, Feng X, Huang Y and Rogers J A 2017 Kinetics and chemistry of hydrolysis of ultrathin, thermally grown layers of silicon oxide as biofluid barriers in flexible electronic systems *ACS Appl. Mater. Interfaces* **9** 42633–8
[99] Xie X, Rieth L, Williams L, Negi S, Bhandari R, Caldwell R, Sharma R, Tathireddy P and Solzbacher F 2014 Long-term reliability of Al2O3 and Parylene C bilayer encapsulated Utah electrode array based neural interfaces for chronic implantation *J. Neural Eng.* **11** 026016–026016
[100] Branch B, Schei J L, Gupta G, Dattelbaum A M, Petsev D N and George J S 2015 Micropillar electrode array: from metal to dielectric interface *IEEE Sens. J.* **15** 4992–5000
[101] Simon D T, Gabrielsson E O, Tybrandt K and Berggren M 2016 Organic bioelectronics: bridging the signaling gap between biology and technology *Chem. Rev.* **116** 13009–41
[102] Cogan S F 2008 Neural stimulation and recording electrodes *Annu. Rev. Biomed. Eng.* **10** 275–309
[103] Gilmour A D, Goding J, Poole-Warren L A, Thomson C E and Green R A 2015 *In vitro* biological assessment of electrode materials for neural interfaces *2015 7th Int. IEEE/EMBS Conf. on Neural Engineering (NER)* 22–24 April 2015pp 450–3
[104] Won S M, Song E, Zhao J, Li J, Rivnay J and Rogers J A 2018 Recent advances in materials, devices, and systems for neural interfaces *Adv. Mater.* **30** 1800534
[105] Garcia-Sandoval A *et al* , 2018 Chronic softening spinal cord stimulation arrays *J. Neural Eng.* **15** 045002
[106] Haldorai Y, Hwang S K, Gopalan A I, Huh Y S, Han Y K, Voit W, Sai-Anand G and Lee K P 2016 Direct electrochemistry of cytochrome c immobilized on titanium nitride/multi-walled carbon nanotube composite for amperometric nitrite biosensor *Biosens. Bioelectron.* **79** 543–52
[107] Wellman S M, Eles J R, Ludwig K A, Seymour J P, Michelson N J, McFadden W E, Vazquez A L and Kozai T D Y 2018 A materials roadmap to functional neural interface design *Adv. Funct. Mater.* **28** 1701269
[108] Li S, Su Y and Li R 2016 Splitting of the neutral mechanical plane depends on the length of the multi-layer structure of flexible electronics *Proceedings. Mathematical, Physical, and Engineering Sciences/The Royal Society* **472** 20160087
[109] Kim W, Lee I, Kim D Y, Yu Y-Y, Jung H-Y, Kwon S, Park W S and Kim T-S 2017 Controlled multiple neutral planes by low elastic modulus adhesive for flexible organic photovoltaics *Nanotechnology* **28** 194002
[110] Fan Z, Zhang Y, Ma Q, Zhang F, Fu H, Hwang K-C and Huang Y 2016 A finite deformation model of planar serpentine interconnects for stretchable electronics *Int. J. Solids Struct.* **91** 46–54
[111] Pan T, Pharr M, Ma Y, Ning R, Yan Z, Xu R, Feng X, Huang Y and Rogers J A 2017 Experimental and theoretical studies of serpentine interconnects on ultrathin elastomers for stretchable electronics *Adv. Funct. Mater.* **27** 1702589
[112] Dong W, Zhu C, Ye D and Huang Y 2017 Optimal design of self-similar serpentine interconnects embedded in stretchable electronics *Appl. Phys.* A **123** 428
[113] Perry A J 1983 Scratch adhesion testing of hard coatings *Thin Solid Films* **107** 167–80
[114] ASTM D3359-17 Standard Test Methods for Rating Adhesion by Tape Test, ASTM International, West Conshohocken, PA, 2017 (https://doi.org/10.1520/D3359-17)

[115] ASTM, Standard Test Method for Peel Resistance of Adhesives (T-Peel Test). American Society for Testing and Materials: 2008; Vol. ASTM D1876–08, p 3 (West Conshohocken, PA: ASTM International) (https://doi.org/10.1520/D1876-08R15E01)
[116] Driesche S. v. d., Habben C, Bödecker A, Lang W and Vellekoop M J 2017 A simple method to allow Parylene-C coatings on gold substrates *Proceedings* **1** 299
[117] Hsu J M, Rieth L, Kammer S, Orthner M and Solzbacher F 2008 Effect of thermal and deposition processes on surface morphology, crystallinity, and adhesion of Parylene-C *Sensors Mater.* **20** 87–102 (https://www.scopus.com/record/display.uri?eid=2-s2.0-46049095897&origin=inward&txGid=1b287a49a35a77999e6d6a95546b623d)
[118] Drnovská H, Lapčík L, Buršíková V, Zemek J and Barros-Timmons A M 2003 Surface properties of polyethylene after low-temperature plasma treatment *Colloid Polym. Sci.* **281** 1025–33
[119] Nomura K, Takagi A, Kamiya T, Ohta H, Hirano M and Hosono H 2006 Amorphous oxide semiconductors for high-performance flexible thin-film transistors *Japan. J. Appl. Phys.* **45** 4303–8
[120] Park J-S, Kim T-W, Stryakhilev D, Lee J-S, An S-G, Pyo Y-S, Lee D-B, Mo Y G, Jin D-U and Chung H K 2009 Flexible full color organic light-emitting diode display on polyimide plastic substrate driven by amorphous indium gallium zinc oxide thin-film transistors *Appl. Phys. Lett.* **95** 013503
[121] Cao Q, Hur S H, Zhu Z T, Sun Y G, Wang C J, Meitl M A, Shim M and Rogers J A 2006 Highly bendable, transparent thin-film transistors that use carbon-nanotube-based conductors and semiconductors with elastomeric dielectrics *Adv. Mater.* **18** 304–9
[122] Ha M, Xia Y, Green A A, Zhang W, Renn M J, Kim C H, Hersam M C and Frisbie C D 2010 Printed, sub-3V digital circuits on plastic from aqueous carbon nanotube inks *ACS Nano* **4** 4388–95
[123] Zhang J, Li Y, Zhang B, Wang H, Xin Q and Song A 2015 Flexible indium-gallium-zinc-oxide Schottky diode operating beyond 2.45 GHz *Nat. Commun.* **6** 7561
[124] Lin C-Y, Tsai C-H, Lin H-T, Chang L-C, Yeh Y-H, Pei Z, Peng Y-R and Wu C-C 2011 High-frequency polymer diode rectifiers for flexible wireless power-transmission sheets *Org. Electron.* **12** 1777–82
[125] Zhang X, Zhai J, Yu X, Ding L and Zhang W 2013 Fabrication and characterization of flexible Ag/ZnO Schottky diodes on polyimide substrates *Thin Solid Films* **548** 623–6
[126] Gutierrez-Heredia G, Martinez-Landeros V H, Aguirre-Tostado F S, Shah P, Gnade B E, Sotelo-Lerma M and Quevedo-Lopez M A 2012 Full bridge circuit based on pentacene schottky diodes fabricated on plastic substrates *Semicond. Sci. Technol.* **27** 085013
[127] Ai Y, Gowrisanker S, Jia H, Trachtenberg I, Vogel E, Wallace R M, Gnade B E, Barnett R, Stiegler H and Edwards H 2007 14 MHz organic diodes fabricated using photolithographic processes *Appl. Phys. Lett.* **90** 262105
[128] Reeder J *et al* Mechanically adaptive organic transistors for implantable electronics *Adv. Mater.* 2014 **26** 4967–73
[129] Avendano-Bolivar A, Ware T, Arreaga-Salas D, Simon D and Voit W 2013 Mechanical cycling stability of organic thin film transistors on shape memory polymers *Adv. Mater.* **25** 3095–9
[130] Gutierrez-Heredia G, Rodriguez-Lopez O, Garcia-Sandoval A and Voit W E 2017 Highly stable indium-gallium-zinc-oxide thin-film transistors on deformable softening polymer substrates *Adv. Electron. Mater.* **3** 1700221
[131] Choi S, Fuentes-Hernandez C, Wang C-Y, Wei A, Voit W, Zhang Y, Barlow S, Marder S R and Kippelen B 2015 *Proc. SPIE 9568, Organic Field-Effect Transistors XIV; and Organic Sensors and Bioelectronics VIII, 95680A (31 August 2015);* ed K Ioannis *et al* (https://doi.org/10.1117/12.2188684)
[132] Gutierrez-Heredia G, Maeng J, Conde J, Rodriguez-Lopez O and Voit W E 2018 Effect of annealing atmosphere on IGZO thin film transistors on a deformable softening polymer substrate *Semicond. Sci. Technol.* **33** 095001
[133] Chasin A, Steudel S, Myny K, Nag M, Ke T-H, Schols S, Genoe J, Gielen G and Heremans P 2012 High-performance a-In-Ga-Zn-O Schottky diode with oxygen-treated metal contacts *Appl. Phys. Lett.* **101** 113505
[134] Chasin A, Nag M, Bhoolokam A, Myny K, Steudel S, Schols S, Genoe J, Gielen G and Heremans P 2013 Gigahertz operation of a-IGZO Schottky diodes *IEEE Trans. Electron Devices* **60** 3407–12
[135] Chasin A, Volskiy V, Libois M, Myny K, Nag M, Rockelé M, Vandenbosch G A E, Genoe J, Gielen G and Heremans P 2014 An integrated a-IGZO UHF energy harvester for passive RFID tags *IEEE Trans. Electron Devices* **61** 3289–95
[136] Zhang J, Wang H, Wilson J, Ma X, Jin J and Song A 2016 Room temperature processed ultrahigh-frequency indium-Gallium–zinc-oxide Schottky diode *IEEE Electron Device Lett.* **37** 389–92
[137] Zhang J, Li Y, Zhang B, Wang H, Xin Q and Song A 2015 Flexible indium–gallium–zinc–oxide Schottky diode operating beyond 2.45 GHz *Nat. Commun.* **6** 7561
[138] FDA 2016 Updated 510(k) sterility review guidance K90-1; Guidence for industry and FDA *US Department of Health and Human Services FaDA, Center for Devices and Radiological Health*
[139] Yakacki C M, Lyons M B, Rech B, Gall K and Shandas R 2008 Cytotoxicity and thermomechanical behavior of biomedical shape-memory polymer networks post-sterilization *Biomed. Mater.* **3** 015010
[140] De Nardo L, Alberti R, Cigada A, Yahia L, Tanzi M C and Farè S 2009 Shape memory polymer foams for cerebral aneurysm reparation: effects of plasma sterilization on physical properties and cytocompatibility *Acta Biomater.* **5** 1508–18
[141] Muschalek R, Nash L, Jones R, Hasan S M, Keller B K, Monroe M B B and Maitland D J 2017 Effects of sterilization on shape memory polyurethane embolic foam devices *Journal of Medical Devices* **11** 031011–031011 -9
[142] ISO 2008 ISO 10993-5 Biological valuation of medical devices, Part 5: Tests for *in vitro* cytotoxicity. (Geneva, Switzerland: International Organization for Standardization)
[143] Black B J, Ecker M, Stiller A, Rihani R, Danda V R, Reed I, Voit W E and Pancrazio J J 2018 *In vitro* compatibility testing of thiol-ene/acrylate-based shape memory polymers for use in implantable neural interfaces *J. Biomed. Mater. Res. Part* A **0**
[144] ISO, 2016 ISO 10993-6 Biological evaluation of medical devices Part 6: Tests for local effects after implantation. (Geneva, Switzerland: International Organization for Standardization)
[145] Lee H C, Gaire J, Currlin S W, McDermott M D, Park K and Otto K J 2017 Foreign body response to intracortical microelectrodes is not altered with dip-coating of polyethylene glycol (PEG) *Frontiers in Neuroscience* **11** 513
[146] Shoffstall A *et al* Characterization of the neuroinflammatory response to thiol-ene shape memory polymer coated intracortical microelectrodes *Micromachines* 2018 **9** 486
[147] Testing M P 2018 Accelerated Aging Calculator. (accessed 05-04-2018) (http://www.medicalpackagetesting.com/page/accelerated-aging-calculato)
[148] ASTM F1980-07(2011) Standard Guide for Accelerated Aging of Sterile Barrier Systems for Medical Devices, ASTM International, West Conshohocken, PA, 2011 (https://doi.org/10.1520/F1980-07R11)
[149] Arrhenius S 1889 Über die Reaktionsgeschwindigkeit bei der Inversion von Rohrzucker durch Säuren In *Z. Phys. Chem.* **4U** 226
[150] Lecomte A, Degache A, Descamps E, Dahan L and Bergaud C 2017 *In vitro* and *in vivo* biostability assessment of chronically-implanted Parylene C neural sensors *Sensors Actuators B: Chem.* **251** (supplement C) 1001–8

[151] Wang Y, Huang M, Luo Y and Li Y 2010 *In vitro* degradation of poly(lactide-co-p-dioxanone)-based shape memory poly(urethane-urea) *Polym. Degrad. Stab.* **95** 549–56
[152] Ahmad Z 2012 Polymer dielectric materials *Dielectric Material* ed M A Silaghi (Rijeka: InTech) (https://doi.org/10.5772/50638)
[153] Farrell R, Goshal T, Cvelbar U, Petkov N and Morris M A 2011 Advances in ultra low dielectric constant ordered porous materials *Electrochem. Soc. Interface* **20** 39–46
[154] Scholvin J, Kinney J P, Bernstein J G, Moore-Kochlacs C, Kopell N J, Fonstad C G and Boyden E S 2016 Heterogeneous neural amplifier integration for scalable extracellular microelectrodes *38th Annual Int. Conf. of the IEEE Engineering in Medicine and Biology Society (EMBC)* Orlando, Florida USA16–20 Aug, 2016(Orlando, Florida USA: IEEE) pp 2789–93
[155] ASTM D257-14 Standard Test Methods for DC Resistance or Conductance of Insulating Materials, ASTM International, West Conshohocken, PA, 2014, (https://doi.org/10.1520/D0257-14)
[156] ASTM D150-11 Standard Test Methods for AC Loss Characteristics and Permittivity (Dielectric Constant) of Solid Electrical Insulation, ASTM International, West Conshohocken, PA, 2011 (https://doi.org/10.1520/D0150-11)
[157] IPC 1986 Permittivity (dielectric constant) and loss tangent (dissipation factor) if insulating material a 1 MHz (contacting electrode systems) *IPC-TM-650* vol 2.5.5.1 (Institute for Inteerconnecting and Packaging ELectronic Circuits) p 5
[158] ASTM D3426-97(2012) Standard Test Method for Dielectric Breakdown Voltage and Dielectric Strength of Solid Electrical Insulating Materials Using Impulse Waves, ASTM International, West Conshohocken, PA, 2012 (https://doi.org/10.1520/D3426-97R12)
[159] Huang Y, Jämbeck J and Unge M 2017 Understanding the ionic conduction in dielectric polymers at high electric fields using molecular dynamics simulations *ACS Macro Letters* **6** 571–4
[160] Zhang X and Tanaka J 1988 Diffusion of ions into polymers *Symp. on Electical Insulating Mateials, IEEE* (https://doi.org/10.1109/ISEIM.1988.763441)
[161] Ciuprina F, Teissèdre G and Filippini J C 2001 Polyethylene crosslinking and water treeing *Polymer* **42** 7841–6
[162] Raider S I, Gregor L V and Flitsch R 1973 Transfer of mobile ions from aqueous-solutions to silicon dioxide surface *J. Electrochem. Soc.* **120** 425–31
[163] Gray F M, Vincent C A and Kent M 1989 A study of the dielectric properties of the polymer electrolyte PEO-LiClO4 over a composition range using time domain spectroscopy *J. Polym. Sci., Part B: Polym. Phys.* **27** 2011–22
[164] Hasted J B, Ritson D M and Collie C H 1948 Dielectric properties of aqueous ionic solutions. Parts I and II *J. Chem. Phys.* **16** 1–21
[165] Murray J N 1997 Electrochemical test methods for evaluating organic coatings on metals: an update. Part I. Introduction and generalities regarding electrochemical testing of organic coatings *Prog. Org. Coat.* **30** 225–33
[166] Murray J N 1997 Electrochemical test methods for evaluating organic coatings on metals: an update. Part III: multiple test parameter measurements *Prog. Org. Coat.* **31** 375–91
[167] Murray J N 1997 Electrochemical test methods for evaluating organic coatings on metals: an update. Part II: single test parameter measurements *Prog. Org. Coat.* **31** 255–64
[168] Nase M, Langer B and Grellmann W 2008 Fracture mechanics on polyethylene/polybutene-1 peel films *Polym. Test.* **27** 1017–25
[169] DIN 2005 *Adhesives—T-peeltest for Flexible -to-flexible Bonded Assemblies.* (Berlin, Germany: German Institute for Standardization) Vol. DIN EN ISO 11339
[170] Vishnuvarthanan M and Rajeswari N 2015 Effect of mechanical, barrier and adhesion properties on oxygen plasma surface modified PP *Innovative Food Science & Emerging Technologies* **30** 119–26
[171] Radun V, von Metzen R P, Stieglitz T, Bucher V and Stett A 2015 Evaluation of adhesion promoters for Parylene C on gold metallization *Current Directions in Biomedical Engineering* **1** 493
[172] Gilja V *et al* Clinical translation of a high performance neural prosthesis *Nat. Med.* 2015 **21** 1142–5
[173] Serruya M D 2014 Bottlenecks to clinical translation of direct brain-computer interfaces *Frontiers in Systems Neuroscience* **8** 226
[174] Sin M L Y, Mach K E, Wong P K and Liao J C 2014 Advances and challenges in biosensor-based diagnosis of infectious diseases *Expert Rev. Mol. Diagn.* **14** 225–44
[175] Eckert M A, Vu P Q, Zhang K, Kang D, Ali M M, Xu C and Zhao W 2013 Novel molecular and nanosensors for *in vivo* sensing *Theranostics* **3** 583–94
[176] Barrese J C, Aceros J and Donoghue J P 2016 Scanning electron microscopy of chronically implanted intracortical microelectrode arrays in non-human primates *J. Neural Eng.* **13** 026003
[177] Kozai T D Y, Catt K, Li X, Gugel Z V, Olafsson V T, Vazquez A L and Cui X T 2015 Mechanical failure modes of chronically implanted planar silicon-based neural probes for laminar recording *Biomaterials* **37** 25–39
[178] Vogt B D, Soles C L, Lee H-J, Lin E K and Wu W.-l. 2005 Moisture absorption into ultrathin hydrophilic polymer films on different substrate surfaces *Polymer* **46** 1635–42
[179] Minnikanti S, Diao G, Pancrazio J J, Xie X, Rieth L, Solzbacher F and Peixoto N 2014 Lifetime assessment of atomic-layer-deposited Al2O3-Parylene C bilayer coating for neural interfaces using accelerated age testing and electrochemical characterization *Acta Biomater. S1742-7061(13)00548-5* **10** 960–7
[180] Amirudin A and Thieny D 1995 Application of electrochemical impedance spectroscopy to study the degradation of polymer-coated metals *Prog. Org. Coat.* **26** 1–28
[181] Huang X, Denprasert P M, Zhou L, Vest A N, Kohan S and Loeb G E 2017 Accelerated life-test methods and results for implantable electronic devices with adhesive encapsulation *Biomed. Microdevices* **19** 46
[182] Fernandez-Sanchez C, McNeil C J and Rawson K 2005 Electrochemical impedance spectroscopy studies of polymer degradation: application to biosensor development *Trac-Trend Anal Chem* **24** 37–48
[183] Cogan S F 2006 *In vivo* and *in vitro* differences in the charge-injection and electrochemical properties of iridium oxide electrodes *Conf Proc IEEE Eng Med Biol Soc* **1** 882–5
[184] Zhou G X, Zhang H, Xu S P, Gui X C, Wei H Q, Leng J S, Koratkar N and Zhong J 2016 Fast triggering of shape memory polymers using an embedded carbon nanotube sponge network *Sci. Rep.* **6** 24148
[185] Cogan S F, Ludwig K A, Welle C G and Takmakov P 2016 Tissue damage thresholds during therapeutic electrical stimulation *J. Neural Eng.* **13** 021001
[186] de la Oliva N, Mueller M, Stieglitz T, Navarro X and del Valle J 2018 On the use of Parylene C polymer as substrate for peripheral nerve electrodes *Sci. Rep.* **8** 5965

NOTE

Potential for thermal damage to the blood–brain barrier during craniotomy: implications for intracortical recording microelectrodes

IOP Publishing Journal of Neural Engineering
J. Neural Eng. **15** (2018) 034001 (11pp) https://doi.org/10.1088/1741-2552/aa9f32

Note

Potential for thermal damage to the blood–brain barrier during craniotomy: implications for intracortical recording microelectrodes

Andrew J Shoffstall[1,2,4,5], Jen E Paiz[1], David M Miller[1], Griffin M Rial[1], Mitchell T Willis[1], Dhariyat M Menendez[1], Stephen R Hostler[3] and Jeffrey R Capadona[1,2]

[1] Department of Biomedical Engineering, Case Western Reserve University, Cleveland, OH 44016, United States of America
[2] Advanced Platform Technology Center, Louis Stokes Cleveland Department of Veterans Affairs Medical Center, 10701 East Blvd, 151 W/APT, Cleveland, OH 44106-1702, United States of America
[3] Department of Mechanical and Aerospace Engineering, Case Western Reserve University, Cleveland, OH 44106, United States of America

E-mail: ajs215@case.edu

Received 5 May 2017, revised 1 December 2017
Accepted for publication 5 December 2017
Published 5 April 2018

Abstract

Objective. Our objective was to determine how readily disruption of the blood–brain barrier (BBB) occurred as a result of bone drilling during a craniotomy to implant microelectrodes in rat cortex. While the phenomenon of heat production during bone drilling is well known, practices to evade damage to the underlying brain tissue are inconsistently practiced and reported in the literature. *Approach.* We conducted a review of the intracortical microelectrode literature to summarize typical approaches to mitigate drill heating during rodent craniotomies. Post mortem skull-surface and transient brain-surface temperatures were experimentally recorded using an infrared camera and thermocouple, respectively. A number of drilling conditions were tested, including varying drill speed and continuous versus intermittent contact. *In vivo* BBB permeability was assayed 1 h after the craniotomy procedure using Evans blue dye. *Main results.* Of the reviewed papers that mentioned methods to mitigate thermal damage during craniotomy, saline irrigation was the most frequently cited (in six of seven papers). In post mortem tissues, we observed increases in skull-surface temperature ranging from +3 °C to +21 °C, dependent on drill speed. *In vivo*, pulsed-drilling (2 s-on/2 s-off) and slow-drilling speeds (1000 r.p.m.) were the most effective methods we studied to mitigate heating effects from drilling, while inconclusive results were obtained with saline irrigation. *Significance.* Neuroinflammation, initiated by damage to the BBB and perpetuated by the foreign body response, is thought to play a key role in premature failure of intracortical recording microelectrodes. This study demonstrates the extreme sensitivity of the BBB to overheating caused by bone drilling. To avoid damage to the BBB, the authors

[4] Author to whom any correspondence should be addressed.
[5] Current address: Louis Stokes Cleveland Department of Veterans Affairs Medical Center, Case Western Reserve University, 2071 Martin Luther King Jr. Drive, Cleveland, OH, United States of America.

recommend that craniotomies be drilled with slow speeds and/or with intermittent drilling with complete removal of the drill from the skull during 'off' periods. While saline alone was ineffective at preventing overheating, its use is still recommended to remove bone dust from the surgical site and to augment other cooling methods.

Keywords: electrophysiology, craniotomy, blood–brain barrier, intracortical, rodent models

S Supplementary material for this article is available online

(Some figures may appear in colour only in the online journal)

Introduction

Intracortical recording microelectrodes have tremendous potential for use in both research and medical applications [1–4]. Intracortical microelectrodes act as an electrical interface that can map and record neural activity [5, 6]. The information captured can be processed to reveal how neuronal cells interact with one another in response to certain stimuli such as in neurological diseases, neurorehabilitation and/or due to environmental factors [6–10]. The signals can also be decoded to reveal practical information for use in medical applications. Most prominently, signal decoding can yield intended movements or actions that can be used as controlling input for prosthetic devices, cursors on a screen or even to restore volitional control of a paralyzed patient's own muscles via functional electrical stimulation [2, 5, 6, 8, 11].

While the promise is great, widespread adoption is challenged by inconsistent device longevity and performance [12–15]. Loss of signal from intracortical microelectrodes is likely a result of a multitude of biological and material factors [12]. Many approaches have been tested to understand and modulate the mechanisms leading to microelectrode failure [12]. While many factors are probably intertwined and together propagate the neurodegenerative and corrosive responses to microelectrode implantation, the process is clearly initiated during device implantation.

Several groups have demonstrated a direct connection between the damage to the neural tissue and surrounding vasculature and the performance of the implanted microelectrode [16–18]. In particular, damage to the blood–brain barrier (BBB) in the presence of a prolonged foreign body response appears to set up a self-perpetuating pro-inflammatory state [19, 20]. While preventative techniques have been developed, damage to the brain tissue during microelectrode insertion is inevitable [21, 22]. Trauma to the BBB allows blood proteins and cells that are not normally present into the immune-privileged brain tissues. Soluble factors that are released from the disrupted BBB play different roles in the inflammatory process, with detrimental effects on neural cells and the electrode [23–29]. The breach allows macrophages to infiltrate the brain tissue and localize at the implanted device [30], while microglia that are normally not activated in the tissues become activated due to both cellular and acellular changes in the microenvironment [30–33]. As a result, the activated monocytes release more soluble factors (including reactive oxygen species) [19, 34–37] at the implant site, further triggering BBB leakage and perpetuating a pro-inflammatory state [20, 38]. While the inflammatory cascade is complex and takes weeks to develop, trauma during the implantation marks its onset and may be a major determining factor in the magnitude of the ultimate response.

To attempt to mitigate the inflammatory response, we therefore focused our attention on the initial surgery to implant the intracortical devices. First and foremost, the procedure requires the removal of bone from the skull to allow for access to the brain [39]. Laboratories carrying out microelectrode work commonly use craniotomies produced by high-speed drills to insert devices into the rodent brain [39]. While many labs regularly take precautions against drill overheating, for example by using saline irrigation [40], the heat of the drill is a potential source of damage that has not been extensively explored with relation to intracortical microelectrode implantation.

New evidence from our ongoing studies of neuroinflammatory response to implanted intracortical microelectrodes indicated that the BBB was disrupted at acute time points (less than 1 h) as a result of the craniotomy procedure alone (i.e. in 'sham' rats). As part of our studies to investigate methods to reduce the neuroinflammatory response to chronically implanted intracortical microelectrodes, we injected Evans blue dye intravenously in rats prior to performing the craniotomy. Evans blue dye binds to circulating albumin in the bloodstream, which cannot normally cross the BBB, therefore making it a sensitive marker of BBB permeability [41–43]. One hour post-craniotomy, we observed a drastic increase in dye concentration in the brain compared with that in animals that had not undergone the craniotomy procedure (i.e. naïve rats). We sought to better characterize the effects of and determine the cause of BBB permeability at acute time points. Since dye extravasation was localized directly under the site of drilling, we hypothesized that the effect was a result of local heating.

While it is generally understood that drill over-heating may cause tissue damage [44–46], a phenomenon particularly well documented in the orthopedics field [47], the impact of craniotomy on highly vascularized brain tissue has not been adequately characterized in the field of intracortical microelectrode research (figure 1). In their comprehensive review of drill bone heating in orthopedic fixation procedures, Pandey *et al* identified a number of factors that influence the degree of drill heating [47]. These factors, as well as others found from our literature review, are shown in table 1.

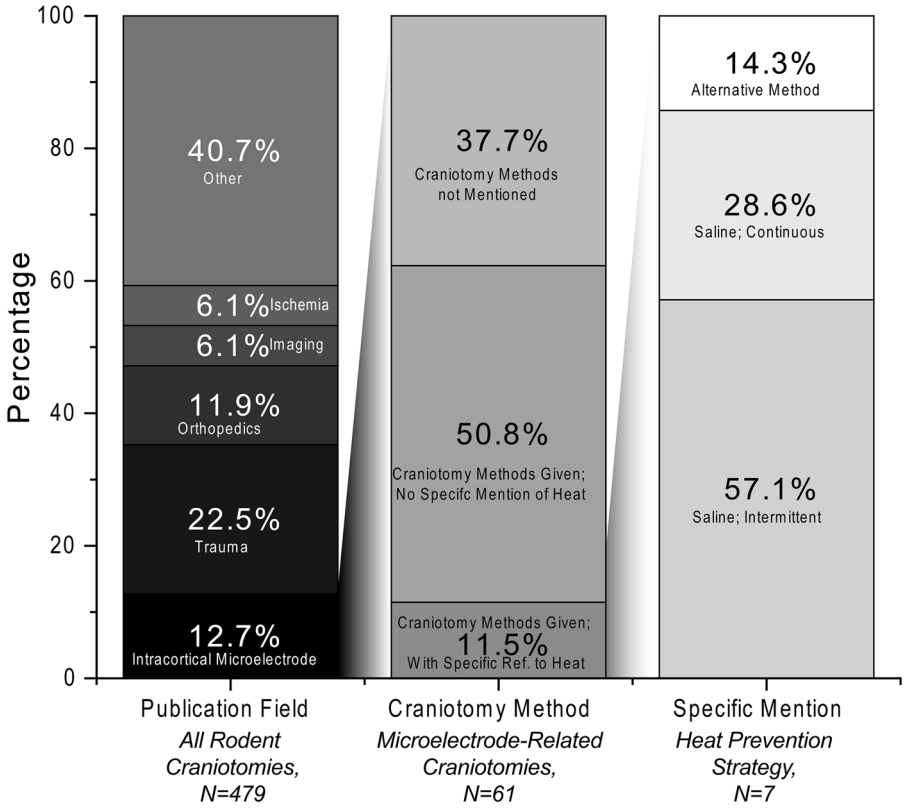

Figure 1. Literature review of rodent craniotomy methods. We identified 479 journal articles from a PubMed database search that included a search for rodent (rat or mouse) craniotomy methods, as well as all papers pertaining to 'intracortical microelectrodes'. Column 1: articles were categorized by their primary field of publication (e.g. 'trauma' versus 'orthopedics'). Column 2: of the subset of journal articles pertaining to 'intracortical microelectrodes' ($N = 61$), 89% did not specifically mention methods for the prevention of drill overheating during craniotomy and 38% provided no details regarding the craniotomy method whatsoever. Column 3: of the subset of intracortical microelectrode papers that described a method to prevent drill overheating ($N = 7$), 4/7 described the use intermittent saline, 2/7 described the use of continuous saline irrigation, and 1/7 described the use of an alternative method for producing the craniotomy, i.e. a biopsy punch.

Table 1. Factors that influence bone drill overheating [44, 45, 47, 71, 72].

- Drill speed
- Contact time
- Feed rate (force of application)
- Bit age (sharp/dullness)
- Bit size (dimensions)

Since visible lesions and/or overt functional damage have not been observed in our study, nor reported in the literature associated with craniotomy procedures, the amount of heating caused by drilling is likely not sufficient to cause *permanent* thermal damage to brain tissues. However, given our interest in investigating the neuroinflammatory response after device implantation, and the role that serum proteins may play in promoting inflammatory cascades, the increased permeability of the BBB may significantly influence or confound the results found in experimental models that require a craniotomy [16, 17, 19].

In the current study we sought to: (1) review the literature for rodent craniotomy procedures for methods to prevent drill over-heating, (2) test our hypothesis that observed BBB damage was due to drill over-heating, (3) better characterize the temperatures and parameters that may lead to drill over-heating and BBB damage, and (4) determine a drilling protocol that avoids damage to the BBB.

Methods

Literature review of rodent craniotomy methods, within the context of microelectrode implantation

An extensive review of rodent craniotomy methods described in the intracortical microelectrode literature was conducted using the PubMed database. We pulled references pertaining to craniotomy procedures in rodent models or intracortical microelectrodes in rodent models.

PubMed search string

'(craniotomy OR (microelectrode AND intracortical)) AND (rat OR mouse OR rodent)'

The initial search yielded approximately 698 results. We then omitted all articles for which access to the full article was not available or which were published prior to 1 January 2000 ($N = 219$ results). The remaining 479 journal articles were then categorized into broad medical fields (e.g. oncology, orthopedics and imaging). To reduce the scope of the search and hone-in on our particular interests, we then focused on the subset of papers related to the intracortical microelectrode field.

We systematically reviewed each paper to determine if the methods sections contained information pertaining to craniotomy methods (e.g. factors mentioned in table 1) and/or the

generation or prevention of heating. We then further analyzed the group of articles that referenced craniotomy methods for a number of other specific factors related to drill-heating and prevention, such as the use of saline irrigation as well as the speed, size and sharpness of a drill bit. It is important to note that the review of specific methods sections was limited to the context of papers related to intracortical microelectrode implantation. The review of heat prevention methods, therefore, omitted other related results such as from fields of *in vivo* optical imaging via cranial windows, implantation of fiber optic or other probes, traumatic brain injury, stroke and other fields, that may also produce craniotomies in rodent models for which the implications of our research findings may be equally relevant.

Materials

Evans blue dye and dimethylformamide (DMF), were purchased from Sigma Aldrich (St Louis, MO, USA). Evans blue solutions for *in vivo* infusion were prepared as 4% w/v solution in 0.9% sterile saline. The solutions were then sterile filtered to remove precipitates with a 0.2 μm syringe filter. All other reagents were used as-received. The high-speed power drill was purchased from Pearson Dental, Osada Model EXL-M40 (Los Angeles, CA, USA). Spherical drill bits were purchased from Stoelting (Wood Dale, IL, USA) and were 1.75 mm in diameter (Stoelting Co., no. 514556).

Rat surgical procedures

All surgeries were performed acutely, i.e. with euthanasia of the animal prior to it waking up [48]. Briefly, rats were anesthetized with 4% isoflurane, shaved and mounted in a stereotaxic frame equipped with blunt ear bars and an incisor bar. A dose of 0.2 ml of 0.25% Marcaine was administered subcutaneously at the incision site, followed by cleaning of the skin with betadine and isopropyl alcohol. Anesthesia was maintained via the oxygen flow path on the stereotaxic frame using 0.5–2% isoflurane. Prior to surgery, the rat received 16 mg kg^{-1} of cefazolin subcutaneously as an antibiotic as an extra precaution to prevent intraoperative infection as well as 1 mg kg^{-1} of meloxicam subcutaneously for pain management.

To perform the craniotomy, a 1-inch incision down midline of the scalp (~2 cm) was followed by removal of superficial soft tissues such that the dry bone skull was exposed. All drilling was completed with a 1.75 mm diameter spherical drill bit (as identified above). While not specifically controlled, the angle was approximated at ~75° (in reference to the table) to allow for simultaneous drilling and visualization by the microscope. A single hole was created using a drill-press style (as opposed to tracing a circle or rectangular hole). After the drilling or heating of the skull was performed, and all measurements taken, rats were euthanized under deep anesthesia via cardiac perfusion with saline. All rat procedures were reviewed and approved by the Louis Stokes Cleveland Department of Veterans Affairs Medical Center Institutional Animal Care and Use Committee.

In vivo Evans blue BBB permeability experiment

Rats were anesthetized and prepared as described above. Once the skull bone was exposed, rat tails were catheterized with a 24-gauge needle, and infused with sterile-filtered 4% Evans blue solution over the course of 1 min at a dose of 2 ml kg^{-1}. Proper infusion was verified by the rat's ears, nose and eyes turning blue. Evans blue was allowed to circulate for 5 min prior to commencement of drilling. Drilling was performed bilaterally (one hole on either side of the midline, −3 mm anteroposterior, ± 3 mm midline). Craniotomies were performed at various speeds (1000, 5000, 10 000, and 15 000 r.p.m) as well as either continuously or with intermittent application (15 000 r.p.m., 2 s-on/2 s-off) to allow the bone to dissipate heat between each application. During 'off' periods, the drill bit was entirely removed from the skull surface to allow for heat dissipation in the air. Another cohort of rats was provided with continuous saline irrigation at 10 ml min^{-1} from a calibrated syringe pump and suction setup (i.e. the continuous drilling group '15k saline').

After drilling, the scalp was temporarily closed and the rat was maintained on isoflurane for 1 h. After 1 h, the rat was euthanized via cardiac perfusion with saline. The brains were harvested, coronally bisected through the area exposed by the craniotomy, and photographed to visualize the extent of blue dye extravasation. Small biopsies of the affected brain tissue were then collected using a 3 mm diameter biopsy punch and suspended in 400 μl DMF overnight. Affected tissue had easily identified margins of blue staining, as seen in the inlaid picture in figure 4. The 3 mm biopsy punch sufficiently captured the entire margins.

After incubation at room temperature, 100 μl of each sample was pipetted into a 96-well glass plate. An Evans blue standard curve was produced, ranging from 25 μg ml^{-1} to ~0.2 μg ml^{-1} in DMF by 2× serial dilution. Samples were read on a plate reader (SpectraMax M3, Molecular Devices, Sunnyvale, CA, USA) using the Evans blue fluorescent spectra peak (620/680 excitation/emission). The results were compiled and graphed in Origin (North Hampton, MA, USA).

Determination of typical drilling times and peak temperatures

Craniotomy holes were drilled with the power-drill at manufacturer-set speeds of 1000, 5000, 10 000 and 15 000 r.p.m. Maximum temperatures and temperature profiles were obtained with an infrared camera (FLIR model E6, Wilsonville, OR, USA). Drilling times were recorded as the time required to perform the full craniotomy, i.e. expose but not disrupt the dura. At least three trials per speed combination were performed and representative infrared images are shown.

Post mortem measurement of transient increase in brain surface temperature from drilling

We sought to understand how the brain surface temperature was transiently affected throughout the drilling procedure. We used a post mortem preparation of rat skulls (post-euthanasia). A single hole was drilled in the skull, through which a temperature measurement probe (miniature type-T thermocouple, 0.02 inch diameter, TC-Direct, Hillside, IL, USA) was placed and tunneled on the surface of the brain, about 2–3 mm away. (figure 3, inlay) The skull was then drilled directly over the

Table 2. Methods to prevent drill overheating during rodent craniotomy procedures referenced from the intracortical microelectrode literature.

	Ref.
'The **biopsy punch prevented heat damage** caused by motorized drills and provided a well-defined 3 mm opening'	[50]
'A craniotomy (5 mm × 3 mm) was made in the parietal bone to expose the somatosensory cortex. **Sterile saline was applied during pauses** while drilling to help dissipate any local heating and to clean the surfaces'	[55]
'A single craniotomy, roughly 2.5 mm in diameter, was made centered at approximately −1.5 mm posterior to bregma and 2.1 mm lateral to midline using a dental drill (Z-35, Henry Schein Inc., Melville, NY). **Sterile saline was applied during pauses** while drilling to help dissipate any local heating'	[40]
'A 3–4 mm diameter craniotomy was created over primary motor cortex using an air driven drill bit with **sterile saline rinses to prevent excessive heating**'	[17]
'A 4 mm by 6 mm craniotomy was made by thinning the skull over the somatosensory and visual cortex using a high speed dental drill and then removed with forceps. The skull was **periodically bathed in saline to ensure that the underlying cortex did not experience thermal damage** from drilling'	[56]
'A small pinhole craniotomy was made over visual cortex with a high-speed dental drill and bone fragments were carefully removed with forceps and saline. **Saline was applied continuously** onto the skull to dissipate heat from the high-speed drill'	[54]
'The top surface of the skull was exposed and a 3 mm by 3 mm craniotomy made over the primary visual cortex using a manual hand drill. **Saline was applied onto the skull continuously to dissipate heat from the high-speed drill**'	[53]

thermocouple, continuously, pulsed for 2 s on/2 s off, or 2 s on/5 s off. Temperature changes were directly recorded via a National Instruments DAQ, USB-6008 (National Instruments, Austin, TX, USA) and the baseline temperature subtracted. Measurements were recorded in triplicate for each drilling method.

Statistics

One-way analysis of variables (ANOVA) was performed to compare the Evans blue dye concentration by drilling method. Tukey tests were used to make pairwise comparisons between groups with the significance level set at $p < 0.05$. Statistics were performed in Minitab (State College, PA, USA). Graphs were produced in Origin.

Results

Literature review of rodent craniotomy methods

During an initial review of the literature on intracortical microelectrodes, we found a wide range and depth of reporting details regarding specific craniotomy methods. Details related to heat dissipation from bone drilling were absent in the majority of papers. As a result, it was often unclear if and how techniques were being applied. We therefore sought to more thoroughly review the currently available literature referencing the performance of rodent craniotomies. Of the 61 articles we categorized as related to the 'intracortical microelectrode' field, 23 (37.7%) had little to no reference to specific techniques used to perform a craniotomy, and 31 (50.8%) referenced a craniotomy method in general terms but did not mention heat and/or methods to mitigate the effects of heat. Overall, only 7 (11.5%) referenced a specific method for the prevention of thermal damage from drill overheating (figure 1). Saline irrigation, either continuous or intermittent was used in six of the seven papers that described specific methods to avoid drill overheating. An alternative drilling method, a biopsy punch, was used in one of the seven papers. Relevant quoted text from the methods sections of the seven articles are provided in table 2.

Typical drilling times and peak temperatures

To determine the magnitude of heating caused by drilling, we performed craniotomies on post mortem rat skulls while simultaneously imaging the surgical field with a thermal infrared camera. Given the wide range of drilling methods we encountered during the literature review, we tested various drill speeds, including 1000, 5000, 10 000 and 15 000 r.p.m. Pictures were recorded for each of the tested speeds at the maximum recorded temperatures. At each of the speeds, from slowest to fastest, temperatures increased by 3, 5, 8 and 21 °C, respectively (figure 2). With fastest drill speed (15 000 r.p.m.) the temperature reached a maximum of 21 °C above baseline, which was much higher than anticipated given the brevity of the procedure. In our experiments we found that there was significant variability in time-to-produce-craniotomy. Typical drilling times ranged from 15 to 30 s. Interestingly, there was only a mild increase in time to complete the craniotomy with 10 000 and 5000 r.p.m. speeds compared with 15 000 r.p.m. (16.4 ± 3.8 s and 17.0 ± 4.1 s, versus 14.9 ± 1.6 s, respectively). Slow drilling at 1000 r.p.m. had the greatest impact on drill time, almost doubling the total time (28.4 ± 1.6 s) when compared with 15 000 r.p.m.

Transient increase in brain surface temperature from drilling

Three types of drilling were tested (continuous, pulsed 2 s on/2 s off, pulsed 2 s on/5 s off, all at 15 000 r.p.m.) in triplicate (figure 3). A thermocouple was used to record the temperature under the skull over time while drilling (figure 3, schematic inset). The continuous drilling had higher peak temperatures (+20.7 to +27.8 °C) than any of the other drilling methods; pulsed 2 s on/2 s off drilling yielded a temperature range of +9.1 to +13.6 °C and pulsed 2 s on/5 s off drilling yielded a range of +3.1 to +7.9 °C.

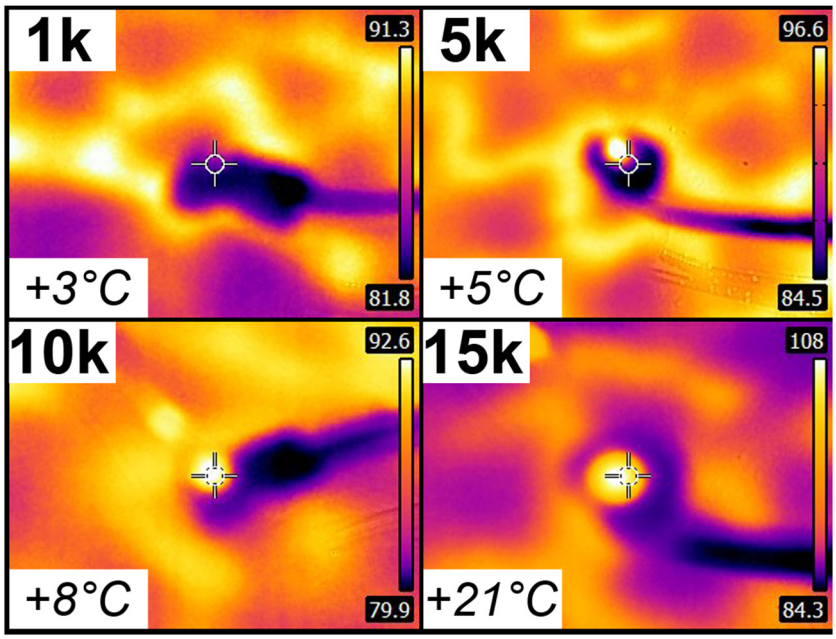

Figure 2. Maximum temperature recorded during drilling of rat craniotomy. To quickly visualize whether we were overheating the skull during drilling, we captured thermal images of the drilling with an infrared camera. Maximum temperatures exceeded an increase of +21 °C from baseline for the 15 000 (15k) r.p.m. drill speed. The image shown was captured using a thermal infrared camera to show the temperature profile of the skull surface. A picture was taken for 1k, 5k, 10k and 15k r.p.m., which increased the baseline temperature by +3 °C, +5 °C, +8 °C and +21 °C, respectively.

The heating rate and cooling rates were approximated by fitting the transient thermal curves with a linear model where the peak temperature value was used as a common point on either side, i.e. as the last point during the heating phase and the first point during the cooling phase. The average rate of heating for the continuous scenario (figure 3(A)) was +2.7 (±2.2) °C s^{-1}, represented as mean (±SD). For the intermittent scenarios, pulsed 2 s on/2 s off (figure 3(B)), and pulsed 2 s on/5 s off (figure 3(C)), the heating rate was +0.5 (±0.1) °C s^{-1} and +0.3 (±0.3) °C s^{-1}, respectively. The average rate of cooling for the continuous, pulsed 2 s on/2 s off and pulsed 2 s on/5 s off scenarios were −0.4 (±0.2) °C s^{-1}, −0.2 (±0.1) °C s^{-1} and −0.1 (±0.02) °C s^{-1}, respectively.

The experiment was performed on post mortem tissue, since placement of the thermocouple was impractical in a live rat preparation. Since the lack of perfusion would have decreased heat dissipation rates via fluid convection, the main heat transfer mode was by conduction through the tissues and air interface. We recapitulated these findings in a simple bio-heat finite-element model (see the supplementary information), comparing our findings with theoretical spatial and temporal mechanics of heat transfer through the skull and brain tissue. As expected, while lack of perfusion was determined to have an effect on heat transfer, at the scale and magnitude relevant for craniotomy, the impact on peak temperatures was projected to be minimal (dashed-line in supplementary figure 1, stacks.iop.org/JNE/15/034001/mmedia). Both the infrared camera technique and direct measurement of brain surface temperature with a thermocouple led to similar peak temperature measurements, with the peaks occurring directly below the site of the drill bit, suggesting rapid and efficient transfer of heat through the skull.

Drilling during rat craniotomy can quickly and unintentionally increase BBB permeability

In order to investigate damage to the BBB caused during craniotomy, a variety of powered drill methods were explored. Rats were subjected to continuous drilling at different speeds (1000, 5000, 10 000, 15 000 r.p.m.), pulsed application (15 000 r.p.m., 2 s on/2 s off) or saline application (15 000 r.p.m. continuous), and compared with naïve rats ('no drill') as controls (figure 4).

Among the drill speeds tested, only 1000 r.p.m. appeared to be slow enough to reliably avoid damage to the BBB. Drilling at 15 000, 10 000, and 5000 r.p.m. led to a significantly higher Evans blue concentration within the brain tissue than the 'no drill' condition ($p < 0.001, p < 0.001, p < 0.05$, respectively). Furthermore, drilling at 1000 r.p.m. led to a lower dye concentration than both 15 000 and 10 000 r.p.m. ($p < 0.01$ and $p < 0.05$, respectively), and did not significantly differ from the 'no drill' condition. Drilling at 5000 r.p.m. led to inconsistent results, with different rats displaying either significant or insignificant BBB permeability, suggesting a potentially narrowly gated threshold for inducing BBB permeability. However, overall, drilling at 5000 r.p.m. led to significantly higher dye concentration in the brain tissue than the 'no drill' condition ($p < 0.05$).

A separate cohort of rats was subjected to pulsed drilling, 2 s on and 2 s off, allowing the drill and tissue to cool off in between drilling periods. The Evans blue concentration from intermittent drilling was very similar to that of the 'no drill' control tissue (n.s.) and was significantly lower than drilling at high speeds (10 000 and 15 000 r.p.m., $p < 0.01$ each). The concentration of Evans blue is visibly higher in the 15 000 r.p.m. continuously drilled side than with 15 000 pulsed drilling on the same rat, as shown in the inlaid picture

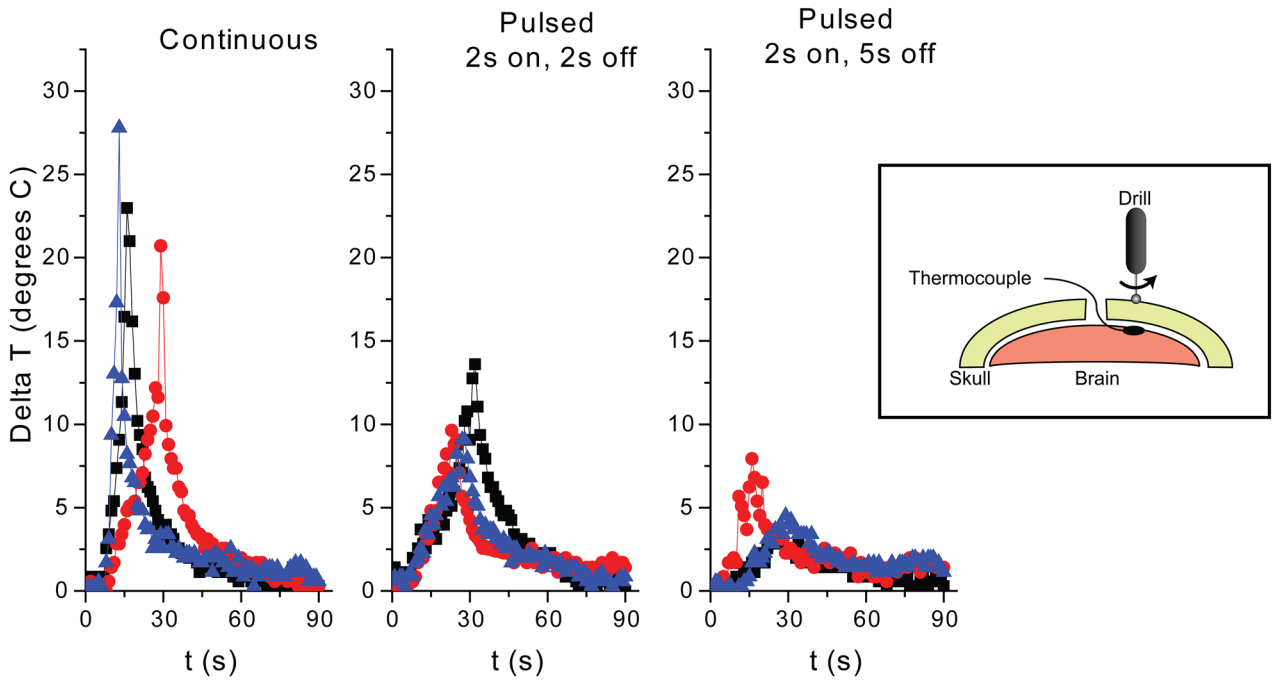

Figure 3. Transient temperature changes at the brain surface during 15 000 r.p.m. drilling (directly below the post mortem rat skull). We placed a small thermocouple on the brain surface from a secondary hole previously drilled about 2 mm away from the site (figure inlay). The experiment was performed with post mortem tissue as placement of the thermocouple was likely to cause damage to the superficial surface of the brain during placement therefore making *in vivo* measurement impractical. Three types of drilling at 15 000 r.p.m. were tested (continuous, pulsed 2 s on/2 s off, pulsed 2 s on/5 s off) in triplicate ($N = 3$ per condition). We observed that continuous application of the drill led to temperature increases greater than 25 °C within 15–30 s. Pulsed application still led to a significant increase in temperature (ranging from +9.1 to +13.6 °C). Further extending the duration of the 'off' period to 5 s during pulsed application of the drill, to allow for additional cooling, resulted in a temperature increase of +3.1 to +7.9 °C. In all tested cases, the brain cooled down back to baseline within 60 s of reaching peak temperature.

in the top right corner of figure 4. Importantly, the damage is not visible without the aid of the dye, and can therefore occur essentially invisibly during the course of a typical experiment.

Discussion

In our study, we examined the role of damage caused by drill overheating during craniotomy on the permeability of the BBB. We found that the damage to the BBB was extraordinarily easy to reproduce with drill speeds of 15 000 r.p.m. and a typical commercially available 1.75 mm drill bit. Furthermore, the damage occurred in under 15–30 s and achieved temperature increases of >25 °C as measured at the brain surface. Intermittent drilling (2 s on, 2 s off), even without saline irrigation (though not recommended as standard practice), was sufficient to prevent damage to the BBB from drill overheating.

The authors are not asserting that all craniotomies performed in the field have incurred BBB damage. In fact, one notable example publication describes robust methods to avoid thermal damage during drilling. Xu *et al* describe the use of intermittent drilling, where cooling of the drill bit with cold artificial cerebrospinal fluid is performed [49]. Furthermore, since visible lesions and/or overt functional damage have not been observed in our previous studies, nor reported in the literature associated with craniotomy procedures, the amount of heating caused by drilling is likely not sufficient to cause *permanent* thermal damage to brain tissues. However, given how quickly changes in BBB permeability can occur, without any visible damage to the surface of the brain (in the absence of a tracer such as Evans blue dye), it seemed appropriate to investigate and share our findings with the research community.

A critical finding of our study is that methods for craniotomy are inconsistently reported in the field. We conducted a comprehensive review of the intracortical microelectrode literature to evaluate the frequency and content of reported craniotomy methods. We found that very few published articles provided explicit details about their craniotomy methods, especially those relating to the prevention of heating (e.g. drill speed, drill bit sharpness, duration etc). Of the reviewed intracortical microelectrode literature, 7 of 61 papers described a craniotomy procedure that detailed a method to prevent overheating. While heat prevention during drilling is regularly practiced by most groups, its use is inconsistently reported, and therefore assumed to be inconsistently performed with various parameters in the literature on rat craniotomy and related electrophysiological recording. Equally important, some researchers opt not to use a power drill approach and instead used a biopsy punch, a manual low-speed hand-drill or rongeurs for craniotomies to presumably avoid overheating of brain tissues [39, 48, 50–53]. While seemingly mundane disclosures, craniotomy procedure parameters may have significant unintended confounding impacts on findings.

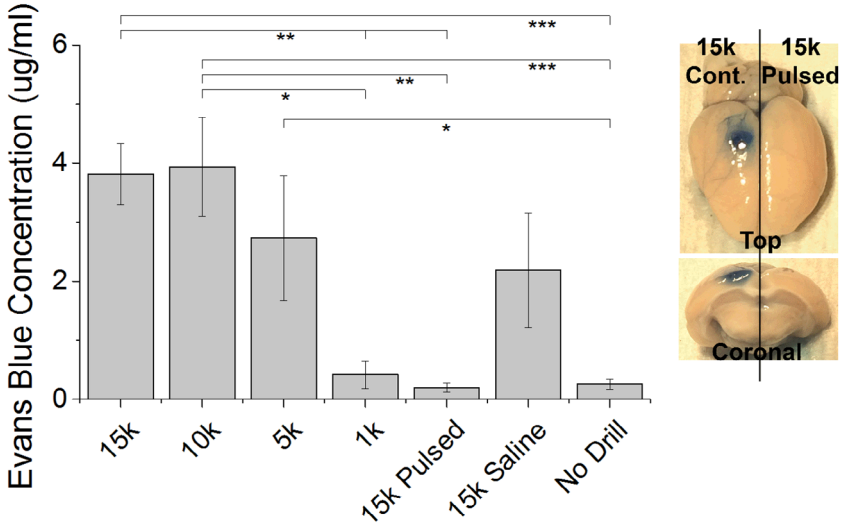

Figure 4. Evans blue dye concentration 1 h after performing various powered drill craniotomy techniques. We measured Evans blue concentrations after drilling at various speeds (15k (15 000), 10k, 5k, 1k r.p.m.) as well as either continuously or pulsed 2 s on/2 s off. There was a nearly 15-fold increase in dye concentration in the brain tissues that were exposed to continuous 10k or 15k speed drilling versus the 'no drill' control. Slow speed (1k) and pulsed application appear to be the most effective means to reduce impacts on BBB permeability. Interestingly, saline application was not an effective or repeatable method to mitigate increases in BBB permeability from 15k continuous drilling. $N = 11$ for 15k and 'no drill' conditions; $N = 4$ per group for 10k, 5k, 1k, '15k pulsed', and '15k saline' conditions. Bars represent mean $\pm$ standard error of the mean. Analysis included ANOVA with pairwise comparisons with Tukey tests: $^{*}p < 0.05$; $^{**}p < 0.01$; $^{***}p < 0.001$.

Of the papers reviewed, external saline irrigation was the most frequently cited method for prevention of heating [17, 40, 54–56]. While it is widely accepted practice in orthopedics, some have suggested that saline alone may not be enough to prevent overheating since the drill bit may be buried deep in the tissue while the saline is only applied at the skull surface [47]. One group demonstrated that light application pressure was required in addition to saline coolant to sufficiently control temperatures [57]. Nonetheless, it would appear that the consensus opinion is that saline irrigation is effective as long as it is applied in the proper manner (e.g. cold saline applied at a high enough rate) [47]. Our experience showed it to be very easy to accidentally overheat brain tissue with the power drill during craniotomy, even with the use of continuous saline irrigation at high flow rates (10 ml min^{-1}). Our findings are consistent with those found in the literature. Others in the traumatic brain injury literature (for controlled cortical impact models) have previously suggested that the craniotomy-only group may not be a 'true sham' as this itself causes damage to the underlying tissues from heat, vibration and removal of a bone flap [58]. Similar results were found by Olesen *et al*, who found that there was significant leakiness of the vasculature after craniotomy [59]. Adelsen *et al* reported on increased extravasation of Evans blue dye at 1 h time points in their craniotomy-sham procedures alone [60]. Specifically, the craniotomy produced a two-fold increase in Evans blue over unoperated controls after 1 h. Importantly, Adelsen *et al* also observed that BBB permeability returned to baseline after just 24 h [60]. While the other groups indicated that their craniotomy procedure may have induced mild trauma, none presented the potential cause as being related to thermal damage from drilling.

From our study, it is apparent the BBB is highly sensitive to temperature change, a finding that is consistent with other studies. In their paper, Kiyatkin *et al* showed that systemic hyperthermia conditions (36–42 °C), induced mild-to-moderate increased permeability of the BBB, resulting in brain edema [61]. In a different study that chronically implanted a cranial window, the authors described heat loss which resulted in temperature dysregulation [62]. They showed that the brain temperature directly under the window was roughly 10 °C cooler than the core temperature of mice [62]. The authors reported lasting effects on blood vessel diameters observed through the window. Similar effects on vasculature were recently observed using optical coherence topography imaging, and it is possible that temperature effects played a role [18]. Kosaras *et al*, described the vascular and innervation structures of the rat skull calvaria and showed the highly vascularized mesh network [63]. Disruption or structural changes to blood vessels in the brain may cause premature and additional activation of inflammatory pathways concurrently with the implantation of intracortical devices, which already elicit a foreign body inflammatory response. Increasing the permeability of the BBB immediately prior to device insertion may act as a priming effect that exacerbates the inflammatory response.

Interestingly, during our transient response experiment, we found that the temperature was still significantly increased by 2 s on/2 s off intermittent application. However, from our *in vivo* experiments we know that the method was sufficient to prevent damage to the BBB. Therefore, we believe that intermittent application, which yielded temperature increases of +9.1 to +13.6 °C, was below the BBB damage threshold for the duration of application. Another potential explanation is that the perfusion of the highly vascularized brain cooled the affected area much more quickly than suggested by our post mortem transient response curves. Unfortunately, it was impractical to place our thermocouple in an *in vivo* preparation

due to potential damage to the brain. Therefore, the brain surface temperature may have varied from the infrared camera measurements of the superficial skull surface. Together, the results seem expected since tissue damage is both a function of the magnitude of the temperature and the duration of the contact [64, 65].

Since drilling times were not significantly altered when different rotational speeds were used this suggests that the feed-rate of the drill was held relatively constant between groups, and therefore not optimized for the particular rotational drill speed. In other words, at faster rotational speeds, the drilling (or raking of bone bits) was essentially less efficient than at slower speeds, where some of the additional work output was heat. In order to prevent this unnecessary build up of heat with faster rotational drilling speeds it may be necessary to drill with faster feed rates. However, faster feed rates to achieve the 'optimal' rate for a fast drill speed are probably contraindicated in this particular application since severe damage may occur if the surgeon were to overshoot the margin of the skull and accidentally penetrate the brain tissue. It is probably better in most hand-driven applications to simply use a slower rotational speed and a slower feed-rate. We therefore reach a similar recommendation to that of Toews *et al*—to use a slow drill speed combined with sufficient axial force to advance the drill as rapidly as possible through the bone [66].

A limitation of our study was the significant trial-to-trial variability in both temperature and time, suggesting that force, feed-rate, angle of application and other variables inherent in manual drilling influenced the heating outcome in each trial. Applied force (and the proportionally related feed-rate parameter) increases the rate of heat generation, as does rotational speed. At the same time, increases in force, feed-rate and rotational speed also decrease the contact time needed to penetrate the bone, which overall decreases the total temperature change of the bone [66–69]. The heat generated during bone drilling is complex and has been extensively studied and modeled in the orthopedics literature [67]. Due to the competing effects of the different mechanical parameters, the impact of each one has a nonlinear relationship with maximum bone temperature during drilling. Surgeons most often use constant-force drilling as opposed to a constant feed rate [67], using the change in load as a feedback detection for knowing when the boundaries of the bone have been reached. During our experiments, every attempt was made to use a consistent force applied to the drill bit, taking great care not to mechanically damage the brain surface after the skull had been breached. While we did not directly assess post mortem tissue histopathology to assess the condition of the meninges, gross anatomy of the brain surfaces appeared intact. The same surgeon performed all procedures and in a similar manner across the study. While these factors were controlled as well as possible, future studies may find better repeatability and accuracy with automated drilling setups such as the one described by Pak *et al*, which can tightly control feed-rate and/or force of application (as well as *x*–*y* controls) [70].

The use of more sophisticated technologies may be able to mitigate the issue of heating during bone drilling. Internally cooled drill bits have been used in orthopedics [45, 47]. While the use of such drilling apparatus in research is currently limited due to added cost and complexity, it is worthwhile noting that it exists and may potentially alleviate heating issues in these applications if it can be adapted to the required size constraints for performing rodent craniotomies. Gupta *et al* recently published an ultrasonic cortical drilling method to reduce the risk of heating [46]. The use of novel cutting methods like this may even further reduce risk to the underlying tissues.

As a final limitation to our study, we did not directly measure the effect of increased acute permeability of the BBB on the evolution of the chronic inflammatory cascade for implanted intracortical microelectrodes. Future work may be aimed at determining if there is a significant impact on the cellular immune/inflammatory response, based on the extent of initial BBB breach during craniotomy, or even device insertion. However, a main conclusion of the present study is that prevention of overheating can be easily and unintentionally achieved. If the nuanced differences between performing the same procedure indeed have an effect on the broader inflammatory response after microelectrode implantation, this may further contribute to the challenge of comparing results across different research groups and surgeons.

Conclusion

We hypothesized that overheating the brain tissues during typically performed craniotomy drilling procedures may inadvertently increase the permeability of the BBB, and that practices to avoid routine iatrogenic injury have been inconsistently reported and practiced in the field. We confirmed that drilling was indeed a source of heat, and that it was capable of producing temperature increases on the brain surface of >25 °C. We consequently determined the root cause of the effect and validated a method to avoid drill overheating in the future, i.e. pulsed drilling with intermittent or continuous irrigation with saline. While pulsed application still produced heat, even momentarily increasing surface brain temperatures to above $+13$ °C, it was apparently below the threshold to produce measureable damage to the BBB.

While the authors are not suggesting that every rat craniotomy method published in the field is confounded as a result of overheating, we are suggesting that it is rather easy to do accidentally, and it should be brought to the forefront of researchers' minds as they are studying the varying impacts of materials implanted in the brain on the neuroinflammatory response. To avoid a systematic and potentially confounding variable, the authors recommend that individual research labs validate their specific and potentially nuanced craniotomy procedures with the use of intravenously injected Evans blue dye, which provides a simple and rapid evaluation of BBB permeability. The authors additionally recommend that researchers use a slow drill speed combined with sufficient axial force to advance the drill as rapidly as possible through the bone, and in conjunction with other prevention methods such as intermittent (pulsed on/off) drilling with complete removal of the drill from the skull during 'off' periods. While saline alone was ineffective at preventing overheating, its use

is still recommended to remove bone dust from the surgical site and to augment other cooling methods.

Acknowledgments

This work was supported in part by the Office of the Assistant Secretary of Defense for Health Affairs through the Peer Reviewed Medical Research Program under award no. W81XWH-15-1-0608, and in part by Merit Review Award no. B1495-R (Capadona) and Presidential Early Career Award for Scientist and Engineers (PECASE, Capadona) from the United States (US) Department of Veterans Affairs Rehabilitation Research and Development Service. The contents do not represent the views of the US Department of Veterans Affairs or the United States Government.

ORCID iDs

Andrew J Shoffstall https://orcid.org/0000-0002-0881-2180
Jeffrey R Capadona https://orcid.org/0000-0001-8030-6947

References

[1] Donoghue J P 2002 Connecting cortex to machines: recent advances in brain interfaces *Nat. Neurosci.* **5** 1085–8
[2] Peckham P H and Knutson J S 2005 Functional electrical stimulation for neuromuscular applications *Annu. Rev. Biomed. Eng.* **7** 327–60
[3] Pancrazio J J and Peckham P H 2009 Neuroprosthetic devices: how far are we from recovering movement in paralyzed patients? *Exp. Rev. Neurother.* **9** 427–30
[4] Bouton C E *et al* 2016 Restoring cortical control of functional movement in a human with quadriplegia *Nature* **533** 247–50
[5] Hochberg L R *et al* 2012 Reach and grasp by people with tetraplegia using a neurally controlled robotic arm *Nature* **485** 372–5
[6] Jarosiewicz B *et al* 2015 Virtual typing by people with tetraplegia using a self-calibrating intracortical brain-computer interface *Sci. Transl. Med.* **7** 313ra179
[7] Gabran S R *et al* 2013 High-density intracortical microelectrode arrays with multiple metallization layers for fine-resolution neuromonitoring and neurostimulation *IEEE Trans. Neural Syst. Rehabil. Eng.* **21** 869–79
[8] Ajiboye A B *et al* 2017 Restoration of reaching and grasping movements through brain-controlled muscle stimulation in a person with tetraplegia: a proof-of-concept demonstration *Lancet* **381** 1821–30
[9] Schwartz A B and Moran D W 2000 Arm trajectory and representation of movement processing in motor cortical activity *Eur. J. Neurosci.* **12** 1851–6
[10] Schwartz A B, Moran D W and Reina G A 2004 Differential representation of perception and action in the frontal cortex *Science* **303** 380–3
[11] Donoghue J 2008 Bridging the brain to the world: a perspective on neural interface systems *Neuron* **60** 511–21
[12] Jorfi M, Skousen J L, Weder C and Capadona J R 2015 Progress towards biocompatible intracortical microelectrodes for neural interfacing applications *J. Neural Eng.* **12** 011001
[13] Barrese J C *et al* 2013 Failure mode analysis of silicon-based intracortical microelectrode arrays in non-human primates *J. Neural Eng.* **10** 066014
[14] Prasad A *et al* 2012 Comprehensive characterization and failure modes of tungsten microwire arrays in chronic neural implants *J. Neural Eng.* **9** 056015
[15] Miranda R A *et al* 2015 DARPA-funded efforts in the development of novel brain-computer interface technologies *J. Neurosci. Methods* **244** 52–67
[16] Saxena T *et al* 2013 The impact of chronic blood–brain barrier breach on intracortical electrode function *Biomaterials* **34** 4703–13
[17] Nolta N F, Christensen M B, Crane P D, Skousen J L and Tresco P A 2015 BBB leakage, astrogliosis, and tissue loss correlate with silicon microelectrode array recording performance *Biomaterials* **53** 753–62
[18] Hammer D X *et al* 2014 Longitudinal vascular dynamics following cranial window and electrode implantation measured with speckle variance optical coherence angiography *Biomed. Opt. Express* **5** 2823–36
[19] Potter K A, Buck A C, Self W K, Callanan M E, Sunil S and Capadona J R 2013 The effect of resveratrol on neurodegeneration and blood brain barrier stability surrounding intracortical microelectrodes *Biomaterials* **34** 7001–15
[20] Potter K A, Buck A C, Self W K and Capadona J R 2012 Stab injury and device implantation within the brain results in inversely multiphasic neuroinflammatory and neurodegenerative responses *J. Neural Eng.* **9** 046020
[21] Kozai T D Y *et al* 2010 Reduction of neurovascular damage resulting from microelectrode insertion into the cerebral cortex using *in vivo* two-photon mapping *J. Neural Eng.* **7** 046011
[22] Hammer D X, Lozzi A, Boretsky A and Welle C G 2016 Acute insertion effects of penetrating cortical microelectrodes imaged with quantitative optical coherence angiography *Neurophotonics* **3** 025002
[23] Quagliarello V J, Wispelwey B, Long W J Jr and Scheld W M 1991 Recombinant human interleukin-1 induces meningitis and blood–brain barrier injury in the rat. Characterization and comparison with tumor necrosis factor *J. Clin. Invest.* **87** 1360–6
[24] Clark I A, Alleva L M and Vissel B 2010 The roles of TNF in brain dysfunction and disease *Pharmacol. Ther.* **128** 519–48
[25] Stamatovic S M *et al* 2005 Monocyte chemoattractant protein-1 regulation of blood–brain barrier permeability *J. Cerebr. Blood Flow Metab.* **25** 593–606
[26] Feuerstein G Z, Liu T and Barone F C 1994 Cytokines, inflammation, and brain injury: role of tumor necrosis factor-alpha *Cerebrovasc. Brain Metab. Rev.* **6** 341–60
[27] Stamatovic S M, Keep R F, Kunkel S L and Andjelkovic A V 2003 Potential role of MCP-1 in endothelial cell tight junction 'opening': signaling via Rho and Rho kinase *J. Cell Sci.* **116** 4615–28
[28] Yadav A, Saini V and Arora S 2010 MCP-1: chemoattractant with a role beyond immunity: a review *Clin. Chim. Acta* **411** 1570–9
[29] Sugama S, Takenouchi T, Cho B P, Joh T H, Hashimoto M and Kitani H 2009 Possible roles of microglial cells for neurotoxicity in clinical neurodegenerative diseases and experimental animal models *Inflamm. Allergy Drug Targets* **8** 277–84
[30] Ravikumar M *et al* 2014 The roles of blood-derived macrophages and resident microglia in the neuroinflammatory response to implanted Intracortical microelectrodes *Biomaterials* **35** 8049–64
[31] Sommakia S, Rickus J L and Otto K J 2014 Glial cells, but not neurons, exhibit a controllable response to a localized inflammatory microenvironment *in vitro Front. Neuroeng.* **7** 41
[32] London A, Cohen M and Schwartz M 2013 Microglia and monocyte-derived macrophages: functionally distinct

populations that act in concert in CNS plasticity and repair *Front. Cell. Neurosci.* **7** 34
[33] Nimmerjahn A, Kirchhoff F and Helmchen F 2005 Resting microglial cells are highly dynamic surveillants of brain parenchyma *in vivo Science* **308** 1314–8
[34] Potter-Baker K A and Capadona J R 2015 Reducing the 'stress': antioxidative therapeutic and material approaches may prevent intracortical microelectrode failure *ACS Macro Lett.* **2015** 275–9
[35] Potter K A, Jorfi M, Householder K T, Foster E J, Weder C and Capadona J R 2014 Curcumin-releasing mechanically-adaptive intracortical implants improve the proximal neuronal density and blood–brain barrier stability *Acta Biomater.* **10** 2209–22
[36] Potter-Baker K A *et al* 2015 Implications of chronic daily anti-oxidant administration on the inflammatory response to intracortical microelectrodes *J. Neural Eng.* **12** 046002
[37] Potter-Baker K A *et al* 2014 Development of superoxide dismutase mimetic surfaces to reduce accumulation of reactive oxygen species surrounding intracortical microelectrodes *J. Mater. Chem.* B **2** 2248–58
[38] Block M L, Zecca L and Hong J-S 2007 Microglia-mediated neurotoxicity: uncovering the molecular mechanisms *Nat. Rev. Neurosci.* **8** 57–69
[39] Gage G J, Stoetzner C R, Richner T, Brodnick S K, Williams J C and Kipke D R 2012 Surgical implantation of chronic neural electrodes for recording single unit activity and electrocorticographic signals *J. Vis. Exp.* **60** e3565
[40] Woolley A J, Desai H A and Otto K J 2013 Chronic intracortical microelectrode arrays induce non-uniform, depth-related tissue responses *J. Neural Eng.* **10** 026007
[41] Saunders N R, Dziegielewska K M, Mollgard K and Habgood M D 2015 Markers for blood–brain barrier integrity: how appropriate is Evans blue in the twenty-first century and what are the alternatives? *Front. Neurosci.* **9** 385
[42] Hue C D *et al* 2016 Time course and size of blood–brain barrier opening in a mouse model of blast-induced traumatic brain injury *J. Neurotrauma* **33** 1202–11
[43] Kawoos U, Gu M, Lankasky J, McCarron R M and Chavko M 2016 Effects of exposure to blast overpressure on intracranial pressure and blood–brain barrier permeability in a rat model *PLoS One* **11** e0167510
[44] Augustin G *et al* 2012 Cortical bone drilling and thermal osteonecrosis *Clin. Biomech.* **27** 313–25
[45] Augustin G, Davila S, Udilljak T, Staroveski T, Brezak D and Babic S 2012 Temperature changes during cortical bone drilling with a newly designed step drill and an internally cooled drill *Int. Orthop.* **36** 1449–56
[46] Gupta V, Pandey P M, Gupta R K and Mridha A R 2017 Rotary ultrasonic drilling on bone: a novel technique to put an end to thermal injury to bone *Proc. Inst. Mech. Eng.* H **231** 189–96
[47] Pandey R K and Panda S S 2013 Drilling of bone: a comprehensive review *J. Clin. Orthop. Trauma* **4** 15–30
[48] Nguyen J K *et al* 2014 Mechanically-compliant intracortical implants reduce the neuroinflammatory response *J. Neural Eng.* **11** 056014
[49] Xu H T, Pan F, Yang G and Gan W B 2007 Choice of cranial window type for *in vivo* imaging affects dendritic spine turnover in the cortex *Nat. Neurosci.* **10** 549–51
[50] Harris J P *et al* 2011 Mechanically adaptive intracortical implants improve the proximity of neuronal cell bodies *J. Neural Eng.* **8** 066011
[51] Nguyen J K *et al* 2016 Influence of resveratrol release on the tissue response to mechanically adaptive cortical implants *Acta Biomater.* **29** 81–93
[52] Stolzberg D, Chrostowski M, Salvi R J and Allman B L 2012 Intracortical circuits amplify sound-evoked activity in primary auditory cortex following systemic injection of salicylate in the rat *J. Neurophysiol.* **108** 200–14
[53] Kolarcik C L *et al* 2015 Elastomeric and soft conducting microwires for implantable neural interfaces *Soft Matter* **11** 4847–61
[54] Kozai T D *et al* 2015 Comprehensive chronic laminar single-unit, multi-unit, and local field potential recording performance with planar single shank electrode arrays *J. Neurosci. Methods* **242** 15–40
[55] De Faveri S *et al* 2014 Bio-inspired hybrid microelectrodes: a hybrid solution to improve long-term performance of chronic intracortical implants *Frontiers Neuroeng.* **7** 7
[56] Kozai T D Y, Vazquez A L, Weaver C L, Kim S-G and Cui X T 2012 *In vivo* two-photon microscopy reveals immediate microglial reaction to implantation of microelectrode through extension of processes *J. Neural Eng.* **9** 066001
[57] Livingston A, Wang T, Christou C, Pelletier M H and Walsh W R 2015 The effect of saline coolant on temperature levels during decortication with a Midas Rex: an *in vitro* model using sheep cervical vertebrae *Frontiers Surg.* **2** 37
[58] Cole J T *et al* 2011 Craniotomy: true sham for traumatic brain injury, or a sham of a sham? *J. Neurotrauma* **28** 359–69
[59] Olesen S P 1987 Leakiness of rat brain microvessels to fluorescent probes following craniotomy *Acta Physiol. Scand.* **130** 63–8
[60] Adelson P D, Whalen M J, Kochanek P M, Robichaud P and Carlos T M 1998 Blood brain barrier permeability and acute inflammation in two models of traumatic brain injury in the immature rat: a preliminary report *Acta Neurochir. Suppl.* **71** 104–6
[61] Kiyatkin E A and Sharma H S 2009 Permeability of the blood–brain barrier depends on brain temperature *Neuroscience* **161** 926–39
[62] Kalmbach A S and Waters J 2012 Brain surface temperature under a craniotomy *J. Neurophysiol.* **108** 3138–46
[63] Kosaras B, Jakubowski M, Kainz V and Burstein R 2009 Sensory innervation of the calvarial bones of the mouse *J. Comp. Neurol.* **515** 331–48
[64] Eriksson A R and Albrektsson T 1983 Temperature threshold levels for heat-induced bone tissue injury: a vital-microscopic study in the rabbit *J. Prosthet. Dent.* **50** 101–7
[65] Yarmolenko P S *et al* 2011 Thresholds for thermal damage to normal tissues: an update *Int. J. Hyperth.* **27** 320–43
[66] Toews A R, Bailey J V, Townsend H G and Barber S M 1999 Effect of feed rate and drill speed on temperatures in equine cortical bone *Am. J. Vet. Res.* **60** 942–4
[67] Davidson S R and James D F 2003 Drilling in bone: modeling heat generation and temperature distribution *J. Biomech. Eng.* **125** 305–14
[68] Bachus K N, Rondina M T and Hutchinson D T 2000 The effects of drilling force on cortical temperatures and their duration: an *in vitro* study *Med. Eng. Phys.* **22** 685–91
[69] Prabhu K S 2007 *Improved Bone Drilling Process Through Modeling and Testing* (Gainesville, FL: University of Florida)
[70] Pak N, Siegle J H, Kinney J P, Denman D J, Blanche T J and Boyden E S 2015 Closed-loop, ultraprecise, automated craniotomies *J. Neurophysiol.* **113** 3943–53
[71] Hou Y, Li C, Ma H, Zhang Y, Yang M and Zhang X 2015 An experimental research on bone drilling temperature in orthopaedic surgery *Open Mater. Sci. J.* **9** 178–88
[72] Li C H *et al* 2015 Simulation study on effect of cutting parameters and cooling mode on bone-drilling temperature field of superhard drill *Int. J. Adv. Manuf. Technol.* **81** 2027–38

CHAPTER

28

Prospects for a Robust Cortical Recording Interface

Andrew Shoffstall[1,2], *Jeffrey R. Capadona*[1,2]

[1]Case Western Reserve University, Cleveland, OH, United States; [2]Louis Stokes Cleveland VA Medical Center, Cleveland, OH, United States

OUTLINE

Neuromodulation, Second Edition
http://dx.doi.org/10.1016/B978-0-12-805353-9.00028-0

This chapter outlines and discusses the history and current state of the neural recording field, specifically in the context of cortical neural prostheses. For in-depth reviews of the subject matter, the reader is referred to excellent reviews by Jorfi et al. (2015), Murphy et al. (2015), Gunasekera et al. (2015), and Tresco and Winslow (2011). Topics covered in this chapter include:

1. Motivation, progress, and challenges for intracortical recording electrodes
2. Commonly used electrodes for intracortical recording
3. Summary of intracortical recording electrode failure mechanisms
4. The biological response to electrode implantation
5. Intracortical electrode technologies to evade the inflammatory response and improve long-term performance
6. Perspectives on the future of cortical neural recording interfaces

MOTIVATION, PROGRESS, AND CHALLENGES FOR INTRACORTICAL RECORDING ELECTRODES

Motivation

The development of a stable intracortical recording electrode has tremendous implications for the rapidly expanding field of neuroprosthetics and, more broadly, brain–machine interfaces (BMIs). BMIs have significant potential to reduce the burden associated with paralysis and limb loss. By bypassing damaged regions of the nervous system, BMIs offer the promise of reducing the burden of injury and enabling injured individuals to live fuller and more interactive lives (Pancrazio and Peckham, 2009). Unfortunately, microelectrodes that are currently used for BMI applications demonstrate poor chronic neural recording performance and reliability. Signal-to-noise ratio degrades over several weeks to months (Burns et al., 1974), resulting from a multifactored failure mechanism having both electromechanical (abiotic) and host tissue (biotic) root causes (Jorfi et al., 2015).

In part due to the potential for BMI applications and the need for further development, on April 2, 2013, President Obama launched an initiative to "accelerate the development and application of new technologies that will enable researchers to… show how individual brain cells and complex neural circuits interact at the speed of thought." In response to this grand challenge, the director of the National Institutes of Health (NIH) released the scientific vision of the Brain Research through Advancing Innovative Neurotechnologies (BRAIN) Working Group, which asked for $4.5 billion over the next 10–12 years to support a strategy for addressing that goal. The BRAIN Initiative looks beyond the current rehabilitative applications proposed for BMIs, to a comprehensive, mechanistic understanding of cognition, emotion, perception, and action in health and disease. The first 5 years of the NIH vision focus largely on developing new "platform" tools and technologies to advance human neuroscience and integrate them into therapeutic interventions. With notable supporters like National Science Foundation (NSF), US Food and Drug Administration (FDA), Defense Advanced Research Projects Agency (DARPA), and many private organizations, the magnitude of the potential impact of the NIH BRAIN Initiative has been compared with that of the Apollo Program and the Human Genome Project (Insel, 2015).

Progress

Intracortical recording electrodes were initially developed in the 1940s to advance our basic understanding of the nervous system (Grundfest, 1942; Grundfest et al., 1950; Renshaw and Morison, 1940). The first devices consisted of glass pipette and microwire electrodes and were used to interrogate the cortical electrophysiology of various animal models. Since that time, the field has achieved significant strides, both in fabrication technologies and in advancing medical applications of intracortical recording electrodes.

For the past two decades, hundreds of publications have been added to the literature involving "intracortical recording" (or "intracortical microelectrodes"), with over one-third being published since 2010 (Fig. 28.1). With the initiation of more than 120 funded projects stemming from the BRAIN Initiative, this number is set to soar exponentially in the coming years (The Brain Initiative Website, 2016). Today, there are intracortical microelectrodes that have FDA approval (namely the Utah Array from Blackrock). Additionally, there are a broad range of advanced materials and devices with novel capabilities in the preclinical pipeline for future implementation and approval. Recent clinical trials have demonstrated tremendous success, enabling quadriplegic patients to feed themselves, not only with robotic arms (Hochberg et al., 2012) but also with their own muscles with applied stimulation (Bouton et al., 2016). Very recent evidence even points to the possibility that brain–computer interfaces may be able to trigger partial lower limb recovery in paraplegic patients (Donati et al., 2016). Wireless communication has been integrated into new generations of devices that simplifies their clinical implementation and overcomes tethering challenges (Rajangam et al., 2016). The use of optogenetic techniques to allow neural recording or stimulation with light currently remains in preclinical study, but may someday soon provide a

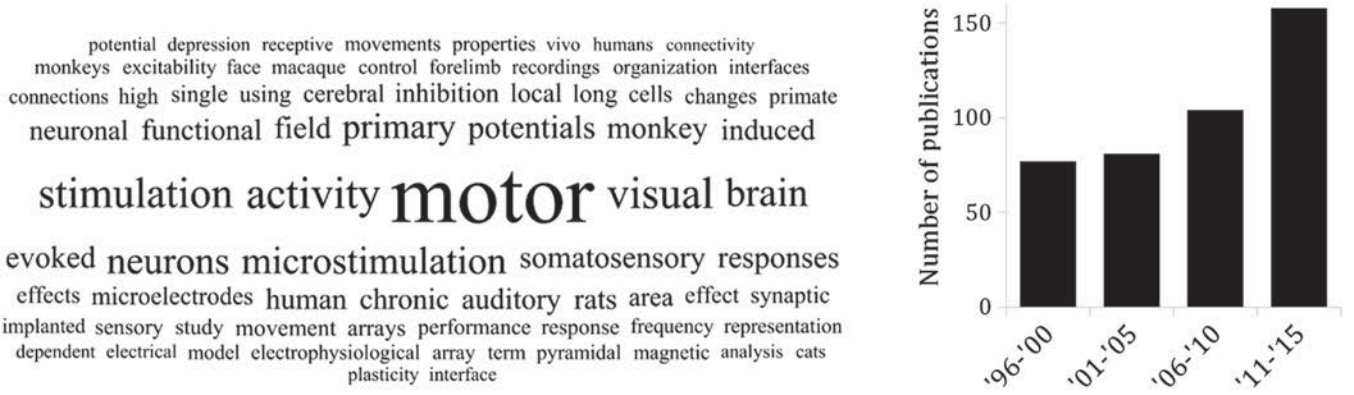

FIGURE 28.1 Wordle depicting the current focus of the intracortical recording field. This wordle and graph of total of publications were created based on titles from a PubMed database search of the term "intracortical AND (recording OR microelectrode)." To create the wordle, we used software freely available from MathWorks (Owen, 2014). Word font size is proportional to the frequency of appearance in the literature search titles.

means for less invasively or more selectively interacting with neural circuits (Yazdan-Shahmorad et al., 2016; Gagnon-Turcotte et al., 2015). The pace of innovation and the achievement of milestones is astonishing.

While the field has made significant progress, BCI has yet to break into the mainstream. To achieve a reliable and natural brain control paradigm, neural signals must be recorded with high-quality and fine spatial resolution such that neuron populations can be triangulated, decoded, and correlated with a person's intended movement (Murphy et al., 2015). Such applications often rely on intracortically implanted microelectrodes. Due to the moderate risk associated with implantation surgery and the limited longevity of current recording configurations, one must consider and balance risk to the patient (or animal) with the potential benefit it may serve. The Holy Grail of neural recording interfaces has yet to be perfected: a device that is minimally invasive but can still provide high-density, chronically stable signals.

Challenges

A central focus of neuromodulation has been on the development of electrodes for *stimulation applications*. Surface chemistries and stimulation paradigms are optimized to balance charge delivery and prevent dissolution and corrosion of the electrode contacts. The host tissue response (including inflammation and encapsulation) is an important consideration, but resulting changes can often be compensated for by tuning stimulation settings (e.g., amplitude, pulse width, direction, etc.) to achieve the desired functional outcome: excitation or blockade of surrounding neurons.

For *intracortical recording applications*, some unique considerations regarding the neural electrode must be made. Researchers working in the field are challenged with a dynamically changing environment, which includes biological, material, and electrical factors, that can be roughly grouped into biotic and abiotic in origin. For a more complete discussion of failure mechanisms, the reader is referred to Jorfi et al. (2015), Polikov et al. (2005), Biran et al. (2005), and Kozai et al. (2015a).

Biotic. In recording applications involving implanted neural electrodes, the host tissue response plays a much larger role in determining long-term recording performance and stability than it does in stimulation applications. Inflammation, the healing response, and encapsulation result in changes to the physical and electrical properties of the tissue (Jorfi et al., 2015). Cellular composition and the normal pattern of neural activity surrounding the electrode are altered.

Abiotic. Electromechanical failures include the breakage of the fine electrode shanks, degradation of insulation, and corrosion of metal contacts. These failures result in changes to an electrode's exposed conductive surface area, conductivity, and, ultimately, its ability to transduce ionic extracellular signals into electrical signals (Jorfi et al., 2015).

There are a wide breadth of neural recoding electrodes available, reflecting the huge motivation in the field to produce a device capable of long-term high-quality intracortical recordings and the diversity of targeted tissue regions for a variety of applications.

COMMONLY USED ELECTRODES FOR INTRACORTICAL RECORDING

There are a number of electrode designs used for cortical recordings, segmented here as: Utah arrays, Michigan-type electrodes, microwires, and encephalography (electrocorticography [ECoG] and electroencephalography [EEG]). The factors that influence the electrode

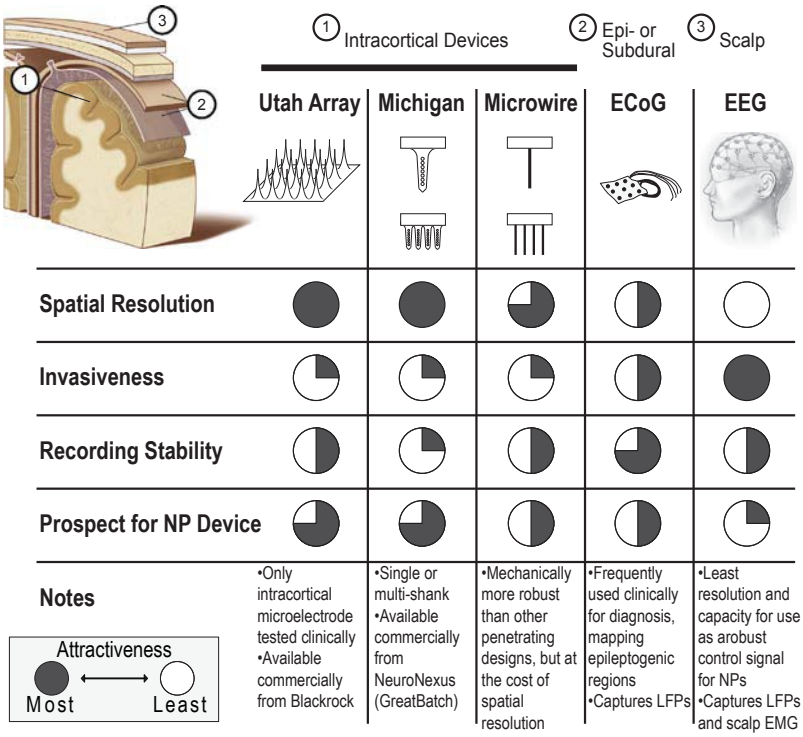

FIGURE 28.2 Neural recording devices, including invasive and noninvasive. *ECoG*, electrocortocography; *EEG*, electrocephalography; *EMG*, electromyography; *LFPs*, local field potential; *NPs*, neuroprostheses. *Modified from Jorfi, M., Skousen, J.L., Weder, C., Capadona, J.R., February 2015. Progress towards biocompatible intracortical microelectrodes for neural interfacing applications. J. Neural Eng. 12 (1), 011001.*

selection primarily include invasiveness, spatial resolution, and relatedly quality and stability of the signal (Fig. 28.2). To date, for neuroprosthetic BMI applications, the Utah and Michigan electrodes have outpaced microwires, ECoG and EEG, owing to their superior spatial resolution.

The Utah Electrode Array

The Utah Electrode Array (UEA) consists of silicon-based microelectrode typically with a 10×10 array of 1.5-mm tines (Campbell et al., 1991). Developed by Normann et al. at the University of Utah in 1991, it has remained at the forefront of the intracortical recording field. It provides extremely high-resolution information, with tines spaced 400 μm apart. Several challenges prevent its wider acceptance and use in broader applications: (1) it requires an invasive procedure, involving high-speed pneumatically driven insertion, and (2) it has suffered from inconsistent performance owing to biological (neuroinflammatory) response and/or manufacturing defects (Miranda et al., 2015). Nonetheless, the UEA is the only high-density, penetrating recording electrode approved by the FDA. It has 510(k) approval for recording or stimulation experiments of less than 30 days and investigational device exemption (IDE) approval for chronic recording or stimulation studies longer than 30 days (Brain Initiative Website, 2017). Additionally, the Utah Array has received the CE mark in Europe.

Variations of the UEA have also been explored, including a slanted-tine design for achieving various tissue depths (Branner and Normann, 2001), a design shape that conforms to complex anatomical geometries (Bhandari et al., 2008), ultra-high aspect ratio devices (Bhandari et al., 2010), and high-density arrays (Wark et al., 2013). Recently, a collaboration between Brown University and Blackrock Microsystems has generated a commercially available wireless version of the UEA (Yin et al., 2013; Borton et al., 2013).

The majority of clinical work with UEA technology to date has focused on rehabilitative applications (Warren et al., 2001; Kim et al., 2006; Suner et al., 2005; Schwartz et al., 1988). As part of the BrainGate clinical trials, Hochberg et al. implanted UEAs into the primary motor cortex of their volunteers with tetraplegia. Using a robotic arm, they were able to restore reach and grasp functions to the individuals by recording and decoding volitional movement intent (Hochberg et al., 2012, 2006). Jarosiewicz et al. (2015) used similar approach to achieve virtual typing for paralyzed individuals, and Ajiboye et al. (2017) demonstrated reaching and grasp through brain-controlled muscle stimulation. Gilja et al. (2015) recently demonstrated neural recording for more than 1 year with UEAs implanted in patients

with amyotrophic lateral sclerosis (ALS). Other groups around the globe have also been making significant advances in the field of BCI, including from Shwartz (Wodlinger et al., 2015; Golub et al., 2014), Andersen (Stetson and Andersen, 2015; Klaes et al., 2015; Graf and Andersen, 2015), and Nicolelis (Rajangam et al., 2016; Vouga et al., 2017).

Despite the tremendous progress that has been achieved, improving recording performance and longevity remains a principal focus (Jorfi et al., 2015; Rousche and Normann, 1998; Barrese et al., 2013). For examples, in their review of DARPA-led efforts in BCIs, Miranda et al. (2015) argue that overcoming interface failure is one of the largest remaining hurdles for BCI researchers and that without overcoming these issues, the vision of life-long BCI systems will remain just out of reach.

Michigan-Style Microelectrodes

Whereas the Utah Arrays consist of a two-dimensional, 10×10 array of shanks, Michigan-style electrode arrays (MEAs) are planar devices with multiple recording contacts located along one or several silicon shanks (Wise, 2005). Developed by Wise et al., first at Bell Labs in 1966 and later at the University of Michigan, these electrodes are frequently studied in preclinical BCI applications (Wise and Angell, 1975; Wise et al., 1970; BeMent et al., 1986; Hetke et al., 1994; Kipke et al., 2003; Vetter et al., 2004). While chronic recording studies have been reported, the consistent longevity of recordings remains among the biggest hurdles (Ludwig et al., 2006). To the authors' knowledge, MEAs have yet to be studied in human clinical trials.

MEAs are sold commercially by NeuroNexus, a subsidiary of GreatBatch Inc. Recent advances have yielded on-board signal digitization (SmartProbe) and a variant that can be used as an optogenetic probe (optoelectrodes or simply "optrode"). For additional details on the development and application of MEAs, the reader is referred to a review by Wise (2005).

Microwires

Microwires were first developed by Salcman, Bak, and Schimdt at the NIH in the early 1970s (Salcman and Bak, 1973, 1976). These electrodes consisted of 2- to 11-μm-diameter iridium (Ir) and platinum (Pt) alloys. In one of the first long-term demonstrations of the technology, Salcman and Schmidt recorded single neuron unit activity for up to 223 days with a microwire implanted in the motor cortex of a nonhuman primate (Salcman and Bak, 1976; Schmidt et al., 1976). Since then, a variety of microwire devices have been developed for BMI applications (Schmidt et al., 1976, 1988; Liu et al., 2006; Kruger et al., 2010). However, as with other microelectrodes, neuroinflammation appears to degrade recording performance over time (Burns et al., 1974; Schmidt et al., 1976; Prasad et al., 2012, 2014), most likely through the degradation of insulating materials and corrosion of metals (Prasad et al., 2012, 2014).

Electrocorticography

ECoG is frequently used clinically to map epileptogenic regions of the brain and facilitate the surgical excision of operable focal lesions. ECoG arrays are placed temporarily intraoperatively and removed immediately or shortly after lesion resection surgery.

Many groups have investigated the use of ECoG arrays placed subdurally or epidurally to collect neural signals for use in BMI applications (Murphy et al., 2015; Schalk and Leuthardt, 2011; King-Stephens et al., 2015; Bouchard and Chang, 2014; Bleichner et al., 2016; Kellis et al., 2012). ECoG arrays pick up LFP signals and are reported to have a spatial resolution of about 4 mm (Murphy et al., 2015). Even with this limitation, applications involving two- and three-dimensional arm movements (Marathe and Taylor, 2013; Chao et al., 2010) that predict arm movement with 3 degrees of freedom (*df*) (Nakanishi et al., 2013), and determine trajectory and kinetics for use in an FES system (Flint et al., 2014) have been developed, with individual reports of chronic recordings up to 7 years (King-Stephens et al., 2015). While ECoG arrays have the distinct benefit of being placed superficial to the meninges, and thus potentially less invasive than implanted MEAs, most applications have focused on gross motor rather than fine motor tasks that may require a higher spatial resolution.

Electroencephalography

Due to noninvasiveness contacts placed on the scalp, EEG benefits from sampling a wider number of areas around the skull. However, its spatial resolution is relatively coarse at about 3 cm (Murphy et al., 2015). To date, the best performance of an EEG BCI system in control of extrinsic operations is 3 *df*, which was achieved only after months of intensive training (McFarland et al., 2010). Other BMI investigations include those by surveying the EEG response to various motor task (Ramos-Murguialday and Birbaumer, 2015) and decoding movement intent in a sitting-to-standing task in healthy volunteers (Bulea et al., 2014). Interestingly, as one group has recently shown, EEG may be used in a complimentary fashion to other sources of neural control (Soekadar et al., 2015): electrooculography in conjunction with EEG to improve hand-grasp task of an exoskeleton.

Optical Microelectrodes

Optical microelectrodes (or "optrodes") are also under development by a number of groups, primarily for use in optogenetic research (Yazdan-Shahmorad et al., 2016; Abaya et al., 2012; Segev et al., 2017; Iseri and Kuzum, 2017; Chamanzar et al., 2014). Notably, Yazdan-Shahmorad et al. (2016) developed a micro-ECoG array that was capable of recording large-scale cortical activity spanning the S1 somatosensory and M1 motor regions in a nonhuman primate. With recent advances in optogentic techniques and novel implantable probe designs, such devices are improving at a rapid rate.

SUMMARY OF INTRACORTICAL RECORDING ELECTRODE FAILURE MECHANISMS

Failure of microelectrode recordings is characterized by a decrease in signal-to-noise ratio, leading to inability to accurately discriminate neuronal firing from background (Burns et al., 1974; Ludwig et al., 2006; Liu et al., 2006, 1999; Freire et al., 2011). There are a number of underlying failure mechanisms that have been described, but, by definition, all lead to either electrical or neural circuit disruption. Failure modes for microelectrode recordings include:

1. **Degradation of insulation** (e.g., dissolution, peeling of polymer coatings) (Schmidt et al., 1988, 1999; Hammerle et al., 2002; Maloney et al., 2005; Hsu et al., 2009; Loeb et al., 1977; Winslow et al., 2010)
2. **Corrosion of electrical contacts** (e.g., oxidation, pitting of electrode contacts and connectors) (Prasad et al., 2014; Merrill, 2010; Patrick et al., 2011; McCarthy et al., 2011; McDord and Fridovich, 1969; Potter et al., 2013)
3. **Local neurodegeneration** (e.g., neuronal loss, dysfunction) (Potter et al., 2012)
4. **Device migration** (e.g., movement of microelectrode away from neuron population of interest) (Barrese et al., 2016)
5. **Direct mechanical damage** (e.g., electrode, lead fractures), (Barrese et al., 2013; Prasad et al., 2012, 2014; Ward et al., 2009)

As suggested in Fig. 28.3, the primary mechanisms are influenced by a number of secondary and tertiary factors, namely:

- Secondary (neuroinflammation, tissue strain, chemical environment, material fatigue)
- Tertiary (acute implantation injury, chronic micromotion and exposure, and manufacturing defects)

These factors are not mutually exclusive and may contribute synergistically to failure. In particular, it seems that neuroinflammation may underpin a number of interrelated failure mechanisms (Prasad et al., 2012; Ward et al., 2009). Neuroinflammation releases a number of cytotoxic substances (leading to neurodegeneration), altering the microenvironment by lowering pH and releasing reactive oxidative species (leading to corrosion and degradation of insulation), and depositing scar tissue (electrically and physically isolating the device from neurons).

Neuroinflammatory Underpinnings

While the dominant mechanism leading to functional loss following intracortical implantation is unresolved, neuroinflammation is thought to play a major role in both biotic and abiotic failure mechanisms (Jorfi et al., 2015; Harris, 2011). Upon implantation, microelectrodes immediately disrupt brain tissue and neurovasculature, initiating a multiphasic inflammatory response (Potter et al., 2012). The acute response plateaus within the first few weeks of implantation, and inflammation thereafter is driven in a chronic state via various mechanisms, including microglial and macrophage activation, the fibrotic glial scar, free radical oxidation, and chronic dysfunction of the blood–brain barrier (BBB) (Potter et al., 2012; Skousen et al., 2015; Potter-Baker et al., 2014b; Nguyen et al., 2012).

To directly demonstrate the impact of neuroinflammation on recording signal quality, Harris et al. administered LPS (lipopolysaccharide, an endotoxin that elicits an inflammatory response) to rats and observed signal degradation within the first 4 weeks (Harris, 2011). Signal degradation was observed as an increase in signal-to-noise ratio a decrease in local field potential power in the LPS-treated group compared with their control group. These results demonstrated that the inflammatory response directly affected signal quality during chronic recordings.

While the inflammatory process has been implicated in recording signal loss, so far no strategies to mitigate it have proved to be safe and effective for long-term use. A deeper understanding of the underlying biology is of significant importance. To better understand how to modulate/mitigate the inflammatory response, one must better understand the underlying cellular and physiologic changes that take place after implantation.

THE BIOLOGICAL RESPONSE TO ELECTRODE IMPLANTATION

Overview

Upon implantation, the microelectrode disturbs the natural resting physiology of the brain tissue. Several groups have shown that the vasculature is immediately and significantly affected (Hammer et al., 2014; Bjornsson

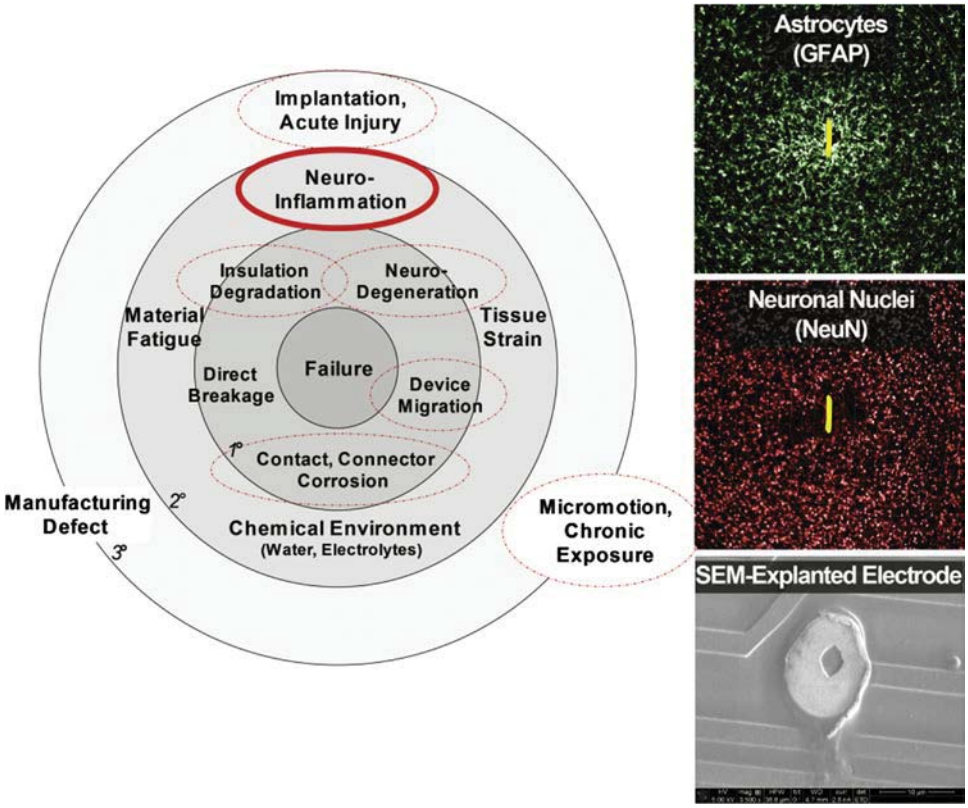

FIGURE 28.3 Failure mechanisms of intracortical microelectrodes. *Innermost circles* denote direct causes of failure, caused by electrical or neural circuit disruption and characterized by a signal-to-noise ratio attenuation. *Outer circles* are secondary (and tertiary) causes for electrode failure that act indirectly to lead to recording malfunction. The neuroinflammatory response plays a key role in affecting a number of failure pathways and, for that reason, has been studied extensively as a means to prolong microelectrode recording performance. Mechanisms related to neuroinflammation, both upstream and downstream, are circled in red. Example images show (1) histology of neuroinflammation (staining for activated astrocytes at 2 weeks after implantation), (2) histology of neurodegeneration (loss of neurons most proximal to implanted microelectrode 2 weeks after implantation), (3) SEM of explanted electrodes showing insulation peeling, contact corrosion, and direct mechanical damage after 2 weeks of implantation (Prasad et al., 2012).

et al., 2006; House et al., 2006). Small and large vessels may be disrupted, which allow cells, large proteins, and molecules that normally cannot pass through the BBB to pass into the extravascular tissue. Consequently, an inflammatory and wound-healing response is simultaneously set into motion (Potter et al., 2012).

In cases of acute and nonsevere instances of brain injury, the BBB typically reforms after 3–4 weeks (Hammer et al., 2014), and weeks later, the inflammatory response subsides (Potter et al., 2012). However, in the case of an implanted material, macrophages and microglia, the cells responsible for clearing debris (Tresco and Winslow, 2011; Polikov et al., 2005; Biran et al., 2005, 2007; Potter et al., 2012), are unable to engulf and phagocytose the microelectrode and continue to promote a proinflammatory state. Therefore, the blood–brain barrier remains chronically leaky (Kozai et al., 2015b). Microglia and astrocytes begin to wall off the electrode, releasing reactive chemical species and depositing extracellular matrix proteins in a process known as astrogliosis. Astrogliosis results in fibrotic encapsulation around the implantation site.

In addition to the inflammation response set off by the initial injury, additional mechanisms, such as motion-induced injury, may promote persistent or chronic inflammation. Since the base materials in traditional electrodes are stiff (e.g., silicon), and the brain is comparatively much softer and in constant motion, albeit micromotion, chronic fluctuating strains are placed on the brain tissue surrounding the implanted electrode (Subbaroyan et al., 2005; Sridharan et al., 2013; Polanco et al., 2016). While the exact underlying biological mechanism for how the strain field is translated into inflammatory response is unknown, in vivo findings support the correlation. When compliant, rather than stiff, electrodes are implanted to minimize the strain/stress in response to motion, a reduced inflammatory response is observed in the rat brain tissue surrounding the electrode (Harris et al., 2011a,b; Nguyen et al., 2014).

Soluble Factors Kill Neurons, Degrade and Corrode Implanted Materials, and Maintain the Inflammatory Response

Soluble factors (e.g., growth factors and cytokines) play a major role in cell signaling to help mediate the wound healing response as well as inflammation after injury

(Skousen et al., 2015). Upon initial injury, the BBB is disrupted, allowing macrophage, serum proteins, and other blood cells to infiltrate the immune-privileged neural space. In particular, macrophages and microglia have been identified as releasing a number of soluble factors that not only act on the tissue immediately touching the electrode but also diffuse from the implant surface, increasing the radius of the cells' effects (Skousen et al., 2011).

Interleukins (tumor necrosis factor [TNF]α, interleukin [IL]-1, IL-6) are upregulated at the microelectrode location (He et al., 2006). MCP-1, a chemoattractant, and metalloproteases (e.g., MMP-2, MMP-9) are also expressed (Jorfi et al., 2015; Biran et al., 2005). TNFα, in particular, has direct cytotoxic effects on neurons, while both TNFα and MCP-1 have been shown to associate with the BBB and to help to recruit macrophages (Block et al., 2007; Chao et al., 1995; Quagliarello et al., 1991; Clark et al., 2010; Feuerstein et al., 1994; Gosselin and Rivest, 2007; Stamatovic et al., 2003, 2005; Sugama et al., 2009; Yadav et al., 2010). Proteases, among other roles, aid in breaking down extracellular matrix proteins. Further, reactive oxygen species appear to accumulate at the implant site (Potter et al., 2013). Together, these soluble factors may have multiple effects, including material corrosion, degradation, and neuronal loss (Takmakov et al., 2015). Importantly, reactive oxygen species and the other factors appear to further afflict the BBB, causing it to be "leaky" and allowing for additional cellular and serum protein infiltration, thus perpetuating an inflammatory cycle (Potter et al., 2012).

Insoluble Factors Serve a Vital Role in Healing and Regeneration but Also Isolate Neurons Electrically and Physically From the Recording Electrode

Extracellular matrix proteins serve an important role after central nervous system injury: reconstruction and walling off the damaged tissue to prevent dysfunction and promote reformation of the BBB (Silver, 2016; Busch and Silver, 2007). While the "dogma" in the field has historically categorized astrocytes as a primary cell type responsible for scarring and for walling off the injury site, new evidence strongly supports its role additionally as both one of regeneration and mediation of the inflammatory response (Silver, 2016; Cregg et al., 2014; Liberto et al., 2004). After injury, glial fibrillary acidic protein (GFAP) and a number of proteoglycans (e.g., chondroitin sulfate [CSPGs]) are upregulated and expressed at the site of the electrode (Busch and Silver, 2007; Zhong and Bellamkonda, 2007). CSPGs are typically considered neuroinhibitory because they form synaptic-like connections with axons, entrapping neurons. However, it has been suggested that CSPGs may also serve a protective role by preventing neuronal destruction from invading macrophages (Silver, 2016; Friedlander et al., 1994; Gopalakrishnan et al., 2008; Hynds and Snow, 1999; Iijima et al., 1991; Kuffler et al., 2009; Nakanishi et al., 2006; Yamada et al., 1997; Filous et al., 2014).

While it may be debated exactly how and what functions these molecules serve, their presence appears to displace neurons as well as change the electrical properties of the surrounding tissue, potentially limiting recording function (Burns et al., 1974; Schmidt et al., 1976; Williams et al., 2007).

Neuronal Loss at the Electrode–Tissue Interface Attenuates the Source Signal

Neuronal density is significantly reduced surrounding implanted electrodes as a result of inflammation and fibrous scar tissue formation (Biran et al., 2005; Potter et al., 2012; Seymour and Kipke, 2007; Thelin et al., 2011; Collias and Manuelidis, 1957; Ravikumar et al., 2014a). Given that electric field potentials decay rapidly, as an inverse square of distance from the source, proximity is an extremely important factor for recording electrode performance. Effective recording ranges have been estimated at 50–150 μm for local field potentials and 25–50 μm for single-unit recordings (Buzsáki, 2004). Unfortunately, neuron survival is not simply a function of the initial injury. Chronic inflammation also appears to reduce neuron populations; however, the exact relationship with recording quality has yet to be identified. Neuron viability is likely more relevant to recording quality than is the density. Regardless, as neurons die back, and are physically separated from the recording electrode by scar tissue, recorded signals are significantly attenuated (Biran et al., 2005; Kozai et al., 2015b).

INTRACORTICAL ELECTRODE TECHNOLOGIES TO EVADE THE INFLAMMATORY RESPONSE AND IMPROVE LONG-TERM PERFORMANCE

Various strategies, specifically aimed at reducing the neuroinflammatory response, have been investigated to achieve recordings over clinically meaningful time frames. The list of strategies broadly include (1) drug administration, (2) material selection/modification, and (3) implantation technique/system design. The following sections and Fig. 28.4 serve as a primer for more in-depth reading on each approach.

Drug Administration

Drug administration is appealing because its effects are temporary and can be tuned to an individual's needs. One must consider the safety, efficacy, ability of the drug

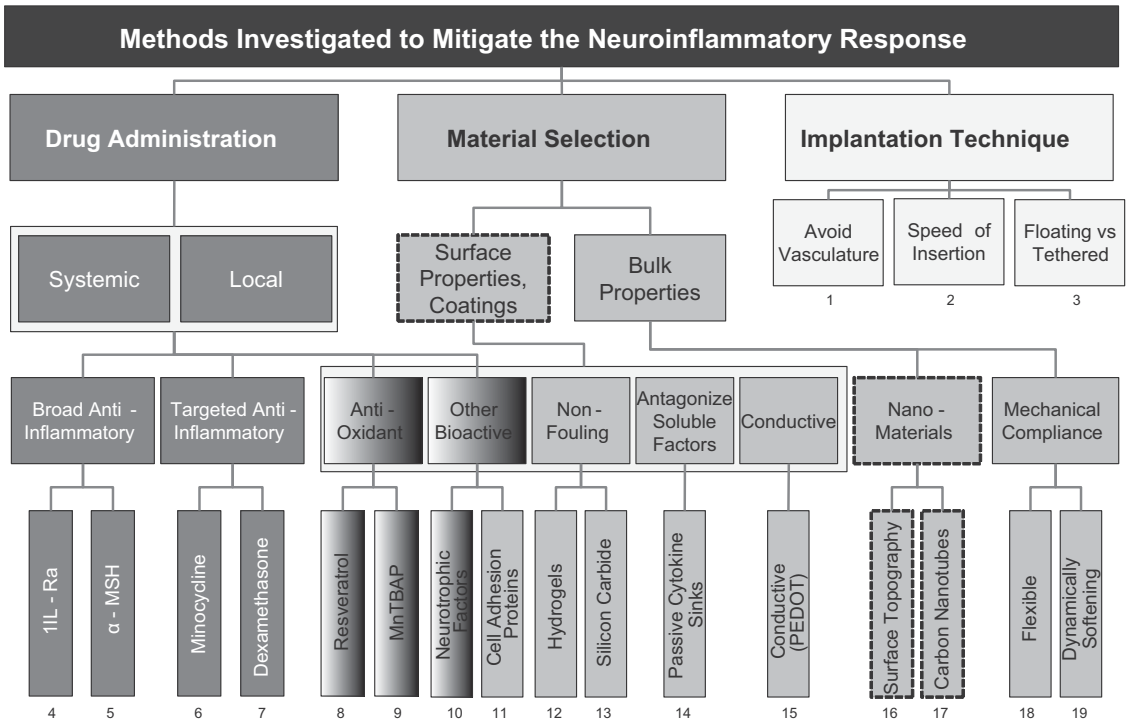

FIGURE 28.4 Methods investigated to mitigate the neuroinflammatory response, broken at the first level into drug administration, material selection, and implantation technique. Note that antioxidant therapies and neurotrophic factors have been studied as both as an administered drug and covalently conjugated onto surfaces of devices (denoted by partial shading). Similarly, nanomaterials, while primarily a novel bulk material, may also have active surface properties (denoted by *dashed-box outline*). References for examples from literature (not an exhaustive list) are provided here: 1, Kozai et al. (2010); 2, Dryg et al. (2015); 3, Karumbaiah et al. (2013); 4, Taub et al. (2012); 5, Zhong and Bellamkonda (2005); 6, Rennaker et al. (2007); 7, Zhong and Bellamkonda (2007), Mercanzini et al. (2010); 8, Potter et al. (2013), Potter-Baker et al. (2015), Nguyen et al. (2016) and Constant et al. (2012); 9, Potter-Baker et al. (2014a,c) and Potter et al. (2014); 10, Winter et al. (2007), Kim et al. (2007) and Gomez and Schmidt (2007); 11, He et al. (2006), Azemi et al. (2008) and Kolarcik et al. (2012); 12, Gutowski et al. (2014), Rao et al. (2012) and Purcell et al. (2009); 13, Knaack et al. (2016) and Cogan et al. (2003); 14, Skousen et al. (2015) and Polikov et al. (2010); 15, Ludwig et al. (2011), Cui and Zhou (2007) and Castagnola et al. (2016); 16, Chapman et al. (2015), Golda et al. (2013) and Ereifej et al. (2013); 17, Vitale et al., 2015, Lu et al. (2010), Baranauskas et al. (2011) and Lewitus et al. (2011); 18, Altuna et al. (2013), Liu et al. (2015) and Luan et al. (2017); 19, Capadona et al. (2008), Ware et al. (2012b, 2013a), Hess et al. (2009, 2011) and Simon et al. (2017).

to cross the BBB, and duration of a drug regimen as well as the desired effect. Some therapies have proved to be effective in the acute phase after implantation but due to safety concerns are not appropriate or practical for long-term use.

Broad-Spectrum Anti-Inflammatory Agents

Local anti-inflammatory treatment after implantation have been shown to reduce histological inflammatory response (dexamethasone) and improve recorded signal quality (minocycline), while vehicle control agents did not (Zhong and Bellamkonda, 2007; Rennaker et al., 2007). While anti-inflammatory drugs helps to confirm the role of inflammation, unfortunately, due to side effects of these therapeutics (i.e., osteoporosis, infection, cataracts, high blood pressure, impaired wound healing), chronic administration is contraindicated (Girbovan et al., 2012; Patel et al., 2011; Khodagholy et al., 2013; Chung et al., 2013). Minocycline is a tetracycline and appears to shift macrophages and microglia toward a quiescent, rather than activated, phenotype (Lee et al., 2004; Kobayashi et al., 2013). Promising in vivo data showed that neural recording from rats receiving minocycline fared better in signal-to-noise ratio and number of simultaneously viable channels. While recording was not investigated, dexamethasone reduced the histologically measured inflammatory response compared with untreated animals (Zhong and Bellamkonda, 2007; Shain et al., 2003; Spataro et al., 2005; Zhong et al., 2005; Wadhwa et al., 2006).

Targeted Anti-Inflammatory Agents

The inflammatory response is extraordinarily complex and composed of many intertwined pathways (Polikov et al., 2005; Potter et al., 2012; Ravikumar et al., 2014b; Cui et al., 2011). Targeted agents may have the ability to more specifically address neuroinflammation in response to device implantation, without inducing

the plethora of unwanted side effects seen with broad-spectrum anti-inflammatory agents. For example, α-melanocyte–stimulating hormone (α-MSH) and IL-1 receptor antagonist (IL-1Ra) are among the agents that have been tested for this purpose (Galimberti et al., 1999; Zhong and Bellamkonda, 2005; He et al., 2007; Taub et al., 2012).

α-MSH is an endogenous tridecapeptide that acts through the inhibition of proinflammatory cytokines and by inhibiting nitric oxide (NO) production (Galimberti et al., 1999; Zhong and Bellamkonda, 2005). By immobilizing α-MSH on a device both in vitro and in vivo, the Bellamkonda laboratory demonstrated a significant reduction in reactive astrocyte (GFAP) and macrophage/microglia (ED1) staining at both 1 and 4 weeks postimplantation (He et al., 2007). Taub et al. (2012) investigated the antagonization of the proinflammatory cytokine IL-1Ra–coated microelectrodes. Short-term histologic studies verified IL-1Ra–coated microelectrodes significantly reduced astrogliosis compared with noncoated microelectrodes. Recently, Gutowski et al. (2015) showed that glial cell attachment to the electrode surface was significantly reduced in vitro with IL-1Ra incorporated in a PEG-based on-demand release system. While their in vivo study in rats produced less resounding results, they found that IgG, a marker for blood proteins, was significantly reduced in their IL-1Ra–positive group at 4 weeks after implantation. For both these targeted agents (α-MSH and IL-1Ra), longer-term histologic and recording outcomes have not been investigated and warrant additional research.

Drug/Coating Combinations

Antioxidants

Given the reported accumulation of reactive oxygen species at the implant site, researchers have investigated the use of antioxidants to combat their negative effects (Potter et al., 2013; Potter-Baker et al., 2015, 2014c; Pangeni et al., 2014). While there are a number of antioxidant agents readily available, a few of the most frequently investigated for use in central nervous system injury associated with microelectrode insertion include resveratrol, curcumin, and superoxide dismutase (SOD) mimetics [e.g., Mn(III) tetrakis (4-benzoic acid)porphyrin (MnTBAP)] (Potter-Baker et al., 2015, 2014c; Liu et al., 2011; Li and Zhou, 2011; Batinić-Haberle et al., 2010).

Potter et al. (2013) found that rats receiving resveratrol showed signs of improved BBB stability and increased neuronal density after 2, but not after 4, weeks at the microelectrode–tissue interface. While these effects were lost at 4 weeks, the authors suggest that the effects may have subsided as it was a single-dose experiment. They later tested repeated intraperitoneal administration and showed continued effects up to 16 weeks and, importantly, a reduction in neurodegeneration by staining with Fluoro-jade C (Potter-Baker et al., 2015).

Surface modification with covalently bound antioxidative catalysts is appealing because the effects are targeted directly at the site of desired action. Additionally, as opposed to local drug delivery, where the bioactive molecule is consumed over time, permanent surface modification may have longer-lasting effects. For an initial proof of concept, Potter et al. coated a microelectrode surface with the SOD mimetic MnTBAP (Potter-Baker et al., 2014b). With this system, they observed a burst release of the molecule, accompanied with a sustained surface immobilized approach. The modified surfaces provided sustained activity, reducing the accumulation of reactive oxygen species up to several days (Potter-Baker et al., 2014c). Long-term histologic and recording outcomes are ongoing.

Neurotrophic Factors

To promote neural growth (neurite extension) toward the electrode surface, as well as to promote cell survival, several groups have investigated the local delivery of neurotrophic factors from electrode coatings (Winter et al., 2007; Kim et al., 2007b). In both studies, nerve growth factor was used for its ability to encourage neurite extension and even attachment on the electrode surface. While initial results have been promising, chronic applications have not been studied to know if the effect persists for prolonged periods of time and in the presence of the chronic inflammatory response. Further, translation of such a technique may prove to be challenging given the high regulatory burden required for biologics and drug-device combinations.

Material Selection/Surface Properties, Coatings

Cell Adhesion Proteins

Two primary reasons exist for the desire to increase cell adhesion to the electrode surface. First, increasing tissue adherence has been suggested to minimize the micromotion between the implant and the tissue. To date, this phenomenon has been demonstrated only in silico (Lee et al., 2005). Additionally, minimizing the distance between electrode contacts and viable neurons has been suggested to increase the signal amplitude to single-unit neural recordings (Buzsáki, 2004). Therefore, several groups have applied biomolecules to electrodes to promote cell adhesion. For example, both laminin (He et al., 2006) and L1 (a transmembrane neuronal cell adhesion molecule) have been used (Azemi et al., 2008; Kolarcik et al., 2012). Unlike laminin, L1 demonstrated an increase in both neuron cell bodies and neuronal filaments at the electrode–tissue interface. Neither approach has been shown to impact neural recording quality, to date.

Hydrogel and Other Nonfouling Surfaces

Immediately on implantation, proteins are adsorbed onto the material's surface. Depending on the protein milieu that is attracted and how those proteins are altered (e.g., denatured by electrostatic interactions), various attachment sites are produced that may help determine the cellular and inflammatory response. Therefore, several groups have investigated methods to prevent cell adhesion to the microelectrode surface.

Garcia et al. developed silicon microelectrodes coated with hydrogels consisting of poly(I-isopropylacrylamide) (pNIPAm) and cross-linked with poly(ethylene glycol diacrylate) (PEG) (Gutowski et al., 2014). A frequently used tactic in surface modification, the PEG chains inhibit protein adsorption (Leckband et al., 1999; Capadona et al., 2005). While the coating was effective at preventing cell adherence, in vivo studies yielded persistent inflammation and lower neuronal density for both uncoated and coated microelectrodes after implantation up to 24 weeks in rat cortex (Gutowski et al., 2014). Similar results were found for Parylene C coatings (Winslow et al., 2010) and additional hydrogel coatings for review (Jorfi et al., 2015).

Silicon carbide (SiC) is an attractive material, given its long track record and documented biocompatibility in other biomedical applications, including orthopedic implants and coronary stents (Knaack et al., 2016). Recently, Knaack et al. (2016) characterized amorphous SiC as a biomaterial for chronic neural implants in vivo, demonstrating that it was not dissimilar to standard silicon device in terms of its histologic response (NeuN, CD68, and DAPI). For a more through discussion of SiC as a biomaterial, readers are referred to Saddow (2012). Overall, while the nonfouling approaches may minimize surface attachment of inflammatory cells, glial scarring and neuron loss are not significantly impacted.

Soluble Factor (Cytokine) Sinks

Soluble factors such as cytokines play a major role in promoting and perpetuating the proinflammatory state. To counteract these soluble factors, researchers have developed passive diffusion "sinks," or porous surface coatings, which absorb and entrap these potentially harmful molecules (Skousen et al., 2015; Winn et al., 1989; Jaeger et al., 1991; Bridge and Tresco, 2008; Kim et al., 2007a; Moxon et al., 2004). While a significant amount of evidence suggests this may be a viable technology, since the hydrogels typically used as passive sinks are themselves soft, it should be caveated that mechanical compliance may confound the interpretation of results (La Flamme et al., 2007; Lopez et al., 2006). Additionally, the implementation of hydrogel coating create the added complexity of increasing the functional distance between electrode contacts and nearby neurons.

Conductive Polymers

To increase the biocompatibility of a material, researchers often look to mimic the native biological environment. While tissue conducts electricity via ionic transport, electronic devices conduct electrons. Conducting polymers complexed with biologically active counterions are unique in that they can act in a hybrid fashion, enabling either electron or ionic transport (Kim et al., 2008). Further, they can be directly deposited onto microelectrode substrates, with relatively simple manufacturing processes (Kim et al., 2008). It is unclear whether conductive polymers indeed increase the biocompatibility of devices as a result of their electrical conduction, or whether it is by other mechanisms, but a number of groups have reported success with poly(3,4-ethylenedioxythiophene) (PEDOT) coatings integrated in microelectrode devices (Mandal et al., 2014; Luo et al., 2011; Ludwig et al., 2011; Cui and Zhou, 2007; Cui and Martin, 2003; Castagnola et al., 2015). Reports of the performance of PEDOT are exceedingly positive, with several recent reports of its inclusion in microelectrode recording applications (Castagnola et al., 2016; Charkhkar et al., 2016; Kozai et al., 2016). However, some skepticism remains as to long-term stability of the polymers in vivo, especially for stimulating applications.

Material Selection/Bulk Properties

Flexible Substrates

A number of flexible microelectrode designs have been described in the literature including those made from polyimide, benzocyclobutene (BCB), polydimethylsiloxane (PDMS), Parylene C, and SU-8 (Rousche et al., 2001; Subbaroyan and Kipke, 2006; Takeuchi et al., 2005; Wester et al., 2009; Fernandez et al., 2009; Mercanzini et al., 2009; Lu et al., 2009; Lacour et al., 2010; Köhler et al., 2015). With these, researchers have been able to successfully record neurons from rat cortex, BCB (Clement et al., 2003), and even record single units, SU-8 (Altuna et al., 2013). Additionally, a number of innovative flexible probe designs have been recently published, including sinusoidal designs (Sohal et al., 2014) and for peripheral applications a flexural neural ribbon (Xiang et al., 2016). Excitingly, Liu et al. (2015) recently demonstrated an injectable mesh microelectrode. Giving more credence to the hypothesis that flexible electrodes may help to evade the inflammatory response, Luan et al. (2017) demonstrated robust cortical recording up to 16 weeks, with minimal inflammatory response, which they deemed "glial scar free." They performed in vivo two-photon imaging and incredibly tracked the same neuronal population over the several-month study and showed that they survived in close proximity to the neural probe. To overcome the flexibility during insertion, they developed a simple introducer system consisting of

a rod with a hook at the end that appears to drag the electrode through the tissue.

While flexible electrode designs show a significant amount of potential, to date, there have been no comprehensive systematic studies comparing recording performance and longevity between stiff and flexible electrodes controlling for all other variables, such as having similar surface chemistry. Further, one of the main drawbacks of an entirely flexible electrode is that it is often impossible to, by itself, be inserted into the brain without buckling.

Methods to address soft microelectrode insertion (namely prevention of buckling) include coating microelectrodes with sacrificial polymers or coatings that dissolve after insertion (Lewitus et al., 2011; Lind et al., 2010; Gilgunn et al., 2012; Lo et al., 2015), fast insertion speed (Dryg et al., 2015), treating implantation site with collagenase to soften the tissue prior to insertion (Paralikar and Clement, 2008), a variety of introducer designs (Kozai and Kipke, 2009; Kim et al., 2013), and materials that dynamically soften after insertion (Capadona et al., 2008, 2009, 2012; Reeder et al., 2014; Simon et al., 2013; Ware et al., 2012a,b, 2013a,b). Each approach is at a different stage of development.

Dynamically Softening Materials

Dynamically softening materials used for intracortical microelectrodes were first introduced as a means to both enable the insertion of a less-rigid device and to minimize the effects of chronic micromotion and mechanical mismatch between the microelectrode and the tissue (Capadona et al., 2008). The first-generation mechanically responsive microelectrodes developed by Capadona et al. mimicked the sea cucumber, which reacts to threats by rapidly transitioning their outer shell from soft to stiff via chemically induced cross-linking. As an initial finding, the team demonstrated the ability of the dry implants to be easily inserted through the pia mater and into the brain cortex of a rat (Harris et al., 2011a; Hess et al., 2013). Histologic evaluations by Nguyen et al. (2014) demonstrated nearly significantly reduced inflammatory response and minimal loss of neuronal density by 16 weeks postimplantation. Additionally, Hess et al. have demonstrated several advances in fabrication techniques leading to the inclusion of a Parylene C coating for additional electric insulation between sputtered contacts (Hess et al., 2009, 2011).

Alternatively to the sea cucumber inspired materials, a few laboratories have also explored the use of shape memory polymers (SMPs) for their tunable thermal and mechanical transitions (Ware et al., 2012b, 2013a; Sharp et al., 2006). For example, the Voit laboratory has developed SMP-based microelectrodes from acrylate and thiolene/acrylate polymers (Ware et al., 2012a,b, 2013a). Initial studies demonstrated that their SMP-based microelectrodes were capable of recording neuronal signals in a rat cortex. However, the team has not yet completed their histologic or electrophysiologic head-to-head comparison to that of traditional microelectrodes (Ware et al., 2013a).

Nanomaterials/Carbon Nanotubes

Nanomaterials are an exciting class of materials that have been tested in a variety of biomedical applications, including for neural interfacing (Aguilar, 2012; Mozafari, 2007; Giersig and Khomutov, 2008; Baldrighi et al., 2016). Notably, nanomaterials have the potential to interact with biological tissues at the cell and even subcellular levels, facilitate transportation of molecules, and have desirable electrical properties (conduct electrical/ionic charges) (Kozai et al., 2016; Wang et al., 2015).

Carbon nanotubes (CNTs), carbon nanofibers (CNFs), and graphene-based materials, due to their extraordinary strength and electrical conductivity and the number of attributes that can be designed into them, CNTs have been widely studied for use in microelectrodes (Voge and Stegemann, 2011; Kotov et al., 2009; Hanein and Bareket-Keren, 2013). However, despite these advantages, CNTs by themselves are rigid and non-compliant and tend to have high electrical impedance due to their extremely small dimensions.

To develop flexible nanotube systems, CNTs have been combined with a number of flexible substrates, including polyimide, PDMS, and Parylene C (Hanein and Bareket-Keren, 2013; Hsu et al., 2010; Gabay et al., 2007; Hanein, 2010). Further, to overcome the challenge of high impedance, several groups have investigated inclusion of PEDOT in their material matrices (Castagnola et al., 2016; Wang et al., 2015; Luo et al., 2013; Kozai et al., 2016). In one study, Kozai et al. (2016) observed chronic spike recording stability up to at least 4 months. Wang et al. (2015) conjugated a bioactive peptide (YIGSR) to the CNT surface to promote cell adhesion. The pace and quality of developments in the field of nanomaterials for recording interfaces are rapid and exciting. When also considering new medical applications that include both electrical stimulation and recording, nanomaterials hold significant potential (Vitale et al., 2015).

Implantation Technique and System Design

Avoidance of Vasculature

Intracortical microelectrodes are invasive by nature, and inevitably damage occurs during surgical implantation. Live imaging of in vivo preparations has made it possible to observe the dynamic and longitudinal response to microelectrode insertion, particularly of the vasculature (Hammer et al., 2014, 2016). The impact on blood vessels is immediate and extensive and persists for a long duration. According to research by Saxena et al. (2013), the chronic breach in the BBB may play a major role in determining electrophysiologic performance. In the future, image-guided techniques such as those taken by Kozai et al. (2010)

may provide a means to minimize damage to the brain tissue during insertion, particularly the vasculature.

Shape and Speed of Insertion

Several groups have investigated electrode shapes and insertion speeds to minimize damage to the tissues (Bjornsson et al., 2006; Casanova et al., 2014; Dryg et al., 2015; Fekete et al., 2015). Bjorssen et al. (2006) suggested, based on computational modeling and ex vivo studies, the sharpest (5 degrees) and fastest (2 mm/s) insertion minimized potential for damage based on blood vessel displacement, rupture, severing and dragging, as well as overall tissue strain. Findings from Bjorssen et al. are consistent with techniques described by Rosuche et al. for extremely fast pneumatic insertion and, more recently, by Dryg et al. for magnetic insertion of microelectrodes (Rousche and Normann, 1992; Dryg et al., 2015).

However, there are a number of other groups that have tested moderately fast insertion speeds ranging from 0.1 to 10 mm/s that suggest perhaps the opposite is true. Their findings suggest that speed may have less impact than tip shape. Specifically, Fekete et al. found that tip shape, namely its sharpness, played a significant role in the peak force of insertion. Fekete was able to reduce insertion force by nearly 5-fold with sharpening of the silicon probe alone (Fekete et al., 2015). Interestingly, in the same study, however, they found that increased speeds led to doubled insertion forces and produced minimal effect on dimpling (Fekete et al., 2015). These findings are echoed by Welkenhuysen et al. (2011), who observed minimal impact of the speed of insertion on neuroinflammatory histologic outcomes among the range of moderate insertion speeds. Therefore, it appears that there may be a more complex answer than simply faster is better, depending on whether one is trying to minimize shear stress, damage to vasculature, or dimpling during insertion. The optimal speed and tip shape appear to be dependent on each other and perhaps specific applications.

Floating Versus Tethered Lead Wires

Most electrode designs currently incorporate tethers cemented into the skull, which mechanically fixes the electrode at its base and therefore limits movement with the brain (particularly for stiff electrodes). Fixation to the skull contributes to a fluctuating strain within the brain tissue that may lead to tissue damage with chronic exposure (Biran et al., 2007; Karumbaiah et al., 2013; Subbaroyan, 2007). Floating designs (Ersen et al., 2015) and designs with extreme flexural compliance (Sohal et al., 2014; Gilgunn et al., 2012) may reduce the tethering effect. Given recent advances in devices with wireless communication capabilities and compliant materials, this challenge may be mitigated even further.

PERSPECTIVES ON THE FUTURE OF NEURAL RECORDING INTERFACES

To develop a robust cortical recording interface, the microelectrode must retain the ability to record distinct action potentials throughout the lifetime of the patient. Many factors contribute independently and synergistically to electrode performance. During the past decade, significant strides have been made in the understanding of the biological and abiological failure modes. Importantly, the field is beginning to come to a consensus on the major factors that affect recording performance. Now, novel materials are being designed for the application, as opposed to simply using what was available at the time of electrode development. The challenge of premature electrode failure is being attacked from a multitude of angles and with a number of innovative technologies. Therefore, there is little doubt that as a field we will develop a chronically stable intracortical device capable of high-fidelity neural recordings.

Moving forward, it will be important to consider the complexity of the biological response and the role that the biological response to the electrodes plays on materials-based failure modes. There will be no single strategy that will ensure the stability of chronic intracortical recordings. The biological response is too complex and dynamic for a single approach. Instead, the implants and anti-inflammatory approaches must become equally as dynamic as the inflammatory response and respond, in time, to the changing neurodegenerative, corrosive environment.

Future studies to better understand failure modes will need to rely more heavily on transgenic animal models, and advances in histological methods, including live animal imaging for real-time correlation between implant/tissue interface and the recording performance. Evasion of the inflammatory response to improve long-term recording performance is possible and certain.

Acknowledgments

The authors thank Erika Woodrum and the FES Center for their assistance in preparing illustrations.

This work was supported by the Office of the Assistant Secretary of Defense for Health Affairs through the Peer Reviewed Medical Research Program under Awards W81XWH-15-1-0607 and W81XWH-15-1-0608. Opinions, interpretations, conclusions, and recommendations are those of the authors and are not necessarily endorsed by the Department of Defense. Additionally, this study was supported by Merit Review Award # B1495-R (Capadona) and the Presidential Early Career Award for Scientist and Engineers (PECASE, Capadona) from the United States (US) Department of Veterans Affairs Rehabilitation Research and Development Service. The contents do not represent the views of the U.S. Department of Veterans Affairs or the United States Government. Finally, funding was also received from the National Institute of Health, National Institute of Neurological Disorders and Stroke, (Grant # 1R01NS082404-01A1). None of the funding sources aided in collection, analysis, and interpretation of the data, in writing of the book chapter or in the decision to submit for publication. The authors have no conflict of interest related to this work to disclose.

References

Abaya, T.V., Diwekar, M., Blair, S., Tathireddy, P., Rieth, L., Clark, G.A., et al., September 1, 2012. Characterization of a 3D optrode array for infrared neural stimulation. Biomed. Opt. Express 3 (9), 2200–2219.

Aguilar, Z., 2012. Nanomaterials for Medical Applications, first ed. Elsevier.

Ajiboye, A.B., Willett, F.R., Young, D.R., Memberg, W.D., Murphy, B.A., Miller, J.P., Walter, B.L., Sweet, J.A., Hoyen, H.A., Keith, M.W., Peckham, P.H., Simeral, J.D., Donoghue, J.P., Hochberg, L.R., Kirsch, R.F., 2017. Restoration of reaching and grasping movements through brain-controlled muscle stimulation in a person with tetraplegia: a proof-of-concept demonstration. Lancet 398, 1821–1830 .

Altuna, A., Bellistri, E., Cid, E., Aivar, P., Gal, B., Berganzo, J., et al., 2013. SU-8 based microprobes for simultaneous neural depth recording and drug delivery in the brain. Lab Chip 13 (7), 1422–1430. http://dx.doi.org/10.1039/C3LC41364K.

Azemi, E., Stauffer, W.R., Gostock, M.S., Lagenaur, C.F., Cui, X.T., 2008. Surface immobilization of neural adhesion molecule L1 for improving the biocompatibility of chronic neural probes: in vitro characterization. Acta Biomater. 1208–1217.

Baldrighi, M., Trusel, M., Tonini, R., Giordani, S., 2016. Carbon nanomaterials interfacing with neurons: an in vivo perspective. Front. Neurosci. 10, 250.

Baranauskas, G., Maggiolini, E., Castagnola, E., Ansaldo, A., Mazzoni, A., Angotzi, G.N., et al., December 2011. Carbon nanotube composite coating of neural microelectrodes preferentially improves the multiunit signal-to-noise ratio. J. Neural Eng. 8 (6), 066013 [Research Support, Non-U.S. Gov't.]

Barrese, J.C., Rao, N., Paroo, K., Triebwasser, C., Vargas-Irwin, C., Franquemont, L., et al., 2013. Failure mode analysis of silicon-based intracortical microelectrode arrays in non-human primates. J. Neural Eng. 10 (6), 066014.

Barrese, J.C., Aceros, J., Donoghue, J.P., April 2016. Scanning electron microscopy of chronically implanted intracortical microelectrode arrays in non-human primates. J. Neural Eng. 13 (2), 026003.

Batinić-Haberle, I., Rebouças, J.S., Spasojević, I., September 15, 2010. Superoxide dismutase mimics: chemistry, pharmacology, and therapeutic potential. Antioxid. Redox Signal. 13 (6), 877–918.

BeMent, S.L., Wise, K.D., Anderson, D.J., Najafi, K., Drake, K.L., February 1986. Solid-state electrodes for multichannel multiplexed intracortical neuronal recording. IEEE Trans. Biomed. Eng. 33 (2), 230–241.

Bhandari, R., Negi, S., Rieth, L., Normann, R.A., Solzbacher, F., 2008. A novel method of fabricating convoluted shaped electrode arrays for neural and retinal prostheses. Sens. Actuators A Phys. 145–146 (1–2), 123–130.

Bhandari, R., Negi, S., Rieth, L., Solzbacher, F., July 1, 2010. A wafer-scale etching technique for high aspect ratio implantable MEMS structures. Sens. Actuators A Phys. 162 (1), 130–136.

Biran, R., Martin, D.C., Tresco, P.A., 2005. Neuronal cell loss accompanies the brain tissue response to chronically implanted silicon microelectrode arrays. Exp. Neurol. 195 (1), 115–126.

Biran, R., Martin, D.C., Tresco, P.A., 2007. The brain tissue response to implanted silicon microelectrode arrays is increased when the device is tethered to the skull. J. Biomed. Mater. Res. A 82 (1), 169–178.

Bjornsson, C.S., Oh, S.J., Al-Kofahi, Y.A., Lim, Y.J., Smith, K.L., Turner, J.N., et al., September 2006. Effects of insertion conditions on tissue strain and vascular damage during neuroprosthetic device insertion. J. Neural Eng. 3 (3), 196–207.

Bleichner, M.G., Freudenburg, Z.V., Jansma, J.M., Aarnoutse, E.J., Vansteensel, M.J., Ramsey, N.F., January 2016. Give me a sign: decoding four complex hand gestures based on high-density ECoG. Brain Struct. Funct. 221 (1), 203–216.

Block, M.L., Zecca, L., Hong, J.S., January 2007. Microglia-mediated neurotoxicity: uncovering the molecular mechanisms. Nat. Rev. Neurosci. 8 (1), 57–69 [Research Support, N.I.H., Extramural, Research Support, N.I.H., Intramural, Research Support, Non-U.S. Gov't, Review].

Borton, D.A., Yin, M., Aceros, J., Nurmikko, A., April 2013. An implantable wireless neural interface for recording cortical circuit dynamics in moving primates. J. Neural Eng. 10 (2), 026010.

Bouchard, K.E., Chang, E.F., 2014. Neural decoding of spoken vowels from human sensory-motor cortex with high-density electrocorticography. Conf. Proc. IEEE Eng. Med. Biol. Soc. 2014, 6782–6785.

Bouton, C.E., Shaikhouni, A., Annetta, N.V., Bockbrader, M.A., Friedenberg, D.A., Nielson, D.M., et al., May 12, 2016. Restoring cortical control of functional movement in a human with quadriplegia. Nature 533 (7602), 247–250.

Brain Initiative Website, 2017. Available from: http://www.braininitiative.org.

Branner, A.S.R., Normann, R.A., 2001. Selective stimulation of cat sciatic nerve using an array of varying-length microelectrodes. J. Neurophysiol. 85 (4), 1585–1594.

Bridge, M.J., Tresco, P.A., 2008. In vivo solute diffusivity in brain tissue surrounding indwelling neural implants. In: Reichert, W.M. (Ed.), Indwelling Neural Implants: Strategies for Contending with the In Vivo Environment. Boca Raton (FL).

Bulea, T.C., Prasad, S., Kilicarslan, A., Contreras-Vidal, J.L., 2014. Sitting and standing intention can be decoded from scalp EEG recorded prior to movement execution. Front. Neurosci. 8, 376.

Burns, B.D., Stean, J.P., Webb, A.C., March 1974. Recording for several days from single cortical neurons in completely unrestrained cats. Electroencephalogr. Clin. Neurophysiol. 36 (3), 314–318.

Busch, S.A., Silver, J., February 2007. The role of extracellular matrix in CNS regeneration. Curr. Opin. Neurobiol. 17 (1), 120–127.

Buzsáki, G., 2004. Large-scale recording of neuronal ensembles. Nat. Neurosci. 7 (5), 446–451.

Campbell, P.K., Jones, K.E., Huber, R.J., Horch, K.W., Normann, R.A., August 1991. A silicon-based, three-dimensional neural interface: manufacturing processes for an intracortical electrode array. IEEE Trans. Biomed. Eng. 38 (8), 758–768.

Capadona, J.R., Petrie, T.A., Fears, K.P., Latour, R.A., Collard, D.M., García, A.J., 2005. Surface-nucleated assembly of fibrillar extracellular matrices. Adv. Mater. 17, 2604–2608.

Capadona, J.R., Shanmuganathan, K., Tyler, D.J., Rowan, S.J., Weder, C., 2008. Stimuli-responsive polymer nanocomposites inspired by the sea cucumber dermis. Science 319 (5868), 1370.

Capadona, J.R., Shanmuganathan, K., Trittschuh, S., Seidel, S., Rowan, S.J., Weder, C., April 13, 2009. Polymer nanocomposites with nanowhiskers isolated from microcrystalline cellulose. Biomacromolecules 10 (4), 712–716.

Capadona, J.R., Tyler, D.J., Zorman, C.A., Rowan, S.J., Weder, C., 2012. Mechanically adaptive nanocomposites for neural interfacing. Mater. Res. Soc. Bull. 37 (06), 581–589.

Casanova, F., Carney, P.R., Sarntinoranont, M., 2014. In vivo evaluation of needle force and friction stress during insertion at varying insertion speed into the brain. J. Neurosci. Methods 237, 79–89.

Castagnola, V., Descamps, E., Lecestre, A., Dahan, L., Remaud, J., Nowak, L.G., et al., May 15, 2015. Parylene-based flexible neural probes with PEDOT coated surface for brain stimulation and recording. Biosens. Bioelectron. 67, 450–457.

Castagnola, E., Maggiolini, E., Ceseracciu, L., Ciarpella, F., Zucchini, E., De Faveri, S., et al., 2016. pHEMA encapsulated PEDOT-PSS-CNT microsphere microelectrodes for recording single unit activity in the brain. Front. Neurosci. 10, 151.

Chamanzar, M., Borysov, M., Maharbiz, M.M., Blanche, T.J., 2014. High-density optrodes for multi-scale electrophysiology and optogenetic stimulation. Conf. Proc. IEEE Eng. Med. Biol. Soc. 2014, 6838–6841.

Chao, C.C., Hu, S., Peterson, P.K., 1995. Glia, cytokines, and neurotoxicity. Crit. Rev. Neurobiol. 9 (2–3), 189–205.

Chao, Z.C., Nagasaka, Y., Fujii, N., 2010. Long-term asynchronous decoding of arm motion using electrocorticographic signals in monkeys. Front. Neuroeng. 3, 3.

Chapman, C.A.R., Chen, H., Stamou, M., Biener, J., Biener, M.M., Lein, P., et al., February 23, 2015. Nanoporous gold as a neural interface coating: effects of topography, surface chemistry, and feature size. ACS Appl. Mater. Interfaces 7 (13), 7093–7100.

Charkhkar, H., Knaack, G.L., McHail, D.G., Mandal, H.S., Peixoto, N., Rubinson, J.F., et al., March 01, 2016. Chronic intracortical neural recordings using microelectrode arrays coated with PEDOT-TFB. Acta Biomater. 32, 57–67.

Chung, K., Wallace, J., Kim, S.Y., Kalyanasundaram, S., Andalman, A.S., Davidson, T.J., et al., May 16, 2013. Structural and molecular interrogation of intact biological systems. Nature 497 (7449), 332–337.

Clark, I.A., Alleva, L.M., Vissel, B., December 2010. The roles of TNF in brain dysfunction and disease. Pharmacol. Therapeutics 128 (3), 519–548 Review.

Neural recordings from a benzocyclobutene (BCB) based intra-cortical neural implant in an acute animal model. In: Clement, R.S., Singh, A., Olson, B., Lee, K., He, J. (Eds.), 2003. Proceedings of the 25th Annual International Conference of the IEEE EMBS. Cancun, Mexico.

Cogan, S.F.E.D., Guzelian, A.A., Ping Liu, Y., Edell, R., 2003. Plasma-enhanced chemical vapor deposited silicon carbide as an implantable dielectric coating. J. Biomed. Mater. Res. A 67 (3), 856–867.

Collias, J.C., Manuelidis, E.E., May 1957. Histopathological changes produced by implanted electrodes in cat brains; comparison with histopathological changes in human and experimental puncture wounds. J. Neurosurg. 14 (3), 302–328.

Constant, J.P., Fraley, G.S., Forbes, E., Hallas, B.H., Leheste, J.R., Torres, G., July 13, 2012. Resveratrol protects neurons from cannulae implantation injury: implications for deep brain stimulation. Neuroscience 222, 333–342.

Cregg, J.M., DePaul, M.A., Filous, A.R., Lang, B.T., Tran, A., Silver, J., March 2014. Functional regeneration beyond the glial scar. Exp. Neurol. 253, 197–207.

Cui, X., Martin, D.C., 2003. Electrochemical deposition and characterization of poly(3,4-ethylenedioxythiophene) on neural microelectrode arrays. Sens. Actuators B 89, 92–102.

Cui, X.T., Zhou, D.D., December 2007. Poly (3,4-ethylenedioxythiophene) for chronic neural stimulation. IEEE Trans. Neural Syst. Rehabil. Eng. 15 (4), 502–508.

Cui, M., Huang, Y., Tian, C., Zhao, Y., Zheng, J., April 2011. FOXO3a inhibits TNF-alpha- and IL-1beta-induced astrocyte proliferation:Implication for reactive astrogliosis. Glia 59 (4), 641–654 [Research Support, N.I.H., Extramural, Research Support, Non-U.S. Gov't.]

Donati, A.R., Shokur, S., Morya, E., Campos, D.S., Moioli, R.C., Gitti, C.M., et al., August 11, 2016. Long-term training with a brain-machine interface-based gait protocol induces partial neurological recovery in paraplegic patients. Sci. Rep. 6, 30383.

Dryg, I., Ward, M., Qing, K., Mei, H., Schaffer, J., Irazoqui, P., 2015. Magnetically inserted neural electrodes: tissue response and functional lifetime. IEEE Trans. Neural Syst. Rehabil. Eng 23 (4), 562–571.

Ereifej, E.S., Matthew, H.W., Newaz, G., Mukhopadhyay, A., Auner, G., Salakhutdinov, I., et al., 2013. Nanopatterning effects on astrocyte reactivity. J. Biomed. Mater. Res. A 101A (6), 1743–1757.

Ersen, A., Elkabes, S., Freedman, D.S., Sahin, M., February 2015. Chronic tissue response to untethered microelectrode implants in the rat brain and spinal cord. J. Neural Eng. 12 (1), 016019.

Fekete, Z., Nemeth, A., Marton, G., Ulbert, I., Pongracz, A., February 2015. Experimental study on the mechanical interaction between silicon neural microprobes and rat dura mater during insertion. J. Mater. Sci. Mater. Med. 26 (2), 70.

Fernandez, L.J., Altuna, A., Tijero, M., Gabriel, G., Villa, R., Rodriguez, M.J., et al., 2009. Study of functional viability of SU-8-based microneedles for neural applications. J. Micromech. Microeng. 19 (2), 025007.

Feuerstein, G.Z., Liu, T., Barone, F.C., 1994. Cytokines, inflammation, and brain injury: role of tumor necrosis factor-alpha. Cerebrovasc. Brain Metab. Rev. 6 (4), 341–360 Winter (Review).

Filous, A.R., Tran, A., Howell, C.J., Busch, S.A., Evans, T.A., Stallcup, W.B., et al., December 3, 2014. Entrapment via synaptic-like connections between NG2 proteoglycan+ cells and dystrophic axons in the lesion plays a role in regeneration failure after spinal cord injury. J. Neurosci. 34 (49), 16369–16384.

Flint, R.D., Wang, P.T., Wright, Z.A., King, C.E., Krucoff, M.O., Schuele, S.U., et al., November 1, 2014. Extracting kinetic information from human motor cortical signals. Neuroimage 101, 695–703.

Freire, M.A., Morya, E., Faber, J., Santos, J.R., Guimaraes, J.S., Lemos, N.A., et al., 2011. Comprehensive analysis of tissue preservation and recording quality from chronic multielectrode implants. PLoS One 6 (11), e27554.

Friedlander, D.R., Milev, P., Karthikeyan, L., Margolis, R.K., Margolis, R.U., Grumet, M., 1994. The neuronal chondroitin sulfate proteoglycan neurocan binds to the neural cell adhesion molecules Ng-CAM/L1/NILE and N-CAM and inhibits neuronal adhesion and neurite outgrowth. J. Cell Biol. 125 (3), 669–680.

Gabay, T., Ben-David, M., Kalifa, I., Sorkin, R., ZeR, A., Ben-Jacob, E., et al., 2007. Electro-chemical and biological properties of carbon nanotube based multi-electrode arrays. Nanotechnology 18 (3), 035201.

Gagnon-Turcotte, G., Kisomi, A.A., Ameli, R., Camaro, C.O., LeChasseur, Y., Neron, J.L., et al., 2015. A wireless optogenetic headstage with multichannel electrophysiological recording capability. Sensors (Basel) 15 (9), 22776–22797.

Galimberti, D., Baron, P., Meda, L., Prat, E., Scarpini, E., Delgado, R., et al., September 16, 1999. α-MSH peptides inhibit production of nitric oxide and tumor necrosis factor-α by microglial cells activated with β-amyloid and interferon γ. Biochem. Biophys. Res. Commun. 263 (1), 251–256.

Giersig, M., Khomutov, G.B. (Eds.), 2008. Nanomaterials for Application in Medicine and Biolog, first ed. Springer.

Gilgunn, P.J., Khilwani, R., Kozai, T.D.Y., Weber, D.J., Cui, X.T., Erdos, G., et al. (Eds.), 2012. An Ultra-Compliant, Scalable Neural Probe with Molded Biodissolvable Delivery Vehicle. IEEE 25th International Conference on Micro Electro Mechanical Systems (MEMS); 2012 Jan. 29, 2012–Feb. 2, 2012.

Gilja, V., Pandarinath, C., Blabe, C.H., Nuyujukian, P., Simeral, J.D., Sarma, A.A., et al., October 2015. Clinical translation of a high-performance neural prosthesis. Nat. Med. 21 (10), 1142–1145.

Girbovan, C., Morin, L., Plamondon, H., February 2012. Repeated resveratrol administration confers lasting protection against neuronal damage but induces dose-related alterations of behavioral impairments after global ischemia. Behav. Pharmacol. 23 (1), 1–13.

Golda, M., Brzychczy-Włoch, M., Faryna, M., Engvall, K., Kotarb, A., 2013. Oxygen plasma functionalization of parylene C coating for implants surface: nanotopography and active sites for drug anchoring. Mater. Sci. Eng. C 33, 4221–4227.

Golub, M.D., Yu, B.M., Schwartz, A.B., Chase, S.M., July 15, 2014. Motor cortical control of movement speed with implications for brain-machine interface control. J. Neurophysiol. 112 (2), 411–429.

Gomez, N., Schmidt, C.E., 2007. Nerve growth factor-immobilized polypyrrole: bioactive electrically conducting polymer for enhanced neurite extension. J. Biomed. Mater. Res. A 81A (1), 135–149.

Gopalakrishnan, S.M., Teusch, N., Imhof, C., Bakker, M.H., Schurdak, M., Burns, D.J., et al., August 1, 2008. Role of Rho kinase pathway in chondroitin sulfate proteoglycan-mediated inhibition of neurite outgrowth in PC12 cells. J. Neurosci. Res. 86 (10), 2214–2226.

Gosselin, D., Rivest, S., March 2007. Role of IL-1 and TNF in the brain: twenty years of progress on a Dr. Jekyll/Mr. Hyde duality of the innate immune system. Brain Behav. Immun. 21 (3), 281–289 [Historical Article, Research Support, Non-U.S. Gov't, Review].

Graf, A.B., Andersen, R.A., January 23, 2015. Predicting oculomotor behaviour from correlated populations of posterior parietal neurons. Nat. Commun. 6, 6024.

Grundfest, H.S.R., Oettinger, W.H., Gurry, R.W., 1950. Stainless steel micro-needle electrodes mae by electrolytic pointing. Rev. Sci. Instrum. 21 (4), 360–362.

Grundfest, H.C.B., 1942. Origin, conduction and termination of impulses in the dorsal spino-cerebellar tract of cats. J. Neurophysiol. 5 (4), 275–294.

Gunasekera, B., Saxena, T., Bellamkonda, R., Karumbaiah, L., 2015. Intracortical recording interfaces: current challenges to chronic recording function. ACS Chem. Neurosci. 6 (1), 68–83.

Gutowski, S.M., Templeman, K.L., South, A.B., Gaulding, J.C., Shoemaker, J.T., Laplaca, M.C., et al., 2014. Host response to microgel coatings on neural electrodes implanted in the brain. J. Biomed. Mater. Res. A 102 (5), 1486–1499.

Gutowski, S.M., Shoemaker, J.T., Templeman, K.L., Wei, Y., Latour Jr., R.A., Bellamkonda, R.V., et al., March 2015. Protease-degradable PEG-maleimide coating with on-demand release of IL-1Ra to improve tissue response to neural electrodes. Biomaterials 44, 55–70.

Hammer, D.X., Lozzi, A., Abliz, E., Greenbaum, N., Agrawal, A., Krauthamer, V., et al., August 1, 2014. Longitudinal vascular dynamics following cranial window and electrode implantation measured with speckle variance optical coherence angiography. Biomed. Opt. Express 5 (8), 2823–2836.

Hammer, D.X., Lozzi, A., Boretsky, A., Welle, C.G., 2016. Acute insertion effects of penetrating cortical microelectrodes imaged with quantitative optical coherence angiography. Neurophotonics 3 (2), 025002.

Hammerle, H., Kobuch, K., Kohler, K., Nisch, W., Sachs, H., Stelzle, M., February 2002. Biostability of micro-photodiode arrays for subretinal implantation. Biomaterials 23 (3), 797–804.

Hanein, Y., Bareket-Keren, L., January 9, 2013. Carbon nanotube based multi electrode arrays for neuronal interfacing: progress and prospects. Front. Neural Circuits 6 [Review].

Hanein, Y., 2010. Carbon nanotube integration into MEMS devices. Phys. Status Solidi (B) 247 (11–12), 2635–2640.

Harris, J.P., Capadona, J.R., Miller, R.H., Healy, B.C., Shanmuganathan, K., Rowan, S.J., et al., 2011a. Mechanically adaptive intracortical implants improve the proximity of neuronal cell bodies. J. Neural Eng. 8 (6), 066011.

Harris, J.P., Hess, A.E., Rowan, S.J., Weder, C., Zorman, C.A., Tyler, D.J., et al., 2011b. In vivo deployment of mechanically adaptive nanocomposites for intracortical microelectrodes. J. Neural Eng. 8 (4), 046010.

Harris, J.P., 2011. The Glia-Neuronal Response to Cortical Electrodes: Interactions with Substrate Stiffness and Electrophysiology. Case Western Reserve University.

He, W., McConnell, G.C., Bellamkonda, R.V., December 2006. Nanoscale laminin coating modulates cortical scarring response around implanted silicon microelectrode arrays. J. Neural Eng. 3 (4), 316–326.

He, W., McConnell, G.C., Schneider, T.M., Bellamkonda, R.V., 2007. A novel anti-inflammatory surface for neural electrodes. Adv. Mater. 19 (21), 3529–3533.

Hess, A., Dunning, J., Harris, J., Capadona, J.R., Shanmuganathan, K., Rowan, S.J., et al. (Eds.), 2009. A Bio-Inspired, Chemo-Responsive Polymer Nanocomposite for Mechanically Dynamic Microsystems. Solid-State Sensors, Actuators and Microsystems Conference; 2009 21–25 June 2009.

Hess, A.E., Capadona, J.R., Shanmuganathan, K., Hsu, L., Rowan, S.J., Weder, C., et al., May 2011. Development of a stimuli-responsive polymer nanocomposite toward biologically optimized, MEMS-based neural probes. J. Micromech. Microeng. 21 (5), 054009.

Hess, A.E., Potter, K.A., Tyler, D.J., Zorman, C.A., Capadona, J.R., August 20, 2013. Environmentally-controlled microtensile testing of mechanically-adaptive polymer nanocomposites for ex vivo characterization. JoVE 78, e50078.

Hetke, J.F., Lund, J.L., Najafi, K., Wise, K.D., Anderson, D.J., April 1994. Silicon ribbon cables for chronically implantable microelectrode arrays. IEEE Trans. Biomed. Eng. 41 (4), 314–321.

Hochberg, L.R., Serruya, M.D., Friehs, G.M., Mukand, J.A., Saleh, M., Caplan, A.H., et al., July 13, 2006. Neuronal ensemble control of prosthetic devices by a human with tetraplegia. Nature 442 (7099), 164–171.

Hochberg, L.R., Bacher, D., Jarosiewicz, B., Masse, N.Y., Simeral, J.D., Vogel, J., et al., May 17, 2012. Reach and grasp by people with tetraplegia using a neurally controlled robotic arm. Nature 485 (7398), 372–375.

House, P.A., Macdonald, J.D., Tresco, P.A., Normann, R.A., 2006. Acute microelectrode array implantation into human neocortex: preliminary technique and histological considerations. Neurosurg. Focus 20 (5), E4.

Hsu, J.M., Rieth, L., Normann, R.A., Tathireddy, P., Solzbacher, F., January 2009. Encapsulation of an integrated neural interface device with Parylene C. IEEE Trans. Biomed. Eng. 56 (1), 23–29.

Hsu, H.-L., Teng, I.J., Chen, Y.-C., Hsu, W.-L., Lee, Y.-T., Yen, S.-J., et al., 2010. Flexible UV-ozone-modified carbon nanotube electrodes for neuronal recording. Adv. Mater. 22 (19), 2177–2181.

Hynds, D.L., Snow, D.M., November 1999. Neurite outgrowth inhibition by chondroitin sulfate proteoglycan: stalling/stopping exceeds turning in human neuroblastoma growth cones. Exp. Neurol. 160 (1), 244–255 [Research Support, Non-U.S. Gov't. Research Support, U.S. Gov't, P.H.S.]

Iijima, N., Oohira, A., Mori, T., Kitabatake, K., Kohsaka, S., February 1991. Core protein of chondroitin sulfate proteoglycan promotes neurite outgrowth from cultured neocortical neurons. J. Neurochem. 56 (2), 706–708.

Insel, T., 2015. Director's Blog: BRAIN Awareness. National Institute of Mental Health. Available from: http://www.nimh.nih.gov/about/director/2015/brain-awareness.shtml.

Iseri, E., Kuzum, D., February 15, 2017. Implantable optoelectronic probes for in vivo optogenetics. J. Neural Eng. 14 (3), 031001.

Jaeger, C.B., Winn, S.R., Tresco, P.A., Aebischer, P., June 14, 1991. Repair of the blood-brain barrier following implantation of polymer capsules. Brain Res. 551 (1–2), 163–170.

Jarosiewicz, B., Sarma, A.A., Bacher, D., Masse, N.Y., Simeral, J.D., Sorice, B., et al., November 11, 2015. Virtual typing by people with tetraplegia using a self-calibrating intracortical brain-computer interface. Sci. Transl. Med. 7 (313) 313ra179.

Jorfi, M., Skousen, J.L., Weder, C., Capadona, J.R., February 2015. Progress towards biocompatible intracortical microelectrodes for neural interfacing applications. J. Neural Eng. 12 (1), 011001.

Karumbaiah, L., Saxena, T., Carlson, D., Patil, K., Patkar, R., Gaupp, E.A., et al., 2013. Relationship between intracortical electrode design and chronic recording function. Biomaterials 34 (33), 8061–8074.

Kellis, S., Hanrahan, S., Davis, T., House, P.A., Brown, R., Greger, B., 2012. Decoding hand trajectories from micro-electrocorticography in human patients. Conf. Proc. IEEE Eng. Med. Biol. Soc. 2012, 4091–4094.

Khodagholy, D., Doublet, T., Quilichini, P., Gurfinkel, M., Leleux, P., Ghestem, A., et al., 2013. In vivo recordings of brain activity using organic transistors. Nat. Commun. 4, 1575.

Kim, S.J., Manyam, S.C., Warren, D.J., Normann, R.A., February 2006. Electrophysiological mapping of cat primary auditory cortex with multielectrode arrays. Ann. Biomed. Eng. 34 (2), 300–309.

Kim, Y.T., Bridge, M.J., Tresco, P.A., April 23, 2007. The influence of the foreign body response evoked by fibroblast transplantation on soluble factor diffusion in surrounding brain tissue. J. Control. Release 118 (3), 340–347 [Comparative Study, Research Support, N.I.H., Extramural].

Kim, D.-H., Richardson-Burns, S.M., Hendricks, J.L., Sequera, C., Martin, D.C., 2007. Effect of Immobilized Nerve Growth Factor on Conductive Polymers: Electrical Properties and Cellular Response, pp. 79–86.

Kim, D.H., Richardson-Burns, S., Povlich, L., Abidian, M.R., Spanninga, S., Hendricks, J.L., et al., 2008. Soft, fuzzy, and bioactive conducting polymers for improving the chronic performance of neural prosthetic devices. In: Reichert, W.M. (Ed.), Indwelling Neural Implants: Strategies for Contending with the in Vivo Environment. CRC Press, Boca Raton. p. xviii, 271 p., [8] p. of plates.

Kim, B.J., Kuo, J.T., Hara, S.A., Lee, C.D., Yu, L., Gutierrez, C.A., et al., August 2013. 3D Parylene sheath neural probe for chronic recordings. J. Neural Eng. 10 (4), 045002.

King-Stephens, D., Mirro, E., Weber, P.B., Laxer, K.D., Van Ness, P.C., Salanova, V., et al., June 2015. Lateralization of mesial temporal lobe epilepsy with chronic ambulatory electrocorticography. Epilepsia 56 (6), 959–967.

Kipke, D.R., Vetter, R.J., Williams, J.C., Hetke, J.F., June 2003. Silicon-substrate intracortical microelectrode arrays for long-term recording of neuronal spike activity in cerebral cortex. IEEE Trans. Neural Syst. Rehabil. Eng. 11 (2), 151–155.

Klaes, C., Kellis, S., Aflalo, T., Lee, B., Pejsa, K., Shanfield, K., et al., November 18, 2015. Hand shape representations in the human posterior parietal cortex. J. Neurosci. 35 (46), 15466–15476.

Knaack, G.L., McHail, D.G., Borda, G., Koo, B., Peixoto, N., Cogan, S.F., et al., 2016. In vivo characterization of amorphous silicon carbide as a biomaterial for chronic neural interfaces. Front. Neurosci. 10, 301.

Kobayashi, K., Imagama, S., Ohgomori, T., Hirano, K., Uchimura, K., Sakamoto, K., et al., 2013. Minocycline selectively inhibits M1 polarization of microglia. Cell Death Dis. 4 (3), e525.

Köhler, P., Wolff, A., Ejserholm, F., Wallman, L., Schouenborg, J., Linsmeier, C.E., 2015. Influence of probe flexibility and gelatin embedding on neuronal density and glial responses to brain implants. PLoS One 10 (3), e0119340.

Kolarcik, C.L., Bourbeau, D., Azemi, E., Rost, E., Zhang, L., Lagenaur, C.F., et al., October 2012. In vivo effects of L1 coating on inflammation and neuronal health at the electrode–tissue interface in rat spinal cord and dorsal root ganglion. Acta Biomater. 8 (10), 3561–3575.

Kotov, N.A., Winter, J.O., Clements, I.P., Jan, E., Timko, B.P., Campidelli, S., et al., 2009. Nanomaterials for neural interfaces. Adv. Mater. 21 (40), 3970–4004.

Kozai, T.D., Kipke, D.R., August 8, 2009. Insertion shuttle with carboxyl terminated self-assembled monolayer coatings for implanting flexible polymer neural probes in the brain. J. Neurosci. Methods 184 (2), 199–205.

Kozai, T.D.Y., Marzullo, T.C., Hooi, F., Langhals, N.B., Majewska, A.K., Brown, E.B., et al., 2010. Reduction of neurovascular damage resulting from microelectrode insertion into the cerebral cortex using in vivo two-photon mapping. J. Neural Eng. 7 (4), 046011.

Kozai, T.D.Y., Catt, K., Li, X., Gugel, Z.V., Olafsson, V.T., Vazquez, A.L., et al., 2015a. Mechanical failure modes of chronically implanted planar silicon-based neural probes for laminar recording. Biomaterials 37, 25–39.

Kozai, T.D.Y., Jaquins-Gerstl, A.S., Vazquez, A.L., Michael, A.C., Cui, X.T., 2015b. Brain tissue responses to neural implants impact signal sensitivity and intervention strategies. ACS Chem. Neurosci. 6 (1), 48–67.

Kozai, T.D., Catt, K., Du, Z., Na, K., Srivannavit, O., Haque, R.U., et al., January 2016. Chronic in vivo evaluation of PEDOT/CNT for stable neural recordings. IEEE Trans. Biomed. Eng. 63 (1), 111–119.

Kruger, J., Caruana, F., Volta, R.D., Rizzolatti, G., 2010. Seven years of recording from monkey cortex with a chronically implanted multiple microelectrode. Front. Neuroeng. 3, 6.

Kuffler, D.P., Sosa, I.J., Reyes, O., October 2009. Schwann cell chondroitin sulfate proteoglycan inhibits dorsal root ganglion neuron neurite outgrowth and substrate specificity via a soma and not a growth cone mechanism. J. Neurosci. Res. 87 (13), 2863–2871.

La Flamme, K.E., Popat, K.C., Leoni, L., Markiewicz, E., La Tempa, T.J., Roman, B.B., et al., June 2007. Biocompatibility of nanoporous alumina membranes for immunoisolation. Biomaterials 28 (16), 2638–2645.

Lacour, S., Benmerah, S., Tarte, E., FitzGerald, J., Serra, J., McMahon, S., et al., October 1, 2010. Flexible and stretchable micro-electrodes for in vitro and in vivo neural interfaces. Med. Biol. Eng. Comput. 48 (10), 945–954.

Leckband, D., Sheth, S., Halperin, A., 1999. Grafted poly(ethylene oxide) brushes as nonfouling surface coatings. J. Biomater. Sci. Polym. 10 (10), 1125–1147.

Lee, S.M., Yune, T.Y., Kim, S.J., Kim, Y.C., Oh, Y.J., Markelonis, G.J., et al., 2004. Minocycline inhibits apoptotic cell death via attenuation of TNF-alpha expression following iNOS/NO induction by lipopolysaccharide in neuron/glia co-cultures. J. Neurochem. 91 (3), 568–578.

Lee, H., Bellamkonda, R.V., Sun, W., Levenston, M.E., 2005. Biomechanical analysis of silicon microelectrode-induced strain in the brain. J. Neural Eng. 2 (4), 81–89.

Lewitus, D., Smith, K.L., Shain, W., Kohn, J., June 2011. Ultrafast resorbing polymers for use as carriers for cortical neural probes. Acta Biomater. 7 (6), 2483–2491.

Lewitus, D.Y., Landers, J., Branch, J., Smith, K.L., Callegari, G., Kohn, J., et al., 2011. Biohybrid carbon nanotube/agarose fibers for neural tissue engineering. Adv. Funct. Mater. 21 (14), 2624–2632.

Li, C., Zhou, H.-M., 2011. The role of manganese superoxide dismutase in inflammation defense. Enzym. Res. 2011, 387176.

Liberto, C.M., Albrecht, P.J., Herx, L.M., Yong, V.W., Levison, S.W., June 2004. Pro-regenerative properties of cytokine-activated astrocytes. J. Neurochem. 89 (5), 1092–1100.

Lind, G., Linsmeier, C.E., Thelin, J., Schouenborg, J., 2010. Gelatine-embedded electrodes—a novel biocompatible vehicle allowing implantation of highly flexible microelectrodes. J. Neural Eng. 7 (4), 046005.

Liu, X., McCreery, D.B., Carter, R.R., Bullara, L.A., Yuen, T.G., Agnew, W.F., September 1999. Stability of the interface between neural tissue and chronically implanted intracortical microelectrodes. IEEE Trans. Rehabil. Eng. 7 (3), 315–326.

Liu, X., McCreery, D.B., Bullara, L.A., Agnew, W.F., March 2006. Evaluation of the stability of intracortical microelectrode arrays. IEEE Trans. Neural Syst. Rehabil. Eng. 14 (1), 91–100 [Research Support, N.I.H., Extramural].

Liu, C., Shi, Z., Fan, L., Zhang, C., Wang, K., Wang, B., 2011. Resveratrol improves neuron protection and functional recovery in rat model of spinal cord injury. Brain Res. 1374, 100–109.

Liu, J., Fu, T.M., Cheng, Z., Hong, G., Zhou, T., Jin, L., et al., July 2015. Syringe-injectable electronics. Nat. Nanotechnol. 10 (7), 629–636.

Lo, M.C., Wang, S., Singh, S., Damodaran, V.B., Kaplan, H.M., Kohn, J., et al., April 2015. Coating flexible probes with an ultra fast degrading polymer to aid in tissue insertion. Biomed. Microdevices 17 (2), 34.

Loeb, G.E., Bak, M.J., Salcman, M., Schmidt, E.M., March 1977. Parylene as a chronically stable, reproducible microelectrode insulator. IEEE Trans. Biomed. Eng. 24 (2), 121–128.

Lopez, C.A., Fleischman, A.J., Roy, S., Desai, T.A., June 2006. Evaluation of silicon nanoporous membranes and ECM-based microenvironments on neurosecretory cells. Biomaterials 27 (16), 3075–3083.

Lu, Y., Wang, D., Li, T., Zhao, X., Cao, Y., Yang, H., et al., 2009. Poly(vinyl alcohol)/poly(acrylic acid) hydrogel coatings for improving electrode-neural tissue interface. Biomaterials 30 (25), 4143–4151.

Lu, Y., Li, T., Zhao, X.Q., Li, M., Cao, Y.L., Yang, H.X., et al., July 2010. Electrodeposited polypyrrole/carbon nanotubes composite films electrodes for neural interfaces. Biomaterials 31 (19), 5169–5181.

Luan, L., Wei, X., Zhao, Z., Siegel, J.J., Potnis, O., Tuppen, C.A., et al., February 2017. Ultraflexible nanoelectronic probes form reliable, glial scar-free neural integration. Sci. Adv. 3 (2), e1601966.

Ludwig, K.A., Uram, J.D., Yang, J., Martin, D.C., Kipke, D.R., 2006. Chronic neural recordings using silicon microelectrode arrays electrochemically deposited with a poly(3,4-ethylenedioxythiophene) (PEDOT) film. J. Neural Eng. 3 (1), 59–70.

Ludwig, K.A., Langhals, N.B., Joseph, M.D., Richardson-Burns, S.M., Hendricks, J.L., Kipke, D.R., February 2011. Poly(3,4-ethylenedioxythiophene) (PEDOT) polymer coatings facilitate smaller neural recording electrodes. J. Neural Eng. 8 (1), 014001 [Comparative Study, Research Support, N.I.H., Extramural, Research Support, Non-U.S. Gov't, Research Support, U.S. Gov't, Non-P.H.S.]

Luo, X., Weaver, C.L., Zhou, D.D., Greenberg, R., Cui, X.T., 2011. Highly stable carbon nanotube doped poly(3,4-ethylenedioxythiophene) for chronic neural stimulation. Biomaterials 32 (24), 5551–5557.

Luo, X., Weaver, C.L., Tan, S., Cui, X.T., 2013. Pure graphene oxide doped conducting polymer nanocomposite for bio-interfacing. J. Mater. Chem. B 1 (9), 1340–1348.

Maloney, J.M., Lipka, S., Baldwin, S.P. (Eds.), 2005. In Vivo Biostability of CVD Silicon Oxide and Silicon Nitride Films. Mater Res Soc Symp Proc.

Mandal, H.S., Knaack, G.L., Charkhkar, H., McHail, D.G., Kastee, J.S., Dumas, T.C., et al., June 2014. Improving the performance of poly(3,4-ethylenedioxythiophene) for brain-machine interface applications. Acta Biomater. 10 (6), 2446–2454.

Marathe, A.R., Taylor, D.M., June 2013. Decoding continuous limb movements from high-density epidural electrode arrays using custom spatial filters. J. Neural Eng. 10 (3), 036015.

McCarthy, P.T., Otto, K.J., Rao, M.P., 2011. Robust penetrating microelectrodes for neural interfaces realized by titanium micromachining. Biomed. Microdevices 13 (3), 503–515.

McDord, J.M., Fridovich, I., 1969. Superoxide dismutase. J. Biol. Chem. 244 (22), 6049–6055.

McFarland, D.J., Sarnacki, W.A., Wolpaw, J.R., June 2010. Electroencephalographic (EEG) control of three-dimensional movement. J. Neural Eng. 7 (3), 036007.

Mercanzini, A., Colin, P., Bensadoun, J.C., Bertsch, A., Renaud, P., July 2009. In vivo electrical impedance spectroscopy of tissue reaction to microelectrode arrays. IEEE Trans. Biomed. Eng. 56 (7), 1909–1918.

Mercanzini, A., Reddy, S.T., Velluto, D., Colin, P., Maillard, A., Bensadoun, J.C., et al., August 3, 2010. Controlled release nanoparticle-embedded coatings reduce the tissue reaction to neuroprostheses. J. Control. Release 145 (3), 196–202.

Merrill, D.R., 2010. The electrochemistry of charge injection at the electrode/tissue interface, 85–138.

Miranda, R.A., Casebeer, W.D., Hein, A.M., Judy, J.W., Krotkov, E.P., Laabs, T.L., et al., April 15, 2015. DARPA-funded efforts in the development of novel brain-computer interface technologies. J. Neurosci. Methods 244, 52–67.

Moxon, K.A., Kalkhoran, N.M., Markert, M., Sambito, M.A., McKenzie, J.L., Webster, J.T., 2004. Nanostructured surface modification of ceramic-based microelectrodes to enhance biocompatibility for a direct brain-machine interface. IEEE Trans. Biomed. Eng. 51 (6), 881–889.

Mozafari, M.R. (Ed.), 2007. Nanomaterials and Nanosystems for Biomedical Applications, first ed. Springer.

Murphy, M.D., Guggenmos, D.J., Bundy, D.T., Nudo, R.J., 2015. Current challenges facing the translation of brain computer interfaces from preclinical trials to use in human patients. Front. Cell Neurosci. 9, 497.

Nakanishi, K., Aono, S., Hirano, K., Kuroda, Y., Ida, M., Tokita, Y., et al., August 25, 2006. Identification of neurite outgrowth-promoting domains of neuroglycan C, a brain-specific chondroitin sulfate proteoglycan, and involvement of phosphatidylinositol 3-kinase and protein kinase C signaling pathways in neuritogenesis. J. Biol. Chem. 281 (34), 24970–24978 [Research Support, Non-U.S. Gov't.]

Nakanishi, Y., Yanagisawa, T., Shin, D., Fukuma, R., Chen, C., Kambara, H., et al., 2013. Prediction of three-dimensional arm trajectories based on ECoG signals recorded from human sensorimotor cortex. PLoS One 8 (8), e72085.

Nguyen, D., Cho, N., Satkunendrarajah, K., Austin, J.W., Wang, J., Fehlings, M.G., 2012. Immunoglobulin G (IgG) attenuates neuroinflammation and improves neurobehavioral recovery after cervical spinal cord injury. J. Neuroinflamm. 9 (1), 224.

Nguyen, J.K., Park, D.J., Skousen, J.L., Hess-Dunning, A., Tyler, D.J., Rowan, S.J., et al., October 2014. Mechanically-compliant intracortical implants reduce the neuroinflammatory response. J. Neural Eng. 11 (5), 056014.

Nguyen, J.K., Jorfi, M., Buchanan, K.L., Park, D.J., Foster, E.J., Tyler, D.J., et al., 2016. Influence of resveratrol release on the tissue response to mechanically adaptive cortical implants. Acta Biomater. 29, 81–93.

Owen, J., 2014. Word Data Visualisation App. Mathworks, Natick, MA.

Pancrazio, J.J., Peckham, P.H., 2009. Neuroprosthetic devices: how far are we from recovering movement in paralyzed patients? Expert Rev. Neurother. 9 (4), 427–430.

Pangeni, R., Sahni, J.K., Ali, J., Sharma, S., Baboota, S., August 2014. Resveratrol: review on therapeutic potential and recent advances in drug delivery. Expert Opin. Drug Deliv. 11 (8), 1285–1298.

Paralikar, K.J., Clement, R.S., September 2008. Collagenase-aided intracortical microelectrode array insertion: effects on insertion force and recording performance. IEEE Trans. Biomed. Eng. 55 (9), 2258–2267.

Patel, K.R., Scott, E., Brown, V.A., Gescher, A.J., Steward, W.P., Brown, K., January 2011. Clinical trials of resveratrol. Ann. N.Y. Acad. Sci. 1215, 161–169 Review.

Patrick, E., Orazem, M.E., Sanchez, J.C., Nishida, T., 2011. Corrosion of tungsten microelectrodes used in neural recording applications. J. Neurosci. Methods 198 (2), 158–171.

Polanco, M., Bawab, S., Yoon, H., 2016. Computational assessment of neural probe and brain tissue interface under transient motion. Biosensors (Basel) 6 (2).

Polikov, V.S., Tresco, P.A., Reichert, W.M., 2005. Response of brain tissue to chronically implanted neural electrodes. J. Neurosci. Methods 148 (1), 1–18.

Polikov, V.S., Hong, J.S., Reichert, W.M., July 15, 2010. Soluble factor effects on glial cell reactivity at the surface of gel-coated microwires. J. Neurosci. Methods 190 (2), 180–187 [Research Support, N.I.H., Extramural. Research Support, Non-U.S. Gov't.]

Potter, K.A., Buck, A.C., Self, W.K., Capadona, J.R., 2012. Stab injury and device implantation within the brain results in inversely multiphasic neuroinflammatory and neurodegenerative responses. J. Neural Eng. 9 (4), 046020.

Potter, K.A., Buck, A.C., Self, W.K., Callanan, M.E., Sunil, S., Capadona, J.R., 2013. The effect of resveratrol on neurodegeneration and blood brain barrier stability surrounding intracortical microelectrodes. Biomaterials 34, 7001–7015.

Potter, K.A., Jorfi, M., Householder, K.T., Foster, E.J., Weder, C., Capadona, J.R., 2014. Curcumin-releasing mechanically-adaptive intracortical implants improve the proximal neuronal density and blood-brain barrier stability. Acta Biomater. 10 (5), 2209–2222.

Potter-Baker, K.A., Nguyen, J.K., Kovach, K.M., Gitomer, M.M., Srail, T.W., Skousen, J.L., et al., 2014a. Development of Superoxide Dismutase Mimetic Surfaces to Mitigate Reactive Oxygen Species-Mediated Intracortical Microelectrode Failure under Review.

Potter-Baker, K.A., Ravikumar, M., Burke, A.A., Meador, W.D., Householder, K.T., Buck, A.C., et al., 2014b. A comparison of neuroinflammation to implanted microelectrodes in rat and mouse models. Biomaterials 34, 5637–5646.

Potter-Baker, K.A., Nguyen, J.K., Kovach, K.M., Gitomer, M.M., Srail, T.W., Stewart, W.G., Skousen, J.L., Capadona, J.R., April 28, 2014c. Development of superoxide dismutase mimetic surfaces to reduce accumulation of reactive oxygen species for neural interfacing applications. J. Mater. Chem. B Mater. Biol. Med. 2 (16), 2248–2258.

Potter-Baker, K.A., Stewart, W.G., Tomaszewski, W.H., Wong, C.T., Meador, W.D., Ziats, N.P., et al., May 27, 2015. Implications of chronic daily anti-oxidant administration on the inflammatory response to intracortical microelectrodes. J. Neural Eng. 12 (4), 046002.

Prasad, A., Xue, Q.S., Sankar, V., Nishida, T., Shaw, G., Streit, W.J., et al., October 2012. Comprehensive characterization and failure modes of tungsten microwire arrays in chronic neural implants. J. Neural Eng. 9 (5), 056015.

Prasad, A., Xue, Q.S., Dieme, R., Sankar, V., Mayrand, R.C., Nishida, T., et al., 2014. Abiotic-biotic characterization of Pt/Ir microelectrode arrays in chronic implants. Front. Neuroeng. 7, 2.

Purcell, E.K., Seymour, J.P., Yandamuri, S., Kipke, D.R., April 2009. In vivo evaluation of a neural stem cell-seeded prosthesis. J. Neural Eng. 6 (2), 26005.

Quagliarello, V.J., Wispelwey, B., Long Jr., W.J., Scheld, W.M., 1991. Recombinant human interleukin-1 induces meningitis and blood-brain barrier injury in the rat. Characterization and comparison with tumor necrosis factor. J. Clin. Investig. 87 (4), 1360–1366.

Rajangam, S., Tseng, P.H., Yin, A., Lehew, G., Schwarz, D., Lebedev, M.A., et al., March 03, 2016. Wireless cortical brain-machine interface for whole-body navigation in primates. Sci. Rep. 6, 22170.

Ramos-Murguialday, A., Birbaumer, N., June 1, 2015. Brain oscillatory signatures of motor tasks. J. Neurophysiol. 113 (10), 3663–3682.

Rao, L., Zhou, H., Li, T., Li, C., Duan, Y.Y., 2012. Polyethylene glycol-containing polyurethane hydrogel coatings for improving the biocompatibility of neural electrodes. Acta Biomater. 8 (6), 2233–2242.

Ravikumar, M., Hageman, D.J., Tomaszewski, W.H., Chandra, G.M., Skousen, J.L., Capadona, J.R., 2014a. The effect of residual endotoxin contamination on the neuroinflammatory response to sterilized intracortical microelectrodes. J. Mater. Chem. B 2, 2517–2529.

Ravikumar, M., Sunil, S., Black, J., Barkauskas, D., Haung, A.Y., Miller, R.H., et al., 2014b. The roles of blood-derived macrophages and resident microglia in the neuroinflammatory response to implanted intracortical microelectrodes. Biomaterials S0142–9612 (35), 8049–8064.

Reeder, J., Kaltenbrunner, M., Ware, T., Arreaga-Salas, D., Avendano-Bolivar, A., Yokota, T., et al., August 6, 2014. Mechanically adaptive organic transistors for implantable electronics. Adv. Mater. 26 (29), 4967–4973.

Rennaker, R.L., Miller, J., Tang, H., Wilson, D.A., June 2007. Minocycline increases quality and longevity of chronic neural recordings. J. Neural Eng. 4 (2), L1–L5.

Renshaw, B.F.A., Morison, B.R., January 1, 1940. Activity of isocortex and hippocampus: electrical studies with micro-electrodes. J. Neurophysiol. 3 (1), 74–105.

Rousche, P.J., Normann, R.A., 1992. A method for pneumatically inserting an array of penetrating electrodes into cortical tissue. Ann. Biomed. Eng. 20 (4), 413–422.

Rousche, P.J., Normann, R.A., 1998. Chronic recording capability of the Utah intracortical electrode array in cat sensory cortex. J. Neurosci. Methods 82 (1), 1–15.

Rousche, P.J., Pellinen, D.S., Pivin, D.P., Williams, J.C., Vetter, R.J., Kipke, D.R., 2001. Flexible polyimide-based intracortical electrode arrays with bioactive capability. IEEE Trans. Biomed. Eng. 48 (3), 361–371.

Saddow, S.E. (Ed.), 2012. Silicon Carbide Biotechnology, first ed. Elsevier Inc, Waltham, MA.

Salcman, M., Bak, M.J., July 1973. Design, fabrication, and in vivo behavior of chronic recording intracortical microelectrodes. IEEE Trans. Biomed. Eng. 20 (4), 253–260.

Salcman, M., Bak, M.J., January 1976. A new chronic recording intracortical microelectrode. Med. Biol. Eng. 14 (1), 42–50.

Saxena, T., Karumbaiah, L., Gaupp, E.A., Patkar, R., Patil, K., Betancur, M., et al., 2013. The impact of chronic blood–brain barrier breach on intracortical electrode function. Biomaterials 34 (20), 4703–4713.

Schalk, G., Leuthardt, E.C., 2011. Brain-computer interfaces using electrocorticographic signals. IEEE Rev. Biomed. Eng. 4, 140–154.

Schmidt, E.M., Bak, M.J., McIntosh, J.S., September 1976. Long-term chronic recording from cortical neurons. Exp. Neurol. 52 (3), 496–506.

Schmidt, E.M., McIntosh, J.S., Bak, M.J., January 1988. Long-term implants of Parylene-C coated microelectrodes. Med. Biol. Eng. Comput. 26 (1), 96–101.

Schmitt, G., Schultze, J.-W., Faßbender, F., Buß, G., Lüth, H., Schöning, M.J., 1999. Passivation and corrosion of microelectrode arrays. Electrochim. Acta 44 (21–22), 3865–3883.

Schwartz, A.B., Kettner, R.E., Georgopoulos, A.P., 1988. Primate motor cortex and free arm movements to visual targets in three-dimensional space. I. Relations between single cell discharge and direction of movement. J. Neurosci. 8 (8), 2913–2927.

Segev, E., Reimer, J., Moreaux, L.C., Fowler, T.M., Chi, D., Sacher, W.D., et al., January 2017. Patterned photostimulation via visible-wavelength photonic probes for deep brain optogenetics. Neurophotonics 4 (1), 011002.

Seymour, J.P., Kipke, D.R., April 5, 2007. Neural probe design for reduced tissue encapsulation in CNS. Biomaterials 28 (25), 3596–3604.

Shain, W., Spataro, L., Dilgen, J., Haverstick, K., Retterer, S., Isaacson, M., et al., 2003. Controlling cellular reactive responses around neural prosthetic devices using peripheral and local intervention strategies. IEEE Trans. Neural Syst. Rehabil. Eng. 11 (2), 186–188.

Sharp, A.A., Panchawagh, H.V., Ortega, A., Artale, R., Richardson-Burns, S., Finch, D.S., et al., December 2006. Toward a self-deploying shape memory polymer neuronal electrode. J. Neural Eng. 3 (4), L23–L30.

Silver, J., June 18, 2016. The glial scar is more than just astrocytes. Exp. Neurol. 286, 147–149.

Simon, D., Ware, T., Marcotte, R., Lund Jr., B.R., Smith, D.W., Prima, M.D., et al., 2013. A comparison of polymer substrates for photolithographic processing of flexible bioelectronics. Biomed. Microdevices 15 (6), 925–939.

Simon, D.M., Charkhkar, H., St John, C., Rajendran, S., Kang, T., Reit, R., et al., January 2017. Design and demonstration of an intracortical probe technology with tunable modulus. J. Biomed. Mater. Res. A 105 (1), 159–168.

Skousen, J.L., Merriam, S.M., Srivannavit, O., Perlin, G., Wise, K.D., Tresco, P.A., 2011. Reducing surface area while maintaining implant penetrating profile lowers the brain foreign body response to chronically implanted planar silicon microelectrode arrays. Prog. Brain Res. 194C, 167–180.

Skousen, J.L., Bridge, M.J., Tresco, P.A., January 2015. A strategy to passively reduce neuroinflammation surrounding devices implanted chronically in brain tissue by manipulating device surface permeability. Biomaterials 36 (0), 33–43.

Soekadar, S.R., Witkowski, M., Vitiello, N., Birbaumer, N., June 2015. An EEG/EOG-based hybrid brain-neural computer interaction (BNCI) system to control an exoskeleton for the paralyzed hand. Biomed. Tech. (Berl.) 60 (3), 199–205.

Sohal, H.S., Jackson, A., Jackson, R., Clowry, G.J., Vassilevski, K., O'Neill, A., et al., 2014. The sinusoidal probe: a new approach to improve electrode longevity. Front. Neuroeng. 7, 10.

Spataro, L., Dilgen, J., Retterer, S., Spence, A.J., Isaacson, M., Turner, J.N., et al., 2005. Dexamethasone treatment reduces astroglia responses to inserted neuroprosthetic devices in rat neocortex. Exp. Neurol. 194 (2), 289–300.

Sridharan, A., Rajan, S.D., Muthuswamy, J., 2013. Long-term changes in the material properties of brain tissue at the implant–tissue interface. J. Neural Eng. 10 (6), 066001.

Stamatovic, S.M., Keep, R.F., Kunkel, S.L., Andjelkovic, A.V., November 15, 2003. Potential role of MCP-1 in endothelial cell tight junction 'opening': signaling via Rho and Rho kinase. J. Cell Sci. 116 (Pt 22), 4615–4628 [Research Support, Non-U.S. Gov't.]

Stamatovic, S.M., Shakui, P., Keep, R.F., Moore, B.B., Kunkel, S.L., Van Rooijen, N., et al., May 2005. Monocyte chemoattractant protein-1 regulation of blood-brain barrier permeability. J. Cereb. Blood Flow Metab. 25 (5), 593–606.

Stetson, C., Andersen, R.A., June 01, 2015. Early planning activity in frontal and parietal cortex in a simplified task. J. Neurophysiol. 113 (10), 3915–3922.

Subbaroyan, J., Kipke, D.R. (Eds.), 2006. The role of flexible polymer interconnects in chronic tissue response induced by intracortical microelectrodes–a modeling and an in vivo study. Conf Proc IEEE Eng Med Biol Soc

.Subbaroyan, J., Martin, D.C., Kipke, D.R., 2005. A finite-element model of the mechanical effects of implantable microelectrodes in the cerebral cortex. J. Neural Eng. 2 (4), 103–113.

Subbaroyan, J., 2007. Investigations of Tethering Induced Injury Response in Brain Tissue by Intracortical Implants through Modeling and In Vivo Experiments. University of Michigan, Ann Arbor, MI.

Sugama, S., Takenouchi, T., Cho, B.P., Joh, T.H., Hashimoto, M., Kitani, H., September 2009. Possible roles of microglial cells for neurotoxicity in clinical neurodegenerative diseases and experimental animal models. Inflamm. Allergy Drug Targets 8 (4), 277–284 [Research Support, Non-U.S. Gov't, Review.]

Suner, S., Fellows, M.R., Vargas-Irwin, C., Nakata, G.K., Donoghue, J.P., 2005. Reliability of signals from a chronically implanted, silicon-based electrode array in non-human primate primary motor cortex. IEEE Trans. Rehabil. Eng. 13 (4), 524–541.

Takeuchi, S., Ziegler, D., Yoshida, Y., Mabuchi, K., Suzuki, T., 2005. Parylene flexible neural probes integrated with microfluidic channels. Lab Chip 5 (5), 519–523.

Takmakov, P., Ruda, K., Scott Phillips, K., Isayeva, I.S., Krauthamer, V., Welle, C.G., April 2015. Rapid evaluation of the durability of cortical neural implants using accelerated aging with reactive oxygen species. J. Neural Eng. 12 (2), 026003.

Taub, A.H., Hogri, R., Magal, A., Mintz, M., Shacham-Diamand, Y., 2012. Bioactive anti-inflammatory coating for chronic neural electrodes. J. Biomed. Mater. Res. A 100A (7), 1854–1858.

The Brain Initiative Website, 2016. National Institutes of Health, Bethesda, MD. Available from: http://www.braininitiative.nih.gov/.

Thelin, J., Jorntell, H., Psouni, E., Garwicz, M., Schouenborg, J., Danielsen, N., et al., 2011. Implant size and fixation mode strongly influence tissue reactions in the CNS. PLoS One 6 (1), e16267 [Research Support, Non-U.S. Gov't.]

Tresco, P.A., Winslow, B.D., 2011. The challenge of integrating devices into the central nervous system. Crit. Rev. Biomed. Eng. 39 (1), 29–44.

Vetter, R.J., Williams, J.C., Nunamaker, E.A., Kipke, D.R., 2004. Chronic neural recording using silicon-substrate microelectrode arrays implanted in cerebral cortex. IEEE Trans. Biomed. Eng. 51 (6), 896–904.

Vitale, F., Summerson, S.R., Aazhang, B., Kemere, C., Pasquali, M., April 28, 2015. Neural stimulation and recording with bidirectional, soft carbon nanotube fiber microelectrodes. ACS Nano 9 (4), 4465–4474.

Voge, C.M., Stegemann, J.P., February 2011. Carbon nanotubes in neural interfacing applications. J. Neural Eng. 8 (1), 011001 Review.

Vouga, T., Zhuang, K.Z., Olivier, J., Lebedev, M.A., Nicolelis, M.A., Bouri, M., et al., February 2017. EXiO-a brain-controlled lower limb exoskeleton for *Rhesus macaques*. IEEE Trans. Neural Syst. Rehabil. Eng. 25 (2), 131–141.

Wadhwa, R., Lagenaur, C.F., Cui, X.T., February 21, 2006. Electrochemically controlled release of dexamethasone from conducting polymer polypyrrole coated electrode. J. Control. Release 110 (3), 531–541.

Wang, K., Tang, R.Y., Zhao, X.B., Li, J.J., Lang, Y.R., Jiang, X.X., et al., November 28, 2015. Covalent bonding of YIGSR and RGD to PEDOT/PSS/MWCNT-COOH composite material to improve the neural interface. Nanoscale 7 (44), 18677–18685.

Ward, M.P., Rajdev, P., Ellison, C., Irazoqui, P.P., 2009. Toward a comparison of microelectrodes for acute and chronic recordings. Brain Res. 1282, 183–200.

Ware, T., Simon, D., Arreaga-Salas, D.E., Reeder, J., Rennaker, R., Keefer, E.W., et al., 2012a. Fabrication of responsive, softening neural interfaces. Adv. Funct. Mater. 22 (16), 3470–3479.

Ware, T., Simon, D., Hearon, K., Liu, C., Shah, S., Reeder, J., et al., 2012b. Three-dimensional flexible electronics enabled by shape memory polymer substrates for responsive neural interfaces. Macromol. Mater. Eng. 297 (12), 1193–1202.

Ware, T., Simon, D., Liu, C., Musa, T., Vasudevan, S., Sloan, A., et al., 2013a. Thiol-ene/acrylate substrates for softening intracortical electrodes. J. Biomed. Mater. Res. B. http://dx.doi.org/10.1002/jbmb.32946.

Ware, T., Simon, D., Rennaker, R.L., Voit, W., 2013b. Smart polymers for neural interfaces. Polym. Rev. 53 (1), 108–129.

Wark, H.A.C., Sharma, R., Mathews, K.S., Fernandez, E., Yoo, J., Christensen, B., Tresco, P., Rieth, L., Solzbacher, F., Normann, R.A., Tathireddy, P., 2013. A new high-density (25 electrodes/mm^2) penetrating microelectrode array for recording and stimulating sub-millimeter neuroanatomical structures. J. Neural Eng. 10 (4).

Warren, D.J., Fernandez, E., Normann, R.A., 2001. High-resolution two-dimensional spatial mapping of cat striate cortex using a 100-microelectrode array. Neuroscience 105 (1), 19–31.

Welkenhuysen, M., Andrei, A., Ameye, L., Eberle, W., Nuttin, B., November 2011. Effect of insertion speed on tissue response and insertion mechanics of a chronically implanted silicon-based neural probe. IEEE Trans. Biomed. Eng. 58 (11), 3250–3259.

Wester, B.A., Lee, R.H., LaPlaca, M.C., April 2009. Development and characterization of in vivo flexible electrodes compatible with large tissue displacements. J. Neural Eng. 6 (2), 024002.

Williams, J.C., Hippensteel, J.A., Dilgen, J., Shain, W., Kipke, D.R., December 2007. Complex impedance spectroscopy for monitoring tissue responses to inserted neural implants. J. Neural Eng. 4 (4), 410–423.

Winn, S.R., Aebischer, P., Galletti, P.M., January 1989. Brain tissue reaction to permselective polymer capsules. J. Biomed. Mater. Res. 23 (1), 31–44.

Winslow, B.D., Christensen, M.B., Yang, W.K., Solzbacher, F., Tresco, P.A., 2010. A comparison of the tissue response to chronically implanted Parylene-C-coated and uncoated planar silicon microelectrode arrays in rat cortex. Biomaterials 31 (35), 9163–9172.

Winter, J.O., Cogan, S.F., Rizzo 3rd, J.F., May 2007. Neurotrophin-eluting hydrogel coatings for neural stimulating electrodes. J. Biomed. Mater. Res. B Appl. Biomater. 81 (2), 551–563.

Wise, K.D., Angell, J.B., May 1975. A low-capacitance multielectrode probe for use in extracellular neurophysiology. IEEE Trans. Biomed. Eng. 22 (3), 212–219.

Wise, K.D., Angell, J.B., Starr, A., July 1970. An integrated-circuit approach to extracellular microelectrodes. IEEE Trans. Biomed. Eng. 17 (3), 238–247.

Wise, K.D., September–October 2005. Silicon microsystems for neuroscience and neural prostheses. IEEE Eng. Med. Biol. Mag. 24 (5), 22–29.

Wodlinger, B., Downey, J.E., Tyler-Kabara, E.C., Schwartz, A.B., Boninger, M.L., Collinger, J.L., February 2015. Ten-dimensional anthropomorphic arm control in a human brain-machine interface: difficulties, solutions, and limitations. J. Neural Eng. 12 (1), 016011.

Xiang, Z., Yen, S.C., Sheshadri, S., Wang, J., Lee, S., Liu, Y.H., et al., June 2016. Progress of flexible electronics in neural interfacing - a self-adaptive non-invasive neural ribbon electrode for small nerves recording. Adv. Mater. 28 (22), 4472–4479.

Yadav, A., Saini, V., Arora, S., November 11, 2010. MCP-1: chemoattractant with a role beyond immunity: a review. Clin. Chim. Acta 411 (21–22), 1570–1579 Review.

Yamada, H., Fredette, B., Shitara, K., Hagihara, K., Miura, R., Ranscht, B., et al., October 15, 1997. The brain chondroitin sulfate proteoglycan brevican associates with astrocytes ensheathing cerebellar glomeruli and inhibits neurite outgrowth from granule neurons. J. Neurosci. 17 (20), 7784–7795 [Research Support, U.S. Gov't, P.H.S.]

Yazdan-Shahmorad, A., Diaz-Botia, C., Hanson, T.L., Kharazia, V., Ledochowitsch, P., Maharbiz, M.M., et al., March 02, 2016. A large-scale interface for optogenetic stimulation and recording in nonhuman primates. Neuron 89 (5), 927–939.

Yin, M., Borton, D.A., Aceros, J., Patterson, W.R., Nurmikko, A.V., April 2013. A 100-channel hermetically sealed implantable device for chronic wireless neurosensing applications. IEEE Trans. Biomed. Circuits Syst. 7 (2), 115–128.

Zhong, Y., Bellamkonda, R.V., 2005. Controlled release of anti-inflammatory agent α-MSH from neural implants. J. Control. Release 106 (3), 309–318.

Zhong, Y., Bellamkonda, R.V., May 7, 2007. Dexamethasone-coated neural probes elicit attenuated inflammatory response and neuronal loss compared to uncoated neural probes. Brain Res. 1148, 15–27.

Zhong, Y., McConnell, G.C., Ross, J.D., DeWeerth, S.P., Bellamkonda, R.V. (Eds.), March 2005. A Novel Dexamethasone-releasing, Anti-inflammatory Coating for Neural Implants. Neural Engineering, 2005 Conference Proceedings 2nd International IEEE EMBS Conference on; 2005, 16–19.

Video Article

Rodent Behavioral Testing to Assess Functional Deficits Caused by Microelectrode Implantation in the Rat Motor Cortex

Monika Goss-Varley[1,2], Andrew J. Shoffstall[1,2], Keith R. Dona[1,2], Justin A. McMahon[1,2], Sydney C. Lindner[1,2], Evon S. Ereifej[1,2], Jeffrey R. Capadona[1,2]

[1]Advanced Platform Technology Center, Rehabilitation Research and Development, Louis Stokes Cleveland Department of Veterans Affairs Medical Center

[2]Department of Biomedical Engineering, Case Western Reserve University

Correspondence to: Jeffrey R. Capadona at jrc35@case.edu

URL: https://www.jove.com/video/57829
DOI: doi:10.3791/57829

Keywords: Bioengineering, Issue 138, Behavior, rat, iatrogenic injury, brain trauma, TBI, ladder, open field grid, grip strength

Date Published: 8/18/2018

Citation: Goss-Varley, M., Shoffstall, A.J., Dona, K.R., McMahon, J.A., Lindner, S.C., Ereifej, E.S., Capadona, J.R. Rodent Behavioral Testing to Assess Functional Deficits Caused by Microelectrode Implantation in the Rat Motor Cortex. *J. Vis. Exp.* (138), e57829, doi:10.3791/57829 (2018).

Abstract

Medical devices implanted in the brain hold tremendous potential. As part of a Brain Machine Interface (BMI) system, intracortical microelectrodes demonstrate the ability to record action potentials from individual or small groups of neurons. Such recorded signals have successfully been used to allow patients to interface with or control computers, robotic limbs, and their own limbs. However, previous animal studies have shown that a microelectrode implantation in the brain not only damages the surrounding tissue but can also result in functional deficits. Here, we discuss a series of behavioral tests to quantify potential motor impairments following the implantation of intracortical microelectrodes into the motor cortex of a rat. The methods for open field grid, ladder crossing, and grip strength testing provide valuable information regarding the potential complications resulting from a microelectrode implantation. The results of the behavioral testing are correlated with endpoint histology, providing additional information on the pathological outcomes and impacts of this procedure on the adjacent tissue.

Video Link

The video component of this article can be found at https://www.jove.com/video/57829/

Introduction

Intracortical microelectrodes were originally used to map the circuitry of the brain, and have developed into a valuable tool to enable the detection of motor intentions which can be used to produce functional outputs[1]. Detected functional outputs can offer individuals suffering from spinal cord injuries, cerebral palsy, amyotrophic lateral sclerosis (ALS), or other movement-limiting conditions the control of a computer cursor[2,3] or robotic arm[4,5,6], or restore function to their own disabled limb[7]. Therefore, intracortical microelectrode technology has emerged as a promising and quickly growing field[8].

Due to the successes seen in the field, clinical studies are underway to improve and better understand the possibilities of BMI technology[5,9,10]. By realizing the full potential of communication with neurons in the brain, the rehabilitation applications are perceived as limitless[8]. Although there is great optimism for the future of intracortical microelectrode technology, it is also well-known that microelectrodes eventually fail[11], possibly due to an acute neuroinflammatory response following implantation. The implantation of a foreign material in the brain results in immediate damage to the surrounding tissue and leads to further damage caused by the neuroinflammatory response that varies depending on properties of the implant[12]. In addition, an implant in the brain can cause a microlesion effect: a reduction in glucose metabolism thought to be caused by acute edema and hemorrhage due to the device insertion[13]. Furthermore, the signal quality and the length of time that useful signals can be recorded are inconsistent, regardless of the animal model[11,14,15,16]. Several studies have demonstrated the connection between neuroinflammation and microelectrode performance[17,18,19]. Therefore, the consensus of the community is that the inflammatory response of the neural tissue that surrounds the microelectrodes, at least in part, compromises electrode reliability.

Many studies have examined local inflammation[11,20,21,22] or explored methods to reduce the damage to the brain caused by insertion[11,23,24,25], with a goal of improving the recording performance over time[14,26]. Additionally, we have recently shown that an iatrogenic injury caused by a microelectrode insertion in the motor cortex of rats causes an immediate and lasting fine motor deficit[27]. Therefore, the purpose of the protocols presented here is to give researchers a quantitative method to assess possible motor deficits as a result of brain trauma following the implantation and persistent presence of intracortical devices (microelectrodes in the case of this manuscript). The behavior tests described here were designed to tease out both gross and fine motor function impairments, and can be used in many models of brain injury. These methods are straightforward, reproducible, and can easily be implemented in a rodent model. Further, the methods presented here allow for a correlation of motor behavior to histological outcomes, a benefit that until recently, the authors have not seen published in the BMI field. Finally, as these methods were designed to test fine motor function[28], the gross motor function[29], and stress and anxiety behavior[29,30], the methods presented here can also be implemented into a variety of head injury models where the researchers want to rule out (or in) any motor function deficits.

Protocol

All procedures and animal care practices were approved by and performed in accordance with the Louis Stokes Cleveland Department of Veterans Affairs Medical Center Institutional Animal Care and Use Committees.

NOTE: To educate researchers on the decision about the use of a stab injury model as a control, it is recommended to review the work done by Potter *et al.*[21].

1. Microelectrode Implantation Surgical Procedure

1. **Pre-surgical animal preparation**
    1. Anesthetize the animal in an induction chamber using isoflurane (2 - 4%). While under anesthesia, continuously monitor the animal using a vital measurement system to monitor the heart rate and the blood-oxygen content.
    2. Move the animal to a nose cone to continue the anesthetic. Subcutaneously (SQ) inject a cephalosporin antibiotic, e.g. cefazolin (25 mg/kg) and a non-steroidal anti-inflammatory, e.g. carprofen (5 mg/kg) to prevent infection and manage the pain, respectively.
    3. Liberally apply ophthalmic ointment to the animal's eyes to prevent them from drying.
    4. Using small animal nail clippers, trim the toenails to prevent the animal from scratching the sutures during the wound healing. Ensure that the nails are not clipped too short, as this can lead to pain and bleeding for the animal.
    5. Shave the animal's head thoroughly from behind the ears to between the eyes using an electric razor trimmer.
    6. Provide a local analgesia with an SQ injection of bupivacaine (0.3 mL of 0.125% bupivacaine diluted from stock solution) at the top of the animal's head in the area of the incision.
    7. Mount the animal on a stereotaxic frame, using ear bars to keep the head from moving during the surgery. Place a circulating water heating pad under the animal to maintain the animal's internal temperature.
    8. Apply a sterile drape, e.g., institutionally-approved sterile plastic wrap, to isolate the surgical field.
    9. Scrub the surgical area using an alternating betadine solution and isopropanol scrubs.
    10. Perform a toe pinch according to the institutional protocol to ensure the animal is under the surgical plane.

2. **Prepare animal for implantation**
    1. Create an incision of approximately 1 in down midline exposing the skull using a No. 10 scalpel blade. Bluntly remove the periosteum using a cotton-tipped applicator, and stop any bleeding using a gauze pad. Retract the surrounding tissue using alligator clips and clean and dehydrate the skull with hydrogen peroxide.
    2. Place a few drops of cyanoacrylate-based tissue adhesive on the exposed skull to improve the dental cement bonding in later steps.
    3. In the chosen hemisphere, mark the region of the motor cortex corresponding to forepaw movement approximately 3 mm lateral to midline and 2 mm anterior to bregma by creating a nick in the bone.
    4. Remove a portion of the skull using a 1.75-mm rounded tip dental drill, taking special consideration not to drill too quickly or too deeply, and supporting one hand on the stereotaxic frame. The drill should be applied to the skull intermittently to avoid overheating[31].
    5. Reflect the dura using a fine hooked 45° dura pick.
    6. Clean any bleeding using a cotton-tipped applicator and saline, taking care to not directly touch the brain surface.

3. **Insertion of microelectrode in motor cortex**
    1. Carefully mount the sterilized microelectrode in the universal holder on the stereotaxic frame, taking caution not to bump the shank of the electrode. Ensure that the headstage interface connector of the electrode is firmly held by the holder.
    NOTE: Here, a non-functional Michigan-style silicon shank electrode measuring 2 mm x 123 µm x 15 µm was used, and the shank was inserted using fine forceps.
    2. Using the micromanipulators on the stereotaxic frame, carefully position the tip of the electrode over the open craniotomy.
    3. Gently lower the electrode approximately 2 mm into the brain using the micromanipulators as a measurement guide (depending on the choice of electrode, an automated insertion at controlled rates may be required.) Take caution to avoid any visible vasculature whenever possible. Once the electrode is in place, carefully release the connector from the universal holder and retract the insertion arm.
    4. Carefully clean any bleeding from around the electrode using a cotton-tipped applicator and saline.
    5. Seal off the craniotomy around the implanted electrode using a silicone elastomer.
    6. Fix the electrode to the skull using dental cement.
    7. Once the cement is completely dry, bring the edges of the incision together at the front and back of the cement headcap and suture them shut.

4. **Post-operative care**
    1. Allow the animal to recover on a circulating water heating pad while continuing to monitor its vital signs. Avoid using heat lamps as the temperature from lamps is more difficult to control and animals can overheat.
    2. Once the animal is fully awake, move the animal to a clean cage with easy access to food and water.
    3. During post-operative days 1 - 3, provide the animals with SQ cephalosporin antibiotic (25 mg/kg) and a non-steroidal anti-inflammatory (5 mg/kg) to prevent infection and manage their pain.
    4. Monitor the animals daily for the signs of pain or discomfort, bleeding, weight change, or suture issues through at least post-operative day 5.

2. Behavioral Testing

1. For all behavior testing, test the animals 2x per test in the week prior to the electrode implantation surgery to calculate their pre-surgery baseline scores. Following the surgery, allow the animals to rest for 1 week before beginning behavior testing 2x per week on each test. Consistent testing conditions should be used throughout the study for both pre- and post-surgical testing to minimize the effects of stress on the performance, which could result in a measurement of anxiety.
    1. Clean all testing equipment with a chlorine dioxide-based sterilant at the beginning of each testing session and after each animal.
    2. Film the open field grid and ladder testing. These tests require a video camera (1080p, minimum of 15 fps, 78° diagonal field of view), a laptop, and room to store the video data.
    3. At the beginning of each testing day, bring the animals to the testing room and allow them to acclimate for at least 20 min before beginning the testing. The room should be light and temperature-controlled, and the same personnel should complete all testing. Ideally, the same room will be used for all animals throughout the course of the testing with no changes to the room.
    4. Use food rewards to encourage the animals to complete the tasks, especially during the ladder training. Cereals or small pieces of banana chips or crackers make good rewards.
    5. Normalize all weekly testing performances to the pre-surgery scores for each individual animal (**Equation 1**).

        Equation 1: $$\%\ change\ in\ performance = \frac{baseline\ score - weekly\ test\ score}{baseline\ score} * (100)$$

2. **Open field grid testing**

    NOTE: The open field grid test was built in-house and has a running surface of 1 m^2 with approximately 40-cm high opaque side walls. The bottom running surface of the grid is divided into 9 equal squares from the underside using tape (**Figure 1A**). The recording camera is permanently mounted above the center of the grid on scaffolding.
    1. To begin open field grid testing, place the animal in the center of the grid facing away from the tester.
    2. Allow the animal to run freely for 3 min while recording a video.
    3. When the animal has completed testing, remove the animal from the grid and return it to the cage. Clean the grid thoroughly with chlorine dioxide-based sterilant.
    4. Test each animal 1x per testing day.
    5. Analyze the number of gridlines crossed, the total distance traveled, and the maximum velocity of the animal as metrics of the gross motor function using a video tracking software.

        NOTE: The data presented here were quantified manually by trained researchers, but it is preferred to use a recently developed in-house tracking algorithm[32].

3. **Ladder testing**

    NOTE: The ladder test was built in-house and consists of 2 clear acrylic side walls, each 1 m in length, connected by 3-mm diameter rungs spaced at 2 cm apart (**Figure 2A**). Ladder testing is a skilled test, and therefore requires 1 week of training prior to recording the pre-surgery baseline scores. The protocol for the training and testing is the same.
    1. Move the animal to a temporary clean holding cage to begin ladder testing.
    2. Set the ladder up so that it bridges 2 cages. The start end of the ladder rests on a clean cage, and the finish end rests on the animal's home cage to serve as a motivation to complete the run.
    3. Position the same (or similar) video camera on a tripod at the center of the ladder. The position of the camera should be at rung height and allow for the whole ladder to be seen.
    4. With the video camera running, hold the animal to the starting line of the ladder, allowing their front paws to touch the first rung.
    5. Allow the animal to cross the ladder at their own pace. The time elapsed between the moment when the animal's paw touches the first rung and the finish line at the third to last rung will determine the animal's time to cross.
    6. If the animal turns around on the ladder or does not move for a period of 20 s, consider the animal to have failed the run. Assign the animals a penalty score time for each failed run. Determine the penalty time by the slowest performance recorded during pre-surgery testing[27].
    7. Allow each animal to cross the ladder 5x per testing day with approximately 1 min rest in between each run.
    8. Average the fastest 3 runs per day as a metric of fine motor function. Additionally, record the number of times each of the front paws slips off the rungs using a video tracking software.

        NOTE: The data presented here were quantified manually by trained researchers, but it is preferred to use a recently developed in-house tracking algorithm using Dona *et al.*[32].

4. **Grip strength testing**
    1. Calibrate the grip strength meter before each testing session, and measure the strength in grams.
    2. Position the grip strength meter on the edge of a counter with the grip handlebars extended over the floor.
    3. Allow the animal to grab the handlebars with both front paws while holding the animal by the base of the tail (**Figure 3A**).
    4. Once the animal has a firm grip with each paw, pull the animal away from the meter by the base of the tail with slow and steady force.
    5. Record the maximum grip strength exerted by the animal which is displayed on the digital output by the grip strength meter.
    6. Test each animal 3x per testing day with approximately 2 min rest in between each test.
    7. As a metric of fine motor function, record and average the maximum grip strength output from each of the 3 trials.

3. Post-behavioral Protocol

1. Following all behavioral testing (*e.g*, 8 - 16 weeks after the implantation), anesthetize the animals deeply using ketamine (160 mg/kg) and xylazine (20 mg/kg), transcardially perfuse them, harvest their brains and cryo-slice them, and stain the tissue using immunohistochemical markers to quantify the cellular response around the site of implantation[33,34,35,36,37,38].

4. Statistical Analysis

NOTE: A prospective power analysis is strongly suggested for any studies seeking to answer a particular research question. The power analysis, which informs the number of animals required to achieve a statistical significance for a particular study design, should be based on the particular research hypothesis, the design of the experiment, the estimated effect size and variability of the intended treatments, as well the effect size required to achieve clinical or scientific relevance.

1. Conduct statistical analyses using common statistical software.
2. Tabulate the descriptive statistics and display them as Mean ± Standard Error.
3. Analyze the behavioral performance [in the open field grid (step 2.2), ladder (step 2.3), and grip strength testing (step 2.4)] at each weekly time point to compare the control *vs.* implanted groups using a two-sample t-test. Consider each weekly time point an independent measure.
4. Quantify the longitudinal performance using a mixed effect linear model. The week and the group are fixed factors and an experimental animal is nested within the group as a random effect. An analysis of variance (ANOVA) is used to determine the factor effect with a significance level of $p < 0.05$.
5. Compare the ladder performance with immunoglobin G (IgG) intensity using a linear regression analysis. Calculate the correlation coefficient by a Pearson's method.

Representative Results

Using the methods presented here, a microelectrode implantation surgery in the motor cortex is completed following established procedures[39,40,41,42], followed by open field grid testing to assess the gross motor function and ladder and grip strength testing to assess the fine motor function[27]. Motor function testing was completed 2x per week for 16 weeks post-surgery in implanted animals, with no surgery non-implanted animals as a control. All post-surgery scores were averaged per week and normalized to each individual animal's pre-surgery baseline scores. All error is reported as standard error of the mean (SEM).

To measure their gross motor function and stress behavior, animals were allowed to run freely in an open field grid test for 3 min (**Figure 1A**). Various metrics from this test can be recorded, including the number of grid lines cross, the total distance traveled, and the maximum speed achieved by the animal. In this previously reported data, the number of grid lines crossed is presented[27]. In the first week following the recovery period (the 2-week timepoint), a significant difference was seen in the open field grid performance between the 2 groups. However, there was no further significance throughout the rest of the study (**Figure 1B**). The control and microelectrode-implanted animals scored similarly throughout testing, and the variance in performance was relatively high in both sets of animals. No significance was seen when comparing the open field grid performance in both sets of animals across the entire experimental time. Because there was no difference in performance between the 2 groups of animals, this result was interpreted to indicate that there is no gross motor deficit or severely limiting stress caused by a microelectrode implantation in the motor cortex[27]. When interpreting the data, a decrease in the number of grid lines crossed, the total distance traveled, or the maximum speed achieved by the animal all indicate a decrease in its gross motor function (**Table 1**).

To measure the coordinated grasp and fine motor function, animals took part in a horizontal ladder test (**Figure 2A**) where the time it took the animal to cross the ladder and the frequency of paw slips were recorded. Post-surgery ladder crossing times were normalized for each animal to each individual animal's pre-surgery scores. Therefore, a positive percentage coincides with a decrease in time to cross the ladder and an increased performance, and a negative percentage coincides with an increase in time to cross the ladder and a decreased performance (**Figure 2B**, **Table 1**).

In this previously reported data, the control animals, having received no implant, displayed the slowest performance times (82.6 ± 26.0%) during the first week of post-surgery testing immediately after the recovery phase[27]. Beginning in the second week of post-surgery ladder testing, the control animals resumed their baseline performance times and maintained scores comparable to their baseline scores over the course of the study with very little variance.

The animals receiving an intracortical microelectrode saw a reduced performance straightaway following surgery. These animals demonstrated an increased ladder crossing time compared to their baseline of 199.1 ± 61.4% in the first week of post-surgery testing. The implanted animals displayed a reduced performance for the duration of the study and their performance did not return to their baseline scores. At their worst, implanted animals decreased in performance during week 11 to an average of 526.9 ± 139.4% compared to their baseline performance. Additionally, the implanted animals showed a higher variance compared to the control animals. There was no significant difference between the control and implanted animals during the first week of testing. However, a significant difference in the percent change compared to the baseline times was seen between the groups at all subsequent weeks in the study ($p < 0.05$) (**Figure 2B**).

Further evidence of fine motor impairment was demonstrated by the frequency of front right paw slips between the 2 groups of animals. The performance of the front right paw was of particular interest because microelectrodes were implanted in the left hemisphere of the brain in the region of the motor cortex responsible for front paw control. By meticulous video analysis, paw slips were chronicled and quantified (**Figure 2C**). While no significant differences were seen in the frequency of left paw slips, it was found that the implanted animals experienced significantly more front right paw slips as compared to the control animals (an average of 0.54 ± 0.07 front right paw slips per week in the implanted animals as compared to an average of 0.32 ± 0.02 front right paw slips per week in the control animals). When interpreting the data, an increase in the time to cross the ladder or an increase in the number of paw slips indicates a decrease in fine motor function (**Table 1**).

As a secondary measure of coordinated grasp and fine motor function, the animals completed a grip strength test (**Figure 3A**) where the maximum grip strength exerted by the animals was recorded. The individual animal's weekly grip scores were normalized to their pre-surgery baseline grip strength. It was seen that the implanted animals' post-surgery grip strength was significantly reduced compared to the control animals' at almost every post-surgery time point. (**Figure 3B**). The control animals' grip strength improved following pre-surgery testing, likely due to the training effect. Further, the control animals' grip strength was significantly greater than the baseline throughout the course of the study ($p < 0.05$). Interestingly, the implanted animals' grip strength performance was significantly worse than the baseline ($p < 0.01$) in the first week of testing following the recovery phase, but slowly returned to their baseline performance. Of note, a decrease in the maximum grip strength achieved by the animal indicates a decrease in fine motor function (**Table 1**).

Various histological markers can be used to visualize the microenvironment near a brain implant, including neuronal nuclei, astrocytes, and blood-brain barrier stability. Here, we performed immunohistochemical staining for IgG, a common blood protein not commonly found in the brain. Earlier work has shown that IgG is a useful indicator of blood-brain barrier integrity as it is an antibody found in the blood, and not normally present in the brain[16,18], and therefore the presence of IgG in the surrounding brain tissue can be correlated to the integrity of the blood-brain barrier[43]. Here, IgG fluorescence intensity was normalized to background brain tissue and quantified starting at the boundary of the electrode explantation hole and moving out in concentric bins until IgG was no longer present in the tissue. The implanted animals showed a significant increase in IgG intensity near the hole out to 150 µm as compared to the control animals. The IgG intensity in the implanted animals gradually returned to background intensity over the distance radiating from the implanted microelectrode hole. In the control animals, having never been implanted with a microelectrode, the normalized IgG intensity was not present in significant quantities above background intensity as the blood-brain barrier was not damaged in these animals.

Because significant differences were seen in both the ladder performance and IgG intensity, the two were correlated (**Figure 4**). Here, the normalized fluorescent intensity of the IgG area under the curve from 0-50 µm from the tissue-electrode interface for each animal was correlated with the average of each animal's ladder performance over the course of the study. A correlation coefficient of 0.90 was determined, demonstrating a very strong correlation between the fine motor performance and damage to the blood-brain barrier.

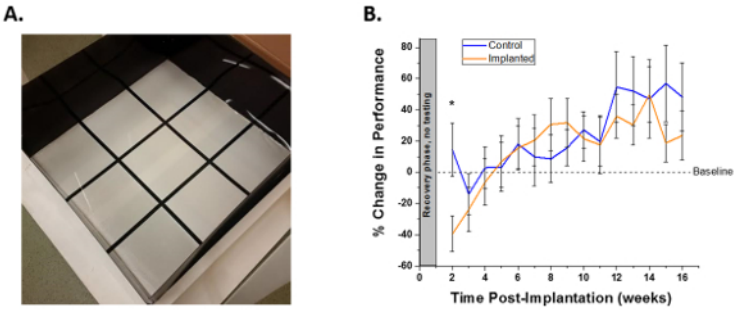

Figure 1. Representative open field grid test results. (**A**) This panel shows a behavioral testing setup for an open field grid test (for gross motor and anxiety testing). The open field grid test consists of a 1 m^2 acrylic sheet with 4 opaque walls of 40 cm in height, and square bottom sections of approximately 33 cm each. (**B**) This panel shows a gross motor function performance measured by the number of grid lines crossed, compared to the baseline performance. A significant difference in performance was seen between the control ($n = 10$) and the implanted ($n = 17$) groups at 2 weeks post-surgery ($p < 0.05$). All error is reported as SEM. This figure is reprinted from Goss-Varley *et al.*[27] with permission from the Nature Publishing Group. Please click here to view a larger version of this figure.

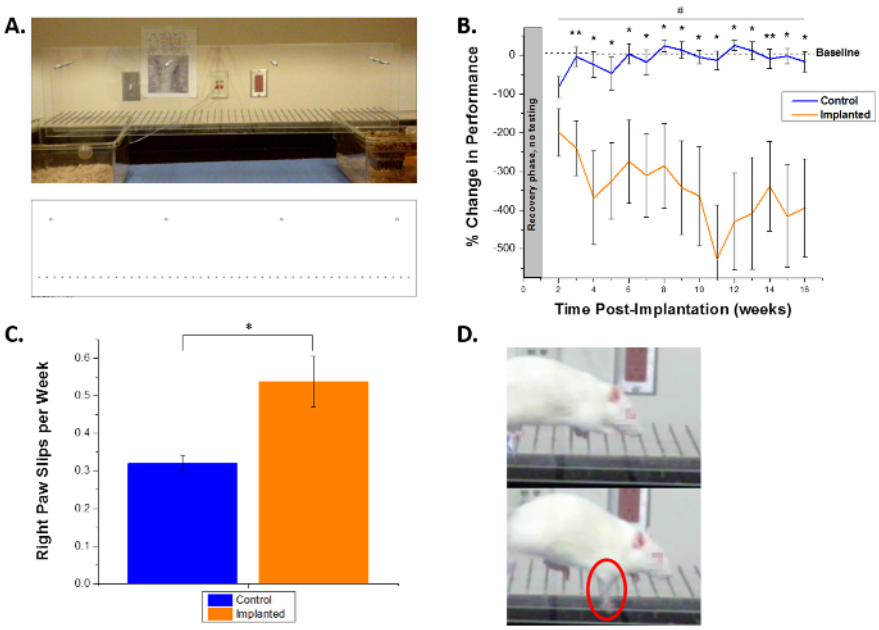

Figure 2. Representative ladder test results. (**A**) This panel shows a behavioral testing setup for a ladder test (for fine motor function testing). The ladder consists of 2 clear acrylic sides of 1 m in length and 25 cm in height, joined by stainless steel rungs spaced at 2 cm with a 3-mm diameter. (**B**) This panel shows fine motor function performance measured by time to cross the ladder, compared to the baseline performance. The results below the dashed line indicate a decrease in performance as compared to the baseline performance. A significant difference in performance was discovered between the control (n = 10) and the implanted (n = 17) groups for the post-surgery weeks 3 - 16 (* = $p < 0.05$, ** = $p < 0.01$) and longitudinally across the entire study (# = $p < 0.05$). (**C**) This panel shows a quantified instance of right front paw slips. A significant difference was discovered in the occurrence of right front paw slips per week when comparing the control and the implanted groups (* = $p < 0.05$). (**D**) This is an example of a paw slip. All error is reported as SEM. This figure is reprinted from Goss-Varley *et al.*[27] with permission from the Nature Publishing Group. Please click here to view a larger version of this figure.

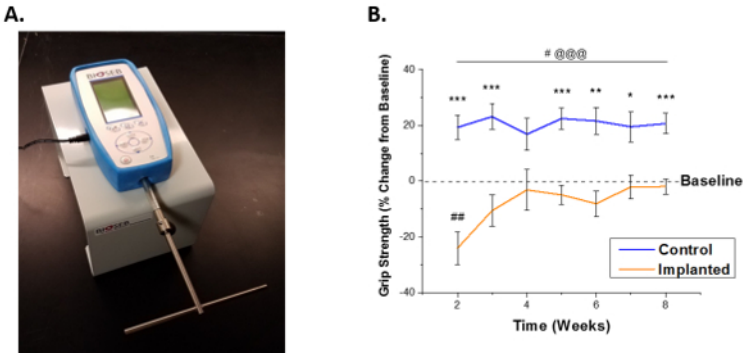

Figure 3. Representative grip strength test results. (**A**) This panel shows a behavioral testing setup for grip strength (for fine motor function testing). The grip strength meter consists of a weighted base with a mounted strength gauge connected to a grip handlebar. (**B**) This panel shows the fine motor function performance, measured by the maximum grip strength exerted compared to the baseline performance. The results below the dashed line indicate a decrease in performance as compared to the baseline performance. Significant differences were seen between the control (n = 5) and the implanted (n = 6) animals for almost all post-surgical weeks (* = $p < 0.05$, ** = $p < 0.01$, *** = $p < 0.001$). Further significance was seen between the control animals' weekly and baseline performances (# = $p < 0.05$) and between the implanted animals' weekly and baseline performances (## = $p < 0.01$). The control and the implanted animals performed significantly different longitudinally across the entire study (@@@ = $p < 0.001$). Please click here to view a larger version of this figure.

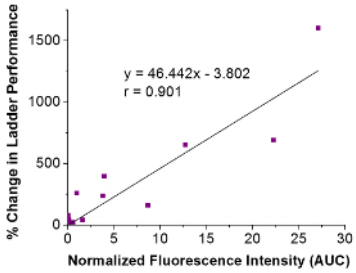

Figure 4. Correlation of IgG and ladder performance. A normalized IgG fluorescence intensity around the site of implantation was correlated with a change in ladder performance, and a correlation coefficient of 0.901 was found ($p < 0.001$). Please click here to view a larger version of this figure.

	Open Field Grid Lines Crossed	Open Field Total Distance Traveled	Open Field Maximum Speed	Ladder Crossing Time	Ladder Paw Slips	Grip Strength Maximum Pull
Increase from Baseline	Improved Performance – No Gross Motor Function or Anxiety Deficits	Improved Performance – No Gross Motor Function or Anxiety Deficits	Improved Performance – No Gross Motor Function or Anxiety Deficits	Reduced Performance – Fine Motor Function Deficit	Reduced Performance – Fine Motor Function Deficit	Improved Performance – No Fine Motor Function Deficit
Decrease from Baseline	Reduced Performance –Gross Motor Function or Anxiety Deficits	Reduced Performance – Gross Motor Function or Anxiety Deficits	Reduced Performance – Gross Motor Function or Anxiety Deficits	Improved Performance – No Fine Motor Function Deficit	Improved Performance – No Fine Motor Function Deficit	Reduced Performance – Fine Motor Function Deficit

Table 1. Overall representative behavior data showing increase and decrease in performance compared to baseline scores for each testing metric. The green boxes represent an improved performance which makes a motor deficit unlikely, and the red boxes represent a reduced performance which makes motor function deficits likely.

Discussion

The protocol outlined here has been used to effectively and reproducibly measure both fine and gross motor deficit in a model of rodent brain injury. Additionally, it allows for the correlation of fine motor behavior to histological outcomes following a microelectrode implantation in the motor cortex. The methods are easy to follow, inexpensive to set up, and can be modified to fit a researcher's individual needs. Further, the behavior testing does not cause great stress or pain to the animals; rather, the researchers believe the animals grew to enjoy the exercise and rewards that came with testing. Previous studies have suggested that motor cortex damage can cause motor, memory, and functional damage[44,45]. However, despite this knowledge, there is limited information on the functional impact caused by a microelectrode implantation in the motor cortex[27], which could negatively impact the clinical outcomes in patients.

Modifications can be made throughout the protocol, both in the surgical procedure and in the behavior testing. This protocol outlines the procedure to implant microelectrodes in the motor cortex of animals in the region affecting the forepaws. This procedure can be easily adapted to vary the implant, including electrodes for electrical stimulation[46] or cannulas for drug delivery[47], or the type of injury, including a TBI model[48]. Further modifications can be made to the scoring metrics used on the open field grid test, and to the ladder testing apparatus. In addition to the number of gridlines crossed, the total distance traveled, and the maximum velocity achieved by the animal, the time spent stagnant and the number of right and left turns can also be recorded as additional parameters of motor performance[32]. In the ladder test, removing rungs[49] or placing the ladder on an incline[50] can increase difficulty, although with the current implants the authors did not find this necessary to tease out fine motor deficits in this application. Finally, although the testing apparatus presented here were designed to be used with rats, the units could be scaled up or down to be used with various-sized rodents. It is important to note that if issues arise where an animal is not able to complete the pre-surgery testing consistently, the animal should be removed from the study.

As with all behavioral testing, it is critical to remain as consistent as possible over the course of the study. It has been shown that test results can vary based on the researcher working with the animals[51], the location in which the testing is performed[52], and environmental factors including animal housing and husbandry procedures[53]. Additionally, research has shown great variability in producing a brain injury by way of skull heating during a craniotomy procedure[31] and models of TBI including the weight-drop model[54] and mechanical variation in a controlled cortical impact model[55]. Researchers should, therefore, take special care to maintain consistency in the surgical procedure, testing and housing conditions, and in the testing personnel, among others.

Future directions of these behavior testing methods could expand upon the testing presented here to provide more thorough results. For example, a water maze test or a rotor rod test could be incorporated to further extract anxiety[56] or gross motor function[57] deficits, respectively. Additionally, future work might also aim to reduce the tissue damage caused by a device insertion in the brain. Current work in this area has focused on inflammation mitigation through anti-oxidant treatments[42,58], mechanically compliant implants[41,59,60], the inhibition of the innate immunity signaling pathway[14,15], and reducing vascular damage during a device implantation[31,61].

Lastly, it must be considered that the current work was completed using healthy, juvenile, male rats that do not necessarily embody the characteristics of the typical human patient receiving a brain implant. Additional research exploring further fine and gross motor function tasks in characteristic disease models is required to ratify the findings presented here. In varying disease models, differences between implanted and non-implanted sham animals may require the above-mentioned modifications to test conditions.

Disclosures

The authors have nothing to disclose.

Acknowledgements

This study was supported in part by the Merit Review Award #B1495-R (Capadona) and the Presidential Early Career Award for Scientist and Engineers (PECASE, Capadona) from the United States (US) Department of Veterans Affairs Rehabilitation Research and Development Service. Additionally, this work was supported in part by the Office of the Assistant Secretary of Defense for Health Affairs through the Peer Reviewed Medical Research Program under Award No. W81XWH-15-1-0608. The contents do not represent the views of the U.S. Department of Veterans Affairs or the United States Government. The authors would like to thank Dr. Hiroyuki Arakawa in the CWRU Rodent Behavior Core for his guidance in designing and testing rodent behavioral protocols. The authors would also like to thank James Drake and Kevin Talbot from the CWRU Department of Mechanical and Aerospace Engineering for their help in designing and manufacturing the rodent ladder test.

References

1. Donoghue, J. P. Bridging the brain to the world: a perspective on neural interface systems. *Neuron.* **60** (3), 511-521 (2008).
2. McFarland, D. J., Sarnacki, W. A., Wolpaw, J. R. Electroencephalographic (EEG) control of three-dimensional movement. *Journal of Neural Engineering.* **7** (3), 036007 (2010).
3. Wolpaw, J. R., McFarland, D. J. Control of a two-dimensional movement signal by a noninvasive brain-computer interface in humans. *Proceedings of the National Academy of Sciences of the United States of America.* **101** (51), 17849-17854 (2004).
4. Bell, C. J., Shenoy, P., Chalodhorn, R., Rao, R. P. Control of a humanoid robot by a noninvasive brain-computer interface in humans. *Journal of Neural Engineering.* **5** (2), 214-220 (2008).
5. Collinger, J. L. *et al.* High-performance neuroprosthetic control by an individual with tetraplegia. *The Lancet.* **381** (9866), 557-564 (2013).
6. Hochberg, L. R. *et al.* Reach and grasp by people with tetraplegia using a neurally controlled robotic arm. *Nature.* **485** (7398), 372-375 (2012).
7. Ajiboye, A. B. *et al.* Restoration of reaching and grasping movements through brain-controlled muscle stimulation in a person with tetraplegia: a proof-of-concept demonstration. *The Lancet.* **389** (10081), 1821-1830 (2017).
8. Bowsher, K. *et al.* Brain-computer interface devices for patients with paralysis and amputation: a meeting report. *Journal of Neural Engineering.* **13** (2), 023001 (2016).
9. Taylor, D. M., Tillery, S. I., Schwartz, A. B. Direct cortical control of 3D neuroprosthetic devices. *Science.* **296** (5574), 1829-1832 (2002).
10. Taylor, D. M., Tillery, S. I., Schwartz, A. B. Information conveyed through brain-control: cursor *versus.* robot. *IEEE Transactions on Neural Systems and Rehabilitation Engineering.* **11** (2), 195-199 (2003).
11. Jorfi, M., Skousen, J. L., Weder, C., Capadona, J. R. Progress towards biocompatible intracortical microelectrodes for neural interfacing applications. *Journal of Neural Engineering.* **12** (1), 011001 (2015).
12. Anderson, D. J. Penetrating multichannel stimulation and recording electrodes in auditory prosthesis research. *Hearing Research.* **242** (1-2), 31-41 (2008).
13. Pourfar, M. *et al.* Assessing the microlesion effect of subthalamic deep brain stimulation surgery with FDG PET. *Journal of Neurosurgery.* **110** (6), 1278-1282 (2009).
14. Hermann, J. K. *et al.* Inhibition of the cluster of differentiation 14 innate immunity pathway with IAXO-101 improves chronic microelectrode performance. *Journal of Neural Engineering.* In Press (2018).
15. Bedell, H. W. *et al.* Targeting CD14 on blood derived cells improves chronic intracortical microelectrode performance in chronic modified state of neuroinflammation. *Biomaterials.* **163**, 163-173 (2018).
16. Kozai, T. D. Y., Jaquins-Gerstl, A. S., Vazquez, A. L., Michael, A. C., Cui, X. T. Brain tissue responses to neural implants impact signal sensitivity and intervention strategies. *ACS Chemical Neuroscience.* **6** (1), 48-67 (2015).
17. Rennaker, R. L., Miller, J., Tang, H., Wilson, D. A. Minocycline increases quality and longevity of chronic neural recordings. *Journal of Neural Engineering.* **4** (2), L1-5 (2007).
18. Saxena, T. *et al.* The impact of chronic blood-brain barrier breach on intracortical electrode function. *Biomaterials.* **34** (20), 4703-4713 (2013).
19. Kozai, T. D. *et al.* Effects of caspase-1 knockout on chronic neural recording quality and longevity: insight into cellular and molecular mechanisms of the reactive tissue response. *Biomaterials.* **35** (36), 9620-9634 (2014).
20. Biran, R., Martin, D., Tresco, P. Neuronal cell loss accompanies the brain tissue response to chronically implanted silicon microelectrode arrays. *Experimental Neurology.* **195** (1), 115-126 (2005).
21. Potter, K. A., Buck, A. C., Self, W. K., Capadona, J. R. Stab injury and device implantation within the brain results in inversely multiphasic neuroinflammatory and neurodegenerative responses. *Journal of Neural Engineering.* **9** (4), 046020 (2012).
22. Szarowski, D. H. *et al.* Brain responses to micro-machined silicon devices. *Brain Research.* **983** (1-2), 23-35 (2003).
23. Gunasekera, B., Saxena, T., Bellamkonda, R., Karumbaiah, L. Intracortical recording interfaces: current challenges to chronic recording function. *ACS Chemical Neuroscience.* **6** (1), 68-83 (2015).
24. Villalobos, J. *et al.* Preclinical evaluation of a miniaturized Deep Brain Stimulation electrode lead. *Conference Proceedings: Annual International Conferences of the IEEE Engineering in Medicine and Biology Society.* **2015** 6908-6911 (2015).
25. Zhong, Y., Bellamkonda, R. V. Controlled release of anti-inflammatory agent alpha-MSH from neural implants. *Journal of Controlled Release.* **106** (3), 309-318 (2005).

26. Gage, G. J. *et al.* Surgical implantation of chronic neural electrodes for recording single unit activity and electrocorticographic signals. *Journal of Visualized Experiments.* (60), e3565 (2012).
27. Goss-Varley, M. *et al.* Microelectrode implantation in motor cortex causes fine motor deficit: implications on potential considerations to brain computer interfacing and human augmentation. *Scientific Reports.* **7**, 15254 (2017).
28. Metz, G. A., Whishaw, I. Q. Cortical and subcortical lesions impair skilled walking in the ladder rung walking test: a new task to evaluate fore- and hindlimb stepping, placing, and co-ordination. *Journal of Neuroscience Methods.* **115** (2), 169-179 (2002).
29. Bailey, K. R., Crawley, J. N. Anxiety-related behaviors in mice. In *Methods of Behavior Analysis in Neuroscience.* edited by Buccafusco, J. J., chapter 5, CRC Press. Boca Raton, FL (2009).
30. Prut, L., Belzung, C. The open field as a paradigm to measure the effects of drugs on anxiety-like behaviors: a review. *European Journal of Pharmacology.* **463** (1-3), 3-33 (2003).
31. Shoffstall, A. J. *et al.* Potential for thermal damage to the blood-brain barrier during craniotomy procedure: implications for intracortical recording microelectrodes. *Journal of Neural Engineering.* In Press (2017).
32. Dona, K. R. *et al.* A novel single animal motor function tracking system using MATLAB's computer vision toolbox to assess functional deficits. *Journal of Visualized Experiments.* Under Review (2018).
33. Ereifej, E. S. *et al.* Implantation of neural probes in the brain elicits oxidative stress. *Frontiers in Bioengineering and Biotechnology.* In Press (2018).
34. Ereifej, E. S. *et al.* The neuroinflammatory response to nanopatterning parallel grooves into the surface structure of intracortical microelectrodes. *Advanced Functional Materials.* (2017).
35. Ravikumar, M. *et al.* The roles of blood-derived macrophages and resident microglia in the neuroinflammatory response to implanted intracortical microelectrodes. *Biomaterials.* **S0142-9612** (35), 8049-8064 (2014).
36. Potter-Baker, K. A. *et al.* A comparison of neuroinflammation to implanted microelectrodes in rat and mouse models. *Biomaterials.* **34**, 5637-5646 (2014).
37. Nguyen, J. K. *et al.* Influence of resveratrol release on the tissue response to mechanically adaptive cortical implants. *Acta Biomaterialia.* **29** 81-93 (2016).
38. Ravikumar, M. *et al.* The effect of residual endotoxin contamination on the neuroinflammatory response to sterilized intracortical microelectrodes. *Journal of Materials Chemistry B.* **2** 2517-2529 (2014).
39. Potter, K. A., Simon, J. S., Velagapudi, B., Capadona, J. R. Reduction of autofluorescence at the microelectrode-cortical tissue interface improves antibody detection. *Journal of Neuroscience Methods.* **203** (1), 96-105 (2012).
40. Potter, K. A. *et al.* Curcumin-releasing mechanically-adaptive intracortical implants improve the proximal neuronal density and blood-brain barrier stability. *Acta Biomaterialia.* **10** (5), 2209-2222 (2014).
41. Nguyen, J. K. *et al.* Mechanically-compliant intracortical implants reduce the neuroinflammatory response. *Journal of Neural Engineering.* **11** 056014 (2014).
42. Potter, K. A. *et al.* The effect of resveratrol on neurodegeneration and blood brain barrier stability surrounding intracortical microelectrodes. *Biomaterials.* **34**, 7001-7015 (2013).
43. McConnell, G. C. *et al.* Implanted neural electrodes cause chronic, local inflammation that is correlated with local neurodegeneration. *Journal of Neural Engineering.* **6** (5), 056003 (2009).
44. Hamm, R. J., Pike, B. R., O'Dell, D. M., Lyeth, B. G., Jenkins, L. W. The rotarod test: an evaluation of its effectiveness in assessing motor deficits following traumatic brain injury. *Journal of Neurotrauma.* **11** (2), 187-196 (1994).
45. Teuber, H. L. Recovery of function after brain injury in man. *Ciba Foundation Symposium.* (34), 159-190 (1975).
46. Carmel, J. B., Kimura, H., Martin, J. H. Electrical stimulation of motor cortex in the uninjured hemisphere after chronic unilateral injury promotes recovery of skilled locomotion through ipsilateral control. *Journal of Neuroscience.* **34** (2), 462-466 (2014).
47. Hayn, L., Koch, M. Suppression of excitotoxicity and foreign body response by memantine in chronic cannula implantation into the rat brain. *Brain Research Bulletin.* **117**, 54-68 (2015).
48. Marklund, N. Rodent models of traumatic brain injury: methods and challenges. *Methods in Molecular Biology.* **1462**, 29-46 (2016).
49. Metz, G. A., Whishaw, I. Q. The ladder rung walking task: a scoring system and its practical application. *Journal of Visualized Experiments.* (28), e1204 (2009).
50. Pajoohesh-Ganji, A., Byrnes, K. R., Fatemi, G., Faden, A. I. A combined scoring method to assess behavioral recovery after mouse spinal cord injury. *Neuroscience Research.* **67** (2), 117-125 (2010).
51. Chesler, E. J., Wilson, S. G., Lariviere, W. R., Rodriguez-Zas, S. L., Mogil, J. S. Influences of laboratory environment on behavior. *Nature Neuroscience.* **5** (11), 1101-1102 (2002).
52. Crabbe, J. C., Wahlsten, D., Dudek, B. C. Genetics of mouse behavior: interactions with laboratory environment. *Science.* **284** (5420), 1670-1672 (1999).
53. Richter, S. H., Garner, J. P., Auer, C., Kunert, J., Wurbel, H. Systematic variation improves reproducibility of animal experiments. *Nature Methods.* **7** (3), 167-168 (2010).
54. Xiong, Y., Mahmood, A., Chopp, M. Animal models of traumatic brain injury. *Nature Reviews Neuroscience.* **14** (2), 128-142 (2013).
55. Osier, N. D., Dixon, C. E. The controlled cortical impact model: applications, considerations for researchers, and future directions. *Frontiers in Neurology.* **7** 134 (2016).
56. Harrison, F. E., Hosseini, A. H., McDonald, M. P. Endogenous anxiety and stress responses in water maze and Barnes maze spatial memory tasks. *Behavioural Brain Research.* **198** (1), 247-251 (2009).
57. Jackson, J. R. *et al.* Reduced voluntary running performance is associated with impaired coordination as a result of muscle satellite cell depletion in adult mice. *Skeletal Muscle.* **5** 41 (2015).
58. Potter-Baker, K. A. *et al.* Implications of chronic daily anti-oxidant administration on the inflammatory response to intracortical microelectrodes. *Journal of Neural Engineering.* **12** (4), 046002 (2015).
59. Ware, T., Simon, D., Rennaker, R. L., Voit, W. Smart polymers for neural interfaces. *Polymer Reviews.* **53** (1), 108-129 (2013).
60. Ecker, M. *et al.* Sterilization of thiol-ene/acrylate based shape memory polymers for biomedical applications. *Macromolecular Materials and Engineering.* **302** (2), 160331 (2017).
61. Kozai, T. *et al.* Reduction of neurovascular damage resulting from microelectrode insertion into the cerebral cortex using *in vivo*. two-photon mapping. *Journal of Neural Engineering.* **7** (4), 046011 (2010).

frontiers in Materials

ORIGINAL RESEARCH
published: 15 November 2018
doi: 10.3389/fmats.2018.00066

Softening Shape Memory Polymer Substrates for Bioelectronic Devices With Improved Hydrolytic Stability

*Seyed Mahmoud Hosseini[1], Rashed Rihani[2], Benjamin Batchelor[3], Allison M. Stiller[2], Joseph J. Pancrazio[2], Walter E. Voit[2,3,4] and Melanie Ecker[2,3,4]**

[1] Department of Chemistry and Biochemistry, The University of Texas at Dallas, Dallas, TX, United States, [2] Department of Bioengineering, The University of Texas at Dallas, Dallas, TX, United States, [3] Center for Engineering Innovation, The University of Texas at Dallas, Dallas, TX, United States, [4] Department of Materials Science and Engineering, The University of Texas at Dallas, Dallas, TX, United States

Candidate materials for next generation neural recording electrodes include shape memory polymers (SMPs). These materials have the capability to undergo softening after insertion in the body, and therefore reduce the mismatch in modulus that usually exists between the device and the tissue. Current SMP formulations, which have shown promise for neural implants, contain ester groups within the main chain of the polymer and are therefore prone to hydrolytic decomposition under physiological conditions over periods of 11–13 months *in vivo*, thus limiting the utility for chronic applications. Ester free polymers are stable in harsh condition (PBS at 75°C or NaOH at 37°C) and accelerated aging results suggest that ester free SMPs are projected to be stable under physiological condition for at least 7 years. In addition, the ester free SMP is compatible with microfabrication processes needed for device fabrication. Furthermore, they demonstrate *in vitro* biocompatibility as demonstrated by high levels of cell viability from ISO 10993 testing.

Keywords: neural interfaces, softening behavior, accelerated aging, hydrolytic stable, shape memory polymer, thiol-ene degradation, chronic viable polymer

OPEN ACCESS

Edited by:
Ulrich G. Hofmann, Universitätsklinikum Freiburg, Germany

Reviewed by:
Ahmed El-Fiqi, Dankook University, South Korea
Ajay Devidas Padsalgikar, St. Jude Medical, United States

***Correspondence:**
Melanie Ecker
melanie.ecker@utdallas.edu

Specialty section:
This article was submitted to Biomaterials, a section of the journal Frontiers in Materials

Received: *09 August 2018*
Accepted: *24 October 2018*
Published: *15 November 2018*

Citation:
Hosseini SM, Rihani R, Batchelor B, Stiller AM, Pancrazio JJ, Voit WE and Ecker M (2018) Softening Shape Memory Polymer Substrates for Bioelectronic Devices With Improved Hydrolytic Stability. Front. Mater. 5:66. doi: 10.3389/fmats.2018.00066

INTRODUCTION

Shape memory polymers (SMPs) are an emerging class of materials. Their capability to restore their original shape after being deformed is outstanding (Dietsch and Tong, 2007; Liu et al., 2007; Mather et al., 2009; Lendlein, 2010; Hu et al., 2012b; Hager et al., 2015) and these materials have found utility in a variety of potential applications, including airspace, (Ishizawa et al., 2003; Barrett et al., 2006; Rory Barrett et al., 2006; Yanju and Jinsong, 2010; Yanju et al., 2014) anti-counterfeiting technology, (Pretsch et al., 2012; Ecker and Pretsch, 2013, 2014a,b) textile industry, (Matilla, 2006; Hu and Chen, 2010; Hu et al., 2012a) and as medical devices (Feninat et al., 2002; Buckley et al., 2006; Baer et al., 2007; Kulshrestha and Mahapatro, 2008; Lendlein and Behl, 2008; Baudis et al., 2014; Wang et al., 2017). The triggers for SMPs to recover to their permanent shape are diverse and include direct heating above the transition temperature of the polymer, indirect heating through electric or magnetic activation, and less commonly, chemical modification including plasticization. The plasticization of the SMP with solvent molecules, e.g., water, leads to a lowering of the glass transition temperature (T_g) of the polymer due to swelling and the resulting increased free volume of the polymer chains

(Immergut and Mark, 1965; Singhal et al., 2013). When the T_g of a polymer is above room temperature (RT) before, but below after plasticization, the SMP may recover its permanent shape upon immersion in aqueous solutions at ambient temperatures. At the same time, the polymer changes from a glassy (stiff) materials to a rubbery (soft) material. This behavior of SMPs is what is of interest for the development of (self)-softening SMP substrates for bioelectronics devices. Especially for cortical neural interfaces, there is a need for devices which are stiff enough during the implantation to enable a sufficient penetration of the tissue with least possible trauma. However, after implantation, materials that soften to a modulus that is much closer to the tissue modulus offer the promise of decreasing the foreign body response and micromotion effects. Previously, the Voit Lab has presented a new generation of neural implants comprising of softening thiol-ene/acrylate polymers used as substrates (Ware et al., 2013, 2014; Do et al., 2017; Ecker et al., 2017; Simon et al., 2017). These devices work well for acute experiments and for chronic experiments on the order of 1–3 months. At least one factor limiting the long term stability of current SMP devices may be the fact that these polymers contain ester groups in their backbone which are vulnerable to hydrolytic degradation under moist conditions. For future applications, including translation to the clinic, it is necessary to have substrate materials with increased durability under *in vivo* conditions to enable chronic experiments over the course of years (Ryu and Shenoy, 2009; Rubehn and Stieglitz, 2010; Takmakov et al., 2015; Teo et al., 2016; Lecomte et al., 2017; ASTM, 2018), Reit et al. (2015) have demonstrated, that the use of ester free thiol-monomers significantly increases the durability of thiol-ene networks while it still allows to tune the glass transition temperature and cross-link density.

Here, we present a thiol-ene SMP formulation that is chemically and structurally similar to the most recent ones, but does not contain any ester groups (Do et al., 2017; Ecker et al., 2017; Simon et al., 2017; Garcia-Sandoval et al., 2018; Shoffstall et al., 2018). We have optimized the synthesis of a new monomer and tailored the polymer composition to have similar *in vivo* softening capabilities as previous reported SMPs. Dynamic mechanical analysis (DMA) of the hydrolytically stable SMP revealed that the SMP has a glass transition temperature above body temperature when dry, but below body temperature after being soaked in phosphate buffered saline (PBS). Thus, the novel SMP is also able to soften under physiological conditions to a modulus that is much closer to the tissue. To verify the improved stability of the new material against hydrolysis, we have performed accelerated aging tests in PBS at elevated temperatures (75°C) for 8 weeks and in one molar sodium hydroxide (NaOH) solution at body temperature over the course of 4 weeks. Weight loss and mechanical properties were determined and compared to a SMP composition that contains ester groups in the main chain. Our results demonstrate that the ester free SMP remained stable over the course of the study whereas the ester-containing counterpart lost about 15% of mass after aging in PBS and even 39% after aging in NaOH. We have also demonstrated that the new softening polymer is biocompatible, can be sterilized, and is compatible with microfabrication methods. That makes this polymer an ideal substrate candidate for future neural implants.

MATERIALS AND METHODS

Synthesis of 1,3,5-tris(3-mercaptopropyl)-1,3,5-triazinane-2,4,6-trione (TTTSH)

Trithiol monomer TTTSH was synthesized following previously reported method (Lundberg et al., 2010) with minor modifications (**Scheme 1**). Briefly, 30 g (120.4 mmol) 1, 3, 5-triallyl-1, 3, 5-triazine-2, 4, 6-trione (TATATO), 82.40 g (1,080 mmol) thioacetic acid, and 1.98 g (12.04 mmol) 2, 2′-azobis (2-methylpropionnitrile) (AIBN) were placed in a 500 mL three-neck round-bottom flask which was equipped with condenser and nitrogen inlet. Afterward, the reaction mixture was stirred at 65°C for 24 h under a nitrogen atmosphere. Excess thioacetic acid was removed by reduced pressure and then was reacted with methanol (100 ml) and concentrated hydrochloric acid (50 ml) at 65°C for 36 h to cleave the thioester bond. After cooling down to room temperature, water was added (300 ml) and extracted for three times with methylene chloride (300 ml). The organic mixture was washed with sodium hydrogen carbonate solution (5%), dried over $MgSO_4$, and concentrated with reduced pressure. After purification by column chromatography with gradient hexane: ethyl acetate mixtures 1:0 to 1:4 yellowish viscous liquid was obtained.

Fabrication of Polymers

1,3,5-Triallyl- 1,3,5-triazine-2,4,6(1H,3H,5H)-trione (TATATO), Trimethylolpropane tris(3-mercaptopropionate) (TMTMP), and 2,2-Dimethoxy-2-phenylacetophenone (DMPA) were purchased from Sigma Aldrich, whereas Tris [2-(3-mercaptopropionyloxy) ethyl] isocyanurate (TMICN) was purchased from Evans Chemicals, and 1,10-Decanedithiol (DDT) from TCI Chemicals. All the chemicals were used as received without further purification. TTTSH was synthesized as described under section Synthesis of 1,3,5-tris(3-mercaptopropyl)-1,3,5-triazinane-2,4,6-trione (TTTSH). Two thiol-ene SMP compositions were prepared, an ester-free (SMP-A) and an ester containing (SMP-B) formulation, each consisting of stoichiometric quantities of thiol to alkene functionalities. Exact mole fractions are: TTTSH/DDT-TATATO = 0.3/0.2–0.5 (SMP-A) and TMTMP/TMICN-TATATO = 0.45/0.05–0.5 (SMP-B) (**Figure 1**). A total of 0.1 wt% DMPA of total monomer weight was dissolved in the solution for the initiation of the photopolymerization of the monomer solution. The vial was covered in aluminum foil to prevent incident light from contacting the monomer solution and kept at room temperature. Without exposing the solution to light, the vial was mixed thoroughly by planetary speed mixing.

The polymer solutions were spin cast on 75 × 50 mm glass microscope slides using a Laurell WS-650-8B spin coater. Spin speed was 350 rpm and time was 45 s for SMP-A and 600 rpm and 25 s for SMP-B in order to achieve thicknesses of about 30 μm, respectively. Polymerization was performed at ambient temperature using an UVP CL-1000 crosslinking chamber with five overhead 365 nm UV bulbs for 60 min under air. Cured

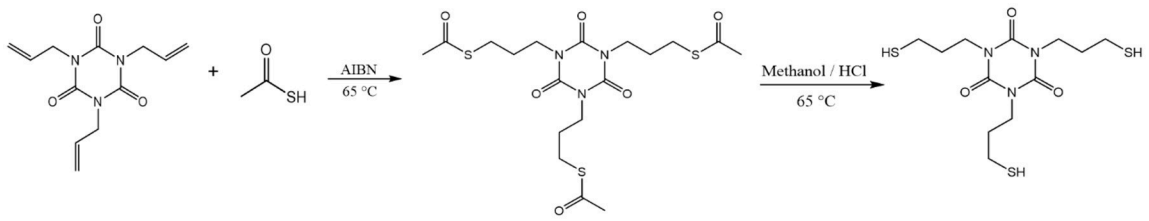

SCHEME 1 | Reaction scheme of the TTT-SH synthesis.

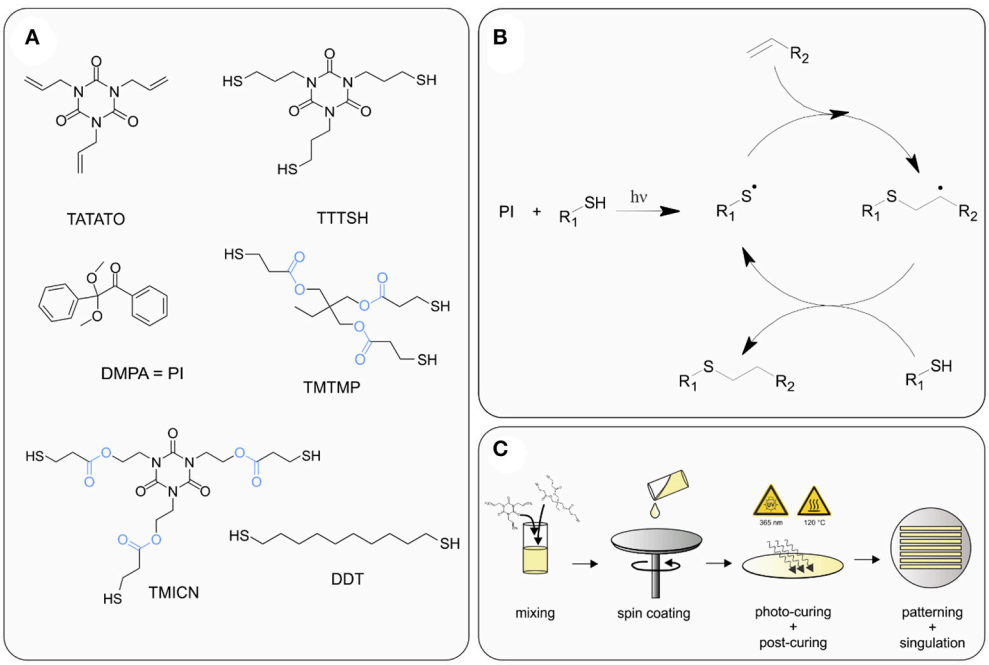

FIGURE 1 | (A) Chemical structures of monomers and photoinitiator (PI) used for synthesis of polymers SMP-A and SMP-B. Ester groups are highlighted in blue, **(B)** reaction mechanism of thiol-ene click reaction, and **(C)** schematic of polymer fabrication.

samples were then placed in a vacuum oven at 120°C and 5 inHg (∼16.9 kPa) for 24 h to further complete network conversion.

Test devices were either fabricated using a CO_2 laser or were fabricated in the UT Dallas Class 10,000 cleanroom facility. The above SMP-on-glass substrates were used as the starting substrates in the cleanroom. Low temperature silicon nitride (using PlasmaTherm-790 PECVD) was deposited to act as a hard mask for the following plasma etching processes in which the device outline/shape was patterned. Adjacently, the nitride hard mask was etched away in the 1:10 HF dip. For some SMP samples top 4 μm thick crust was etched away in oxygen plasma (Technics RIE). In a final step, the test devices having dimensions of 4.5 × 50 mm × 30 μm were delaminated from the glass slide by soaking in water.

Accelerated Aging

SMP-A and B were subjected to two different accelerated aging scenarios; test samples were either immersed in 20 ml phosphate buffered saline (PBS) at 75°C or in 1 M sodium hydroxide (NaOH) solution at 37°C, respectively. A number of $N = 3$ samples were removed after 7, 14, 21, and 28 days immersion in NaOH and after 7, 14, 21, 28, 35, 42, 49, and 56 days after immersion in PBS. After removal, the samples were rinsed in de-ionized water before they were dried with a lint-free cloth. The accelerated aging in PBS follows the Arrhenius equation under the conservative assumption for biomedical polymers (Hemmerich, 1998) that $Q_{10} = 2$:

$$Accelerated\ Aging\ Time\ (t_{AA}) = \frac{Real\ Aging\ Time\ (t_{RT})}{Q_{10}^{\frac{(T_{AA}-T_{RT})}{10}}} \quad (1)$$

where t_{AA} is the accelerated aging time, t_{RT} the real aging time, T_{AA} temperature for accelerated aging, T_{RT} temperature for real time aging and Q_{10} the temperature coefficient. According to the Q_{10} temperature coefficient, which is a derivation of the Arrhenius equation, 1 week in PBS at 75°C is equal to 14 weeks at 37°C.

Weight and Thickness Loss

The dry weight of all samples was determined with 0.01 mg precision before and after aging. The weight loss was calculated according the following equation:

$$mass\ loss\ (\%) = \frac{m_0 - m_T}{m_0} \times 100 \quad (2)$$

where m_0 is the weight of the neat samples and m_T is the weight of the samples after aging. A Marathon micrometer with 0.001 mm precision was applied to determine thickness of samples before and after the aging study. The mean value and standard deviation was calculated for $N = 3$ samples per aging time.

Dynamic Mechanical Analysis (DMA)

DMA was performed using a TA Instruments RSA-G2 Solids Analyzer with the immersion system in tension mode in order to quantify the storage modulus *E*' and tan δ of dry or in PBS soaked samples. All measurements were performed on rectangular samples as received after the clean room processing or CO_2 laser cutting, having a width of 4.5 ± 0.1 mm and thicknesses of 30 ± 3 μm. The following parameters were selected: clamping distance of 15 mm, a preload force of 0.1 N, a frequency of 1 Hz, and a deformation amplitude of 0.275% strain. Dry experiments were run from 10 to 100°C or from 20 to 120°C using a heating rate of 2°C min^{-1}. Soaking experiments were performed using the immersion system of the RSA-G2 filled with PBS. The first step (the soaking) included the heating from room temperature to 37°C followed by isothermal oscillating for 60 or 120 min. The second step comprised first cooling down to the start temperature with a rate of 3 C min^{-1} followed by heating from 10 to 80°C applying a heating rate of 2°C min^{-1}. All measurements were performed on three independent specimens in order to gather statistical results. Graphics show representative measurements only.

Termogravimetric Analysis (TGA)

A Mettler Toledo TGA/DSC 1 was used to perform Thermal Gravimetric Analysis on $N = 3$ samples before and after accelerated aging. The polymer samples were heated from 25 to 700°C at a heating rate of 20°C/min and flow of 50 ml/min nitrogen gas. Samples were approximately 5 mg each.

Cytotoxicity Test

Cytotoxicity assays were carried out as previously described (Black et al., 2018) and in accordance with the International Organization for Standards (ISO) protocol "10993-5: Biological evaluation of medical devices"(ISO, 2008). Briefly, 50% and 100% concentration shape-memory polymer (SMP-A) extract was evaluated against Tygon-F-4040-Lubricant Tubing extract (positive control) and cell medium (negative control). Material extracts which reduced normalized cell viability percentages below 70% were considered cytotoxic in accordance with the ISO protocol (ISO, 2008).

Material extracts were made by soaking 3 cm^2/ml of positive control and SMP A in Dulbecco's Modified Eagle Medium (DMEM) at 37°C, 5% CO_2, and 95% relative humidity for 24 h in a polystyrene, glass-bottom 24 well plate (Greiner Bio-One, Austria). NCTC clone 929 fibroblasts (ATCC, USA) were routinely sub-cultured and seeded in a separate 24 well plate at a density of 100,000 cells per well in complete cell medium (DMEM with 10% horse serum) and allowed to incubate at 37°C, 5% CO_2, and 95% relative humidity for 24 h until a semi-confluent monolayer of cells was formed. Cell media was replaced with the respective material extract for 24 h before being stained using a LIVE/DEAD Cytotoxicity kit for mammalian cells (Thermo Fisher, L3324) using manufacturer protocol. Briefly, Cells were washed three times with sterile PBS and incubated at 37°C with 2 μM Calcein AM (CaAM) and 4 μM Ethidium Homodimer (EthD-1) for 15 min. CaAM dye stained the cytoplasm of live cells while EthD-1 stained the nucleus of apoptotic cells. 2 × 2 field stitched fluorescent images (10x objective) were taken in each well using an inverted microscope (Nikon Ti eclipse).

Live/dead cell counts were quantified using ImageJ (NIH). Briefly, images were treated with a 2.0 Gaussian Blur then automatically counted based on local intensity maxima. Further analysis using a MATLAB program identified cells that exhibited both live and dead stains based on cell-to-cell proximity through and were removed from the live count. Cell viability percentage was defined as the ratio of live cells to the total number of cells. Cell viability percentages reported were normalized to the negative control.

RESULTS

Synthesis of Ester Free Monomer

Trifunctional thiol (TTTSH) was synthesized by radical addition reaction between TATATO and thioacetic acid followed by hydrolysis in acidic media. Column chromatography was applied to remove byproducts. Yield: 30 g (71%). ^{1}H NMR, ^{13}C NMR and FTIR, support the successful synthesis (detailed plots are shown in SI, **Supplementary Figures 1–3**). ^{1}H NMR [600 MHz, $CDCl_3$, δ (ppm)]: 3.98 (t, $J = 7$ Hz, 6H, -N-C**H2**-CH2-), 2.54 (dt, $J = 7$ Hz/ $J = 8$ Hz, -C**H2**-SH), 1.94 (quintet, $J = 7$ Hz, 6H, -CH2-C**H2**-CH2-), 1.52 (t, 3H, $J = 8$ Hz, -S**H**).^{13}C NMR [150 MHz, $CDCl_3$, δ (ppm)]: 149.03(–**C**=O), 41.84 (–N**C**H_2–), 31.87 (–**C**H2–), 21.95 (–**C**H_2SH). FT-IR (cm^{-1}): 2962, 2933, 2854, 2566 (ν_{S-H}), 1671 ($\nu_{C=O}$), 1454, 1423, 1373, 1334, 1288, 1230, 759.

Softening Effect on Pristine SMPs

Our aim was to synthesize an ester free SMP formulation with similar softening properties as previously used ester-containing thiol-ene and thiol-ene/acrylate polymer compositions. In order to mimic the effect of body fluids on mechanical properties of the polymer SMP-A, dynamic mechanical analysis was performed in dry and soaked conditions (**Figure 2A**). The glass transition temperature (T_g) and storage modulus (*E*') in the glassy and rubbery state was tuned to be similar to the previously used SMP-B (**Figure 2B**). Soaked conditions were achieved by immersing the polymers in phosphate buffered saline (PBS) at 37°C and monitoring the storage modulus loss until the modulus no longer decreases. We determined that the composition consisting of TTTSH/DDT-TATATO = 0.3/0.2–0.5 had comparable values.

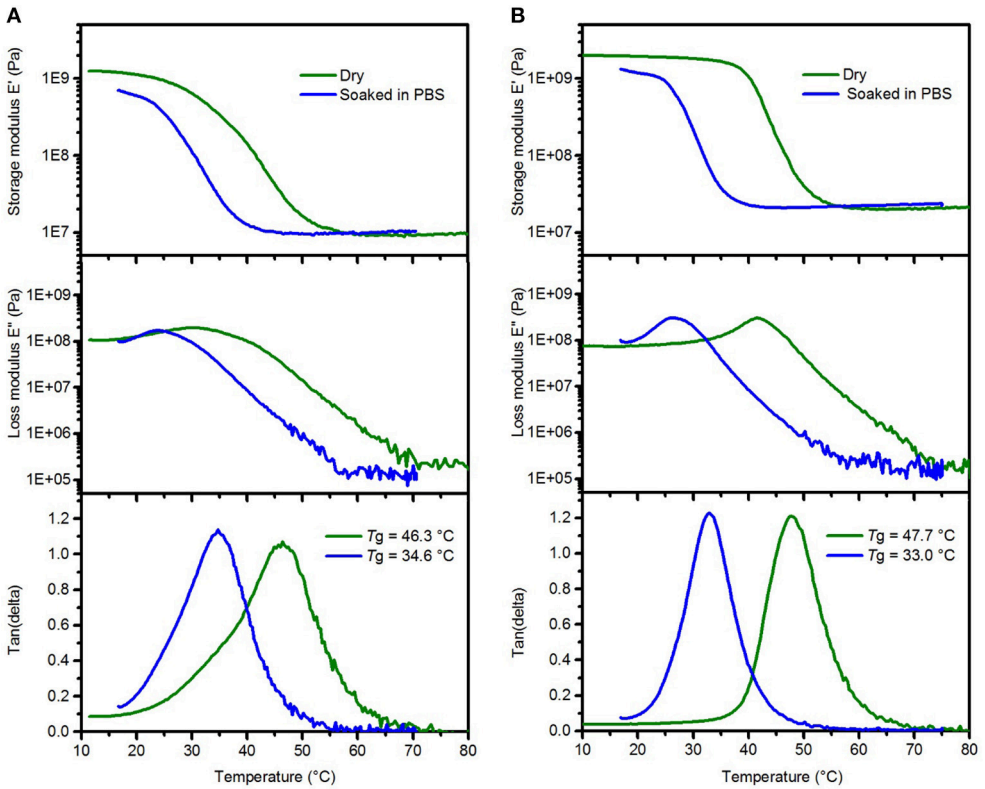

FIGURE 2 | Representative DMA data of SMP-A **(A)** and SMP-B **(B)** showing the changes in the storage modulus (top), loss modulus (center), and tan delta (bottom) after softening in PBS, respectively.

Soaking in PBS led to a modulus decrease for SMP-A from 1,020 ± 67 MPa at room temperature (23°C) to 22.1 ± 0.3 MPa after 20 min at 37°C, while the modulus of SMP-B dropped from 2,187 ± 98 MPa to 28.8 ± 0.4 MPa. After soaking in PBS, the peaks of loss modulus and tan (delta) which show the glass transition temperature of both SMPs decreased by 12–14°C compared to the dry values (**Figure 2**). For SMP-A, T_g dropped from 46.3 ± 0.7 to 34.6 ± 0.8°C and for the SMP-B, fell from 47.8 ± 0.4 to 33.0 ± 0.6°C.

Accelerating Aging Test in PBS at 75°C

Chronic implantable bioelectronic devices must consist of stable substrate materials in biological environment to enable operation for many years *in vivo* (Lyu and Untereker, 2009). To compare the hydrolytic stability of the sample's network in physiological conditions, aging in PBS was performed. In order to accelerate the aging process, the temperature was increased to 75°C. The effect of the aging conditions on mass change (**Figure 3**) and viscoelastic behavior (**Figure 4**) of the samples were then assessed. As shown in **Figure 3A**, the SMP-B was stable for nearly 4 weeks, but thereafter began to continually lose mass until the test was stopped. After 8 weeks at elevated temperature, SMP-B lost 14.7 ± 0.9% of its original mass. On the other hand, SMP-A exhibited no weight loss. A similar trend is seen in **Figure 3B**, where SMP-A displayed no change in thickness over the testing period, whereas SMP-B began to thin after 5 weeks. At the end of 8 weeks SMP-B lost 9.8 ± 1.6% of its original thickness.

The DMA data of the SMPs aged in PBS indicates that T_g increased each week, which can be seen in the peak shifts of tan delta and the loss modulus, respectively. As seen in **Figure 4**, the $T_g$for both SMP-A and SMP-B displayed higher glass transition temperatures after soaking in PBS at 75°C (shifting from 47 to∼61°C). **Figure 4B** indicates that rubbery modulus of SMP-B decreases gradually and tan delta peak is getting wider and asymmetric with increasing aging time. On the other hand SMP-A does not show any changes in the shape of graphs.

Accelerated Aging Test in 1 M NaOH Solution

The effect of harsh conditions (1.0 M NaOH, 37°C) on our two different polymers (SMP-A and B) was investigated. Mass and thickness changes (**Figure 5**) and mechanical properties (**Figure 6**) of the polymers were compared to the initial pristine and dry polymers. **Figure 5A** shows the change in polymer mass over time. Over the course of the 4 weeks investigation, SMP-A had no appreciable loss of mass, whereas SMP-B showed remarkable mass change during 4 weeks with a final mass loss of 38.7 ±

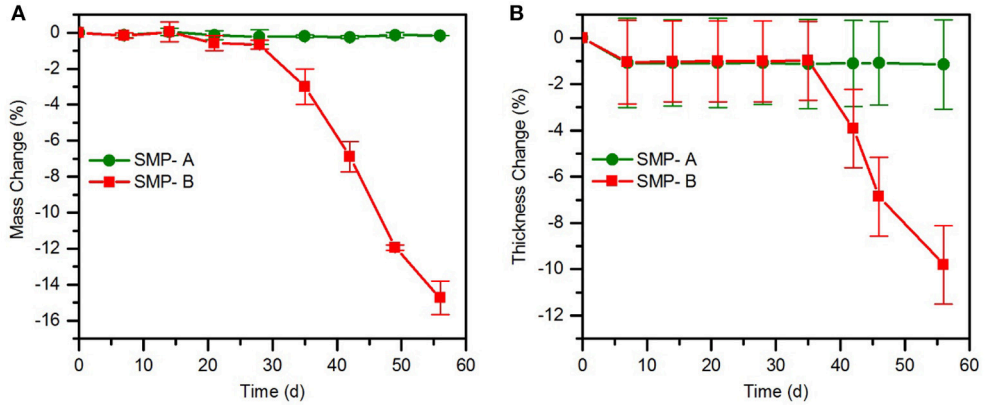

FIGURE 3 | Mass change **(A)** and thickness change **(B)** of SMP-A and SMP-B after various aging times in PBS at 75°C.

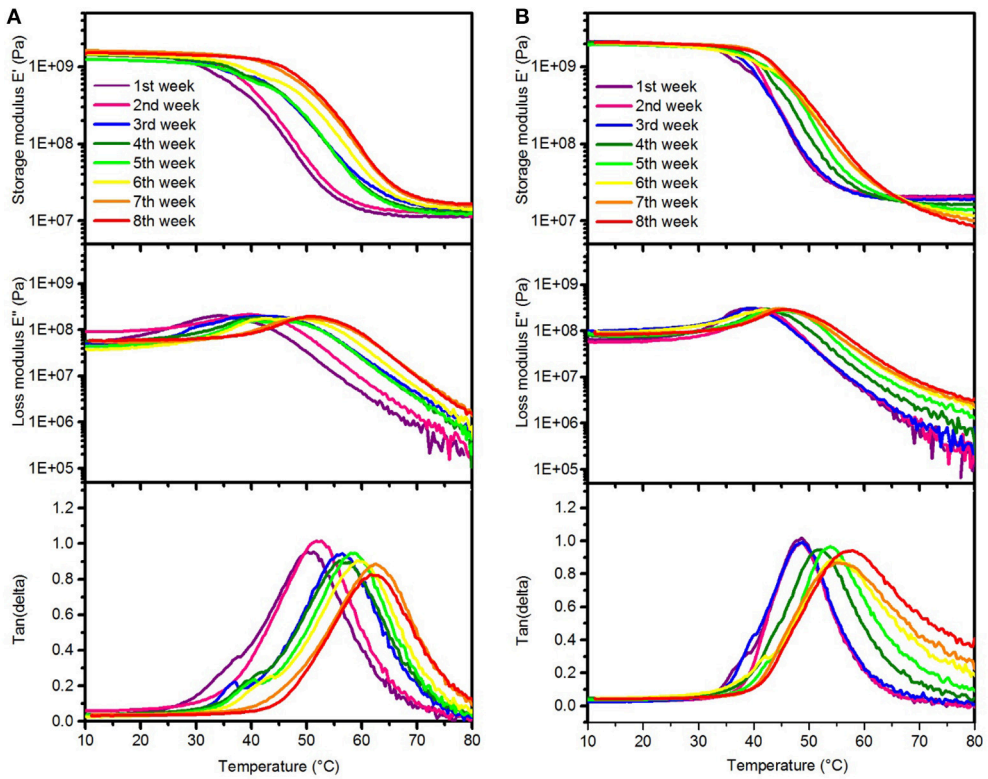

FIGURE 4 | Representative DMA measurements of SMP-A **(A)** and SMP-B **(B)** showing changes in the storage modulus (top), loss modulus (center), and tan delta (bottom) after various aging times in PBS at 75°C, respectively.

0.3%. In addition to the weight loss study, the thickness of each polymer was monitored during the aging. **Figure 5B** indicates significant thickness loss (42.1 ± 1.7%) for SMP-B over the course of the aging test, while SMP-A was stable.

Dynamic mechanical analysis (DMA) was performed to investigate the stability of thermomechanical properties of both SMPs after aging in NaOH (**Figure 6**). It can be seen that there are no changes in the profiles of the storage/loss moduli, and tan delta. We could not measure the thermomechanical properties of SMP-B after 4 weeks of aging in NaOH, since the polymers were already too degraded and the specimen were brittle and ruptured (see **Supplementary Figure 4** in SI). These findings are in line with the weight loss and thickness measurements, which also revealed drastic changes. Thermal gravimetric analysis (TGA) was performed in order to compare

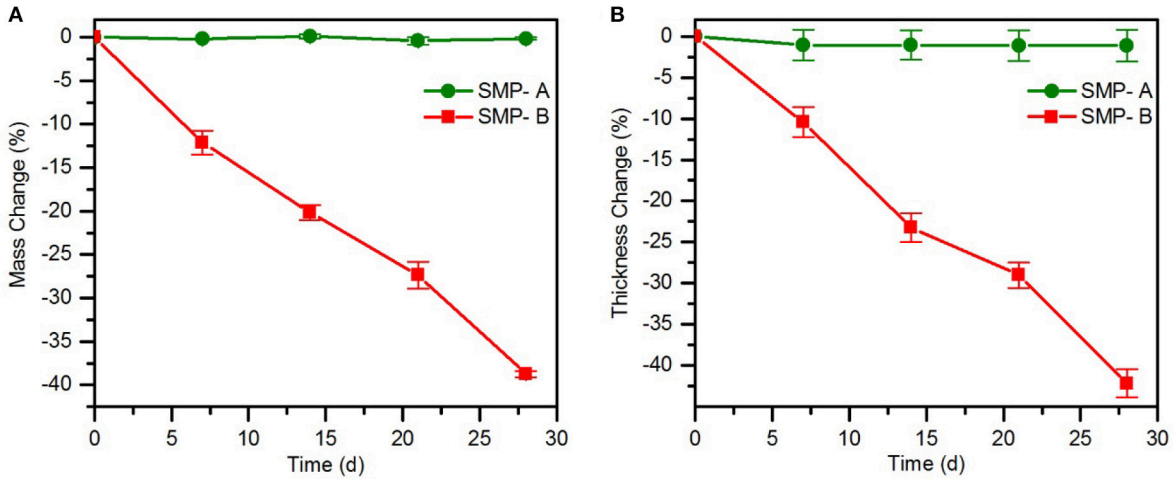

FIGURE 5 | (A) Mass change of SMP-A and SMP-B in 1 M NaOH with **(B)** corresponding thickness loss.

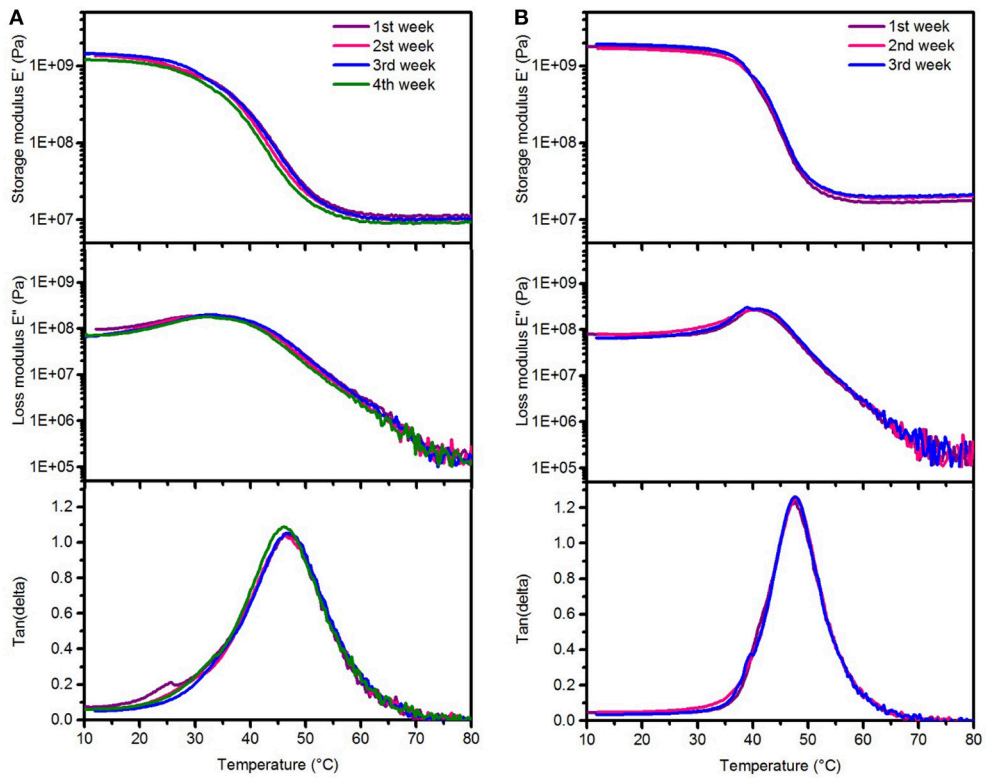

FIGURE 6 | Representative dynamic mechanical analysis after aging test in 1 M NaOH solution showing changes in the storage modulus (top), loss modulus (center), and tan delta (bottom) after various aging times at 37°C **(A)** SMP-A **(B)** SMP-B.

thermal stability of materials before and after the aging study in NaOH and PBS (**Figure 7**). It can be seen in **Figure 7A** that SMP-A (top) was not affected by the aging study in both media and degradation temperature and mass loss rate did not change. However, SMP-B (bottom) displays a slightly lower onset in the decomposition temperature after 4 weeks in NaOH (from 320 to 300°C) and even larger shift (from 320 to 250°C) after 8 weeks in PBS media. **Figure 7B** displays a more detailed view on the aging effects of 75°C PBS on SMP-B. The onset of the decomposition temperature shifts downward

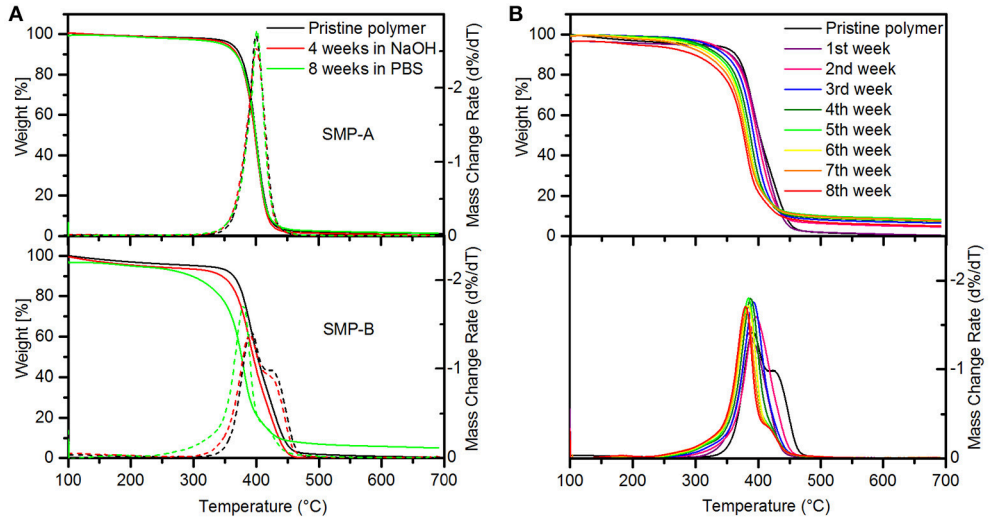

FIGURE 7 | Thermal gravimetric analysis of SMPs. **(A)** Showing weight loss and mass change rate of SMP-A (top) and SMP-B (bottom) after 4 weeks in 1 M NaOH solution at 37°C (red line) and 8 weeks in PBS at 75°C (green line). **(B)** Weight loss (top) and mass change rate (bottom) of SMP-B in PBS over 8 weeks.

about 8–10°C per week. In addition, the mass loss rate pattern changes over time, in detail the shoulder at higher temperature diminishes.

Cytotoxicity Test

To evaluate the cytotoxicity of SMP-A *in vitro*, we carried out live/dead assays based on material extract treatments in accordance with ISO protocol 10993-5. After fibroblasts were incubated for 24 h in the material extract, cell viability percentages were calculated and normalized to the negative control (**Figure 8**). SMP A at 50 and 100% concentrations had normalized viability percentages of 97.8 ± 0.8% (mean ± SEM, $n = 6$) and 93.6 ± 1% (mean ± SEM, $n = 6$), respectively. The positive control had a significantly lower viability percentage of 21.8 ± 4.7% (mean ± SEM, $n = 6$) (**Figure 8B**). Normalized viability percentages for SMP A at both 50 and 100% concentrations were both above the 70% threshold and deemed non-cytotoxic in accordance with ISO protocol 10993-5.(ISO, 2008) The *in vitro* cytotoxicity of SMP-B was evaluated in a different study (Black et al., 2018) and is therefore not shown detailed herein. The other study revealed that SMP-B (which was named FS SMP in the other study) had normalized viability percentages of 99.1 ± 0.7 % in the case of NCTC fibroblasts.

DISCUSSION

The focus of this study was to compare the stability of two types of SMPs that are applicable for flexible bioelectronic devices. Finding the appropriate substrate for the use in self-softening bioelectronic devices requires an understanding of the chemical structure and composition of the monomers for fine-tuning of the glass transition temperature of the final polymer. Glass transition (T_g) is critical to designing polymeric substrates for softening bioelectronic devices, since the T_g must be higher than body temperature prior to insertion for easy handling. After insertion however, a T_g higher than body temperature may cause an inflammatory response because the polymer is still in its glassy (stiff) state. Both SMP-A and SMP-B were synthesized utilizing a thiol-click polymerization mechanism and the glass transitions were tuned to be between 42 and 46°C in dry conditions and around 34°C when immersed in PBS. The mechanical properties of the SMPs change in the aqueous environments due to the plasticization effect of water molecules on polymer films. The storage modulus E' decreased significantly after 25 and 10 min immersion in PBS at 37°C, for SMP-A and SMP-B, respectively. Therefore, the glass transition in dry condition is high enough for handling during insertion and low enough to minimize an inflammatory response under physiological conditions. After finding the proper composition for both SMPs, the polymers were evaluated for long-term stability in two different media; PBS to mimic the aqueous environment *in vivo* at elevated temperature (75°C) and a harsher alkaline solution (NaOH) at 37°C. Afterward, the weight loss and thermomechanical properties of the SMPs were investigated.

The weight loss and thickness loss data of polymers in PBS (**Figure 3**) indicates that SMP-B is stable until the fourth week but thereafter begins to continually lose weight and thickness up to 15 and 10%, respectively. According to equation 1, aging test at 75°C for 1 week is equivalent to 14 weeks at body temperature. Therefore, SMP-B is expected to start to degrade after about 56 weeks (14 months) under physiological conditions. While this time span might be long enough for many chronic and sub-chronic studies on animals, which usually last 3 months to a year, it would not be sufficient for long-term chronic applications, which may take several years to decades. In contrast, SMP-A data shows that ester-free polymers are stable under these conditions until the end of this study, which was 8 weeks (projected to ∼26 months under physiological conditions) without any signs of

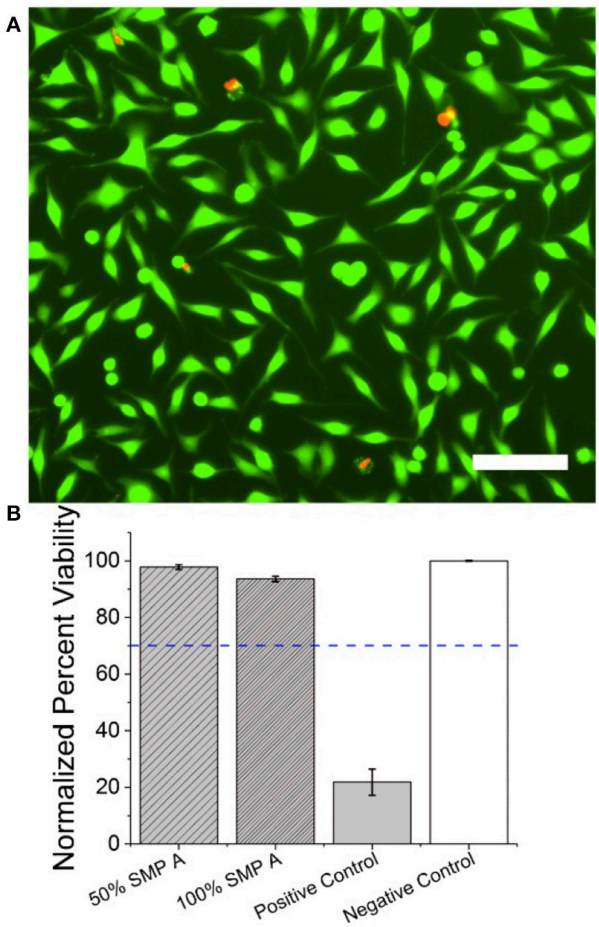

FIGURE 8 | SMP-A Cytotoxicity assays using NCTC fibroblasts (A) Fluorescent image of NCTC fibroblasts stained with CaAM (green) and EthD-1 (red). Green cells represent live cells while red cells represent apoptotic cells. Scale bar represents 100 μ m (B) Mean normalized cell viability percentage of SMP A at 50 and 100% concentrations, positive control, and negative control. Blue dotted line represents the 70% threshold based on ISO protocols (ISO, 2008) needed to pass for non-cytotoxic materials.

degradation. Harsh conditions (1 M NaOH) were used to further accelerate aging, which will be discussed later.

DMA data (**Figure 4**) reveals that the glass transition temperature of both polymers shifts to a higher temperature with increasing aging time, which is indicated by shifted loss modulus and tan delta peaks. In order to investigate whether this effect is due to the PBS or due to the relatively high temperature (this effect was not seen upon aging on NaOH at 37°C), additional experiments were performed. We aged SMP-A samples in de-ionized (DI) water at 75°C for up to 3 weeks, respectively, before DMA measurements were conducted and compared to the aging study in PBS at the same temperature. DMA data (shown in SI, **Supplementary Figure 5**) revealed that the samples aged in water showed similar shifting in T_g, which shows that the elevated temperature causes annealing effects. We do not expect to see such effects at body temperature. In addition, the DMA data shows that after 4 weeks of aging test in PBS, the rubbery storage modulus started to decrease and tan delta got wider which means the SMP-B started to lose the crosslink density. Since accelerating aging test was performed at 75°C (above the glass transition of the polymer), the mobility of polymer chains and diffusion of water molecules were increased. Therefore, the water migration into the polymer was faster than the reaction rate of the hydrolysis, which leads to bulk degradation (Lyu and Untereker, 2009). TGA data (**Figure 7B**) also confirms that at higher temperature water molecules can diffuse into the polymer structure and hydrolize ester functional groups. That causes a loss in the crosslink density of polymer. With that, the thermal stability of the polymer was reduced as shown by decreased decomposition temperatures. The diminishing shoulder at higher temperatures can be attributed to the fact that the polymer network got already broken down by hydrolysis. Fragments of the hydrolyzed TMICN and TMTMP monomers have already left the polymeric network and therefore do no longer contribute to the thermal decomposition profile of the polymer. To further investigate the degradation of the polymers, gas chromatography-mass spectroscopy (GS-MS) was applied on the PBS solution after aging. GC-MS data (shown in SI, **Supplementary Figure 7**) indicates that tris(hydroxymethyl)propane was released from SMP-B. In contrast, however, SMP-A did not reveal any degradation products in the PBS after aging. That confirms our assumption that the ester-containing SMP-B undergoes hydrolysis since tris(hydroxymethyl)propane is a fragment of the monomer TMTMP, which used for the synthesis of this polymer (**Supplementary Scheme 1**).

Figure 5 shows the weight loss and thickness loss of SMP-A and SMP-B in NaOH solution. According to the graphs, SMP-A, which does not contain ester groups, is completely stable and the weight and thickness did not change over the course of the aging study. On the other hand, ester-group containing SMP-B started to hydrolize which leads to a 38% and 42% decrease in weight and thickness, respectively after 4 weeks. It was seen that SMP-B had a maximum weight loss of 15% after 8 weeks in PBS at 75°C, which was approximately the same as for aging in NaOH for 9 days. Therefore, we assume that the aging in NaOH at 37°C is roughly six times faster than in PBS at 75°C. Based on the equation 1, 1 week in PBS at 75°C is equal to 14 weeks at 37°C. Taking both considerations into account, we estimate that 4 weeks degradation in NaOH at 37°C is equal to 24 weeks at 75°C. Therefore, it could be concluded that SMP-A is projected to be completely stable for at least 7 years under physiological conditions.

The DMA data of SMP-A and SMP-B after aging in NaOH (**Figure 6**) indicates that T_g, loss and storage moduli of SMP-A are completely conserved, while SMP-B degrades too rapidly for data collection after 4 weeks. All of the SMP-B samples tore apart during testing before obtaining a glass transition temperature (see **Supplementary Figure 4** in SI). Since salts and ions have low solubility in polymer chains, hydroxide ions did not diffuse into the polymer structure and hydrolysis took place on the surface (Lyu and Untereker, 2009). Therefore, erosion of the polymer occurred from the outside to the inside of the film. Another finding was, that in contrast to the aging in

PBS, the rubbery modulus of SMP-B did not decrease. That indicates that there are no changes in the polymeric network and the crosslink density. These findings support the hypothesis that aging in NaOH follows surface erosion rather than bulk degradation. We have also noticed, that the aging at 37°C was not affecting the T_g of the polymers, which indicates that no annealing took place at this temperature. Additionally, we have performed ATR-FTIR of polymers SMP-A and SMP-B before and after both aging scenarios (**Supplementary Figure 8** in SI). SMP-A shows as expected no changes in surface chemistries after both aging studies. SMP-B however has shown only minor changes after 4 weeks in NaOH, wheras it shows more distinct changes after aging for 8 weeks in PBS. It can be seen for example a broad peak appearing between 2,500 and 3,500 cm^{-1}, which can be assigned to the hydroxyl (OH) and carboxyl (OH) streching vibration signatures, which is due to hydrolized polymer fragments. These measurements support the bulk vs. surface erosion theory further. Even if ATR is a surface method, the penetration depth of the IR beam is between 0.5 and 5 μm into the bulk of the sample. Therefore, the bulk degraded sample (PBS aged) shows a higher number of degraded moieties per volume measured.

Thermogravimetric analysis graph (**Figure 7**) displays SMP data before and after aging in NaOH. **Figure 7A** indicates that SMP-A is completely stable, while for SMP-B the onset of decomposition shifts about 30–40°C toward lower temperatures after aging. In general, polymers with decomposition temperatures higher than ∼300°C are favorable for the fabrication of bioelectronic devices. The micro-fabrication of such devices uses processes such as photolithography, metal deposition, reactive ion etching, and chemical etching.

It should be noted that long term implants are not only subjected to hydrolytic degradation in an *in vivo* environment. Takmakov et al. (2015) pointed out that hydrolytic degradation alone may not adequately capture the aggressive chemical environment that is created by activated immune cells, which release digestive enzymes and reactive oxygen species (ROS). They have developed an *in vitro* system to simulate degradation of neural implants that can occur in a stressful environment by using hydrogen peroxide to mimic the effect of ROS generation during the brain's injury response. While this presents an important part of real live conditions, the focus of the present study is on the hydrolytic degradation only, because we wanted to demonstrate the improved durability of the ester free SMP-A against the ester containing SMP-B. In future studies however, we will perform experiments to evaluate the durability of thiol-ene and thiol-ene/acrylate formulations against oxidative species such as hydrogen peroxide. We do not expect to see any differences between ester containing and ester free versions because the ester groups are reported in literature to be not susceptible for oxidation (Lyu and Untereker, 2009). The sulfide groups however, may undergo oxidation to sulfoxides and sulfones using 30% aqueous hydrogen peroxide (Jeyakumar and Chand, 2006; Gregori et al., 2008).

The ultimate goal is to utilize the hydrolytically stable SMP-A as a substrate for neural interfaces and therefore have an alternative to the currently used softeing SMP versions (Simon et al., 2017; Garcia-Sandoval et al., 2018). To validate that the polymer is compatible with microfabrication processes, SMP-A was spin-coated on silicon wafers and subjected to photolithography as previously decribed (Ecker et al., 2017). Briefly, the polymer was covered by a silicon nitride (SiN) hard mask before it was coated with positive photoresist. Afterward, a photomask was used to pattern the pacifier probe through the photoresist by exposure to UV light. Next, the probe was subjected to dry etch with SF_6 to remove unpatterned hard mask. Subsequently, oxygen plasma was applied to remove excess polymer and patterned photoresist. Finally, the sample was etched with hydrofluoric acid to remove SiN that was on the SMP (Garcia-Sandoval et al., 2018). The micro-fabricated pacifier probes were also used for the *in vitro* cytotoxicity test.

Another important aspect is that materials for biomedical applications should be biocompatible and sterilizable. The materials need to be able to show a desirable performance with respect to a specific medical treatment, without any unwanted effects on the tissues (Johnson and Shiraishi, 2014; Huang et al., 2017). One of the tests for evaluating prospective biocompatibility of biomedical devices before clinical survey is *in vitro* cytotoxicity (Johnson and Shiraishi, 2014). To investigate the potential toxicity without affecting the mechanical or chemical properties of the polymer, cytotoxicity tests were performed on pacifier probes by incubating fibroblasts with extract of SMP-A for 24 h. **Figure 8** confirms that the extract of the polymer at both concentrations is reliable and the polymer is expected to be safe for biomedical applications. We have seen, that SMP-B produces some water soluble byproducts after hydrolysis. These byproducts may undergo some deleterious reactions including oxidation *in vivo*. Therefore, the degraded polymer may not prove to be as biocompatible as the original polymer. Additional studies, such as functional neurotoxicity or cytotoxicity assays using primary cortical neurons, (Charkhkar et al., 2014) need to be performed to further investigate potential harm of degradation product. On the other hand, SMP-A sustained even in harsh conditions without any signs of degradation and therefore is less of a biocompatibility concern. Biomedical devices need to be sterilized properly for *in vivo* studies. To inquire the effect of sterilization on mechanical properties, SMP-A was subjected to sterilization with ethylene oxide (EtO) as previously described (Ecker et al., 2017). Since the sterilization with EtO was performed at a low temperature, it has negligible effects on the mechanical properties of SMPs. DMA data (shown in SI, **Supplementary Figure 6**) before and after sterilization shows that storage modulus and glass transition did not change remarkably.

CONCLUSION

Ester free (SMP-A) and ester containing (SMP-B) polymers with comparable thermomechanical properties and softening capabilities were prepared and their stability *in vitro* was evaluated. Accelerated aging tests were performed on both polymers and their stability was compared. According to the test

results, ester free polymers are projected to be stable for at least 7 years in the biological environment, whereas the ester containing polymer should be stable for approximately 1 year. Therefore, the new ester-free polymer (SMP-A) is a good candidate for future devices. It was stable under the tested conditions and is therefore much more reliable and robust than SMP-B, but still biocompatible. Furthermore, fabrication of pacifier probes demonstrated that SMP-A was stable in cleanroom processes and conserved its mechanical properties. Next steps will include the fabrication of fully functional neural interfaces and their testing *in vitro* as well as *in vivo*.

AUTHOR CONTRIBUTIONS

SH and ME: Conceptualization; SH, RR, BB, and AS: Methodology; SH, RR, BB, and ME: Formal Analysis; SH, RR, and BB: Data Curation; SH and ME: Writing–Original Draft Preparation; SH and ME: Writing–Review and Editing; SH, RR, and BB: Visualization; ME: Supervision; ME: Project Administration; WV and JP: Resources; JP and WV: Funding Acquisition; All authors approved the final version to be published and agreed to be accountable for all aspects of the work.

ACKNOWLEDGMENTS

This work was supported by the Center for Engineering Innovation and in parts by the Office of the Assistant Secretary of Defense for Health Affairs through the Peer Reviewed Medical Research Program under Award No. W81XWH-15-1-0607. Opinions, interpretations, conclusions and recommendations are those of the authors and are not necessarily endorsed by the Department of Defense. Additionally, the contents do not represent the views of the U.S. Department of Veterans Affairs or the United States Government. The authors want to thank Dr. Taylor Ware for allowing us to use the environmental DMA.

SUPPLEMENTARY MATERIAL

The Supplementary Material for this article can be found online at: https://www.frontiersin.org/articles/10.3389/fmats.2018.00066/full#supplementary-material

REFERENCES

ASTM (2018). *Standard Guide for Accelerated Aging of Sterile Barrier Systems for Medical Devices*. ASTM F1980–07.

Baer, G., Wilson, T. S., Matthews, D. L., Maitland, D. (2007). Shape-memory behavior of thermally stimulated polyurethane for medical applications. *J. Appl. Polym. Sci.* 103, 3882–3892. doi: 10.1002/app.25567

Barrett, R., Francis, W., Abrahamson, E., Lake, M. S., and Scherbarth, M. (2006). "Qualification of elastic memory composite hinges for spaceflight applications," in *47th AIAA/ASME/ASCE/AHS/ASC Structures, Structural Dynamics, and Materials Conference* (Newport, RI). doi: 10.2514/6.2006-2039

Baudis, S., Behl, M., and Lendlein, A. (2014). Smart polymers for biomedical applications. *Macromol. Chem. Phys.* 215, 2399–2402. doi: 10.1002/macp.201400561

Black, B. J., Ecker, M., Stiller, A., Rihani, R., Danda, V. R., Reed I., et al. (2018). *In vitro* compatibility testing of thiol-ene/acrylate-based shape memory polymers for use in implantable neural interfaces. *J. Biomed. Mater. Res. A* doi: 10.1002/jbm.a.36478. [Epub ahead of print].

Buckley, P. R., McKinley, G. H., Wilson, T. S., Small, W., Benett W.J., Bearinger J.P., et al. (2006). Inductively heated shape memory polymer for the magnetic actuation of medical devices. *IEEE Transac. Biomed. Eng.* 53, 2075–2083. doi: 10.1109/TBME.2006.877113

Charkhkar, H., Frewin, C., Nezafati, M., Knaack, G. L., Peixoto, N., Saddow S. E., et al. (2014). Use of cortical neuronal networks for *in vitro* material biocompatibility testing. *Biosensors Bioelectron.* 53, 316–323. doi: 10.1016/j.bios.2013.10.002

Dietsch, B., and Tong, T. (2007). A review - Features and benefits of shape memory polymers (SMPs). *J. Adv. Mater.* 39, 3–12. Available online at: http://apps.webofknowledge.com/full_record.do?product=WOS&search_mode=GeneralSearch&qid=8&SID=8BSUhmnqWxNvZmIqxlx&page=1&doc=1

Do, D. H., Ecker, M., and Voit, W. E. (2017). Characterization of a Thiol-Ene/acrylate-based polymer for neuroprosthetic implants. *ACS Omega* 2, 4604–4611. doi: 10.1021/acsomega.7b00834

Ecker, M., Danda, V., Shoffstall, A. J., Mahmood, S. F., Joshi-Imre A., Frewin C. L., et al. (2017). Sterilization of Thiol-ene/Acrylate based shape memory polymers for biomedical applications. *Macromol. Mater. Eng.* 302:1600331. doi: 10.1002/mame.201600331

Ecker, M., and Pretsch, T. (2013). Durability of switchable QR code carriers under hydrolytic and photolytic conditions. *Smart Mater. Struct.* 22:094005. doi: 10.1088/0964-1726/22/9/094005

Ecker, M., and Pretsch, T. (2014a). Multifunctional poly(ester urethane) laminates with encoded information. *RSC Adv.* 4, 286–292. doi: 10.1039/C3RA45651J

Ecker, M., and Pretsch, T. (2014b). Novel design approaches for multifunctional information carriers. *RSC Adv.* 4, 46680–46688. doi: 10.1039/C4RA08977D

Feninat, F. E., Laroche, G., Fiset, M., and Mantovani, D. (2002). Shape Memory materials for biomedical applications. *Adv. Eng. Mater.* 4, 91–104. doi: 10.1002/1527-2648(200203)4:3<91::AID-ADEM91>3.0.CO;2-B

Garcia-Sandoval, A., Pal, A., Mishra, A. M., Sherman, S., Parikh, A., Joshi-Imre A., et al. (2018). Chronic softening spinal cord stimulation arrays. *J. Neural Eng.* 15:045002. doi: 10.1088/1741-2552/aab90d

Gregori, F., Nobili, I., Bigi, F., Maggi, R., Predieri, G., and Sartori, G. (2008). Selective oxidation of sulfides to sulfoxides and sulfones using 30% aqueous hydrogen peroxide and silica-vanadia catalyst. *J. Mol. Catal. A Chem.* 286, 124–7. doi: 10.1016/j.molcata.2008.02.004

Hager, M. D., Bode, S., Weber, C., and Schubert, U. S. (2015). Shape memory polymers: past, present and future developments. *Prog. Polym. Sci.* 49–50, 3–33. doi: 10.1016/j.progpolymsci.2015.04.002

Hemmerich, K. J. (1998). General aging theory and simplified protocol for accelerated aging of medical devices. *Medi. Plastic Biomater.* 5, 16–23.

Hu, J., and Chen, S. (2010). A review of actively moving polymers in textile applications. *J. Mater. Chem.* 20, 3346–3355. doi: 10.1039/b922872a

Hu, J., Meng, H., Li, G., and Ibekwe, S. I. (2012a). A review of stimuli-responsive polymers for smart textile applications. *Smart Mater. Struct.* 21:053001. doi: 10.1088/0964-1726/21/5/053001

Hu, J., Zhu, Y., Huang, H., and Lu, J. (2012b). Recent advances in shape memory polymers: structure, mechanism, functionality, modeling and applications. *Prog. Polym. Sci.* 37, 1720–1763. doi: 10.1016/j.progpolymsci.2012.06.001

Huang, Y., Zhou, J., Hakamivala, A., Wu, J., Hong, Y., Borrelli, J., et al. (2017). An optical probe for detecting chondrocyte apoptosis in response to mechanical injury. *Sci. Rep.* 7:10906. doi: 10.1038/s41598-017-10653-y

Immergut, E. H., and Mark, H. F. (1965). Principles of plasticization. plasticization and plasticizer processes. *Am. Chem. Soc.* 48, 1–26. doi: 10.1021/ba-1965-0048.ch001

Ishizawa, J., Imagawa, K., Minami, S., Hayashi, S., and Miwa, N. (2003). "Research on Application of Shape Memory Polymers to Space Inflatable Systems," in

Proceeding of the 7th International Symposium on Artificial Intelligence, Robotics and Automation in Space: i-SAIRAS (Nara).

ISO (2008). *ISO 10993-5 Biological Valuation of Medical Devices, Part 5: Tests for in vitro Cytotoxicity*. Geneva: International Organization for Standardization.

Jeyakumar, K., and Chand, D. K. (2006). Selective oxidation of sulfides to sulfoxides and sulfones at room temperature using H_2O_2 and a Mo(VI) salt as catalyst. *Tetrahedron Lett.* 47, 4573–4576. doi: 10.1016/j.tetlet.2006.04.153

Johnson, A. and Shiraishi, T. (2014). "Biocompatibility of precious metals for medical applications," in *Precious Metals for Biomedical Applications*, eds N. Baltzer and T. Copponnex (Woodhead Publishing), 37–55. doi: 10.1533/9780857099051.1.37

Kulshrestha, A. S., and Mahapatro, A. (2008). Polymers for biomedical applications. *Polym. Biomed. Appl.* 977, 1–7. doi: 10.1021/bk-2008-0977.ch001

Lecomte, A., Degache, A., Descamps, E., Dahan, L., and Bergaud, C. (2017). *In vitro* and *in vivo* biostability assessment of chronically-implanted Parylene C neural sensors. *Sensors Actuators B Chemical* 251(Suppl. C):1001–8. doi: 10.1016/j.snb.2017.05.057

Lendlein, A. (2010). *Shape-Memory Polymers*. Berlin; Heidelberg: Springer.

Lendlein, A., and Behl, M. (2008). "Shape-memory polymers for biomedical applications," in *CIMTEC 2008 - Proceedings of the 3rd International Conference on Smart Materials, Structures and Systems - Smart Materials and Micro/Nanosystems* (Acireale), 96–102.

Liu, C., Qin, H., and Mather, P. T. (2007). Review of progress in shape-memory polymers. *J. Mater. Chem.* 17, 1543–1558. doi: 10.1039/b615954k

Lundberg, P., Bruin, A., Klijnstra, J. W., Nystrom, A. M., Johansson M., Malkoch M., et al. (2010). Poly(ethylene glycol)-based thiol-ene hydrogel coatings-curing chemistry, aqueous stability, and potential marine antifouling applications. *ACS Appl. Mater. Interfaces* 2, 903–912. doi: 10.1021/am900875g

Lyu, S., and Untereker, D. (2009). Degradability of polymers for implantable biomedical devices. *Int. J. Mol. Sci.* 10:4033. doi: 10.3390/ijms10094033

Mather, P. T., Luo, X., and Rousseau, I. A. (2009). Shape memory polymer research. *Annu. Rev. Mater. Res.* 39, 445–471. doi: 10.1146/annurev-matsci-082908-145419

Matilla, H. R. (2006). *Intelligent Textiles and Clothing*. Cambridge, UK: Woodhead Publishing in Textiles.

Pretsch, T., Ecker, M., Schildhauer, M., and Maskos, M. (2012). Switchable information carriers based on shape memory polymer. *J. Mater. Chem.* 22, 7757–7766. doi: 10.1039/c2jm16204k

Reit, R., Zamorano, D., Parker, S., Simon, D., Lund, B., Voit, W., et al. (2015). Hydrolytically stable thiol–ene networks for flexible bioelectronics. *ACS Appl. Mater. Interfaces* 7, 28673–28681. doi: 10.1021/acsami.5b10593

Rory Barrett, W. F., Erik, A., Mark Lake, S., and Mark, S. (2006). "Qualification of elastic memory composite hinges for spaceflight applications,"in *47nd IAA/ASME/ASCE/AHS/ASC SDM Conference*. (Newport, RI: AIAA-2006-2039).

Rubehn, B., and Stieglitz, T. (2010). In vitro evaluation of the long-term stability of polyimide as a material for neural implants. *Biomaterials* 31, 3449–3458. doi: 10.1016/j.biomaterials.2010.01.053

Ryu, S. I., and Shenoy, K. V. (2009). Human cortical prostheses: lost in translation? *Neurosurg. Focus* 27:E5. doi: 10.3171/2009.4.FOCUS0987

Shoffstall, A. J., Srinivasan, S., Willis, M., Stiller, A. M., Ecker, M., Voit W. E., et al. (2018). A mosquito inspired strategy to implant microprobes into the brain. *Sci. Rep.* 8:122. doi: 10.1038/s41598-017-18522-4

Simon, D. M., Charkhkar, H. C., St John, Rajendran, S., Kang, T., Reit, R., et al. (2017). Design and demonstration of an intracortical probe technology with tunable modulus. *J. Biomed. Mater. Res. A* 105, 159–168. doi: 10.1002/jbm.a.35896

Singhal, P., Boyle, A., Brooks, M. L., Infanger, S., Letts, S., Small W., et al. (2013). Controlling the actuation rate of low-density shape-memory polymer foams in water. *Macromol. Chem. Phys.* 214, 1204–1214. doi: 10.1002/macp.201200342

Takmakov, P., Ruda, K., Scott Phillips, K., Isayeva, I. S., Krauthamer, V., and Welle C. G., (2015). Rapid evaluation of the durability of cortical neural implants using accelerated aging with reactive oxygen species. *J. Neural Eng.* 12:026003. doi: 10.1088/1741-2560/12/2/026003

Teo, A. J. T., Mishra, A., Park, I., Kim, J., Park, T., and, Yoon, J. (2016). Polymeric biomaterials for medical implants and devices. *ACS Biomater. Sci. Eng.* 2, 454–472. doi: 10.1021/acsbiomaterials.5b00429

Wang, K., Strandman, S., and Zhu, X. X. (2017). A mini review: shape memory polymers for biomedical applications. *Front. Chem. Sci. Eng.* 11, 143–153. doi: 10.1007/s11705-017-1632-4

Ware, T., Simon, D., Hearon, K., Kang, T. H., Maitland, D., et al. (2013). Thiol-click chemistries for responsive neural interfaces. *Macromol. Biosci.* 13, 1640–1647. doi: 10.1002/mabi.201300272

Ware, T., Simon, D., Liu, C., Musa, T., Vasudevan, S., Sloan, A., et al. (2014). Thiol-ene/acrylate substrates for softening intracortical electrodes. *J. Biomed. Mater. Res. B Appl. Biomater.* 102, 1–11. doi: 10.1002/jbmb.32946

Yanju, L., Haiyang, D., Liwu, L., and Jinsong, L. (2014). Shape memory polymers and their composites in aerospace applications: a review. *Smart Mater. Struct.* 23:23001. doi: 10.1088/0964-1726/23/2/023001

Yanju, L., and Jinsong, L. (2010). "Applications of shape-memory polymers in aerospace," in *Shape-Memory Polymers and Multifunctional Composites*, eds J. Leng and S. Du (Boca Raton, FL: CRC Press), 233–266. doi: 10.1201/9781420090208-c8

Conflict of Interest Statement: The authors declare that the research was conducted in the absence of any commercial or financial relationships that could be construed as a potential conflict of interest.

Sterilization of Thiol-ene/Acrylate Based Shape Memory Polymers for Biomedical Applications

Melanie Ecker,* Vindhya Danda, Andrew J. Shoffstall, Samsuddin F. Mahmood, Alexandra Joshi-Imre, Christopher L. Frewin, Taylor H. Ware, Jeffrey R. Capadona, Joseph J. Pancrazio, Walter E. Voit*

A fundamental study on the sterilization of thiol-ene/acrylate polymers for biomedical applications is presented. These polymer networks belong to the emerging field of shape memory polymers and have the capability to undergo softening after insertion into the body. The impact of various sterilization methods, such as radiation, steam, and ethylene oxide on the thermomechanical properties of these stimuli responsive materials is investigated. Time and temperature dependent thermomechanical properties of sterilized and nonsterilized samples are determined by means of dynamic mechanical analysis in an aqueous environment to allow testing of polymers in phosphate buffered saline. The findings show that ethylene oxide sterilization is appropriate for thiol-ene and thiol-ene/acrylate based shape memory polymers. This method does not adversely affect thermomechanical and self-softening properties and after sterilization, endotoxin levels remain below the thresholds recommended in the FDA Guidance.

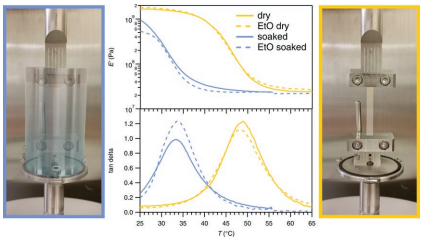

Dr. M. Ecker, V. Danda, Dr. A. Joshi-Imre, Prof. W. E. Voit
Department of Materials Science and Engineering
The University of Texas at Dallas
800 W. Campbell Rd., Richardson, TX 75080, USA
E-mail: melanie.ecker@utdallas.edu; walter.voit@utdallas.edu
V. Danda, Dr. C. L. Frewin, Prof. T. H. Ware, Prof. J. J. Pancrazio, Prof. W. E. Voit
Department of Bioengineering
The University of Texas at Dallas
800 W. Campbell Rd., Richardson, TX 75080, USA
Dr. A. J. Shoffstall, Prof. J. R. Capadona
Department of Biomedical Engineering
Case Western Reserve University
2071 Martin Luther King Jr. Drive, Cleveland, OH 44106, USA
Dr. A. J. Shoffstall, Prof. J. R. Capadona
Advanced Platform Technology Center
Louis Stokes Cleveland Department of Veterans Affairs Medical Center, 10701 East Blvd, 151 W/APT, Cleveland OH 44106-1702, USA
Dr. S. F. Mahmood, Prof. W. E. Voit
Department of Chemistry and Biochemistry
The University of Texas at Dallas
800 W. Campbell Rd., Richardson, TX 75080, USA

1. Introduction

Polymers and polymer-composites are increasingly used for in vivo biomedical applications and have become an indispensable part of modern medicine.[1] This is attributed to their versatility: polymers can be designed and prepared with a wide variety of structures with customized physical, chemical, and surface properties. Applications include, but are not limited to, polymeric therapeutics and diagnostics, dental implants, catheters, joint replacements, ligaments, vascular grafts, and heart valves.[2]

Polymer classes used for biomedical applications include biodegradable polymers,[3] polymeric micelles and vesicles,[4] nanoparticles,[5] hydrogels,[6] and dendrimers.[7] Recently, shape memory polymers (SMPs) have been under extensive investigation for their use for biomedical applications.[8]

In general, SMPs are stimuli responsive materials.[9] They have the capability to change their shape in response to certain external stimuli, such as temperature, electricity, magnetic fields, pH, or moisture. Beyond that,

DOI: 10.1002/mame.201600331

their phase (and thus, their shape) transition temperature can be shifted in response to plasticizing effects of solvents, including water, resulting in a lower modulus at a given temperature. With regard to biomedical applications, current studies focus on surgical and implantable devices for therapeutics and diagnosis, such as self-expanding stents,[10] intelligent sutures,[11] active catheters,[12] and microscale neural interfaces.[13] In fact, our group focuses on the development and demonstration of self-softening devices for recording and stimulation of neural systems, taking advantage of the thermomechanical properties of SMPs.[14] The principle of these devices is that they are rigid (glassy) during insertion but become elastic (rubbery) during use to minimize the modulus differential between neural tissue and the device that has been associated with neuroinflammation.[15]

Medical devices undergo sterilization to be used in clinical environments in order to remove various microorganisms.[16] Established methods, which are listed in the FDA Guidance[17] include steam, ethylene oxide (EtO), and radiation.[16,18] However, these techniques may influence the material properties of the polymers significantly. Therefore, it is important to study the physical impact of the sterilization methods on medical devices,[19] especially on heat sensitive materials such as SMPs, which may alter their thermomechanical properties.[20] Hence, it is no surprise that in 2014, Wong et al. raised significant concerns about the biomedical practicality of SMPs, given the uncertainties related to sterilization.[21]

In this paper, we examine the effects of sterilization on the thermomechanical properties of neural probe test structures comprised of SMP. We verify sterilization efficacy by performing chromogenic residual endotoxin assays with samples composed of SMP formulations. Our findings indicate that SMPs composed of thiol-ene and thiol-ene/acrylates are sensitive to various sterilization approaches, where shifts in transition temperature and modulus are evident. We show that with the use of a mild plasma etch prior to steam and EtO sterilization, the SMP based test devices exhibit homogenous mechanical behavior that is consistent with well-defined polymer network structures. The overall procedure does not affect the functionality of the SMPs, such that the test devices still undergo controlled softening after immersion in aqueous solution.

2. Results

2.1. Fabrication of SMP Test Devices

To create SMPs which could undergo different degrees of softening, we prepared thiol-ene (SMP-FS, fully softening) and thiol-ene/acrylate (SMP-SS, slightly softening) polymers with stoichiometric thiol to ene contents using photoinitiated thiol-ene click chemistry (Scheme 1).[22] In order to mimic the conditions actual devices would undergo, both SMP substrates were photolithographically defined using cleanroom processing methods such as nitride deposition, plasma, and hydrofluoric acid (HF) etch to receive rectangular specimens having dimensions of 4.5 mm × 50 mm × 30 μm. Some of the samples were subjected to an additional oxygen plasma etching step before they were singulated. This removed ≈4 μm of the top surface but was accompanied by the nontransparent, milky appearance of the samples due to light scattering at the roughened surface.

In contrast to prior studies, where cast samples with thicknesses in the mm range were used for thermomechanical investigations due to a limitation of traditional techniques in their ability to measure thin films,[14a,c] we herein prepared spin coated samples in the μm thickness range, which is the thickness of devices used for in vivo studies. Unexpectedly, the thermal and mechanical

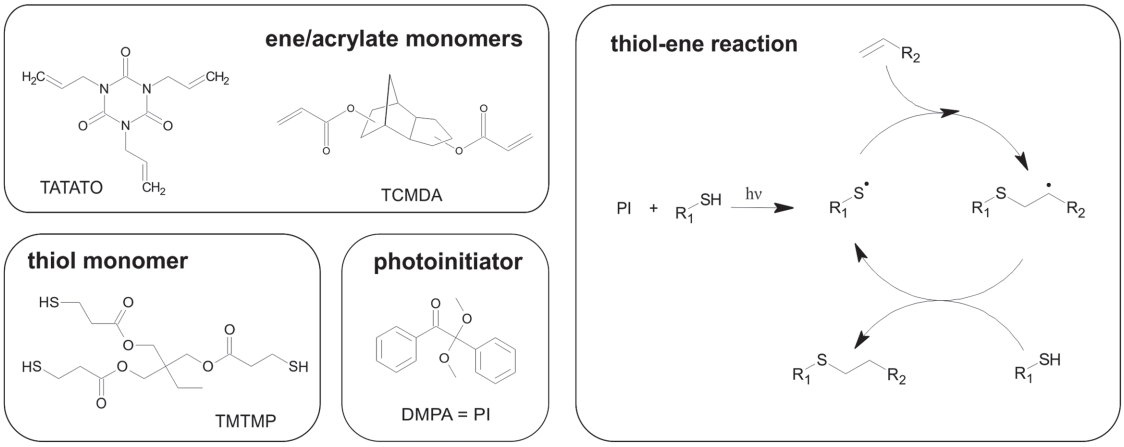

Scheme 1. Chemical structures of monomers used for the different polymer compositions and the used photoinitiator (left) and scheme of thiol-ene reaction (right).

properties were strongly dependent on the preparation method. The T_g of cast samples was significantly lower than spin coated samples having the same monomer composition. This might be explained by different curing scenarios: namely, the cast samples were covered by a glass slide which absorbs a part of the UV radiation and thus leads to lower energy transfer to the polymer solution including the photoinitiator compared to the spin cast samples which were uncovered. In addition, the exposure of the polymer solution to oxygen as part of the atmosphere in case of the spin cast samples might influence the cross-linking behavior as well. It is known, that oxygen can inhibit the cross-link reaction of acrylates.[23] In case of the thiol-ene reaction, oxygen is not acting as inhibitor, but however can be incorporated into side chains of the polymer network through a well-described mechanism.[24] In order to eliminate possible effects caused by oxygen, some samples were cured under varied curing scenarios, namely irradiation under 254 nm for 2 h under nitrogen and argon atmosphere instead of air. The thermomechanical properties of SMP-FS after the different curing scenarios are shown in Figure 1. The properties did not significantly differ from each other after curing under varied atmospheres, indicating that the presence of oxygen during the curing did not influence the bulk thermomechanical properties of thick polymer networks. However, a removal of the top 4 μm from the top surface by an oxygen plasma etch changed the polymer properties noticeably. The drop in modulus was more pronounced and the glass transition region was narrower, which is representative of more homogenous networks as prior to etching. This surface treatment was used prior to all following sterilization procedures in order to assure consistent conditions.

In addition, the differences in surface chemistries before and after etching were investigated by means of attenuated total reflectance Fourier transform infrared spectroscopy (ATR-FTIR) (shown in Figure S1, Supporting Information). The oxygen plasma etching resulted in an increased absorbance from 3580 to 3060 cm^{-1}, which is attributed to hydroxyl groups. Beyond that, the peaks at 2961, 2926, and 2854 cm^{-1}, which are attributed to asymmetrical and symmetrical CH stretching vibration of CH_3 and CH_2 groups, increased noticeably. The rest of the spectra showed no significant changes. This observation indicates that the oxygen plasma etching causes changes in the number of the alkyl and hydroxyl groups within the polymer surface, possibly through bond breaking, formation of radicals, and reformation of new bonds.[25]

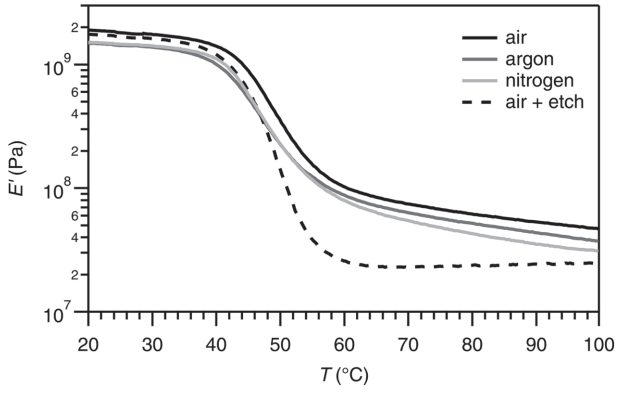

Figure 1. DMA measurements of SMP-FS samples after curing in different atmospheres, namely air, argon, and nitrogen. The dashed graph shows the storage modulus E' of a sample cured under air, but with postetching of the first 4 μm.

2.2. Sterilization of SMP Test Devices

Surface etched SMP samples were subjected to different sterilization methods. All specimens were mounted in a manner that they were hanging downward and were free floating (not attaching any surface) in order to prevent them from bending or twisting. The impact of sterilization on thermomechanical properties appeared to depend on the sterilization method rather than on the polymer composition. For example, SMP-FS and SMP-SS showed similar shifts in T_g after EtO exposure (Figure 2). In addition, the surface properties of the SMP samples were investigated by means of ATR-FTIR spectroscopy to see if there are any changes caused by the sterilization procedures (Figure 3). The IR spectra of both investigated SMP networks showed only minor changes in the peak intensities after the applied sterilization methods. This suggests that sterilization does not alter the chemical properties of the SMP materials.

2.2.1. UV Sterilization

After 120 min of UV irradiation at 254 nm, the glass transition region was less narrow than for neat samples (Figure 2). At the same time, the characteristics of the drop in storage modulus E' when passing the glass transition region changes drastically where the curve shows a twofold transition. The initial modulus change was similar to neat samples, but after 8–10 °C the slope changed to a smaller value. In the tan δ curves of the UV sterilized samples, there was also a second, less distinct but broad peak/plateau visible. In case of the SMP-FS, the second T_g was found around 68 °C, in case of the SMP-SS the tan δ curve remained at a plateau after the T_g peak. However, the main T_g remained almost unaffected at the same temperature.

These findings indicate that the resulting polymer network within the sample is inhomogeneous. In order to verify whether this behavior was due to any plasticizing effects caused by the ethanol dip prior to UV exposure, we also investigated the material properties for UV treatment only. The effects appeared to not be related to the ethanol dip, since the modulus followed the same characteristics

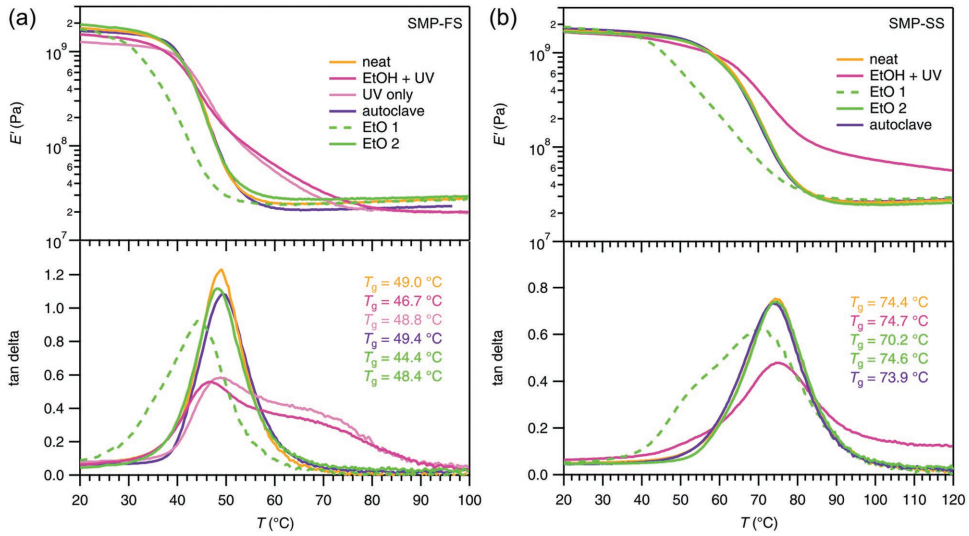

Figure 2. DMA measurements of the a) SMP-FS and b) SMP-SS samples after surface etch followed by various sterilization methods. Top shows the storage modulus *E′*, the bottom the tan *δ*, respectively.

in both cases. However, a removal of the top 4 µm from the UV exposed surface by an additional oxygen plasma etch changed the overall materials properties back to a uniform glass transition (not shown herein). This observation suggests that the bulk properties remained unaffected while the surface properties were changed by the intense UV irradiation.

2.2.2. Autoclave

The thermomechanical properties of the different polymer compositions were not affected by the autoclave sterilization, which includes exposure to steam at 121 °C followed by a drying cycle. The temperature dependent storage modulus *E′* did not show any significant differences after treatment with steam and pressure as visible by almost congruent dynamic mechanic analysis (DMA) curves (Figure 2). Beyond that, no shift in T_g was evident, indicating that the SMPs are stable with respect to their network structures and hence with their thermomechanical properties as well.

2.2.3. Ethylene Oxide

When measuring DMA of SMP samples shortly after sterilization with EtO gas, the glass transition region broadened and T_g shifted 5–7 °C toward lower temperatures (dashed green lines in Figure 2). The storage modulus *E′* of both SMPs remained the same in the glassy state (at temperatures below the T_g) as well as in the rubbery regime (at temperatures above T_g) post sterilization. However, when repeating the same DMA measurements on samples sterilized at least 7 d prior to measurement on the DMA, the T_g shifted back to the value of nonsterilized samples (solid green lines in Figure 2). This observation suggests that EtO gas has a reversible plasticizing effect on the polymer, and that the exposed SMP samples need a longer aeration phase for removal of EtO gas as compared to other materials. The degassing time could be reduced to 3 d by keeping the samples under low vacuum (0.62 bar). It might be possible that the degassing time could be reduced even further by simultaneously increasing the temperature.

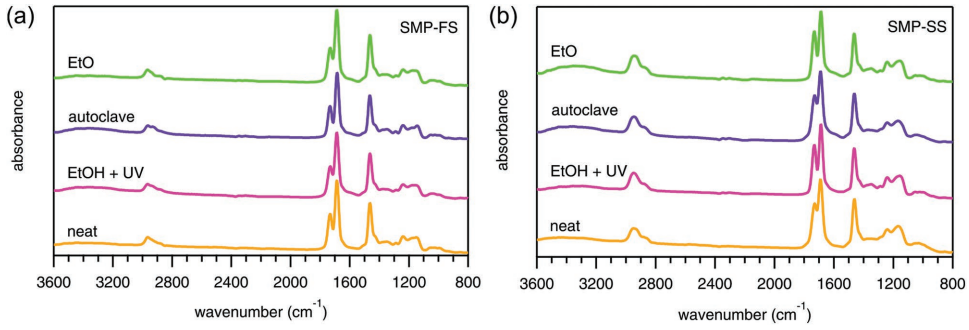

Figure 3. Normalized ATR-FTIR spectra of surface etched a) SMP-FS and b) SMP-SS samples after various sterilization methods.

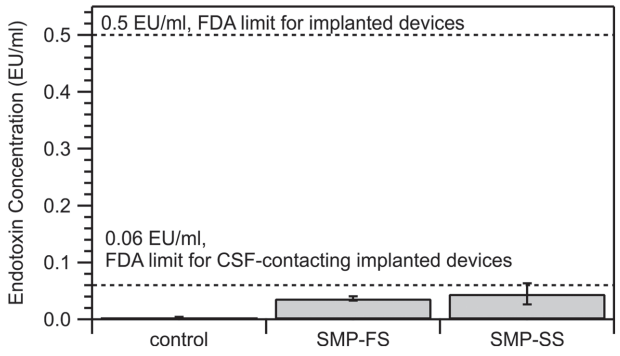

Figure 4. Results of endotoxin testing for SMP-FS and SMP-SS samples after sterilization with EtO. Control sample is certified endotoxin-free water exposed to the incubation period, handling, and preparation as the test devices. Thresholds of acceptable endotoxin concentration (EU mL^{-1}) limits, as set forth by FDA Guidance for Industry for implantable devices, are indicated by horizontally dashed lines.

In order to further investigate this phenomenon, we performed ATR-FTIR measurements on samples before and after EtO sterilization. We observed only minor changes in the surface chemistry of the SMP (Figure 3). The broad peak at 3580–3060 cm^{-1} was slightly increasing, indicating the incorporation of hydroxyl groups. Since the ATR-FTIR measures only surface effects, we also extracted the remaining EtO from sterilized SMP-FS samples in acetone after different degassing times and performed ^{1}H-NMR spectroscopy (shown in Figure S2, Supporting Information). Directly after the sterilization, a peak at 2.6 ppm was evident. This peak diminished significantly after additional degassing time.

2.3. Endotoxin Measurements of Sterilized Test Devices

Endotoxin tests were performed on SMP-FS and SMP-SS test devices that were sterilized by EtO using a 24 h cycle, followed by 15 d of outgassing under standard ambient temperature and pressure. Both samples showed minimal endotoxin contamination, achieving levels below the threshold suggested in the FDA Guidance for Industry for cerebrospinal fluid (CSF)-contacting implanted devices (0.06 EU mL^{-1}, Figure 4).[26] In particular, the samples revealed values of 0.037 (SMP-FS) and 0.045 EU mL^{-1} (SMP-SS), respectively.

2.4. Soaking of Neat and Sterilized SMP Test Devices in Phosphate Buffered Saline (PBS)

We investigated the soaking behavior of the different SMP compositions before and after sterilization. DMA measurements were performed using the RSA-G2 with Immersion System (Figure 5).

The specimens were clamped, the PBS added, and the measurement was started immediately. The first step consisted of rapid heating from room temperature to

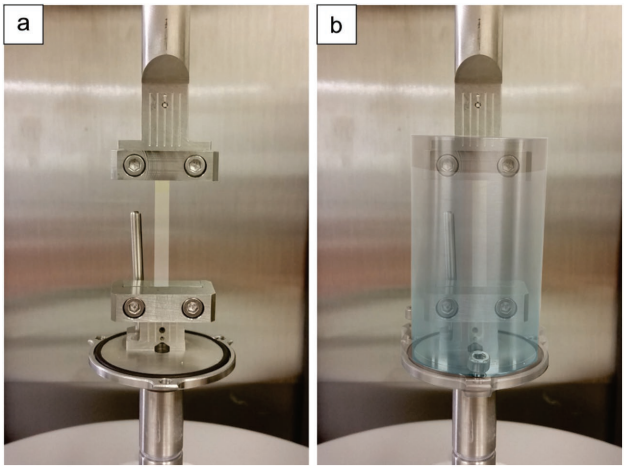

Figure 5. Setup for a) dry and b) immersed DMA measurements.

37 °C followed by isothermal soaking of the polymer films (Figure 6). The second step included cooling from 37 to 20 °C followed by application of a heating ramp from 20 to 70 °C while still immersed in PBS (Figure 7). As expected, the aqueous environment altered the mechanical properties of the SMP. For both compositions, the storage modulus *E′* dropped noticeably after 10–20 min immersion in PBS at 37 °C, for the fully softening SMP more pronounced than for the slightly softening SMP (Figure 6). After the initial drop, the modulus remained at a constant plateau for the remaining soaking interval. The behavior before and after sterilization with EtO was

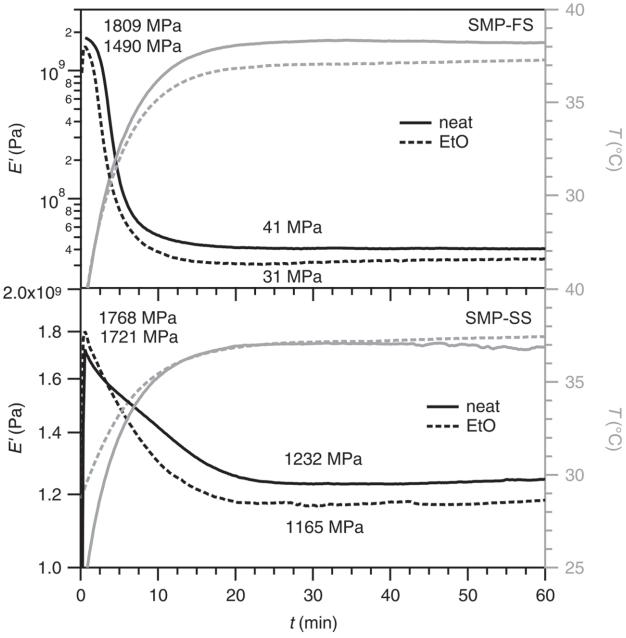

Figure 6. DMA measurements of surface-etched SMP-FS (top) and SMP-SS (bottom) before and after EtO sterilization. Shown are the storage modulus *E′* (black) and the respective temperature (grey) during soaking in PBS over the immersion time.

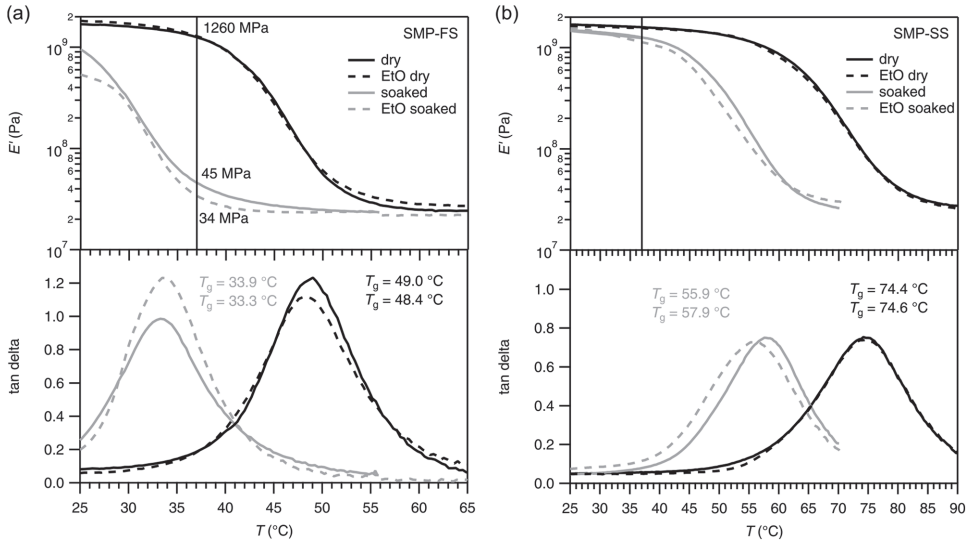

Figure 7. DMA measurements of surface-etched a) SMP-FS and b) SMP-SS before and after EtO sterilization. Showing the storage modulus E' (top) and the tan δ (bottom) of dry (black) and of in PBS soaked (grey) samples, respectively. Vertical line indicates the values at 37 °C.

similar. The modulus of nonsterilized SMP-FS dropped from 1809 MPa at room temperature directly after insertion to 41 MPa after 20 min in PBS at 37 °C, whereas the modulus of sterilized SMP-FS dropped from 1490 to 31 MPa. For the SMP-SS, E' dropped from 1768 to 1232 MPa before, and from 1721 to 1165 MPa after sterilization. After 60–120 min soaking in PBS, the T_g of both compositions was observed to decrease by 15–20 °C compared to the dry values (Figure 7). The glass transition temperature for nonsterilized SMP-FS (control) dropped from 49.0 to 33.3 °C; the sterilized SMP-FS dropped from 48.4 to 33.9 °C. The T_g values for the nonsterilized SMP-SS samples changed from 74.6 to 57.9 °C, whereas the sterilized samples changed from 74.4 to 55.9 °C. The storage moduli in the glassy and rubbery states after soaking have been almost the same for both compositions, before and after sterilization with EtO. The only difference was observed for the SMP-FS at 25 °C, where the glassy modulus for sterilized samples was lower (540 MPa) as for the nonsterilized equivalents (950 MPa). This might be caused by plasticization effects, but has no impact to the functionality of devices since these are values of soaked samples. For dry samples, the storage modulus in the glassy state is in any case high enough for a reliable handling during insertion. Although the maximum temperature to which the immersed samples could be heated was limited to 70 °C, which was attributed to the experimental setup, this was high enough to verify the tan δ peak and the rubbery modulus of both compositions after softening because the glass transition of both polymers was within this temperature range.

The softening characteristics of the herein tested thiol-ene and thiol-ene/acrylate were not impaired. This indicates, that sterilization with EtO gas has insignificant influence on modulus as a function of temperature and does not affect the degree of softening of the SMP.

3. Discussion

We have shown for the first time that SMP-based structures designed for neural implantation tolerate sterilization procedures necessary for reliable preclinical studies and eventual clinical use.

One key challenge, when using biomedical devices in vivo, is their proper sterilization. A common way to sterilize temperature sensitive polymeric devices is the use of 254 nm UV light. However, the thermomechanical properties of SMP-SF and SMP-SS were significantly affected through the UV treatment (Figure 2). The inhomogeneity between surface and core could be explained by accelerated ageing effects of the polymer caused by irradiation for 2 h at 254 nm. These include chain scissions and formation of new bonds. In particular, thioether bonds are relatively weak and are known to be susceptible to photoinduced cleavage.[27] Further investigations would be necessary to clarify the specific underlying mechanisms in these particular networks.

In contrast, sterilization with steam and EtO did not significantly affect the thermomechanical properties of the SMP test devices or their surface characteristics as demonstrated by DMA (Figure 2) and ATR-FTIR (Figure 3) measurements, respectively. These findings are in line with the findings of Yakacki et al.,[20] who studied the thermomechanical behavior of acrylate-based SMPs after various sterilization methods.

However, with regard to the fabrication of functionalized devices, steam sterilization is inappropriate. The deposited metals and electronic connecters might be corroded by the harsh conditions. From a more general viewpoint, it would also be difficult to sterilize temporary deformed SMPs having a transition temperature below 120 °C without triggering the shape memory effect.

Unlike sterilization by steam, EtO sterilization is performed at low temperatures and therefore more suitable for temperature sensitive materials such as SMP. Even though the T_g is depressed shortly after sterilization by a few degrees due to plasticization, this effect was shown to be reversible (Figure 2). After an extended degassing step, the material behaved the same as before sterilization.

Sterilization methods, including EtO, steam, and dry heat, were previously tested to compare their ability to remove endotoxins from silicon microelectrodes. Ravikumar et al. demonstrated that decreased levels of endotoxin contamination left on sterilized implants directly corresponded to decreases in acute neuroinflammation surrounding microelectrodes implanted in mice brains.[28] Specifically, EtO gas sterilized implants had less residual endotoxins, resulting in less neurodegenerative effects than autoclaved or heat treated implants. Consequently, we strived to apply an EtO-based sterilization method for SMP devices. In fact, SMP-FS and SMP-SS met the FDA-recommended criteria for maximum residual endotoxin concentration for CSF-contacting implanted devices (<0.06 EU mL^{-1}) (Figure 4).

With regard to the application of SMP as softening neural probes, equally as relevant as the room temperature behavior of dry test devices, is their behavior under conditions representative of in vivo use. Therefore, we soaked the test devices before and after sterilization in PBS at 37 °C and monitored the change of their thermomechanical properties. The water uptake accompanied rapid reduction of both the modulus and glass transition temperature, faster than prior studies.[13b] After 10 min of immersion, the storage modulus of SMP-FS decreased by two orders of magnitude, while the modulus of SMP-SS decreased just by a few hundred MPa (Figure 6), which is in line with the proposed softening characteristics of the individual polymers. For both compositions, the modulus was stabilized at a plateau after 15–20 min, and therefore the softening of the SMP test devices was considered to be complete. This gives the surgical timeframe for the reliable insertion of devices (≈10 min) into the body before they become too elastic and may buckle when attempting to penetrate tissue. The values for the EtO sterilized samples were comparable to the non-sterilized equivalents, showing that the degree of softening and the time required for plasticization, was not impaired.

The second part of the measurement of the soaked samples comprised a heating ramp from 20 to 70 °C to validate the material properties after plasticization caused by the aqueous solution (Figure 7). It is widely known that molecular interaction between water and the polymer chains leads to increased free volume which allows increased chain segment mobility.[29] As expected from prior studies with similar thiol-ene and thiol-ene/acrylate networks,[13b] the shift in T_g from the dry to the soaked state was ≈15 °C for both, the fully softening and the slightly softening SMP. Once again, the sterilization with EtO gas had only a minor influence on the thermomechanical properties of the herein tested thiol-ene and thiol-ene/acrylate, showing that the functionality of the SMP was not affected. Thus, this sterilization method seems to be promising for functionalized devices using the herein presented SMPs as a substrate. However, the properties of fully functionalized and packaged devices may differ from the herein investigated test structures, and therefore it is important to investigate in how far sterilization has an impact on the electrical behavior and overall performance on bioelectronic devices.

4. Conclusions

We have demonstrated that softening SMPs composed of either thiol-ene or thiol-ene/acrylate networks are compatible with various sterilization methods. In particular, the treatment with EtO gas did not damage thin photolithographically defined polymer films and seems to be a promising method to sterilize softening neural probes. Using DMA equipped with an immersion system, we observed that EtO sterilized samples showed only minor changes in their thermomechanical properties, and more importantly, the engineered softening behavior of SMPs was not impaired. In addition, sterilization of the samples met the FDA Guidance for residual endotoxin concentrations. Our findings have significant implications for the commercial biomedical application of SMP-based devices including neural electrodes. By building sterilization methods into our fabrication processes and factoring sterilization effects into material design, the biomedical application potential of novel materials such as SMPs can be realized.

5. Experimental Section

5.1. Polymer Solutions

1,3,5-Triallyl-1,3,5-triazine-2,4,6(1H,3H,5H)-trione (TATATO), tricyclo[5.2.1.$0^{2,6}$]decanedimethanol diacrylate (TCMDA), trimethylolpropane tris(3-mercaptopropionate) (TMTMP), 2,2-dimethoxy-2-phenylacetophenone (DMPA) were purchased from Sigma-Aldrich (Scheme 1). All the chemicals were used as received without further purification.

Two SMP compositions were prepared, a thiol-ene and a thiol-ene/acrylate, each consisting of stoichiometric quantities of thiol to ene functionalities. Exact mole fractions were: TMTMP-TATATO = 0.5-0.5 (SMP-FS) and TMTMP-TATATO/TCMDA = 0.345-0.345/0.31 (SMP-SS). A total of 0.1 wt% DMPA of total monomer weight was dissolved in the solution for the initiation of the photopolymerization of the monomer solution. The vial was covered in aluminum foil to prevent incident light from contacting the monomer solution and kept at room temperature. Without exposing the solution to light, the vial was mixed thoroughly by planetary speed mixing.

5.2. Sample Preparation

The polymer solutions were spin cast on 75 mm × 50 mm glass microscope slides using a Laurell WS-650-8B spin coater. Spin speed was 600 rpm and time was 30 s for SMP-FS and 25 s for SMP-SS in order to achieve thicknesses of about 30 μm, respectively. Polymerization was performed at ambient temperature using an UVP CL-1000 cross-linking chamber with five overhead 254 nm UV bulbs for 120 min under air. In addition, some samples were cured in the UV chamber floated with either nitrogen or argon gas. Cured samples were then placed in a vacuum oven at 120 °C and five in Hg for 24 h to further complete network conversion.

5.3. Nonfunctional Devices

Test devices were fabricated in the UT Dallas Class 10 000 cleanroom facility. The above SMP-on-glass substrates were used as the starting substrates in the cleanroom. Low temperature silicon nitride (using PlasmaTherm-790 plasma-enhanced chemical vapor deposition (PECVD)) was deposited to act as a hard mask for the following plasma etching processes in which the device outline/shape was patterned. Adjacently, the nitride hard mask was etched away in the 1:10 HF dip. For some SMP samples, top 4 μm thick crust was etched away in oxygen plasma (Technics reactive ion etch (RIE)). In a final step, the test devices having dimensions of 4.5 mm × 50 mm × 30 μm were delaminated from the glass slide by soaking in water.

5.4. DMA

DMA was performed using a TA RSA-G2 with Immersion System in tension mode in order to quantify the storage modulus E' and tan δ of dry or in PBS soaked samples (Figure 5). All measurements were performed on rectangular samples as received after the cleanroom processing, having a width of 4.5 ± 0.1 mm and thicknesses of 30 ± 3 μm. The following parameters were selected: clamping distance of 15 mm, a preload force of 0.05 N, a frequency of 1 Hz, and a deformation amplitude of 0.275% strain. Dry experiments were run from 10 to 100 °C or from 20 to 120 °C using a heating rate of 2 °C min^{-1}. Soaking experiments were run using the immersion system of the RSA-G2 filled with PBS. The first step (the soaking) included the heating from room temperature to 37 °C followed by isothermal oscillating for 60 or 120 min. The second step comprised first cooling down to the start temperature with a rate of 3 °C min^{-1} followed by heating from 10 to 80 °C applying a heating rate of 2 °C min^{-1}. It should be noted, that there was an offset of about 10 °C between the set temperature and the measured temperature inside the solution, based on the experimental setup. All measurements were performed on three independent specimens in order to gather statistical results.

5.5. Infrared Spectroscopy

ATR-FTIR measurements were performed with an IRAffinity-1 spectrometer from Shimadzu using a deuterated, L-alanine doped triglycine sulfate (DLATGS) detector. The ATR cell was equipped with a ZnSe crystal. The spectra were recorded from 4000 to 800 cm^{-1} as the average of 32 scans at a resolution of 2 cm^{-1}. Analysis of data included baseline correction, ATR correction, and normalization.

5.6. UV Sterilization

Specimens were dipped in ethanol (EtOH) and immediately transferred to a UV chamber equipped with five overhead 254 nm UV bulbs, in which they were irradiated for 120 min.

5.7. Autoclave Sterilization

Specimens were mounted inside containers and loaded into a Getinge 400/500LS-E series steam sterilizer. Small strips of autoclave indicator tape were applied to the containers before they were placed into the autoclave. Superdry cycle was selected, which includes exposure to steam for 30 min at 121 °C and 15 psi, followed by 75 min drying cycle. Post sterilization cycle, the stripe color of the indicator tape was inspected to verify whether or not the desired temperature of 121 °C was reached.

5.8. Ethylene Oxide Sterilization

Specimens were mounted inside appropriate size glass petri dishes, sealed, and loaded into a liner bag along with gas indicator tape and biological indicators, such as a Dosimeter and a Steritest. Next, the packed samples were loaded into the ethylene oxide sterilizer (AN 74i, Anprolene, Andersen Sterilizers Inc.) along with a Humidichip to ensure a minimum of 35% relative humidity inside the sterilization liner bag. After a minimum of 4 h of prehumidification, the glass ampoule containing 18 g of liquid EtO was added to the liner bag which was then sealed using velcro wrap. The room temperature and atmospheric pressure 24 h sterilization cycle was then started and samples were retrieved after the 2 h purge/aeration and degassing cycles following sterilization, to remove the residual EtO. All indicators were inspected for color changes to make sure the gas came in contact with the specimens.

5.9. Measurement of Residual Endotoxins

A Kinetic-QCL chromogenic limulus amebocyte lysate (LAL) endotoxin assay (Lonza, Inc., Catalog Number: 50-650U) was used to determine the level of residual endotoxins on the surface etched SMP test devices after EtO sterilization. The Kinetic-QCL assay was a quantitative assay for the detection of

gram-negative endotoxins. Endotoxin level was indirectly measured as a function of the reaction time associated with endotoxin-activation of an enzyme that catalyzed the release of the chromogen p-nitroaniline.

Three independently prepared test devices were assayed, in triplicate, for each SMP composition ($n = 3$). Residual endotoxins were extracted from test devices via incubation with certified endotoxin-free water for 24 h at 37 °C (LAL Reagent Water, Lonza). All glassware and handling instruments were rendered endotoxin-free by dry heat or EtO prior to use. Endotoxin activity on a given microelectrode sample was calculated from a five-point log–log standard curve generated from the Kinetic-QCL kit following methods described by the vendor (Lonza). Negative (blank) controls confirmed the absence of contamination from handling and preparation of the assay. A positive-spike control test confirmed that the SMP materials did not interfere with the assay.

Supporting Information

Supporting Information is available from the Wiley Online Library or from the author.

Acknowledgements: This work was supported by the Office of the Assistant Secretary of Defense for Health Affairs through the Peer Reviewed Medical Research Program under Award Nos. W81XWH-15-1-0607 and W81XWH-15-1-0608. Opinions, interpretations, conclusions, and recommendations were those of the authors and were not necessarily endorsed by the Department of Defense. Additionally, the contents did not represent the views of the U.S. Department of Veterans Affairs or the United States Government.

Received: July 26, 2016; Revised: September 8, 2016; Published online: October 12, 2016; DOI: 10.1002/mame.201600331

Keywords: biocompatibility; shape memory polymers; sterilization; stimuli-sensitive polymers; thermomechanical properties

[1] A. S. Kulshrestha, A. Mahapatro, in *Polymers for Biomedical Applications*, American Chemical Society, Washington, DC **2008**, p. 1.
[2] a) D. F. Williams, *Biomaterials* **1981**, *2*, 133; b) S. Ramakrishna, J. Mayer, E. Wintermantel, K. W. Leong, *Compos. Sci. Technol.* **2001**, *61*, 1189; c) R. Duncan, *Nat. Rev. Drug Discovery* **2003**, *2*, 347; d) L. Hartmann, S. Haefele, R. Peschka-Suess, M. Antonietti, H. G. Borner, *Chem. - Eur. J.* **2008**, *14*, 2025; e) A. Bertin, *Macromol. Chem. Phys.* **2012**, *213*, 2329.
[3] a) R. W. Lenz, *Adv. Polym. Sci.* **1993**, *107*, 1; b) L. S. Nair, C. T. Laurencin, *Prog. Polym. Sci.* **2007**, *32*, 762; c) T. Ware, A. R. Jennings, Z. S. Bassampour, D. Simon, D. Y. Son, W. Voit, *RSC Adv.* **2014**, *4*, 39991.
[4] D. E. Discher, A. Eisenberg, *Science* **2002**, *297*, 967.
[5] a) O. Koshkina, C. Bantz, C. Wuerth, T. Lang, U. Resch-Genger, M. Maskos, in *Advanced Polymers in Medicine* (Eds: A. Lendlein, D. W. Grijpma), WILEY-VCH Verlag GmbH & Co. KGaA, Weinheim **2011**, p. 141; b) A. F. Thünemann, R. Bienert, D. Appelhans, B. Voit, *Macromol. Chem. Phys.* **2012**, *213*, 2362; c) O. Koshkina, T. Lang, R. Thiermann, D. Docter, R. H. Stauber, C. Secker, H. Schlaad, S. Weidner, B. Mohr, M. Maskos, A. Bertin, *Langmuir* **2015**, *31*, 8873.
[6] J. Wu, Z.-G. Su, G.-H. Ma, *Int. J. Pharm.* **2006**, *315*, 1.
[7] S. E. Stiriba, H. Frey, R. Haag, *Angew. Chem., Int. Ed.* **2002**, *41*, 1329.
[8] a) W. Sokolowski, A. Metcalfe, S. Hayashi, L. Yahia, J. Raymond, *Biomed. Mater.* **2007**, *2*, 23; b) W. Small, P. Singhal, T. S. Wilson, D. J. Maitland, *J. Mater. Chem.* **2010**, *20*, 3356; c) M. C. Serrano, G. A. Ameer, *Macromol. Biosci.* **2012**, *12*, 1156; d) P. Singhal, W. Small, E. Cosgriff-Hernandez, D. J. Maitland, T. S. Wilson, *Acta Biomater.* **2014**, *10*, 67.
[9] a) C. Liu, H. Qin, P. T. Mather, *J. Mater. Chem.* **2007**, *17*, 1543; b) D. Ratna, J. Karger-Kocsis, *J. Mater. Sci.* **2008**, *43*, 254; c) A. Lendlein, *Shape-Memory Polymers*, Springer, Berlin Heidelberg **2010**, p. 209; d) T. Pretsch, *Polymers* **2010**, *2*, 120; e) M. D. Hager, S. Bode, C. Weber, U. S. Schubert, *Prog. Polym. Sci.* **2015**, *49–50*, 3; f) Q. Zhao, H. J. Qi, T. Xie, *Prog. Polym. Sci.* **2015**, *49–50*, 79.
[10] a) M. C. Chen, H. W. Tsai, Y. Chang, W. Y. Lai, F. L. Mi, C. T. Liu, H. S. Wong, H. W. Sung, *Biomacromolecules* **2007**, *8*, 2774; b) W. Small, P. R. Buckley, T. S. Wilson, W. J. Benett, J. Hartman, D. Saloner, D. J. Maitland, *IEEE Trans. Biomed. Eng.* **2007**, *54*, 1157; c) L. Xue, S. Dai, Z. Li, *Biomaterials* **2010**, *31*, 8132.
[11] A. Lendlein, R. Langer, *Science* **2002**, *296*, 1673.
[12] K. Kratz, U. Voigt, A. Lendlein, *Adv. Funct. Mater.* **2012**, *22*, 3057.
[13] a) T. Ware, D. Simon, R. L. Rennaker II, W. Voit, *Polym. Rev.* **2013**, *53*, 108; b) T. Ware, D. Simon, C. Liu, T. Musa, S. Vasudevan, A. Sloan, E. W. Keefer, R. L. Rennaker II, W. Voit, *J. Biomed. Mater. Res., Part B* **2014**, *102*, 1.
[14] a) T. Ware, D. Simon, K. Hearon, C. Liu, S. Shah, J. Reeder, N. Khodaparast, M. P. Kilgard, D. J. Maitland, R. L. Rennaker, II, W. E. Voit, *Macromol. Mater. Eng.* **2012**, *297*, 1193; b) T. Ware, D. Simon, D. E. Arreaga-Salas, J. Reeder, R. Rennaker, E. W. Keefer, W. Voit, *Adv. Funct. Mater.* **2012**, *22*, 3470; c) T. Ware, D. Simon, K. Hearon, T. H. Kang, D. J. Maitland, W. Voit, *Macromol. Biosci.* **2013**, *13*, 1640.
[15] a) J. P. Harris, J. R. Capadona, R. H. Miller, B. C. Healy, K. Shanmuganathan, S. J. Rowan, C. Weder, D. J. Tyler, *J. Neural Eng.* **2011**, *8*, 066011; b) J. P. Harris, A. E. Hess, S. J. Rowan, C. Weder, C. A. Zorman, D. J. Tyler, J. R. Capadona, *J. Neural Eng.* **2011**, *8*, 046010; c) A. E. Hess, J. R. Capadona, K. Shanmuganathan, L. Hsu, S. J. Rowan, C. Weder, D. J. Tyler, C. A. Zorman, *J. Micromech. Microeng.* **2011**, *21*, 054009; d) J. R. Capadona, D. J. Tyler, C. A. Zorman, S. J. Rowan, C. Weder, *MRS Bull.* **2012**, *37*, 581; e) J. K. Nguyen, D. J. Park, J. L. Skousen, A. E. Hess-Dunning, D. J. Tyler, S. J. Rowan, C. Weder, J. R. Capadona, *J. Neural Eng.* **2014**, *11*, 056014; f) M. Jorfi, J. L. Skousen, C. Weder, J. R. Capadona, *J. Neural Eng.* **2015**, *12*, 011001; g) J. K. Nguyen, M. Jorfi, K. L. Buchanan, D. J. Park, E. J. Foster, D. J. Tyler, S. J. Rowan, C. Weder, J. R. Capadona, *Acta Biomater.* **2016**, *29*, 81.
[16] P. D. Nair, *J. Biomater. Appl.* **1995**, *10*, 121.
[17] FDA, "Updated 510(k) sterility review guidance K90-1; Guidence for industry and FDA", US Department of Health and Human Services FDA, Center for Devices and Radiological Health, **2016**.
[18] a) J. C. Kelsey, *J. Clin. Pathol.* **1961**, *14*, 59; b) I. P. Matthews, C. Gibson, A. H. Samuel, *Clin. Mater.* **1994**, *15*, 191.
[19] a) L. De Nardo, R. Alberti, A. Cigada, L. Yahia, M. C. Tanzi, S. Farè, *Acta Biomater.* **2009**, *5*, 1508; b) L. De Nardo,

M. Moscatelli, F. Silvi, M. C. Tanzi, L. H. Yahia, S. Farè, *J. Mater. Sci.: Mater. Med.* **2010**, *21*, 2067; c) L. De Nardo, S. Bertoldi, M. C. Tanzi, H. J. Haugen, S. Farè, *Smart Mater. Struct.* **2011**, *20*, 035004; d) S. Todros, C. Venturato, A. N. Natali, G. Pace, V. Di Noto, *J. Polym. Sci., Part B: Polym. Phys.* **2014**, *52*, 1337; e) T. A. M. Valente, D. M. Silva, P. S. Gomes, M. H. Fernandes, J. D. Santos, V. Sencadas, *ACS Appl. Mater. Interfaces* **2016**, *8*, 3241; f) C. Yavuz, S. N. B. Oliaei, B. Cetin, O. Yesil-Celiktas, *J. Supercrit. Fluids* **2016**, *107*, 114; g) L. De Nardo, S. Bertoldi, A. Cigada, M. C. Tanzi, H. J. Haugen, S. Farè, *J. Appl. Biomater. Funct. Mater.* **2012**, *10*, 119; h) M. C. Tanzi, L. De Nardo, S. Bertoldi, S. Farè, in *Shape Memory Polymers for Biomedical Applications* (Ed: L. Yahia), Elsevier Ltd, Cambridge, UK **2015**, p. 133; i) S. Bertoldi, S. Farè, H. J. Haugen, M. C. Tanzi, *J. Mater. Sci.: Mater. Med.* **2015**, *26*, 1.

[20] C. M. Yakacki, M. B. Lyons, B. Rech, K. Gall, R. Shandas, *Biomed. Mater.* **2008**, *3*, 015010.

[21] Y. Wong, J. Kong, L. K. Widjaja, S. S. Venkatraman, *Sci. China: Chem.* **2014**, *57*, 476.

[22] a) C. E. Hoyle, T. Y. Lee, T. Roper, *J. Polym. Sci., Part A: Polym. Chem.* **2004**, *42*, 5301; b) C. E. Hoyle, C. N. Bowman, *Angew. Chem., Int. Ed.* **2010**, *49*, 1540.

[23] a) H. Cao, E. Currie, M. Tilley, Y. C. Jean, in *Photoinitiated Polymerization*, American Chemical Society, Washington, DC **2003**, p. 152; b) J. A. Arceneaux, *UV + EB Technol. – Print. Packag. Innovations* **2015**, *1*, 48.

[24] N. B. Cramer, C. N. Bowman, *J. Polym. Sci., Part A: Polym. Chem.* **2001**, *39*, 3311.

[25] a) H. Drnovská, L. Lapčík, V. Buršíková, J. Zemek, A. M. Barros-Timmons, *Colloid Polym. Sci.* **2003**, *281*, 1025; b) C. Corbella, S. Grosse-Kreul, A. von Keudell, *Plasma Processes Polym.* **2015**, *12*, 564; c) M. Vishnuvarthanan, N. Rajeswari, *Innovative Food Sci. Emerging Technol.* **2015**, *30*, 119.

[26] F. D. A. United States Department of Health and Human Services – Office of Regulatory Affairs (ORA), "Guidance for Industry Pyrogen and Endotoxins Testing: Questions and Answers," United States Department of Health and Human Services – Office of Regulatory Affairs (ORA), Food and Drug Administration, **2012**.

[27] a) P. J. Kropp, G. E. Fryxell, M. W. Tubergen, M. W. Hager, G. D. Harris, T. P. McDermott, R. Tornero-Velez, *J. Am. Chem. Soc.* **1991**, *113*, 7300; b) P. Filipiak, G. L. Hug, B. Marciniak, *J. Photochem. Photobiol. A: Chem.* **2006**, *177*, 295.

[28] M. Ravikumar, D. J. Hageman, W. H. Tomaszewski, G. M. Chandra, J. L. Skousen, J. R. Capadona, *J. Mater. Chem. B, Mater. Biol. Med.* **2014**, *2*, 2517.

[29] H. Levine, L. Slade, *Water Science Reviews 3*, Cambridge University Press, Cambridge, UK **1988**.

frontiers in Neuroscience

ORIGINAL RESEARCH
published: 31 October 2018
doi: 10.3389/fnins.2018.00772

Understanding the Effects of Both CD14-Mediated Innate Immunity and Device/Tissue Mechanical Mismatch in the Neuroinflammatory Response to Intracortical Microelectrodes

*Hillary W. Bedell[1,2], Sydney Song[1,2], Xujia Li[1], Emily Molinich[1], Shushen Lin[1], Allison Stiller[3], Vindhya Danda[3,4], Melanie Ecker[3,4,5], Andrew J. Shoffstall[1,2], Walter E. Voit[3,4,5,6], Joseph J. Pancrazio[3] and Jeffrey R. Capadona[1,2]**

[1] Department of Biomedical Engineering, School of Engineering, Case Western Reserve University, Cleveland, OH, United States, [2] Advanced Platform Technology Center, L. Stokes Cleveland VA Medical Center, Rehab. R&D, Cleveland, OH, United States, [3] Department of Bioengineering, The University of Texas at Dallas, Richardson, TX, United States, [4] Center for Engineering Innovation, The University of Texas at Dallas, Richardson, TX, United States, [5] Department of Materials Science and Engineering, The University of Texas at Dallas, Richardson, TX, United States, [6] Department of Mechanical Engineering, The University of Texas at Dallas, Richardson, TX, United States

OPEN ACCESS

Edited by:
Mikhail Lebedev,
Duke University, United States

Reviewed by:
Takashi D. Y. Kozai,
University of Pittsburgh, United States
Erkin Seker,
University of California, Davis, United States

***Correspondence:**
Jeffrey R. Capadona
jrc35@case.edu

Specialty section:
This article was submitted to Neural Technology, a section of the journal Frontiers in Neuroscience

Received: *26 July 2018*
Accepted: *04 October 2018*
Published: *31 October 2018*

Citation:
Bedell HW, Song S, Li X, Molinich E, Lin S, Stiller A, Danda V, Ecker M, Shoffstall AJ, Voit WE, Pancrazio JJ and Capadona JR (2018) Understanding the Effects of Both CD14-Mediated Innate Immunity and Device/Tissue Mechanical Mismatch in the Neuroinflammatory Response to Intracortical Microelectrodes. Front. Neurosci. 12:772. doi: 10.3389/fnins.2018.00772

Intracortical microelectrodes record neuronal activity of individual neurons within the brain, which can be used to bridge communication between the biological system and computer hardware for both research and rehabilitation purposes. However, long-term consistent neural recordings are difficult to achieve, in large part due to the neuroinflammatory tissue response to the microelectrodes. Prior studies have identified many factors that may contribute to the neuroinflammatory response to intracortical microelectrodes. Unfortunately, each proposed mechanism for the prolonged neuroinflammatory response has been investigated independently, while it is clear that mechanisms can overlap and be difficult to isolate. Therefore, we aimed to determine whether the dual targeting of the innate immune response by inhibiting innate immunity pathways associated with cluster of differentiation 14 (CD14), and the mechanical mismatch could improve the neuroinflammatory response to intracortical microelectrodes. A thiol-ene probe that softens on contact with the physiological environment was used to reduce mechanical mismatch. The thiol-ene probe was both softer and larger in size than the uncoated silicon control probe. *Cd14*$^{-/-}$ mice were used to completely inhibit contribution of CD14 to the neuroinflammatory response. Contrary to the initial hypothesis, dual targeting worsened the neuroinflammatory response to intracortical probes. Therefore, probe material and CD14 deficiency were independently assessed for their effect on inflammation and neuronal density by implanting each microelectrode type in both wild-type control and *Cd14*$^{-/-}$ mice. Histology results show that 2 weeks after implantation, targeting CD14 results in higher neuronal density and decreased glial scar around the probe, whereas the thiol-ene probe results in more microglia/macrophage activation and greater blood–brain barrier (BBB) disruption around the probe. Chronic histology demonstrate no differences in

the inflammatory response at 16 weeks. Over acute time points, results also suggest immunomodulatory approaches such as targeting CD14 can be utilized to decrease inflammation to intracortical microelectrodes. The results obtained in the current study highlight the importance of not only probe material, but probe size, in regard to neuroinflammation.

Keywords: intracortical microelectrodes, neuroinflammation, innate immunity, softening electrode, shape memory polymer

INTRODUCTION

Intracortical microelectrodes allow researchers to record single-unit and multi-unit activity from individual or groups of neurons by detecting changes to the extracellular potential as a result of neurons generating action potentials (Renshaw et al., 1940; Wessberg et al., 2000). Recorded neural signals afford neuroscientists insight into the activity of specific populations of neurons. Thus, intracortical microelectrodes provide a valuable research tool to the field of cognitive and sensorimotor neuroscience. Intracortical microelectrodes are also utilized in brain–computer interfacing (BCI) applications to record neural activity as an input signal to decode and extract motor intent (Schwartz, 2004; Hochberg et al., 2012). Recorded neural signal informs the generation of a desired action for an external device, prosthetic, or muscles (*via* muscle stimulators) for a patient suffering from paralysis or limb loss. Thus, intracortical microelectrodes are a promising technology for both basic research and the development of clinical neuroprosthetic devices.

For both clinical and research applications, intracortical microelectrodes must be able to record from single cortical neurons for long periods (months to years). Unfortunately, there are limitations to intracortical microelectrodes that impede device reliability. Many studies document the failure of intracortical microelectrodes exemplified by both decrease of signal to noise ratio and loss of number of channels detecting single units (Polikov et al., 2005; Liu et al., 2006; Rennaker et al., 2007; Barrese et al., 2013). There are multiple factors that contribute to the failure of intracortical microelectrodes, including but not limited to a biological response to chronically implanted intracortical microelectrodes (Rennaker et al., 2007; Saxena et al., 2013; Kozai et al., 2014b; Hermann et al., 2017).

Inflammation ensues after the device damages tissue during implantation when blood vessels are unavoidably severed leading to blood infiltration and serum protein adsorption onto the device. Implantation results in the release of endogenous damage signals such as high mobility growth box 1 (HMGB1) and inflammatory lipids from damaged cells (Potter et al., 2014). Plasma proteins and damage-associated molecular patterns (DAMPs) are recognized by cellular receptors such as the toll-like receptor (TLR)/cluster of differentiation 14 (CD14) complex. As a result, microglial and infiltrating macrophage cells become inflammatory or "activated" and subsequently release of pro-inflammatory molecules (Kim S. et al., 2013; Zanoni et al., 2017). Glial encapsulation, neurodegeneration, and neuronal death follow this inflammatory cascade. Since the long-term success of the devices depends on the presence of healthy, active neurons immediately adjacent to the recording sites of the probe, the inflammatory process leads to a reduction of detectable signals necessary for BCI and other neuroscience research applications (Schwartz, 2004; Bjornsson et al., 2006; Jorfi et al., 2015).

In addition to the primary injurious events caused by the initial implantation, a persistent inflammatory response is present at the probe–tissue interface under chronic conditions. The pro-inflammatory microenvironment resulting from probe implantation leads to further breakdown of the blood–brain barrier (BBB) and increased vascular permeability perpetuating the inflammatory cascade (Abdul-Muneer et al., 2015).

Furthermore, the mechanical mismatch between a traditional probe (with a metal or silicon substrate) and the brain can exacerbate inflammation (Harris et al., 2011; Moshayedi et al., 2014; Nguyen et al., 2014; Du et al., 2017; Lee et al., 2017a). The mechanical discrepancy in modulus between the non-compliant probe and the pliant brain results in tissue strain and compression at the tissue–device interface. We have shown that reducing the modulus of the probe from 100 to 1000 s of GPa, to 1–10 s of MPa to more closely match that of gray matter in brain tissue (E = ∼3–6 kPa (Green et al., 2008)) reduces the micromotion-induced strain (Sridharan et al., 2015). As a result, after implantation of such relatively compliant materials, the inflammatory response to intracortical microelectrodes is significantly reduced, but not completely eliminated, providing neuroprotection and a more stable BBB (Harris et al., 2011; Nguyen et al., 2014).

Increased BBB permeability can facilitate the infiltration of myeloid cells into the injured brain tissue. These peripheral immune cells become activated and perpetuate the inflammatory response leading to neuronal death by the probe–tissue interface (Ravikumar et al., 2014). To combat the inflammatory response from microglia and infiltrating myeloid cells triggered by recognition of DAMPs and serum proteins, our lab has explored targeting the TLR/CD14 pathway involved in the recognition of DAMPs as a method to improve the chronic recording performance and reduce inflammation around the brain–electrode interface (Hermann et al., 2017). More recently, we have also shown that targeting the TLR/CD14 pathway in only infiltrating blood-derived cells leads to an improvement in chronic recording quality (Bedell et al., 2018).

Our initial softening probes used in the Capadona Lab yielded desirable mitigation of the neuroinflammatory response to

intracortical microelectrodes (Capadona et al., 2008; Nguyen et al., 2014). However, these initial materials swelled up to 70% in aqueous conditions, making fabrication into functional electrodes problematic. In collaboration with the Voit and Pancrazio labs, we have begun exploring similar softening materials, thiol-ene and thiol-ene/acrylate shape memory polymers (softening from ∼1.7 GPa down to ∼35 MPa (Ecker et al., 2017)) that possess fabrication benefits over the initial nanocomposite softening probes. These polymers soften under physiological conditions due to plasticization effects, but swell only up to 3%. The strong interaction between thiols and noble metals commonly used for electrodes yields improved adhesion between substrate and thin film metals (Nuzzo et al., 1987). Moreover, thiol-ene and thiol-ene/acrylates are more compatible with high yield, high-resolution photolithographic processes enabling manufacturability. Most importantly, a functional device, comprised of a thiol-ene/acrylate substrate, has been synthesized which was able to record single units for more than 2 months (Simon et al., 2017). Therefore, in the current study, thiol-ene was used as a probe substrate material that more closely matches the modulus of the brain to reduce BBB breakdown while also targeting an innate immune pathway involved in the recognition of serum proteins. Our work combines these approaches using a softening material and targeting CD14 through $Cd14^{-/-}$ mice, to reduce neuroinflammation in response to single-shank intracortical microelectrode probes.

RESULTS

The current study aimed to determine whether the dual targeting of the innate immune response and the mechanical mismatch between tissue and a single-shank probe, which generates tissue damage, results in combinatorial or synergistic effects to improve neuronal density and reduce inflammation at the probe–tissue interface. We utilized a thiol-ene probe, which is stiff when inserted, but softens at physiological temperatures as the probe that more closely matches the brain tissue modulus. A $Cd14^{-/-}$ knock-out model was used to target the innate immune response while immunohistochemistry was used to evaluate the neuroinflammatory response. A neuronal nuclear protein, NeuN, was used as an immunohistochemical marker for cortical neurons around the probe (Mullen et al., 1992). The glial scar is an indicator of neuroinflammation, so glial fibrillary acidic protein (GFAP), a type of intermediate filament protein upregulated by reactive astrocytes, was examined *via* immunohistochemistry (Landis, 1994). To explore microglia and macrophage activation, an antibody to CD68, was used to detect activated microglia/macrophages around the probe interface. CD68 is an lysosomal-associated membrane protein which may play a role in antigen processing and presenting (Song et al., 2011). Furthermore, BBB dysfunction characterizes inflammation resulting from a neural implant such as an intracortical probe. BBB disruption was evaluated by quantifying the presence of IgG, a prolific plasma protein not found in the brain parenchyma under normal conditions, using an anti-IgG antibody (Potter et al., 2012a).

Comparing Dual Innate Immune Response and Mechanical Mismatch to Control

We first aimed to determine whether knocking out CD14 while using a softening probe would lead to reduced neuroinflammation and improved neuronal density around the probe at 2 weeks post implantation. For both experimental and control conditions, neuronal density at 0–50 μm from the implant surface was significantly lower than that at the background (300–350 μm from probe surface). Additionally, neuronal density surrounding softening (thiol-ene) probes in $Cd14^{-/-}$ animals was significantly higher than control animals at each 50 μm interval from 100 to 250 μm from the probe surface (**Figure 1A**). There was no difference in glial scar between these two conditions at any distance interval from the probe (**Figure 1B**). However, the combinatorial targeting approach increases BBB disruption and activated macrophages and microglia at each 50 μm interval from 0 to 150 μm from the probe (**Figures 1C,D**). Altogether, these data suggest that dual targeting the innate immune response while using the thiol-ene softening probe actually worsens the neuroinflammatory response. Thus, subsequent experiments were conducted to delineate the role of each strategy – targeting CD14 versus using a thiol-ene probe.

Delineating Effect of Each Variable – Probe Stiffness and CD14 Expression

To elucidate if either factor (probe stiffness or CD14 expression) drove the increased neuroinflammatory response of the combinatorial targeting, additional animals were set up as controls for each factor resulting in four different conditions (silicon shank + WT, silicon shank + $Cd14^{-/-}$, thiol-ene + WT, thiol-ene + $Cd14^{-/-}$). Additional animals were also set up to examine more chronic (16 weeks post-implantation) time points for each of the four experimental conditions. Comparisons were made between levels of each independent variable – responses of softening thiol-ene probes versus stiff silicon probes and comparisons between $Cd14^{-/-}$ and wild-type animals.

Neuronal Density

At both 2 and 16 weeks post implant, neuronal density at 0–50 μm from the electrode surface was significantly lower than that at the background for all conditions regardless of substrate material or genotype (**Figures 2A,B**). In the absence of CD14, neuronal density at each interval from 0 to 300 μm was significantly higher than that of wild-type at 2 weeks post implant (**Figures 2A,C**). However, at the chronic time point, 16 weeks, CD14 deficiency seemed to play a lesser role as there were no significant differences between wild-type and $Cd14^{-/-}$ animals (**Figures 2B,D**). At both 2 and 16 weeks post implant, the thiol-ene probe did not result in increased neuronal density compared to the control silicon probe (**Figure 2**). Furthermore, the combinatorial approach of using a softening substrate and targeting CD14 did not significantly improve neuronal density over the other conditions (**Figure 2**). Thus, targeting CD14 results in higher neuronal density around the probe at 2 weeks,

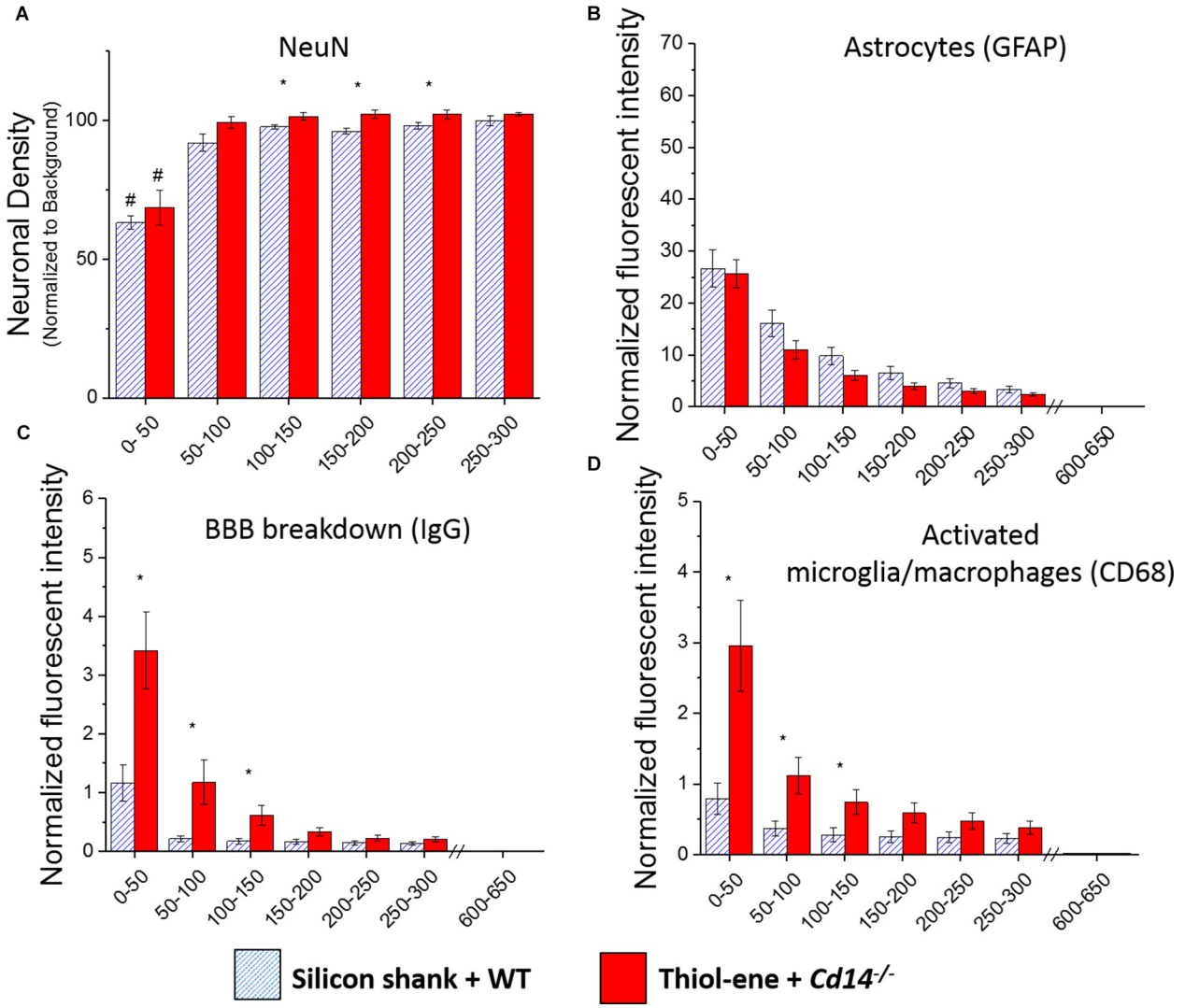

FIGURE 1 | Immunohistochemical evaluation comparing the dual targeting of the innate immune response and mechanical mismatch to control at 2 weeks after implantation. All analyses were evaluated with respect to distance from the explanted microelectrode hole (μm). **(A)** Neuronal density evaluated as $NeuN^+$ cells. **(B)** Astrocyte encapsulation evaluated as GFAP expression. **(C)** Blood-brain barrier permeability evaluated as IgG expression. **(D)** Microglial and macrophage activation evaluated as CD68 expression. * Denotes significance between silicon shank + WT and thiol-ene + $Cd14^{-/-}$; # denotes significant difference from background neuronal density.

but combining CD14 inhibition with a reduction in probe stiffness was counterproductive.

Glial Scarring

In all conditions, the glial scar was the densest closest to the probe and decreased as a function of distance from the probe–tissue interface (**Figure 3**). The glial scar became denser from 2 to 16 weeks post-implantation for all conditions (**Figure 3**), indicated by more intense GFAP staining from 0 to 50 μm from the surface of the implants. In animals that do not express CD14, there is less glial scar compared to wild-type animals at each 50 μm interval from 100 to 300 μm from the probe-tissue interface at 2 weeks post-implantation (**Figures 3A,C**), but not 16 weeks post-implantation (**Figures 3B,D**). Notably, there were no significant differences in the glial scar between the thiol-ene probe and control silicon probe at either time point (**Figure 3**).To summarize, targeting CD14 decreases glial scar around probe at 2 weeks.

Microglia/Macrophage Expression

Overall, microglial/macrophage activation as assessed *via* CD68 expression was heavily increased at the probe–tissue interface, and declined to background levels (zero expression) as a function of distance from the interface (**Figure 4**). The thiol-ene probes resulted in more activated microglia/macrophages than the silicon probes at 2 weeks post-implantation at each interval 0–200 μm from the probe–tissue interface (**Figures 4A,C**). However, there were no significant differences

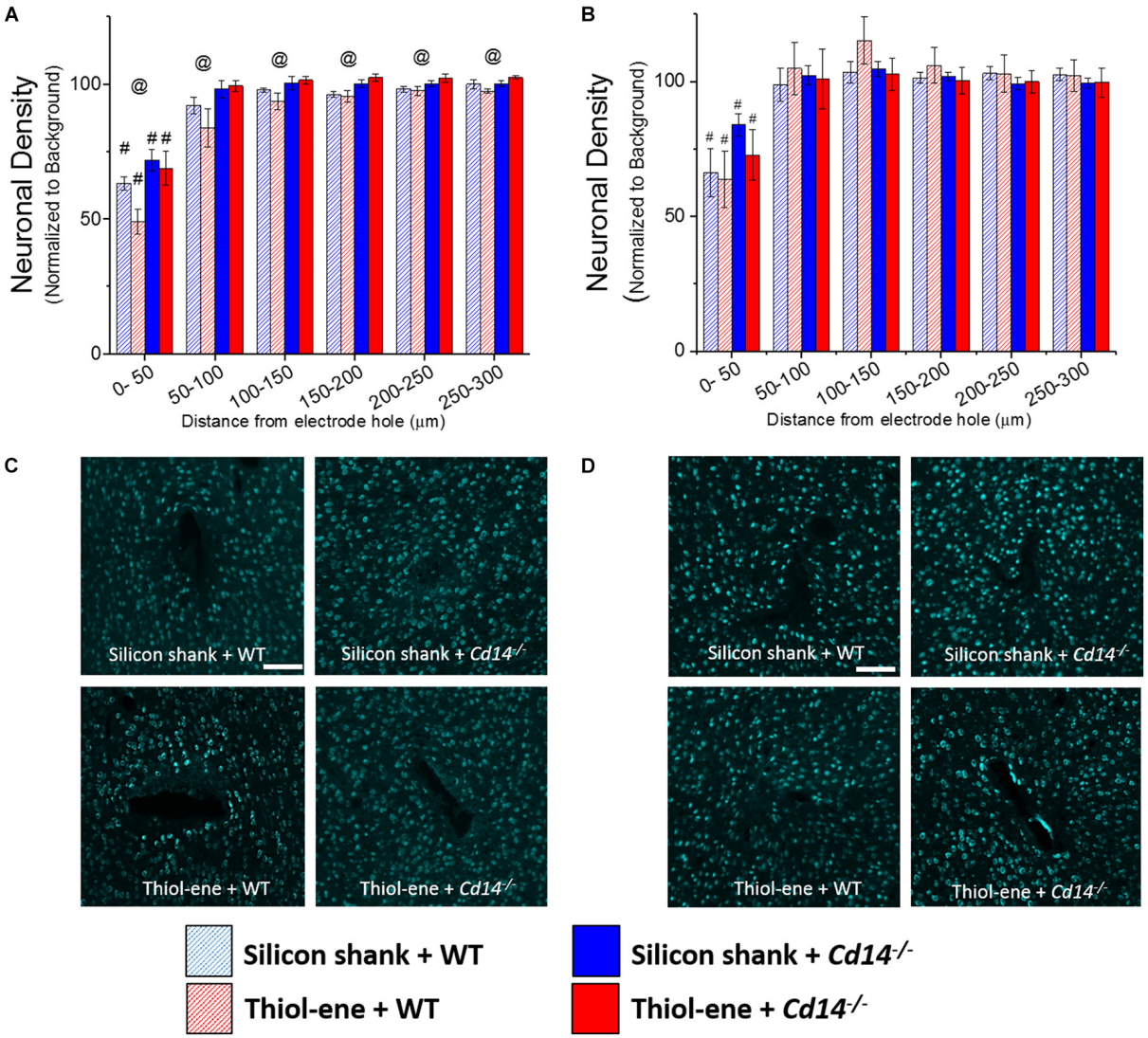

FIGURE 2 | Immunohistochemical evaluation of neuronal density. Neuronal density evaluated as $NeuN^+$ cells with respect to distance from the explanted microelectrode hole (μm). **(A)** 2 weeks. **(B)** 16 weeks. **(C)** Representative images of 2 weeks neuronal density. **(D)** Representative images of 16 weeks neuronal density. Scale bar: 100 μm. $^{@}$ Denotes significance between WT and $Cd14^{-/-}$; $^{\#}$ denotes significant difference from background neuronal density.

between wild-type and $Cd14^{-/-}$ groups at 2 weeks post-implantation (**Figures 4A,C**). By 16 weeks post-implant, activated microglia/macrophages for all groups had decreased compared to 2 weeks post-implantation (**Figures 4A,B**). Additionally, there were no differences in activation of microglia/macrophages among the conditions at 16 weeks (**Figures 4B,D**). Altogether, thiol-ene probe results in more microglia/macrophage activation around the probe at 2 weeks, but not 16 weeks post-implantation.

BBB Disruption

Similar to the glial scar and activated microglia/macrophages, BBB disruption (IgG expression) was found to be greatest at the probe-tissue interface and decreased in intensity as distance from probe-tissue interface increased (**Figure 5**). The only significant differences found between the groups were at 2 weeks post-implantation (**Figures 5A,C**). At 2 weeks post-implantation, the softer thiol-ene probes yielded significantly greater BBB breakdown compared to the stiff silicon probes (at each interval examined between 0 and 250 μm from probe interface, **Figures 5A,C**). In summary, thiol-ene probe results in greater BBB disruption around the probe at 2 weeks.

DISCUSSION

The current study explores how a softening thiol-ene probe and/or targeting the TLR/CD14 innate immune pathway affects inflammation and neuronal density at both 2 and 16 weeks post-implantation of intracortical microelectrode probes. Because

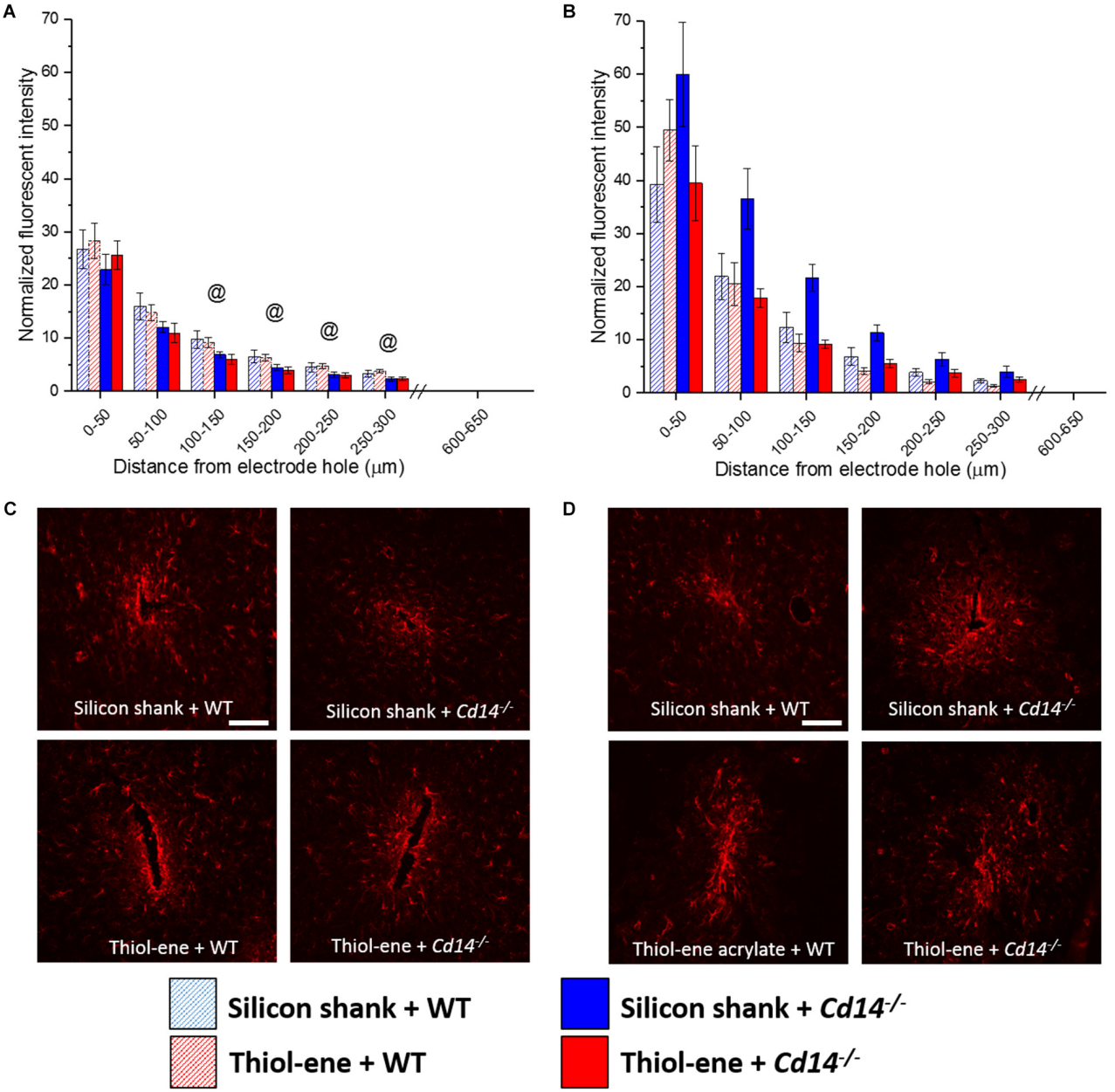

FIGURE 3 | Immunohistochemical evaluation of glial scarring assessed *via* astrocyte encapsulation. Astrocyte encapsulation evaluated as GFAP expression with respect to distance from the explanted microelectrode hole (μm). **(A)** 2 weeks. **(B)** 16 weeks. **(C)** Representative images of 2 weeks glial scar. **(D)** Representative images of 16 weeks glial scar. Scale bar: 100 μm. [@] Denotes significance between WT and $Cd14^{-/-}$.

initial results exploring synergistic effects of two different approaches resulted in increased neuroinflammation, we set out to parse out the response of each variable to gain a better understanding of each strategy alone. Our results demonstrate targeting CD14 results in higher neuronal density and decreased astroglial scarring around the probe at 2 weeks (**Figures 2A,C**, **3A,C**). We also describe the use of the thiol-ene probe with a modulus 3 orders of magnitude lower and a cross-sectional area 4× greater than the control silicon probes. Our observations demonstrate that a probe with a lower modulus but larger implantation footprint resulted in more BBB breakdown and activated microglia/macrophages than the control silicon probes. However, in spite of these markers of inflammation, the softening thiol-ene probes did not result in significantly decreased neuronal density or increased astroglial scarring around the implant at either acute (2 weeks) or chronic (16 weeks) time points.

Physiological sources such as respiration and vascular pulsations result in micromotion of an intracortical probe against brain tissue resulting in strain on brain tissue which can induce tissue damage (Subbaroyan et al., 2005; Gilletti

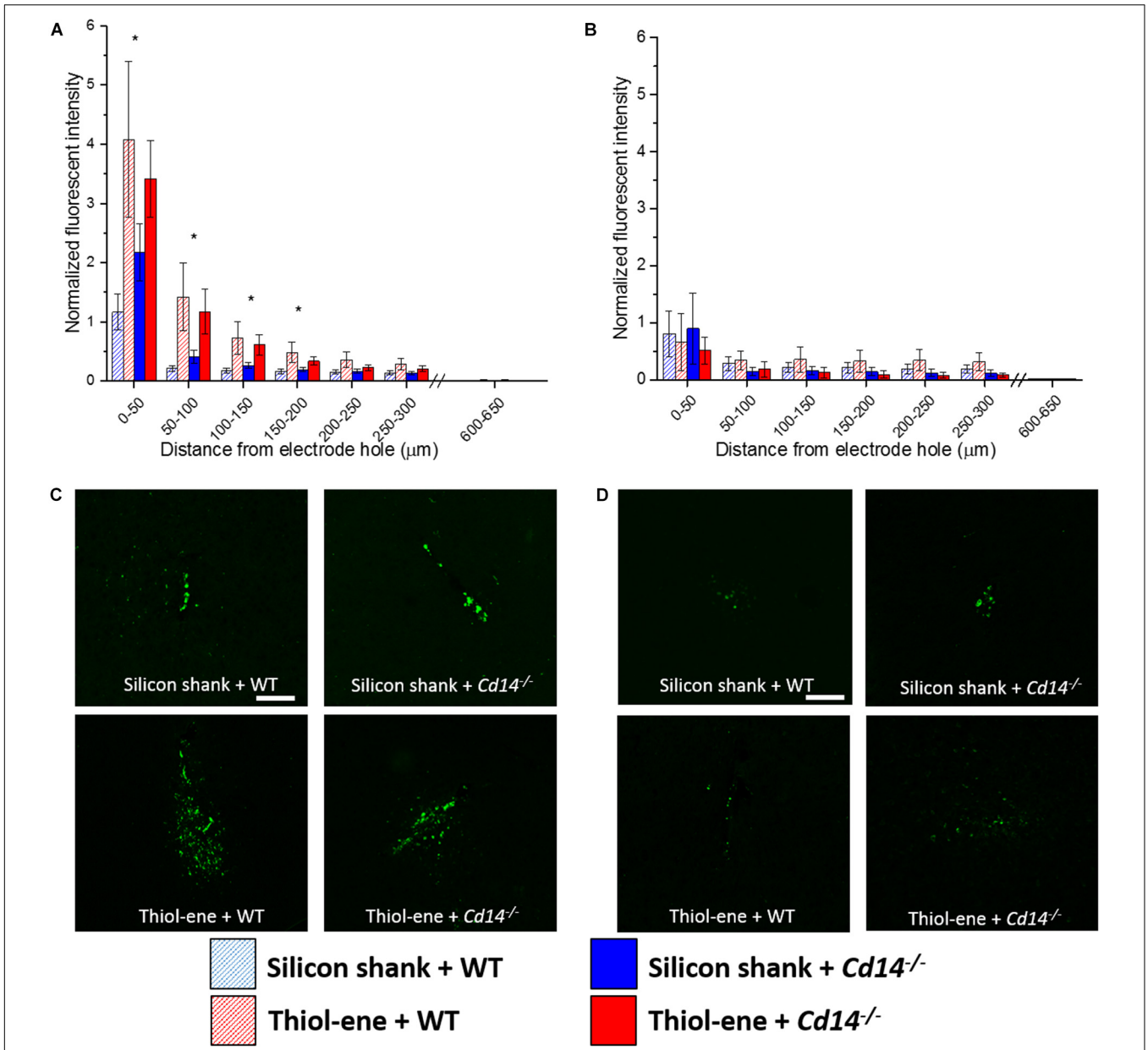

FIGURE 4 | Immunohistochemical evaluation of activated microglia and macrophages. Microglial and macrophage activation evaluated as CD68 expression with respect to distance from the explanted probe hole (μm). **(A)** 2 weeks. **(B)** 16 weeks. **(C)** Representative images of 2 weeks activated microglia and macrophages. **(D)** Representative images of 16 weeks activated microglia and macrophages. Scale bar: 100 μm. * Denotes significance between silicon and thiol-ene probes.

and Muthuswamy, 2006). One of the approaches to reduce the effects of micromotion is to increase probe flexibility. Decreasing the modulus of the probe material is one commonly explored/hypothesized methods to increase flexibility of the device. Probes made of polymers with a modulus or overall stiffness closer to brain tissue such as PDMS, polyimide, and SU-8 have been explored (Rousche et al., 2001; McClain et al., 2011; Altuna et al., 2013). However, implanting such soft probes present challenges with their insertion into the brain. A probe with too soft of a modulus will buckle during insertion and compress the brain tissue during the insertion process (Hess et al., 2013; Jorfi et al., 2015). Current methods used to implant soft electrodes while avoiding buckling include temporarily increasing the stiffness of the probe by use of a coating that dissolves after implantation or a stiff shuttle that accompanies the soft probe and is later removed (Lewitus et al., 2011; Kim B.J. et al., 2013; Kozai et al., 2014a; Vitale et al., 2015). Unfortunately, both approaches increase the footprint of the primary implant which can exacerbate the acute damage to brain tissue during implantation and lead to an increase in inflammation.

Materials which are innately stiff enough to implant, but soften while residing in tissue minimize the modulus

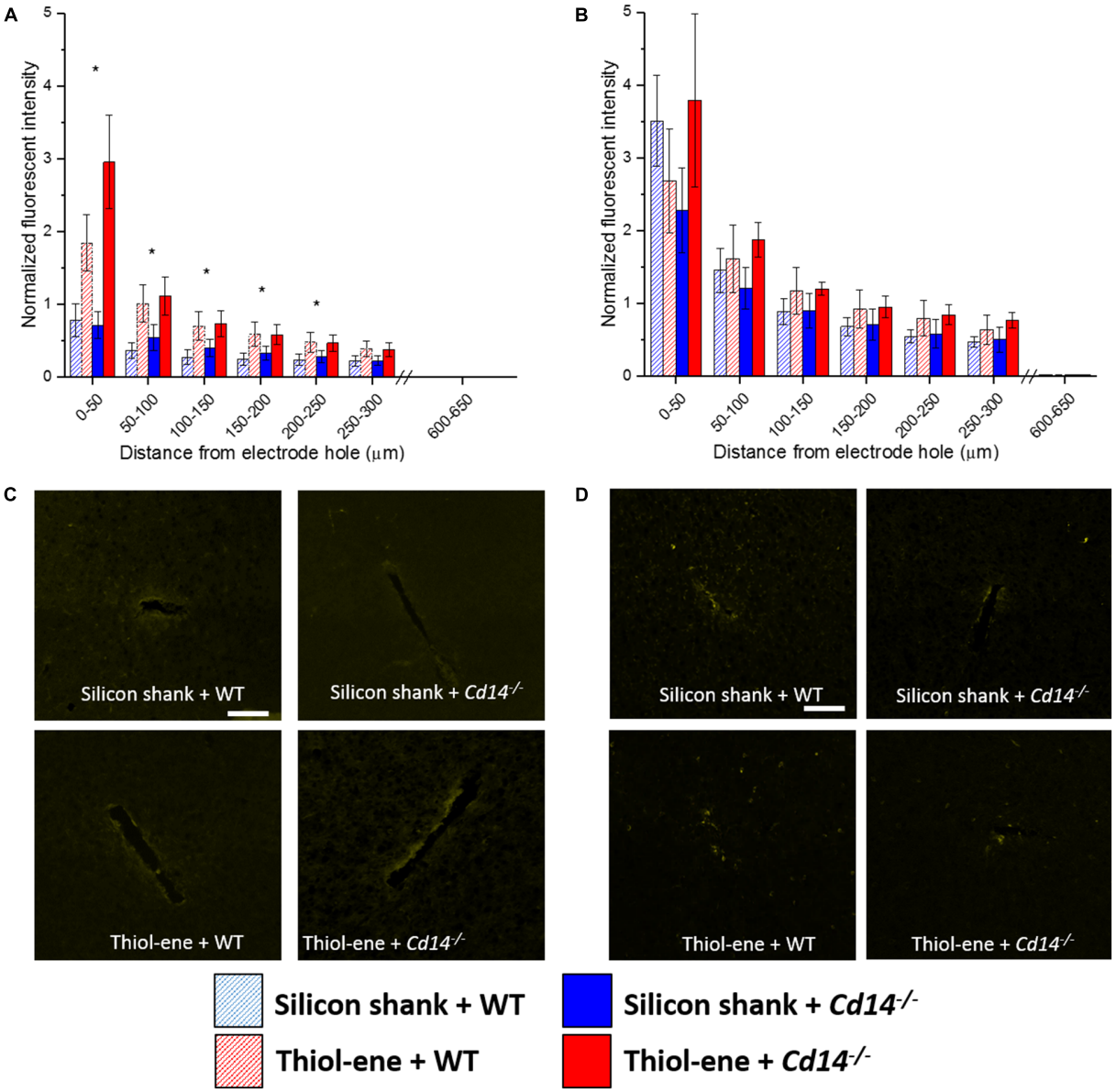

FIGURE 5 | Immunohistochemical evaluation of blood-brain barrier permeability. Blood–brain barrier permeability evaluated as IgG expression with respect to distance from the explanted microelectrode hole (μm). **(A)** 2 weeks. **(B)** 16 weeks. **(C)** Representative images of 2 weeks BBB permeability. **(D)** Representative images of 16 weeks BBB permeability. Scale bar: 100 μm. * Denotes significance between silicon and thiol-ene probes.

difference between probe and brain tissue. Previous literature has suggested that a softening material can compensate for increased damage footprint generated by a device with a larger cross-sectional area compared to a stiff silicon control probe (Nguyen et al., 2014). However, we found this phenomenon to be inconsistent in the current study as the larger thiol-ene probes had a larger cross-sectional area and resulted in more activated microglia/macrophages and increased evidence of BBB breakdown at 2 weeks compared to the smaller, stiffer silicon probes (**Figures 4A,C**, **5A,C**).

The thiol-ene probes used in the current study had a cross-sectional area of about 9000 μm^2, which is a 4× increase over the silicon probes utilized. The bending stiffness of the probe is determined by both the Young's modulus (E) and the probe dimensions. Although modulus of the probe material affects flexibility of the device, the probe dimensions play more of a role in reducing stiffness; bending stiffness is proportional to Et^3, where t is the cross-sectional area of the probe (Salatino et al., 2017).

A larger implant confers more acute tissue damage during implantation leading to greater extravasation of blood cells and proteins (Saxena et al., 2013). However, Nguyen et al. showed that a polyvinyl acetate, another softening material, can overcome increased inflammation induced by a slightly larger penetration

profile. The polyvinyl acetate probes used in Nguyen et al. (2014) had a pre-implant cross-sectional area that was 1.5× larger than control polyvinyl acetate dip-coated silicon probes. However, findings by Nguyen et al. (2014) were not recapitulated with thiol-ene, as the thiol-ene resulted in more activated microglia and macrophages and increased BBB permeability compared to the silicon probes (**Figures 4**, **5**). Therefore, there might be a size threshold to where a probe comprised of a softer material cannot overcome the increased inflammation resulting from an increased penetration profile.

The results from the current study suggest that the degree of initial trauma influences acute but not chronic inflammatory response, as there were significant results at 2 weeks post implantation, but there were no differences in the inflammatory response or neuronal density at 16 weeks between implants of different sizes (**Figures 2B**, **3B**, **4B**, **5B**). Current findings are consistent with Szarowski et al. (2003) which suggests initial glial response is correlated with the cross-sectional area of the electrode; however, sustained response of the implant was independent of probe size.

The different swelling properties of thiol-ene and polyvinyl acetate could also elicit differences in inflammation. The polyvinyl acetate swells ∼70% by volume under physiological conditions (Nguyen et al., 2014), while the thiol-ene substrate yields very minimal (<3%) swelling in physiologic environment (Ware et al., 2014). From a fabrication standpoint, minimal swelling is desirable as fluid uptake from the substrate results in cracking of thin film conductors used for the electrodes. However, as posited by Skousen et al. (2015), the thick hydrogel formed by the swollen polyvinyl acetate could have functioned as a sink for pro-inflammatory cytokines and chemokines at the probe–tissue interface, both of which facilitate inflammation. Reduced pro-inflammatory molecules at the device interface can lead to decreased inflammation and neuronal death. Future studies will need to explore the aforementioned theory.

In the current study, the thiol-ene probe resulted in an increased inflammatory response, likely because of its greater surface area and vascular damage during implantation, consistent with previously published research (Karumbaiah et al., 2013; Lee et al., 2017b; Spencer et al., 2017). The thiol-ene materials utilized in the present study have previously undergone testing to control for material surface chemistry. Shoffstall et al. (2018a) demonstrated that intracortical silicon probes dip-coated with the SMP material (SI, Section "Materials and Methods") generated similar histological responses (with respect to neuronal survival, activated microglia/macrophages, and BBB permeability) as compared to size-matched bare-silicon probes. While there was a statistically significant reduction in reactive astrocyte staining (GFAP) with the dip-coated probes, taken by itself it is unclear if the effects are substantially different from the bare silicon probes. Similar results suggestive of the effects of cross-sectional dimensions are found using a chemistry-controlled experiment (**Supplementary Figure S1**). Thiol-ene probes with larger cross-sectional width were compared to silicon probes dip-coated with the thiol-ene material, hereby setting up a chemistry-controlled comparison. Neuronal survival around the larger thiol-ene probes appears to be consistently lower compared to the smaller dip-coated probes, at both 2 and 16 weeks after implantation. Thus, the differences in size of the two probes in the current study are the most likely driver for the heightened inflammatory response of the thiol-ene probes.

Our study adds to the current body of research which suggests that size of the implant is a very important consideration in intracortical microelectrode design and too large of an implant can counteract benefit conferred by improved material selection or approaches to target the biology (Seymour and Kipke, 2007). Based on these and other findings from the field, size of the implant needs to be a major consideration for electrode design.

The current study further highlights the importance of CD14 for microglial and macrophage responses to DAMPs. As previously reported, CD14 is central for microglial responses to damage signals in the brain (Janova et al., 2016). In this current study, $Cd14^{-/-}$ resulted in higher neuronal density (**Figures 2A,C**) and decreased glial scar (**Figures 3A,C**) at 2 weeks post implantation, further revealing the importance of CD14 as a molecular target to reduce neuroinflammation. In our past work, we have demonstrated that partial inhibition of CD14 (in myeloid cells) was shown to improve single-shank, multi-channel electrode performance over time, whereas a complete CD14 inhibition did not result in such promising electrode performance (Bedell et al., 2018). In the current study, coupling complete inhibition of CD14 with the thiol-ene probe not only prevented exaggerated frustrated phagocytosis but also inhibited proper wound healing; the promising effects afforded by targeting CD14 were not able overcome the detriments of a larger probe size. However, the promising results of partial CD14 inhibition suggest that controlled of the thiol-ene inhibition of CD14 with a drug may still be promising for the integration of softer probes.

The dimensions of the thiol-ene probe are larger than that of the silicon probe, likely contributing to the increased inflammation seen on the thiol-ene probes compared to the uncoated silicon probes. The length of the thiol-ene probe taper (1.4 mm) is greater than that of the uncoated silicon probe taper (0.6 mm). However, the angle of their tips are similar, at 41.6° and 47°, respectively. As such, the differences in the angle between the tips are not expected to contribute significantly to vascular damage and hence tissue response; it is unlikely to affect our study. It also should be noted that there are conflicting reports in the literature to the benefits/disadvantages of different insertion speeds. Although Bjornsson et al. (2006) report that *fast* insertion (2 mm/s) results in less vascular damage and tissue strain, there are other reports indicating that slower insertion speeds afford time for tissue to adapt to probe thus decreasing compressive forces (Edell et al., 1992; Andrei et al., 2011).

Together, the results found in the current study suggest that large cross-sectional area probes comprised of a minimally swelling, yet softening material cannot overcome inflammation driven by large penetration profile differences. Accordingly, the differences in the size of the electrodes is a major limitation of our study. Overall, the results presented here highlight the detriment of only considering one or two aspects of probe design and mitigation of biological response. When approaching translatable strategies to improve chronic intracortical microelectrode

performance by decreasing inflammation, one needs to consider many characteristics in tandem.

CONCLUSION

The current manuscript demonstrates the impact of size of the probe on the initial stages of inflammation. To reduce inflammation, the cross-sectional area of the probe should be minimized. The current study also characterizes the acute benefits of targeting CD14 and further confirms the TLR/CD14 pathway as a mechanism amenable for therapeutic targeting. In the initial weeks after probe implantation, the benefits a minimally swelling soft probe affords does not exceed the inflammation driven by a probe with 4× the cross-sectional area. When optimizing probe design for intracortical microelectrodes, many elements of the probe need to be carefully considered, especially size.

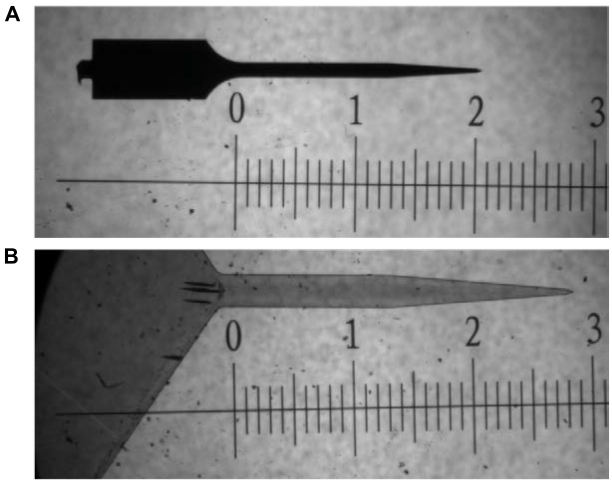

FIGURE 6 | Bright field microscope image comparing dimensions of probes used in study. **(A)** uncoated silicon probe and **(B)** thiol-ene probe. Both images are taken at 5× magnification. Scale is in mm.

MATERIALS AND METHODS

Electrodes

Single shank, uncoated, Michigan style silicon probes (2 mm × 15 μm × 123 μm; 47° taper angle) and thiol-ene based shape memory polymer (SMP) probes (3 mm × 30 μm × 290 μm; 41.6° taper angle) were used as intracortical probes (**Figure 6**). Polymer films were fabricated as previously described (Ecker et al., 2017). Briefly, 0.5 mol% 1,3,5-triallyl-1,3,5-triazine-2,4,6(1H,3H,5H)-trione (TATATO), 0.45 mol% trimethylolpropane tris(3-mercaptopropionate) (TMTMP), and 0.05 mol% Tris[2-mercaptopropionyloxy)ethyl] isocyanurate (TMICN) were mixed with 0.1 wt% of photoinitiator 2,2-dimethoxy-2-phenylacetophenone (DMPA). The polymer solution was then spin coated on glass slides using a spin coater (Laurell WS-650-23B) to receive ∼33 μm films before they were cured for 2 h at 254 nm (UVP CL-1000 cross-linking chamber) followed by an overnight post-cure at 120 °C under vacuum. Dummy probes were fabricated in the UT Dallas Class 10000 cleanroom facility. The 33-μm SMP-on-glass substrates were used as the starting substrates in the cleanroom. Low temperature silicon nitride (using PlasmaTherm-790 PECVD) was deposited to act as a hard mask for the following plasma etching processes. The device outline/shape was then patterned using standard lithography techniques. The hard mask and the SMP layer were plasma etched in Technics RIE using SF_6 and O_2 plasma, respectively. After the 30-μm SMP layer was plasma etched down to the glass slide, the remaining silicon nitride hard mask was etched away in diluted 10:1 HF dip. A ∼3 μm SMP layer from the surface of these devices was etched in Technics RIE using O_2 plasma. The devices were then released by soaking in DIW. The material is characterized by a glass transition temperature (T_g) of 52°C before, and 35 °C after softening under physiological conditions as measured by dynamic mechanical analysis (TA RSA-G2). The storage modulus E' at 37°C (measured in tension) changes from 1.2 GPa (dry) to 35 MPa (soaked). Stainless-steel wires (∼3 mm length) were used as dummy ground and reference wires to mimic the implants involved with functional probes. Probes and wires were sterilized *via* a cold ethylene oxide gas cycle as previously described.

Animals

C57/BL6 (strain #000664) and $Cd14^{-/-}$ (C57/BL6 background) (strain #003726) were bred in-house. Strain of $Cd14^{-/-}$ mice was verified *via* genotyping according to the protocols established by the vendor (Jackson Laboratories). Both male and female mice between 8 and 12 weeks of age were used for surgeries. Prior to surgery, mice were group housed with food and water *ad libitium* while maintained on a 12-h light/dark cycle. After surgery, mice were individually housed. All animal handling was performed in a class II sterile hood using microisolator techniques. All procedures and animal care practices comply with the protocol approved by the Case Western Reserve University Institutional Animal Care and Use Committee.

Surgical Implantation of Electrodes

A total of three holes were drilled in the exposed skull using a 0.45 mm size bit (Stoetling Co.) with adequate breaks in the drilling pulses to prevent overheating of the skull (Shoffstall et al., 2018b). The probe hole was created in the skull over the motor region of the brain (1.5 mm lateral and 0.5 mm anterior to bregma) (Tennant et al., 2011). Two additional craniotomies were conducted for dummy ground and reference wires which were implanted in the contralateral hemisphere to the probe (∼2 mm lateral, ∼2 mm rostral and caudal to bregma). The dummy probes and dummy wires were manually inserted (∼2–3 mm/s) into the cortex. Silicone elastomer (Kwik-Sil, World Precision Instruments) and dental acrylic (Fusio/Flow-it ALC, Patterson Dental) tethered the probe and wires to the skull. The incision site was then sutured closed using 5-0 monofilment polypropylene suture. To minimize variability, the same surgeon performed all implantation surgeries.

TABLE 1 | Number of experimental animals for each condition at each time point.

	2 weeks post implantation	16 weeks post implantation
Silicon shank + WT	10	6
Thiol-ene + WT	10	4
Silicon shank + *Cd14*$^{-/-}$	8	6
Thiol-ene + *Cd14*$^{-/-}$	9	4

Immunohistochemistry

At each 2 and 16 weeks post-implantation, mice were sacrificed and brain tissue was harvested. At the respective time point, mice were anesthetized with an intraperitoneal injection of ketamine/xylazine cocktail. Each animal was then transcardially perfused with phosphate buffered saline (PBS) followed by 4% paraformaldehyde (PFA) to fix the tissue. Mouse heads were post-fixed for an additional 2 days in 4% PFA at 4°C. After fixation, brains were extracted and immersed in 30% sucrose for at least 48 h. After dummy electrodes and wires were removed, brain tissue was cryopreserved in optimal cutting temperature compound (OCT) (Tissue-Tek). Horizontal brain tissue sections (16 μm thick) were obtained using a cryostat and stored at −80°C.

To compare neuroinflammation and neuronal density in the area adjacent the implanted dummy shank among conditions, immunohistochemistry was utilized using previously established methodology (Potter et al., 2014). Only tissue slices between ∼320 and 1000 μm from the surface of the cortex were used as this depth corresponds with Layers III–VI of the mouse motor cortex, the layers from which functional probes aim to record (Oswald et al., 2013). After blocking the tissue (4% chicken serum, 0.3% Trition-X-100 in 1× PBS), the following primary antibodies (in 4% chicken serum, 0.3% Trition-X-100 in 1× PBS) were added to incubate overnight at 4 °C: Rabbit anti-GFAP (1:500, Z0334, Dako), mouse anti-neuronal nuclei (NeuN) (1:250, MAB377, Millipore), rat anti-CD68 (1:500, ab53444, Abcam), and rabbit anti-immunoglobulin G (IgG) (1:500, STAR26B, Bio-Rad). Visualization of the inflammatory and neuronal markers was achieved with respective Alexa Fluor® secondary antibodies (1:1000) (in 4% chicken serum, 0.3% Trition-X-100 in 1× PBS). DAPI (Molecular Probes D3571) was incorporated in secondary antibody solution to visualize cell nuclei. Furthermore, tissue autofluorescence was reduced by incubating tissue sections with of 0.5 mM copper sulfate buffer solution for 10 min (Potter et al., 2012b). Finally, copper sulfate buffer was washed off thoroughly with MilliQ H_2O, and slides were coverslipped using Fluoromount-G. Slides were stored in the dark at 4 °C until imaged.

Imaging and Quantitative Analysis

Images were acquired using a 10× objective on a Carl Zeiss AxioObserver.Z1 (Zeiss Inc.) inverted epifluorescence microscope. Fluorescent markers were imaged on single optical sections using an AxioCam MRm monochrome camera with fixed exposure times for each marker.

Images of fluorescent markers were analyzed using SECOND, a custom-written MATLAB program previously used in the Capadona lab (Goss-Varley et al., 2017). The fluorescent intensity of each marker in concentric rings at fixed distances (normalized by area) from the probe–tissue interface was measured as a function of distance from the implant. Prior to measurement, the user defines the implant hole and any imperfections in the brain slice to omit from the analysis. For each slice, raw fluorescent intensities were then normalized to background signal, defined as the fluorescent intensity of the concentric ring 600–650 μm from the interface. The area under the curve (AUC) was calculated from the intensity profile.

Neuronal densities at the interface were determined using AfterNeuN, another custom-written MATLAB program. Using AfterNeuN, the user manually defines the electrode implant region, any areas to be excluded from analysis, and neuronal cell bodies. The program then outputs the density of neurons at fixed radial distances from the electrode interface. Neuronal densities at uniform binned distances (50 μm bins) were then normalized to background counts from the same brain tissue slice 300–350 μm away from the interface.

Immunohistochemistry Statistical Analysis

Table 1 indicates number of animals for each condition at each time point. Measurements from all brain tissue slices for a given animal were first averaged together (four to six brain slices per animal, average of 5.29 ± 0.87). Average intensity or count for a given condition was calculated using independent animal averages. Statistical analyses for the first experiment, comparing thiol-ene + *Cd14*$^{-/-}$ to silicon shank + WT were performed using unpaired *t*-tests. All statistical analyses assessing immunohistochemical results comparing all four conditions were performed using a general linear model with a two-way analysis of variance (ANOVA) using Minitab software with genotype (WT or *Cd14*$^{-/-}$) and electrode material (uncoated silicon or thiol-ene) as separate factors. Results were considered significant at $p < 0.05$ and expressed as mean ± standard error of mean.

AUTHOR CONTRIBUTIONS

HB, WV, JP, and JC contributed substantially to the conception or design of the work, analysis, and interpretation of data for the work, drafting, and revising the manuscript for important intellectual content, approved the final version to be published, and agreed to be accountable for all aspects of the work. HB, SS, XL, EM, AJS, and SL aided in the collection and analysis of histological data. AS, ME, and VD fabricated and characterized the SMP probes. All authors approved the final version to be published and agreed to be accountable for all aspects of the work.

FUNDING

The current work was supported in part by the Department of Biomedical Engineering and Case School of Engineering at

Case Western Reserve University through laboratory start-up funds, the National Institute of Health, National Institute of Neurological Disorders and Stroke (Grant # 1R01NS082404-01A1), and the NIH Neuroengineering Training Grant 5T-32EB004314-16. Additional support was provided by the Presidential Early Career Award for Scientists and Engineers (PECASE, JR. Capadona), by Merit Review Awards B1495-R and B2611-R from the United States Department of Veterans Affairs Rehabilitation Research and Development Service, and in part by the Office of the Assistant Secretary of Defense for Health Affairs through the Peer Reviewed Medical Research Program under Award no. W81XWH-15-1-0607 and W81XWH-15-1-0608. None of the funding sources aided in collection, analysis, and interpretation of the data, in writing of the manuscript, or in the decision to submit the manuscript for publication. The contents do not represent the views of the U.S. Department of Veterans Affairs or the United States Government.

SUPPLEMENTARY MATERIAL

The Supplementary Material for this article can be found online at: https://www.frontiersin.org/articles/10.3389/fnins.2018.00772/full#supplementary-material

REFERENCES

Abdul-Muneer, P., Chandra, N., and Haorah, J. (2015). Interactions of oxidative stress and neurovascular inflammation in the pathogenesis of traumatic brain injury. *Mol. Neurobiol.* 51, 966–979. doi: 10.1007/s12035-014-8752-3

Altuna, A., Bellistri, E., Cid, E., Aivar, P., Gal, B., Berganzo, J., et al. (2013). SU-8 based microprobes for simultaneous neural depth recording and drug delivery in the brain. *Lab Chip* 13, 1422–1430. doi: 10.1039/c3lc41364k

Andrei, A., Welkenhuysen, M., Nuttin, B., and Eberle, W. (2011). A response surface model predicting the in vivo insertion behavior of micromachined neural implants. *J. Neural Eng.* 9:016005. doi: 10.1088/1741-2560/9/1/016005

Barrese, J. C., Rao, N., Paroo, K., Triebwasser, C., Vargas-Irwin, C., Franquemont, L., et al. (2013). Failure mode analysis of silicon-based intracortical microelectrode arrays in non-human primates. *J. Neural Eng.* 10:066014. doi: 10.1088/1741-2560/10/6/066014

Bedell, H. W., Hermann, J. K., Ravikumar, M., Lin, S., Rein, A., Li, X., et al. (2018). Targeting CD14 on blood derived cells improves intracortical microelectrode performance. *Biomaterials* 163, 163–173. doi: 10.1016/j.biomaterials.2018.02.014

Bjornsson, C. S., Oh, S. J., Al-Kofahi, Y. A., Lim, Y. J., Smith, K. L., Turner, J. N., et al. (2006). Effects of insertion conditions on tissue strain and vascular damage during neuroprosthetic device insertion. *J. Neural Eng.* 3, 196–207. doi: 10.1088/1741-2560/3/3/002

Capadona, J. R., Shanmuganathan, K., Tyler, D. J., Rowan, S. J., and Weder, C. (2008). Stimuli-responsive polymer nanocomposites inspired by the sea cucumber dermis. *Science* 319, 1370–1374. doi: 10.1126/science.1153307

Du, Z. J., Kolarcik, C. L., Kozai, T. D., Luebben, S. D., Sapp, S. A., Zheng, X. S., et al. (2017). Ultrasoft microwire neural electrodes improve chronic tissue integration. *Acta Biomater.* 53, 46–58. doi: 10.1016/j.actbio.2017.02.010

Ecker, M., Danda, V., Shoffstall, A. J., Mahmood, S. F., Joshi-Imre, A., Frewin, C. L., et al. (2017). Sterilization of Thiol-ene/Acrylate based shape memory polymers for biomedical applications. *Macromol. Mater. Eng.* 302:1600331. doi: 10.1002/mame.201600331

Edell, D. J., Toi, V., McNeil, V. M., and Clark, L. (1992). Factors influencing the biocompatibility of insertable silicon microshafts in cerebral cortex. *IEEE Trans. Biomed. Eng.* 39, 635–643. doi: 10.1109/10.141202

Gilletti, A., and Muthuswamy, J. (2006). Brain micromotion around implants in the rodent somatosensory cortex. *J. Neural Eng.* 3, 189–195. doi: 10.1088/1741-2560/3/3/001

Goss-Varley, M., Dona, K. R., McMahon, J. A., Shoffstall, A. J., Ereifej, E. S., Lindner, S. C., et al. (2017). Microelectrode implantation in motor cortex causes fine motor deficit: implications on potential considerations to brain computer interfacing and human augmentation. *Sci. Rep.* 7:15254. doi: 10.1038/s41598-017-15623-y

Green, M. A., Bilston, L. E., and Sinkus, R. (2008). In vivo brain viscoelastic properties measured by magnetic resonance elastography. *NMR Biomed.* 21, 755–764. doi: 10.1002/nbm.1254

Harris, J., Hess, A. E., Rowan, S. J., Weder, C., Zorman, C., Tyler, D., et al. (2011). In vivo deployment of mechanically adaptive nanocomposites for intracortical microelectrodes. *J. Neural Eng.* 8:046010. doi: 10.1088/1741-2560/8/4/046010

Hermann, J. K., Ravikumar, M., Shoffstall, A., Ereifej, E. S., Kovach, K., Chang, J., et al. (2017). Inhibition of the cluster of differentiation 14 innate immunity pathway with IAXO-101 improves chronic microelectrode performance. *J. Neural Eng.* 15:025002. doi: 10.1088/1741-2552/aaa03e

Hess, A. E., Potter, K. A., Tyler, D. J., Zorman, C. A., and Capadona, J. R. (2013). Environmentally-controlled microtensile testing of mechanically-adaptive polymer nanocomposites for ex vivo characterization. *J. Vis. Exp.* 78:e50078. doi: 10.3791/50078

Hochberg, L. R., Bacher, D., Jarosiewicz, B., Masse, N. Y., Simeral, J. D., Vogel, J., et al. (2012). Reach and grasp by people with tetraplegia using a neurally controlled robotic arm. *Nature* 485, 372–375. doi: 10.1038/nature11076

Janova, H., Böttcher, C., Holtman, I. R., Regen, T., van Rossum, D., Götz, A., et al. (2016). CD14 is a key organizer of microglial responses to CNS infection and injury. *Glia* 64, 635–649. doi: 10.1002/glia.22955

Jorfi, M., Skousen, J. L., Weder, C., and Capadona, J. R. (2015). Progress towards biocompatible intracortical microelectrodes for neural interfacing applications. *J. Neural Eng.* 12:011001. doi: 10.1088/1741-2560/12/1/011001

Karumbaiah, L., Saxena, T., Carlson, D., Patil, K., Patkar, R., Gaupp, E. A., et al. (2013). Relationship between intracortical electrode design and chronic recording function. *Biomaterials* 34, 8061–8074. doi: 10.1016/j.biomaterials.2013.07.016

Kim, B. J., Kuo, J. T., Hara, S. A., Lee, C. D., Yu, L., Gutierrez, C., et al. (2013). 3D Parylene sheath neural probe for chronic recordings. *J. Neural Eng.* 10:045002. doi: 10.1088/1741-2560/10/4/045002

Kim, S., Kim, S. Y., Pribis, J. P., Lotze, M., Mollen, K. P., Shapiro, R., et al. (2013). Signaling of high mobility group box 1 (HMGB1) through toll-like receptor 4 in macrophages requires CD14. *Mol. Med.* 19, 88–98. doi: 10.2119/molmed.2012.00306

Kozai, T. D., Gugel, Z., Li, X., Gilgunn, P. J., Khilwani, R., Ozdoganlar, O. B., et al. (2014a). Chronic tissue response to carboxymethyl cellulose based dissolvable insertion needle for ultra-small neural probes. *Biomaterials* 35, 9255–9268. doi: 10.1016/j.biomaterials.2014.07.039

Kozai, T. D., Li, X., Bodily, L. M., Caparosa, E. M., Zenonos, G. A., Carlisle, D. L., et al. (2014b). Effects of caspase-1 knockout on chronic neural recording quality and longevity: insight into cellular and molecular mechanisms of the reactive tissue response. *Biomaterials* 35, 9620–9634. doi: 10.1016/j.biomaterials.2014.08.006

Landis, D. M. D. (1994). The early reactions of nonneuronal cells to brain injury. *Annu. Rev. Neurosci.* 17, 133–151. doi: 10.1146/annurev.ne.17.030194.001025

Lee, H. C., Ejserholm, F., Gaire, J., Currlin, S., Schouenborg, J., Wallman, L., et al. (2017a). Histological evaluation of flexible neural implants; flexibility limit for reducing the tissue response? *J. Neural Eng.* 14:036026. doi: 10.1088/1741-2552/aa68f0

Lee, H. C., Gaire, J., Currlin, S. W., McDermott, M. D., Park, K., and Otto, K. J. (2017b). Foreign body response to intracortical microelectrodes is not altered with dip-coating of polyethylene glycol (PEG). *Front. Neurosci.* 11:513. doi: 10.3389/fnins.2017.00513

Lewitus, D., Smith, K. L., Shain, W., and Kohn, J. (2011). Ultrafast resorbing polymers for use as carriers for cortical neural probes. *Acta Biomater.* 7, 2483–2491. doi: 10.1016/j.actbio.2011.02.027

Liu, X., McCreery, D. B., Bullara, L. A., and Agnew, W. F. (2006). "Evaluation of the stability of intracortical microelectrode arrays," in *Proceedings of the IEEE Transactions on Neural Systems and Rehabilitation Engineering*, Vol. 14, (Piscataway, NJ: IEEE), 91–100.

McClain, M. A., Clements, I. P., Shafer, R. H., Bellamkonda, R. V., LaPlaca, M. C., and Allen, M. G. (2011). Highly-compliant, microcable neuroelectrodes fabricated from thin-film gold and PDMS. *Biomed. Microdevices* 13, 361–373. doi: 10.1007/s10544-010-9505-3

Moshayedi, P., Ng, G., Kwok, J. C., Yeo, G. S., Bryant, C. E., Fawcett, J. W., et al. (2014). The relationship between glial cell mechanosensitivity and foreign body reactions in the central nervous system. *Biomaterials* 35, 3919–3925. doi: 10.1016/j.biomaterials.2014.01.038

Mullen, R. J., Buck, C. R., and Smith, A. M. (1992). NeuN, a neuronal specific nuclear protein in vertebrates. *Development* 116, 201–211.

Nguyen, J. K., Park, D. J., Skousen, J. L., Hess-Dunning, A., Tyler, D. J., Rowan, S. J., et al. (2014). Mechanically-compliant intracortical implants reduce the neuroinflammatory response. *J. Neural Eng.* 11:056014. doi: 10.1088/1741-2560/11/5/056014

Nuzzo, R. G., Fusco, F. A., and Allara, D. L. (1987). Spontaneously organized molecular assemblies. 3. Preparation and properties of solution adsorbed monolayers of organic disulfides on gold surfaces. *J. Am. Chem. Soc.* 109, 2358–2368. doi: 10.1021/ja00242a020

Oswald, M. J., Tantirigama, M. L., Sonntag, I., Hughes, S. M., and Empson, R. M. (2013). Diversity of layer 5 projection neurons in the mouse motor cortex. *Front. Cell. Neurosci.* 7:174. doi: 10.3389/fncel.2013.00174

Polikov, V. S., Tresco, P. A., and Reichert, W. M. (2005). Response of brain tissue to chronically implanted neural electrodes. *J. Neurosci. Methods* 148, 1–18. doi: 10.1016/j.jneumeth.2005.08.015

Potter, K. A., Buck, A. C., Self, W. K., and Capadona, J. R. (2012a). Stab injury and device implantation within the brain results in inversely multiphasic neuroinflammatory and neurodegenerative responses. *J. Neural Eng.* 9:046020. doi: 10.1088/1741-2560/9/4/046020

Potter, K. A., Simon, J. S., Velagapudi, B., and Capadona, J. R. (2012b). Reduction of autofluorescence at the microelectrode-cortical tissue interface improves antibody detection. *J. Neurosci. Methods* 203, 96–105. doi: 10.1016/j.jneumeth.2011.09.024

Potter, K. A., Jorfi, M., Householder, K. T., Foster, E. J., Weder, C., and Capadona, J. R. (2014). Curcumin-releasing mechanically adaptive intracortical implants improve the proximal neuronal density and blood–brain barrier stability. *Acta Biomater.* 10, 2209–2222. doi: 10.1016/j.actbio.2014.01.018

Ravikumar, M., Sunil, S., Black, J., Barkauskas, D., Haung, A. Y., Miller, R. H., et al. (2014). The roles of blood-derived macrophages and resident microglia in the neuroinflammatory response to implanted intracortical microelectrodes. *Biomaterials* 35, 8049–8064. doi: 10.1016/j.biomaterials.2014.05.084

Rennaker, R. L., Miller, J., Tang, H., and Wilson, D. A. (2007). Minocycline increases quality and longevity of chronic neural recordings. *J. Neural Eng.* 4, L1–L5.

Renshaw, B., Forbes, A., and Morison, B. (1940). Activity of isocortex and hippocampus: electrical studies with micro-electrodes. *J. Neurophysiol.* 3, 74–105. doi: 10.1152/jn.1940.3.1.74

Rousche, P. J., Pellinen, D. S., Pivin, D. P., Williams, J. C., Vetter, R. J., and Kipke, D. R. (2001). Flexible polyimide-based intracortical electrode arrays with bioactive capability. *IEEE Trans. Biomed. Eng.* 48, 361–371. doi: 10.1109/10.914800

Salatino, J. W., Ludwig, K. A., Kozai, T. D., and Purcell, E. K. (2017). Glial responses to implanted electrodes in the brain. *Nat. Biomed. Eng.* 1, 862–877. doi: 10.1038/s41551-017-0154-1

Saxena, T., Karumbaiah, L., Gaupp, E. A., Patkar, R., Patil, K., Betancur, M., et al. (2013). The impact of chronic blood–brain barrier breach on intracortical electrode function. *Biomaterials* 34, 4703–4713. doi: 10.1016/j.biomaterials.2013.03.007

Schwartz, A. B. (2004). Cortical neural prosthetics. *Annu. Rev. Neurosci.* 27, 487–507. doi: 10.1146/annurev.neuro.27.070203.144233

Seymour, J. P., and Kipke, D. R. (2007). Neural probe design for reduced tissue encapsulation in CNS. *Biomaterials* 28, 3594–3607. doi: 10.1016/j.biomaterials.2007.03.024

Shoffstall, A. J., Danda, V., Joshi-Imre, A., Stiller, A., Yu, M., Paiz, J., et al. (2018a). Characterization of the neuroinflammatory response to thiol-ene shape memory polymer coated intracortical microelectrodes. *Micromachines* 9:486. doi: 10.3390/mi9100486

Shoffstall, A. J., Paiz, J. E., Miller, D. M., Rial, G. M., Willis, M. T., Menendez, D. M., et al. (2018b). Potential for thermal damage to the blood–brain barrier during craniotomy: implications for intracortical recording microelectrodes. *J. Neural Eng.* 15:034001. doi: 10.1088/1741-2552/aa9f32

Simon, D. M., Charkhkar, H., St John, C., Rajendran, S., Kang, T., Reit, R., et al. (2017). Design and demonstration of an intracortical probe technology with tunable modulus. *J. Biomed. Mater. Res. A* 105, 159–168. doi: 10.1002/jbm.a.35896

Skousen, J. L., Bridge, M. J., and Tresco, P. A. (2015). A strategy to passively reduce neuroinflammation surrounding devices implanted chronically in brain tissue by manipulating device surface permeability. *Biomaterials* 36, 33–43. doi: 10.1016/j.biomaterials.2014.08.039

Song, L., Lee, C., and Schindler, C. (2011). Deletion of the murine scavenger receptor CD68. *J. Lipid Res.* 52, 1542–1550. doi: 10.1194/jlr.M015412

Spencer, K. C., Sy, J. C., Ramadi, K. B., Graybiel, A. M., Langer, R., and Cima, M. J. (2017). Characterization of mechanically matched hydrogel coatings to improve the biocompatibility of neural implants. *Sci. Rep.* 7:1952. doi: 10.1038/s41598-017-02107-2

Sridharan, A., Nguyen, J. K., Capadona, J. R., and Muthuswamy, J. (2015). Compliant intracortical implants reduce strains and strain rates in brain tissue in vivo. *J. Neural Eng.* 12:036002. doi: 10.1088/1741-2560/12/3/036002

Subbaroyan, J., Martin, D. C., and Kipke, D. R. (2005). A finite-element model of the mechanical effects of implantable microelectrodes in the cerebral cortex. *J. Neural Eng.* 2, 103–113. doi: 10.1088/1741-2560/2/4/006

Szarowski, D., Andersen, M., Retterer, S., Spence, A., Isaacson, M., Craighead, H., et al. (2003). Brain responses to micro-machined silicon devices. *Brain Res.* 983, 23–35. doi: 10.1016/S0006-8993(03)03023-3

Tennant, K. A., Adkins, D. L., Donlan, N. A., Asay, A. L., Thomas, N., Kleim, J. A., et al. (2011). The organization of the forelimb representation of the C57BL/6 mouse motor cortex as defined by intracortical microstimulation and cytoarchitecture. *Cereb. Cortex* 21, 865–876. doi: 10.1093/cercor/bhq159

Vitale, F., Summerson, S. R., Aazhang, B., Kemere, C., and Pasquali, M. (2015). Neural stimulation and recording with bidirectional, soft carbon nanotube fiber microelectrodes. *ACS Nano* 9, 4465–4474. doi: 10.1021/acsnano.5b01060

Ware, T., Simon, D., Liu, C., Musa, T., Vasudevan, S., Sloan, A., et al. (2014). Thiol-ene/acrylate substrates for softening intracortical electrodes. *J. Biomed. Mater. Res. B Appl. Biomater.* 102, 1–11. doi: 10.1002/jbmb.32946

Wessberg, J., Stambaugh, C. R., Kralik, J. D., Beck, P. D., Laubach, M., Chapin, J. K., et al. (2000). Real-time prediction of hand trajectory by ensembles of cortical neurons in primates. *Nature* 408, 361–365. doi: 10.1038/35042582

Zanoni, I., Tan, Y., Di Gioia, M., Springstead, J. R., and Kagan, J. C. (2017). By capturing inflammatory lipids released from dying cells, the receptor CD14 induces inflammasome-dependent phagocyte hyperactivation. *Immunity* 47, 697.e3–709.e3. doi: 10.1016/j.immuni.2017.09.010

Conflict of Interest Statement: The authors declare that the research was conducted in the absence of any commercial or financial relationships that could be construed as a potential conflict of interest.

Critical Reviews™ *in Biomedical Engineering*, 46(4):341–367 (2018)

Understanding the Role of Innate Immunity in the Response to Intracortical Microelectrodes

John K. Hermann[a,b] & Jeffrey R. Capadona[a,b,*]

[a]Department of Biomedical Engineering, Case Western Reserve University, 2071 Martin Luther King Jr. Drive, Wickenden Bldg, Cleveland, OH 44106; [b]Advanced Platform Technology Center, Rehabilitation Research and Development, Louis Stokes Cleveland VA Medical Center, 10701 East Blvd. Mail Stop 151 AW/APT, Cleveland, OH 44106-1702

*Address all correspondence to: Jeffrey R. Capadona, Ph.D., Case Western Reserve University, 2071 Martin Luther King Jr. Drive, Cleveland, OH; Tel.: 216-368-5486, E-mail: jeffrey.capadona@case.edu

ABSTRACT: Intracortical microelectrodes exhibit enormous potential for researching the nervous system, steering assistive devices and functional electrode stimulation systems for severely paralyzed individuals, and augmenting the brain with computing power. Unfortunately, intracortical microelectrodes often fail to consistently record signals over clinically useful periods. Biological mechanisms, such as the foreign body response to intracortical microelectrodes and self-perpetuating neuroinflammatory cascades, contribute to the inconsistencies and decline in recording performance. Unfortunately, few studies have directly correlated microelectrode performance with the neuroinflammatory response to the implanted devices. However, of those select studies that have, the role of the innate immune system remains among the most likely links capable of corroborating the results of different studies, across laboratories. Therefore, the overall goal of this review is to highlight the role of innate immunity signaling in the foreign body response to intracortical microelectrodes and hypothesize as to appropriate strategies that may become the most relevant in enabling brain-dwelling electrodes of any geometry, or location, for a range of clinical applications.

KEY WORDS: intracortical microelectrodes, brain machine interfaces, neuroinflammatory response, neurodegeneration, biocompatibility, innate immunity

ABBREVIATIONS: ALS, amyotrophic lateral sclerosis; **CE**, Conformité Européene; **COX-2**, cyclooxygenase 2; **CD14**, cluster of differentiation 14; **DAMPs**, damage (or danger) associated molecular patterns; **DLB**, dementia with Lewy bodies; **ECM**, extracellular matrix; **FDA**, Food and Drug Administration; **HSP**, heat shock proteins; **HNMGB1**, High Mobility Group Box 1; **iNOS**, inducible nitric oxide synthetase; **IFN-α**, interferon-α; **IL**, interleukin; **LPS**, lipopolysaccharide; **LRR**, leucine-rich repeat; **MIP-1α**, macrophage inflammatory protein-1α; **MHC**, major histocompatibility complex; **MMP**, matrix metalloprotease; **MS**, multiple sclerosis; **MSA**, multiple system atrophy; **NLRs**, Nod-like receptors; **NO**, nitrous oxide; **PD**, Parkinson's disease; **PAMPs**, pathogen associated molecular patterns; **PRRs**, pattern-recognition receptors; **PACAP**, pituitary adenylate cyclase-activating polypeptide; **ROS**, reactive oxygen species; **RLRs**, retinoic acid-inducible gene-I-like receptors; **SSL3**, staphylococcal superantigen-like protein 3; **TLRs**, Toll-like receptors; **TNF** or **TNF-α**, tumor necrosis factor

I. INTRODUCTION

A. Failure of Intracortical Microelectrodes

In order to become a clinical solution for many brain interfacing applications, intracortical microelectrodes should ideally operate consistently over time ranges of years to decades to prevent the repetition of highly invasive brain surgeries. Unfortunately, intracortical microelectrodes fail to consistently record neural signals over extended periods. Many labs studying various chronically implanted intracortical microelectrodes have demonstrated trends of the decreasing number of units detected,[1–6] the number of channels detecting units,[1,2,7–11] signal amplitudes,[4,10,12] and decoder performance,[4] as well as generally inconsistent recording performance[1,7,13] and recording longevity,[8,10,13] regardless of the animal model. Together, such characteristics are not ideal for the long-term performance of brain-computer and brain-machine interfaces.

Declining and inconsistent recording performance has been ascribed to many failure mechanisms, typically grouped into mechanical, material, or biological mechanisms.[10] In their review, Barrese et al. defined mechanical failures as physical relocation or damage of the electrode array and hardware,

0278-940X/18 $35.00

material failures as breakdown of electrode array materials, and biological failures as a consequence of the foreign body response or implantation trauma following device insertion.[10] Mechanical and materials related failure modes have recently been reviewed and will not be discussed here (see Prasad et al., Barrese et al., Jorfi et al., and Kozai et al. for examples[7,9,10,14,15]). Biological failures are typically associated with the interruption of electrical signals between cortical neurons and recording contacts. They will be further described and discussed in the sections that follow.

B. Foreign Body Response to Intracortical Microelectrodes

Intracortical microelectrodes fail, in part, due to biological mechanisms, many of which result from the foreign body response to the implant and subsequent chronic inflammatory cascades (for review, see Jorfi et al.[14]). As a microelectrode array is inserted in the brain, blood vessels are ruptured,[16] releasing blood proteins into the brain parenchyma. Several components of blood, including proteins, can be neurotoxic.[17] Furthermore, tissue is displaced and neurons and glia cells along the insertion path are damaged or killed.[18] Blood proteins will adsorb to the surface of the electrode array and denature, upon which they are recognized by the brain's major inflammatory cells, the microglia.[19,20] Subsequently, microglia transition from a dormant ramified state to a pro-inflammatory amoeboid phenotype by retracting processes and upregulating lytic enzymes.[18] In the activated state, microglia are able to release a variety of soluble pro-inflammatory and cytotoxic factors, such as nitric oxide, reactive nitrogen species, and reactive oxygen species.[21–24] Evidence of oxidative gene expression and cellular oxidative damage have been detected at the electrode tissue interface.[25] Factors released by pro-inflammatory microglia likely contribute to neuronal death and neurodegeneration (Fig. 1).[21–24] Additionally, soluble factors released by microglia may damage the blood-brain barrier by disrupting tight adherens junctions connecting endothelial cells of the vasculature.[26] Furthermore, oxidative factors may also contribute to material degradation (Fig. 1).[27] Thus, consequences of electrode implantation and early inflammatory activation may contribute to the decline or unreliability of electrode performance.

Attracted by the release of soluble factors by nearby microglia, more microglia migrate from the parenchyma. Likewise, additional monocytes and other myeloid cells are recruited from circulation across the leaky blood-brain barrier.[28,29] Blood proteins and necrotic cells from insertion damage, as well as the early inflammatory response and leaky blood-brain barrier promote pro-inflammatory activation in the newly recruited inflammatory cells.[20,28,30] One pathway by which microglia and macrophages recognize such damage and enact pro-inflammatory responses is through Toll-like receptors (TLRs).[31] Later sections of this paper will discuss TLRs in depth. Soluble factors from the total collection of inflammatory cells around the implant may cause further damage to neurons, recording materials (Fig. 1), and the blood-brain barrier.[21–24] Repeated damage to cells and blood-vessels resulting in the recruitment and activation of more inflammatory cells is hypothesized to propagate self-perpetuated chronic inflammatory cascades indefinitely.[20,28] The neuronal and material damage resulting from self-perpetuating inflammatory cascades may contribute to long-term biological failure mechanisms.[20,28]

As the microglial and macrophage response matures, within days to weeks, the fibroblast of the brain, astrocytes, begin their response to the implantation of the microelectrode. Astrocytes proliferate, become hypertrophic, and migrate to the implantation site, ultimately resulting in a dense encapsulation layer around the electrode.[18] Astrocytic responses typically start wider and more diffuse, and then become denser and more compact over the course of several weeks.[18] Astrocytic encapsulation isolates the inflammatory or damaged region around the electrode from the surrounding parenchyma. In addition to astrocytes, meningeal fibroblasts may migrate to the electrode-tissue interface and contribute to electrode encapsulation.[6,10] Together, encapsulation of the electrode may interfere with diffusion of neuroactive substances,[32] increase the electrical impedance between the electrode and neurons,[13,33] increase the distance between neurons and electrodes,[13] or in extreme cases promote extrusion of electrode arrays.[10]

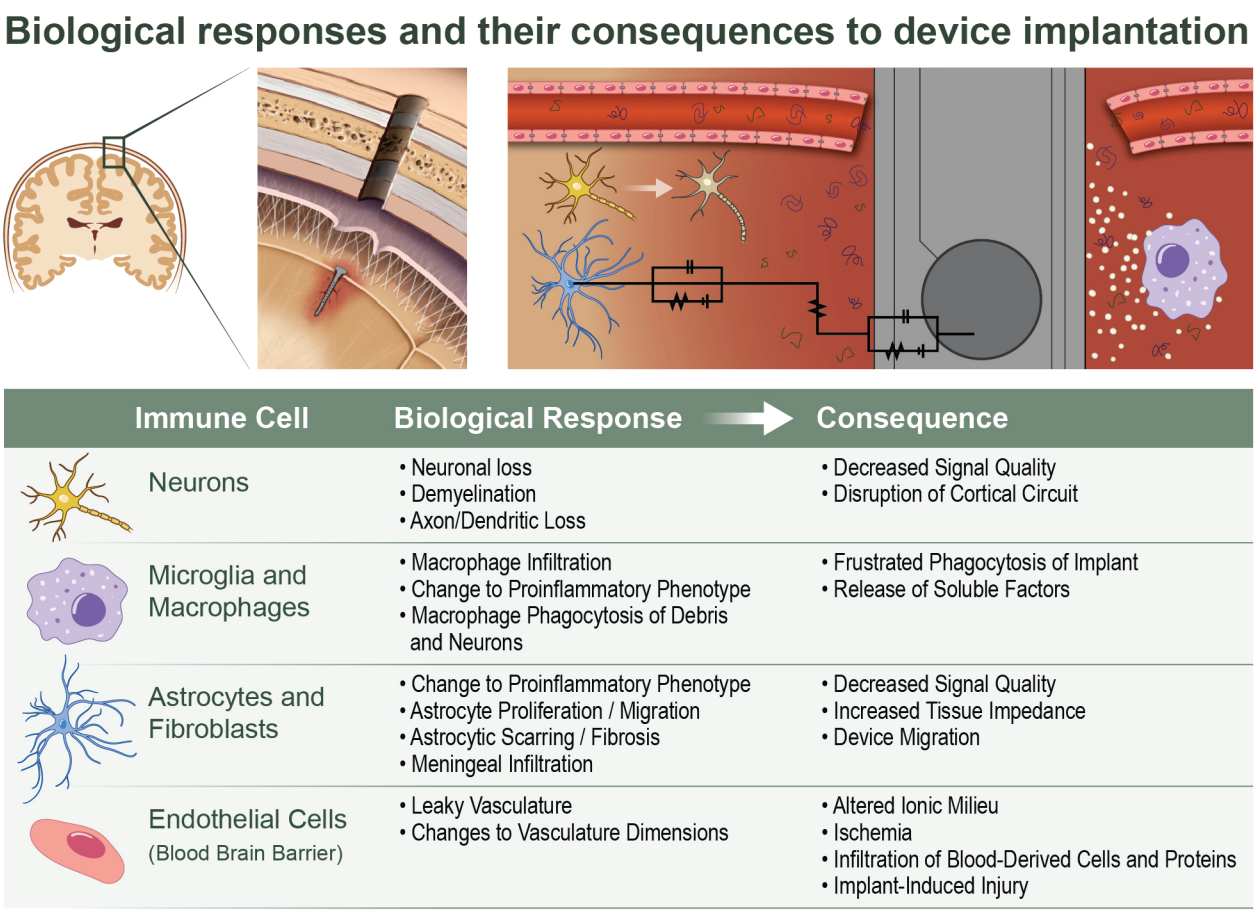

FIG. 1: Oxidative stress following neural probe implantation. The implantation of neural probes leads to the overproduction of reactive oxygen species (ROS), which can consequently (1) perpetuate the foreign body response, (2) facilitate neuronal death, and (3) facilitate corrosion and delamination of the microelectrode surface. (Reprinted from Ereifej et al.[25] under a Creative Commons Attribution International License, Copyright 2018: https://creativecommons.org/licenses/by/4.0/.)

Overall, chronic inflammation, neuronal loss, blood-brain barrier permeability, and encapsulation of microelectrode arrays may stem from the foreign body response to implanted intracortical microelectrodes and can be implicated in the recording performance of the implanted device.

C. Studies Linking Neuroinflammation to Electrode Failure

Despite all the efforts to overcome biological intracortical failure mechanisms (see Jorfi et al. or Hermann[14,34]), only a handful of studies have directly compared neuroinflammation to electrode performance. Interestingly, each study can be linked to the innate immunity, the body's fast-acting response to pathogenic threats. Here we briefly discuss the studies directly comparing neuroinflammation to electrode performance and their links to innate immunity.

Rennaker et al. were the first to demonstrate a correlation between microelectrode recording performance and the inflammatory response.[35] Specifically, in their study, Rennaker et al. investigated the effects of minocycline, chosen for its neuroprotective and neurorestorative effects,[36] on intracortical microelectrode recording performance.[35] Rats that were administered minocycline via water for two days before surgery through five days after surgery exhibited improved recording performance over

controls after the first week of implantation, upon which the signal-to-noise ratio of controls steadily dropped.[35] End-point histological analyses revealed that astrocytic encapsulation was decreased at one- and four-week time points after implantation in animals treated with minocycline.[35] Improved recording performance was hypothesized to be caused by decreased inflammation, neuronal dieback, and microglia activation in addition to the observed decrease in astrocyte encapsulation. Minocycline was later shown to inhibit the pro-inflammatory phenotype of macrophages.[37] Alternative explanations could factor in the antibiotic activity of minocycline. Perhaps a lower bacterial load activated less inflammation via innate immunity pathways. Regardless of the mechanism of action, minocycline is not suitable for long-term administration due to detrimental side effects including bone discoloration.[38,39] The long-term clinical significance of minocycline induced bone discoloration remains unknown, yet is reported to be worrisome to orthopedic surgeons while further characterization is completed.[40,41]

In contrast to the previous study administering an anti-inflammatory compound, Harris[42] examined the effects of a pro-inflammatory compound on intracortical microelectrode performance in an unpublished thesis study. At the end of a four-week study, rats administered a one-time surgical dose of the pro-inflammatory agent lipopolysaccharide (LPS) exhibited significantly lower neuronal density within the first 50 μm away from the implant.[42] Additionally, administration of LPS significantly reduced firing rates in evoked neural recordings.[42] Thus, inflammation is associated with poor neuronal survival and recording performance. Interestingly, the pro-inflammatory agent LPS is derived from the bacterial cell walls of gram-negative bacteria and predominantly recognized by the innate immunity receptors cluster of differentiation 14 (CD14) and Toll-like receptor 4 (TLR4) to induce robust inflammatory responses.[43] The results of Harris[42] indicate that activation of innate immunity can result in detrimental effects in recording performance and tissue integration.

Furthermore, Saxena et al. examined the effects of blood-brain barrier permeability on recording performance.[28] In this study, extravasation of blood proteins and myeloid cells into the brain parenchyma around intracortical microelectrodes implanted in rats coincided with poor recording performance.[28] The team hypothesized that chronic blood-brain barrier permeability following intracortical microelectrode implantation was part of a positive feedback loop with chronic inflammation, resulting in neurodegeneration,[28] similar to the self-perpetuating neurodegenerative response described by Potter et al.[20] One mechanism by which microglia and macrophages may recognize blood proteins and promote inflammation is through the innate immunity receptor Toll-like receptors.[31,44] Thus, innate immunity may play a role in the positive feedback loop of blood-brain barrier permeability and chronic inflammation that leads to intracortical microelectrode failure.

Finally, Kozai et al. investigated the role of caspase-1 in the recording performance of intracortical microelectrodes.[11] Caspase-1 was studied for its role in the activation of the pro-inflammatory cytokine IL-1β, as well as its role in neuronal death related to ischemia and chronic neurodegeneration.[11] Knockout mice lacking caspase-1 implanted with intracortical microelectrodes exhibited significantly improved single unit yields over wild type controls out to ~ 150 days after implantation with similar yields extending to the end of the experiment around 180 days after implantation.[45] Coincidentally, caspase-1 is involved in several innate immunity mechanisms, including inflammasome, RIG-like receptor, and TLR signaling.[45] In this instance, attenuation of innate immunity improved chronic intracortical microelectrode performance. Thus, innate immunity appears to play a role in the failure of intracortical microelectrodes.

Overall, studies linking inflammation to intracortical microelectrode performance reveal several connections by which innate immunity may be involved in intracortical microelectrode performance.

II. DISCUSSION

A. Innate Immunity

As indicated above, innate immunity has ties to the foreign body response to intracortical microelectrodes. Thus, further understanding of the innate

immunity may inform strategies to mitigate intracortical microelectrode failures.

Innate immunity is often described as the body's first line of defense against pathogenic threats.[46] Innate immunity should be distinguished from the body's other defense system, adaptive immunity, by several characteristics. Innate immunity activates much more quickly, responding within minutes or hours, as compared to several days.[46,47] The quickness in responses is, in part, due to the widely distributed germline encoded effectors.[47] In contrast, the adaptive immunity requires genetic recombination and clonal expansion of specific effectors.[46,47] The disadvantage of germline encoded effectors is that innate immunity has less diversity and specificity of responses.[47] However, the recognition of general patterns conserved among classes of pathogens allows the innate immunity to be versatile and have capable effector cells distributed throughout the body.[46,47] In further contrast, the adaptive immunity features memory, meaning that adaptive responses to a previously encountered threat may be activated more quickly and with greater intensity.[47] Innate immunity is not traditionally thought to feature memory; thus, innate immune responses enact with a relatively consistent activation time and intensity. However, there is growing evidence that innate immunity may feature some degree of memory.[48] Innate and adaptive immunity are not completely independent, as the innate immunity often aids in the activation and regulation of adaptive immunity effectors.[47]

Innate immunity is comprised of physical barriers, chemical barriers, and cellular responses.[47] Physical barriers include epithelial layers, mucosal tissues, and glandular tissues.[47] Chemical barriers include acidic fluids, anti-microbial proteins, and anti-microbial peptides that reside near the physical barriers.[47] Cellular innate immune responses are typically mediated by phagocytic cells, such as macrophages, neutrophils, dendritic cells, monocytes, and microglia, but can also involve natural killer cells, leukocytes, epithelial cells, and endothelial cells.[47] Additionally, complement glycoproteins found in serum are included in innate immunity.[47]

In the event that pathogens bypass the physical and chemical barriers of the body, cellular effectors may address the threat. Cellular effectors of the innate immunity are generally activated via pattern-recognition receptors (PRRs), which recognize molecular patterns common to categories of pathogens referred to as pathogen associated molecular patterns (PAMPs). Some PRRs may also recognize molecular patterns on endogenous molecules released by the body called damage (or danger) associated molecular patterns (DAMPs).[47] The family of PRRs employed by the innate immunity are TLRs,[49] C-type lectin receptors,[50] Retinoic acid-inducible gene-I-like receptors (RLRs),[51,52] and Nod-like receptors (NLRs).[53,54] The TLRs and CLRs are transmembrane proteins expressed across plasma membranes; however, TLRs may also be expressed on endosomes and lysosomes.[47] In contrast, RLRs and NLRs are expressed in the cytosol.[47] Both TLRs and NLRs have demonstrated recognition of DAMPs in addition to PAMPs.[47] Activation of the various PRRs may result in pro-inflammatory activation, apoptosis, phagocytosis, coagulation cascades, opsonization, or complement activation.[46]

In the context of foreign body responses to implanted intracortical microelectrodes, TLRs may be the most relevant. Some TLRs are expressed on plasma membranes,[55,56] so they may be able to respond to external threats directly. The TLRs also have the capability to recognize DAMPs and PAMPs,[31,57] enabling the potential detection of tissue, cellular, and vascular damage associated with intracortical microelectrode implantation, in addition to pathogens introduced with the microelectrode. Thus, we will also discuss TLRs and their adaptor molecule, CD14.

1. Toll-Like Receptors and CD14

One major group of effectors in innate immunity is a class of PRRs called TLRs.[58] The TLRs are transmembrane proteins that recognize molecular patterns associated with either pathogens or tissue damage and enact downstream inflammatory activation.[58,59] The TLRs are expressed on peripheral immune cells, such as macrophages and dendritic cells, as well as several cells of the central nervous system, including microglia, astrocytes, and neurons.[58,60,61]

Toll-like receptors are named for their similarity to Toll,[62,63] a protein responsible for directing dor-

sal-ventral patterning in *Drosophila* embryos[64] and involved in innate immunity in adult *Drosophila*.[65] The TLRs were later identified in humans based on their shared molecular structure and downstream signaling pathways.[66]

Toll-like receptors are type 1 transmembrane proteins that feature leucine-rich repeat (LRR) domains on the extracellular side and a Toll/IL-1 receptor (TIR) domain.[58,62,66,67] The LRRs are sequence motifs with frequent interspersed instances of the amino acid leucine and are found on many proteins involved in protein-protein interactions such as signal transduction.[58,68] The other major component of Toll-like receptors, the TIR domain, is a protein-protein interaction module found involved in the host responses of both plants and animals.[58,69]

Building off the common structural elements of LRR and TIR domains, the TLR family gives rise to at least 12 different functional members in mice and 10 different functional members in humans.[49,51,58] The TLRs 1–9 are functional in both mice and humans, TLR10 is functional in humans but not mice,[70] and TLRs 11–13 have been identified in mice but not humans.[49] The members of the TLR family vary in membrane location and ligand specificity.[58] Some TLRs, such as TLR 1, 2, 4–6, 8, and 11, are located on the cell membrane, with the LRR domain facing the extracellular environment and the TIR domain facing the cytosol.[49,71,72] With an outward-facing ligand-binding domain, TLRs on the cell membrane monitor for external threats like bacteria. Other TLRs, such as TLR 3, 7, 8, and 9, are located on intracellular vesicles, with the LRR domains facing the interior of the vesicle and the TIR domain facing the cytosol.[49,71,72] With a vesicle-facing ligand-binding domain, TLRs on vesicle membranes monitor for internal threats, such as viruses. Each TLR recognizes its own set of ligands, which may be pathogen associated molecular patterns (PAMPs) or damage/danger associated molecular patterns (DAMPs).

The PAMPs recognized by TLRs and other PRRs are molecular patterns shared among broad categories of pathogens, allowing rapid and versatile innate immune responses with a handful of widely available receptor types.[58] The broad, fast-acting nature of TLRs contrasts against the highly specialized receptors and antibodies of the adaptive immunity, which require time-consuming clonal expansion to distribute effector cells to combat pathogens.[58] The PAMPs are effective targets for immune recognition because they occur in pathogens but not host cells, allowing inflammatory effector cells to discriminate between self and non-self.[58] Furthermore, PAMPs are typically molecular patterns involved in critical pathogenic survival mechanisms.[58] Mutations in pathogens removing PAMPs are typically deadly, allowing TLR signaling to remain effective across many generations of evolution.[58]

Of note, PAMPs can be utilized in the recognition of bacterial, fungal, parasitic, and viral pathogens (for a detailed summary, see Akira et al.[73]). As opposed to PAMPs, DAMPs are patterns found in endogenous molecules released in the event of noninfectious tissue damage (Table 1) from Pineau and Lacroix,[31] Tsan and Gao,[57] and Beg.[59] The DAMPs recognized by TLRs include heat shock proteins (HSP), extracellular matrix (ECM) components, components of necrotic cells, surfactant protein A, RNA, DNA, and fibrinogen.[31,59] Heat shock proteins are molecules released when cells are exposed to various stresses.[31,57,74,75] TLRs can recognize HSP22,[76] HSP60,[77–79] HSP70,[80,81] and Gp96.[82] Molecules may be cleaved from the ECM by proteolytic enzymes during the inflammatory response to traumatic injury,[31] and TLRs can recognize heparan sulfate,[83–85] hyaluronan-derived oligosaccharide,[86,87] biglycan,[88] and fibronectin extra domain A.[89] Necrotic cells promote inflammation via TLR recognition of the released chromatin binding protein high mobility group box 1 (HMGB1)[30,90–93] or unidentified ligands.[94,95] Surfactant protein A is a component of pulmonary surfactant and may activate TLRs.[96] Host RNA[97–99] and DNA[97,100] can activate TLRs, but the method of endosome localization is unclear.[97] Fibrinogen escapes vasculature during inflammation and can bind TLRs to further propagate inflammatory mechanisms.[44]

Upon binding of a PAMP or DAMP to the sequence of LRR domains on a TLR, cytoplasmic signaling events occur (for a more detailed review, see Akira and Takeda[107]). Genes induced by TLR activation have been implicated in the production of pro-inflammatory cytokines, chemokines, major

TABLE 1: Summary of major damage associated molecular patterns (DAMPs) recognized by Toll-like receptors (TLRs), based on data from Pineau and Lacroix,[31] Tsan and Gao,[57] and Beg[59]

DAMP	TLR	Factors Produced	Refs.
Heat shock proteins (HSPs)			
HSP60	TLR2, TLR4	TNF, NO	77–79
HSP70	TLR2, TLR4	TNF, IL-1b, IL-6, IL-12	80, 81
Gp96	TLR2, TLR4	TNF, IL-12	82
HSP22	TLR4	TNF, IL-6, IL-12	76
Extracellular matrix components			
Heparan sulfate	TLR4	TNF	83–85
Hyaluronan-derived oligosaccharide	TLR2, TLR4	TNF, MIP-1a, MIP-2, KC	86, 87
Biglycan	TLR2, TLR4	TNF, MIP-2	88
Fibronectin extra domain A	TLR4	MMP-9	89
Decorin	TLR2, TLR4	PDCD4, IL-10	101
Versican	TLR2, TLR6	TNF-α, IL-6	102
Necrotic cells	TLR2, TLR3	TNF, IL-8, MIP-2, KC, MMP-3, iNOS	94, 95
RNA	TLR3, TLR7	IL-12, IFN-α	97, 98
DNA (in the form of immune complexes)	TLR9	IFN-α	97, 100
High mobility group box 1 protein (HMGB1)	TLR2, TLR4	TNF, IL-1a,IL-1b, IL-6, IL-8, MIP-1a, MIP-1b, COX-2, iNOS	30, 90–93
Lung surfactant protein A	TLR4	TNF-α, IL-10	96
Fibrinogen	TLR4	MIP-1α, MIP-1β, MIP-2, MCP-1	44
S100A8	TLR4	TNF-α	103
S100A9	TLR4	IL-1β, TNF-α, IL-6, IL-8 and IL-10	104
Fibrillar β-amyloid	TLR2, TLR4	Superoxide radical	105
α-synuclein	TLR4	TNF-α, IL-6, CXCL1, ROS	106

histocompatibility complex (MHC), co-stimulatory molecules, and antimicrobial peptides.[58] Although cytokines and chemokines promote innate immunity and inflammatory responses, MHC and co-stimulatory molecules facilitate adaptive immune responses. Cytokines released in response to TLR activation include the interleukins (IL) IL-1α,[90] IL-1β,[90] IL-6,[76,108] and IL-12,[81,97] tumor necrosis factor (TNF, also listed as TNF-α),[78,86–88,90,92,94,97,108] interferon-α (IFN- α),[97] and the chemokines macrophage inflammatory protein-1α (MIP-1α),[86,90,95] MIP-1β,[90] MIP-2,[86,88,95] MCP-1,[109] and KC.[86,95] Cytokines can promote further inflammatory activation and edema, and chemokines can promote cellular extravasation and trafficking.[110]

Other factors released after TLR activation include the free radical signaling molecule nitric oxide (NO)[77,78] and an enzyme that produces NO, inducible nitric oxide synthetase (iNOS).[92,94] Additionally, TLR activation may result in release of the matrix metalloprotease (MMP) 3 or MMP9,[95] which are involved in tissue repair.[89] Finally, TLR activation may release the pro-inflammatory enzyme cyclooxygenase 2 (COX-2),[92] which activates arachidonic acid/prostaglandin inflammatory mechanisms.[111] Overall, TLR signaling pathways utilize a broad range of downstream effectors to respond to pathogenic and endogenous threats, which can be a likely source of the self-perpetuating inflammatory response to microelectrodes described above.

Because of established roles of particular PRR in neurodegenerative disorders, we have taken particular interest in the potential role of TLR2, TLR4, and the co-receptor cluster of differentiation 14 (CD14) in the foreign body response to intracortical microelectrodes.

The cell-surface receptor TLR2 is expressed on endothelial cells and antigen-presenting cells, including macrophages and microglia.[58,112,113] Rather

than forming homodimers to activate downstream signaling pathways, TLR2 typically forms heterodimers with TLR1 or TLR6.[58] The main function of TLR2 is the recognition of Gram-positive bacteria via peptidoglycan (disputed by Travassos et al.[114]) and lipoteichoic acid,[115–119] but it also binds the PAMPs lipoproteins/lipopeptides,[120] lipoarabinomannan,[121] phenol-soluble modulin,[122] glycoinositolphospholipids,[123] porins,[124] atypical LPS,[125,126] and zymosan.[107,113] In addition to the aforementioned PAMPs, TLR2 recognizes the DAMPs HSP60,[79] HSP70,[80,81] GP96,[82] hyaluronan-derived oligosaccharide,[86] biglycan,[88] necrotic cells,[94,95] and HMGB1.[91,93] The broad range of recognized ligands makes TLR2 an effective innate immunity activator throughout the body, but the important role of TLR2 in CNS inflammation and neurodegeneration will be discussed below.

In contrast to TLR2, TLR4 communicates via homodimerization and recognizes Gram-negative bacteria.[58,127–129] The cell-surface receptor TLR4 is expressed on macrophages, microglia, and several immune cells.[58,66,130] In addition to bacterial recognition via LPS, TLR4 also recognizes several other PAMPs,[73,107] including mannan,[131] glucuronoxylomannan,[73,132] viral fusion protein,[133] and viral envelope proteins.[134] Also, TLR4 is also involved in the recognition of several DAMPs,[31,59] such as HSP60,[77,78] HSP70,[80,81] Gp96,[82] HSP22,[76] heparan sulfate,[83–85] hyaluronan-derived oligosaccharide,[86,87] biglycan,[88] fibronectin extra domain A,[89] HMGB1,[91,93] and fibrinogen.[44] Involvement of TLR4 signaling in CNS inflammation and neurodegeneration will also be discussed in below.

The co-receptor CD14, a 55 kD glycoprotein closely associated with TLR2 and TLR4, is predominantly known for its role in the recognition of LPS.[135] Briefly, CD14 binds LPS monomers extracted from LPS aggregates by LPS binding protein (LBP)[136,137] and the TLR4-MD2 complex subsequently binds LPS.[135,138] Although the exact mechanism of LPS transfer from CD14 to TLR4-MD2 has not been elucidated, the presence of CD14 greatly improves the sensitivity of LPS recognition by effector cells.[139] Macrophages and to a lesser extent microglia express CD14,[140–142] either linked to a membrane by a glycophosphoinositol or released in a soluble form.[58,135] In addition to LPS recognition, CD14 acts as a co-receptor to TLR2 in the recognition of the various PAMPs, such as virions[143] and the cell wall components peptidoglycan (disputed by Travassos et al.[114]) and LTA.[119,144] The co-receptor CD14 is thought to be an adaptor molecule to the TLRs for the binding of both PAMPs and DAMPs.[144] For example, CD14 acts as a co-receptor to TLR2 and/or TLR4 in the recognition of HMGB1,[145] β amyloid plaques,[105] and HSP70.[80,146] Furthermore, CD14 signals independently of TLR2 and TLR4, such as in the endosomal recognition of viral nucleic acids by TLR7 and TLR9,[147] and the non-TLR mediated recognition of necrotic cells[144] and apoptotic cells.[148–150] Finally, CD14 facilitates the internalization of several molecules, such as phosphatidylinositol.[151] The role of CD14 in CNS inflammation and neurodegeneration will also be discussed further in below.

2. *TLR2, TLR4, and CD14 in Neurodegenerative Disorders*

The innate immunity receptors TLR2, TLR4, and CD14 play a prominent role in several neurodegenerative disorders due to their expression in CNS tissue and ability to promote potent inflammatory mechanisms.[152] The receptors TLR2 and TLR4 are expressed on microglia and astrocytes in both human and mice and on neurons in mice only.[60,153] Additionally, TLR2 is expressed on oligodendrocytes.[153] Although constitutive expression of CD14 in the brain is limited to perivascular, leptomeningeal, and choroid plexus macrophages, it can be upregulated in parenchymal microglia following injury.[154,155] Subsequently, activation of TLR2, TLR4, and/or CD14 on microglia can induce neurodegeneration.[156–158] In addition to parenchymal cells of the brain, TLR2 and TLR4 are expressed on cerebral endothelial cells[159] and soluble CD14 may participate in the ligand recognition of endothelial cells lacking membrane-bound CD14.[160] Injuries of the CNS may also recruit CD14 positive macrophages to enact and propagate inflammatory responses.[154] The receptors TLR2 and TLR4 are commonly expressed in macrophages as well.

Neuroinflammatory mechanisms involving TLR2, TLR4, and CD14 activation have been

demonstrated to contribute to neurodegeneration.[156–158] Resident microglia or infiltrating macrophages may respond to TLR2, TLR4, and CD14 ligands linked to CNS disorders and injuries, such as α-synuclein,[106,161] fibrillar β-amyloid,[105] heparan sulfate proteoglycans,[162] heat shock proteins,[77,163,164] necrotic neurons,[94,165] and whole and partial bacteria.[156,166] Activation of TLRs on microglia can lead to microglial activation and the subsequent release of cytokines, chemokines, reactive oxygen species,[106] and nitric oxide,[156] as well as induce phagocytosis of both damaged and viable neurons.[167] The release of reactive oxygen species by activated microglia can cause damage to neuronal membranes and dendrites.[168] Additionally, activation of TLRs has been shown to interfere with remyelination.[169] In summary, overreaction of microglia to TLR2, TLR4, and CD14 can cause neuronal damage in many ways.

Contrary to the major role of TLR2, TLR4, and CD14 signaling in neurodegeneration, TLR2, TLR4, and CD14 have also been linked to neuroprotection.[170] Activation of TLR2, TLR4, and CD14 may protect neurons by reverting microglia to a pro-healing activation state,[171] inducing cytokine release in a beneficial context,[172] or to facilitate clearing of dangerous molecules from the CNS.[173] Thus, well-regulated innate immune signaling is useful for maintaining neuronal health. These results contradict many reports of the current understanding of TLR2, TLR4, and CD14, but should be further explored for a more complete understanding of the role of innate immunity in microelectrode performance.

Activation of TLR2, TLR4, and CD14 has been implicated in the neurodegeneration caused by a variety of CNS diseases and injuries, including Parkinson's disease (PD),[174] dementia with Lewy bodies (DLB),[174] multiple system atrophy (MSA),[174] multiple sclerosis (MS),[175] amyotrophic lateral sclerosis (ALS),[176] Alzheimer's disease,[105,177] neuropathic pain,[178] subarachnoid hemorrhage,[179,180] traumatic brain injury,[181] focal cerebral ischemia,[182] spinal cord injury,[183] and brain injury.[184] Synucleinopathies (PD, DLB, and MSA), Alzheimer's disease, and ALS will be discussed in further detail due to the involvement of multiple receptors of interest and heavy innate immunity involvement.

Alzheimer's disease is a memory disorder involving plaques made of β amyloid in the parenchyma of the brain.[185,186] Bystander damage caused by the chronic inflammatory mechanisms directed against β amyloid plaques is hypothesized to be a major source of neurodegeneration.[187] The receptors TLR2, TLR4, and CD14 on microglia recognize fibrillar β amyloid and induce a pro-inflammatory state involving phagocytosis and ROS release.[105] Inhibiting TLR2 and TLR4 by various means has resulted in decreased generation of pro-inflammatory factors and subsequent neurotoxicity.[158,185,188–190] On the other hand, activation of TLR2, TLR4, and CD14 signaling has been shown to facilitate the clearance of β amyloid,[191] and the removal of neurons damaged by Aβ.[192] Thus, some degree of TLR activation while limiting neuronal damage is likely the optimal scenario for treating Alzheimer's disease.

Recent studies have identified participation of TLR2 and TLR4 in synucleinopathies, such as Parkinson's disease, dementia with Lewy bodies, and multiple system atrophy.[106,161,173,174] Synucleinopathies involve misfolding and buildup of the protein α-synuclein, resulting in TLR-mediated neuroinflammation and neurodegeneration.[106,193] Activation of TLR2 disrupts the clearance of α-synuclein via autophagy.[161] Contrarily, activation of TLR4 promotes the clearance of α-synuclein via phagocytosis, while simultaneously promoting neurodegenerative inflammatory mechanisms.[106,173] Thus, a proper balance of clearing harmful materials and limiting self-inflicted damage must be maintained to combat synucleinopathies. Alternatively, a TLR4 ligand similar to LPS, mono-phosphoryl lipid A, has been identified to selectively promote clearance and not destructive inflammatory cascades.[174] Therefore, approaches more nuanced than simply shutting down the signaling of entire TLRs must be considered in the mitigation of TLR-mediated neuroinflammation and neurodegeneration.

Amyotrophic lateral sclerosis is a disorder involving death of motoneurons in the motor cortex and spinal cord resulting in muscle atrophy and paralysis.[185,194,195] Although the initial cause of motoneuron damage is unclear, activated microglia with mutations in SOD1 have been shown to exacerbate neurodegeneration via the release of superoxide,

nitrate, and nitrite.[185,196] TLR2, TLR4, and CD14 have been shown to activate microglia by binding extracellular mutated SOD1.[197] Furthermore, knocking out TLR4 resulted in increased survival and improved functional outcomes in a mouse model of ALS.[198] Recently, natural and synthetic TLR4 antagonists have been shown to mitigate neurodegeneration and nitric oxide release (natural TLR4 antagonist only) by microglia, *in vitro*.[176] Overall, persistent activation of microglia via TLR2, TLR4, and CD14 in ALS leads to further neurodegeneration, and inhibiting these pathways mitigates harmful outcomes.

In summary, TLR2, TLR4, and CD14 are expressed on tissues of the CNS, recognize PAMPS and DAMPS in the CNS, and promote inflammatory mechanisms involved in neurodegenerative disorders. Temporal and regulated inhibition of TLR2, TLR4, and CD14 holds the potential to mitigate neurodegenerative disorders, because clearance of the ligands that generate inflammation must be considered for proper healing to occur.

B. TLR2, TLR4, and CD14 in Foreign Body Response to Intracortical Microelectrodes

Although there is currently little direct evidence for TLR2, TLR4, and CD14 signaling in the foreign body response to intracortical microelectrodes, several connections exist that suggest their role in the recognition of damage to promote and perpetuate inflammation. Particularly, TLR2, TLR4, and CD14 are expressed in the cells at the electrode tissue interface;[60,153–155] ligands recognized by TLR2, TLR4, and CD14 have been reported at the electrode tissue interface;[89,199] and outcomes associated with the activation of TLR2, TLR4, and CD14 pathways have been reported by several groups.[61,66,157,200–205] Together, the concurrent presence of receptors, ligands, and downstream effectors strengthens the likelihood for participation of TLR2, TLR4, and CD14 in the foreign body response to intracortical microelectrodes.

As discussed above, resident parenchymal microglia express TLR2 and TLR4 constitutively,[60,153] and may express CD14 following injury.[154,155] Additionally, infiltrating macrophages constitutively express TLR2, TLR4, and CD14. Following intracortical microelectrode implantation, both resident microglia and infiltrating macrophages accumulate at the electrode-tissue interface and revert to a pro-inflammatory activated state.[29] Therefore, the receptors TLR2, TLR4, and CD14 may play a role in the pro-inflammatory activation of microglia and macrophages through the recognition of ligands.

Several of the ligands that activate TLR2, TLR4, and CD14 may be present at the electrode tissue interface. Starting with PAMPs, residual endotoxin (LPS) has been detected at levels above FDA guidelines for CNS devices on intracortical microelectrode probes even following standard sterilization protocols with ethylene oxide.[199] Ravikumar et al. compared sterilization methods and found that probes with higher endotoxin levels exhibited higher microglial activation, astrocytic encapsulation, blood-brain barrier permeability, and neuronal dieback at acute time points.[199] Since TLR4 and CD14 are involved in the main pathway of endotoxin recognition,[58] their findings indicate that activation of TLR4 and CD14 may contribute to unfavorable inflammatory mechanisms at the electrode tissue interface. Immunohistochemical differences between sterilization methods were not observed 16 weeks after implantation, suggesting that endotoxin or LPS may not be a significant activating ligand for chronic inflammatory responses once the LPS introduced by the electrode has been cleared. Additionally, as mentioned above, Harris administered LPS systemically to rats at the time of intracortical microelectrode implantation and observed decreased neuronal survival paired with lower firing rates in evoked recordings compared to control rats,[42] indicating that activation of TLR4 and CD14 may contribute to declining recording performance as well as the foreign body response to the electrode. Of note, Gram-positive bacterial cell wall components, recognized by TLR2, were not quantified in the sterilization study but may be present following imperfect sterilization methods.

In addition to PAMPs, several DAMPs may be present at the electrode tissue interface due to the damage caused by insertion trauma, micromotion, and chronic inflammatory mechanisms.[199] Enhanced

expression of fibronectin, a ligand to TLR4,[89] has been detected in the reactive tissue around implanted intracortical microelectrodes,[206] as well as cortical impact injures.[207] HMGB1, recognized by TLR2,[91,93] TLR4,[91,93] and CD14,[145] was observed to be upregulated around implanted intracortical microelectrodes[208] as well as in the brain following ischemia.[92,209,210] Furthermore, necrotic cells, recognized by TLR2[94,95] and CD14,[144] have been observed around implanted intracortical microelectrodes.[211] Other DAMPs have been observed in various brain injuries and illnesses. A ligand to TLR4, HSP70, has been observed in the brain following focal cerebral ischemia.[212,213] *In vitro* studies of CNS cells also indicate evidence of DAMP release following nervous system injuries. The ligands HSP60 and HSP70, recognized by TLR2,[79–81] TLR4,[77,78,80,81] and CD14 (HSP60 only),[80,146] were observed on the axons of cultured DRG neurons that were explanted from rats following sciatic nerve injury.[163,164] Furthermore, HSP60 was observed being released from apoptotic and necrotic cells in mixed CNS culture (embryonic forebrain-derived cells of unspecified composition).[77] Additionally, fibrinogen, a blood protein that activates TLR4,[44] has been speculated to be present around implanted intracortical microelectrodes.[14,21,214] The disruption of vasculature upon intracortical microelectrode implantation[16] and chronic permeability of the blood brain barrier likely results in the presence of fibrinogen in the brain at both acute and chronic time points.[28,215] Overall, a variety of DAMPs may be released in the brain following intracortical microelectrode implantation.

Finally, the downstream consequences of TLR2, TLR4, and CD14 activation may indicate a role in the foreign body response to implanted intracortical microelectrode. Activation of TLR2, TLR4, and CD14 on microglia and macrophages leads to the activation of NF-κB, which mediates pro-inflammatory genes responsible for the release of cytokines, chemokines, cyclooxygenase-2, and matrix metalloproteinase-9 (MMP-9).[66,216,217] The factors generated following NF-κB activation may perpetuate chronic inflammatory mechanisms around the implanted device. Activated microglia and macrophages are present at the electrode tissue interface long after device implantation.[29,215] Activation of TLRs has the capability to induce neuronal damage,[61,157] and neuronal dieback is commonly observed along with the foreign body response to intracortical microelectrodes.[21,215,218] Activation of TLRs by DAMP recognition may contribute to the loss of neurons around the implant. Additionally, the neurons killed around implanted intracortical microelectrodes may provide further stimulus for TLR activation via necrosis or the release of HSP60, HSP70, or HMGB1, thus self-perpetuating chronic inflammation. Furthermore, activation of TLRs may contribute to chronic blood-brain barrier permeability via the release of nitric oxide pro-inflammatory cytokines, NO, and reactive oxygen species (ROS), and MMP-9.[26,66,200–205] Blood-brain barrier permeability is a persistent problem of the foreign body response to intracortical microelectrodes and has been associated with poor recording performance.[28,215]

Overall, the evidence presented here suggests that TLR2, TLR4, and CD14 play a role in the foreign body response to intracortical microelectrodes via the recognition of PAMPs and DAMPs by microglia and macrophages and subsequent pro-inflammatory, neurotoxic, and blood-brain barrier damaging actions (Fig. 2).

1. Current Strategies to Inhibit TLR2, TLR4, and CD14

Several strategies exist for inhibiting TLR2-, TLR4-, and CD14-mediated signaling, varying in target and molecular composition. The most direct strategies target the receptors themselves, however, inhibition strategies may target other components of the TLR2/TLR4/CD14 signal transduction pathways. A variety of peptides, antibodies, and RNA sequences may disrupt signaling at the various targets. In this section, several TLR2/TLR4/CD14 inhibition strategies under different stages of investigation will be reviewed (see Table 2).

The first major option for inhibiting TLR2/TLR4/CD14 signaling we will discuss utilizes methods to alter the cell-surface expression of TLR2/TLR4/CD14, either by downregulation or internalization. Administration of rosmarinic acid,[219] siRNA,[220] oxymatrine,[181] glycyrrhizin,[221] argon,[222] pituitary adenylate cyclase-activating polypeptide

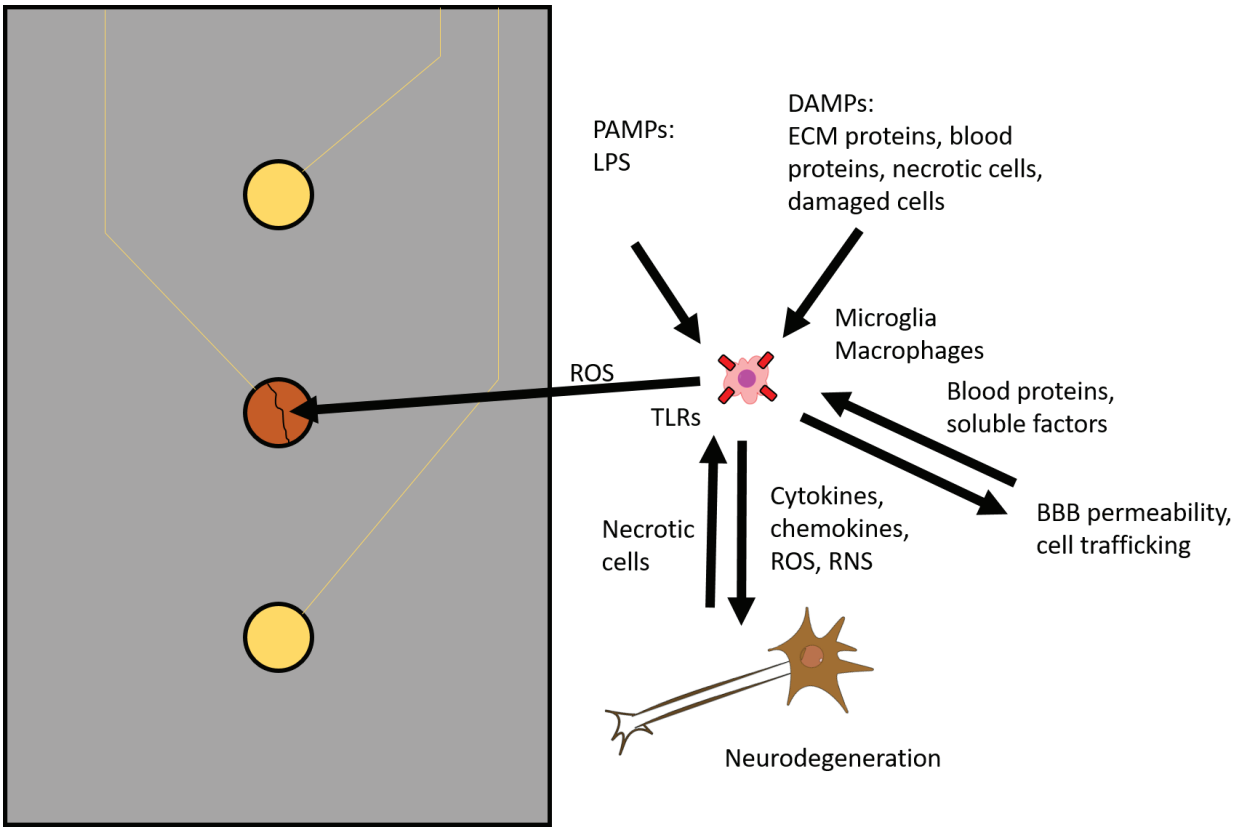

FIG. 2: Potential role of TLR2, TLR4, and CD14 in the foreign body response to intracortical microelectrodes. Microglia and macrophages at the electrode tissue interface may recognize PAMPs and DAMPs at the electrode tissue interface via TLR2, TLR4, and CD14, resulting in the release of soluble factors such as cytokines, chemokines, reactive oxygen species, and reactive nitrogen species. The released soluble factors may damage neurons, blood vessels, and electrode materials, leading to poor intracortical microelectrode performance. Cells damaged and killed by the soluble inflammatory factors may release DAMPs that activate microglia and macrophages. Blood proteins released following damage to the blood brain barrier may also act as DAMPs. Inflammatory cells infiltrating across the blood-brain barrier permeability may become activated by DAMPs and contribute to the foreign body response. Thus, TLR2, TLR4, and CD14 signaling may contribute to the activation and perpetuation of chronic inflammatory mechanisms in the foreign body response to intracortical microelectrodes.

(PACAP),[223] melatonin,[224] apigenin,[225] and ursolic acid,[226] resulted in reduced TLR2, TLR4, and/or CD14 expression; whereas, walnut extract was shown to promote receptor internalization.[227] Of note, intrathecal siRNA that reduces TLR4 expression attenuated neuropathic pain in a rat model.[220] Oxymatrine and PACAP conferred neuroprotection in a rat models of traumatic brain injury by inhibiting the expression and upregulation of TLR4.[181,223] Glycyrrhizin inhibited TLR2-HMGB1 signaling, resulting in reduced lymphocyte trafficking in experimental autoimmune thyroiditis in mice.[221] Melatonin, apigenin, and ursolic acid attenuated the effects of subarachnoid hemorrhage, including neurobehavioral deficits, blood-brain barrier permeability, and neuronal apoptosis.[224–226] Even more promising, administration of melatonin has resulted in improved intracortical microelectrode recording and neuronal viability.[228] Although melatonin was chosen for its ability to inhibit caspase activation, cytochrome c release, and oxidative stress, inhibition of TLR4 may have contributed to improved microelectrode integration and performance.[224,228] Reducing the expression of TLR2, TLR4, and/or

TABLE 2: Strategies for the inhibition of TLR2, TLR4, and CD14

Inhibition Target Mechanism	Type of Therapeutic	Receptor Targeted	Therapeutic	Application(s)
Ligand binding	Small molecule	CD14/TLR4	IAXO-101	Sepsis,[233] neuropathic pain,[178] malaria[234]
Ligand binding	Small molecule	CD14/TLR4	IAXO-102	Aneurysm[235]
Ligand binding/ receptor dimerization	Small molecule	TLR2	SSL3236	N/A
Ligand binding	Antibody	CD14	IC14	LPS responsiveness,[241] sepsis[242,243]
Co-receptors (non-CD14)	Small molecule	TLR4 (via MD-2)	Eritoran	Sepsis[250]
Co-receptors (non-CD14)	Small molecule	TLR4 (via MD-2)	TAP2	Inflammation[251]
Co-receptors (non-CD14)	Small molecule (natural)	TLR4 (via MD-2)	Curcumin	Integration of intracortical microelectrodes[208]
TLR4-MyD88 Complex formation	Small molecule	TLR4	Wogonin	Inflammation in DRG neurons,[255] traumatic brain injury[216]
Intracellular TLR domain interactions	Small molecule	TLR4	TAK-242/resatorvid	Sepsis,[260] endotoxic shock,[259] traumatic brain injury,[261] cerebral ischemia,[257] intracerebral hemorrhage,[257] optic nerve crush[262]
Receptor expression at cell surface	siRNA	TLR4	N/A	Neuropathic pain[220]
Receptor expression at cell surface	Small molecule	TLR4	Oxymatrine	Traumatic brain injury[181]
Receptor expression at cell surface	Small molecule	TLR4	PACAP	Traumatic brain injury[223]
Receptor expression at cell surface	Small molecule	TLR2	Glycyrrhizin	Autoimmune thyroiditis[221]
Receptor expression at cell surface	Small molecule	TLR4	Melatonin	Subarachnoid hemorrhage,[224] integration of intracortical microelectrode[228]
Receptor expression at cell surface	Small molecule	TLR4	Apigenin	Subarachnoid hemorrhage[225]
Receptor expression at cell surface	Small molecule	TLR4	Ursolic acid	Subarachnoid hemorrhage[226]

CD14 effectively attenuates the negative effects of overactive TLR signaling. Again, the success of cell-surface expression in CNS injuries and disorder demonstrate a potential application for integrating intracortical microelectrodes. Therefore, we utilized transgenic TLR2, TLR4, or CD14 knockout mice to investigate the effects of removal of each receptor in the integration and performance of intracortical microelectrodes. Studies with TLR2/TLR4 utilized dummy implants and investigated only the histological response.[229] Endpoint histology at 2 and 16 weeks after implantation demonstrated that *Tlr4*$^{-/-}$ mice exhibited significantly lower BBB permeability at acute and chronic time points but also demonstrated significantly lower neuronal survival at the chronic time point. Additionally, inhibition of the TLR2 pathway had no significant histological effect compared to control animals. Together,

our results indicate that complete genetic removal of TLR4 was detrimental to the integration of intracortical neural probes, while inhibition of TLR2 had no impact within the tests performed in this study. Implanting functional recording intracortical microelectrodes into *Cd14*$^{-/-}$ mice exhibited acute but not chronic improvements in intracortical microelectrode performance without significant differences in end point histology.[230] However, when we used a mouse bone marrow chimera model to selectively knockout CD14 from either brain resident microglia or blood-derived macrophages, we were able to understand the most effective targets for future therapeutic options—brain-derived microglia or infiltrating blood-derived cells.[231] Using single-unit recordings, we demonstrate that inhibiting CD14 from the blood-derived macrophages improves recording quality over the 16-week long study. We conclude that targeting CD14 in blood-derived cells should be part of the strategy to improve the performance of intracortical microelectrodes and that the daunting task of delivering therapeutics across the blood-brain barrier may not be needed to increase intracortical microelectrode performance. Knowing that both TLR4 and CD14 are important mediators of intracortical microelectrode integration and performance, other strategies to inhibit their activation must be explored.

Our next step was to consider inhibiting TLR2/TLR4/CD14 signaling via antagonism of the binding domain with a small molecule. The glycolipid IAXO-101 has demonstrated success as a CD14-TLR4 antagonist by competitively occupying CD14,[232] resulting in mitigation of sepsis, neuropathic pain, and experimental malaria in mice.[178,233,234] Therefore, we explored the use of IAXO-101 in an intracortical microelectrode model. Interestingly, mice receiving IAXO-101 exhibited significant improvements in recording performance over the entire 16-week duration without significant differences in endpoint histology.[230] Combined with our chimera studies, we hypothesized that some degree of CD14 signaling may be necessary over chronic time ranges to facilitate wound healing mechanisms. We also remained unsure if IAXO-101 was simply not the most optimal method for small molecule inhibition and are exploring other options. For example, a similar compound IAXO-102 attenuated the development of an experimental form of aneurysm.[235] The naturally derived antagonist to TLR2 staphylococcal superantigen-like protein 3 (SSL3) may inhibit TLR2 signaling by both blocking binding sites and disrupting heterodimerization.[236] Because of the diversity of molecular structures recognized by the same TLR, the effectiveness of small molecule antagonists to interfere with ligand-receptor interactions may vary between ligand.[237] Small molecule antagonists to the TLR2/TLR4/CD14 pathways have demonstrated varying degrees of success. The capability of small molecule antagonists to mitigate TLR2/TLR4/CD14 activity and attenuate detrimental inflammatory outcomes is promising for their utilization in intracortical microelectrode integration. When contemplating the effectiveness of a small molecule antagonist approach, it is important to consider delivery to the brain. Depending on the approach, delivery through the blood-brain barrier is complicated, despite the known "leakiness" associated with the neuroinflammatory response to intracortical microelectrodes.

Another mechanism of inhibiting TLR2/TLR4/CD14 signaling by blocking the ligand-receptor interactions utilizes blocking antibodies. Antibodies that bind a cellular receptor and prevent ligand binding have demonstrated success in various inflammatory disorders.[238] Anti-CD14 antibodies may disrupt CD14 signaling by blocking the binding of LPS to CD14[239,240] or through mechanisms independent of LPS binding.[239] The commercially available monoclonal antibody IC14 recognizes human CD14 and saturates CD14 on monocytes and granulocytes.[241] Intravenous administration of IC14 in humans reduced responsiveness to LPS, specifically attenuating the release of pro-inflammatory cytokines (TNF, IL-6, and IL-10), the activation of leukocytes and endothelial cells, the acute phase protein response, and various symptoms.[241] The administration of IC14 has produced less promising results in severe cases of sepsis.[242,243] One potential setback for the use of blocking antibodies is activation of the complement pathway by the Fc region of the antibody.[244] Recent studies employing hybrid antibodies with inert Fc regions have been successful in attenuating CD14-mediated inflammatory responses without activating complement-related side effects

in both *in vivo* porcine models and *ex vivo* human whole blood models of sepsis.[244] Furthermore, pairing complement inhibition with hybrid anti-CD14 antibodies has demonstrated enhanced survival in a porcine model of polymicrobial sepsis.[245] Finally, hybrid anti-CD14 antibodies with and without concurrent complement inhibition has outperformed the synthetic small molecule antagonist eritoran in mitigating monocyte activation in response to sepsis.[246] Therapeutic antibodies have demonstrated success in mitigating TLR2/TLR4/CD14 mediated disorders despite potential complications. Thus, therapeutic antibodies may be applicable for integrating intracortical microelectrodes within the brain.

Alternative inhibition strategies to inhibit TLR2 and TLR4 focus on the non-CD14 co-receptors. The protein MD-2 (myeloid differentiation 2) is the other major cell-surface co-receptor involved in the recognition of LPS. Where CD14 is thought to facilitate recognition of both PAMPs and DAMPs, MD-2 is thought to facilitate response to PAMPs only.[144] Limiting the types of ligands inhibited will likely result in different outcomes. Small molecule antagonists to TLR4-MD-2 may be derived from synthetic and natural sources, such as olive oil and curcumin.[237] Synthetic antagonists to TLR4-MD-2 are typically similar in structure to the LPS component lipid A that is recognized by the TLR4 receptor complex.[237] Eritoran is a synthetic small molecule antagonist derived from lipid A that binds MD-2 without promoting the dimerization of TLR4.[237,247] Despite promising *in vitro*[248] and animal model results,[249] eritoran was unable to reduce mortality in clinical trials of severe sepsis.[250] More recently, the TLR4/MD-2 antagonist peptide TAP2, hypothesized to bind the LPS-binding pocket of MD-2, was shown to attenuate LPS-induced inflammatory activation *in vitro* and in mice.[251] However, clinical trials with TAP2 have not been reported. Becaust of the predominant interaction of MD-2 with PAMPS,[144] the authors did not initially expect TLR4-MD-2 antagonists to be effective in mitigating chronic inflammation associated with the damage caused by intracortical microelectrodes. However, Potter et al. previously demonstrated that the natural TLR4-MD-2 antagonist curcumin improves neuronal survival and blood-brain barrier stability around intracortical microelectrodes implanted in rats.[208] Their results may indicate a larger role of pathogens at the electrode tissue interface, involvement of MD-2 in DAMP recognition, or promiscuous activity of curcumin as an antioxidant, which was the author's intended application. Regardless of the mechanism, this finding indicates the potential for TLR4-MD-2 inhibitors in the integration of intracortical microelectrodes.

Additional inhibition strategies to inhibit TLR2/TLR/CD14 signaling target downstream intracellular signal transduction pathways. Antagonists have been developed or identified to target the adaptor molecules MyD88 adaptor-like (Mal) and TRIF-related adaptor molecule (TRAM),[252] the TLR2 TIR domain,[253] JNK,[166] ubiquitin chains,[254] TLR4-MyD88 interactions,[255] TLR1-TLR2 heterodimerization,[256] and the intracellular domain of TLR4.[257,258] Of note, administration of the flavonoid wogonin attenuated LPS-induced inflammation in dorsal root ganglion neurons[255] and improved outcomes in a model of traumatic brain injury[216] by interfering with TLR4-MyD88 complex formation.[255] Furthermore, cyclohexene-derived TAK-242/resatorvid inhibits TLR4 signaling by binding the intracellular domain of TLR4 and preventing interactions with downstream adapter molecules.[257,259] *In vivo* administration of TAK-242 for the treatment of sepsis,[260] endotoxic shock,[259] traumatic brain injury,[261] cerebral ischemia,[257] intracerebral hemorrhage,[257] and optic nerve crush[262] resulted in positive outcomes, such as attenuated inflammation and neuroprotection. A phase III clinical trial (NCT00633477) investigated the utilization of TAK-242 to treat sepsis, but the trial was discontinued due to business concerns unrelated to safety.[263] Strategies to inhibit TLR2/TLR4/CD14 signaling have demonstrated preliminary efficacy but have not demonstrated clinical success to this date. Nonetheless, many of the *in vivo* experiments have demonstrated efficacy in conditions related to the foreign body response to intracortical microelectrodes. Traumatic brain injury involves similar phenomena exhibited in the foreign body response to intracortical microelectrodes, such as blood-brain barrier permeability, neuroinflammation, and neuronal death.[264] Additionally, ischemic conditions have been observed around intracortical microelectrodes.[265] The efficacy of inhibiting intracellular signal transduction path-

ways downstream of TLR2/TLR4/CD14 in CNS applications is promising for the utilization in the integration of intracortical microelectrodes.

Overall, TLR2, TLR4, and CD14 may be attenuated at different points along their respective signaling pathways (Table 2). Many promising findings have been observed *in vitro* and *in vivo*, but strong clinical performance in humans has not been demonstrated. Human clinical trials mainly failed in severe cases of sepsis, which is likely not the best predictor of efficacy mitigating the foreign body response to intracortical microelectrodes. However, promising *in vivo* results in CNS injuries and diseases, coupled with our preliminary work in the role of TLR4/CD14 in microelectrode performance clearly indicate the potential success of additional strategies for integrating intracortical microelectrodes.

III. CONCLUSION: FUTURE PERSPECTIVES AND DIRECTIONS

Electrical signals recorded from the neurons of human patients by intracortical microelectrodes have been used to communicate with computers, control robotic limbs, and to control the patient's own arm. The signal quality and the length of time that useful signals can be recorded are inconsistent. The widely held view of the community is that the inflammatory response of neural tissue that surrounds the microelectrodes, at least in part, compromises electrode reliability. Several studies have demonstrated the connection between neuroinflammation and microelectrode performance.

Inflammation is initiated when inflammatory cells recognize foreign biologics (i.e., damaged/infiltrating proteins and cells). Serum proteins and blood-derived cells invade the central nervous system following microelectrode implantation and aggravate the neuroinflammatory response. Cells and tissue are damaged from the trauma of microelectrode implantation. At the microelectrode surface, accumulation of pro-inflammatory molecules causes neuronal degeneration and increases the permeability of the blood-brain barrier, self-perpetuating the process. In rodents, the neuroinflammatory response to implanted microelectrodes in the motor cortex has been linked to decreased fine motor skills.[266]

Many labs, including ours, have worked to develop new microelectrode designs to reduce to neuroinflammatory response to intracortical microelectrodes. The extent to which neuroinflammation has been altered by electrode design varies between labs and designs. In the near term, the field must remember the effort that was taken to obtain FDA and CE approvals for clinical trials. The most direct route to translation is working with the devices further along in development. Ultimately, one electrode design will be unable to reach all the targets of the brain that may require interfacing. Therefore, simply making the intracortical microelectrode smaller, thinner, more flexible, mechanically dynamic, or inert may not be enough. We believe that the most likely route to enabling intracortical microelectrodes to interface with any region of the brain is to intimately understand the neuroinflammatory process, to allow for the most directed strategies for mitigation without interruption of the normal healthy response to disease or injury.

Here, we have outlined the rationale behind our hypothesis for the importance of the innate immune system in intracortical microelectrode performance. We have introduced our preliminary efforts and attempted to inspire others to also implement approaches that target the controlled immunosuppression of the localized and specific parts of the innate immune response to intracortical microelectrodes, as opposed to broader approaches that may lead to greater side effects. Much of the work reported here in understanding the role of specific innate immunity pathways was performed in mice. Although most basic neuroscience studies of the brain are also performed in mice, the majority of brain computer interface studies in rodents chose the rat over the mouse.[267] We have previously reported that there is no difference in the inflammatory response to microelectrode in the mouse and rat models[268] and thus chose to focus on the mouse as more transgenic models are available in mice than rats. The number and type of TLRs in mice varies to that found in humans; so as with all animal work, precaution should be taken in overanalyzing results from transgenic studies in mice when deciding pathways to clinical translation. Additionally, as chemists and biomaterialists, we appreciate the role of new materials and

electrode designs in the overall picture. In the end, no one approach will work alone, indefinitely. Only after we understand the body's temporally driven process for rejection of implanted devices can we better engineer the neural interface and our complete strategy for long-term integration.

ACKNOWLEDGMENTS

This work was supported in part by the Department of Biomedical Engineering and Case School of Engineering at Case Western Reserve University through laboratory start-up funds and the National Institute of Health, National Institute of Neurological Disorders and Stroke, (Grant No. 1R01NS082404-01A1). Additional support was provided by the Presidential Early Career Award for Scientists and Engineers (PECASE, JR. Capadona) and by Merit Review Award B1495-R from the United States (U.S.) Department of Veterans Affairs Rehabilitation Research and Development Service. None of the funding sources aided in collection, analysis, and interpretation of the data, in writing of the paper, or in the decision to submit the paper for publication. The authors have no conflict of interest related to this work to disclose. The contents do not represent the views of the U.S. Department of Veterans Affairs or the United States Government.

REFERENCES

1. Williams JC, Rennaker RL, Kipke DR. Long-term neural recording characteristics of wire microelectrode arrays implanted in cerebral cortex. Brain Res Brain Res Protoc. 1999;4(3):303–13.
2. Rousche PJ, Normann RA. Chronic recording capability of the Utah Intracortical Electrode Array in cat sensory cortex. J Neurosci Methods. 1998;82(1):1–15.
3. Freire MA, Morya E, Faber J, Santos JR, Guimaraes JS, Lemos NA, Sameshima K, Pereira A, Ribeiro S, Nicolelis MA. Comprehensive analysis of tissue preservation and recording quality from chronic multielectrode implants. PLoS One. 2011;6(11):e27554.
4. Perge JA, Zhang S, Malik WQ, Homer ML, Cash S, Friehs G, Eskandar EN, Donoghue JP, Hochberg LR. Reliability of directional information in unsorted spikes and local field potentials recorded in human motor cortex. J Neural Eng. 2014;11(4):046007.
5. Nolta NF, Christensen MB, Crane PD, Skousen JL, Tresco PA. BBB leakage, astrogliosis, and tissue loss correlate with silicon microelectrode array recording performance. Biomaterials. 2015;53:753–62.
6. Cody PA, Eles JR, Lagenaur CF, Kozai TD, Cui XT. Unique electrophysiological and impedance signatures between encapsulation types: An analysis of biological Utah array failure and benefit of a biomimetic coating in a rat model. Biomaterials. 2018;161:117–128.
7. Prasad A, Xue Q-S, Sankar V, Nishida T, Shaw G, Streit WJ, Sanchez JC. Comprehensive characterization and failure modes of tungsten microwire arrays in chronic neural implants. J Neural Eng. 2012;9(5):056015.
8. Liu X, McCreery DB, Bullara LA, Agnew WF. Evaluation of the stability of intracortical microelectrode arrays. IEEE Trans Neural Syst Rehabil Eng. 2006;14(1):91–100.
9. Prasad A, Xue Q-S, Dieme R, Sankar V, Mayrand R, Nishida T, Streit WJ, Sanchez JC. Abiotic-biotic characterization of Pt/Ir microelectrode arrays in chronic implants. Front Neurosci. 2014;7.
10. Barrese JC, Rao N, Paroo K, Triebwasser C, Vargas-Irwin C, Franquemont L, Donoghue JP. Failure mode analysis of silicon-based intracortical microelectrode arrays in non-human primates. J Neural Eng. 2013;10(6):066014.
11. Kozai TD, Li X, Bodily LM, Caparosa EM, Zenonos GA, Carlisle DL, Friedlander RM, Cui XT. Effects of caspase-1 knockout on chronic neural recording quality and longevity: Insight into cellular and molecular mechanisms of the reactive tissue response. Biomaterials. 2014;35(36):9620–34.
12. Chestek CA, Gilja V, Nuyujukian P, Foster JD, Fan JM, Kaufman MT, Churchland MM, Rivera-Alvidrez Z, Cunningham JP, Ryu SI, Shenoy KV. Long-term stability of neural prosthetic control signals from silicon cortical arrays in rhesus macaque motor cortex. J Neural Eng. 2011;8(4):045005.
13. Liu X, McCreery DB, Carter RR, Bullara LA, Yuen TG, Agnew WF. Stability of the interface between neural tissue and chronically implanted intracortical microelectrodes. IEEE Trans Rehabil Eng. 1999;7(3):315–26.
14. Jorfi M, Skousen JL, Weder C, Capadona JR. Progress towards biocompatible intracortical microelectrodes for neural interfacing applications. J Neural Eng. 2015;12(1):011001.
15. Kozai TDY, Catt K, Li X, Gugel ZV, Olafsson VT, Vazquez AL, Cui XT. Mechanical failure modes of chronically implanted planar silicon-based neural probes for laminar recording. Biomaterials. 2015;37:25–39.
16. Bjornsson CS, Oh SJ, Al-Kofahi YA, Lim YJ, Smith KL, Turner JN, De S, Roysam B, Shain W, Kim SJ. Effects of insertion conditions on tissue strain and vascular damage during neuroprosthetic device insertion. J Neural Eng. 2006;3(3):196–207.
17. Abbott NJ, Patabendige AA, Dolman DE, Yusof SR, Begley DJ. Structure and function of the blood–brain barrier. Neurobiol Dis. 2010;37(1):13–25.

18. Polikov V, Tresco P, Reichert W. Response of brain tissue to chronically implanted neural electrodes. J Neurosci Methods. 2005;148(1):1–18.
19. Anderson JM, Rodriguez A, Chang DT. Foreign body reaction to biomaterials. Semin Immunol. 2008;20: 86–100.
20. Potter KA, Buck AC, Self WK, Callanan ME, Sunil S, Capadona JR. The effect of resveratrol on neurodegeneration and blood brain barrier stability surrounding intracortical microelectrodes. Biomaterials. 2013;34:7001–15.
21. Biran R, Martin DC, Tresco PA. Neuronal cell loss accompanies the brain tissue response to chronically implanted silicon microelectrode arrays. Exp Neurol. 2005;195(1):115–26.
22. Block ML, Zecca L, Hong J-S. Microglia-mediated neurotoxicity: uncovering the molecular mechanisms. Nat Rev Neurosci. 2007;8(1):57–69.
23. Yadav A, Saini V, Arora S. MCP-1: chemoattractant with a role beyond immunity: a review. Clinica chimica acta; international journal of clinical chemistry. 2010;411(21-22):1570–9.
24. Quagliarello VJ, Wispelwey B, Long WJ Jr, Scheld WM. Recombinant human interleukin-1 induces meningitis and blood-brain barrier injury in the rat. Characterization and comparison with tumor necrosis factor. J Clin Invest. 1991;87(4):1360–6.
25. Ereifej ES, Rial GM, Hermann JK, Smith CS, Meade SM, Rayyan JM, Chen K, Feng H, Capadona JR. Implantation of neural probes in the brain elicits oxidative stress. Front Bioeng Biotechnol. 2018;6(9):1–12.
26. Bennett C, Samikkannu M, Mohammed F, Dietrich WD, Rajguru SM, Prasad A. Blood brain barrier (BBB)-disruption in intracortical silicon microelectrode implants. Biomaterials. 2018;164:1–10.
27. Takmakov P, Ruda K, Phillips KS, Isayeva IS, Krauthamer V, Welle CG. Rapid evaluation of the durability of cortical neural implants using accelerated aging with reactive oxygen species. J Neural Eng. 2015;12(2):026003.
28. Saxena T, Karumbaiah L, Gaupp EA, Patkar R, Patil K, Betancur M, Stanley GB, Bellamkonda RV. The impact of chronic blood–brain barrier breach on intracortical electrode function. Biomaterials. 2013;34(20):4703–13.
29. Ravikumar M, Sunil S, Black J, Barkauskas D, Haung AY, Miller RH, Selkirk SM, Capadona JR. The roles of blood-derived macrophages and resident microglia in the neuroinflammatory response to implanted intracortical microelectrodes. Biomaterials. 2014;S0142-9612(35):8049–64.
30. Scaffidi P, Misteli T, Bianchi ME. Release of chromatin protein HMGB1 by necrotic cells triggers inflammation. Nature. 2002;418(6894):191–5.
31. Pineau I, Lacroix S. Endogenous signals initiating inflammation in the injured nervous system. Glia. 2009;57(4):351–61.
32. Roitbak T, Sykova E. Diffusion barriers evoked in the rat cortex by reactive astrogliosis. Glia. 1999;28(1):40–8.
33. Schultz RL, Willey TJ. The ultrastructure of the sheath around chronically implanted electrodes in brain. J Neurocytol. 1976;5(6):621–42.
34. Hermann JK. The role of innate immunity in the response to intracortical microelectrodes [dissertation]: Cleveland, OH, Case Western Reserve University; 2018.
35. Rennaker RL, Miller J, Tang H, Wilson DA. Minocycline increases quality and longevity of chronic neural recordings. J Neural Eng. 2007;4(2):L1–5.
36. Shultz RB, Zhong Y. Minocycline targets multiple secondary injury mechanisms in traumatic spinal cord injury. Neural Regen Res. 2017;12(5):702–13.
37. Kobayashi K, Imagama S, Ohgomori T, Hirano K, Uchimura K, Sakamoto K, Hirakawa A, Takeuchi H, Suzumura A, Ishiguro N, Kadomatsu K. Minocycline selectively inhibits M1 polarization of microglia. Cell Death Dis. 2013;4(3):e525.
38. Ochsendorf F. Minocycline in acne vulgaris: benefits and risks. Am J Clin Dermatol. 2010;11(5):327–41.
39. Reed DN, Gregg FO, Corpe RS. Minocycline-induced black bone disease encountered during total knee arthroplasty. Orthopedics. 2012;35(5):e737–9.
40. Yang S, Takakubo Y, Kobayashi S, Asano T, Sasaki A, Sasaki K, Ohki H, Tamaki Y, Takagi M. Minocycline-induced periarticular black bones in inflamed joints which underwent arthroplastic reconstruction. Clin Orthop Surg. 2012;4:181–7.
41. Ashukem MT, Levy JC, Formaini N. Minocycline induced black bone disease: an incidental finding during total shoulder arthroplasty. Curr Orthop Pract. 2016;27(6):698–701.
42. Harris JP. The glia-neuronal response to cortical electrodes: interactions with substrate stiffness and electrophysiology [dissertation]. Cleveland (OH): Case Western Reserve University; 2012.
43. Dobrovolskaia MA, Vogel SN. Toll receptors, CD14, and macrophage activation and deactivation by LPS. Microb Infect. 2002;4:903–14.
44. Smiley ST, King JA, Hancock WW. Fibrinogen stimulates macrophage chemokine secretion through Toll-like receptor 4. J Immunol. 2001;167(5):2887–94.
45. Kozai TDY, Li X, Bodily LM, Caparosa EM, Zenonos GA, Carlisle DL, Friedlander RM, Cui XT. Effects of caspase-1 knockout on chronic neural recording quality and longevity: Insight into cellular and molecular mechanisms of the reactive tissue response. Biomaterials. 2014;35(36):9620–34.
46. Medzhitov R, Janeway CJ. Innate immunity. N Engl J Med. 2000;343(5):338-44.
47. Owen J, Punt J, Stranford S, Jones P. Kuby immunology, 7th ed. New York: WH Freeman. 2013;27(692): 109–130.
48. Netea MG, Latz E, Mills KHG, O'Neill LAJ. Innate im-

mune memory: a paradigm shift in understanding host defense. Nat Immunol. 2015;16:675–9.
49. Kawai T, Akira S. The role of pattern-recognition receptors in innate immunity: update on Toll-like receptors. Nat Immunol. 2010;11(5):373–84.
50. Geijtenbeek TB, Gringhuis SI. Signalling through C-type lectin receptors: shaping immune responses. Nat Rev Immunol. 2009;9(7):465–79.
51. Kawai T, Akira S. Toll-like receptor and RIG-1-like receptor signaling. Ann N Y Acad Sci. 2008;1143(1):1–20.
52. Yoneyama M, Fujita T. RNA recognition and signal transduction by RIG-I-like receptors. Immunol Rev. 2009;227(1):54–65.
53. Martinon F, Mayor A, Tschopp J. The inflammasomes: guardians of the body. Annu Rev Immunol. 2009;27: 229–65.
54. Franchi L, Eigenbrod T, Muñoz-Planillo R, Nuñez G. The inflammasome: a caspase-1-activation platform that regulates immune responses and disease pathogenesis. Nat Immunol. 2009;10(3):241–7.
55. Takeda K, Kaisho T, Akira S. Toll-like receptors. Annu Rev Immunol. 2003;21(1):335–76.
56. Takeda K, Akira S. Toll-like receptors in innate immunity. Int Immunol. 2005;17(1):1–14.
57. Tsan MF, Gao B. Endogenous ligands of Toll-like receptors. J Leukoc Biol. 2004;76(3):514–9.
58. Medzhitov R. Toll-like receptors and innate immunity. Nat Rev Immunol. 2001;1(2):135–45.
59. Beg AA. Endogenous ligands of Toll-like receptors: implications for regulating inflammatory and immune responses. Trends Immunol. 2002;23(11):509–12.
60. Kong Y, Le Y. Toll-like receptors in inflammation of the central nervous system. Int Immunopharmacol. 2011;11(10):1407–14.
61. Lehnardt S. Innate immunity and neuroinflammation in the CNS: The role of microglia in Toll-like receptor-mediated neuronal injury. Glia. 2010;58(3):253–63.
62. Rock FL, Hardiman G, Timans JC, Kastelein RA, Bazan JF. A family of human receptors structurally related to Drosophila Toll. Proc Natl Acad Sci U S A. 1998;95(2):588–93.
63. Chiang C, Beachy PA. Expression of a novel Toll-like gene spans the parasegment boundary and contributes to hedgehog function in the adult eye of Drosophila. Mech Dev. 1994;47(3):225–39.
64. Morisato D, Anderson KV. The spätzle gene encodes a component of the extracellular signaling pathway establishing the dorsal-ventral pattern of the Drosophila embryo. Cell. 1994;76(4):677–88.
65. Lemaitre B, Nicolas E, Michaut L, Reichhart J-M, Hoffmann JA. The dorsoventral regulatory gene cassette spätzle/Toll/cactus controls the potent antifungal response in Drosophila adults. Cell. 1996;86(6):973–83.
66. Medzhitov R, Preston-Hurlburt P, Janeway CA. A human homologue of the Drosophila Toll protein signals activation of adaptive immunity. Nature. 1997;388(6640): 394–7.
67. Hashimoto C, Hudson KL, Anderson KV. The Toll gene of drosophila, required for dorsal-ventral embryonic polarity, appears to encode a transmembrane protein. Cell. 1988;52(2):269–79.
68. Kobe B, Deisenhofer J. Proteins with leucine-rich repeats. Curr Opin Struct Biol. 1995;5(3):409–16.
69. Aravind L, Dixit VM, Koonin EV. Apoptotic molecular machinery: vastly increased complexity in vertebrates revealed by genome comparisons. Science. 2001;291(5507):1279–84.
70. Oosting M, Cheng S-C, Bolscher JM, Vestering-Stenger R, Plantinga TS, Verschueren IC, Arts P, Garritsen A, van Eenennaam H, Sturm P. Human TLR10 is an anti-inflammatory pattern-recognition receptor. Proc Natl Acad Sci U S A. 2014;111(42):E4478–E84.
71. Kawasaki T, Kawai T. Toll-like receptor signaling pathways. Front Immunol. 2014;5:461–8.
72. Celhar T, Magalhaes R, Fairhurst A-M. TLR7 and TLR9 in SLE: when sensing self goes wrong. Immunol Res. 2012;53(1-3):58–77.
73. Akira S, Uematsu S, Takeuchi O. Pathogen recognition and innate immunity. Cell. 2006;124(4):783–801.
74. Lindquist S. The heat-shock response. Annu Rev Biochem. 1986;55(1):1151–91.
75. Tsan M-F, Gao B. Heat shock protein and innate immunity. Cell Mol Immunol. 2004;1(4):274–9.
76. Roelofs MF, Boelens WC, Joosten LA, Abdollahi-Roodsaz S, Geurts J, Wunderink LU, Schreurs BW, van den Berg WB, Radstake TR. Identification of small heat shock protein B8 (HSP22) as a novel TLR4 ligand and potential involvement in the pathogenesis of rheumatoid arthritis. J Immunol. 2006;176(11):7021–7.
77. Lehnardt S, Schott E, Trimbuch T, Laubisch D, Krueger C, Wulczyn G, Nitsch R, Weber JR. A vicious cycle involving release of heat shock protein 60 from injured cells and activation of toll-like receptor 4 mediates neurodegeneration in the CNS. J Neurosci. 2008;28(10): 2320–31.
78. Ohashi K, Burkart V, Flohé S, Kolb H. Cutting edge: heat shock protein 60 is a putative endogenous ligand of the toll-like receptor-4 complex. J Immunol. 2000;164(2):558–61.
79. Zanin-Zhorov A, Nussbaum G, Franitza S, Cohen IR, Lider O. T cells respond to heat shock protein 60 via TLR2: activation of adhesion and inhibition of chemokine receptors. FASEB J. 2003;17(11):1567–9.
80. Asea A, Rehli M, Kabingu E, Boch JA, Baré O, Auron PE, Stevenson MA, Calderwood SK. Novel signal transduction pathway utilized by extracellular HSP70 role of Toll-like receptor (TLR) 2 and TLR4. J Biol Chem. 2002;277(17):15028–34.
81. Vabulas RM, Ahmad-Nejad P, Ghose S, Kirschning CJ, Issels RD, Wagner H. HSP70 as endogenous stimulus

of the Toll/interleukin-1 receptor signal pathway. J Biol Chem. 2002;277(17):15107–12.
82. Vabulas RM, Braedel S, Hilf N, Singh-Jasuja H, Herter S, Ahmad-Nejad P, Kirschning CJ, Da Costa C, Rammensee H-G, Wagner H. The endoplasmic reticulum-resident heat shock protein Gp96 activates dendritic cells via the Toll-like receptor 2/4 pathway. J Biol Chem. 2002;277(23):20847–53.
83. Brunn GJ, Bungum MK, Johnson GB, Platt JL. Conditional signaling by Toll-like receptor 4. FASEB J. 2005;19(7):872-4.
84. Johnson GB, Brunn GJ, Kodaira Y, Platt JL. Receptor-mediated monitoring of tissue well-being via detection of soluble heparan sulfate by Toll-like receptor 4. J Immunol. 2002;168(10):5233–9.
85. Johnson GB, Brunn GJ, Platt JL. Cutting edge: an endogenous pathway to systemic inflammatory response syndrome (SIRS)-like reactions through Toll-like receptor 4. J Immunol. 2004;172(1):20–4.
86. Jiang D, Liang J, Fan J, Yu S, Chen S, Luo Y, Prestwich GD, Mascarenhas MM, Garg HG, Quinn DA. Regulation of lung injury and repair by Toll-like receptors and hyaluronan. Nat Med. 2005;11(11):1173–9.
87. Termeer C, Benedix F, Sleeman J, Fieber C, Voith U, Ahrens T, Miyake K, Freudenberg M, Galanos C, Simon JC. Oligosaccharides of Hyaluronan activate dendritic cells via Toll-like receptor 4. J Exp Med. 2002;195(1):99–111.
88. Schaefer L, Babelova A, Kiss E, Hausser H-J, Baliova M, Krzyzankova M, Marsche G, Young MF, Mihalik D, Götte M. The matrix component biglycan is proinflammatory and signals through Toll-like receptors 4 and 2 in macrophages. J Clin Invest. 2005;115(8):2223–33.
89. Okamura Y, Watari M, Jerud ES, Young DW, Ishizaka ST, Rose J, Chow JC, Strauss JF. The extra domain A of fibronectin activates Toll-like receptor 4. J Biol Chem. 2001;276(13):10229–33.
90. Andersson U, Wang H, Palmblad K, Aveberger A-C, Bloom O, Erlandsson-Harris H, Janson A, Kokkola R, Zhang M, Yang H. High mobility group 1 protein (HMG-1) stimulates proinflammatory cytokine synthesis in human monocytes. J Exp Med. 2000;192(4):565–70.
91. Park JS, Svetkauskaite D, He Q, Kim J-Y, Strassheim D, Ishizaka A, Abraham E. Involvement of Toll-like receptors 2 and 4 in cellular activation by high mobility group box 1 protein. J Biol Chem. 2004;279(9):7370–7.
92. Kim J-B, Choi JS, Yu Y-M, Nam K, Piao C-S, Kim S-W, Lee M-H, Han P-L, Park J-s, Lee J-K. HMGB1, a novel cytokine-like mediator linking acute neuronal death and delayed neuroinflammation in the postischemic brain. J Neurosci. 2006;26(24):6413–21.
93. Park JS, Gamboni-Robertson F, He Q, Svetkauskaite D, Kim J-Y, Strassheim D, Sohn J-W, Yamada S, Maruyama I, Banerjee A. High mobility group box 1 protein interacts with multiple Toll-like receptors. Am J Physiol Cell Physiol. 2006;290(3):C917–C24.
94. Lee H, Jo E-K, Choi S-Y, Oh SB, Park K, Kim JS, Lee SJ. Necrotic neuronal cells induce inflammatory Schwann cell activation via TLR2 and TLR3: implication in Wallerian degeneration. Biochem Biophys Res Commun. 2006;350(3):742–7.
95. Li M, Carpio DF, Zheng Y, Bruzzo P, Singh V, Ouaaz F, Medzhitov RM, Beg AA. An essential role of the nf-kb/toll-like receptor pathway in induction of inflammatory and tissue-repair gene expression by necrotic cells. J Immunol. 2001;166:7128–35.
96. Guillot L, Balloy V, McCormack FX, Golenbock DT, Chignard M, Si-Tahar M. Cutting edge: the immunostimulatory activity of the lung surfactant protein-A involves Toll-like receptor 4. J Immunol. 2002;168(12):5989–92.
97. Barrat FJ, Meeker T, Gregorio J, Chan JH, Uematsu S, Akira S, Chang B, Duramad O, Coffman RL. Nucleic acids of mammalian origin can act as endogenous ligands for Toll-like receptors and may promote systemic lupus erythematosus. J Exp Med. 2005;202(8):1131–9.
98. Karikó K, Ni H, Capodici J, Lamphier M, Weissman D. mRNA is an endogenous ligand for Toll-like receptor 3. J Biol Chem. 2004;279(13):12542–50.
99. Ni H, Capodici J, Cannon G, Communi D, Boeynaems J-M, Karikó K, Weissman D. Extracellular mRNA induces dendritic cell activation by stimulating tumor necrosis factor-α secretion and signaling through a nucleotide receptor. J Biol Chem. 2002;277(15):12689–96.
100. Leadbetter EA, Rifkin IR, Hohlbaum AM, Beaudette BC, Shlomchik MJ, Marshak-Rothstein A. Chromatin–IgG complexes activate B cells by dual engagement of IgM and Toll-like receptors. Nature. 2002;416(6881):603–7.
101. Merline R, Moreth K, Beckmann J, Nastase MV, Zeng-Brouwers J, Tralhão JG, Lemarchand P, Pfeilschifter J, Schaefer RM, Iozzo RV. Signaling by the matrix proteoglycan decorin controls inflammation and cancer through PDCD4 and MicroRNA-21. Sci Signal. 2011;4(199):75–90.
102. Kim S, Takahashi H, Lin W-W, Descargues P, Grivennikov S, Kim Y, Luo J-L, Karin M. Carcinoma-produced factors activate myeloid cells through TLR2 to stimulate metastasis. Nature. 2009;457(7225):102–6.
103. Vogl T, Tenbrock K, Ludwig S, Leukert N, Ehrhardt C, van Zoelen MAD, Nacken W, Foell D, van der Poll T, Sorg C, Roth J. Mrp8 and Mrp14 are endogenous activators of Toll-like receptor 4, promoting lethal, endotoxin-induced shock. Nat Med. 2007;13:1042–9.
104. Riva M, Källberg E, Björk P, Hancz D, Vogl T, Roth J, Ivars F, Leanderson T. Induction of nuclear factor-κB responses by the S100A9 protein is Toll-like receptor-4-dependent. Immunology. 2012;137(2):172–82.
105. Reed-Geaghan EG, Savage JC, Hise AG, Landreth GE. CD14 and Toll-like receptors 2 and 4 are required for fibrillar a-stimulated microglial activation. J Neurosci. 2009;29(38):11982–92.
106. Fellner L, Irschick R, Schanda K, Reindl M, Kli-

maschewski L, Poewe W, Wenning GK, Stefanova N. Toll-like receptor 4 is required for α-synuclein dependent activation of microglia and astroglia. Glia. 2013;61(3):349–60.
107. Akira S, Takeda K. Toll-like receptor signalling. Nat Rev Immunol. 2004;4(7):499–511.
108. Agalave NM, Larsson M, Abdelmoaty S, Su J, Baharpoor A, Lundbäck P, Palmblad K, Andersson U, Harris H, Svensson CI. Spinal HMGB1 induces TLR4-mediated long-lasting hypersensitivity and glial activation and regulates pain-like behavior in experimental arthritis. PAIN®. 2014;155(9):1802–13.
109. Gaudreault E, Fiola S, Olivier M, Gosselin J. Epstein-Barr virus induces MCP-1 secretion by human monocytes via TLR2. J Virol. 2007;81(15):8016–24.
110. Hanisch U-K. Microglia as a source and target of cytokines. Glia. 2002;40(2):140–55.
111. Dubois RN, Abramson SB, Crofford L, Gupta RA, Simon LS, Van De Putte LB, Lipsky PE. Cyclooxygenase in biology and disease. FASEB J. 1998;12(12):1063–73.
112. Laflamme N, Soucy G, Rivest S. Circulating cell wall components derived from Gram-negative, not Gram-positive, bacteria cause a profound induction of the gene-encoding Toll-like receptor 2 in the CNS. J Neurochem. 2001;79(3):648–57.
113. Underhill DM, Ozinsky A, Hajjar AM, Stevens A, Wilson CB, Bassetti M, Aderem A. The Toll-like receptor 2 is recruited to macrophage phagosomes and discriminates between pathogens. Nature. 1999;401(6755): 811–15.
114. Travassos LH, Girardin SE, Philpott DJ, Blanot D, Nahori MA, Werts C, Boneca IG. Toll-like receptor 2-dependent bacterial sensing does not occur via peptidoglycan recognition. EMBO Rep. 2004;5(10):1000–6.
115. Alexopoulou L, Thomas V, Schnare M, Lobet Y, Anguita J, Schoen RT, Medzhitov R, Fikrig E, Flavell RA. Hyporesponsiveness to vaccination with Borrelia burgdorferi OspA in humans and in TLR1-and TLR2-deficient mice. Nat Med. 2002;8(8):878–84.
116. Ozinsky A, Underhill DM, Fontenot JD, Hajjar AM, Smith KD, Wilson CB, Schroeder L, Aderem A. The repertoire for pattern recognition of pathogens by the innate immune system is defined by cooperation between toll-like receptors. Proc Natl Acad Sci U S A. 2000;97(25):13766–71.
117. Takeuchi O, Kawai T, Mühlradt PF, Morr M, Radolf JD, Zychlinsky A, Takeda K, Akira S. Discrimination of bacterial lipoproteins by Toll-like receptor 6. Int Immunol. 2001;13(7):933–40.
118. Takeuchi O, Sato S, Horiuchi T, Hoshino K, Takeda K, Dong Z, Modlin RL, Akira S. Cutting edge: role of Toll-like receptor 1 in mediating immune response to microbial lipoproteins. J Immunol. 2002;169(1):10–4.
119. Schwandner R, Dziarski R, Wesche H, Rothe M, Kirschning CJ. Peptidoglycan-and lipoteichoic acid-induced cell activation is mediated by Toll-like receptor 2. J Biol Chem. 1999;274(25):17406–9.
120. Aliprantis AO, Yang R-B, Mark MR, Suggett S, Devaux B, Radolf JD, Klimpel GR, Godowski P, Zychlinsky A. Cell activation and apoptosis by bacterial lipoproteins through toll-like receptor-2. Science. 1999;285(5428):736–9.
121. Means TK, Wang S, Lien E, Yoshimura A, Golenbock DT, Fenton MJ. Human toll-like receptors mediate cellular activation by Mycobacterium tuberculosis. J Immunol. 1999;163(7):3920–7.
122. Hajjar AM, O'Mahony DS, Ozinsky A, Underhill DM, Aderem A, Klebanoff SJ, Wilson CB. Cutting edge: functional interactions between toll-like receptor (TLR) 2 and TLR1 or TLR6 in response to phenol-soluble modulin. J Immunol. 2001;166(1):15–9.
123. Coelho PS, Klein A, Talvani A, Coutinho SF, Takeuchi O, Akira S, Silva JS, Canizzaro H, Gazzinelli RT, Teixeira MM. Glycosylphosphatidylinositol-anchored mucin-like glycoproteins isolated from Trypanosoma cruzi trypomastigotes induce in vivo leukocyte recruitment dependent on MCP-1 production by IFN-γ-primed-macrophages. J Leukoc Biol. 2002;71(5):837–44.
124. Massari P, Henneke P, Ho Y, Latz E, Golenbock DT, Wetzler LM. Cutting edge: Immune stimulation by neisserial porins is toll-like receptor 2 and MyD88 dependent. J Immunol. 2002;168(4):1533–7.
125. Werts C, Tapping RI, Mathison JC, Chuang T-H, Kravchenko V, Saint Girons I, Haake DA, Godowski PJ, Hayashi F, Ozinsky A. Leptospiral lipopolysaccharide activates cells through a TLR2-dependent mechanism. Nat Immunol. 2001;2(4):346–52.
126. Hirschfeld M, Weis JJ, Toshchakov V, Salkowski CA, Cody MJ, Ward DC, Qureshi N, Michalek SM, Vogel SN. Signaling by toll-like receptor 2 and 4 agonists results in differential gene expression in murine macrophages. Infect Immun. 2001;69(3):1477–82.
127. Poltorak A, He X, Smirnova I, Liu M-Y, Van Huffel C, Du X, Birdwell D, Alejos E, Silva M, Galanos C. Defective LPS signaling in C3H/HeJ and C57BL/10ScCr mice: mutations in Tlr4 gene. Science. 1998;282(5396):2085–8.
128. Qureshi ST, Larivière L, Leveque G, Clermont S, Moore KJ, Gros P, Malo D. Endotoxin-tolerant mice have mutations in Toll-like receptor 4 (Tlr4). J Exp Med. 1999;189(4):615–25.
129. Hoshino K, Takeuchi O, Kawai T, Sanjo H, Ogawa T, Takeda Y, Takeda K, Akira S. Cutting Edge: Toll-like receptor 4 (TLR4)-deficient mice are hyporesponsive to lipopolysaccharide: evidence for TLR4 as the LPS gene product. J Immunol. 1999;162:3749–52.
130. Lehnardt S, Lachance C, Patrizi S, Lefebvre S, Follett PL, Jensen FE, Rosenberg PA, Volpe JJ, Vartanian T. The toll-like receptor TLR4 is necessary for lipopolysaccharide-induced oligodendrocyte injury in the CNS. J Neurosci. 2002;22(7):2478–86.

131. Tada H, Nemoto E, Shimauchi H, Watanabe T, Mikami T, Matsumoto T, Ohno N, Tamura H, Shibata Ki, Akashi S. Saccharomyces cerevisiae-and Candida albicans-derived mannan induced production of tumor necrosis factor alpha by human monocytes in a CD14-and Toll-like receptor 4-dependent manner. Microbiol Immunol. 2002;46(7):503–12.
132. Shoham S, Huang C, Chen J-M, Golenbock DT, Levitz SM. Toll-like receptor 4 mediates intracellular signaling without TNF-α release in response to Cryptococcus neoformans polysaccharide capsule. J Immunol. 2001;166(7):4620–6.
133. Kurt-Jones EA, Popova L, Kwinn L, Haynes LM, Jones LP, Tripp RA, Walsh EE, Freeman MW, Golenbock DT, Anderson LJ, Finberg RW. Pattern recognition receptors TLR4 and CD14 mediate response to respiratory syncytial virus. Nat Immunol. 2000;5:398–401.
134. Kurt-Jones EA, Chan M, Zhou S, Wang J, Reed G, Bronson R, Arnold MM, Knipe DM, Finberg RW. Herpes simplex virus 1 interaction with Toll-like receptor 2 contributes to lethal encephalitis. Proc Natl Acad Sci U S A. 2004;101(5):1315–20.
135. Wright SD, Ramos RA, Tobias PS, Ulevitch RJ, Mathison JC. CD14, a receptor for complexes of lipopolysaccharide (LPS) and LPS binding protein. Science. 1990;249(4975):1431–3.
136. Yu B, Wright SD. Catalytic properties of lipopolysaccharide (LPS) binding protein transfer of LPS to soluble CD14. J Biol Chem. 1996;271(8):4100–5.
137. Thomas CJ, Kapoor M, Sharma S, Bausinger H, Zyilan U, Lipsker D, Hanau D, Surolia A. Evidence of a trimolecular complex involving LPS, LPS binding protein and soluble CD14 as an effector of LPS response. FEBS Lett. 2002;531(2):184–8.
138. Fitzgerald KA, Rowe DC, Golenbock DT. Endotoxin recognition and signal transduction by the TLR4/MD2-complex. Microb Infect. 2004;6(15):1361–7.
139. Haziot A, Ferrero E, Kontgen F, Hijiya N, Yamamoto S, Silver J, Stewart CL, Goyer SM. Resistance to endotoxin shock and reduced dissemination of gram-negative bacteria in CD14-deficient mice. Immunity. 1996;4:407–14.
140. Franklin W, Mason D, Pulford K, Falini B, Bliss E, Gatter K, Stein H, Clarke L, McGee J. Immunohistological analysis of human mononuclear phagocytes and dendritic cells by using monoclonal antibodies. Lab Invest. 1986;54(3):322–35.
141. Beschorner R, Nguyen TD, Gozalan F, Pedal I, Mattern R, Schluesener HJ, Meyermann R, Schwab JM. CD14 expression by activated parenchymal microglia/macrophages and infiltrating monocytes following human traumatic brain injury. Acta Neuropathol (Berl). 2002;103(6):541–9.
142. Ziegler-Heitbrock HWL, Ulevitch RJ. CD14: Cell surface receptor and differentiation marker. Immunol Today. 1993;14(3):121–5.
143. Compton T, Kurt-Jones EA, Boehme KW, Belko J, Latz E, Golenbock DT, Finberg RW. Human cytomegalovirus activates inflammatory cytokine responses via CD14 and Toll-like receptor 2. J Virol. 2003;77(8):4588–96.
144. Chun KH, Seong SY. CD14 but not MD2 transmit signals from DAMP. Int Immunopharmacol. 2010;10(1):98–106.
145. Kim S, Kim SY, Pribis JP, Lotze M, Mollen KP, Shapiro R, Loughran P, Scott MJ, Billiar TR. Signaling of High Mobility Group Box 1 (HMGB1) through Toll-like receptor 4 in macrophages requires CD14. Mol Med. 2013;19(1):88–98.
146. Asea A, Kraeft S-K, Kurt-Jones EA, Stevenson MA, Chen LB, Finberg RW, Koo GC, Calderwood SK. HSP70 stimulates cytokine production through a CD14-dependant pathway, demonstrating its dual role as a chaperone and cytokine. Nat Med. 2000;6(4):435–42.
147. Baumann CL, Aspalter IM, Sharif O, Pichlmair A, Bluml S, Grebien F, Bruckner M, Pasierbek P, Aumayr K, Planyavsky M, Bennett KL, Colinge J, Knapp S, Superti-Furga G. CD14 is a coreceptor of Toll-like receptors 7 and 9. J Exp Med. 2010;207(12):2689–701.
148. Devitt A, Moffatt OD, Raykundalia C, Capra JD, Simmons DL, Gregory CD. Human CD14 mediates recognition and phagocytosis of apoptotic cells. Nature. 1998;392(6675):505–9.
149. Devitt A, Marshall LJ. The innate immune system and the clearance of apoptotic cells. J Leukoc Biol. 2011;90(3):447–57.
150. Gregory CD. CD14-dependent clearance of apoptotic cells: relevance to the immune system. Curr Opin Immunol. 2000;12(1):27–34.
151. Wang P-y, Munford RS. CD14-dependent internalization and metabolism of extracellular phosphatidylinositol by monocytes. J Biol Chem. 1999;274(33):23235–41.
152. Arroyo DS, Soria JA, Gaviglio EA, Rodriguez-Galan MC, Iribarren P. Toll-like receptors are key players in neurodegeneration. Int Immunopharmacol. 2011;11(10):1415–21.
153. Bsibsi M, Ravid R, Gveric D, Van Noort JM. Broad expression of Toll-like receptors in the human central nervous system. J Neuropathol Exp Neurol. 2002;61(11):1013–21.
154. Beschorner R, Schluesener HJ, Gözalan F, Meyermann R, Schwab JM. Infiltrating CD14+ monocytes and expression of CD14 by activated parenchymal microglia/macrophages contribute to the pool of CD14+ cells in ischemic brain lesions. J Neuroimmunol. 2002;126(1-2):107–15.
155. Nadeau S, Rivest S. Role of microglial-derived tumor necrosis factor in mediating CD14 transcription and nuclear factor κ B activity in the brain during endotoxemia. J Neurosci. 2000;20(9):3456–68.
156. Lehnardt S, Henneke P, Lien E, Kasper DL, Volpe JJ, Bechmann I, Nitsch R, Weber JR, Golenbock DT, Vartanian T. A mechanism for neurodegeneration induced by group

B streptococci through activation of the TLR2/MyD88 pathway in microglia. J Immunol. 2006;177(1):583–92.
157. Lehnardt S, Massillon L, Follett P, Jensen FE, Ratan R, Rosenberg PA, Volpe JJ, Vartanian T. Activation of innate immunity in the CNS triggers neurodegeneration through a Toll-like receptor 4-dependent pathway. Proc Natl Acad Sci U S A. 2003;100(14):8514–9.
158. Fassbender K, Walter S, Kuhl S, Landmann R, Ishii K, Bertsch T, Stalder AK, Muehlhauser F, Liu Y, Ulmer AJ, Rivest S, Lentschat A, Gulbins E, Jucker M, Staufenbiel M, Brechtel K, Walter J, Multhaup G, Penke B, Adachi Y, Hartmann T, Beyreuther K. The LPS receptor (CD14) links innate immunity with Alzheimer's disease. FASEB J. 2004;18(1):203–5.
159. Nagyoszi P, Wilhelm I, Farkas AE, Fazakas C, Dung NT, Hasko J, Krizbai IA. Expression and regulation of toll-like receptors in cerebral endothelial cells. Neurochem Int. 2010;57(5):556–64.
160. Andersson J, Nagy S, Bjourk L, Abrams J, Holm S, Andersson U. Bacterial toxin-induced cytokine production studied at the single-cell level. Immunol Rev. 1992;127(1):69–96.
161. Kim C, Rockenstein E, Spencer B, Kim H-K, Adame A, Trejo M, Stafa K, Lee H-J, Lee S-J, Masliah E. Antagonizing neuronal toll-like receptor 2 prevents synucleinopathy by activating autophagy. Cell Rep. 2015;13(4):771–82.
162. O'Callaghan P, Li J-P, Lannfelt L, Lindahl U, Zhang X. Microglial heparan sulfate proteoglycans facilitate the cluster-of-differentiation 14 (CD14)/toll-like receptor 4 (TLR4)-dependent inflammatory response. J Biol Chem. 2015;290(24):14904–14.
163. Willis D, Li KW, Zheng J-Q, Chang JH, Smit A, Kelly T, Merianda TT, Sylvester J, Van Minnen J, Twiss JL. Differential transport and local translation of cytoskeletal, injury-response, and neurodegeneration protein mRNAs in axons. J Neurosci. 2005;25(4):778–91.
164. Willis DE, van Niekerk EA, Sasaki Y, Mesngon M, Merianda TT, Williams GG, Kendall M, Smith DS, Bassell GJ, Twiss JL. Extracellular stimuli specifically regulate localized levels of individual neuronal mRNAs. J Cell Biol. 2007;178(6):965–80.
165. Pais TF, Figueiredo C, Peixoto R, Braz MH, Chatterjee S. Necrotic neurons enhance microglial neurotoxicity through induction of glutaminase by a MyD88-dependent pathway. J Neuroinflammation. 2008;5:43–55.
166. Leow-Dyke S, Allen C, Denes A, Nilsson O, Maysami S, Bowie AG, Rothwell NJ, Pinteaux E. Neuronal Toll-like receptor 4 signaling induces brain endothelial activation and neutrophil transmigration in vitro. J Neuroinflammation. 2012;9(1):230–42.
167. Neher JJ, Neniskyte U, Brown GC. Primary phagocytosis of neurons by inflamed microglia: potential roles in neurodegeneration. Front Pharmacol. 2012;3:27–36.
168. Milatovic D, Zaja-Milatovic S, Montine KS, Shie F-S, Montine TJ. Neuronal oxidative damage and dendritic degeneration following activation of CD14-dependent innate immune response in vivo. J Neuroinflammation. 2004;1(1):20–6.
169. Sloane J, Batt C, Ma Y, Harris Z, Trapp B, Vartanian T. Hyaluronan blocks oligodendrocyte progenitor maturation and remyelination through TLR2. Proc Natl Acad Sci U S A. 2010;107(25):11555–60.
170. Hanisch U-K, Johnson TV, Kipnis J. Toll-like receptors: roles in neuroprotection? Trends Neurosci. 2008;31(4):176–82.
171. Hayakawa K, Okazaki R, Morioka K, Nakamura K, Tanaka S, Ogata T. Lipopolysaccharide preconditioning facilitates M2 activation of resident microglia after spinal cord injury. J Neurosci Res. 2014;92(12):1647–58.
172. Lambertsen KL, Clausen BH, Babcock AA, Gregersen R, Fenger C, Nielsen HH, Haugaard LS, Wirenfeldt M, Nielsen M, Dagnaes-Hansen F, Bluethmann H, Faergeman NJ, Meldgaard M, Deierborg T, Finsen B. Microglia protect neurons against ischemia by synthesis of tumor necrosis factor. J Neurosci. 2009;29(5):1319–30.
173. Stefanova N, Fellner L, Reindl M, Masliah E, Poewe W, Wenning GK. Toll-like receptor 4 promotes α-synuclein clearance and survival of nigral dopaminergic neurons. Am J Pathol. 2011;179(2):954–63.
174. Venezia S, Refolo V, Polissidis A, Stefanis L, Wenning GK, Stefanova N. Toll-like receptor 4 stimulation with monophosphoryl lipid A ameliorates motor deficits and nigral neurodegeneration triggered by extraneuronal α-synucleinopathy. Mol Neurodegener. 2017;12(1):52–64.
175. Hossain MJ, Tanasescu R, Gran B. Innate immune regulation of autoimmunity in multiple sclerosis: Focus on the role of Toll-like receptor 2. J Neuroimmunol. 2017;304:11–20.
176. De Paola M, Sestito SE, Mariani A, Memo C, Fanelli R, Freschi M, Bendotti C, Calabrese V, Peri F. Synthetic and natural small molecule TLR4 antagonists inhibit motoneuron death in cultures from ALS mouse model. Pharmacol Res. 2016;103:180–7.
177. Reed-Geaghan EG, Reed QW, Cramer PE, Landreth GE. Deletion of CD14 attenuates Alzheimer's disease pathology by influencing the brain's inflammatory milieu. J Neurosci. 2010;30(46):15369–73.
178. Bettoni I, Comelli F, Rossini C, Granucci F, Giagnoni G, Peri F, Costa B. Glial TLR4 receptor as new target to treat neuropathic pain: Efficacy of a new receptor antagonist in a model of peripheral nerve injury in mice. Glia. 2008;56(12):1312–9.
179. Kawakita F, Fujimoto M, Liu L, Nakano F, Nakatsuka Y, Suzuki H. Effects of Toll-like receptor 4 antagonists against cerebral vasospasm after experimental subarachnoid hemorrhage in mice. Mol Neurobiol. 2016:1-10.
180. Hanafy KA. The role of microglia and the TLR4 pathway in neuronal apoptosis and vasospasm after subarachnoid hemorrhage. J Neuroinflammation. 2013;10(1):868–77.

181. Dong X-Q, Yu W-H, Hu Y-Y, Zhang Z-Y, Huang M. Oxymatrine reduces neuronal cell apoptosis by inhibiting Toll-like receptor 4/nuclear factor kappa-B-dependent inflammatory responses in traumatic rat brain injury. Inflamm Res. 2011;60(6):533–9.
182. Hyakkoku K, Hamanaka J, Tsuruma K, Shimazawa M, Tanaka H, Uematsu S, Akira S, Inagaki N, Nagai H, Hara H. Toll-like receptor 4 (TLR4), but not TLR3 or TLR9, knock-out mice have neuroprotective effects against focal cerebral ischemia. Neuroscience. 2010;171(1): 258–67.
183. Kigerl KA, Lai W, Rivest S, Hart RP, Satoskar AR, Popovich PG. Toll-like receptor (TLR)-2 and TLR-4 regulate inflammation, gliosis, and myelin sparing after spinal cord injury. J Neurochem. 2007;102(1):37–50.
184. Babcock AA, Wirenfeldt M, Holm T, Nielsen HH, Dissing-Olesen L, Toft-Hansen H, Millward JM, Landmann R, Rivest S, Finsen B. Toll-like receptor 2 signaling in response to brain injury: an innate bridge to neuroinflammation. J Neurosci. 2006;26(49):12826–37.
185. Trotta T, Porro C, Calvello R, Panaro MA. Biological role of Toll-like receptor-4 in the brain. J Neuroimmunol. 2014;268(1-2):1–12.
186. Landreth GE, Reed-Geaghan EG. Toll-like receptors in Alzheimer's disease. 2009;336:137–53.
187. Akiyama H, Barger S, Barnum S, Bradt B, Bauer J, Cole GM, Cooper NR, Eikelenboom P, Emmerling M, Fiebich BL. Inflammation and Alzheimer's disease. Neurobiol Aging. 2000;21(3):383–421.
188. Walter S, Letiembre M, Liu Y, Heine H, Penke B, Hao W, Bode B, Manietta N, Walter J, Schulz-Schüffer W. Role of the toll-like receptor 4 in neuroinflammation in Alzheimer's disease. Cell Physiol Biochem. 2007;20(6): 947–56.
189. Jana M, Palencia CA, Pahan K. Fibrillar amyloid-β peptides activate microglia via TLR2: implications for Alzheimer's disease. J Immunol. 2008;181(10):7254–62.
190. Udan ML, Ajit D, Crouse NR, Nichols MR. Toll-like receptors 2 and 4 mediate Aβ (1–42) activation of the innate immune response in a human monocytic cell line. J Neurochem. 2008;104(2):524–33.
191. Tahara K, Kim H-D, Jin J-J, Maxwell JA, Li L, Fukuchi K-i. Role of Toll-like receptor signalling in Aβ uptake and clearance. Brain. 2006;129(11):3006–19.
192. Bate C, Veerhuis R, Eikelenboom P, Williams A. Microglia kill amyloid-β1-42 damaged neurons by a CD14-dependent process. Neuroreport. 2004;15(9):1427–30.
193. Fellner L, Jellinger KA, Wenning GK, Stefanova N. Glial dysfunction in the pathogenesis of α-synucleinopathies: emerging concepts. Acta Neuropathol. 2011;121(6): 675–93.
194. Casula M, Iyer AM, Spliet WG, Anink JJ, Steentjes K, Sta M, Troost D, Aronica E. Toll-like receptor signaling in amyotrophic lateral sclerosis spinal cord tissue. Neuroscience. 2011;179:233–43.
195. Zhang R, Hadlock KG, Do H, Yu S, Honrada R, Champion S, Forshew D, Madison C, Katz J, Miller RG. Gene expression profiling in peripheral blood mononuclear cells from patients with sporadic amyotrophic lateral sclerosis (sALS). J Neuroimmunol. 2011;230(1): 114–23.
196. Beers DR, Henkel JS, Xiao Q, Zhao W, Wang J, Yen AA, Siklos L, McKercher SR, Appel SH. Wild-type microglia extend survival in PU. 1 knockout mice with familial amyotrophic lateral sclerosis. Proc Natl Acad Sci U S A. 2006;103(43):16021–6.
197. Zhao W, Beers DR, Henkel JS, Zhang W, Urushitani M, Julien JP, Appel SH. Extracellular mutant SOD1 induces microglial-mediated motoneuron injury. Glia. 2010;58(2):231–43.
198. Lee JY, Lee JD, Phipps S, Noakes PG, Woodruff TM. Absence of toll-like receptor 4 (TLR4) extends survival in the hSOD1 G93A mouse model of amyotrophic lateral sclerosis. J Neuroinflammation. 2015;12(1):90–7.
199. Ravikumar M, Hageman DJ, Tomaszewski WH, Chandra GM, Skousen JL, Capadona JR. The effect of residual endotoxin contamination on the neuroinflammatory response to sterilized intracortical microelectrodes. J Mater Chem B. 2014;2:2517–29.
200. Xie Z, Wei M, Morgan TE, Fabrizio P, Han D, Finch CE, Longo VD. Peroxynitrite mediates neurotoxicity of amyloid β-peptide1–42-and lipopolysaccharide-activated microglia. J Neurosci. 2002;22(9):3484–92.
201. Caso JR, Pradillo JM, Hurtado O, Lorenzo P, Moro MA, Lizasoain I. Toll-like receptor 4 is involved in brain damage and inflammation after experimental stroke. Circulation. 2007;115(12):1599–608.
202. Hua F, Ma J, Ha T, Xia Y, Kelley J, Williams DL, Kao RL, Browder IW, Schweitzer JB, Kalbfleisch JH. Activation of Toll-like receptor 4 signaling contributes to hippocampal neuronal death following global cerebral ischemia/reperfusion. J Neuroimmunol. 2007;190(1):101–11.
203. Thiel VE, Audus KL. Nitric oxide and blood–brain barrier integrity. Antioxid Redox Signal. 2001;3(2):273–8.
204. Merrill JE, Murphy SP. Inflammatory events at the blood brain barrier: regulation of adhesion molecules, cytokines, and chemokines by reactive nitrogen and oxygen species. Brain Behav Immun. 1997;11(4):245–63.
205. Banks WA, Erickson MA. The blood–brain barrier and immune function and dysfunction. Neurobiol Dis. 2010;37(1):26–32.
206. Kim YT, Hitchcock RW, Bridge MJ, Tresco PA. Chronic response of adult rat brain tissue to implants anchored to the skull. Biomaterials. 2004;25(12):2229–37.
207. Tate CC, Tate MC, LaPlaca MC. Fibronectin and laminin increase in the mouse brain after controlled cortical impact injury. J Neurotrauma. 2007;24(1):226–30.
208. Potter KA, Jorfi M, Householder KT, Foster EJ, Weder C, Capadona JR. Curcumin-releasing mechanically-adaptive intracortical implants improve the proximal neuronal

density and blood-brain barrier stability. Acta Biomater. 2014;10(5):2209-22.
209. Liesz A, Dalpke A, Mracsko E, Antoine DJ, Roth S, Zhou W, Yang H, Na S-Y, Akhisaroglu M, Fleming T. DAMP signaling is a key pathway inducing immune modulation after brain injury. J Neurosci. 2015;35(2):583–98.
210. Faraco G, Fossati S, Bianchi M, Patrone M, Pedrazzi M, Sparatore B, Moroni F, Chiarugi A. High mobility group box 1 protein is released by neural cells upon different stresses and worsens ischemic neurodegeneration in vitro and in vivo. J Neurochem. 2007;103(2):590–603.
211. Turner JN, Shain W, Szarowski DH, Andersen M, Martins S, Isaacson M, Craighead H. Cerebral astrocyte response to micromachined silicon implants. Exp Neurol. 1999;156(1):33–49.
212. Kinouchi H, Sharp FR, Hill MP, Koistinaho J, Sagar SM, Chan PH. Induction of 70-kDa heat shock protein and hsp70 mRNA following transient focal cerebral ischemia in the rat. J Cereb Blood Flow Metab. 1993;13(1):105–15.
213. Kinouchi H, Sharp FR, Koistinaho J, Hicks K, Kamii H, Chan PH. Induction of heat shock hsp70 mRNA and HSP70 kDa protein in neurons in the 'penumbra' following focal cerebral ischemia in the rat. Brain Res. 1993;619(1-2):334–8.
214. Skousen J, Merriam S, Srivannavit O, Perlin G, Wise K, Tresco P. Reducing surface area while maintaining implant penetrating profile lowers the brain foreign body response to chronically implanted planar silicon microelectrode arrays. Prog Brain Res. 2011;194C:167–80.
215. Potter KA, Buck AC, Self WK, Capadona JR. Stab injury and device implantation within the brain results in inversely multiphasic neuroinflammatory and neurodegenerative responses. J Neural Eng. 2012;9(4):046020.
216. Chen C-C, Hung T-H, Wang Y-H, Lin C-W, Wang P-Y, Lee C-Y, Chen S-F. Wogonin improves histological and functional outcomes, and reduces activation of TLR4/NF-κB signaling after experimental traumatic brain injury. PLoS One. 2012;7(1):e30294.
217. Kumar A, Takada Y, Boriek AM, Aggarwal BB. Nuclear factor-κB: its role in health and disease. J Mol Med. 2004;82(7):434–48.
218. McConnell GC, Rees HD, Levey AI, Gutekunst CA, Gross RE, Bellamkonda RV. Implanted neural electrodes cause chronic, local inflammation that is correlated with local neurodegeneration. J Neural Eng. 2009;6(5):056003.
219. Wei Y, Chen J, Hu Y, Lu W, Zhang X, Wang R, Chu K. Rosmarinic acid mitigates lipopolysaccharide-induced neuroinflammatory responses through the inhibition of TLR4 and CD14 expression and NF-κB and NLRP3 inflammasome activation. Inflammation. 2018:1–9.
220. Wu F-x, Bian J-j, Miao X-r, Huang S-d, Xu X-w, Gong D-j, Sun Y-m, Lu Z-j, Yu W-f. Intrathecal siRNA against Toll-like receptor 4 reduces nociception in a rat model of neuropathic pain. Int J Med Sci. 2010;7(5):251–9.
221. Li C, Peng S, Liu X, Han C, Wang X, Jin T, Liu S, Wang W, Xie X, He X. Glycyrrhizin, a direct HMGB1 antagonist, ameliorates inflammatory infiltration in a model of autoimmune thyroiditis via inhibition of TLR2-HMGB1 signaling. Thyroid. 2017;27(5):722–31.
222. Ulbrich F, Kaufmann K, Roesslein M, Wellner F, Auwärter V, Kempf J, Loop T, Buerkle H, Goebel U. Argon mediates anti-apoptotic signaling and neuroprotection via inhibition of toll-like receptor 2 and 4. PLoS One. 2015;10(12):e0143887.
223. Mao SS, Hua R, Zhao XP, Qin X, Sun ZQ, Zhang Y, Wu YQ, Jia MX, Cao JL, Zhang YM. Exogenous administration of PACAP alleviates traumatic brain injury in rats through a mechanism involving the TLR4/MyD88/NF-small ka, CyrillicB pathway. J Neurotrauma. 2012;29(10):1941–59.
224. Wang Z, Wu L, You W, Ji C, Chen G. Melatonin alleviates secondary brain damage and neurobehavioral dysfunction after experimental subarachnoid hemorrhage: possible involvement of TLR4-mediated inflammatory pathway. J Pineal Res. 2013;55(4):399–408.
225. Zhang T, Su J, Guo B, Wang K, Li X, Liang G. Apigenin protects blood–brain barrier and ameliorates early brain injury by inhibiting TLR4-mediated inflammatory pathway in subarachnoid hemorrhage rats. Int Immunopharmacol. 2015;28(1):79–87.
226. Zhang T, Su J, Guo B, Zhu T, Wang K, Li X. Ursolic acid alleviates early brain injury after experimental subarachnoid hemorrhage by suppressing TLR4-mediated inflammatory pathway. Int Immunopharmacol. 2014;23(2):585–91.
227. Willis LM, Bielinski DF, Fisher DR, Matthan NR, Joseph JA. Walnut extract inhibits LPS-induced activation of BV-2 microglia via internalization of TLR4: possible involvement of phospholipase D2. Inflammation. 2010;33(5):325–33.
228. Golabchi A, Wu B, Li X, Carlisle DL, Kozai TD, Friedlander RM, Cui XT. Melatonin improves quality and longevity of chronic neural recording. Biomaterials. 2018;180:225–39.
229. Hermann JK, Lin S, Soffer A, Wong C, Srivastava V, Chang J, Sunil S, Sudhakar S, Tomaswzeski W, Protasiewicz G, Selkirk S, Miller R, Capadona JR. The role of Toll-like receptor 2 and 4 innate immunity pathways in intracortical microelectrode-induced neuroinflammation. Front Bioeng Biotechnol. 2018;6:113–30.
230. Hermann JK, Ravikumar M, Shoffstall AJ, Ereifej ES, Kovach KM, Chang J, Soffer A, Wong C, Srivastava V, Smith P, Protasiewicz G, Jiang J, Selkirk SM, Miller RH, Sidik S, Ziats NP, Taylor DM, Capadona JR. Inhibition of the cluster of differentiation 14 innate immunity pathway with IAXO-101 improves chronic microelectrode performance. J Neural Eng. 2018;15(2):025002.
231. Bedell HW, Hermann JK, Ravikumar M, Lin S, Rein A, Li X, Molinich E, Smith PD, Selkirk SM, Miller RH,

Sidik S, Taylor DM, Capadona JR. Targeting CD14 on blood derived cells improves intracortical microelectrode performance. Biomaterials. 2018;163:163–73.
232. Piazza M, Yu L, Teghanemt A, Gioannini T, Weiss J, Peri F. Evidence of a specific interaction between new synthetic antisepsis agents and CD14. Biochemistry. 2009;48(51):12337–44.
233. Piazza M, Rossini C, Della Fiorentina S, Pozzi C, Comelli F, Bettoni I, Fusi P, Costa B, Peri F. Glycolipids and benzylammonium lipids as novel antisepsis agents: synthesis and biological characterization. J Med Chem. 2009;52(4):1209–13.
234. Barboza R, Lima FA, Reis AS, Murillo OJ, Peixoto EPM, Bandeira CL, Fotoran WL, Sardinha LR, Wunderlich G, Bevilacqua E. TLR4-mediated placental pathology and pregnancy outcome in experimental malaria. Sci Rep. 2017;7(1):8623–34.
235. Huggins C, Pearce S, Peri F, Neumann F, Cockerill G, Pirianov G. A novel small molecule TLR4 antagonist (IAXO-102) negatively regulates non-hematopoietic toll like receptor 4 signalling and inhibits aortic aneurysms development. Atherosclerosis. 2015;242(2): 563–70.
236. Koymans KJ, Feitsma LJ, Brondijk THC, Aerts PC, Lukkien E, Lössl P, van Kessel KP, de Haas CJ, van Strijp JA, Huizinga EG. Structural basis for inhibition of TLR2 by staphylococcal superantigen-like protein 3 (SSL3). Proc Natl Acad Sci U S A. 2015;112(35):11018–23.
237. Peri F, Calabrese V. Toll-like receptor 4 (TLR4) modulation by synthetic and natural compounds: an update: miniperspective. J Med Chem. 2013;57(9):3612–22.
238. Chan AC, Carter PJ. Therapeutic antibodies for autoimmunity and inflammation. Nat Rev Immunol. 2010;10(5):301–16.
239. Leturcq DJ, Moriarty AM, Talbott G, Winn RK, Martin TR, Ulevitch RJ. Antibodies against CD14 protect primates from endotoxin-induced shock. J Clin Invest. 1996;98(7):1533–8.
240. Schimke J, Mathison J, Morgiewicz J, Ulevitch RJ. Anti-CD14 mAb treatment provides therapeutic benefit after in vivo exposure to endotoxin. Proc Natl Acad Sci U S A. 1998;95:13875–80.
241. Verbon A, Dekkers PE, ten Hove T, Hack CE, Pribble JP, Turner T, Souza S, Axtelle T, Hoek FJ, van Deventer SJ. IC14, an anti-CD14 antibody, inhibits endotoxin-mediated symptoms and inflammatory responses in humans. J Immunol. 2001;166(5):3599–605.
242. Axtelle T, Pribble J. An overview of clinical studies in healthy subjects and patients with severe sepsis with IC14, a CD14-specific chimeric monoclonal antibody. J Endotoxin Res. 2003;9(6):385–9.
243. Reinhart K, Glück T, Ligtenberg J, Tschaikowsky K, Bruining A, Bakker J, Opal S, Moldawer LL, Axtelle T, Turner T. CD14 receptor occupancy in severe sepsis: results of a phase I clinical trial with a recombinant chimeric CD14 monoclonal antibody (IC14). Crit Care Med. 2004;32(5):1100–8.
244. Lau C, Gunnarsen KS, Høydahl LS, Andersen JT, Berntzen G, Pharo A, Lindstad JK, Ludviksen JK, Brekke O-L, Barratt-Due A. Chimeric anti-CD14 IGG2/4 Hybrid antibodies for therapeutic intervention in pig and human models of inflammation. J Immunol. 2013;191(9): 4769–77.
245. Skjeflo EW, Sagatun C, Dybwik K, Aam S, Urving SH, Nunn MA, Fure H, Lau C, Brekke O-L, Huber-Lang M. Combined inhibition of complement and CD14 improved outcome in porcine polymicrobial sepsis. Crit Care. 2015;19(1):415–22.
246. Gustavsen A, Nymo S, Landsem A, Christiansen D, Ryan L, Husebye H, Lau C, Pischke SE, Lambris JD, Espevik T. Combined inhibition of complement and CD14 attenuates bacteria-induced inflammation in human whole blood more efficiently than antagonizing the Toll-like receptor 4–MD2 complex. J Infect Dis. 2016;214(1): 140–50.
247. Kim HM, Park BS, Kim J-I, Kim SE, Lee J, Oh SC, Enkhbayar P, Matsushima N, Lee H, Yoo OJ. Crystal structure of the TLR4-MD-2 complex with bound endotoxin antagonist Eritoran. Cell. 2007;130(5):906–17.
248. Rossignol DP, Lynn M. Antagonism of in vivo and ex vivo response to endotoxin by E5564, a synthetic lipid A analogue. J Endotoxin Res. 2002;8(6):483–8.
249. Mullarkey M, Rose JR, Bristol J, Kawata T, Kimura A, Kobayashi S, Przetak M, Chow J, Gusovsky F, Christ WJ. Inhibition of endotoxin response by e5564, a novel Toll-like receptor 4-directed endotoxin antagonist. J Pharmacol Exp Ther. 2003;304(3):1093–102.
250. Opal SM, Laterre P-F, Francois B, LaRosa SP, Angus DC, Mira J-P, Wittebole X, Dugernier T, Perrotin D, Tidswell M. Effect of eritoran, an antagonist of MD2-TLR4, on mortality in patients with severe sepsis: the ACCESS randomized trial. JAMA. 2013;309(11):1154–62.
251. Park S, Shin H-J, Shah M, Cho H-Y, Anwar MA, Achek A, Kwon H-K, Lee B, Yoo TH, Choi S. TLR4/MD2 specific peptides stalled in vivo LPS-induced immune exacerbation. Biomaterials. 2017;126:49–60.
252. Lysakova-Devine T, Keogh B, Harrington B, Nagpal K, Halle A, Golenbock DT, Monie T, Bowie AG. Viral inhibitory peptide of TLR4, a peptide derived from vaccinia protein A46, specifically inhibits TLR4 by directly targeting MyD88 adaptor-like and TRIF-related adaptor molecule. J Immunol. 2010;185(7):4261–71.
253. Mistry P, Laird MH, Schwarz RS, Greene S, Dyson T, Snyder GA, Xiao TS, Chauhan J, Fletcher S, Toshchakov VY. Inhibition of TLR2 signaling by small molecule inhibitors targeting a pocket within the TLR2 TIR domain. Proc Natl Acad Sci U S A. 2015;112(17):5455–60.
254. McGuire VA, Diez TR-Z, Emmerich CH, Strickson S, Ritorto MS, Sutavani RV, Weiβ A, Houslay KF, Knebel A, Meakin PJ. Dimethyl fumarate blocks pro-inflam-

matory cytokine production via inhibition of TLR induced M1 and K63 ubiquitin chain formation. Sci Rep. 2016;6:31159–76.
255. Chen S, Xiong J, Zhan Y, Liu W, Wang X. Wogonin inhibits LPS-induced inflammatory responses in rat dorsal root ganglion neurons via inhibiting TLR4–MyD88–TAK1-mediated NF-κB and MAPK signaling pathway. Cell Mol Neurobiol. 2015;35(4):523–31.
256. Zhong Z, Liu L-J, Dong Z-Q, Lu L, Wang M, Leung C-H, Ma D-L, Wang Y. Structure-based discovery of an immunomodulatory inhibitor of TLR1–TLR2 heterodimerization from a natural product-like database. Chem Commun. 2015;51(56):11178–81.
257. Matsunaga N, Tsuchimori N, Matsumoto T, Ii M. TAK-242 (resatorvid), a small-molecule inhibitor of Toll-like receptor (TLR) 4 signaling, binds selectively to TLR4 and interferes with interactions between TLR4 and its adaptor molecules. Mol Pharmacol. 2011;79(1):34–41.
258. Takashima K, Matsunaga N, Yoshimatsu M, Hazeki K, Kaisho T, Uekata M, Hazeki O, Akira S, Iizawa Y, Ii M. Analysis of binding site for the novel small-molecule TLR4 signal transduction inhibitor TAK-242 and its therapeutic effect on mouse sepsis model. Br J Pharmacol. 2009;157(7):1250–62.
259. Sha T, Sunamoto M, Kitazaki T, Sato J, Ii M, Iizawa Y. Therapeutic effects of TAK-242, a novel selective Toll-like receptor 4 signal transduction inhibitor, in mouse endotoxin shock model. Eur J Pharmacol. 2007;571(2-3):231–9.
260. Fenhammar J, Rundgren M, Hultenby K, Forestier J, Taavo M, Kenne E, Weitzberg E, Eriksson S, Ozenci V, Wernerson A. Renal effects of treatment with a TLR4 inhibitor in conscious septic sheep. Crit Care. 2014;18(5):488–500.
261. Zhang D, Li H, Li T, Zhou M, Hao S, Yan H, Yu Z, Li W, Li K, Hang C. TLR4 inhibitor resatorvid provides neuroprotection in experimental traumatic brain injury: implication in the treatment of human brain injury. Neurochem Int. 2014;75:11–8.
262. Nakano Y, Shimazawa M, Ojino K, Izawa H, Takeuchi H, Inoue Y, Tsuruma K, Hara H. Toll-like receptor 4 inhibitor protects against retinal ganglion cell damage induced by optic nerve crush in mice. J Pharmacol Sci. 2017;133(3):176–83.
263. Hennessy EJ, Parker AE, O'Neill LAJ. Targeting Toll-like receptors: emerging theraputics? Nat Rev Drug Discov. 2010;9:293–307.
264. Shlosberg D, Benifla M, Kaufer D, Friedman A. Blood–brain barrier breakdown as a therapeutic target in traumatic brain injury. Nat Rev Neurol. 2010;6(7):393–403.
265. Kozai TDY, Vazquez AL, Weaver CL, Kim S-G, Cui XT. In vivo two-photon microscopy reveals immediate microglial reaction to implantation of microelectrode through extension of processes. J Neural Eng. 2012;9(6):066001.
266. Goss-Varley M, Dona KR, McMahon JA, Shoffstall AJ, Ereifej ES, Lindner SC, Capadona JR. Microelectrode implantation in motor cortex causes fine motor deficit: Implications on potential considerations to brain computer interfacing and human augmentation. Sci Rep. 2017;7:15254–65.
267. Jorfi M, Skousen JL, Weder C, Capadona JR. Progress towards biocompatible intracortical microelectrodes for neural interfacing applications. J Neural Eng. 2015;12(1):011001.
268. Potter-Baker KA, Ravikumar M, Burke AA, Meador WD, Householder KT, Buck AC, Sunil S, Stewart WG, Anna JP, Tomaszewski WH, Capadona JR. A comparison of neuroinflammation to implanted microelectrodes in rat and mouse models. Biomaterials. 2014;34:5637–46.